Numerical and Experimental Study of Rock Fracture Creep Under Dry Conditions

by

Hao Kang

B.Eng. Civil Engineering
The University of Hong Kong, 2014

S.M. Civil and Environmental Engineering
Massachusetts Institute of Technology, 2015

SUBMITTED TO THE DEPARTMENT OF CIVIL AND ENVIRONMENTAL ENGINEERING IN PARTIAL FUFILLMENT OF THE REQUIREMENTS FOR THE DEGREE OF

DOCTOR OF PHILOSOPHY IN CIVIL AND ENVIRONMENTAL ENGINEERING

AT THE

MASSACHUSETTS INSTITUTE OF TECHNOLOGY

June 2021

Signature of Author .....
Department of Civil and Environmental Engineering
May 13, 2021

Certified by .....
Herbert Einstein
Professor of Civil and Environmental Engineering
Thesis Supervisor

Accepted by .....
Colette L. Heald
Professor of Civil and Environmental Engineering
Chair, Graduate Program Committee

Numerical and Experimental Study of Rock Fracture Creep Under Dry Conditions

by

Hao Kang

Submitted to the Department of Civil and Environmental Engineering
on May 13th 2021, in partial fulfillment of the
requirements for the degree of
Doctor of Philosophy in Civil and Environmental Engineering

Abstract

In many rock engineering projects such as hydrocarbon extraction or geothermal energy utilization, the hydro-mechanical behavior of rock fractures has a strong effect on the safety and profitability of the project. In field conditions, the hydraulic and mechanical behavior of rock fractures changes with time (the rock fractures creep). Rock fracture creep is a coupled process of four mechanisms: mechanical compression, pressure solution, dissolution, and erosion. To obtain systematic results, it is important to consider these mechanisms separately. Previous research indicates that rock fracture creep under dry conditions is not negligible, and under dry conditions, mechanical compression is the only mechanism.

Experimental work has been conducted to investigate the size and time dependency of the creep of Musandam limestone (a reservoir rock). The elastic and strength properties of Musandam limestone were obtained from triaxial and indentation tests. The results indicate that linear elasticity and von Mises plasticity can reasonably well describe the contacting asperity deformation. Then, triaxial, micro- and nano-indentation creep tests were conducted, and their creep patterns were compared. The results imply that the creep patterns of triaxial and indentation tests are different. In addition, micro- and nano-indentation test results show a time-hardening and a time-softening behavior, respectively. The experimental results can provide a reference for rock creep measurements and modeling.

To study the effect of surface geometry on fracture dry creep, initial steps considering visco-elasticity have been taken. A numerical model was developed to investigate the effect of surface geometry on rock fracture visco-elastic deformation. First, synthetic fracture surfaces were generated based on Brown's (1995) model: the Hurst exponent, root mean square roughness, and mismatch length were varied systematically. Then, an in-house numerical code was developed to simulate the visco-elastic deformation of rough fractures. The results indicate that by increasing the Hurst exponent or decreasing the mismatch length or decreasing the root mean square roughness, the fracture mean aperture decreases, and the contact ratio (the number of contacting cells / total number of cells) increases faster with time. The numerical results can be used to predict visco-elastic deformation of rough rock fractures.

Thesis Supervisor: Herbert H. Einstein
Title: Professor of Civil and Environmental Engineering

Acknowledgements

This thesis would not have been possible without the support and help from some important people.

First, I would like to express my utmost and sincerest gratitude to Prof. Herbert Einstein, for his support, guidance, and enthusiasm for this work. It has been a great honor and pleasure working with him. His knowledge from a wide range of backgrounds and critical insights helped me overcome a lot of challenges in my research. He never imposes anything on me – instead, he encourages me to think out of the box and try different ideas. He is always supportive in my research, job-hunting, and personal life.

I would also like to express my gratitude to Prof. John Germaine. His crucial advice and hands-on expertise in geotechnical experiments greatly helped me. The early Monday group meetings with Prof. Germaine have been extremely productive and insightful. He also gave me a lot of useful suggestions related to my career plan and personal life.

I must thank my committee members: Dr. Stephen Brown, Prof. John Williams, and Prof. Brian Evans. I would like to thank Dr. Brown for his creative ideas in rough surface generation and elastic deformation simulation of rough surfaces. I would like to thank Prof. John Williams for his critical and insightful questions in numerical simulation. I would like to thank Prof. Brian Evans for his crucial suggestions in triaxial and indentation creep data interpretation and fracture-scale creep simulation. In addition, I would like to thank Prof. Andrew Whittle for teaching me soil mechanics, soil behavior, and geotechnical engineering. I learned a lot from his expertise.

I must thank Stephen Rudolph for his generous support in my experimental design and testing. Whenever I had a question or made a mistake, he was always there to help. He has spent a lot of hours teaching me experimental skills and machining the metal pieces for me. I must also thank Dr. Uli Mok for his generous help in NER and Paterson triaxial tests, and Dr. Asheesh Shukla for his help in nano-indentation tests. My thanks also go out to Carolyn Jundzilo-Comer for her administrative support and cookies. I cannot forget to give my gratitude to Jeanette Marchocki, Kiley Clapper, Sarah Smith, and Max Martelli for their administrative support.

My friends at MIT have been a great support to me. In particular, I would like to thank my colleagues in geotechnical engineering, including by not limited to Stephen Morgan, Bruno Goncalves da Silva, Wei Li, Bing Qiuyi Li, Omar Al-Dajani, Hejian ‘Patrick’ Zhu, Ignacio Arzuaga, Yixing Yuan, Rafael Villamor Lora, Chunwei Ge, Mariana Rodriguez, Ivo Montenegro, Zhandos Orazalin, Majed Almubarak, Randy Pietersen, Paris Smalls, Michael Martello, Mauro Sottile, Xin Zhang, Hao Wang, Dohyun Kim, Arabelle de Saussure, Mohamad Zaarour, Irina Seidler, and Michela Casanova. I would also acknowledge my friends at MIT ERL, including but not limited to Haitao Shang, Yu Qiu, Yue Meng, Ke Xu, Hua Wang, Wenlian Xiao, and Tiange Xing,

Finally, it is important to thank my family: Changsheng (father) and Weihong (mother), for their love and support. I would also thank my dearest wife, Wenqing Jiang, for her love and support. Wenqing, wo ai ni (I love you)!

Contents

List of Figures

List of Tables

1. Introduction

In many rock engineering projects, the hydraulic and mechanical behavior of rock fractures has a strong effect on the safety and profitability of the project. Specifically, extracting geothermal energy or extracting hydrocarbons require natural rock fractures to remain open or artificial fractures to be created. In contrast, in CO_2 sequestration, to prevent CO_2 leakage through naturally or artificially induced fractures in the caprock, the fractures in the caprock should remain closed. In field conditions, under constant tectonic stress, rock fractures may deform with time. In other words, rock fractures may creep, and rock fracture creep may affect the hydraulic and mechanical behavior of rock fractures. Therefore, rock fracture creep has been studied extensively both experimentally and theoretically.

Rock fracture creep is a coupled process of four mechanisms: mechanical compression, pressure solution, dissolution, and erosion. Kang et al. (2019) reported that for Musandam limestone fractures, the creep deformation under dry conditions is not negligible. Under dry conditions, mechanical compression is the primary creep mechanism suggesting that it should be systematically studied. However, there is not much work systematically studying the creep caused by mechanical compression. Therefore, rock fracture creep caused by mechanical compression should be investigated both with numerical models and experiments.

1.1 Research objective

To systematically investigate the effect of mechanical compression on rock fracture creep, the following two tasks need to be accomplished: (1): understand the creep behavior of rock at the scale of contacting asperities in the fracture; (2) build numerical models to simulate the creep behavior caused by mechanical compression at the fracture scale. To accomplish these two tasks, an experimental component and a numerical component are proposed in this research.

The experimental component intends to understand the effect of time and scale on rock creep behavior. The experimental research is done on Musandam Limestone, the reservoir formation underlying Abu Dhabi, which is of primary interest to the sponsor of this research, ADNOC. The elastic and strength properties of Musandam limestone are obtained from triaxial and indentation tests. It is essential to understand rock creep behavior at the scale of contacting asperities because the creep of contacting asperities dominates the fracture-scale creep. According to Dieterich and Kilgore (1994), the scale of contacting asperities is generally between 100 nm and 100 μm. To cover the scale range, triaxial creep tests, micro-indentation tests, and nano-indentation tests need to be conducted. The creep patterns from triaxial, micro-indentation, and nano-indentation tests are compared. In addition, to study the effect of time duration on rock creep behavior, micro- and nano-indentation tests at different time durations (3-min and 6-hr) are conducted. The experimental results can provide a reference for rock creep modeling.

The numerical modeling component intends to simulate fracture-scale creep caused by mechanical compression. Fracture mechanical creep consists of two components: visco-elastic deformation and visco-elasto-plastic deformation. In this numerical study, initial steps are taken by simulating the visco-elastic deformation of rough fractures. Previous experiments suggest that the fracture surface geometry has a dominant effect on fracture deformation (Iwano and Einstein, 1995; Brown, 1998; Watanabe et al., 2008; Kang et al., 2019). Therefore, the effect of surface geometry on fracture visco-elastic deformation should be systematically investigated. Synthetic fracture

surfaces are generated based on Brown's (1995) model. In this model, a rock fracture surface can be completely described by three parameters: the Hurst exponent, the mismatch length, and the root mean square roughness. The three parameters are varied systematically to investigate the effect of surface geometry on fracture visco-elastic deformation. The numerical simulation results are compared with experimental results to demonstrate the significance of visco-elastic deformation.

In short, this research aims at understanding the effect of size and time duration on Musandam limestone creep behavior, and at understanding the effect of surface geometry on visco-elastic deformation of rough fractures. These have not been investigated systematically before and are, therefore, the major contribution of this research.

1.2 Thesis structure

This thesis is organized as follows:

Chapter 2 provides the reader with background information on 1) rock creep at different scales, including triaxial creep, micro-indentation creep, and nano-indentation creep, 2) common visco-elastic and visco-elasto-plastic creep models, 3) rock fracture characterization methods, 4) mechanisms of rock fracture creep, 5) the current state of elasto-plastic and visco-elastic deformation simulation of rough fractures in tribology and rock mechanics.

Chapter 3 describes the methodology of the numerical simulation. The ABAQUS simulation methods for micro-indentation and a limited number of contacting asperities (not more than five) are introduced. The methods for simulating the elastic and visco-elastic deformation of rough fractures are described in detail. The numerical results are validated against analytical results for specific surface geometry, and the limitations of the rough fracture deformation simulation methods are briefly discussed. In addition, the method for synthetic fracture surface generation is presented.

Chapter 4 summarizes and discusses the numerical simulation results. The generated synthetic fracture surfaces with different surface geometrical parameters are compared. The visco-elastic deformations of rough fracture surfaces with different geometries are compared. The physical meaning of the creep curves (creep deformation vs. time curves) and the factors affecting the shape and magnitude of the creep curves are also discussed.

Chapter 5 documents the experimental setup and methodology. The geology of the rock used in this research, Musandam limestone, is characterized in detail. The equipment and experimental processes of the fracture creep tests and intact rock creep tests are shown. Then, the experimental processes and data analysis methods for micro- and nano-indentation tests are described. The methods for SEM and SEM-EDS tests are also briefly introduced.

Chapter 6 summarizes and discusses the experimental results. The mineralogy, dissolution properties, and mechanical properties (including the elastic and strength properties) of Musandam limestone are characterized in detail. The fracture creep test results are presented to illustrate the significance of fracture creep under dry conditions. Then, the micro- and nano-indentation test results are shown and discussed in detail. The triaxial creep test results are also presented and

discussed. Finally, the creep behavior in triaxial and indentation tests are compared to reveal the scale effect on rock creep behavior.

Chapter 7 compares the numerical simulation results and experimental results of rock fracture creep under dry conditions. The differences between numerical and experimental results are discussed.

Chapter 8 summarizes the results of this research and provides recommendations for future work.

2. Background

This background chapter includes the definition of rock creep and the creep mechanisms of rock fractures, as well as an extensive literature review of the current state of elasto-plastic and creep simulation of rough fractures. A definition of rock creep will be presented in Section 2.1. Then, the creep behavior of rock at micro-indentation and nano-indentation scales will be described in Section 2.2. The characterization methods of rock fractures will be introduced in Section 2.3. This will be followed by a review of the creep mechanisms of rock fractures in Section 2.4. Finally, the chapter finishes with a review of the numerical simulation of the deformation of rough fractures subjected to normal compressive stress, in both rock mechanics and tribology, in Sections 2.5 and 2.6.

2.1 Definition and a brief introduction of rock creep

In this section, rock creep will be defined. Then, common curve-fitting and rheological models for creep will be described. In this section, only the creep of intact rock will be discussed; the creep of rock with fractures will be discussed later in Sections 2.4 and 2.6.

2.1.1 Definition of rock creep

In rock engineering, there are many situations in which the time-dependent behavior of rock must be considered, such as predicting the long-term deformation of pillars in salt mines and the long-term behavior of hydrocarbon reservoirs (Cook et al., 2006; Zoback and Kohli, 2019). Therefore, the time-dependent behavior of rock has been studied extensively both experimentally and theoretically. Before conducting a comprehensive literature review, it is important to define the rock time-dependent behavior, or rock creep. Rock creep is defined as the time-dependent deformation of rock under constant compressive stress (Cook et al., 2006; Zoback and Kohli, 2019). At any given compressive stress, the strain continues to increase with time, as the stress is held constant. The creep rate increases with increasing compressive stress.

Figure 2.1 shows the typical creep strain behavior during compression or shearing or tension (Cook et al., 2006; Brantut et al., 2013). As shown in Figure 2.1, the creep of rock has often been described by three sequential regimes: primary creep (decelerating rate), secondary creep (constant rate, or steady-state), and tertiary creep (accelerating rate). At time zero, a uniform stress field is applied to the rock specimen, which immediately gives rise to an elastic strain, as indicated by point A. In the transient creep stage, the specimen continues to deform, but the strain rate decreases with time. Then, in the steady-state creep stage, the strain rate is constant (the strain increases linearly with time). Finally, in the tertiary creep stage, the strain rate increases with time until final failure. The schematic in Figure 2.1 assumes that the applied stress does not exceed the yield strength, and the yield strength is defined as the stress at which the permanent deformation occurs. This implies that the creep deformation is not necessarily equal to the permanent deformation.

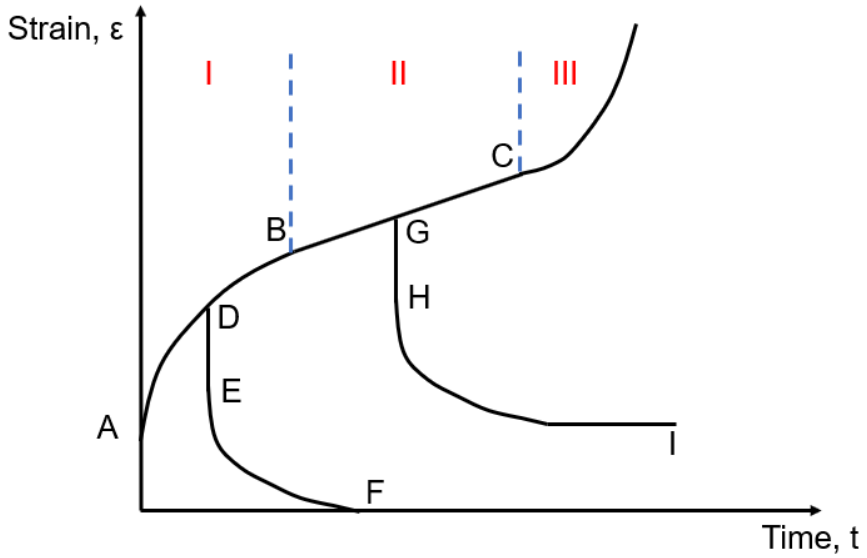

Figure 2.1 Schematic of rock creep at different stages. Region 'I', 'II', and 'III' represent the transient creep stage, steady-state creep stage, and tertiary creep stage, respectively.

Cook et al. (2006) stated that if the applied stress is suddenly reduced to zero in the transient creep stage, the strain will eventually relax back to zero. Curve DEF in Figure 2.1 shows one example strain path. However, if the applied stress is removed during the steady-state creep, the strain will not relax back to zero, and one example strain path is shown in Curve GHI in Figure 2.1.

The above description is a very generalized description, which depends on several different creep mechanisms (Mighani et al., 2019). Some creep mechanisms include micro-crack growth (Brantut et al., 2013; Chester et al., 2007; Heap et al., 2015), pressure solution (Brantut et al., 2012; Geng et al., 2018), and particle rearrangement (Vandamme and Ulm, 2009). The relative magnitudes of creep mechanisms vary for different rock types, different differential stresses (Evans and Dresen, 1991; Kemeny, 1991), different confining stresses (Evans and Kohlstedt, 1995), pore fluid composition (Chester et al., 2007), temperature (Brantut et al., 2013; Geng et al., 2018), and experiment duration. Brantut et al. (2013) stated that small changes in any of these above-mentioned parameters can generate order of magnitude changes in creep strain rates and the time to final failure.

Given that creep behavior is affected by these coupled mechanisms, and that there is still a lot of uncertainty in identifying them, it is challenging to construct accurate mechanical models to simulate creep behavior. As a result, many phenomenological models have been proposed to describe creep behavior. In this section, two types of phenomenological models will be introduced: curve-fitting models and rheological models. Curve-fitting models provide mathematical equations that best fit the laboratory measurements, while rheological models conceptualize the laboratory measurements as a combination of mechanistic elements, such as springs and dashpots.

2.1.2 Simple curve-fitting models

Some researchers have proposed curve-fitting models to match the results from laboratory creep tests. The curve-fitting models for different creep stages (shown in Figure 2.1) will be introduced here.

For the transient creep, the creep strain can be expressed as:

$$\varepsilon(t) = At^n,\ 0 < n < 1 \qquad \text{(Cottrell, 1952)} \qquad (2.1)$$

$$\varepsilon(t) = A\ ln\ t\ + at + b \qquad \text{(Griggs, 1939)} \qquad (2.2)$$

$$\varepsilon(t) = A\ ln\ (1 + at) \qquad \text{(Lomnitz, 1956)} \qquad (2.3)$$

$$\varepsilon(t) = A[(1 + at)^n - 1] \qquad \text{(Jeffreys, 1958)} \qquad (2.4)$$

where *A*, *n*, *a*, and *b* are empirically fitted parameters, t is the time, and ε is the creep strain. These models can provide a reasonably good fit for the strain data over limited periods of time. However, they may not be able to fit the strain data accurately at very small or large values of t. For example, at very small t, Eqns. 2.1 and 2.2 predict infinite large strain rate. For Eqn. 2.1, when t → 0, the strain rate $\dot{\varepsilon} = nAt^{n-1}$; since 0 < n < 1, t^{n-1} becomes infinite (t^{n-1} equals to one divided by a very small number). For Eqn. 2.2, when t → 0, the strain rate $\dot{\varepsilon} = \frac{A}{t}$, and $\frac{1}{t}$ becomes infinite.

For the steady-state creep, the creep strain rate can be expressed as:

$$\dot{\varepsilon} = \dot{\varepsilon_0}\ exp\ (\sigma/\sigma_0) \qquad \text{(Ludwik, 1909)} \qquad (2.5)$$

$$\dot{\varepsilon} = \dot{\varepsilon_0}(\sigma/\sigma_0)^n \qquad \text{(Robertson, 1964)} \qquad (2.6)$$

where $\dot{\varepsilon_0}$ is the reference strain rate, n is the empirically fitted parameter (dimensionless), and σ_0 is the reference differential stress. Robertson (1964) collected data from a wide range of rocks and concluded that n ranges from 1 to 8. Eqns. 2.5 and 2.6 suggest that when $\dot{\varepsilon_0}$ and σ_0 are constant, the steady-state creep rate $\dot{\varepsilon}$ increases with increasing differential stress σ.

For the tertiary creep, it appears that there is no curve-fitting model that only focuses on tertiary creep. However, some rheological models consider the tertiary stage.

It is worth noting that the above-mentioned models were obtained from laboratory results of uniaxial compression and triaxial compression tests. In these tests, the stress distributions were uniform, and the specimen geometries were either cylindrical or cuboid. However, in rock engineering, there exist more general problems with different boundary conditions and geometries. For example, in problems concerning time-dependent deformation of rock fractures, the fracture surface geometry is not cylindrical or cuboid, and the contacting stress distribution is not uniform. Therefore, it is necessary to have stress-strain relations which hold for all types of boundary conditions and geometries. To solve this problem, rheological models have been proposed.

2.1.3 Simple rheological models

The term 'rheology' originates from Greek, meaning the study of flow. Rheological models assume that the time-dependent stress-strain behavior of materials is caused by material's viscosity. Simple rheological models can be constructed by a combination of three simple mechanistic elements: spring, dashpot, and the Saint Venant element. In this section, the three mechanistic elements will be introduced first, followed by four simple rheological models.

2.1.3.1 Simple mechanistic elements

In this section, the mechanistic elements discussed in detail by Bland (1960) are used. The simple mechanistic elements The first mechanistic element is the spring element. As shown in Figure 2.2, the spring element represents an elastic Hookean material in which the stress and strain are related by Hooke's law:

$$\sigma = k\varepsilon \tag{2.7}$$

where k is the spring stiffness (it can be either elastic or shear modulus. They can be mathematically related to each other), σ is the stress, and ε is the strain. This element describes the instantaneous elastic response of rock materials and does not have any time-dependency.

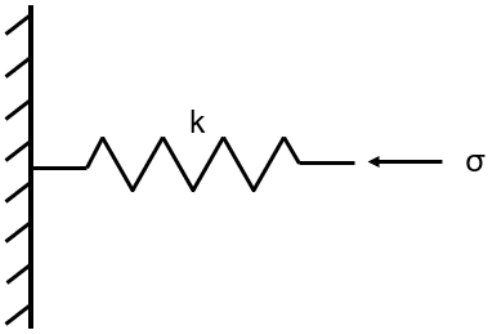

Figure 2.2 Schematic of the spring element.

The second mechanistic element is the viscous dashpot element, which is also called the Newtonian element. It represents a Newtonian viscous material that follows the stress-strain law:

$$\sigma = \eta \frac{d\varepsilon}{dt} \tag{2.8}$$

where η is the viscosity constant with units of [Pressure * Time], σ is the stress, and ε is the strain. Figure 2.3 shows the dashpot element. Since Eqn. 2.8 includes time dimensions, the dashpot element is an essential part of rheological models. If an instantaneous stress σ_0 is applied to this element, starting from a stress-free and strain-free state, Eqn. 2.8 can be integrated to obtain the strain ε changing with time t:

$$\varepsilon = \frac{\sigma_0 t}{\eta} \tag{2.9}$$

Eqn. 2.9 indicates that under constant stress, the strain will increase linearly with time and has no upper bound.

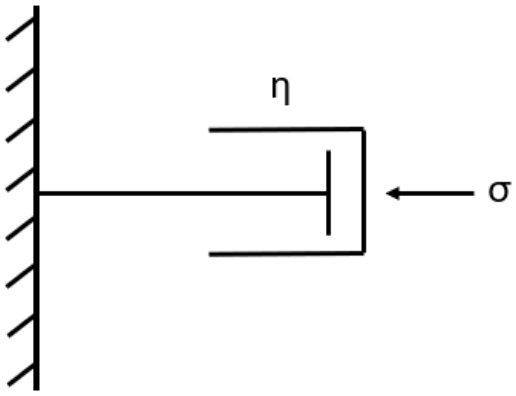

Figure 2.3 Schematic of the dashpot element.

The third mechanistic element is the Saint Venant element, and its schematic is shown in Figure 2.4. This element can be represented by a block of mass sliding on a surface, with a frictional resistance of σ_{pl}. If the applied stress σ is less than σ_{pl}, the block of mass will not move, and the strain ε will be zero; if the applied stress σ is larger than σ_{pl}, the block of mass will move, but the strain ε will be indeterminate. Mathematically, the deformation law can be expressed as:

$$\sigma = \sigma, \varepsilon = 0, if\ \sigma < \sigma_{pl} \tag{2.10}$$

$$\sigma = \sigma_{pl}, \varepsilon\ indeterminate, if\ \sigma \geq \sigma_{pl} \tag{2.11}$$

If only the Saint Venant element is used, when σ is larger than σ_{pl}, the strain is indeterminate. However, to describe the rheological behavior of rock, at any given compressive stresses, the strain value needs to be determinate. Therefore, the Saint Venant element is always combined with other elements, and this will be explained in Section 2.1.3.2.

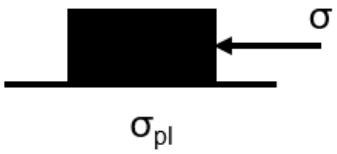

Figure 2.4 Schematic of the Saint Venant element.

2.1.3.2 Simple rheological models

In this section, four simple rheological models will be introduced; the Maxwell model, the Standard Linear Solid (SLS) model, the Burger model, and the Bingham model. The information

for the Maxwell, SLS, and Burger model is from Johnson (1985), and for the Bingham-Maxwell model is from Bland (1960).

The Maxwell model consists of a spring and a dashpot in series. The spring represents elasticity, with a shear modulus of G; and the dashpot represents viscosity, with a viscosity of η (unit: time * pressure). Shear modulus is defined as the ratio of an applied shear stress to a corresponding shear strain. Figures 2.5 (a) and (b) shows the schematic of shear modulus and the Maxwell model, respectively. Under constant stress σ_0, the strain ε(t) can be expressed as:

$$\varepsilon(t) = \sigma_0\left(\frac{1}{G} + \frac{t}{\eta}\right) \tag{2.12}$$

Eqn. 2.12 implies that when σ_0 is applied, instantaneous strain σ_0/G will occur due to elasticity. Then, the strain will increase linearly with time, at a rate of σ_0/η.

(a):

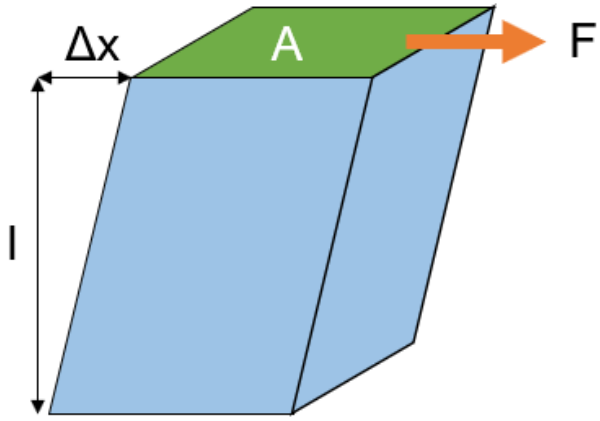

(b):

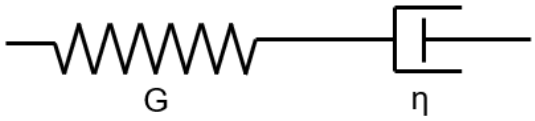

Figure 2.5 Schematic of shear modulus and the Maxwell model. (a): Schematic of shear modulus. F is the applied shear force, and A is the area on which F is acting, Δx is the shear displacement, and l is the initial length. By definition, $G = \frac{Fl}{A\Delta x}$; (b): Schematic of the Maxwell model.

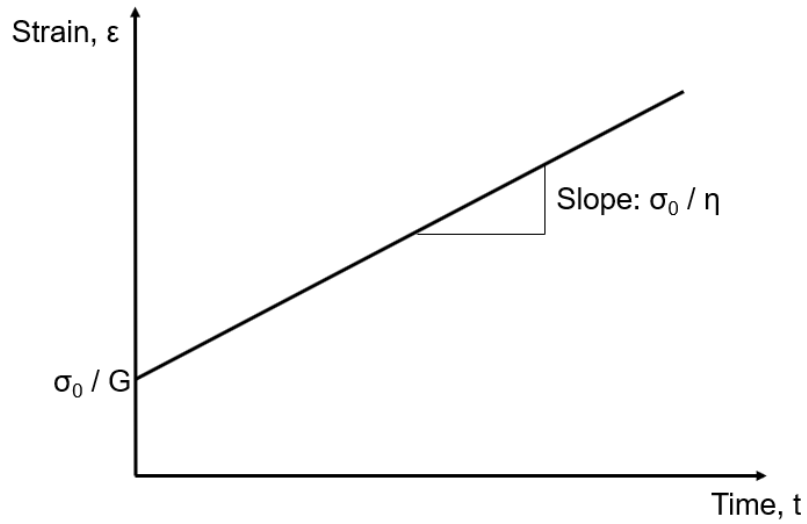

Figure 2.6 Strain changing with time for the Maxwell model.

Before introducing the SLS model, the Kelvin element needs to be defined. The Kelvin element is defined as a spring joining in parallel with a dashpot, illustrated by the right part of Figure 2.7. As shown in Figure 2.7, the SLS model consists of a spring and a Kelvin element in series. The Kelvin element has a shear modulus of G_2, and a viscosity of η; and the spring has a shear modulus of G_1. If a constant stress σ_0 is applied to the SLS model, σ_0 can be expressed by the strain ε(t) as:

$$\sigma_0 = \frac{G_1 G_2}{G_1+G_2}\varepsilon(t) + \frac{G_1 \eta}{G_1+G_2}\frac{d\varepsilon(t)}{dt} \tag{2.13}$$

The strain ε(t) can be obtained by integrating Eqn. 2.13:

$$\varepsilon(t) = \sigma_0\left(\frac{1}{G_1} + \frac{1-e^{-\frac{tG_2}{\eta}}}{G_2}\right) \tag{2.14}$$

Eqn. 2.14 implies that when σ_0 is applied, instantaneous strain σ_0/G_1 will occur due to elasticity. Then, the strain will increase with time with a decreasing strain rate. When $t \to \infty$, $e^{-\frac{tG_2}{\eta}} \to 0$, so the strain $\varepsilon(t) \to (\sigma_0/G_1 + \sigma_0/G_2)$. In addition, as $t \to \infty$, the strain rate will become zero, which means that as time increases, the material will eventually stop creeping. Figure 2.8 shows the strain changing with time for the SLS model. For materials showing a time-decaying creep rate, the SLS model can be used to describe the creep behavior.

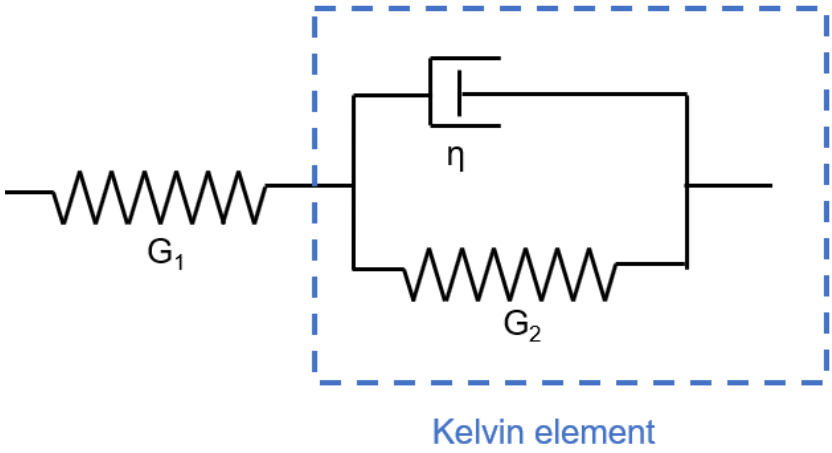

Figure 2.7. Schematic of the SLS model.

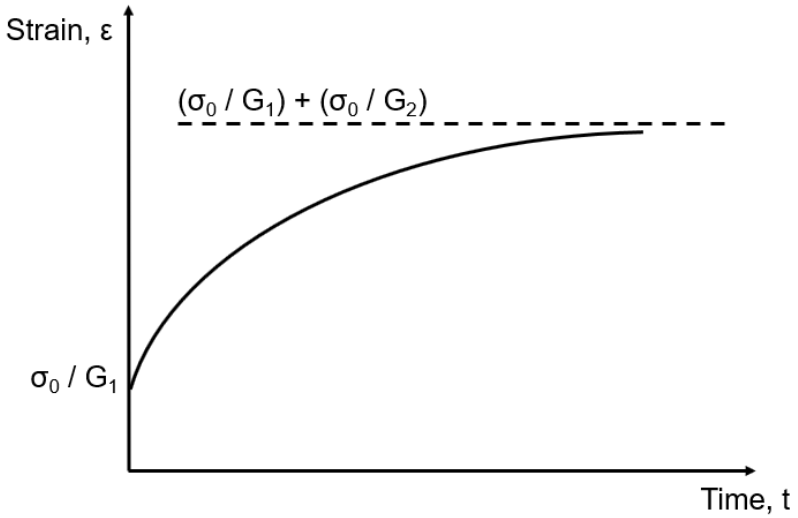

Figure 2.8. Strain changing with time for the SLS model.

The Burger model consists of a spring, a dashpot, and a Kelvin element in series, as shown in Figure 2.9. The Kelvin element in the right has a shear modulus of G_2 and a viscosity of η_2; the spring in the left has a shear modulus of G_1; and the dashpot in the middle has a viscosity of η_1. Under constant stress σ_0, the strain $\varepsilon(t)$ can be related to σ_0 as:

$$\varepsilon(t) = \sigma_0\left(\frac{1}{G_1} + \frac{1-e^{-\frac{tG_2}{\eta_2}}}{G_2} + \frac{t}{\eta_1}\right) \tag{2.15}$$

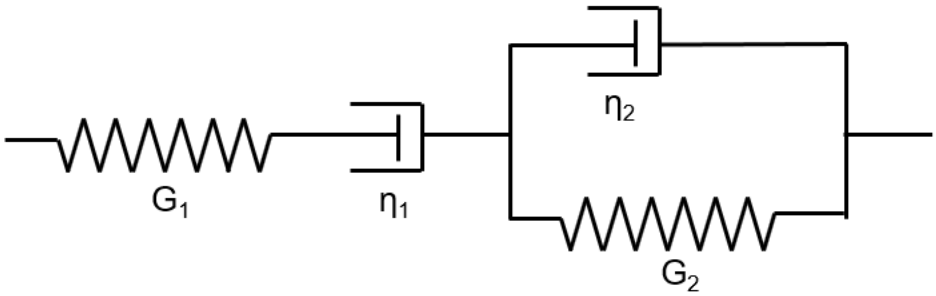

Figure 2.9 Schematic of the Burger model.

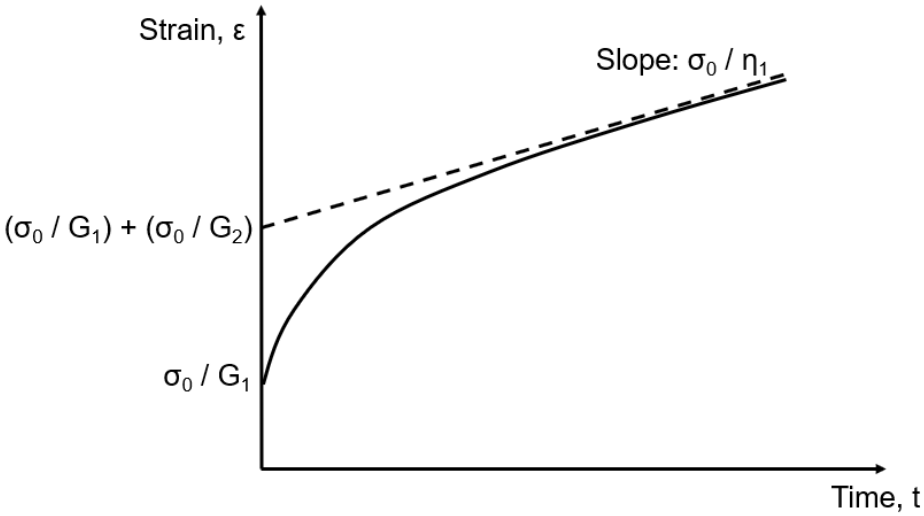

Figure 2.10. Strain changing with time for the Burger model

Figure 2.10 shows the schematic of strain changing with time for the Burger model. When σ_0 is applied, instantaneous strain σ_0/G_1 will occur due to elasticity. Then, the strain will increase with time but the strain rate will decrease. When $t \rightarrow \infty$, the strain rate will asymptotically reach the value of σ_0/G_1, which is the slope of the dashed line. Physically, the Burger model can be used to define two creep stages in rock defined in Section 2.1.1: the initial creep stage and secondary creep stage. From Figure 2.10, initially, the creep rate decreases with time, which corresponds to the initial creep stage; later the creep rate asymptotically reaches a constant value of σ_0/G_1 (the slope of the dashed line), which corresponds to the secondary creep stage.

The Bingham-Maxwell model consists of a spring and a joint element in series, where the joint element consists of a dashpot and a Saint Venant element in parallel. Figure 2.11 shows the schematic of the model. The spring represents elasticity, with a shear modulus of G; the dashpot represents viscosity, with a viscosity of η_1; the Saint Venant element represents plasticity, with a yield strength of σ_{pl}.

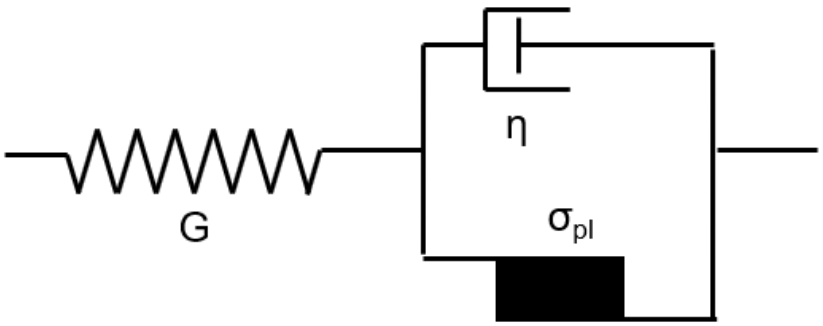

Figure 2.11 Schematic of the Bingham-Maxwell model.

Mathematically, under constant stress σ_0, the strain can be expressed as:

$$\varepsilon(t) = \frac{\sigma_0}{G},\ \sigma_0 < \sigma_{pl} \tag{2.16}$$

$$\varepsilon(t) = \frac{\sigma_0}{G} + \frac{\sigma_0 - \sigma_{pl}}{\eta} t,\ \sigma_0 \geq \sigma_{pl} \tag{2.17}$$

Eqns. 2.16 and 2.17 imply that when the stress is less than the yield strength, no creep strain will occur (the elastic strain will be $\frac{\sigma_0}{G}$ and will not change with time). When the stress exceeds the yield strength σ_{pl}, the Saint Venant element will take the stress σ_{pl}, and the stress transmitted to the dashpot will be (σ_0 - σ_{pl}) due to stress balance. Therefore, the creep strain will increase with time at a constant rate $\frac{\sigma_0 - \sigma_{pl}}{\eta}$. Figure 2.12 shows the creep strain changing with time for the Bingham-Maxwell model when $\sigma_0 > \sigma_{pl}$, and the slope corresponds to the creep rate.

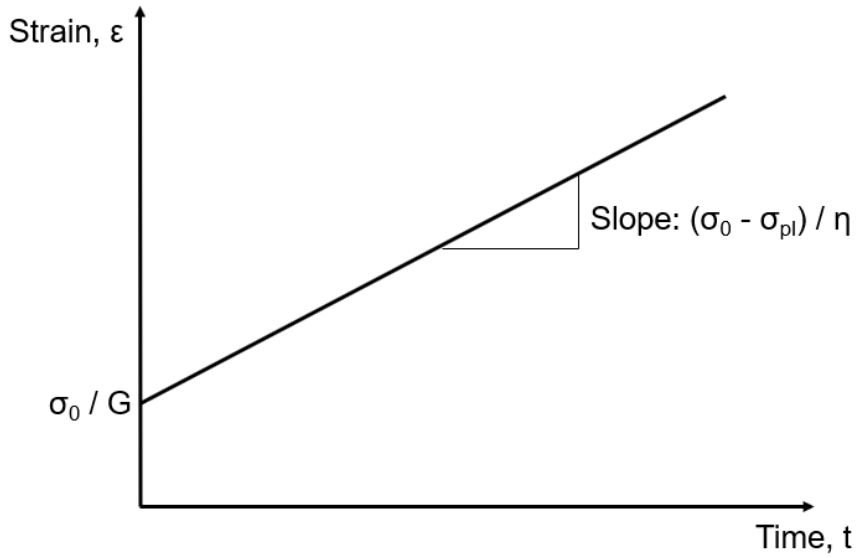

Figure 2.12 Strain changing with time for the Bingham-Maxwell model when σ0 > σpl. When σ_0 < σ_{pl}, no creep will occur (the strain will be $\frac{\sigma_0}{G}$ and will not change with time).

The four above-mentioned rheological models are often used to describe the uniaxial compression creep behavior or triaxial creep behavior.

2.2 Rock creep at different scales – triaxial, micro-indentation, and nano-indentation

In Section 2.1, the creep behavior of rock and common rheological models for rock creep were explained. In this section, rock creep at different scales – triaxial creep, micro-indentation creep, and nano-indentation creep will be introduced. The uniaxial compression creep and triaxial compression creep has already been briefly introduced in Figure 2.1 in Section 2.1.1; therefore, this section will mainly focus on micro-indentation creep and nano-indentation creep.

2.2.1 Micro-indentation creep

To study small volumes of material and understand their mechanical properties at a micron scale, indentation tests are used. An indentation test consists of pushing an indenter with known geometry and mechanical properties perpendicularly to a horizontal polished material surface, at a certain loading or displacement rate. Indentation machines are capable of controlling the load acting on the indenter and continuously measuring the indentation penetration depth. Indenters with different tip geometries are used in indentation tests; in this research, a Berkovich indenter will be used. As shown in Figure 2.13, the Berkovich tip is a three-sided pyramid; geometrically, it is equivalent to a cone with a half-angle of 70.32˚. For micro-indentation, the typical indentation load is around 5 N, and the typical indentation depth is around 10 μm (Slim, 2016).

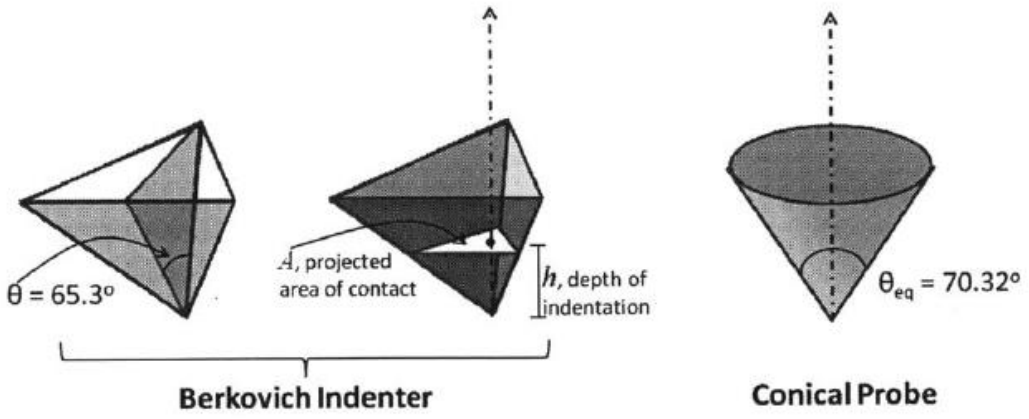

Figure 2.13 Schematic of the Berkovich tip (Brooks, 2013). To simplify analysis, the Berkovich indenter is simplified as a conical probe. A conical probe with a half-angle θ_{eq} of 70.32˚ gives the same projected contact area at a given depth as the Berkovich tip. The projected contact area corresponds to the contact area projected on the horizontal surface.

Figure 2.15 shows that an indentation test typically consists of three chronological stages: loading stage, creep stage (at constant load), and unloading stage. Oliver and Pharr (1992) proposed a methodology to calculate the indentation modulus M and indentation hardness H for the Berkovich indenter.

Before introducing indentation modulus, M, it is essential to introduce a parameter, E_1, which is defined as:

$$E_1 = \beta \frac{S}{2a_u} \tag{2.18}$$

and

$$S = \frac{dP}{d\Delta h}\Big|_{\Delta h = \Delta h_{max}} \tag{2.19}$$

where S is the initial slope of the unloading curve, P is the applied load, Δh is the indentation depth, β is a correction factor (1.05 in this study), and a_u is the radius of the contact area between the indented surface and the indenter at the beginning of unloading (see Figure 2.14). Figure 2.15 shows a typical indentation load versus depth curve and the above-mentioned parameters.

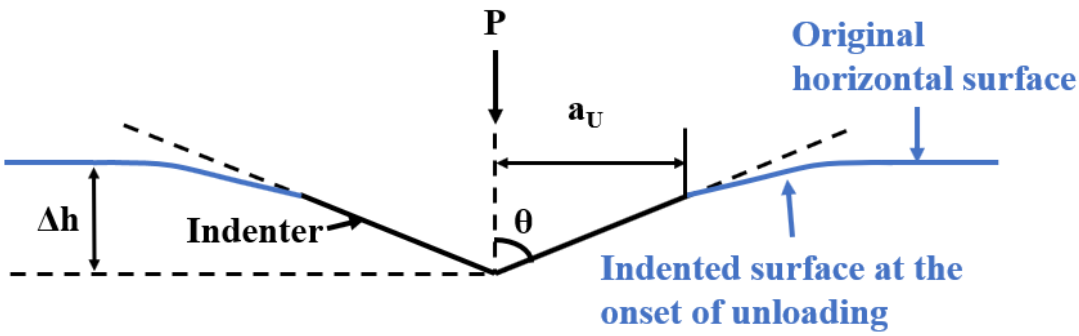

Figure 2.14. Illustration of indenter geometry and a_u. θ is the half-angle of the indenter (70.32˚ for Berkovich indenter).

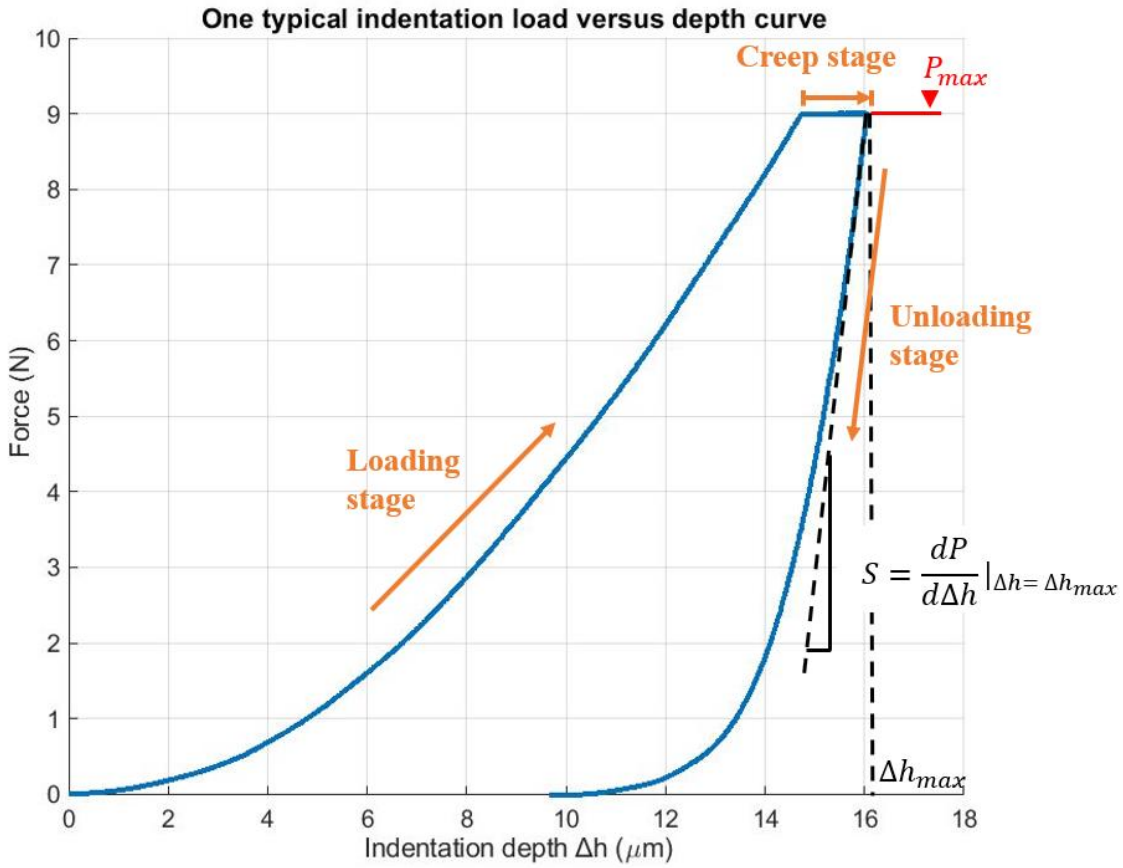

Figure 2.15. Load versus indentation depth curve from a typical indentation test. P_{max} corresponds to the maximum force (load).

If the indented material and the indenter are isotropic, the indentation modulus M can be calculated as:

$$M = \left(\frac{1}{E_1} - \frac{1}{M_{ind}}\right)^{-1} \tag{2.20}$$

where M_{ind} is the indentation modulus of the diamond indenter (1147 GPa) in this study.

The indentation hardness H can also be determined:

$$H = \frac{P_{max}}{\pi a_u^2} \tag{2.21}$$

where P_{max} is the maximum load. Here H is equivalent to the average compressive stress beneath the indenter.

Ulm and Vandamme (2009) proposed another parameter, the indentation creep modulus C, to quantify the material's creep behavior. Under the same indentation load, smaller C values correspond to larger creep deformation. Figure 2.16 shows a typical indentation creep curve (Δh versus t), where Δh is the indentation creep depth, and t is the creep time. The creep curve

corresponds to the creep stage (when the load was constant) shown in Figure 2.15. The indentation creep modulus C can be obtained based on the parameter x_1:

$$C = \frac{P_{max}}{2a_u x_1} \tag{2.22}$$

where x_1 is obtained from Figure 2.16 using curve fitting:

$$\Delta h = x_1 \, ln\,(x_2 t + 1) + x_3 t + x_4 \tag{2.23}$$

where x_1 (unit: length) and x_2 (unit: time^{-1}) are curve fitted parameters characteristic of the tested material. x_3 and x_4 are related to the drifting of the indentation machine and are independent of testing materials. In Figure 2.16, the blue curve corresponds to the measured data, and the red curve corresponds to the fitted curve based on Eq. 2.23. Ulm and Vandamme (2009) stated that for micro-indentation, the machine drifting is much less than the indentation creep depth. Therefore, x_3 and x_4 can be ignored in the analysis. In the curve fitting, Δh and t are measured by indentation tests; while x_1 and x_2 are the unknown parameters. The x_1 and x_2 are fitted by the least square method.

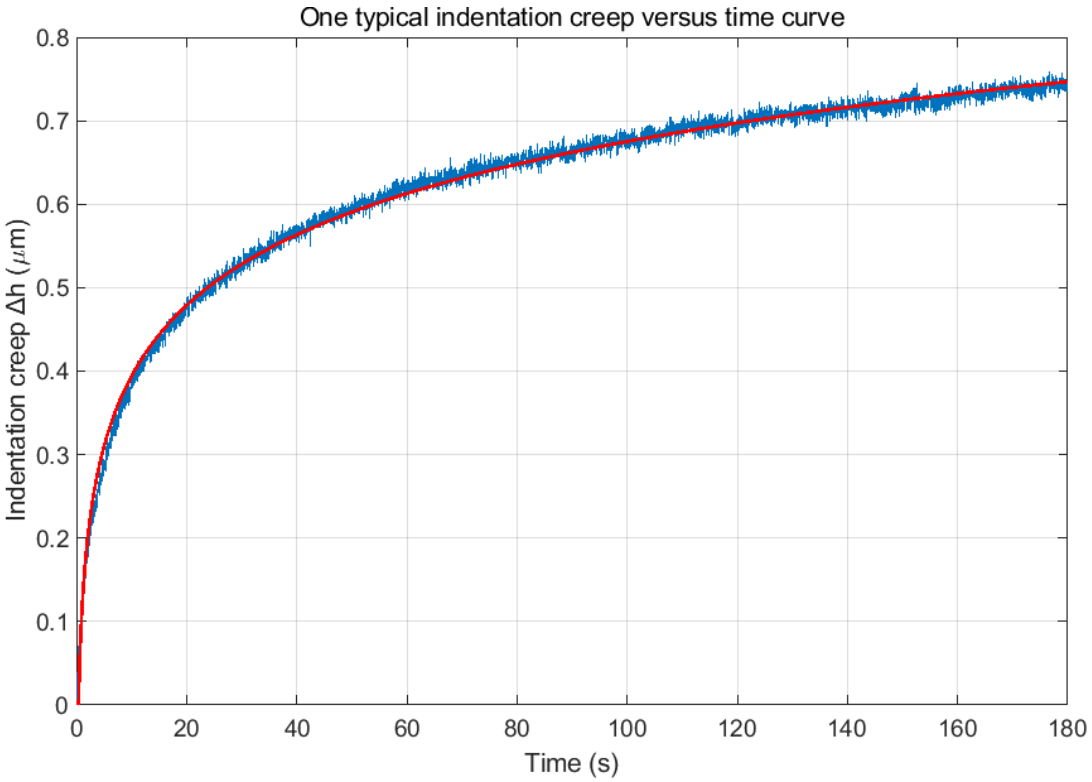

Figure 2.16. A typical indentation creep versus time curve. The blue curve corresponds to the measured data, and the red curve corresponds to the fitted curve based on Eq. 2.23.

The indentation modulus M, hardness H, and creep modulus C are often used to characterize the mechanical properties of rock materials at the sub-micron scale.

2.2.2 Nano-indentation creep

The principles and methods of nano-indentation test are similar to those of the micro-indentation test: indenters with known geometries and mechanical properties are pushed against a horizontal material surface. However, the indentation load and depth are different. For nano-indentation tests, the typical indentation load is around 5 mN, and the typical indentation depth is around 300 nm.

The indentation modulus M, hardness H, and creep modulus C can be determined from nano-indentation measurements. M and H values can be determined using the same methodology as for micro-indentation tests. However, in nano-indentation tests, the machine drifting is comparable to the indentation depth. Therefore, when calculating x_1 (unit: length) and x_2 (unit: time^{-1}) (shown in Eqn. 2.23), the x_3 and x_4 terms must be considered. The x_3 and x_4 terms are dependent on the machine type and the creep time duration, so the x_3 and x_4 values for the specific machine and designated time-duration need to be determined. In this research, the CSM Instruments Nanoindentation Testing NHT is used as the nano-indentation machine. The x_3 and x_4 for 3-min duration are 0.005 nm/s and 0, respectively.

It appears that the creep time duration for most micro- and nano-indentation tests on rock is not longer than 3 minutes. In other words, the rock indentation creep behavior for a relatively longer duration (i.e. a few hours) has not been adequately researched.

2.2.3 Relation between yield strength and indentation hardness H

Tabor (1948) conducted many indentation tests on metals. He noted that when using the conical indenters with a half-angle of 70.26˚ (geometry equivalent to the Berkovich indenter), the hardness can be *empirically* related to the material yield strength:

$$H \cong 3\sigma_Y \tag{2.24}$$

where H is the indentation hardness and σ_Y is the yield strength (the yield strength has been defined in Section 2.1.1).

2.3 Characterization methods of rock fractures

This section presents the definition of rock fracture mechanical aperture and hydraulic aperture. Then, common techniques for fracture surface geometry measurement and common fracture surface geometry models will be reviewed.

2.3.1 Rock fracture mechanical and hydraulic aperture definition

In Sections 2.1 and 2.2 we discussed the intact rock creep behavior. However, in natural conditions, almost all rock masses contain fractures. The fractures have a dominant effect on the mechanical behavior of rock masses because existing fractures provide planes of weakness on which further

displacements can more readily occur. In addition, the fractures can provide major fluid flow conduits, which will significantly change the hydraulic conductivity of rock mass. Thus, the hydraulic and mechanical behavior of rock fractures has been studied extensively (Cook et al., 2006; Iwano and Einstein, 1995; Kang et al., 2020).

To investigate the hydromechanical behavior of rock fractures, it is essential to define the mechanical and hydraulic aperture. Figure 2.17 illustrates the definition of fracture mechanical aperture. According to Hakami et al. (1995), the overall fracture surfaces are assumed to be parallel to the reference plane. The distance between the two surfaces at a certain point, in the direction perpendicular to the reference plane, is the aperture, b, at that point (Hakami et al., 1995). The rock fracture aperture is not the local perpendicular distance between the two surfaces.

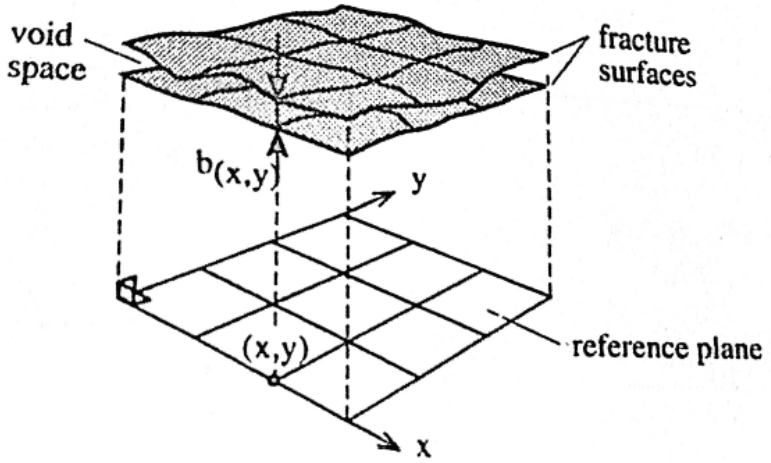

Figure 2.17 Illustration of rock fracture mechanical aperture (Hakami et al., 1995).

The simplest assumption of fluid flow through rock fractures is the parallel plate assumption. As shown in Figure 2.18, the flow in rock fractures is often idealized as flow between two parallel plates. If the flow is steady-state, laminar, and there is no relative flow velocity at the interface between the fracture surface and fluid, the governing flow equation can be derived by simplifying the Navier-Stokes Equation:

$$\frac{\partial P}{\partial x} = \mu \frac{\partial^2 u_x}{\partial x^2} \tag{2.25}$$

where P is the pressure, u_x is the flow velocity in the x-direction, and μ is the fluid dynamic viscosity. The flow velocity profile, $u_x(z)$, can be solved as:

$$u_x(z) = -\frac{1}{2\mu}\frac{\partial P}{\partial x}\left(\left(\frac{h}{2}\right)^2 - z^2\right) \tag{2.26}$$

where $-h/2 \leq z \leq h/2$. The laminar flowrate in the x-direction, Q_x, can be integrated as:

$$Q_x = -\frac{wh^3}{12\mu}\frac{\partial P}{\partial x} \tag{2.27}$$

The parameter h is defined as the hydraulic aperture, which can be expressed as:

$$h = \sqrt[3]{(\frac{-12\mu Q_x}{w})/(\frac{\partial P}{\partial x})} \tag{2.28}$$

Another parameter, $T = wh^3/12$, is defined as the fracture transmissivity.

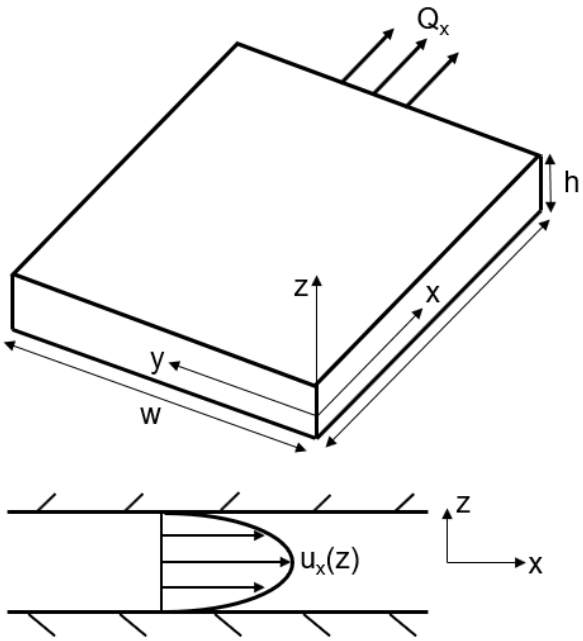

Figure 2.18 Schematic of the parallel plate model.

The parallel plate model provides a convenient theoretical estimation of laminar rock fracture flow. However, in natural conditions, the rock fracture flow is much more complicated than the parallel plate flow. The complicated fracture surface causes flow channelization and complicated fracture deformation behavior under normal stress. To fully understand and simulate rock fracture deformation and fracture fluid flow fields, it is very important to measure and model fracture surface geometry.

2.3.2 Rock fracture surface measurement methods

The fracture surface measurement methods can be grouped based on the measurement technique. Currently, four surface measurement methods have been used: surface profilometer, injection, casting, and X-ray / NMR scanning. In this section, the surface profilometer and X-ray / NMR scanning will be introduced in detail.

Surface profilometers have been widely used to measure fracture surface geometry. The surface profilometer used to be a contacting system: the pin moves on the surface and the pin elevation is recorded. Now the surface profilometer is a non-contact optical system employing a laser beam; it measures the surface profile by digitizing a surface in three dimensions along a series of parallel

trace lines on the object surface. Figure 2.19 shows the schematic of surface digitizing. The x-scanline is parallel to the core axis; the y-scanline is perpendicular to the x-scanline; the z-direction is perpendicular to the surface. Before scanning, the origin of the surface, the sampling interval, and both sets of the trace lines in the x- and y-direction are defined. The laser detector measures the distance to the surface as it moves along the x-direction. At the end of one x-scanline, the laser detector position is stepped in the y-direction and a new trace along the x-direction begins. The resolution (measurement error) of the surface profilometer in the z-direction can be smaller than 1μm.

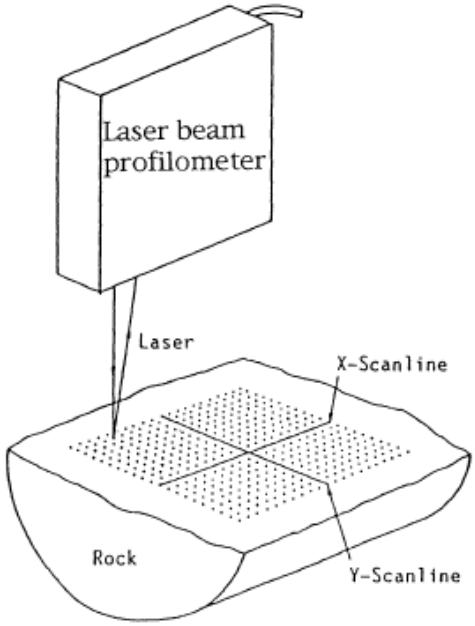

Figure 2.19. Schematic of surface digitizing (Iwano, 1995).

After measuring the elevation of two surfaces, the trend of the measured surface is removed by the linear regression method. Then, as shown in Figure 2.20, the aperture field can be derived as:

$$h = d - z_{upper} - z_{lower} \tag{2.19}$$

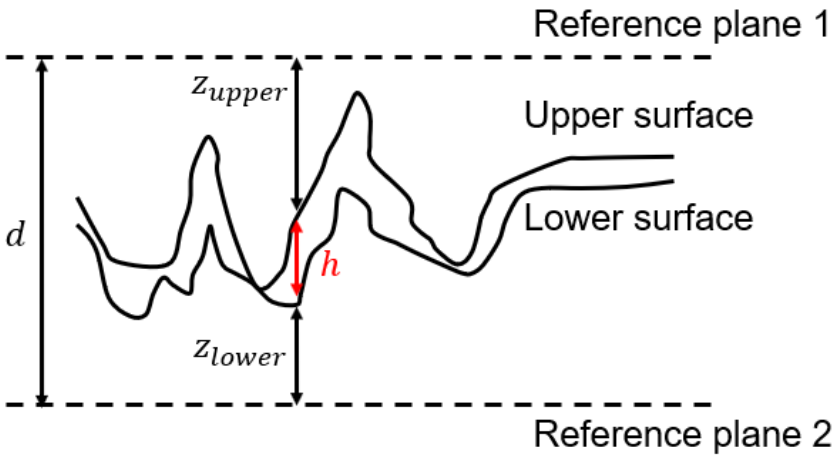

Figure 2.20 Schematic of aperture field derivation based on profilometer measurements.

Although a profilometer can accurately measure fracture surface heights, it has some disadvantages. First, the surface profiles can only be measured before and after experiments. In other words, the surface profiles under confining pressures cannot be measured. In addition, it is difficult to match the two surfaces back to their original positions if the fracture has been opened for surface scanning. The surface mismatch may significantly change the aperture field.

To tackle the disadvantages, the X-ray / NMR scanning technique has been used in recent years (Deng et al., 2015; Carey et al., 2018). Figure 2.21 shows the schematic of X-ray / NMR scanning. The fractured rock is placed inside the core holder and is subject to confining pressure, and CO_2-acidified brine is used as the fracture fluid. The core holder is placed into the scanning chamber for X-ray / NMR, and the holder is connected with the pipeline system to provide confining pressure and pressurized fracture fluid. During scanning, the X-ray source and the panel detector are fixed; the core holder is rotated. The fracture void is differentiated from the rock matrix by comparing the detected X-ray intensity difference. The material for the core holder is generally carbon fiber or aluminum or PEEK/S-glass for X-ray, and PEEK/S-glass for NMR. Most core holders are made by CORE LAB located in Tulsa.

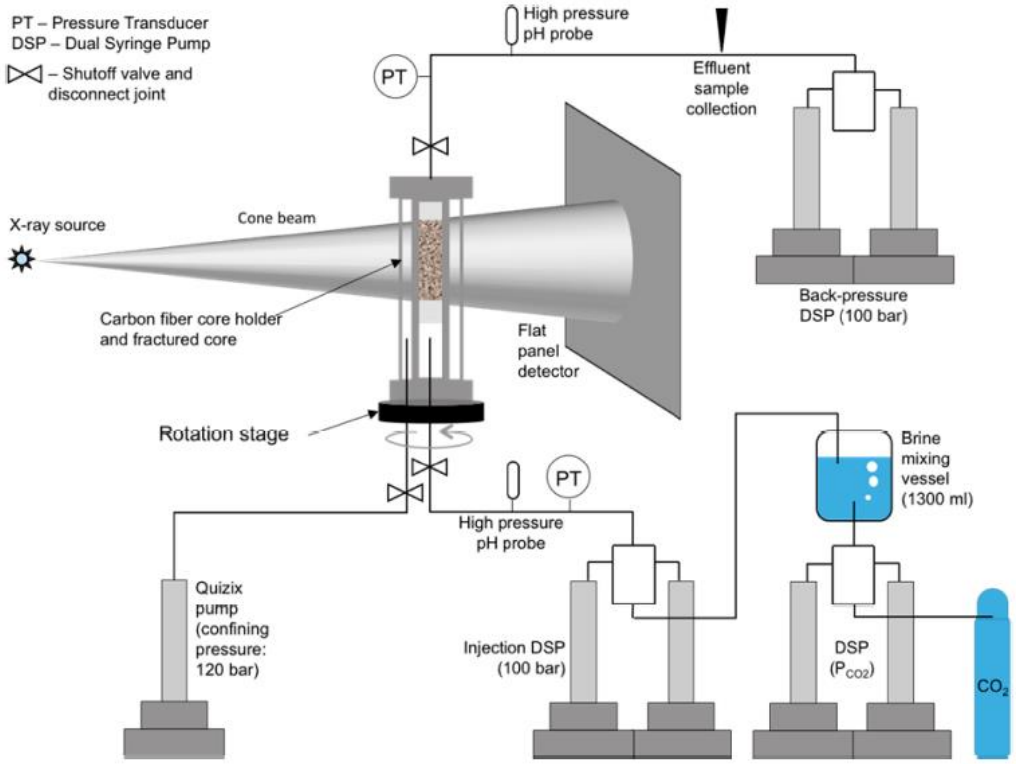

Figure 2.21 Schematic for X-ray / NMR scanning (Deng et al., 2015). The bottom right represents (1) the mixing system for providing pressurized CO_2-acidified brine as the fracture fluid and (2) the inlet pressure control system, the bottom left represents the control system for the confining pressure, and the top right represents the effluent collection and back-pressure control system. The core holder is placed inside the scanning chamber. During scanning, the X-ray source and panel detector is fixed, and the core holder is rotated.

Some research labs, such as the Los Alamos National Lab and the National Energy Technology Lab, have been using this technique to measure the fracture surface heights under confining stresses. The advantage is that the rock fracture aperture field can be obtained during the tests. However, the resolution is not as good as that of the profilometer. The resolution (measurement error) of X-ray or NMR can be larger than 5 μm (Deng et al., 2015; Carey et al., 2018).

The injection method has also been widely used (Hakami et al., 1995; Iwano, 1995; Gale, 1990). As shown in Figure 2.22, resin can be injected into the fracture under confining stresses. After the resin is cured, the fracture is unloaded and cut into thin slices. The thickness of the resin along the thin slices is measured. The disadvantage is that once the fracture void is filled with resin, the fracture cannot be used for further experiments.

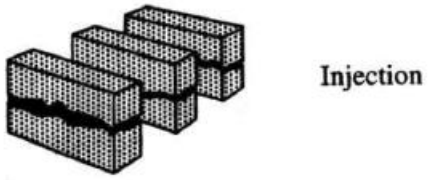

Figure 2.22 Schematic of injection (Hakami et al., 1995).

The casting method has been used to make fracture replicas (Gentier, 1989; Hakami and Barton, 1990). Figure 2.23 shows the schematic of the casting method. A transparent epoxy replica can be made from each joint surface, and the surface replicas can be matched together to form a realistic joint aperture field. Then, water with dye is injected into the replica; the flow velocity field and aperture can be measured. The advantage is that the flow paths and the aperture field become visible. The disadvantage is that the mechanical properties of the epoxy replica are different from those of real rock fractures. In addition, small differences in the geometry between joints and replicas can occur due to the hardening effects of epoxy (shrinking or wrapping) or imperfect copying procedure (Iwano, 1995; Hakami et al., 1995).

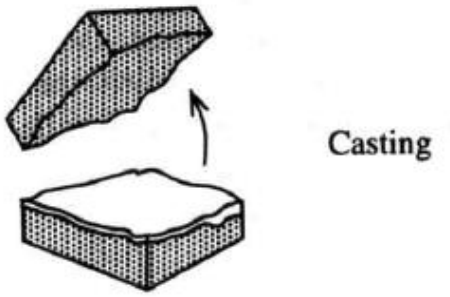

Figure 2.23 Schematic of casting (Hakami et al., 1995).

2.3.3 Rock fracture surface geometry models

Section 2.3.2 showed that under laboratory conditions, the rock fracture surface geometry could be measured. However, at the field scale, it is usually impossible to obtain the detailed description

of the surface geometry. Without fracture surface geometry information, it is extremely difficult to model the hydromechanical behavior. Therefore, many researchers have been trying to characterize fracture surfaces in terms of a small number of statistical parameters and to develop theories that relate the hydromechanical properties of the fracture to the statistical parameters.

To completely describe the surface elevation field, two sets of functions are required: (1) the probability density function of surface heights and (2) the autocovariance function, which is equivalent to the power spectrum (Brown, 1995). The probability density function describes the distribution of surface heights about the mean value without regard to the horizontal spatial position, and the autocovariance function describes the spatial correlation of heights on the surface. Below, five commonly used parameters/functions will be explained: mean and standard deviation for describing the probability density function; autocovariance function, variogram, and power spectrum for describing the spatial correlation. Then, the surface height probability density function and power spectrum used in this research will be introduced.

The basic parameter to describe surface elevation is the mean value, which is defined as:

$$\mu_z = E\{z\} = \frac{1}{A}\int_{y_{min}}^{y_{max}}\int_{x_{min}}^{x_{max}} z(x,y)\,dxdy \tag{2.20}$$

where z(x,y) is the surface elevation, A is the surface area, E{z} is the mathematical expectation of z, and μ_z is the mean value.

The standard deviation, σ_z, is defined as:

$$\sigma_z = \sqrt{E\{z^2(x,y)\} - \mu_z^2} \tag{2.21}$$

The autocovariance function, cov_z, can be used to describe the spatial correlation of surface heights. The autocovariance function represents the degree of correlation between the value of z at one location x and at another location with a distance ξ from location x. Mathematically, it is expressed as:

$$cov_z(\xi) = E\{z(x)z(x+\xi)\} - \mu_z^2 \tag{2.22}$$

Another parameter that can be used to quantify spatial correlation is the variogram function, $\gamma_z(\xi)$:

$$\gamma_z(\xi) = E\{[z(x+\xi) - z(x)]^2\} = 2\sigma_z^2 - 2cov_z(\xi) \tag{2.23}$$

Based on Eqns. 2.22 and 2.23, a decrease in autocorrelation is equivalent to an increase in variogram. Mathematically, larger autocovariance values or smaller variogram values correspond to stronger degree of correlation. Figure 2.24 shows the schematic of autocovariance function and variogram function. From Figure 2.24 (a), the autocovariance decreases with increasing ξ. This implies that between different locations, the degree of correlation reduces with increasing distance. In addition, when the distance $\xi = 0$, the autocovariance becomes the variance (σ_z^2). Figure 2.24 (b) indicates that the variogram increases with increasing ξ.

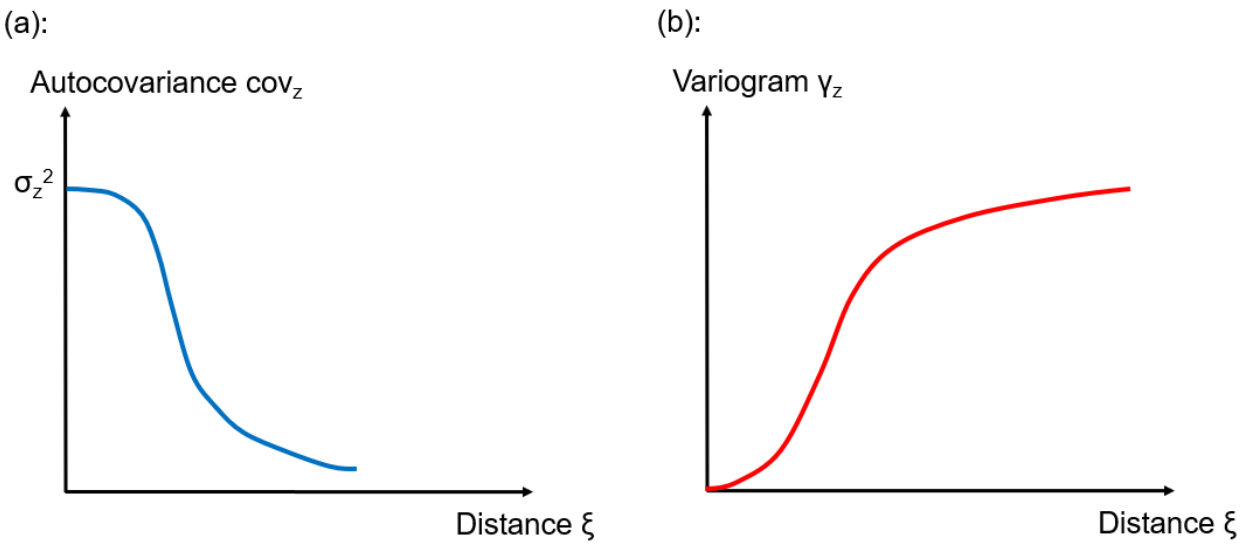

Figure 2.24. Schematic of autocovariance function and variogram function. (a): autocovariance function; (b): variogram function.

The power spectrum is calculated by decomposing the surface into a sum of sinusoidal waves, each with its amplitude, phase, and wavelength. Figure 2.25 shows the process of wave decomposition. In the wave decomposition process, the Fourier transform is used to decompose the random rough surface into a series of sinusoidal wave components. The squared amplitude of each wave component (A^2) is defined as the power, and a plot of power versus the inverse of wavelength ($q = 2\pi/\lambda$) is defined as the power spectrum (see Figure 2.26 for a schematic). The power spectrum is bounded by q_{max} and q_{min}. The upper frequency end, q_{max}, is defined as $q_{max} = 2\pi / \lambda_1$, where λ_1 is the smallest representable or measurable size of scanning devices (i.e. surface profilometers). The lower frequency end, q_{min}, is defined as $q_{min} = 2\pi / \lambda_L$, where λ_L is the surface length.

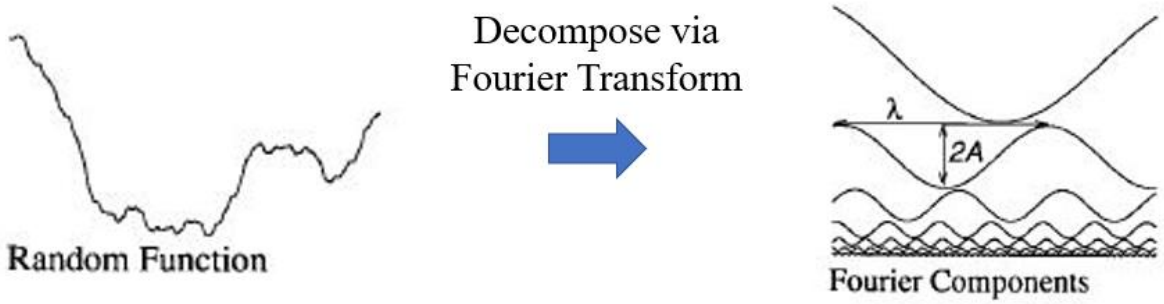

Figure 2.25. Schematic of surface profile breakdown. Each component is characterized by its wavelength (λ), amplitude (A), and phase (relative position of the first peak of the sinusoid to that of all others).

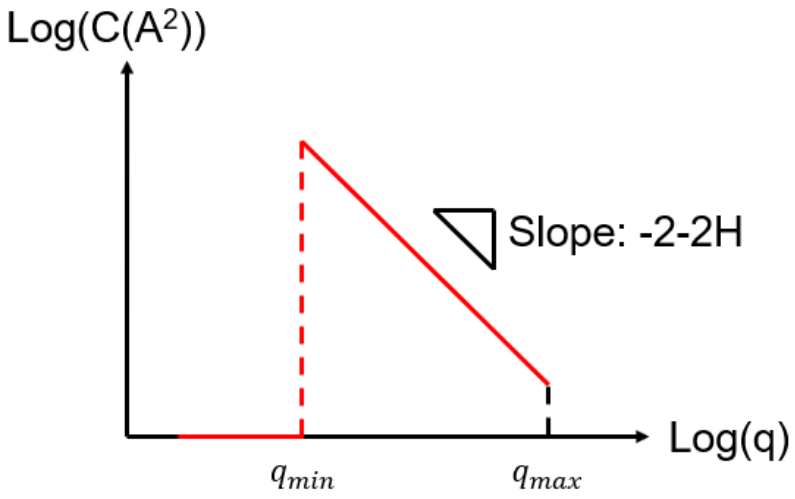

Figure 2.26. Schematic of the power spectrum. The horizontal axis is the frequency q (1/λ), and the vertical axis is the power C (A^2). C (A^2) can also be related to q by Eqn. 2.24. The unit for q is (1/length). The slope and the meaning of H will be explained later.

Mathematically, the power C (A^2) can be related to the autocovariance function by the Fourier transform:

$$C(A^2) = \frac{1}{2\pi}\int_{-\infty}^{+\infty} cov_z(\xi)e^{-iq\xi}d\xi \tag{2.24}$$

Since the autocovariance function and power spectrum can be mathematically related, only one of them is required to describe the surface elevation field.

In this research, the Gaussian distribution will be used as the probability density function to describe fracture surface heights, and the self-affine power spectrum will be used as the spatial correlation function. The Gaussian distribution can be expressed as:

$$p_z(z) = \frac{1}{\sigma_z\sqrt{2\pi}}e^{-\frac{(z-\mu_z)^2}{2\sigma_z^2}} \tag{2.25}$$

where $p_z(z)$ is the probability density function of surface height z. Log-normal and exponential distribution of surface heights have also been used in other research articles (Iwano, 1995; Cook et al., 2006), but those two models will be not used in this research. Therefore, in this section, only the distribution formula will be provided.

The log-normal distribution can be expressed as:

$$p_z(z) = \frac{1}{z\sigma_z\sqrt{2\pi}}e^{-\frac{((\ln z)-\mu_z)^2}{2\sigma_z^2}} \tag{2.26}$$

where $p_z(z)$ is the probability density function of surface height z.

The exponential distribution can be expressed as:

$$p_z(z) = \lambda e^{-\lambda z} \tag{2.27}$$

where $p_z(z)$ is the probability density function of surface height z.

For the spatial correlation function, rock fractures typically follow a self-affine fractal distribution (Mandelbrot, 1983; Brown and Scholz, 1985a; Odling, 1994). A self-affine surface can be described as:

$$z(x) \sim \varepsilon^{-H} z(\varepsilon x) \tag{2.28}$$

where z is the surface elevation, ε is a constant for x-direction scaling, and H is the Hurst exponent. The H value is between 0 to 1; a larger H value corresponds to a smoother local surface profile, as shown in Figure 2.27. In addition, the H value can be related to the power spectrum. If the surface is self-affine, after Fourier transform (shown in Figure 2.25), the power spectrum of the surface will be linear, with a slope of -2-2H. Figure 2.26 shows the schematic of the self-affine power spectrum. Mathematically, C (A^2) can be expressed as:

$$C(A^2) \sim q^{-2(1+H)} \tag{2.29}$$

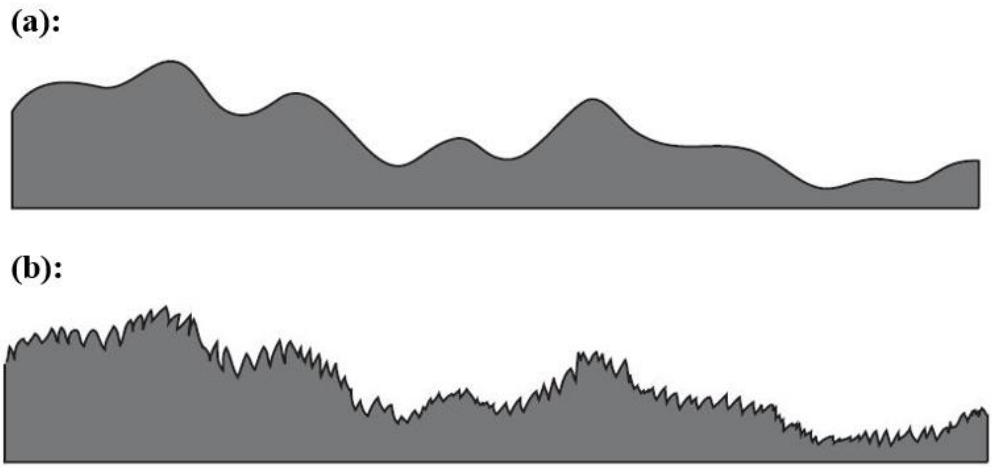

Figure 2.27 Schematic of two self-affine surfaces with different H values (Persson, 2006). (a): H = 1; (b): H = 0.

According to the literature review on rock fracture characterization, the fracture surface can be described by a Gaussian surface height distribution function and a self-affine spatial correlation function. In this research, the Gaussian function of surface heights and the self-affine spatial correlation will be used to generate fracture surfaces, and the generation process will be explained in detail in the Methodology Section (Section 3).

2.4 Creep mechanisms of rock fractures

The following section introduces the creep mechanisms of rock fractures caused by mechanical compression, pressure solution, dissolution, and erosion. Current research related to creep mechanisms will be briefly reviewed.

2.4.1 Creep mechanisms of rock fractures

Mechanical compression occurs in both dry and wet conditions. Figure 2.28 shows a schematic of mechanical compression creep. To balance the external normal stress, the fracture contacting asperities are subjected to compressive stresses. Due to the viscous properties of the rock material, under constant stress, the contacting asperities undergo visco-elastic or visco-elasto-plastic deformations. As a result, the contacting surface area changes, and fracture closes. The change of contacting surface area will further change the stresses acting on the contacting asperities. Besides visco-elastic or visco-elasto-plastic deformations, micro-cracking or asperity breakage may occur, which will further change the contacting surface area and the contacting stresses.

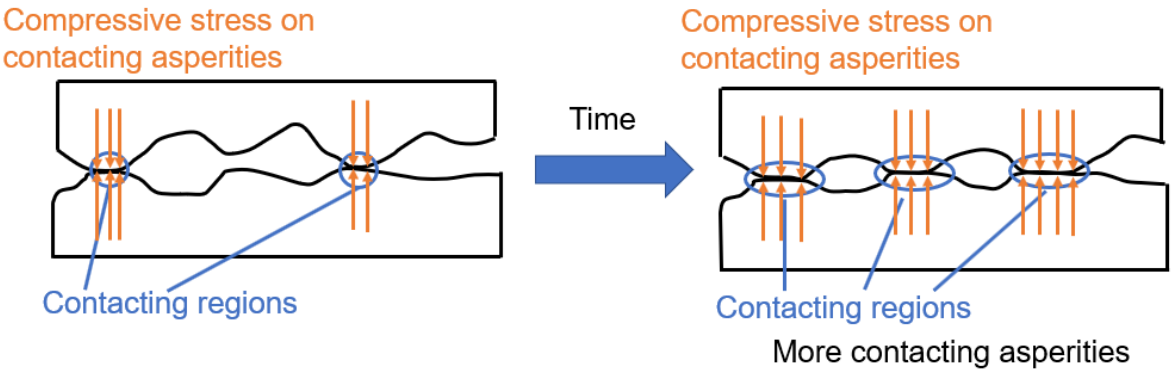

Figure 2.28 Schematic for mechanical compression of the fracture surfaces.

Pressure solution is another important mechanism of rock fracture creep (Yasuhara et al., 2004; Bernabe and Evans, 2007; Ishibashi et al., 2013). As shown in Figure 2.29, pressure solution consists of three main steps: dissolution at contacting asperities; diffusion along the interfacial water film, and precipitation on the free surface. First, at the contacting asperities, the mineral dissolves under high localized compressive stress. Then, the dissolved minerals diffuse from the center of the contacting region to the periphery of the contacting region along the water film contact between the asperities. Finally, the minerals precipitate on the free surfaces, on which there is no contacting stress. The pressure solution process will only occur under wet conditions; it will increase the contacting areas of the fracture and reduce the average aperture.

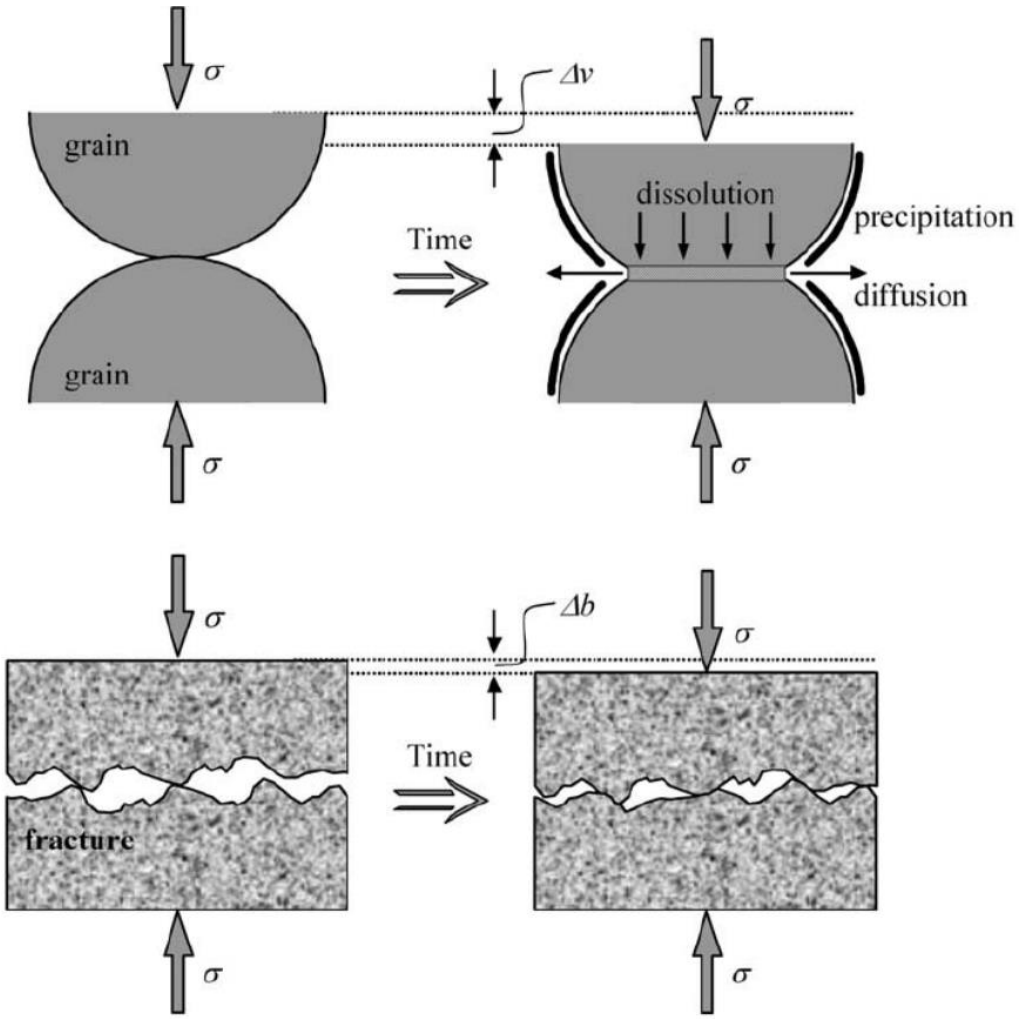

Figure 2.29 Schematic for pressure solution (Yasuhara et al., 2004). The upper figure represents the pressure solution for single grain pair, and the lower figure represents the pressure solution for a fracture. σ is the applied external compressive stress, Δv is the closure for the single grain pair, and Δb is the fracture closure.

Dissolution will also significantly affect fracture creep rate. The dissolution process refers to a solid mixing into the aqueous solution, and it can occur on both contacting asperities and free surfaces. The dissolution consists of two steps: the chemical reaction process at the solid-fluid interface, and the mass transport process of dissolved ions away from the solid-fluid interface (Li, 2019). Figure 2.30 shows a schematic of dissolution. Li (2019) stated that dissolution will occur under fluid conditions, and the common water-soluble minerals are carbonates, sulfates, and chlorides.

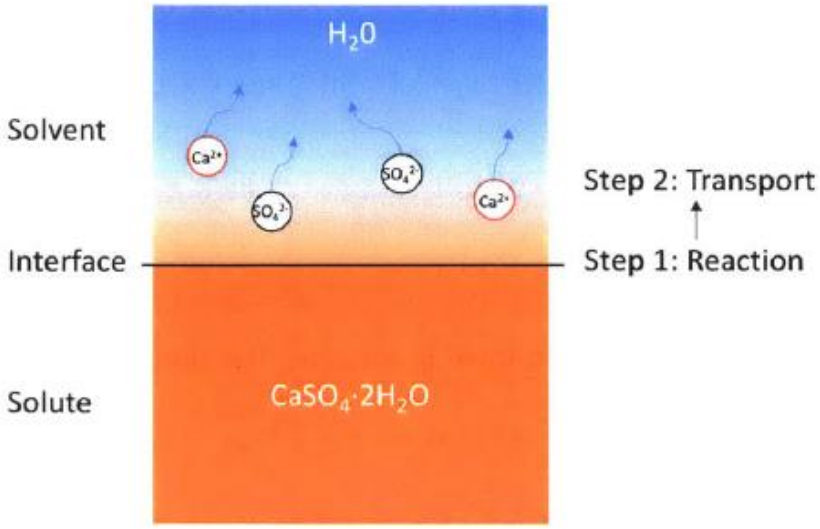

Figure 2.30 Schematic of dissolution process (Li, 2019). The dissolution of gypsum ($CaSO_4 \cdot 2H_2O$) is shown as an example.

As dissolution continues, the fracture surface geometry will be changed. The change of fracture surface geometry may further change the fluid flow paths, and as a result, the fracture hydraulic conductivity may be altered. Figure 2.31 shows one example. It plots the aperture field of a limestone fracture evolving with time, and CO_2-acidified brine was used as the fracture fluid. The results indicate that as dissolution continues, the fracture aperture field changes with time and becomes more heterogeneous. The details of the experiment will be reviewed in Section 2.4.2.

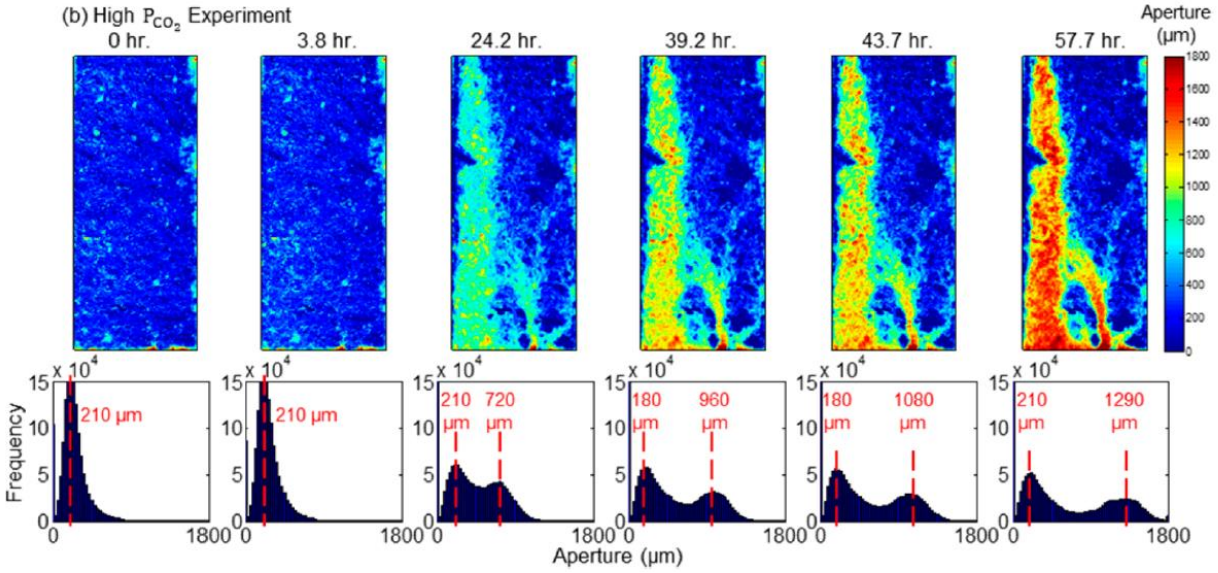

Figure 2.31. The evolution of aperture field of a limestone fracture (Deng et al., 2015). The fracture surface was dissolved by CO_2-acidified brine.

Erosion can also change the fracture surface geometry. Noiriel et al. (2013) and Deng et al. (2017) stated that erosion often occurs together with dissolution in heterogeneous rock fractures. Figure 2.32 shows a schematic of erosion. In Figure 2.32, white circles and brown matrix represent minerals with higher and lower dissolution rates, respectively. As shown in Figure 2.32 (a), under water or brine flow conditions, minerals with higher dissolution rates (white circles) may be dissolved first. As dissolution continues, some minerals with lower dissolution rates may become unstable (shown by the green rectangle). As a result, under the effect of fluid flow, the unstable particles may detach from fracture surfaces. The released particles may be transported downstream and may be clogged at a downstream location. The detachment and clogging of particles will enlarge and reduce the aperture value, respectively.

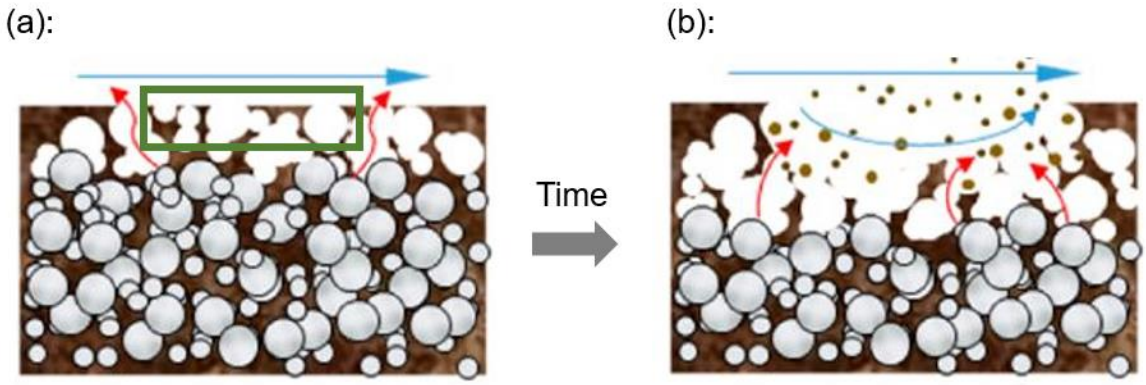

Figure 2.32 Schematic of surface erosion (Deng et al., 2017). The blue arrows represent fluid flow directions, red arrows represent the dissolution of minerals with higher dissolution rates, and the green rectangle represents the unstable minerals with lower dissolution rates.

2.4.2 Very brief summary of current literature investigating the creep mechanisms

Many papers have discussed numerical modeling and laboratory experiments on creep mechanisms of rock fractures. It appears that most experiments and numerical models focus on the mechanisms of pressure solution (at contacting asperities) and dissolution (on free surfaces). The effect of pressure solution on rock fracture creep has been studied extensively (Yasuhara et al., 2006; McGuire et al., 2013; Ishibashi et al., 2013; Beeler and Hickman, 2004). A common finding is that pressure solution will reduce the fracture mechanical and hydraulic aperture by causing compression on the contacting asperities. One example will be reviewed here. Yasuhara et al. (2015) measured the long-term permeability change of saw-cut sandstone fractures under different temperatures. Figure 2.33 shows the schematic of the experiment. The confining pressures were 7.5 and 15 MPa, and the differential pore pressure (pore pressure difference between the inlet and outlet) was fixed at 9.8 kPa. Deionized water was used as the injection fluid, and the effluent was collected at the outlet. The permeability test was intermittently conducted every five days – every five days, the permeability experiment was halted for a very short amount of time. During the halt time, the effluent in the sampling tube (shown in Figure 2.33) was collected for chemical analysis. Figure 2.34 shows the schematic of the testing procedure. The element concentration (Si, K, Ca,

Mg, Al, Fe, and Na) in the effluent was measured with the inductively coupled plasma technique. The flow tube was completely plugged so no-flow conditions were maintained. After the sampling tube was emptied, the flow tube was carefully unplugged, and another five-day permeability experiment started. The results indicate that temperature has a dominant effect on the aperture change (see Figure 2.35). Figure 2.35 shows the results of two specimens.

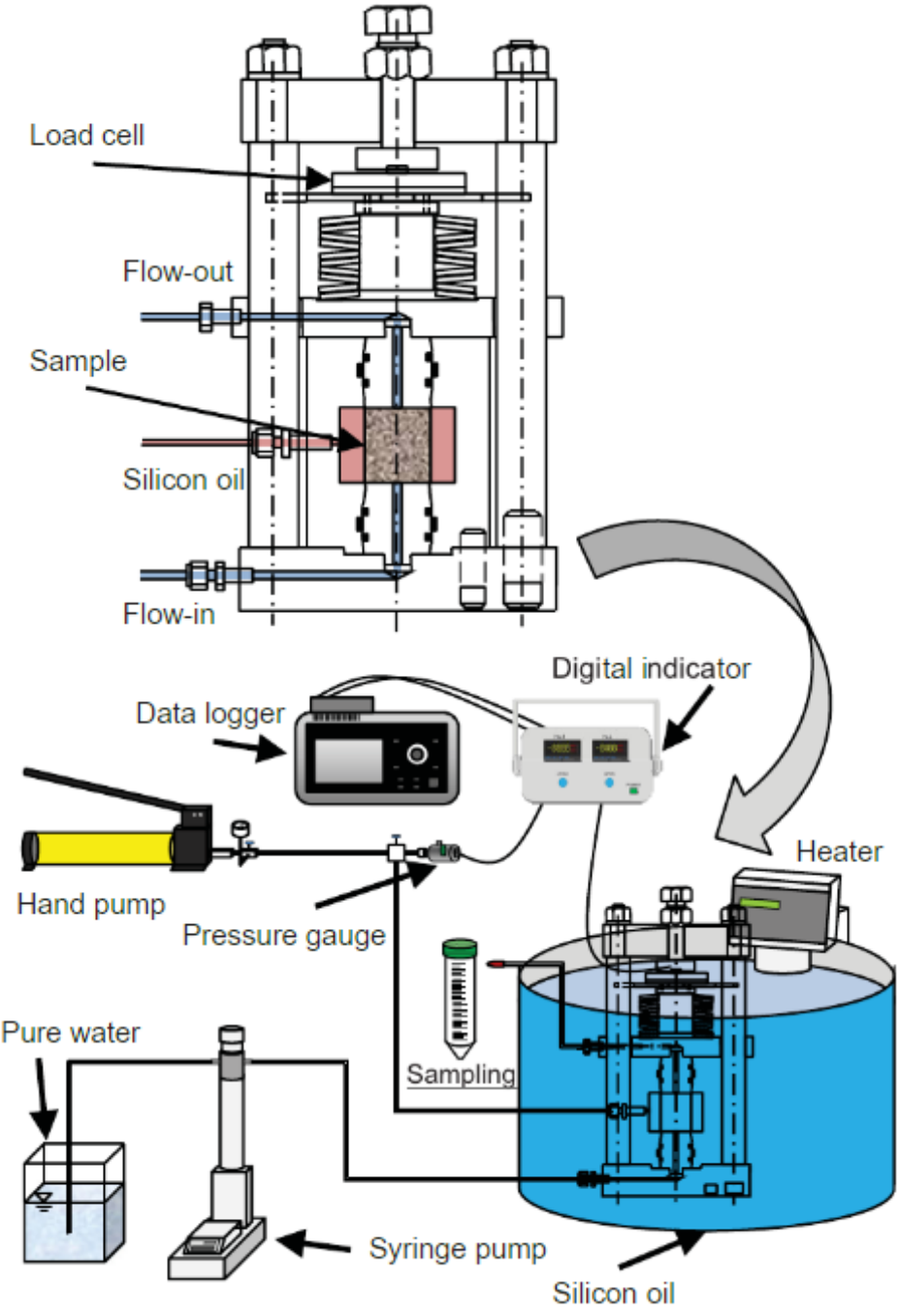

Figure 2.33 Schematic of long-term pressure solution experiments on saw-cut sandstone fractures (Yasuhara et al., 2015). The top part represents the triaxial cell, and the bottom part

represents the entire testing system. The triaxial cell was submerged in a cylindrical container (marked by the blue cylinder) that was filled with a liquid whose temperature was maintained by the heater. The bottom left part represents the fluid injection system. Deionized water was injected into the rock fracture by the syringe pump, and the effluent was collected by the sampling tube. The inlet pressure was controlled by the syringe pump, while the outlet pressure was zero (atmospheric pressure). The confining pressure was controlled by the hand pump. The flow rates (average flowrate for five days) was calculated by weighting the effluent fluid in the sampling tube.

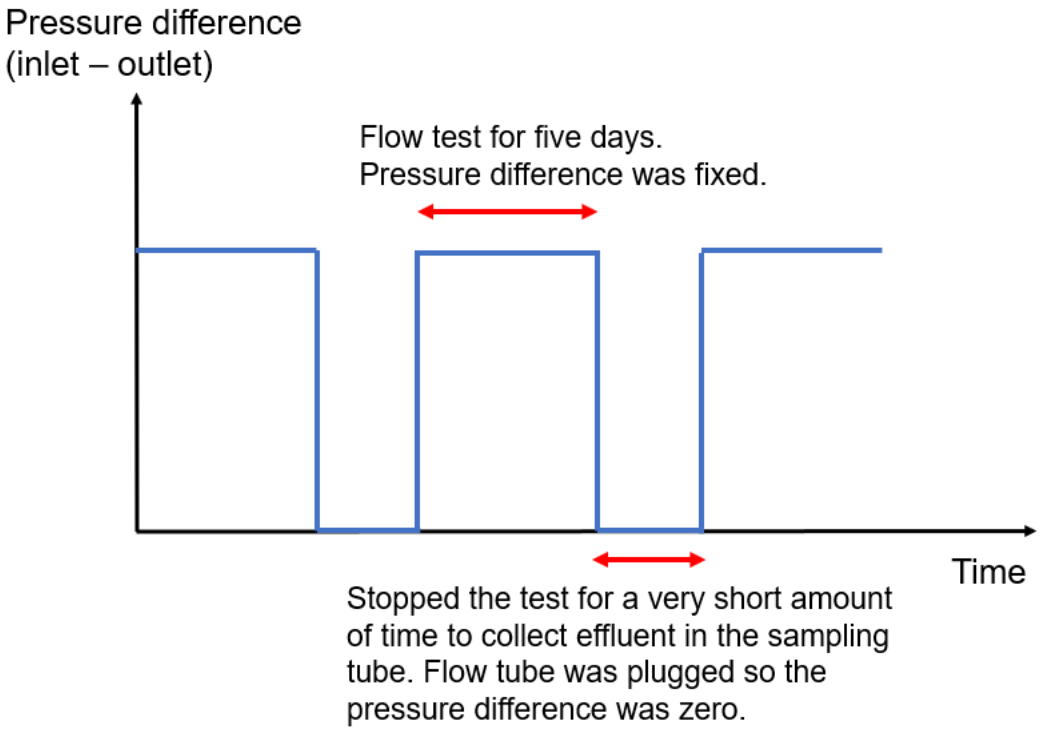

Figure 2.34 Schematic of the testing procedure.

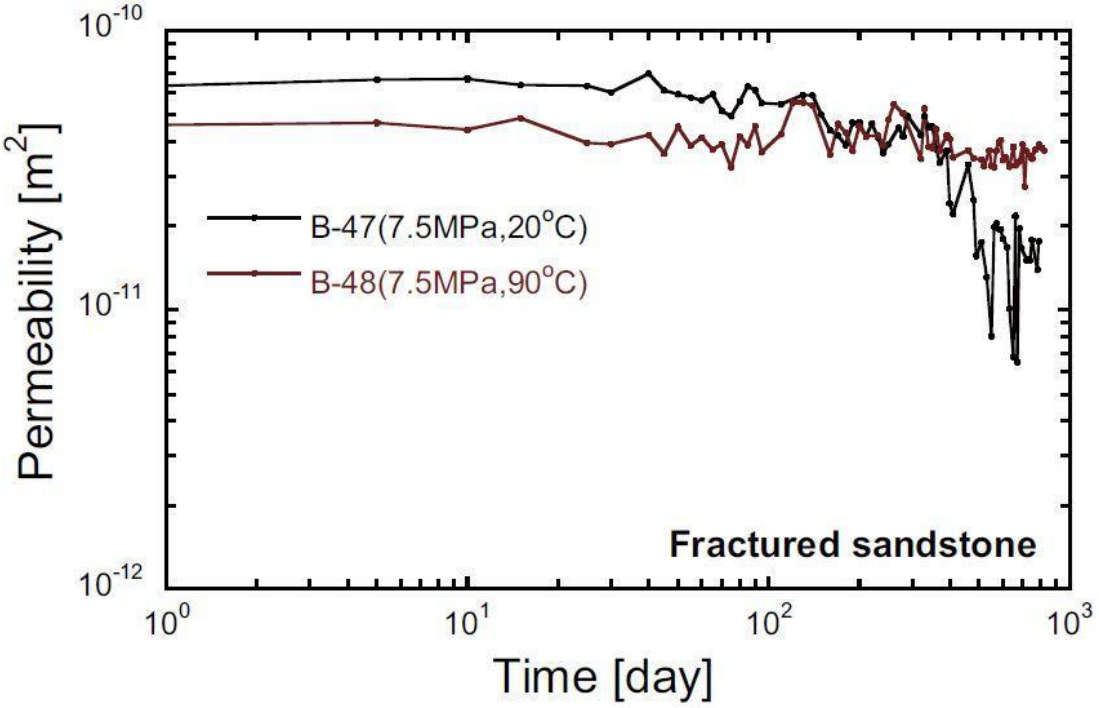

Figure 2.35 Permeability evolution for two saw-cut sandstone fracture specimens (Yasuhara et al., 2015). The confining pressure was 7.5 MPa, and the temperature for specimen B-47 and B-48 was 20 ˚C and 90 ˚C, respectively. The authors did not explain the trend of permeability change or the permeability fluctuation.

In recent years, some numerical models, which simulate fracture-scale pressure solution, have been proposed (Yasuhara and Elsworth, 2004; Bernabe and Evans, 2007; Neretnieks, 2014; Zhao et al., 2014; Lang et al., 2015; Li et al., 2015; Zou et al., 2020). One example will be introduced here. Lang et al. (2015) numerically simulated the effect of pressure solution on fracture asperity field change. Figure 2.36 shows the schematic of the numerical model. First, synthetic rock surfaces were generated by assuming the surfaces were self-affine. For each step, the elastic deformation of the fracture surface under compressive stress was solved (the method will be introduced in Section 2.5). Then, the surface change caused by pressure solution was obtained by using either Bernabe and Evans' (2007) model (BE model) or Lehner and Leroy's (2004) model (LL model). The surface geometry was updated, and a new step is begun.

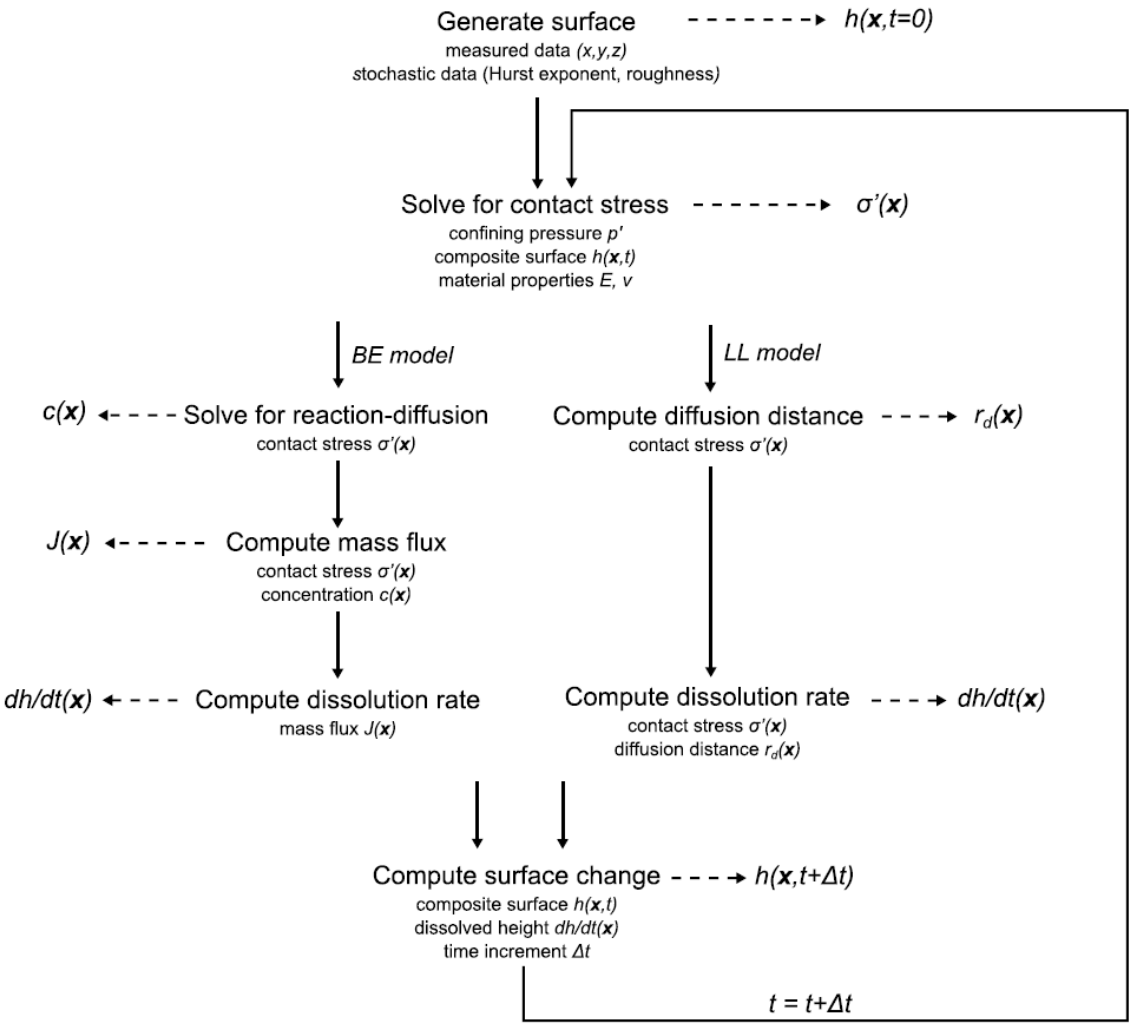

Figure 2.36 Schematic of Lang et al.'s numerical model (Lang et al., 2015). BE model and LL model represent the pressure-solution models proposed by Bernabe and Evans (2007) and Lehner and Leroy (2004), respectively.

Before introducing the results, it is essential to briefly introduce the LL and BE model. The LL model is an analytical model which calculates the dissolution rate. The model makes two important assumptions: (1) the contacting grains are spherical; (2) the dissolution rate is uniform over the entire grain contact at all times during pressure solution. The dissolution over the grain contact is illustrated in the upper figure of Figure 2.29. Based on the two above assumptions, the dissolution rate can be expressed as:

$$\frac{dh}{dt} = \frac{2\frac{\Omega_S}{k_B T}\bar{\sigma}}{\frac{2}{k_d} + \frac{\rho_S}{\rho_f}\frac{r_c^2}{4c_{eq}wD^*}} \tag{2.30}$$

where h (m) is the asperity height, ρ_s (kg/m^3) is the rock grain density, ρ_f (kg/m^3) is the fluid density, T (K) is the temperature, k_B (J/K) is the Boltzmann constant, Ω_s (m^3) is the molecular volume, c_{eq} (kg/m^3) is the equilibrium mineral concentration in pore space, $\bar{\sigma}$ (Pa) is the averaged compressive

stress acting along the grain contact, r_c (m) is the radius of the contacting area, D^* (m^2/s) is the temperature-dependent diffusion constant, k_d (m/s) is a temperature-dependent dissolution constant, and w (m) is the thickness of the interface layer of the grain-to-grain contact (see Figure 2.37). Based on the dissolution rate dh/dt, the surface geometry change caused by dissolution at each time step can be determined.

The LL analytical model provides a convenient theoretical estimation of dissolution rate. However, Bernabe and Evans (2007) pointed out that in reality, the contacting stress distribution along the grain contact is non-uniform, and the dissolution rate is dependent on the contacting stress. As a result, the dissolution rate along the grain contact is non-uniform. Figure 2.37 shows the schematic of non-uniform contacting stress distribution. To relax the constraint of uniform dissolution rate, Bernabe and Evans (2007) proposed a numerical model. As shown in the left part of Figure 2.36, the numerical model first uses the reaction-diffusion equation to calculate the solute concentration from stress distribution along the contacting area. Based on the solute concentration, the mass flux is calculated; and based on the mass flux, the dissolution rate is determined. The surface geometry change caused by dissolution at each time step can therefore be determined from the dissolution rate.

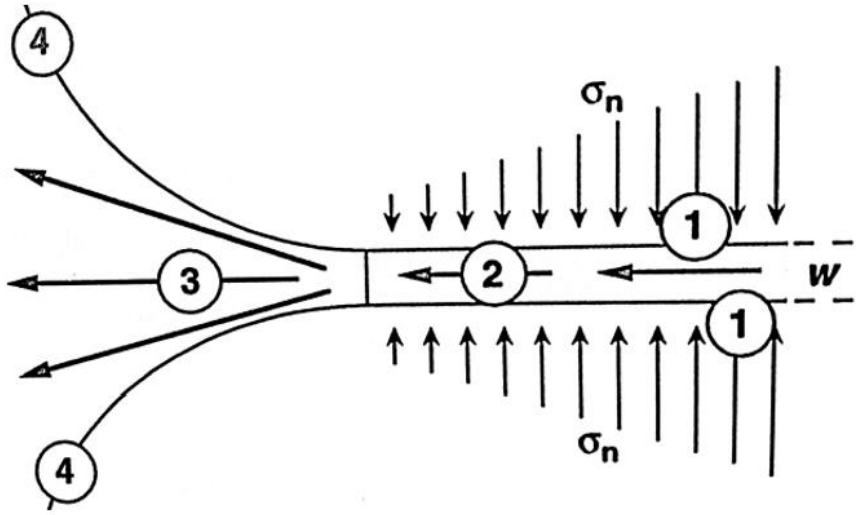

Figure 2.37 Schematic of non-uniform contacting stress distribution (Bernabe and Evans, 2007). It describes the pressure solution process at a single symmetric grain-to-grain contact. Due to symmetry, only half of the grain contact is shown. The solid-solid interface is represented as a thin layer with a thickness of w, and the contacting stress is represented by σ_n. For the numbers: (1): dissolution at the solid-solid interface; (2): diffusion along the interface; (3): diffusion in the pore fluid outside the interface; (4): precipitation along the unstressed fluid-solid interface.

Figure 2.38 shows some of the results. It plots the contacting stress and flow velocity field changing with time for four different time durations. The external pressure (normal pressure acting on the fracture surface) is 10 MPa, and the temperature is 423K. Each sub-plot is a superposition of two figures: the grey figure which represents the flow velocity field, and the colored figure (ranging from red to blue) which represents the contacting stress distribution. The flow is from left

to right. For the grey figure (flow velocity field figure), darker color corresponds to larger flow velocity. For the colored figure (contacting stress field), increasing shades from blue to red represent increasing contacting pressure (red represents the largest contacting stress). The regions without colors (ranging from red to blue) correspond to non-contacting regions. The results indicate that the growth of contact areas due to pressure solution reduces the contacting stress acting on the contacting regions, and changes the fluid flow path. For example, at initial state, there are two major flow channels, and the area of contacting region is relatively small; after 100 years, there is only one major flow channel, and the area of contacting region becomes significantly larger.

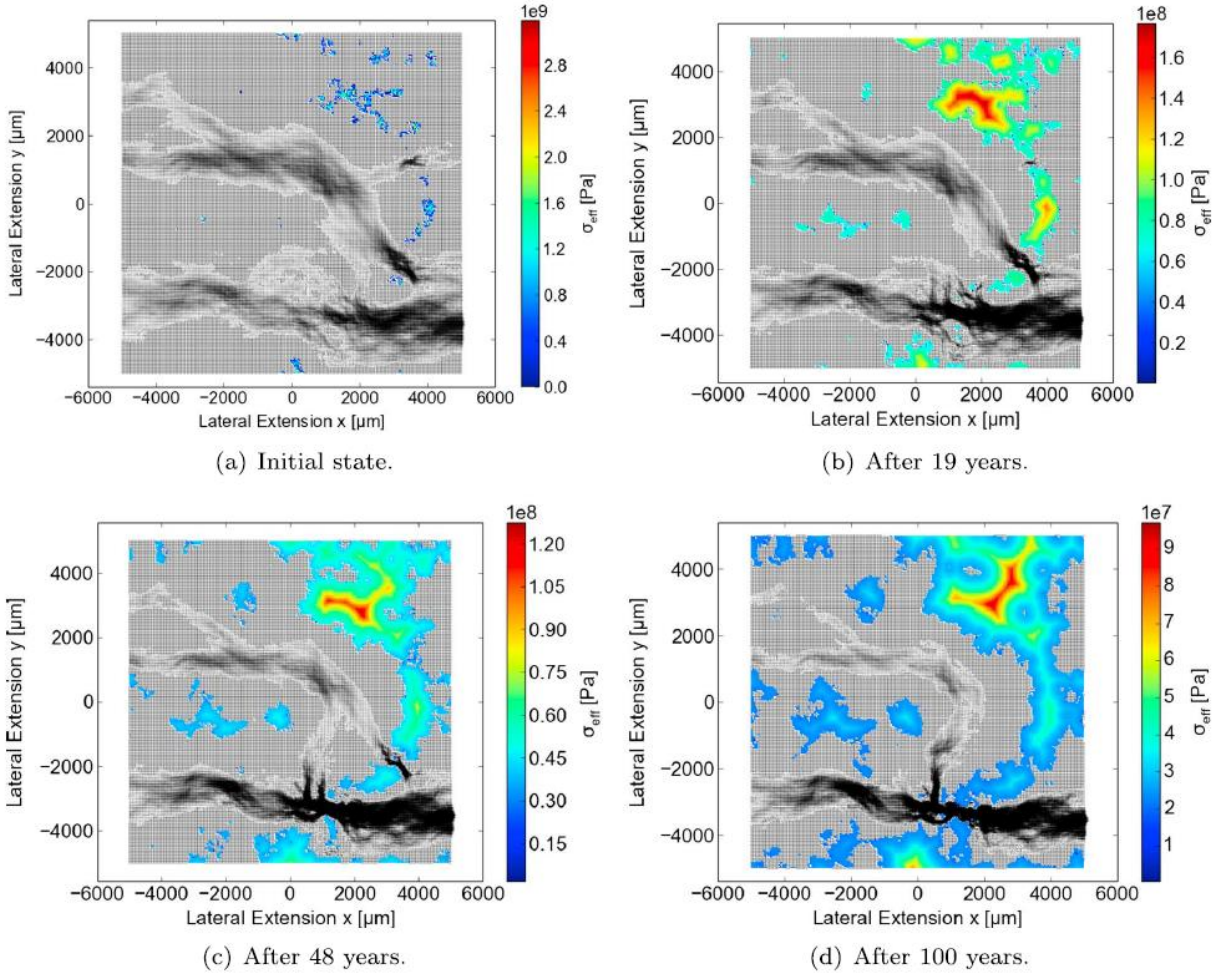

Figure 2.38 One example result of contacting stress and flow field changing with time (Lang et al., 2015). The contacting stress field is displayed as colored regions, and the flow velocity field is displayed as grey. For the colored figures, the scales of the color bar are different. For example, in Figure (a), red color represents the regions with the contacting stress larger than 2.5 GPa; while in Figure (d), red color represents the regions with the contacting stress larger than 80 MPa.

For dissolution, fracture permeability evolution under the influence of acidic solutions has been widely investigated via fracture flow experiments (Durham et al., 2001; Polak et al., 2004; Detwiler, 2008; Elkhoury et al., 2013; Noiriel et al., 2013; Deng et al., 2015; Garcia-Rios et al.

2017). A common conclusion is that for calcite rock, when the pH of the fluid in the fracture is less than 6, fracture aperture distribution becomes more heterogeneous, as a result of acidic dissolution. One example is reviewed here. Deng et al. (2015) conducted dissolution experiments on Indiana limestone fractures, and they used CO_2-acidified brine as the fracture fluid. Figure 2.39 shows the schematic of the experimental setup. The confining pressure and pore pressure were held at 12 MPa and 10 MPa, respectively. The confining vessel was placed inside an X-ray CT scanner, and the fracture aperture field could be obtained from the scanning images. Figure 2.40 shows the results. Due to dissolution, the fracture becomes more heterogeneous, and the average mechanical aperture increases.

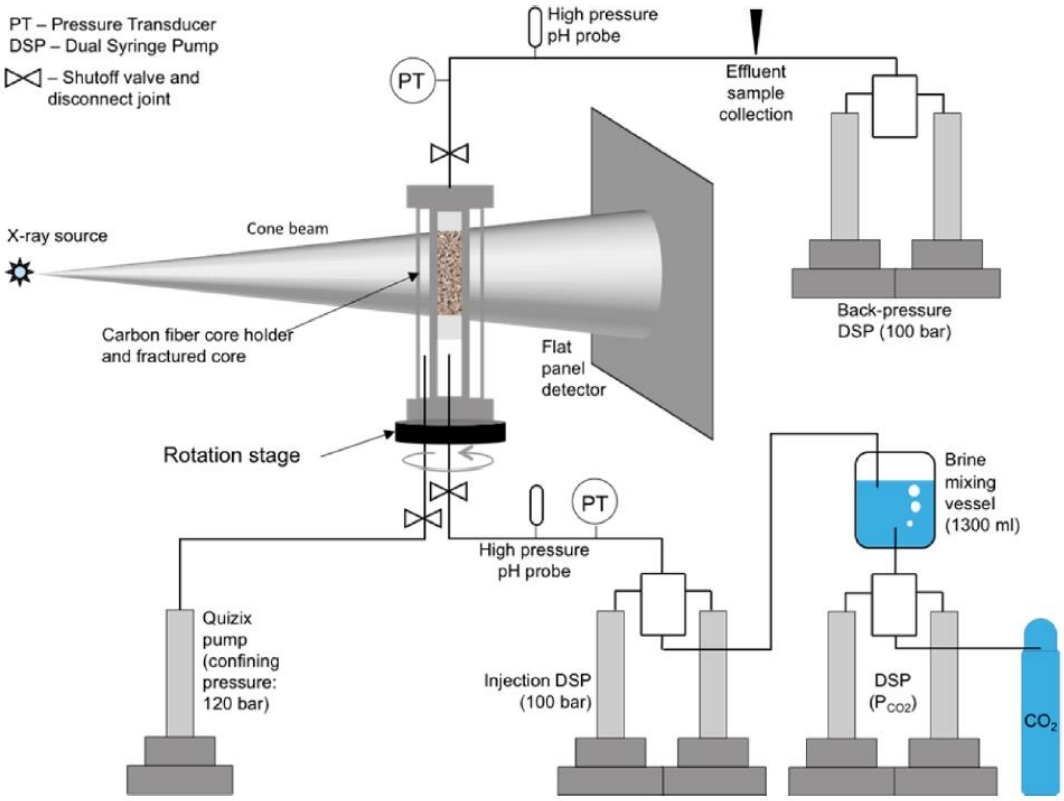

Figure 2.39 Schematic of the experimental setup (Deng et al., 2015). The experimental method has been explained by Figure 2.21 in Section 2.3.2.

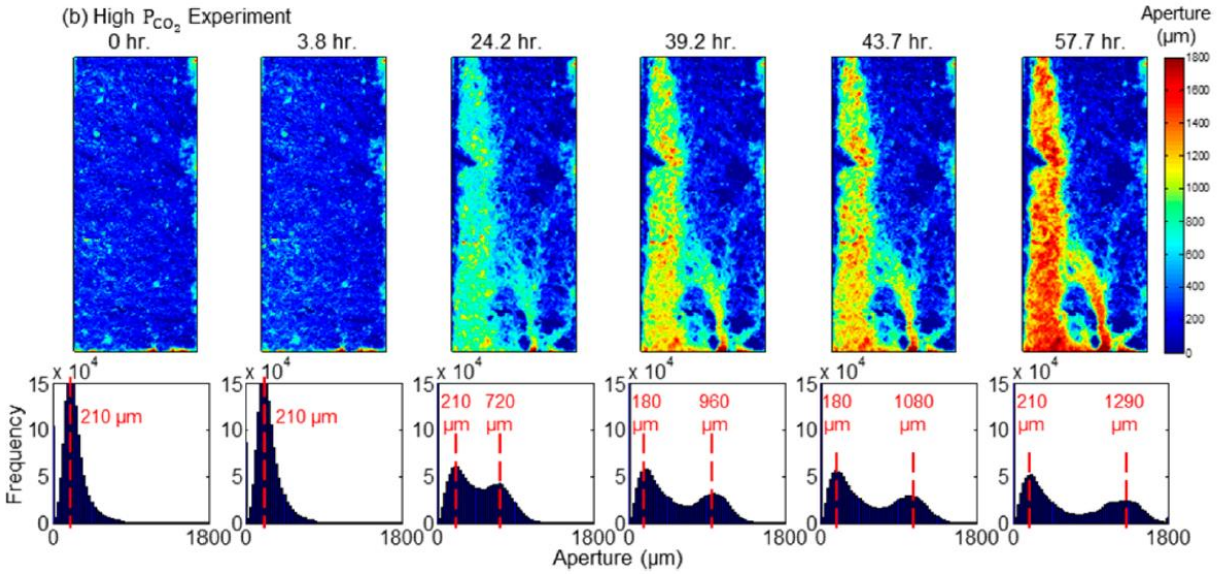

Figure 2.40 Aperture field evolving with time (Deng et al., 2015). As dissolution continues, the fracture aperture field becomes more heterogeneous.

Numerical modeling has also been conducted to simulate the dissolution process, and some researchers have proposed coupled mechanical-chemical numerical models. One example is shown here. Ameli et al. (2014) proposed a coupled mechanical-chemical numerical model to simulate fracture deformation due to time-dependent dissolution and mechanical deformation (mechanical creep was not considered; only the elastic deformation of fracture was calculated). Figure 2.41 shows the schematic of the model. At each step, the local cubic law is used to calculate the flow velocity field. The reactive transport model proposed by Detwiler and Rajaram (2007) is used to calculate the surface geometry change caused by dissolution. Then, the surface geometry is updated, and the elastic deformation (see the 'mechanical equilibrium' and 'elastic deformation' in Figure 2.31) is calculated again by the mechanical model proposed by Pyrak-Nolte and Morris (2000). The results shown in Figure 2.42 indicate that the flowrate had a dominant impact on the fracture aperture change. The initial aperture fields for the four cases are identical. Under the larger flowrate, the aperture fields are more uniform. In addition, if the mechanical deformation mechanism is considered, the average aperture value is smaller.

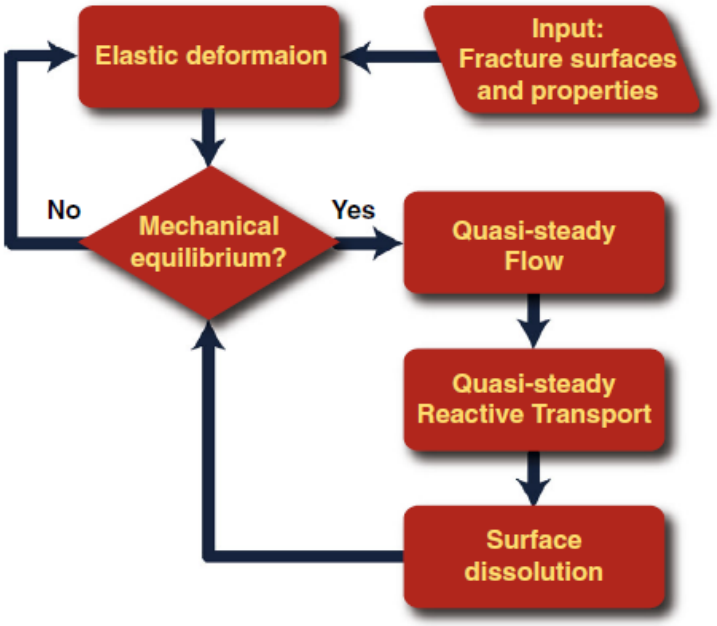

Figure 2.41 Schematic of a coupled mechanical-chemical numerical model to simulate fracture mechanical deformation and dissolution (Ameli et al., 2014). It does not consider the mechanical creep, and the creep is caused only by dissolution. At each time step, the dissolution is calculated, and the fracture surface geometry is changed by dissolution. The fracture surface geometry changed by dissolution is considered as the surface input for the next step. In the next step, the elastic deformation of the fracture is calculated, and the surface geometry is updated again. The new dissolution rate is calculated based on the updated surface geometry.

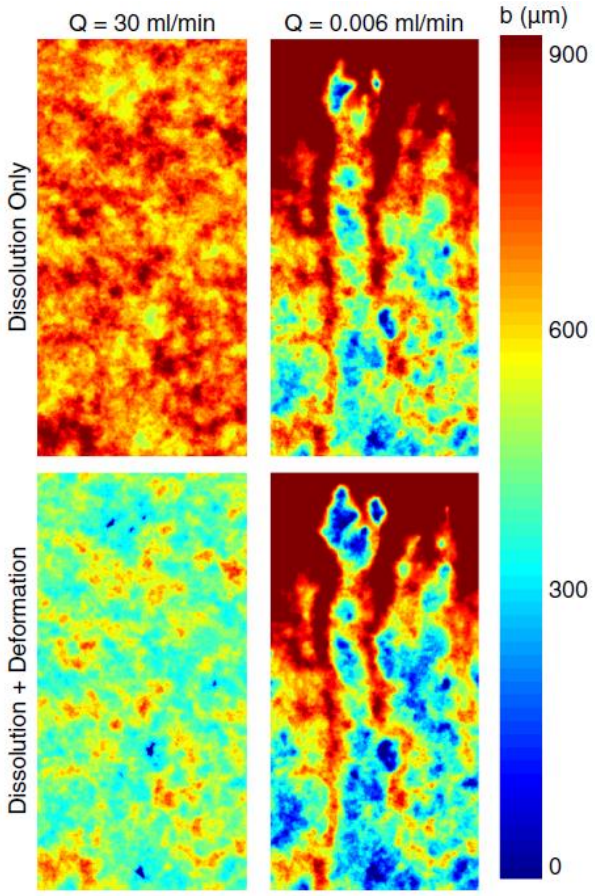

Figure 2.42 The aperture field evolution under different mechanisms and flowrates (Ameli et al., 2014). The top two figures correspond to the simulation results only considering dissolution (mechanical deformation of the fracture is not considered), while the bottom two figures correspond to the simulation results considering both mechanical deformation and time-dependent dissolution. The flow is from top to bottom. The initial aperture fields and the time durations are identical. Under higher dissolution rates (30 ml/min), the aperture field is less heterogeneous compared with lower dissolution rates (0.006ml/min). In addition, the aperture value considering both mechanical deformation and time-dependent deformation is smaller than that considering only dissolution.

Based on the literature review on rock fractures, there is not much work systematically studying the creep mechanism caused by mechanical compression. Kang et al. (2019) reported that for Musandam limestone fractures, the creep deformation under dry conditions is not negligible. Under dry conditions, mechanical compression is the only creep mechanism, suggesting that it should be systematically studied.

2.5 Rough fracture deformation simulation in tribology

Under dry conditions, mechanical compression consists of two mechanisms – viscous deformation of contacting asperities and micro-cracking of contacting asperities – that will cause rock fracture time-dependent deformation. Neither mechanism has been systematically investigated. In this research, the mechanism of micro-cracking will not be considered; only the viscous deformation of contacting asperities will be studied.

In rock mechanics, only the elasto-plastic deformation (no time effect) of rock fractures has been investigated. On the contrary, in tribology, both elasto-plastic and viscous deformation of rough metal or polymer fractures have been explored. Table 2.1 summarizes the current research progress in rock mechanics and tribology. In this research, the methodology used to simulate the viscous deformation of rough fractures in tribology will be used to simulate the viscous deformation of rough rock fractures. In addition, in rock mechanics, a few research groups have been using the same methodologies proposed in tribology to simulate the elasto-plastic deformation of rough rock fractures. Therefore, rough fracture deformation simulation work in tribology will be reviewed first. In this section, three types of deformation simulation work will be reviewed: elastic deformation, elasto-plastic deformation, and visco-elastic deformation.

Table 2.1. Research progress in rock mechanics and tribology related to rough fracture deformation. '√' indicates the area has been investigated, '×'the reverse, and '−'represents uncertain.

Research Field	Topics		
	Elasto-plastic deformation	Visco-elastic deformation	Visco-elasto-plastic deformation
Tribology	√	√	−
Rock Mechanics	√	×	×

Note: It appears that for tribology, the visco-elasto-plastic deformation of rough fractures has not been systematically investigated.

2.5.1 Elastic deformation simulation

In the early years of tribology, theoretical studies were conducted to calculate the rough metal fracture elastic deformation under applied stress in the direction normal to the fracture surface. Before reviewing the theoretical studies, the basic concepts of the Hertz theory (Hertz, 1882) need to be introduced. The Hertz theory has been widely applied in contact mechanics. As shown in Figure 2.43, the Hertz theory describes the contact between two elastic spherical bodies, with a radius of R_1 and R_2, respectively. The radius of the contact area, r_0, can be expressed as:

$$r_0 = \left(\frac{R_1 R_2}{R_1+R_2}\right)^{1/3}\left(\frac{3F(1-\nu^2)}{4E}\right)^{1/3} \tag{2.31}$$

and

$$\frac{1-\nu^2}{E} = \frac{1-\nu_1^2}{E_1} + \frac{1-\nu_2^2}{E_2} \tag{2.32}$$

where E_1 and E_2 are the elastic moduli of the solids and v_1 and v_2 are their Poisson's ratios. The relative movement between the centers of two spheres, s, can be expressed as:

$$s = \left(\frac{R_1+R_2}{R_1R_2}\right)^{1/3}\left(\frac{3F(1-\nu^2)}{4E}\right)^{2/3} \tag{2.33}$$

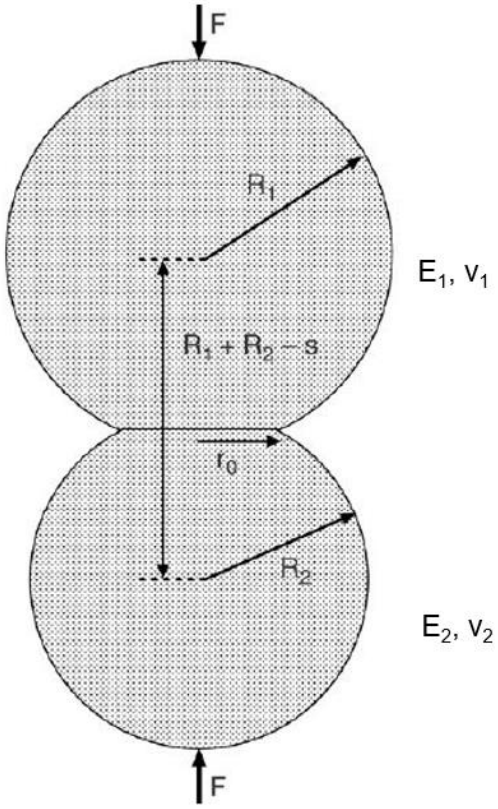

Figure 2.43 Schematic of the Hertz theory – contact between two elastic spheres (Persson, 2005). F is the applied external force, r_0 is the radius of the contact area, and s is the relative movement between two spherical centers.

Greenwood and Williamson (1966) developed closed-form solutions for rough fracture surface elastic deformation using the Hertz theory. They considered a single rough elastic surface being compressed against a rigid horizontal plane. It is worth noting that this assumption is idealized and may not be realistic. For example, if a rough aluminum surface is compressed against a horizontal steel surface, both surfaces will deform. The asperities of the rough surface are spherical and have a radius of curvature R, and the surface height distribution function is $\phi(z)$, where z is the surface elevation. Figure 2.44 shows the schematic of the surface geometry. The contacting stress σ can be calculated as:

$$\sigma = \frac{4E}{3(1-\nu^2)} n_0 \int_d^{+\infty} (z-d)^{\frac{3}{2}} R^{\frac{1}{2}} \phi(z) dz \tag{2.34}$$

where E is the elastic modulus of the rough surface, v is the Poisson's ratio of the rough surface, and n_0 is the number of asperities per unit area.

Figure 2.44 Schematic of Greenwood and Williamson's assumption for surface geometry (1966). All the asperities are circular and have the same radius of curvature R, but the asperity heights (z) are different. All asperities with height z greater than the separation d make contact. The top and bottom surface correspond to the elastic and rigid surface, respectively.

Greenwood and Williamson's model provides a convenient theoretical relation between rough fracture closure and applied compressive stress. However, their model assumes that the contacting asperities are spherical and ignores the interactions of neighboring contacting asperities. In reality, the contacting asperities may not be spherical and may interact with each other. As the applied compressive stress increases, the asperity contacts become more crowded, and the neighboring contacting asperities may interact with each other. To accurately account for the asperity interaction effects, extensive numerical modeling work has been conducted by many research groups. The numerical work includes the finite element method, discrete element method, and boundary element method. For example, Stanley and Kato (1997), Polonsky and Keer (1999), Sahlin et al. (2010), and Wang et al. (2010) used the boundary element method; Fillot et al. (2007) used the discrete element method; Liu et al. (2001) and Pei et al. (2005) used the finite element method.

In this section, the boundary element method will be reviewed. The boundary element method (BEM) has been extensively used in solving rough surface contacting problems for its computational efficiency compared with the traditional finite element method (FEM). The BEM only requires discretization and calculation on the boundaries of the calculation domain, which is two-dimensional. In contrast, the FEM requires discretization and calculation for the whole domain. As a result, to achieve the same stress calculation resolution, the BEM requires many fewer numbers of elements and, therefore, much less calculation time.

In recent years, researchers have been combining the BEM and fast numerical algorithms to achieve more efficient numerical simulations for contacting problems. Before introducing the fast numerical algorithms, it is very important to introduce the equations which need to be solved iteratively in the numerical simulation.

First, the aperture distribution function h (x, y) is defined as:

$$h(x,y) = h_0(x,y) + u_e(x,y) - \delta \tag{2.35}$$

where δ is the rigid-body movement between two surfaces under applied stress in the direction normal to the fracture surface (compression is defined as positive), $h_0(x, y)$ is the initial aperture, and $u_e(x, y)$ is the elastic displacement field between the two contacting surfaces inside the contacting area. Figure 2.45 shows the schematic of Eqn. 2.35.

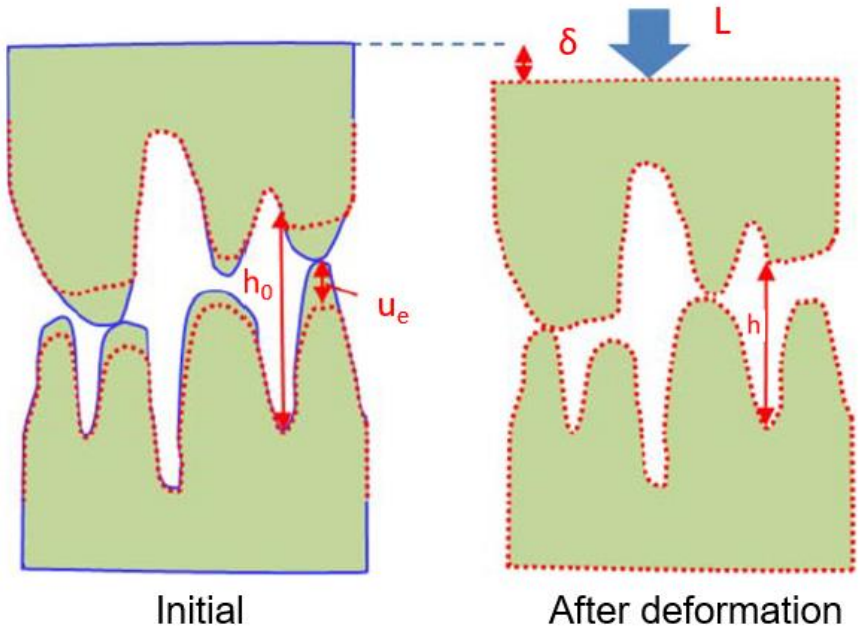

Figure 2.45 Schematic of Eqn. 2.35 (Modified from Wu and Sharma, 2017). The blue solid curves represent the initial surface geometry, and the red dashed curves represent the deformed surface geometry. L represents the load applied normal to the fracture surface.

For two rough surfaces contacting each other, the boundary conditions below need to be satisfied:

$$p(x,y) > 0 \text{ and } h(x,y) = 0 \tag{2.36}$$

$$p(x,y) = 0 \text{ and } h(x,y) > 0 \tag{2.37}$$

where p(x,y) is the contact pressure (in the normal direction) acting on location (x,y). This indicates that the contact pressure is zero at non-contacting areas, and is larger than zero at contacting areas. Compressive stress is defined as positive. Figure 2.46 shows the schematic of Eqns. 2.36 and 2.37.

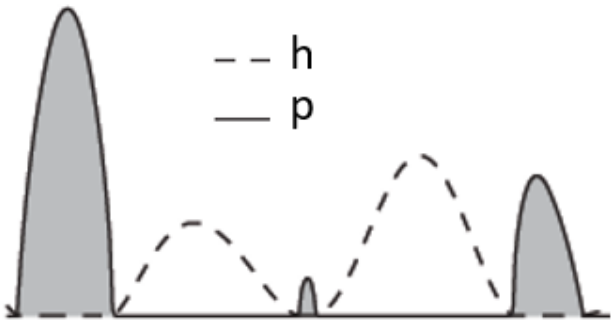

Figure 2.46 Schematic of Eqns. 2.36 and 2.37 (modified from Sahlin et al., 2010). The dashed line represents the aperture field, and the solid line represents the contacting pressure. When the aperture is larger than zero, the contacting pressure is zero; when the aperture is zero, the contacting pressure is larger than zero.

The vertical elastic displacement $u_e(x,y)$ can be calculated from the generalized equation below:

$$u_e(x,y) = \int_{-\infty}^{+\infty}\int_{-\infty}^{+\infty} K(x,y,x',y')p(x',y')dx'dy' \tag{2.38}$$

where $K(x, y, x', y')$ is the influence matrix for normal displacement at surface location B(x,y) due to a normal unit stress applied at location $A(x', y')$, and $p(x', y')$ is the normal stress applied at location $A(x', y')$. Figure 2.47 shows the schematic of the influence matrix.

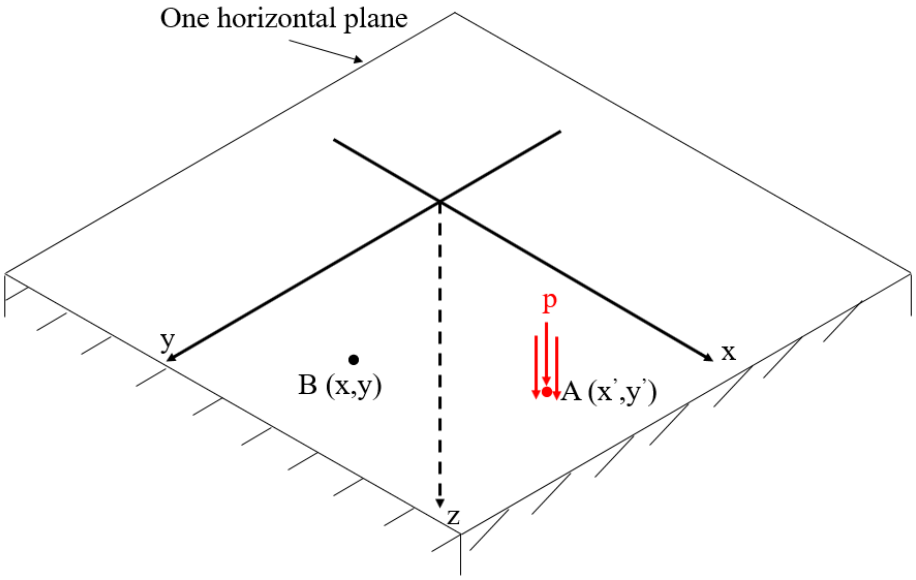

Figure 2.47. Illustration of the Boussinesq solution. A normal stress field p is applied surrounding the location A (x', y'), and $u_e(x,y)$ represents the z-direction elastic displacement at point B (x,y).

The force balance also needs to be satisfied:

$$F = \int_{-\infty}^{+\infty} \int_{-\infty}^{+\infty} p(x', y')\, dx' dy' \tag{2.39}$$

where F is the applied external force on the two fracture surfaces.

Eqns. 2.35, 2.36, 2.37, 2.38, and 2.39 need to be solved iteratively in the numerical simulation. Two numerical algorithms, which greatly reduce the required computational time, will be introduced below.

Stanley and Kato (1997) published the first paper using the fast Fourier Transform (FFT) method to calculate the elastic deformation of rough surfaces under normal stresses. They considered a rigid horizontal plane being compressed against a rough elastic. The rough surface elevation (in 2D) can be described by a cosine function:

$$z(x) = \sum_{n=1}^{5} \cos(nx + \alpha_n) \tag{2.40}$$

where z is the surface elevation, α_n is the phase shift, and is a constant in this example. The initial generated surface is shown in Figure 2.48. They applied a pressure field $p(x', y')$, and used the FFT method to replace Eqn. 2.38:

$$u_e(x, y) = FFT^{-1}(K(x, y, x', y') \times FFT(p(x', y'))) \tag{2.41}$$

By comparing Eqns. 2.38 and 2.41, the FFT method turns complicated convolution into simple matrix multiplication. For a horizontal surface with M and N elements in the x- and y-direction, respectively, the FFT method reduces the number of operations from $N^2 * M^2$ to N*M*log(N*M). Therefore, when N and M values are relatively large, the FFT method can greatly reduce the computational time.

Figure 2.48 shows the simulation results of Stanley and Kato (1997). In their simulation, a rigid horizontal plane was moved downwards against a rough elastic surface. The two figures in the top row represent the undeformed surface and the corresponding contacting pressure distribution field, respectively. The three lower rows represent the deformed surfaces and the corresponding contacting pressure distribution fields. The left column represents the surface profiles, and the right column represents the pressure fields. The pressure field was normalized by the elastic modulus of the surface, E^*.

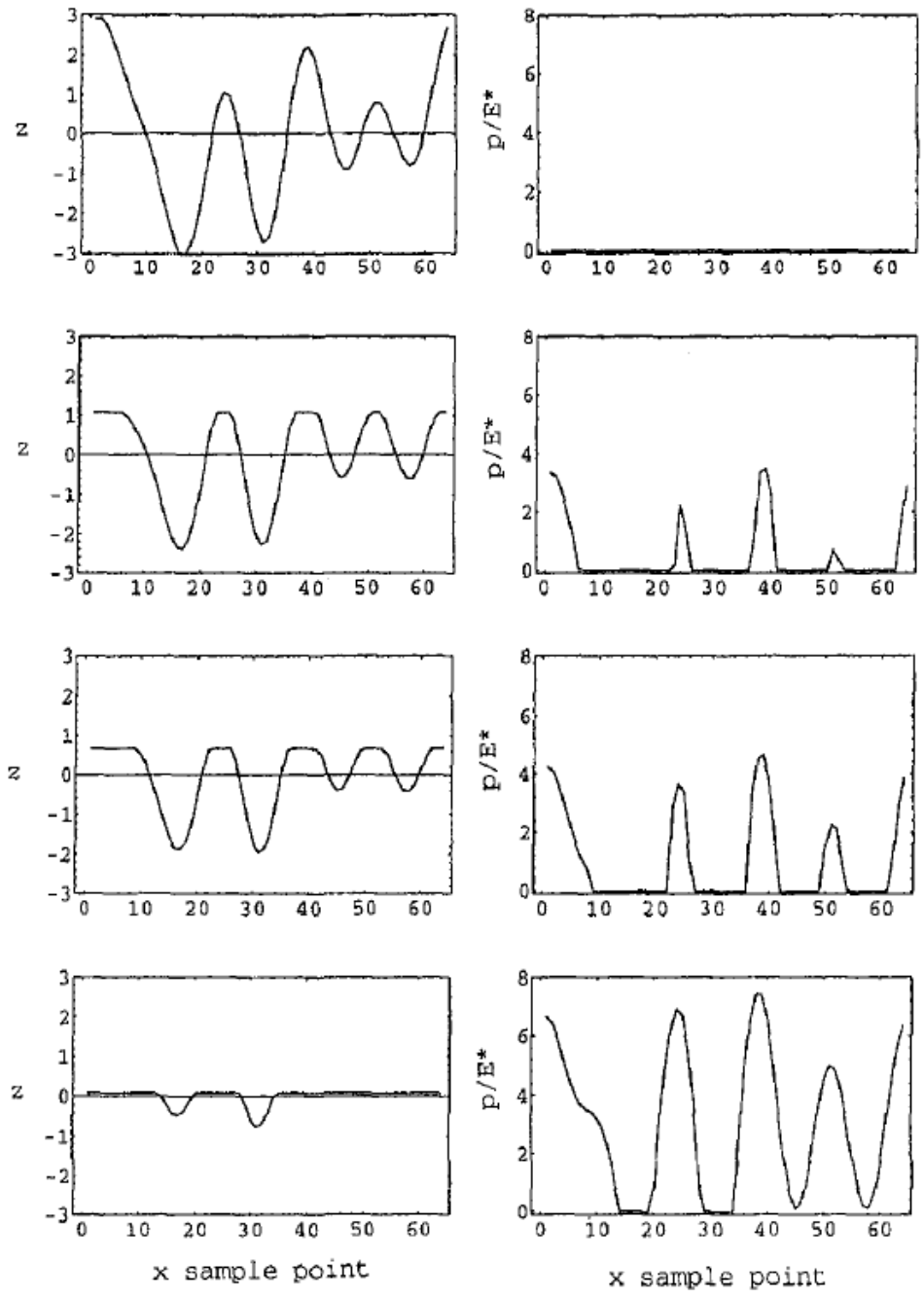

Figure 2.48 Simulation results of Stanley and Kato (1997). Left column: surface profiles. Right column: pressure distribution fields. Top row: the undeformed surface and the pressure distribution field. The rigid horizontal plane is at z = 3, and there is not contacting pressure between the two surfaces. Second row: the deformed surface and the pressure distribution field. The rigid horizontal plane moves downwards to z = 1. As a result, the rough surface becomes flat at z = 1 (the maximum surface elevation is z = 1), and the contacting pressure at z = 1 becomes non-zero. Third row: the deformed surface and the pressure distribution field. The rigid horizontal plane moves downwards to z = 0.75. As a result, the rough surface becomes flat at z =

0.75 (the maximum surface elevation is z = 0.75), and the contacting pressure at z = 0.75 becomes non-zero. Bottom row: the deformed surface and the pressure distribution field. The rigid horizontal plane moves downwards to z = 0.05. As a result, the rough surface becomes flat at z = 0.05 (the maximum surface elevation is z = 0.05), and the contacting pressure at z = 0.05 becomes non-zero. Most regions of the rough surface are in contact with the rigid horizonal plane.

Later, Polonsky and Keer (1999) implemented another efficient numerical method, which is called the conjugate gradient (CG) method. The CG method is an iterative method for solving systems of linear equations, and it was originally developed for optimization. There exists a rigorous mathematical proof of the method convergence. The proof is provided in Hestenes' (1980) book (*Conjugate Direction Method in Optimization*), and will not be shown in this section. They used the CG method to solve Eqns. 2.35, 2.36, 2.37, 2.38, and 2.39 iteratively; for Eqn. 2.38, they used the Boussinesq equation. The details of implementing the CG method and the Boussinesq solution will be introduced in the methodology section. Polonsky and Keer (1999) reported that the CG method greatly reduces the required computation time. It is worth noting that they did not apply the FFT technique (see Eqn. 2.41) to further increase the calculation speed when solving Eqn. 2.38.

Figure 2.49 shows the simulation results of one of the examples of Polonsky and Keer (1999). The example considered an elastic rough surface moving against a horizontal rigid plane. The elastic modulus of the surface is 210 GPa, the Poisson's ratio of the surface is 0.28, and the applied compressive stress on the surface is 848 MPa. The top figure represents the surface geometry before applying the compressive stress, and the bottom figure represents the pressure distribution field after applying the compressive stress.

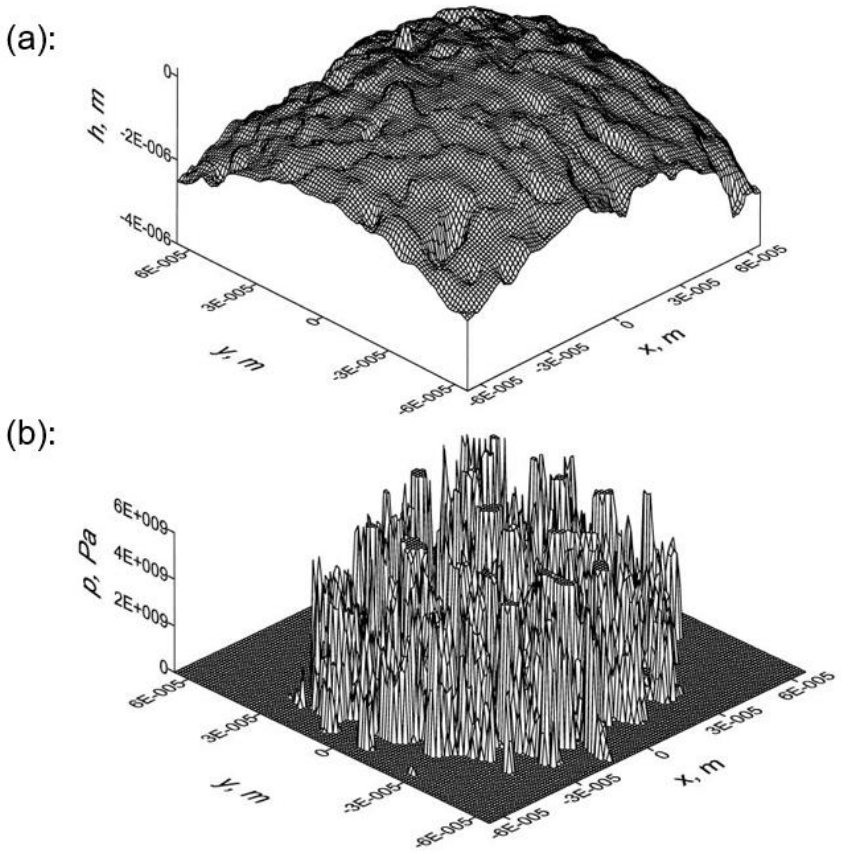

Figure 2.49 Results summary for a rough contact problem (Polonsky and Keer, 1999). (a): surface elevation before applying compressive stress; (b): contact pressure distribution after applying compressive stress (They did not provide the deformed surface profile). The contact pressure at some asperities exceeds 4 GPa.

Soon after Polonsky and Keer (1999), Ai and Sawamiphakdi (1999) combined the CG method and the FFT method to solve elastic contact between rough surfaces. After Ai and Sawamiphakdi (1999), most research groups have been combining the CG and the FFT methods to calculate the elastic deformation of rough surfaces.

2.5.2 Elasto-plastic deformation simulation

When a rough fracture is subjected to compressive stresses, the contacting pressure at some asperities can reach the magnitude of GPa. If only the elastic deformation is considered, there is no upper limit on the contacting pressure. However, under such a high contacting pressure, plastic yielding may occur, especially for rough metal surfaces. Therefore, to obtain more accurate simulation results, extensive research work has been conducted on elasto-plastic deformation simulation, which considers the plastic yielding of contacting asperities. In this section, two typical examples will be reviewed. The first example is the '1-D criterion': an element will start to deform plastically once the vertical compressive stress reaches a threshold value, only considering the

vertical compressive stress (Sahlin et al., 2010). The second example considers the '3-D criterion': an element will start to deform plastically once the von Mises stress (this will be defined later) reaches a threshold value (Jacq et al., 2002), considering the stress in three dimensions. Mathematically, the '1-D criterion' can be expressed as:

$$0 \leq \mathrm{p} \leq p_{max} \tag{2.42}$$

where p is the vertical compressive stress and p_{max} is the threshold value. The indentation hardness value is often used as p_{max}.

The '3-D criterion can be mathematically expressed as:

$$0 \leq \sigma_{Mises} \leq \sigma_{yield} \tag{2.43}$$

where σ_{Mises} is the von Mises stress, and σ_{yield} is the yield strength.

For the '1-D criterion', Sahlin et al. (2010) first proposed a numerical approach that uses the FFT method to calculate the elastic-perfectly plastic displacement due to surface asperity contact. The approach is similar to that proposed by Stanley and Kato (1997), but a major difference is that Sahlin et al.'s model considers the plastic deformation of the asperities. In Sahlin et al.'s model, once the vertical compressive pressure in the contacting asperity reaches a threshold value, the contacting asperity will deform and the vertical compressive pressure will not increase. Figure 2.50 shows the schematic of the model. (Note: to fully explain the numerical model, I need at least five more pages. In addition, in my research, I did not model the plastic deformation of contacting asperities. Therefore, I only used one page to briefly summarize their work.)

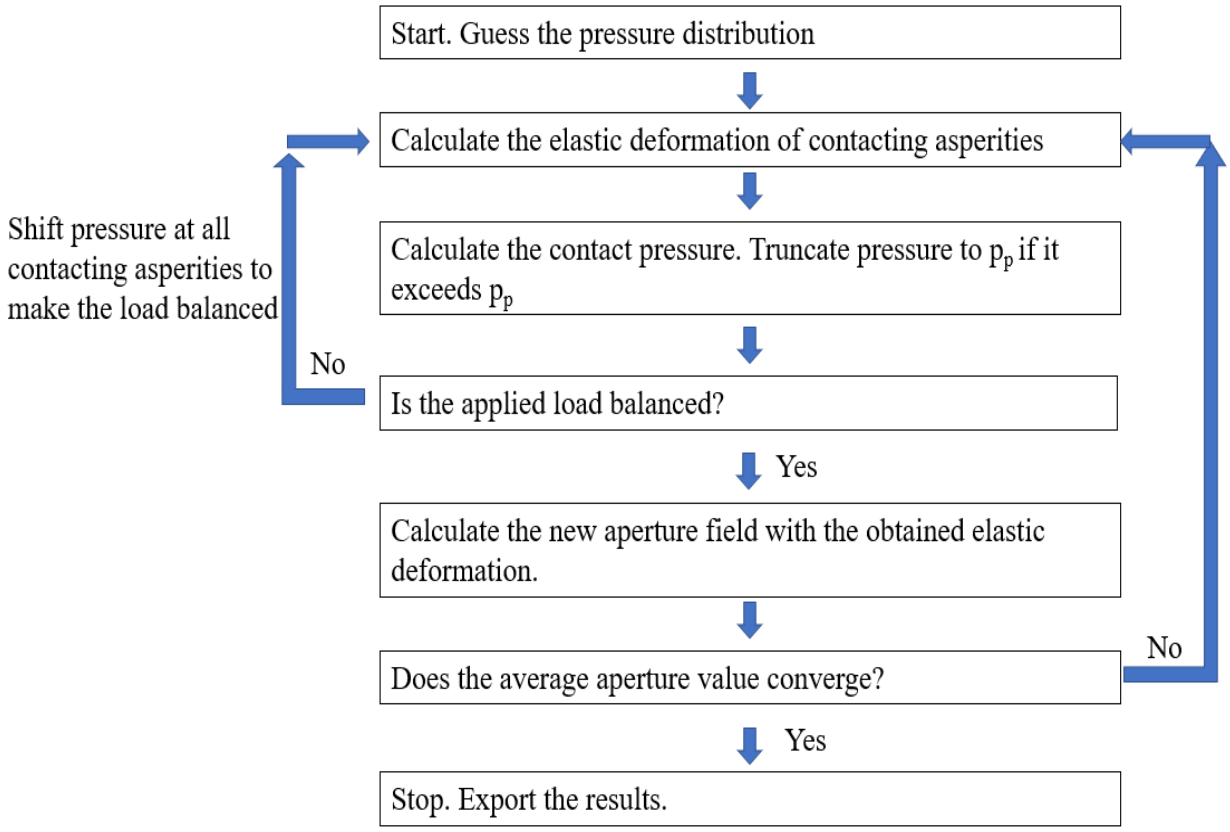

Figure 2.50 Schematic of Sahlin et al.'s (2010) numerical model (modified from Sahlin et al., 2010). p_p is the upper limit of contact pressure acting on the contacting asperities.

For the '3-D criterion', Jacq et al. (2002) first proposed a numerical approach that uses the FFT method to calculate the elastic perfectly plastic displacement due to surface asperity contact. They developed a numerical code which calculates the stresses in 3D (σ_{11}, σ_{22}, σ_{33}, σ_{12}, σ_{23}, σ_{13}), and Figure 2.51 shows the schematic of 3D stresses. In contrast, Sahlin's (2010) model or previous elastic deformation simulation models only calculate σ_{22}. The von Mises stress could therefore be calculated:

$$\sigma_{Mises} = \sqrt{0.5(\sigma_{11} - \sigma_{22})^2 + 0.5(\sigma_{22} - \sigma_{33})^2 + 0.5(\sigma_{33} - \sigma_{11})^2 + 3\sigma_{12}^2 + 3\sigma_{23}^2 + 3\sigma_{13}^2} \quad (2.44)$$

and Figure 2.52 shows the schematic of the von Mises stress. Once the von Mises stress exceeds the yield stress, the asperity will deform plastically.

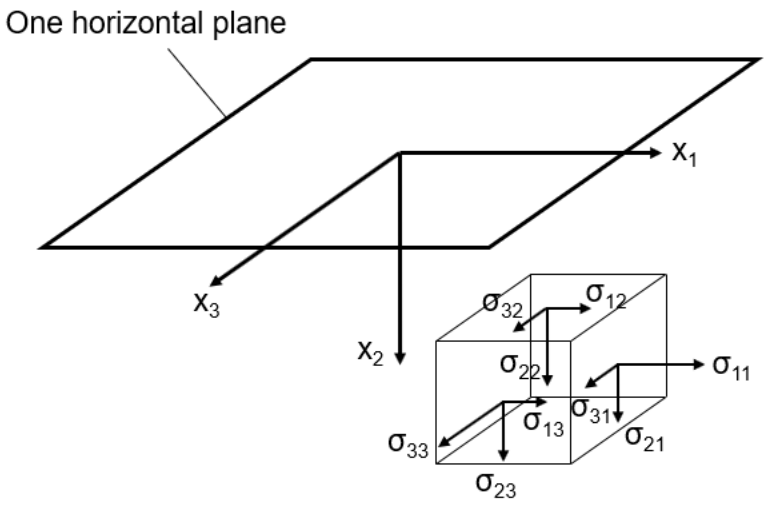

Figure 2.51 Schematic of σ_{11}, σ_{22}, σ_{33}, σ_{12}, σ_{23}, σ_{13}. Direction x_2 is identical to the z-direction in Figure 2.39.

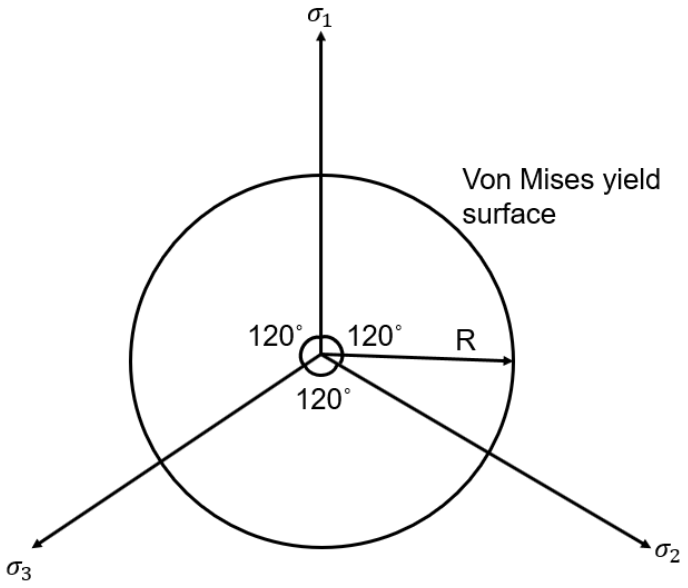

Figure 2.52. Schematic of the von Mises yield surface in principal stress coordinates. σ_1, σ_2, and σ_3 represent three principal stresses, and the hydrostatic axis ($\sigma_1 = \sigma_2 = \sigma_3$) is perpendicular to the paper. The von Mises yield surface circumscribes a cylinder around the hydrostatic axis, and the radius $R = \sqrt{2/3}\sigma_{Mises}$.

Wang et al. (2010) used Jacq et al.'s approach to simulate an indentation problem. In their simulation, a rigid plane was moved against a quarter circle under normal load, as shown in Figure 2.53. The normal load was 800 N, the hemisphere radius was 20 mm, the elastic modulus was 100 GPa, the Poisson's ratio v was 0.3, and the yield strength σ_{yield} was 600 MPa. Figure 2.54 compares the von Mises stress field obtained by their numerical code and that obtained by ABAQUS. The

results indicate that the stress fields are very similar. Thus, Wang et al. (2010) stated that using the '3-D criterion' can accurately predict the displacement and stress fields.

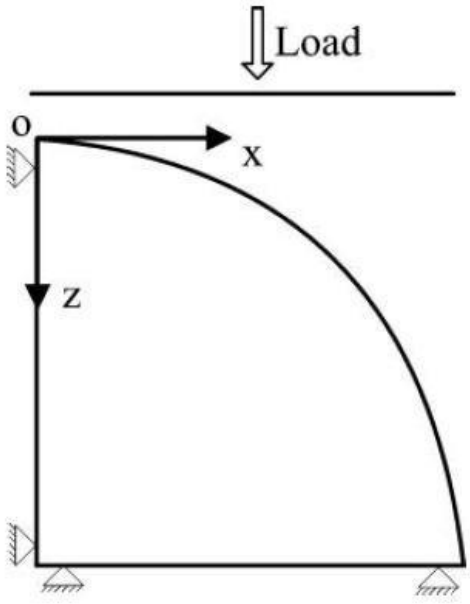

Figure 2.53 Schematic of the geometry setup in Wang et al.'s (2010) simulation.

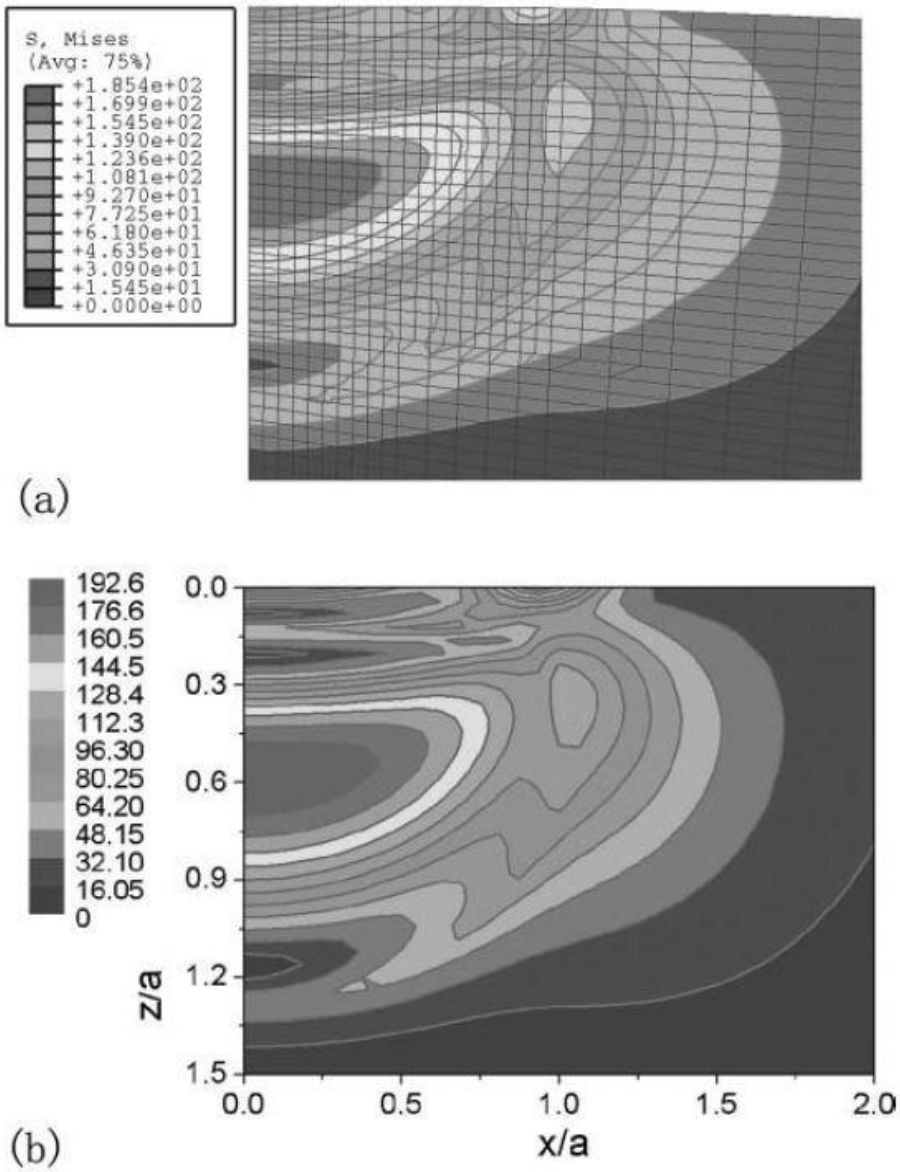

Figure 2.54 Comparison of von Mises stress fields obtained by the numerical code of Wang et al. (2010) and ABAQUS (also simulated by Wang et al. 2010). The upper figure represents the results produced by ABAQUS, and the lower figure represents the results simulated by the code. a is the radius of the contact area when no plasticity is applied (purely elastic model).

2.5.3 Visco-elastic deformation simulation

Chen et al. (2011) first used the CG and FFT method to simulate visco-elastic deformations of rough polymer fractures, and their method will be used in this research. In this section, their simulation work will be introduced briefly. To simulate the visco-elastic deformation, they made two key assumptions.

First, they assumed that the material is linearly visco-elastic. This means that the stress/strain response scales linearly with the stress/strain input, and follows the law of linear superposition. For any arbitrary series of stress or strain inputs, the outputs can be expressed as:

$$\varepsilon(t) = \int_0^t J(t-\tau)\frac{d\sigma(\tau)}{dt}d\tau \tag{2.45}$$

$$\sigma(t) = \int_0^t E_r(t-\tau)\frac{d\varepsilon(\tau)}{dt}d\tau \tag{2.46}$$

where $E_r(t)$ and $J(t)$ are the relaxation modulus function and creep compliance function, respectively. $E_r(t)$ (unit: pressure) describes the time-dependent stress response to a step-change in strain, and $J(t)$ (unit: 1 / pressure) describes the time-dependent strain response to a step-change in stress. τ represents the time variable in the integration, and its range is $0 \leq \tau \leq t$ (this means that t is a constant and τ is the variable). Figure 2.55 explains the creep compliance and relaxation modulus.

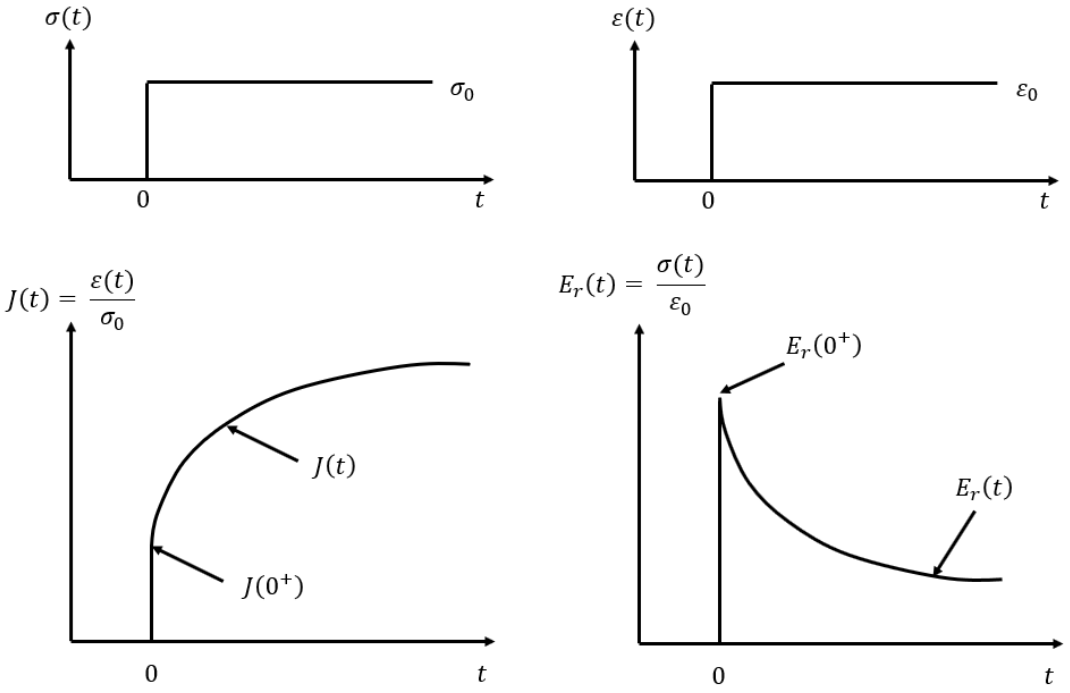

(a): Schematic for creep compliance (b): Schematic for relaxation modulus

Figure 2.55. Schematic for creep compliance and relaxation modulus. (a): schematic for creep compliance under a constant stress σ_0. $J(0^+)$ represents the creep compliance at the moment when σ_0 is applied, and $J(0^+)$ is equal to the elastic modulus. (b): schematic for relaxation modulus under a constant strain ε_0. $E_r(0^+)$ represents the relaxation modulus at the moment when ε_0 is applied, and $E_r(0^+)$ is equal to the elastic modulus.

Compared with linear elastic simulations, the difficulty for linear visco-elastic simulations comes from the stress history. Based on Eqns. 2.45 and 2.46, determination of surface deformation and contact pressure at the present time relies on the pressure history during the past time. To simplify the calculation, Chen et al. (2011) discretized the time into many small time steps, with a uniform

time interval. They made the second assumption: the time interval is sufficiently small such that the pressure field at each time step is unchanged. Between different time steps, the pressure fields are different. This assumption will be further explained in the Methodology Section. Within each time step, the CG and FFT methods (introduced in Section 2.5.1) are used to calculate the pressure and displacement fields. The pressure field will be saved as pressure history. Then, a new time step will be added, and the new pressure and displacement fields will be solved. Figure 2.56 shows the schematic of the calculation procedure. The details of Chen et al.'s method will be explained in the Methodology Section (Section 3).

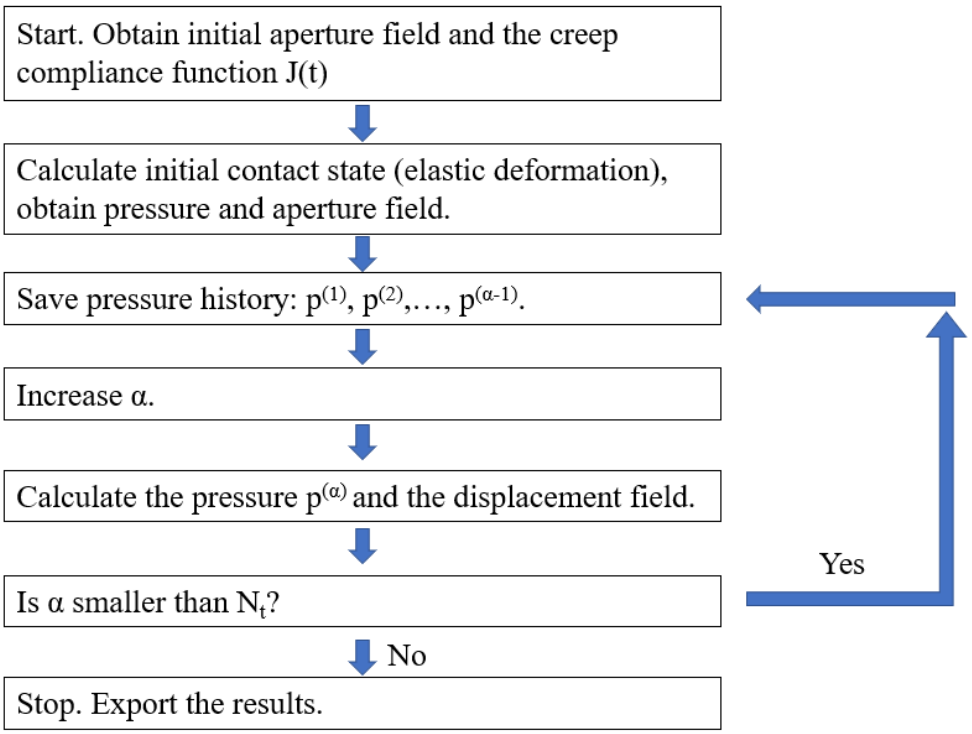

Figure 2.56 Schematic of the calculation procedure. N_t corresponds to the total number of time steps, and $\alpha = 1, 2, \ldots, N_t$. After each step, α is increased by one. The effect of pressure history on the displacement field will be explained in the Methodology Section (Section 3).

They validated their numerical simulation results against analytical solutions. In their simulation, a spherical rigid body is indented into a flat surface, and the flat surface satisfies the Maxwell visco-elastic model (see Section 2.1.3.2 for detailed explanations). Figure 2.57 shows the geometry for the validation example, and Figure 2.58 compares the pressure distribution fields beneath the spherical rigid body for numerical and analytical solutions. The solid lines represent analytical solutions obtained by Lee and Radok (1960), and the dots represent the numerical solutions obtained by Chen et al. (2011). p represents the pressure field acting on the contacting region, p_0 represents the maximum pressure when the time is zero (no creep, the solution is a Hertzian contact solution), a_0 represents the radius of the contacting region when the time is zero, and τ represents the relaxation time ($\tau = \eta / G$, see Figure 2.5 for the definitions). Based on Figure 2.58, the

difference between the numerical and analytical solutions is less than 10%. Thus, Chen et al. (2011) stated that the numerical results match analytical results well.

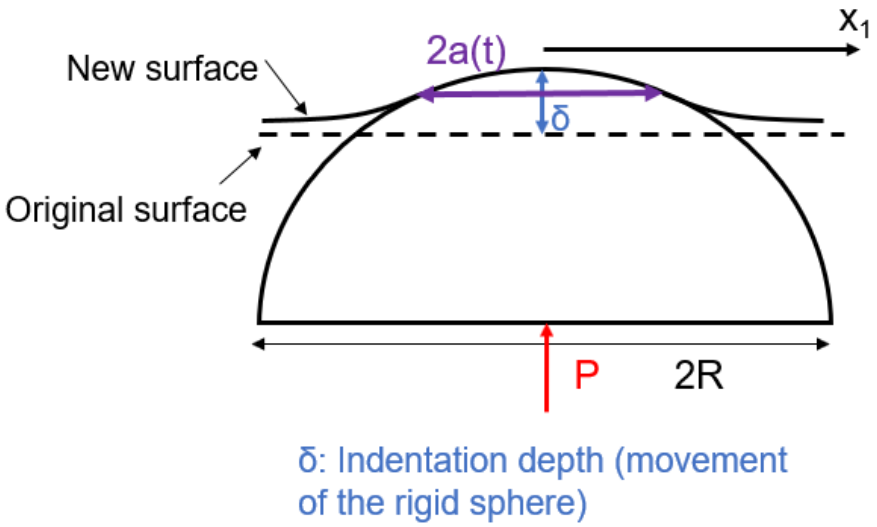

Figure 2.57 Geometry of the validation example (modified from Chen et al, 2011). x_1 represents the distance from the center of the contacting region, P represents the applied load, R represents the radius of the rigid spherical body, and a(t) represents the radius of the contacting region (the radius changes with time).

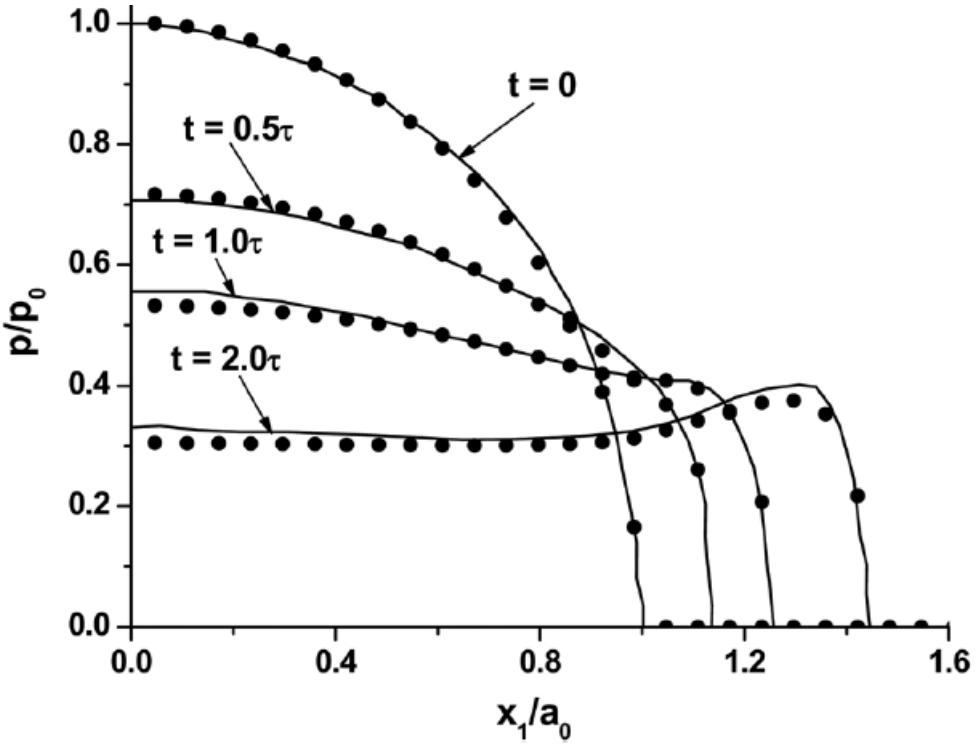

Figure 2.58. Comparison of numerical and analytical solutions (Chen et al., 2011).

To further demonstrate the numerical model's capacity, Chen et al. (2011) simulated the visco-elastic displacement of rough surfaces (this was a new surface geometry compared with that of the previous example). A spherical rigid body, with a radius of 3.5 mm, was indented into a rough surface, and the rough surface satisfies the Maxwell visco-elastic model. Three rough surfaces, with different root mean square (RMS) roughness values (1.0, 2.5, and 5.0 mm), were used. The applied load was 100 N and the time duration was 300 sec. Figure 2.59 shows the simulation results. The results indicate that as the root mean square roughness value decreased, the contact area increased faster with time.

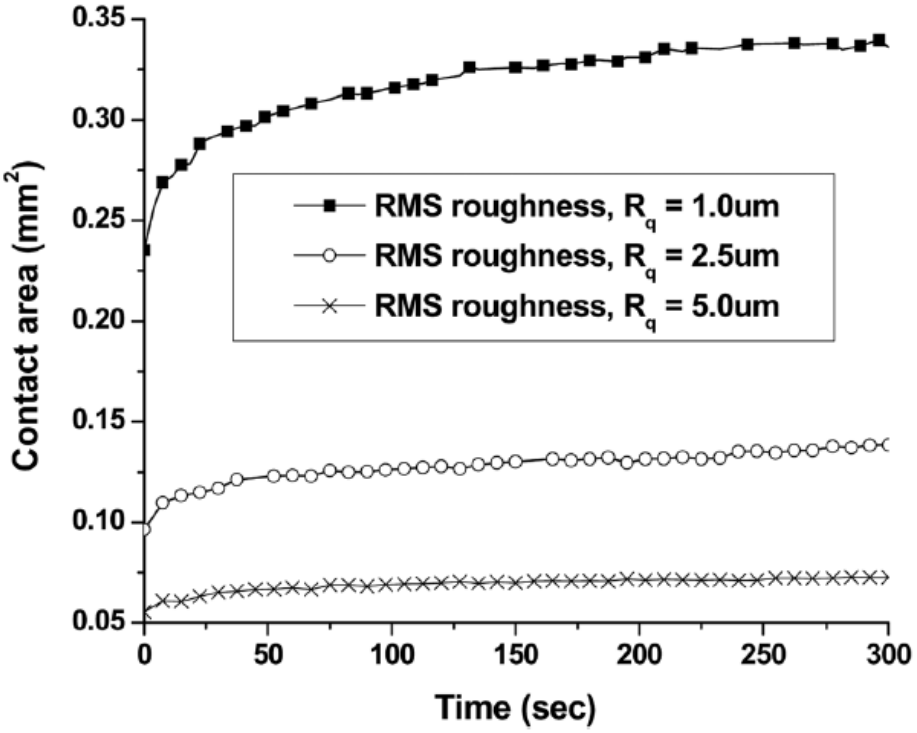

Figure 2.59. Contact area evolution of three surfaces with different root mean square roughness values (Chen et al., 2011).

Hence, in tribology, the elastic, elasto-plastic, and visco-elastic deformations of rough fracture surfaces have been extensively investigated, and mature numerical simulation methods have been developed. Therefore, a few research groups in rock mechanics have been applying the techniques in tribology to rock fracture deformation simulation. For example, Hansen et al. (2000), Lang et al. (2015), and Kang et al. (2016) used the techniques in tribology to simulate the elastic deformation of rough rock fractures, and Kling et al. (2018) and Zou et al. (2020) used the techniques in tribology to simulate the elasto-plastic deformation of rough rock fractures. The literature on rough rock fracture deformation simulation will be reviewed.

2.6 Rock fracture surface deformation simulation under dry conditions

In this section, the literature related to rough rock fracture deformation simulation under normal stresses will be reviewed. The early theoretical and numerical models will be briefly introduced first, followed by the work using the CG + FFT method.

2.6.1 Early theoretical and numerical models

Extensive theoretical and numerical studies have been conducted to establish relationships between normal stress and normal deformation of rock fracture. In the early years, empirical relationships between normal stress and rock fracture normal closure were obtained via experiments (Goodman, 1976; Barton et al., 1985; Bandis et al., 1983). Theoretical studies were also conducted to calculate rock fracture deformation (Brown and Scholz, 1985; Brown and Scholz, 1986; Myer, 2000). Most of these theoretical studies used the Greenwood-Williamson (GW) model, which describes the elastic contact of a random and nominally flat surface based on the elastic Hertzian contact theory (Greenwood and Williamson, 1966; Brown and Scholz, 1985; Brown and Scholz, 1986). However, as stated before, the GW model assumes that the contacting asperities are spherical and ignores the interactions of neighboring contacting asperities. In reality, the contacting asperities may not be spherical and may interact with each other.

Numerical studies have also been conducted to consider the asperity interaction. Hopkins (1991) developed a numerical model that simplifies the asperity geometry as circular disks with varying heights. Figure 2.60 shows the schematic of the model. The model considers three elastic deformable components, including the cylindrical asperities, the upper surface, and the lower surface. Different circular disk heights correspond to different aperture values, and the circular disks have the same radius a. The deformation of the upper and lower surface is calculated using the Boussinesq solution for the normal deformation of a surface under a uniformly loaded circle (Timoshenko, 1970). Hopkins (1991) assumed that for each contacting asperity (the cylindrical disks touching both the upper and lower surfaces), the contacting stress distribution along the contacting area is uniform. For the points beneath the loaded circle, the deformation w is given by:

$$w(r < a) = \frac{4(1-\upsilon^2)qa}{\pi E}\int_0^{\pi/2}(1 - \frac{r^2}{a^2}sin^2\theta)d\theta \tag{2.47}$$

where r is the distance to the center of the loaded circle, v is the Poisson's ratio, E is the elastic modulus, a is the radius of the circle, and q is the average compressive stress acting on the loaded circle. For the points outside the loaded circle, the deformation w is given by:

$$w(r > a) = \frac{4(1-\upsilon^2)qa}{\pi E}[\int_0^{\frac{\pi}{2}}\left(1 - \frac{r^2}{a^2}sin^2\theta\right)d\theta - (1 - \frac{r^2}{a^2})\int_0^{\pi/2}\frac{d\theta}{1-\frac{r^2}{a^2}sin^2\theta}] \tag{2.48}$$

The deformation of the circular disks is calculated as:

$$\Delta h_i = \frac{qh_i}{E} \tag{2.49}$$

where h_i and Δh_i are the initial height and the deformation of the circular disk, respectively. Eqns. 2.47, 2.48, and 2.49 are used to determine the deformation of the upper surface, the lower surface, and the asperities under applied normal load. The other details of this numerical method are shown in Hopkins (1991) or Pyrak-Nolte and Morris (2000).

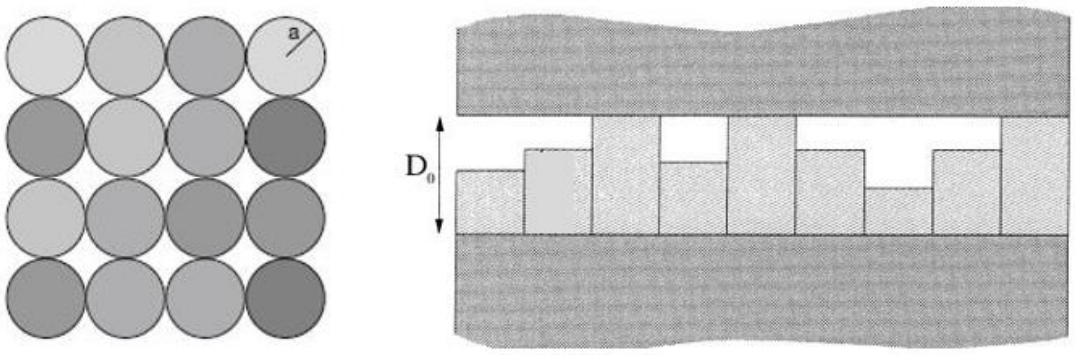

Figure 2.60. A schematic of the Hopkins (1991) model (the figure is from Pyrak-Nolte and Morris, 2000). The left figure represents the plan view of the fracture. The fracture surface is assumed as cylindrical asperities arranged in a regular grid. The radius of the cylinders is a, and the shades of grey represent different asperity heights. Darker color corresponds to larger asperity heights. The right figure represents the font view of the fracture. The upper and lower surfaces are separated by the cylindrical asperities, and the initial separation distance is D_0. As the fracture is being compressed, the separation distance will be reduced, and more cylindrical disks will be in contact with the upper and lower surfaces.

Since the Hopkins' model considers the interactions of neighboring contacting asperities, it was used in many later numerical studies (Hopkins, 2000; Pyrak-Nolte and Morris, 2000; Gentier et al., 2013; Pyrak-Nolte and Nolte, 2016; Wang and Cardenas, 2016). In this section, the numerical study of Pyrak-Nolte and Morris (2000) will be very briefly introduced. Pyrak-Nolte and Morris (2000) numerically generated different fracture surface geometries with different degrees of spatial correlation. Then, compressive stress normal to the fracture surface was applied. Under each compressive stress, the asperity deformation was calculated using the Hopkins's (1991) numerical model. In addition, the hydraulic conductivity of the fracture was numerically determined using the local cubic law. When the applied normal stress was increased from one step to the next, the fracture specific stiffness was calculated as:

$$\kappa = \frac{\Delta\sigma}{\Delta\delta} \tag{2.50}$$

where κ is the fracture specific stiffness, $\Delta\sigma$ is the change of applied stress normal to the fracture surface, and $\Delta\delta$ is the fracture closure when the normal stress was increased from one step to the next.

Figure 2.61 shows different fracture surface geometries under different normal compressive stresses, and Figure 2.62 shows the fracture specific stiffness changing with normal compressive

stress for different surface geometries. The results indicate that the fracture surface geometry has a dominant effect on the fracture specific stiffness and the contacting region distribution.

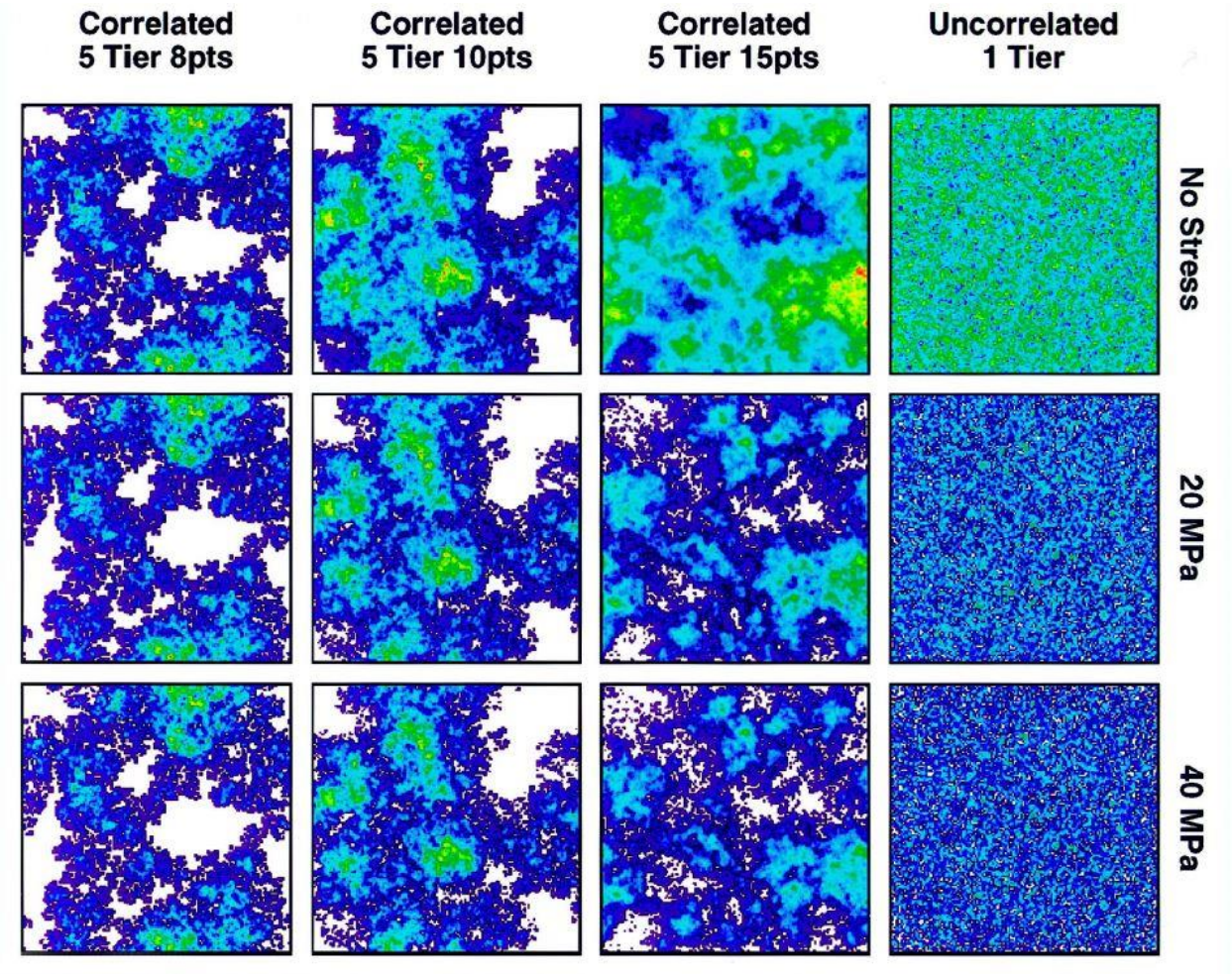

Figure 2.61 Different fracture surface geometries under different normal compressive stresses (Pyrak-Nolte and Morris, 2000). White regions represent contact area, and increasing shades from purple to red represent increasing aperture (red represents the largest aperture, and purple represents the smallest aperture). The same color scale was used for all three stresses but varies among the 1 tier, 5 tier 8 points, 5 tier 10 points, and 5 tier 15 points simulated fractures. The degree of spatial correlation increases with increasing tier number or decreasing point number. 'Tier' meant scale in their work; the scale decreased with increasing number of tiers (the scale of the first tier was the largest). In the surface generation process, several (n points per tier) randomly positioned, equal size squares were chosen within the array defining the fracture plane (first tier). Within each square (the second tier), n smaller squares were chosen. The sub-squares were reduced in linear size by a constant scale factor relative to the previous tier square size. The process was continued until the final tier was reached. Each time a point overlaps a previously plotted point, the aperture was increased by one unit. The details could be found in Pyrak-Nolte and Morris' (2000) paper. From left to right are 5 tier 8 points correlated fracture, 5 tier 10 points

correlated fracture, 5 tier 15 points correlated fracture, and uncorrelated fracture 1 tier. From top to bottom are the fracture geometries under no stress, 20 MPa normal stress, and 40 MPa normal stress. As the applied stress increases, the fracture aperture is reduced, and the contact area increases.

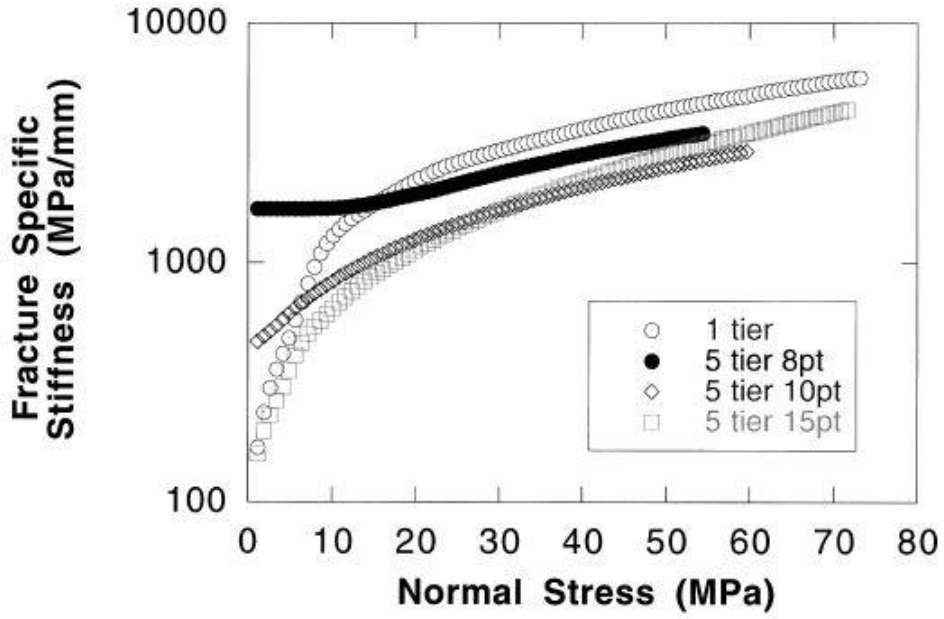

Figure 2.62 Fracture specific stiffness changing with normal stress for different surface geometries (Pyrak-Nolte and Morris, 2000).

2.6.2 Numerical simulation work using the CG + FFT method

Although the Hopkins' (1991) model considers asperity interaction, it still simplifies the asperity geometry. As described in Section 2.5, in tribology, the CG + FFT method does not require specific geometrical simplifications on the shape of the asperities. Therefore, in recent years, a few research groups in rock mechanics have started using the CG + FFT method to simulate fracture deformation (Hansen et al., 2000; Lang et al., 2015; Li et al., 2015; Kang et al., 2016; Wu and Sharma, 2017; Kling et al., 2018; Zou et al., 2020). Most of the studies only simulated the elastic deformation of rough fractures (Hansen et al., 2000; Lang et al., 2015; Kang et al., 2016), while the studies conducted by Li et al. (2015), Wu and Sharma (2017), Kling et al. (2018), and Zou et al. (2020) used the '1-D criterion' (explained in Section 2.5.2) to simulate the elasto-plastic deformation of rough fractures. Table 2.2 summarizes the fracture deformation simulation work in rock mechanics using the CG + FFT method.

For elasto-plastic deformation simulation, elastic modulus E, Poisson's ratio ν, and indentation hardness H were the input parameters. The indentation hardness H was considered as the maximum contacting pressure (see Eqn. 2.42). Therefore, the '1-D criterion' was expressed as:

$$0 \leq p \leq H \tag{2.51}$$

Eqns. 2.35, 2.36, 2.37, 2.39, 2.41, and 2.51 were solved iteratively using the CG method.

Table 2.2. Summary of fracture deformation simulations in rock mechanics using the CG + FFT method. The input parameters were elastic modulus E, Poisson's ratio ν, and indentation hardness H (modified from Kling et al. (2018)).

References	Fracture surface type	Surface generation method	Deformation type	Input parameters
Hansen et al. (2000)	Tensile granite fracture	Profilometer measurement	Elastic deformation	E, ν
Lang et al. (2015)	Synthetic (computer-generated) fracture surface	Fractal surface	Elastic deformation	E, ν
Li et al. (2015)	Tensile novaculite fracture	Profilometer measurement	Elasto-plastic deformation, '1-D criterion'	E, ν, H
Kang et al. (2016)	Synthetic fracture surface	Fractal surface	Elastic deformation	E, ν
Wu and Sharma (2017)	Synthetic fracture surface	Gaussian surface	Elasto-plastic deformation, '1-D criterion'	E, ν, H
Kling et al. (2018)	Tensile granodiorite fracture	Profilometer measurement	Elasto-plastic deformation, '1-D criterion'	E, ν, H
Zou et al. (2020)	Tensile granite fracture	Profilometer measurement	Elasto-plastic deformation, '1-D criterion'	E, ν, H

(continued)

References	Purpose of the numerical model	Was the model validated against fracture closure experimental data?
Hansen et al. (2000)	Study the effect of surface geometry parameters on fracture elastic deformation (sensitivity analysis)	No
Lang et al. (2015)	Obtain the stress field at the contacting asperities to predict pressure solution	No
Li et al. (2015)	Obtain the stress field at the contacting asperities to predict pressure solution	No

Kang et al. (2016)	Simulation of fracture closure, then study the transport pattern	No
Wu and Sharma (2017)	Predict fracture hydraulic conductivity under normal stresses	No
Kling et al. (2018)	Simulate fracture deformation under dry conditions	Yes
Zou et al. (2020)	Simulate fracture deformation under dry conditions, and relate fracture stiffness to surface roughness parameters	Yes

Based on Table 2.2, all the elasto-plastic work used the '1-D criterion'. In other words, it appears that no elasto-plastic work used the '3-D criterion'. For the elastic or elasto-plastic simulations, only Kling et al. (2018) and Zou et al. (2020) validated their numerical results against fracture closure experimental data. In their validation processes, they fitted their simulated stress – displacement curves to the experimental data by adjusting the H values. Figure 2.63 shows the schematic of the validation process.

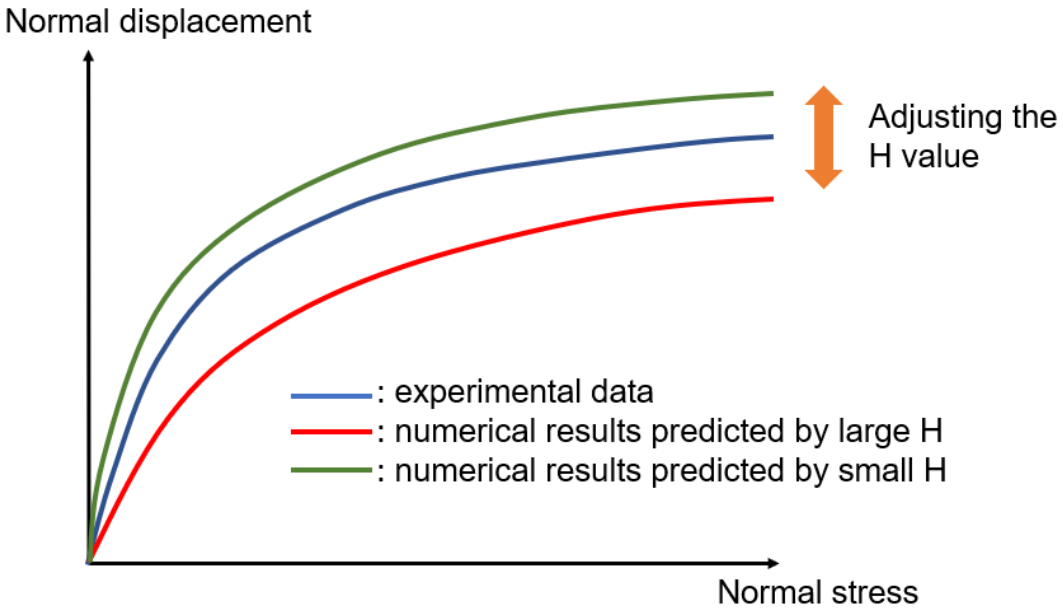

Figure 2.63. Schematic of the validation work conducted by Kling et al. (2018) and Zou et al. (2020). It is worth noting that to make the simulated curve match the measured curve, the H value was adjusted by trial and error; it was not obtained directly from indentation measurements.

Kling et al. (2018) reported that for a tensile granodiorite fracture, when $H = 0.14\ E^*$ ($E^* = 2(1 - \nu^2) / E$, E is the elastic modulus, and ν is the Poisson's ratio), the simulated displacement-stress curve matches experimental data reasonably well. Zou et al. (2020) stated that for tensile granite fracture, when $H = 0.13\ E^*$, the simulated displacement-stress curve fits the measured curve.

However, neither group compared the locations and areas of the contacting regions between numerical results and experimental measurements. Therefore, the numerical models proposed by Kling et al. (2018) and Zou et al. (2020) may not be able to accurately predict the locations and areas of the contacting regions. In addition, both groups obtained the H / E^* value for only one type of rock and only one type of fracture. Between different rock types (igneous rocks, sedimentary rocks, and metamorphic rocks) and different fracture types (tensile and shear fractures), the H / E^* values may be different.

It appears that in rock mechanics, no group has used the CG + FFT method to simulate visco-elastic or visco-elasto-plastic deformations of rock fractures. Kang et al. (2019) reported that for Musandam limestone fractures, the time-dependent deformation under dry conditions is not negligible. Under dry conditions, two mechanisms – viscous deformation of contacting asperities and micro-cracking of contacting asperities – will cause rock fracture time-dependent deformation. Therefore, the visco-elastic or visco-elasto-plastic deformations of rock fractures can be systematically simulated to investigate their significance, and the CG + FFT method can be used.

2.7 Literature review summary and research motivation

As stated in the Introduction Chapter, the research goal of this thesis is to study: (1) the effect of fracture surface geometry on fracture visco-elastic deformation; (2) the effect of size and time duration on rock creep behavior. To that end, the literature review results presented in this thesis and the corresponding knowledge gaps can be summarized as follows:

(i) As shown in Section 2.4, rock fracture creep is caused by four mechanisms: mechanical compression, pressure solution, dissolution, and erosion. The effects of pressure solution, dissolution, and erosion on rock fracture creep have been extensively investigated both experimentally and numerically. However, the effect of mechanical compression on rock fracture creep has not been adequately researched.

(ii) Based on Section 2.5, in tribology, the elastic, elasto-plastic, and visco-elastic deformations of rough fracture surfaces has been extensively investigated, and mature numerical simulation methods have been developed. According to Section 2.6, some research groups in rock mechanics have been applying the methods in tribology to simulate the elastic and elasto-plastic deformations of rock fractures. However, it appears that no group in rock mechanics has numerically simulated visco-elastic deformations of rock fractures. The visco-elastic deformations of rock fractures could be numerically determined using the techniques developed in tribology.

(iii) As shown in Section 2.3, the fracture surface geometry can be well described by a Gaussian surface height distribution function and a self-affine spatial correlation function. Those two functions will be used to generate and describe fracture surfaces, and the detailed generation process will be introduced in the Methodology Section (Section 3).

(iv) As described in Section 2.2, micro- and nano-indentation tests have been extensively applied to characterize the mechanical and creep properties of rock materials at micron

and nano scale. However, the creep time duration for most micro- and nano-indentation tests on rock materials is not longer than 3 minutes. In other words, the rock indentation creep behavior for a relatively longer duration (i.e. a few hours) has not been adequately researched.

Based on the above summary, both numerical and experimental work has been conducted. To address (i), (ii), and (iii), the visco-elastic deformations of rock fractures has been simulated numerically. Fracture surfaces have been generated using the Gaussian surface height distribution function and self-affine spatial correlation function. The visco-elastic deformations of the generated fracture surfaces have been numerically determined according to the methods described in Section 2.5.3. The simulation methodology and results will be explained in Sections 3 and 4, respectively. To address (iv), the effect of time duration on rock creep behavior has been studied experimentally. The experimental methods and the rock material will be described in Section 5, and the experimental results will be presented and discussed in Section 6.

3. Numerical Simulation Methodology

This chapter presents the numerical simulation methodology used in this research. The methods for simulating micro-indentation using ABAQUS will be introduced in Section 3.1. The methods for simulating elastic and visco-elastic deformations of rough fractures will then be discussed in Sections 3.2 and 3.3, respectively. This will be followed by validation against analytical solutions in Section 3.4. Section 3.5 briefly discusses the limitations of the numerical methods. Finally, this chapter finishes with an introduction of the synthetic rough fracture surface generation method in Section 3.6.

3.1 Simulating micro-indentation using ABAQUS

In this section, the simulation work using ABAQUS will be described. The simulation work consists of two parts: (1) simulating the loading stage of micro-indentation. (2): simulating the elasto-plastic deformation of a single and a few cylindrical asperities. The purpose of the first part is to find the correct constitutive models to simulate fracture-scale elasto-plastic deformation, while the second part intends to check the degree of asperity interaction.

3.1.1 Simulation methodology for the loading stage of micro-indentation

Numerical simulations of the micro-indentation tests are conducted using ABAQUS. Figure 3.1 shows the meshing. An axisymmetric mesh is used. The red line represents the Berkovich indenter, with a half-cone angle of 70.32˚; and the light blue elements represent the rock. The mesh near the indenter is refined to 0.1 μm, which is 0.24% of the contact area radius (approximately 42 μm). The standard triangular mesh is used and the mesh geometric order is linear.

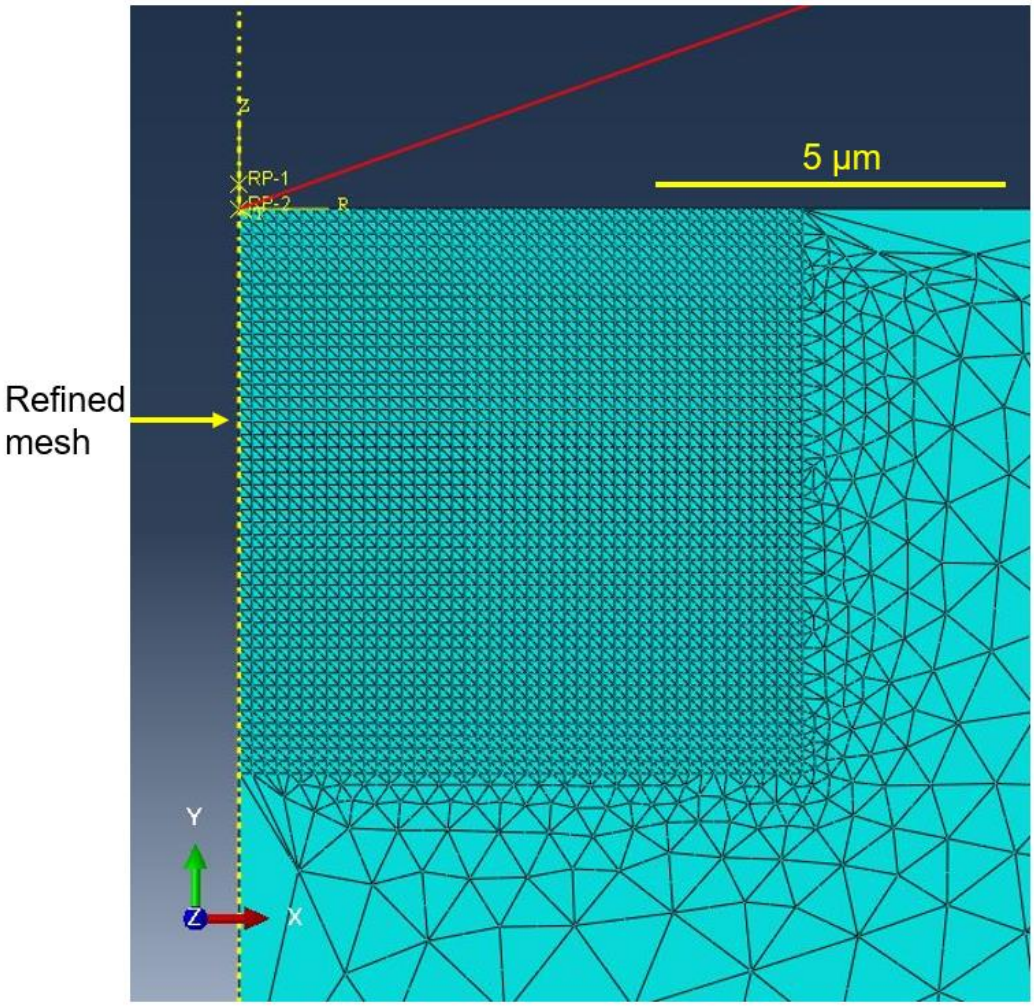

Figure 3.1 Meshing for micro-indentation simulation. The x-, y-, and z-directions are shown in the bottom left of the figure. The mesh near the indenter was refined (the size of the triangle is 0.1 μm and is not visible in this figure).

The constitutive models of the rock are summarized below:

1) Linear elasticity. The elastic modulus is 67 GPa and the Poisson's ratio is 0.3. The elastic properties are obtained from the triaxial tests.
2) Perfect plasticity. The von Mises yield criterion is used. An element will yield if the von Mises stress (see Eqn. 1 below for the definition) reaches the yield strength σ_Y. At the scale and the stress level of micro-indentation, the yield strength of the rock is not dependent on the confining pressure (Wu and Sharma, 2017; Kling, 2018; Evans, 2020), and the von Mises criterion can be used. Bowden and Tabor (1950) stated that using the Berkovich indenter, the indentation hardness is approximately three times the yield strength. Hence, the yield strength σ_Y is H / 3, 560 MPa.

The von Mises stress σ is expressed as:

$$\sigma = \sqrt{0.5(\sigma_{11} - \sigma_{22})^2 + 0.5(\sigma_{22} - \sigma_{33})^2 + 0.5(\sigma_{33} - \sigma_{11})^2 + 3\sigma_{12}^2 + 3\sigma_{23}^2 + 3\sigma_{13}^2} \quad (3.1)$$

Figures 3.2 and 3.3 show the schematic of different stress components and the von Mises stress, respectively.

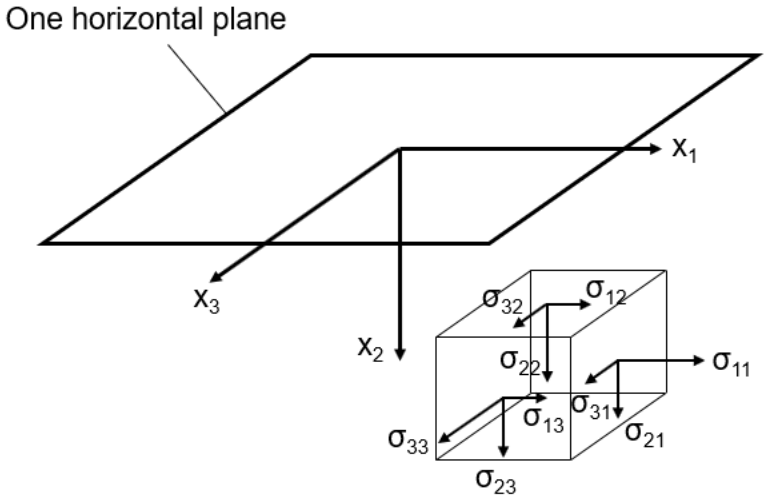

Figure 3.2 Schematic of σ_{11}, σ_{22}, σ_{33}, σ_{12}, σ_{23}, σ_{13}. Direction x_2 corresponds to the y-direction in Figure 3.1.

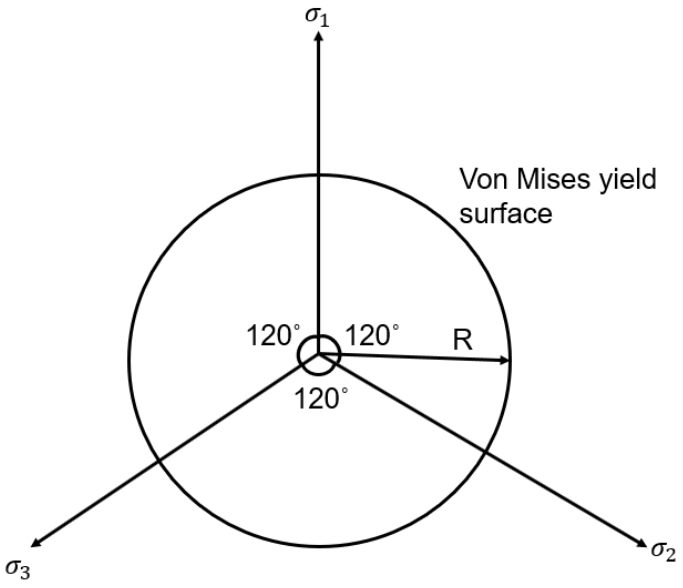

Figure 3.3 Schematic of the von Mises yield surface in principal stress coordinates. σ_1, σ_2, and σ_3 represent three principal stresses, and the hydrostatic (space) axis ($\sigma_1 = \sigma_2 = \sigma_3$) is perpendicular to the paper. The von Mises yield surface circumscribes a cylinder around the hydrostatic axis, and the radius R = $\sqrt{2/3}\sigma_Y$.

3.1.2 Simulation methodology for single and a few cylindrical asperities

The elasto-plastic deformation of a single and a few contacting asperities are simulated to study the effect of contacting asperity interaction. In the simulation, the asperity is deformable, and a rigid horizontal plane is moved against the asperity. Figure 3.4 shows the meshing for the single asperity case. A plane strain mesh is used. The asperity is a cylinder: infinitely long in the z-direction, and the radius in the x- and y-direction is 10 μm. The red line represents the rigid plane, and the light blue elements represent the rock. The mesh near the horizontal plane is refined to 0.04 μm, which is 0.4% of the radius of the cylinder. The standard triangular mesh is used and the mesh geometric order is linear.

(a):

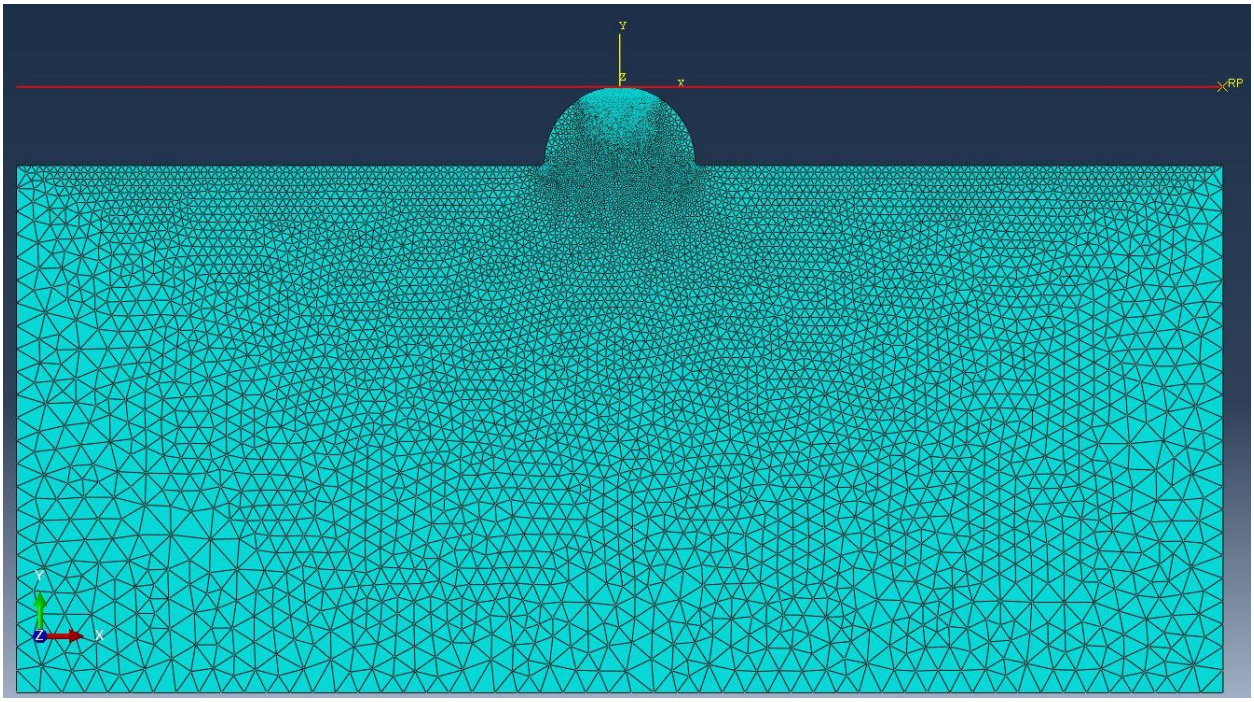

(b):

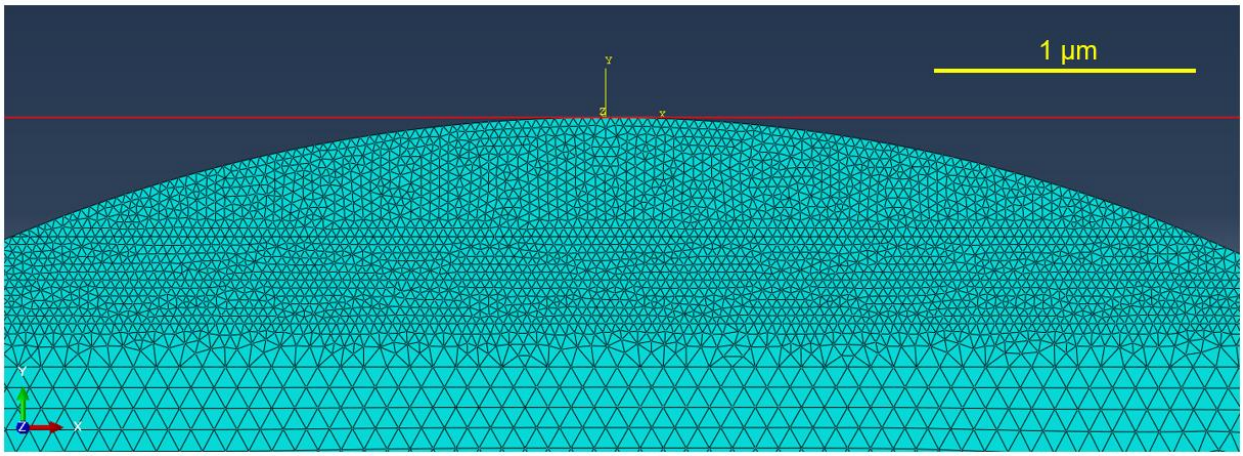

Figure 3.4. Meshing for the single asperity simulation. (a): the whole mesh. The x-, y-, and z-directions are shown in the bottom left of the figure. (b): mesh near the horizontal plane.

The elasto-plastic deformations of two and five cylindrical asperities are also simulated. Figure 3.5 shows the schematic of the multiple-asperity geometry and the definitions of d, r, and σ_1. Table 3.1 summarizes all the cases. Between different cases, the d value and the number of asperities are changed, while the r value is constant. σ_1 is defined as the average compressive stress acting on the contacting asperity. For all the cases, r is fixed at 10 μm, and σ_1 is varied between 100 MPa and 500 MPa. Several papers (Kling et al., 2018; Wu and Sharma, 2017; Lang et al., 2015) reported that for real rock fractures, the average compressive stress acting on the contacting asperities can easily exceed 100 MPa and can reach 500 MPa. Therefore, in this study, the range of average compressive stress σ_1 is chosen between 100 MPa and 500 MPa.

Table 3.1. Summary of different cases (r = 10 μm)

Case No.	d / r	No. of asperities
1	-	1
2	1.3	2
3	1.6	2
4	2.0	2
5	1.3	5
6	1.6	5
7	2.0	5

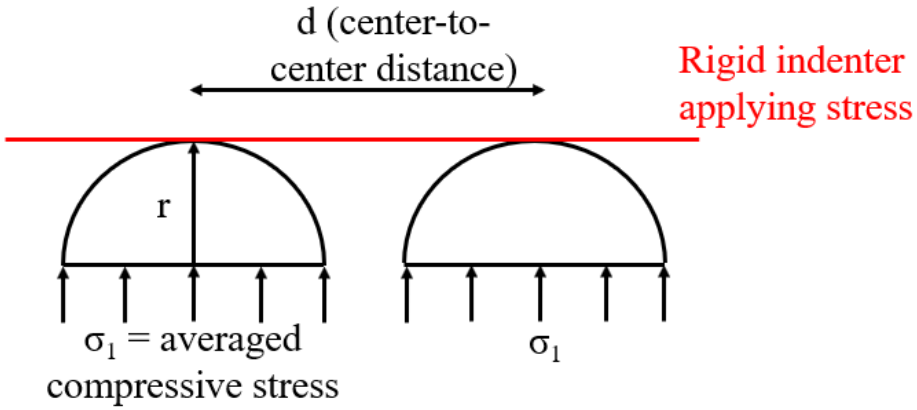

Figure 3.5. Schematic of the multiple-asperity geometry. σ_1 is defined as the average compressive stress acting on the contacting asperity.

Figure 3.6 shows the meshing for case No.6. A plane strain mesh is used. The asperities are five cylinders: each of them is infinitely long in the z-direction, and the radius in the x- and y-direction is 10 μm. The red line represents the rigid plane, and the light blue elements represent the rock. The mesh near the indenter is refined to 0.04 μm, which is 0.4% of the radius of the cylinder. The standard triangular mesh is used and the mesh geometric order is linear.

(a):

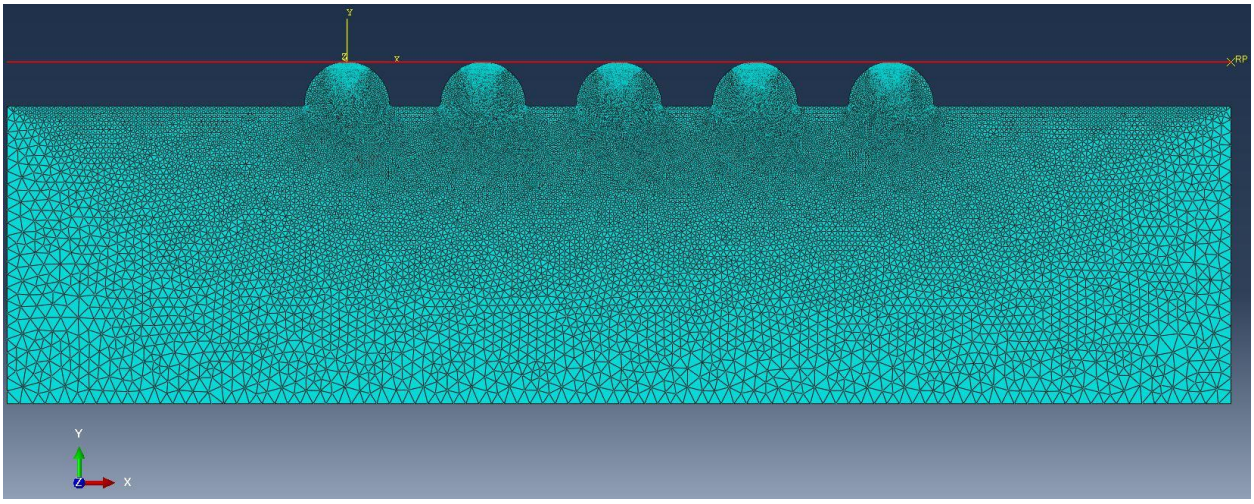

(b):

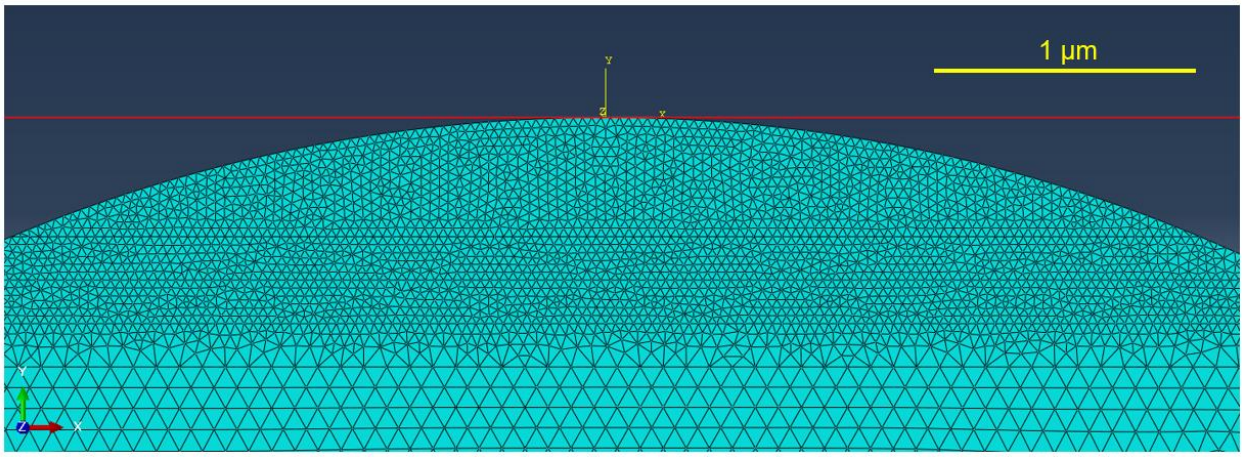

Figure 3.6. Meshing for case No. 6. (a): the whole mesh. The x-, y-, and z-directions are shown in the bottom left of the figure. (b): mesh near the horizontal plane.

The constitutive models used are summarized below:

1) Linear elasticity. Similar to Section 3.1.1, the elastic modulus is 67 GPa and the Poisson's ratio is 0.3. The elastic properties are obtained from the triaxial tests.
2) Perfect plasticity. Similar to Section 3.1.1, the von Mises yield criterion is used. An element will yield if the von Mises stress reaches the yield strength σ_Y. At the scale and the stress level of micro-indentation, the yield strength of the rock is not dependent on the confining pressure (Wu and Sharma, 2017; Kling, 2018; Evans, 2020), and the von Mises criterion can be used. Bowden and Tabor (1950) stated that using the Berkovich indenter, the indentation hardness is approximately three times the yield strength. Hence, the yield strength σ_Y is H / 3, 560 MPa.

3.1.3 Numerical simulation results for micro-indentation in the loading stage (see Section 3.1.1 for definitions)

Figure 3.7 compares the simulated and measured indentation displacements of the loading stage in micro-indentation tests (see Figures 2.14 and 2.15 in the background chapter for micro-indentation test explanation and loading stage explanation, respectively). The micro-indentation tests are conducted on Musandam limestone, and the experimental methodology will be explained in detail in Section 5.3. For each indent, the applied force is increased from 0 to 9N, and the indentation depth is measured. The green curve represents the ABAQUS simulation results, and the other four curves represent the measured curves for four indents. Figure 3.7 shows that the combination of linear elasticity and von Mises criterion gives a reasonably good fit for the loading stage. Therefore, the von Mises criterion is a suitable model to simulate the deformation (at the loading stage) of fracture contacting asperities.

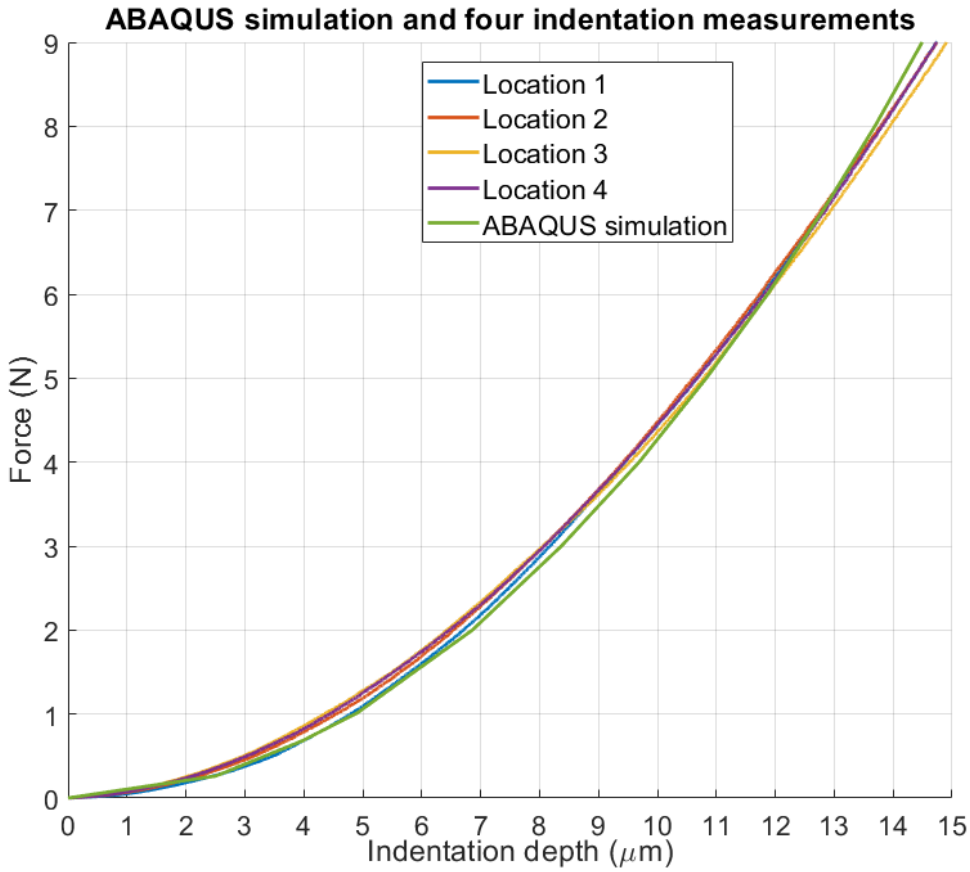

Figure 3.7. Force versus indentation depth curves. The green curve corresponds to the ABAQUS simulation result, while the other four curves correspond to micro-indentation measurements.

Figures 3.8 and 3.9 show the von Mises stress distribution and the y-direction displacement near the indenter, respectively (see Figure 3.1 for the x-, y-, and z-directions). Figure 3.8 indicates that most elements right beneath the indenter have yielded. As defined in Section 3.1.1, under von Mises yielding criterion, the von Mises stress of the yielded elements is equal to the yield strength, which is 560 MPa. In Figure 3.8, the red color corresponds to 560 MPa von Mises stress. Figure

3.9 shows that the y-direction displacement increases if the element is closer to the contacting region.

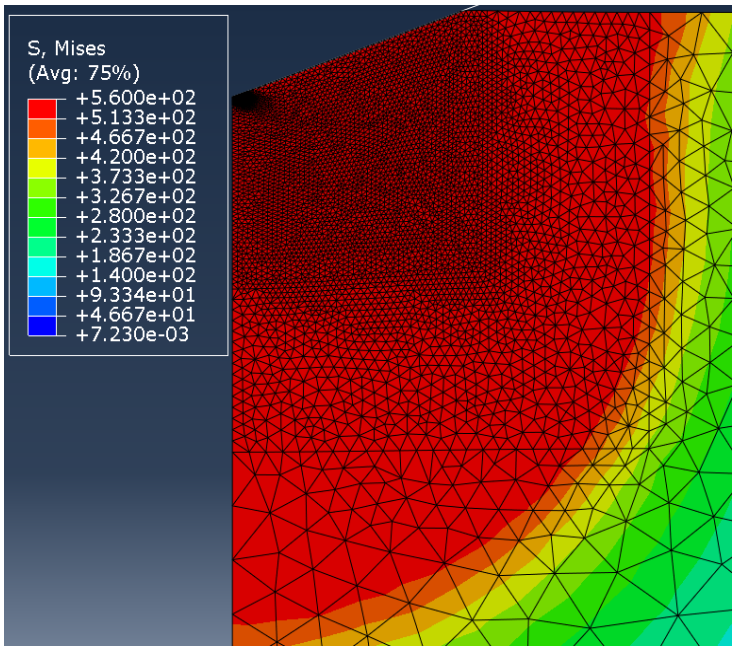

Figure 3.8 Von Mises stress distribution beneath the indenter. The maximum von Mises stress is 560 MPa, which corresponds to the red color. The unit is MPa.

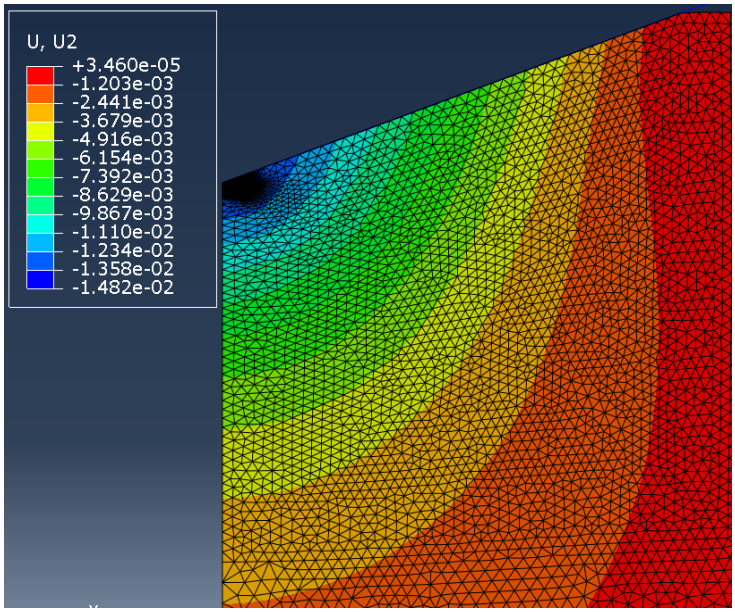

Figure 3.9 Y-direction displacement beneath the indenter. The unit is mm, and the blue color corresponds to larger vertical displacement.

3.1.4 Numerical simulation results for single and a few cylindrical asperities (see Section 3.1.2 for definitions)

Under the same σ_1, the displacement values for the seven cases (listed in Table 3.1) are simulated. In this study, the difference percentage is used to quantify the degree of interaction, and it is defined as:

$$\text{Difference percentage} = \frac{\delta_{mul} - \delta_{sin}}{\delta_{sin}} * 100 \tag{3.2}$$

Where δ_{sin} is the displacement for the single-asperity case, and δ_{mul} is the displacement for multiple-asperity cases (in this study, two and five asperities). If the asperities do not interact with each other, under the same σ_1, the δ_{sin} and δ_{mul} should be identical. The difference between δ_{sin} and δ_{mul} indicates the asperity interaction, and a larger difference percentage corresponds to a higher degree of interaction.

Figure 3.10 compares the difference percentage for the seven cases. The difference percentage increases with decreasing d/r ratio or increasing number of asperities. For example, for cases 5 and 6, when σ_1 is not larger than 300 MPa, the difference percentage is larger than 10%. In other words, the displacement considering asperity interaction is more than 10% larger than that without considering asperity interaction. This implies that if the number of contacting asperities reaches five, the d/r ratio is less than 1.6, and the average compressive stress σ_1 is less than 300 MPa, to accurately predict the asperity deformation, the asperity interaction may need to be considered.

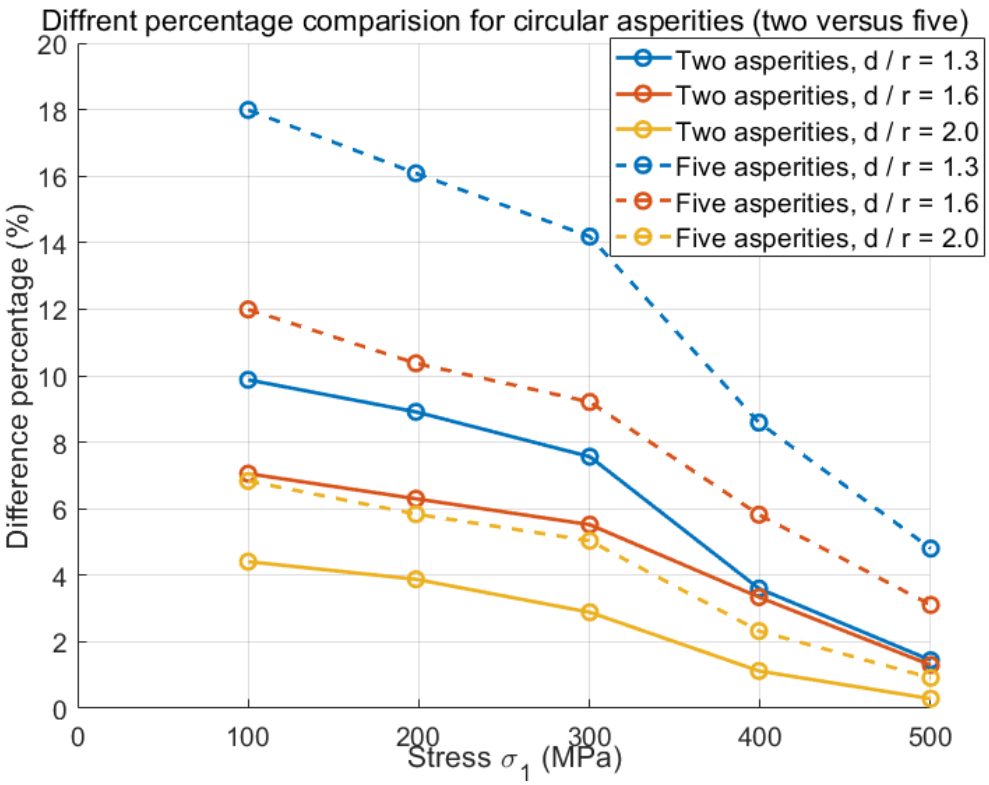

Figure 3.10 Difference percentage comparison for the seven cases. The solid curves represent the two-asperity cases, and the dashed curves represent the five-asperity cases. The stress σ_1 was varied between 100 MPa and 500 MPa.

3.1.5 Summary and conclusions

In this section, the micro-indentation and cylindrical asperity interaction were simulated using ABAQUS. Based on the simulation results, the following key conclusions can be drawn:

1) In the loading stage of micro-indentation, the combination of linear elasticity and von Mises criterion provides a good fit with the experimental results.
2) Based on the results in Figure 3.10, for fracture surfaces with multiple contacting asperities (equal to or more than five), if the d/r ratio (d and r are defined in Figure 3.5) is less than 1.6 and the average compressive stress σ_1 is less than 300 MPa, the asperity interaction may need to be considered.

Based on the above conclusions, to obtain accurate simulation results, the asperity interaction needs to be considered. It is also worth noting that using ABAQUS is not computationally efficient. For example, for case 5 in Section 3.1.2 (five asperities), the simulation took more than one hour. Rough fractures may contain multiple contacting asperities, and as a result, the required computational time may be much longer. Therefore, it is necessary to find another numerical method which is relatively more efficient and considers asperity interaction. The boundary element method (BEM) will be used and it will be introduced in Section 3.2.

3.2 Methods for simulating elastic deformation of rough fractures

The boundary element method (BEM) has been extensively used in solving rough surface contacting problems for its computational efficiency compared with the traditional finite element method (FEM). BEM only requires discretization and calculation on the boundaries of the calculation domain, which is two-dimensional. In contrast, FEM requires discretization and calculation for the whole domain. As a result, to achieve the same stress calculation resolution, BEM requires many fewer numbers of elements and, therefore, much less calculation time.

In recent years, the BEM and fast numerical algorithms have been combined to achieve more efficient numerical simulations for contacting problems. As mentioned in the background chapter, researchers in tribology have been combing the conjugate gradient (CG) method proposed by Polonsky and Keer (1999) and the Fast Fourier Transform (FFT) method proposed by Stanley and Kato (1997) to simulate rough fracture elastic deformations. In this research, an in-house contact simulation code has been developed, and the method is similar to that formulated by Polonsky and Keer (1999). In this section, the key mathematical aspects will be presented. The details can be found in Appendix A1 or Polonsky and Keer (1999).

First, the aperture distribution function h (x, y) is defined as:

$$h(x,y) = h_0(x,y) + u_e(x,y) - \delta \tag{3.3}$$

where δ is the rigid-body movement between two surfaces under applied stress in the direction normal to the fracture surface (compression is defined as positive), h_0(x, y) is the initial aperture, u_e(x, y) is the elastic displacement field between the two contacting surfaces inside the contacting area.

It is important to note that when applying a normal stress to a rough fracture, both normal and shear displacements may occur, as shown in Figures 3.11 (a) and (b), respectively. However, in this numerical model, the shear displacement is not considered; in other word, only the normal displacement is considered.

(a):

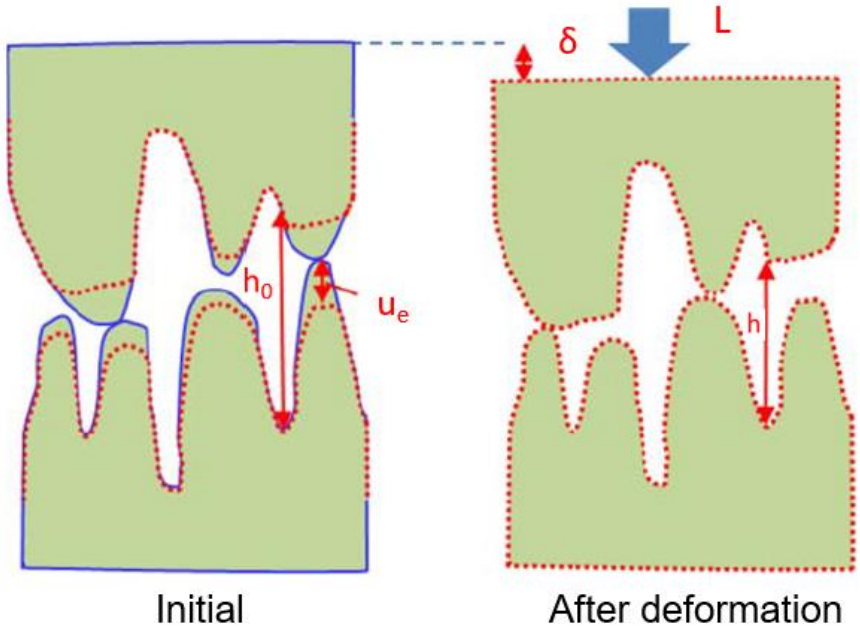

(b):

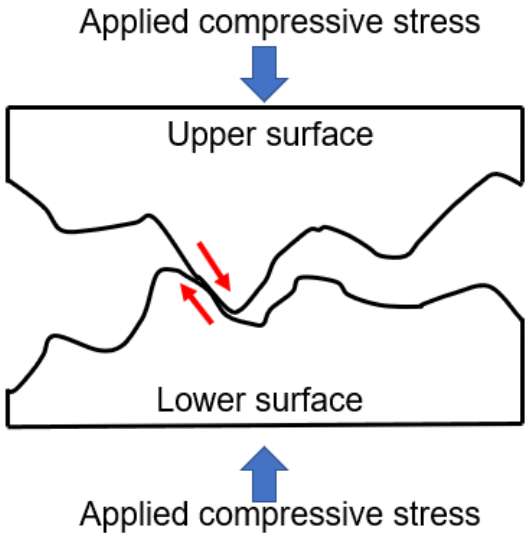

Figure 3.11. Two schematics. (a): schematic of Eqn. 3.3 (Modified from Wu and Sharma, 2017). The blue solid curves represent the initial surface geometry, and the red dotted curves represent the deformed surface geometry. L represents the load applied normal to the fracture surface. (b): schematic of shearing between contacting asperities. The red arrows represent the relative shearing directions.

For two rough surfaces contacting each other, the boundary conditions below need to be satisfied:

$$p(x,y) > 0 \; and \; h(x,y) = 0 \tag{3.4}$$

$$p(x,y) = 0 \; and \; h(x,y) > 0 \tag{3.5}$$

where p(x,y) is the contact pressure (in the normal direction) acting at location (x,y). This indicates that the contact pressure is zero at non-contacting areas, and is larger than zero at contacting areas. Compressive stress is defined as positive. Figure 3.12 shows the schematic of Eqns. 3.4 and 3.5.

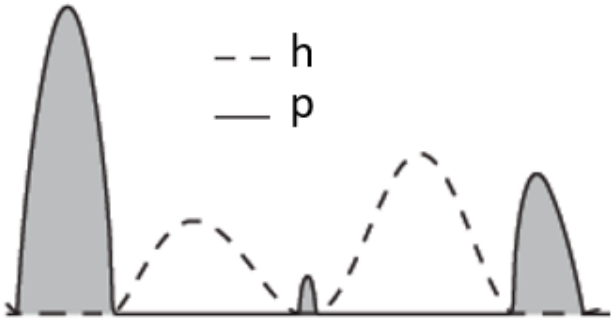

Figure 3.12 Schematic of Eqns. 3.4 and 3.5 (modified from Sahlin et al., 2010). The dashed line represents the aperture field, and the solid line represents the contacting pressure. When the aperture is larger than zero, the contacting pressure is zero; when the aperture is zero, the

contacting pressure is larger than zero. The height of the shaded area represents the magnitude of contacting pressure p. The taller the shaded area, the larger the contacting pressure p.

The vertical elastic displacement $u_e(x,y)$ can be calculated from the Boussinesq and Cerrutti (1885) equation:

$$u_e(x,y) = \int_{-\infty}^{+\infty}\int_{-\infty}^{+\infty} K(x,y,x',y')p(x',y')dx'dy' \tag{3.6}$$

where K(x, y, x', y') is the influence matrix for normal displacement at surface location B(x,y) due to a normal unit stress applied at location A(x', y'), and p(x', y') is the normal stress applied at location A(x', y'). Figure 3.13 shows the schematic of the underlying Boussinesq and Cerrutti equation.

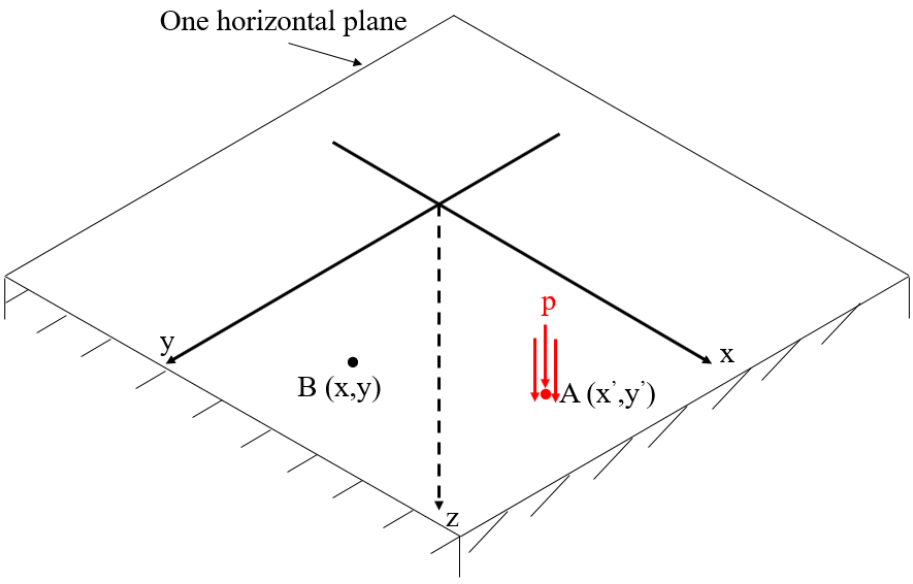

Figure 3.13 Illustration of the Boussinesq solution. A normal stress field p is applied surrounding the location A (x', y'), and $u_e(x,y)$ represents the z-direction elastic displacement at point B (x,y).

The influence matrix K(x, y, x', y') is defined as:

$$K(x,y,x',y') = \frac{1-\upsilon}{2\pi G\sqrt{(x-x')^2+(y-y')^2}} \tag{3.7}$$

where G and υ are the shear modulus and Poisson's ratio, respectively.

The elastic displacement of two rough surfaces with partial contact usually cannot be solved analytically, but can be solved numerically. For numerical simulation, the analytical equations need to be discretized into numerical equations. First, as shown in Figure 3.14, the surface is discretized into a regular grid:

$$x_i = i\Delta x, \qquad i = 1,2,\dots,N \tag{3.8}$$

and

$$y_j = j\Delta y, \qquad j = 1,2,\dots,M \tag{3.9}$$

where x_i and y_j are x and y coordinates, respectively; Δx and Δy are the grid spacings in the x and y direction, respectively; and N and M are the total number of grids in the x- and y-direction, respectively.

The aperture field can be calculated as:

$$h_{i,j} = (h_0)_{i,j} + (u_e)_{i,j} - \delta \tag{3.10}$$

The boundary conditions become:

$$p_{i,j} > 0 \; and \; h_{i,j} = 0 \tag{3.11}$$

$$p_{i,j} = 0 \; and \; h_{i,j} > 0 \tag{3.12}$$

Love (1929) discretized the Boussinesq and Cerrutti equation as:

$$(u_e)_{i,j} = \sum_{k=1}^{N} \sum_{l=1}^{M} (p_{k,l} \times K_{i,k,j,l}) \tag{3.13}$$

and

$$K_{i,k,j,l} = \frac{1-\nu}{2\pi G}\left(a \ln \frac{c+\sqrt{a^2+c^2}}{d+\sqrt{a^2+d^2}} + b \ln \frac{d+\sqrt{b^2+d^2}}{c+\sqrt{b^2+c^2}} + c \ln \frac{a+\sqrt{a^2+c^2}}{b+\sqrt{b^2+c^2}} + d \ln \frac{b+\sqrt{b^2+d^2}}{a+\sqrt{a^2+d^2}}\right) \tag{3.14}$$

where

$$a = x_i - x_k + {\Delta x}/{2}\,, b = x_i - x_k - {\Delta x}/{2}\,, c = y_j - y_l + {\Delta y}/{2}\,, d = y_j - y_l - {\Delta y}/{2} \tag{3.15}$$

Figure 3.14 illustrates the indices.

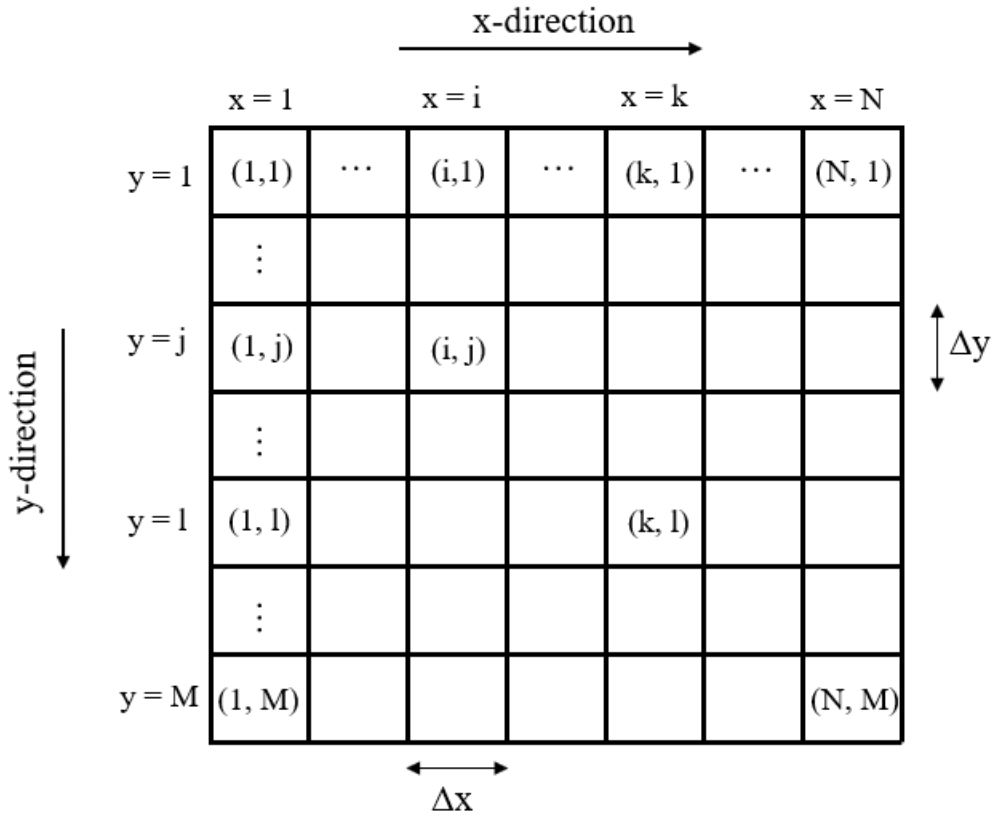

Figure 3.14. Illustration of the grid discretization and discretized Boussinesq equation. Indices i and k represent the coordinates in the x-direction, with $1 \le i \le N$ and $1 \le k \le N$. Indices j and l represent the coordinates in the y-direction, with $1 \le j \le M$ and $1 \le l \le M$. In Eqn.3.13, the vertical pressure $p_{k,l}$ is applied on grid (k,l), and $(u_e)_{i,j}$ represents the z-direction elastic displacement on grid (i,j). Δx and Δy are the grid sizes in the x-direction and y-direction, respectively.

Andrews (1988) first used the fast Fourier transform (FFT) method to solve the Boussinesq and Cerrutti equation in rock fractures. Later, Stanley and Kato (1997) used this method in tribology. Fast Fourier transform is an algorithm that calculates the discrete Fourier transform of a sequence. In engineering, people often use Fourier analysis to convert a signal from its original domain (space or time) to a representation in the frequency domain. Discrete Fourier transform is obtained by decomposing the sequence of values into components of different frequencies, and using the fast Fourier transform can save computation time. The detailed explanation of the FFT method can be found in Stanley and Kato (1997). Using the FFT method, the $(u_e)_{i,j}$ can be expressed as:

$$(u_e)_{i,j} = FFT^{-1}\left[FFT\left(K_{i,k,j,l}\right) \times FFT(p_{k,l})\right] \tag{3.16}$$

where FFT^{-1} means inverse fast Fourier transform (IFFT). In mathematics, the FFT changes the convolution (see Eqn. 3.13) to simple multiplication (see Eqn. 3.16).

If the FFT method is not used, calculating Eq.12 requires $N^2 \times M^2$ operations; while by using the FFT method, calculating Eq.3.13 requires $N \times M \times \ln (N \times M)$ operations. Therefore, when N and M are large, using the FFT method can save computation time.

In addition, force balance needs to be achieved:

$$F = \sum_{k=1}^{N}(\sum_{l=1}^{M}(p_{k,l})) \tag{3.17}$$

where F is the applied external force on the two fracture surfaces, and $p_{k,l}$ represents the pressure acting on grid (k,l) (see Eqn.3.13 and Figure 3.14). The indices k and l are explained in Figure 3.14.

Equations 3.10, 3.11, 3.12, 3.13, and 3.17 are solved iteratively using the conjugate gradient (CG) algorithm proposed by Polonsky and Keer (1999), where the details can be found.

3.3 Methods for simulating visco-elastic deformation of rough fractures

Chen et al. (2011) proposed a numerical method to solve the visco-elastic deformation of rough fracture surfaces. In this research, an inhouse visco-elastic contact simulation code has been developed, and the method the same as that formulated by Chen et al. (2011). Here the details of the numerical method will be introduced.

Before describing the methodology, it is essential to review the basic concepts of visco-elasticity. As described in Section 2.1.1, visco-elastic responses can be modeled by a group of dashpots and springs, in which the springs represent elasticity, and dashpots represent viscosity. In this research, we assume that the material is linearly viscoelastic. This means that the stress/strain response scales linearly with the stress/strain input, and follows the law of linear superposition. For any arbitrary series of stress or strain inputs, the outputs can be expressed as:

$$\varepsilon(t) = \int_0^t J(t-\tau)\frac{d\sigma(\tau)}{dt}d\tau \tag{3.18}$$

$$\sigma(t) = \int_0^t E_r(t-\tau)\frac{d\varepsilon(\tau)}{dt}d\tau \tag{3.19}$$

where $E_r(t)$ and J(t) are the relaxation modulus function and creep compliance function, respectively. $E_r(t)$ (unit: pressure) describes the time-dependent stress response to a step-change in strain, and J(t) (unit: 1 / pressure) describes the time-dependent strain response to a step-change in stress. τ represents the time variable in the integration, and its range is $0 \leq \tau \leq t$ (this means that t is a constant and τ is the variable). Figure 3.15 explains the creep compliance and relaxation modulus.

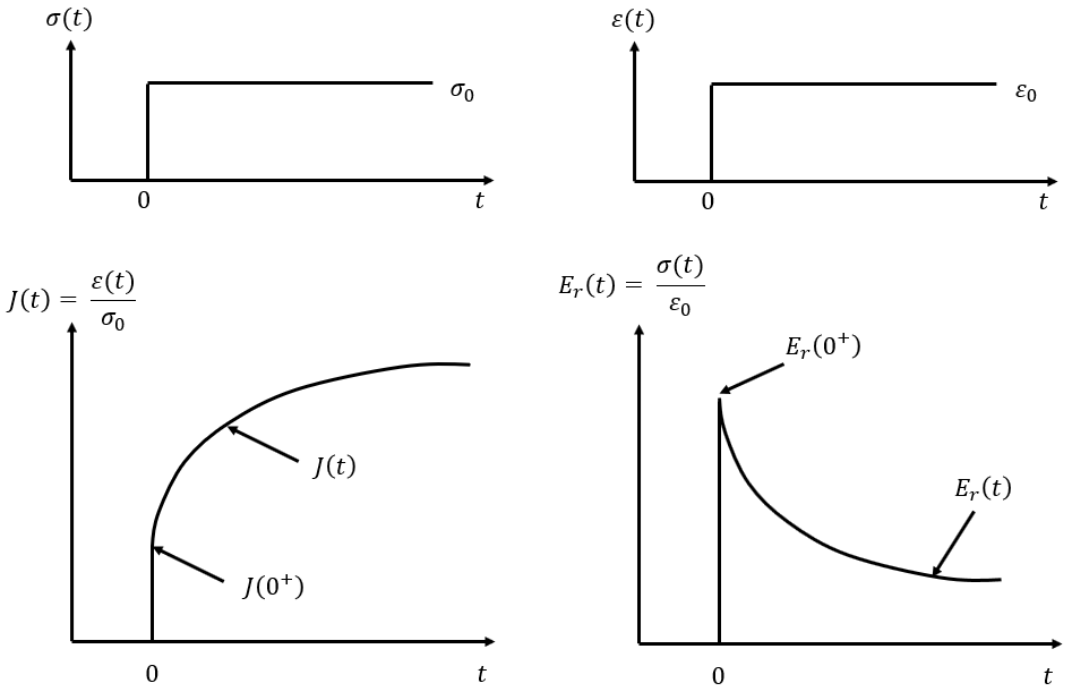

(a): Schematic for creep compliance (b): Schematic for relaxation modulus

Figure 3.15. Schematics for creep compliance and relaxation modulus. (a): schematic for creep compliance under a constant stress σ_0. $J(0^+)$ represents the creep compliance at the moment when σ_0 is applied, and $J(0^+)$ is equal to the elastic modulus. (b): schematic for relaxion modulus under a constant strain ε_0. $E_r(0^+)$ represents the relaxation modulus at the moment when ε_0 is applied, and $E_r(0^+)$ is equal to the elastic modulus.

The analytical solution for the Boussinesq and Cerrutti equation can be modified by adding time-dependent visco-elasticity. Adding the creep compliance function into the Boussinesq and Cerrutti equation (Eqns. 3.6 and 3.7) yields:

$$u_e(x,y,t) = \int_0^t J(t-\tau)\frac{\partial}{\partial\tau}\left[\int_{-\infty}^{+\infty}\int_{-\infty}^{+\infty}\frac{p(x',y',\tau)(1-\nu)}{\pi\sqrt{(x-x')^2+(y-y')^2}}dx'dy'\right]d\tau \tag{3.20}$$

In Eqn. 3.20, the shear modulus 1/2G (in Eqn. 3.7) is replaced by the creep compliance J(t-τ).

Rearranging Eqn. 3.20 yields:

$$u_e(x,y,t) = \int_0^t\int_{-\infty}^{+\infty}\int_{-\infty}^{+\infty}\frac{J(t-\tau)(1-\nu)}{\pi\sqrt{(x-x')^2+(y-y')^2}}\frac{\partial p(x',y',\tau)}{\partial\tau}dx'dy'd\tau \tag{3.21}$$

Eqn. 3.21 cannot be solved analytically. However, it can be solved numerically, if it can be decomposed into a linear equation system. Compared with Eqn. 3.6, an additional integration over the time duration ($\int_0^t \frac{\partial p(x',y',\tau)}{\partial\tau}d\tau$) is added in Eqn. 3.21. Therefore, the time duration also needs to be discretized into many small time steps. Here the total time duration t is discretized into N_t time steps with a uniform interval Δt. It is assumed that Δt is sufficiently small that the pressure field at each time step is unchanged. In addition, according to the fundamental theorem of calculus,

the term $\partial p(x', y', \tau) d\tau / \partial \tau$ in Eqn. 3.21 can be expressed as $p(x', y', \tau + d\tau) - p(x', y', \tau)$. Based on the sufficiently-small time step assumption and the fundamental theorem of calculus, Eqn. 3.21 can be rewritten as a summation:

$$u_e(x, y, \alpha\Delta t) = \sum_{\alpha'=1}^{\alpha} \left\{ \int_{-\infty}^{+\infty} \int_{-\infty}^{+\infty} \frac{J(\alpha\Delta t - \alpha'\Delta t)(1-\nu)}{\pi\sqrt{(x-x')^2+(y-y')^2}} \times [p(x', y', \alpha') - p(x', y', \alpha' - 1)] dx' dy' \right\} \tag{3.22}$$

where $\alpha = 1, 2, \ldots, N_t$.

Within each time duration, in a given surface, the pressure field does not change with time. Therefore, $[p(x', y', \alpha') - p(x', y', \alpha' - 1)]$ can be factored out from the integral. Eqn. 3.22 becomes:

$$u_e(x, y, \alpha\Delta t) = \sum_{\alpha'=1}^{\alpha} [p(x', y', \alpha') - p(x', y', \alpha' - 1)] \left\{ \int_{-\infty}^{+\infty} \int_{-\infty}^{+\infty} \frac{J(\alpha\Delta t - \alpha'\Delta t)(1-\nu)}{\pi\sqrt{(x-x')^2+(y-y')^2}} dx' dy' \right\} \tag{3.23}$$

The integral part of Eqn. 3.23 can be discretized. From Section 3.2 (Eqns. 3.6, 3.7, and 3.13), the following discretization relationship can be obtained:

$$\int_{-\infty}^{+\infty} \int_{-\infty}^{+\infty} \frac{(1-\nu)}{2\pi G\sqrt{(x-x')^2+(y-y')^2}} dx' dy' \xrightarrow{Discretize} \sum_{k=1}^{N} \sum_{l=1}^{M} K_{i,k,j,l} \tag{3.24}$$

By multiplying both sides of Eqn. 3.24 by $2GJ((\alpha - \alpha')\Delta t)$, the left-hand side of Eqn. 3.24 becomes the integral part of Eqn. 3.23. Therefore, the integral part of Eqn. 3.23 can be discretized as:

$$\int_{-\infty}^{+\infty} \int_{-\infty}^{+\infty} \frac{J(\alpha\Delta t - \alpha'\Delta t)(1-\nu)}{\pi\sqrt{(x-x')^2+(y-y')^2}} dx' dy' \xrightarrow{Discretize} \sum_{k=1}^{N} \sum_{l=1}^{M} 2GJ((\alpha - \alpha')\Delta t) K_{i,k,j,l}$$

where G is the shear modulus.

Thus, Eqn. 3.23 can be rewritten as:

$$u_e(i, j, \alpha\Delta t) = \sum_{\alpha'=1}^{N_t} \sum_{k=1}^{N} \sum_{l=1}^{M} 2GJ((\alpha - \alpha')\Delta t) K_{i,k,j,l} (p_{k,l,\alpha'} - p_{k,l,\alpha'-1}) \tag{3.25}$$

Eqn. 3.25 can be decomposed into Eqns. 3.26 and 3.27:

$$u_e(i, j, \alpha\Delta t) = \sum_{\alpha'=1}^{N_t} (u_e)_{\alpha'} \tag{3.26}$$

and

$$(u_e)_{\alpha'} = \sum_{k=1}^{N} \sum_{l=1}^{M} 2GJ((\alpha - \alpha')\Delta t) K_{i,k,j,l} (p_{k,l,\alpha'} - p_{k,l,\alpha'-1}) \tag{3.27}$$

It is worth noting that Eqn. 3.27 is analogous to Eqn. 3.13. Therefore, to save computation time, Eqn. 3.27 can also be solved using the FFT method, similar to Eqn. 3.16:

$$(u_e)_{\alpha'} = FFT^{-1}\left[FFT\left(2GJ((\alpha - \alpha')\Delta t) K_{i,k,j,l}\right) \times FFT(p_{k,l,\alpha'} - p_{k,l,\alpha'-1})\right] \tag{3.28}$$

where $(u_e)_{\alpha'}$, $2GJ((\alpha-\alpha')\Delta t)K_{i,j,k,l}$, and $(p_{k,l,\alpha'}-p_{k,l,\alpha'-1})$ in Eqn. 3.28 are equivalent to $(u_e)_{i,j}$, $K_{i,k,j,l}$, and $p_{k,l}$ in Eqn. 3.16, respectively.

Eqns. 3.26 and 3.28 will be used for numerical simulation. At each specific time step, Eqns. 3.10, 3.11, 3.12, 3.17, 3.26, and 3.28 will be solved iteratively using the CG method (Polonsky and Keer, 1999), and the pressure and displacement fields at each step can be obtained. Then, α will be increased (a new time step will be added), and the new pressure and displacement fields will be solved.

Based on the above mathematical concepts, the numerical algorithm is developed. The main algorithm is summarized below:

1. Obtain the loading history F(t), initial discretized aperture field $h_{i,j}$, and the creep compliance function J(t) for the viscoelastic material.
2. Calculate the $J((\alpha - \alpha')\Delta t)$ for each time step and the stiffness matrix $K_{i,k,j,l}$.
3. Use the method described in Section 3.2, calculate the initial contact state and the pressure distribution (α = 1). In this case, there is no creep effect, and the stress and displacement fields are calculated based on elasticity.
4. Save the historical pressure distribution field.
5. Now increase α (apply a new time increment). Since the historical pressures p(k, l, 1), …, p(k, l, α-1) are known, the pressure distribution field and displacement field at time step α can be calculated by the CG method.
6. If α reaches N_t (the total number of time steps), stop the program, and export the pressure and displacement field. Otherwise, go back to step 4.

Figure 3.16 shows the flowchart of the main algorithm. According to Eqns. 3.18, 3.26, and 3.28, in each time step, the strain at the specific time step is obtained. To obtain the total strain, the strain values at each previous time step need to be accumulated. Since the strain rates from all previous time steps need to be accumulated, the pressure history (the pressure fields of all previous steps) needs to be saved.

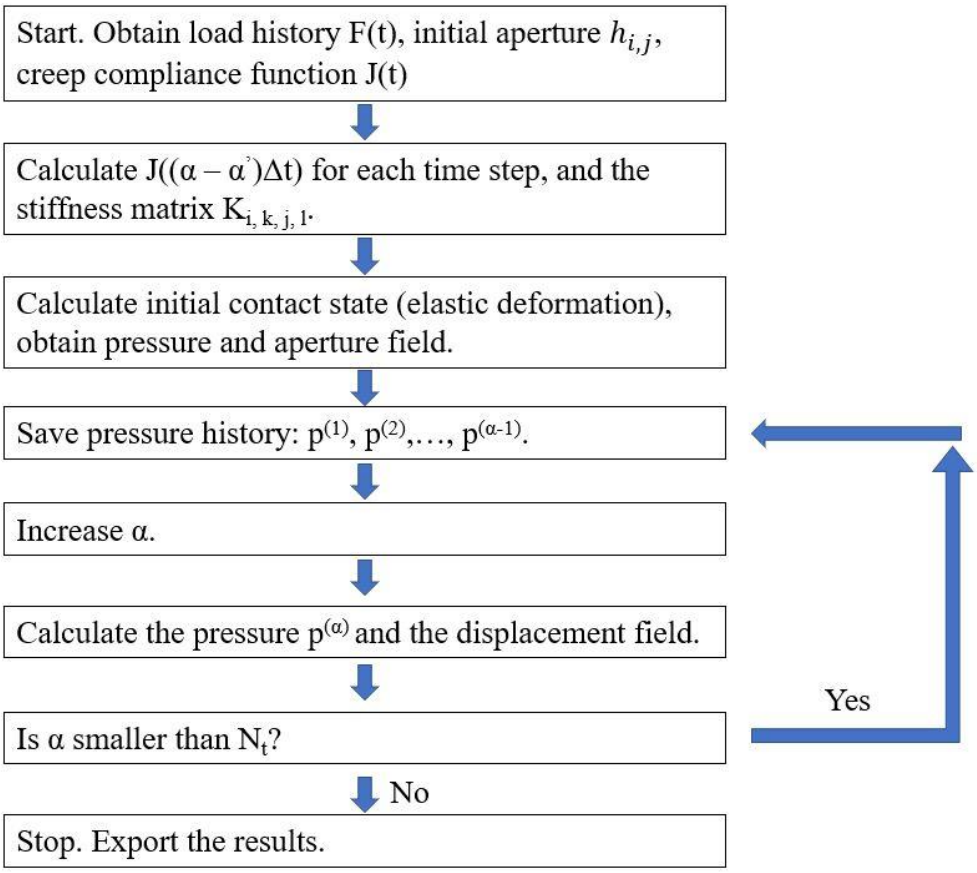

Figure 3.16. Flowchart of the main algorithm.

3.4 Validation of the visco-elastic deformation simulation method

The results of the numerical program need to be validated against analytical solutions. In this research, the cases for validation will be the Maxwell and Standard Linear Solid (SLS) viscoelastic half-spaces being compressed against a spherical rigid body. Lee and Radok (1960) developed the analytical solutions for the two above-mentioned cases, and the pressure distribution along the contacting region will be compared.

It is essential to explain the concept of the Maxwell and Standard Linear Solid (SLS) constitutive models. The two models have been explained in Section 2.2.1, and will be recapped in this section. Figures 3.17 (a) and (b) show the schematic for the Maxwell model and SLS model, respectively.

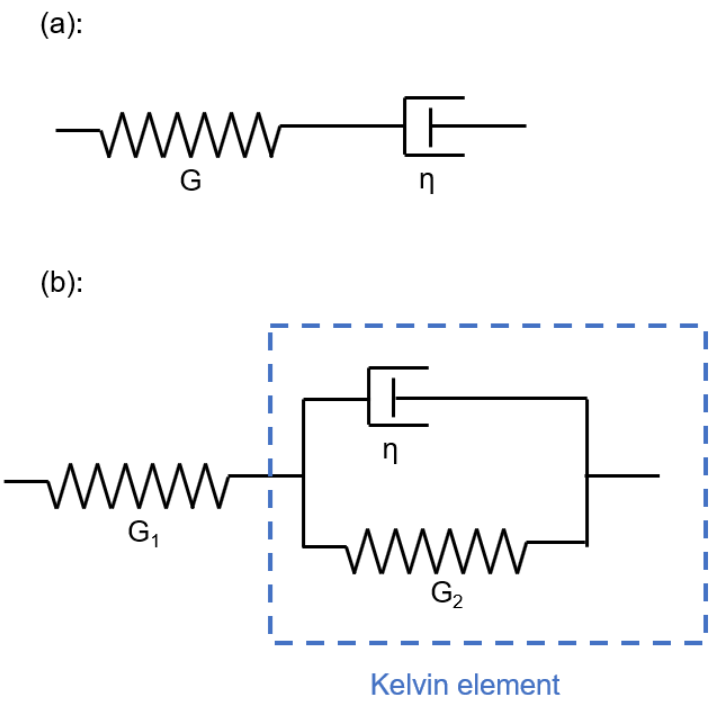

Figure 3.17 (a): Schematic of the Maxwell model; (b): Schematic of the SLS model.

The Maxwell model consists of a spring and a dashpot in series. The spring represents elasticity, with a shear modulus of G; and the dashpot represents viscosity, with a viscosity of η (unit: time * pressure). Under constant stress σ_0, the strain can be expressed as:

$$\varepsilon(t) = \sigma_0\left(\frac{1}{G} + \frac{t}{\eta}\right) \tag{3.29}$$

Eqn. 3.29 indicates that under constant stress, the strain rate (creep rate) is constant.

The creep compliance function can therefore be defined as:

$$J(t) = \frac{1}{G} + \frac{t}{\eta} \tag{3.30}$$

where t is the time. The relaxation time for the Maxwell model, T, is defined as:

$$T = \frac{\eta}{G} \tag{3.31}$$

As explained in Section 2.2.1 and shown in Figure 3.17 (b), the SLS model consists of a spring and a Kelvin element in series. The Kelvin element has a shear modulus of G_2, and a viscosity of η (unit: time * pressure); and the spring has a shear modulus of G_1. Under constant stress σ_0, the strain ε(t) can be related to σ_0 as:

$$\varepsilon(t) = \sigma_0\left(\frac{1}{G_1} + \frac{1-e^{-\frac{tG_2}{\eta}}}{G_2}\right) \tag{3.32}$$

The creep compliance function can be expressed as:

$$J(t) = \frac{1}{G_1} + \frac{1-e^{-tG_2/\eta}}{G_2} \tag{3.33}$$

where t is the time. The relaxation time for the SLS model, T, is defined as:

$$T = \frac{\eta}{G_2} \tag{3.34}$$

In the numerical code developed in this research, if the Maxwell model is chosen as the visco-elastic model, Eqn. 3.30 is substituted into Eqn. 3.25, and the pressure and displacement fields are solved as described in Section 3.3; if the SLS model is chosen as the visco-elastic model, Eqn. 3.33 is substituted into Eqn. 3.25, and the pressure and displacement fields are solved as described in Section 3.3.

Lee and Radok (1960) stated that if a spherical rigid body is moved against a visco-elastic flat surface (see Figure 3.18), and the flat surface satisfies the Maxwell model, the pressure distribution field can be expressed as:

$$p(t,r) = \frac{2}{\pi R(1-\upsilon)} \int_0^t G e^{-(t-t')G/\eta} \frac{d}{dt'} [a^2(t') - r^2]^{1/2} dt' \tag{3.35}$$

and

$$a(t) = \sqrt[3]{\frac{3(1-\nu)RP}{4}\left(\frac{1}{G} + \frac{t}{\eta}\right)} \tag{3.36}$$

where p is the pressure, r is the distance from the center of the contacting region, t is the total time duration, a(t) is the radius of the contacting region, R is the spherical diameter, G is the shear modulus, η is the viscosity, and P is the total load. Figure 3.18 illustrates the physical parameters.

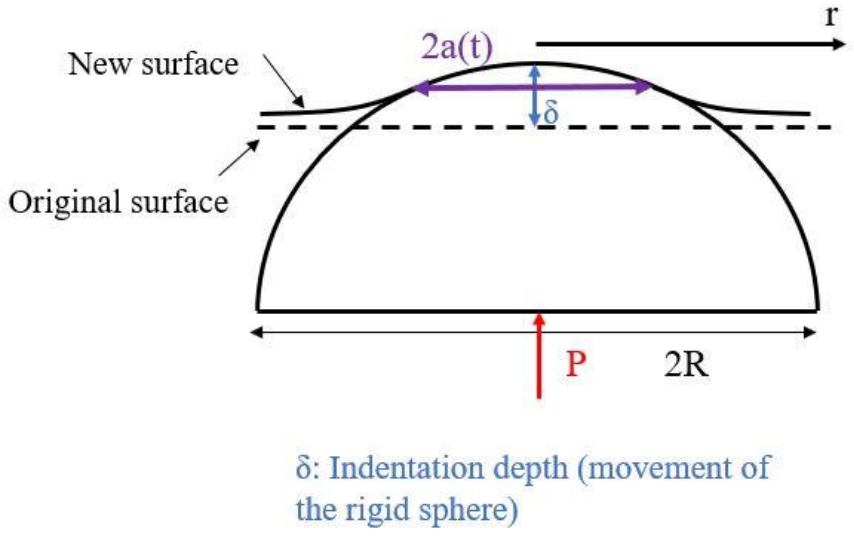

Figure 3.18 Illustration of the physical parameters in Eqns. 3.35, 3.36, 3.37, and 3.38.

Lee and Radok (1960) also suggested that if the flat surface satisfies the SLS model, the pressure distribution field can be expressed as:

$$p(t,r) = \frac{2}{\pi R(1-\upsilon)} \int_0^t \frac{G_1}{G_1+G_2} [G_2 + G_1 e^{-(t-t')(G_1+G_2)/\eta}] \frac{d}{dt'} [a^2(t') - r^2]^{1/2} dt' \quad (3.37)$$

and

$$a(t) = \sqrt[3]{\frac{3(1-\nu)RP}{4} (\frac{1}{G_1} + \frac{1}{G_2}(1 - e^{-tG_2/\eta}))} \quad (3.38)$$

where p is the pressure, r is the distance from the center of the contacting region, t is the total time duration, a(t) is the radius of the contacting region, R is the spherical diameter, G_1 and G_2 are the shear moduli, η is the viscosity, and P is the total load. The physical parameters are also illustrated in Figure 3.18.

Johnson (1985) solved Lee and Radok's analytical equations. Figures 3.19 and 3.20 compare the analytical and numerical solutions for the Maxwell and SLS model, respectively. The analytical solutions are calculated by Johnson (1985), and the numerical solutions are calculated by the code developed in this research. In the comparison, the absolute values of p and r do not matter, because the pressure distribution p and the radius of the contacting region r are normalized. p is divided by p_h, and p_h represents the maximum pressure when the time is zero (no creep, the solution is Hertzian contact solution); r is divided by r_h, and r_h represents the radius of the contacting region when the time is zero (no creep, the solution is Hertzian contact solution).

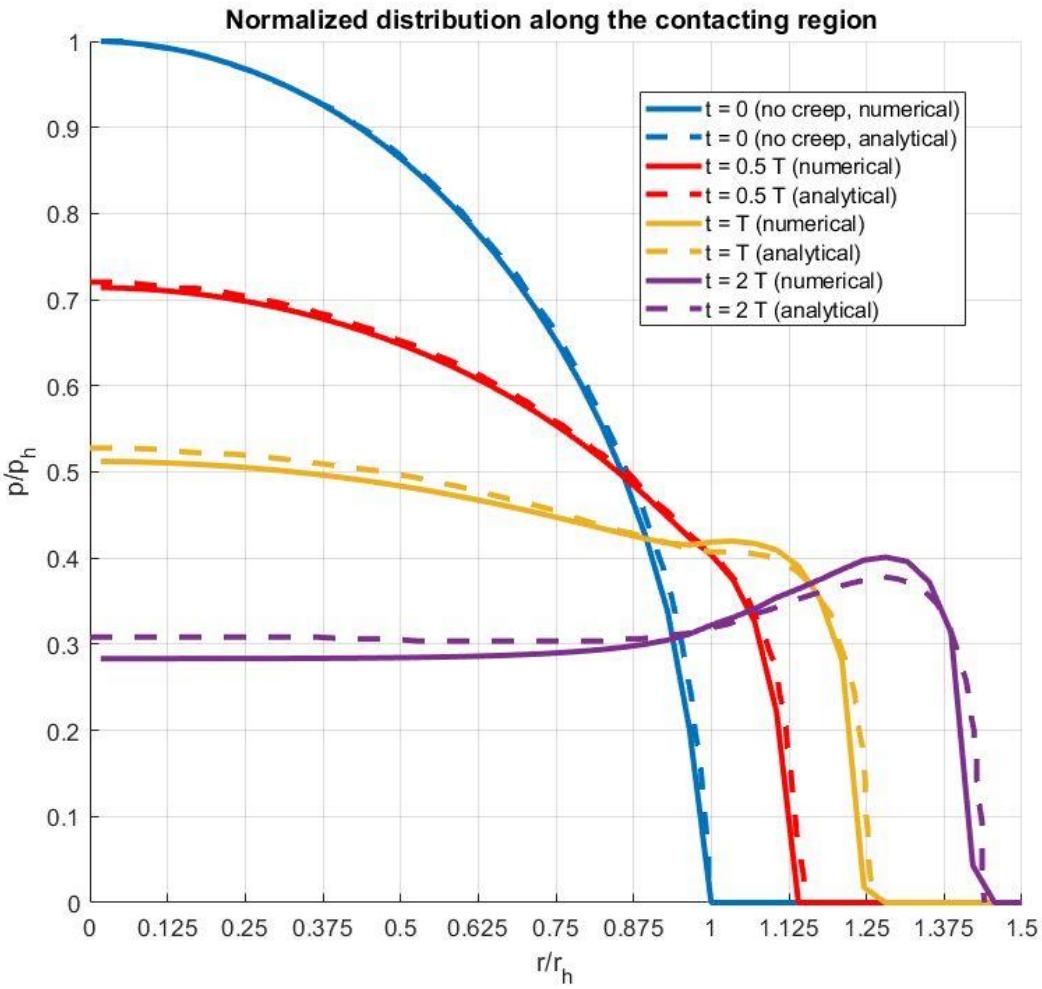

Figure 3.19 Comparison between analytical solutions (Lee and Radok, 1960; Johnson, 1985) and numerical solutions for the Maxwell model. p_h represents the maximum pressure when the time is zero (no creep, the solution is Hertzian contact solution), and r_h represents the radius of the contacting region when the time is zero.

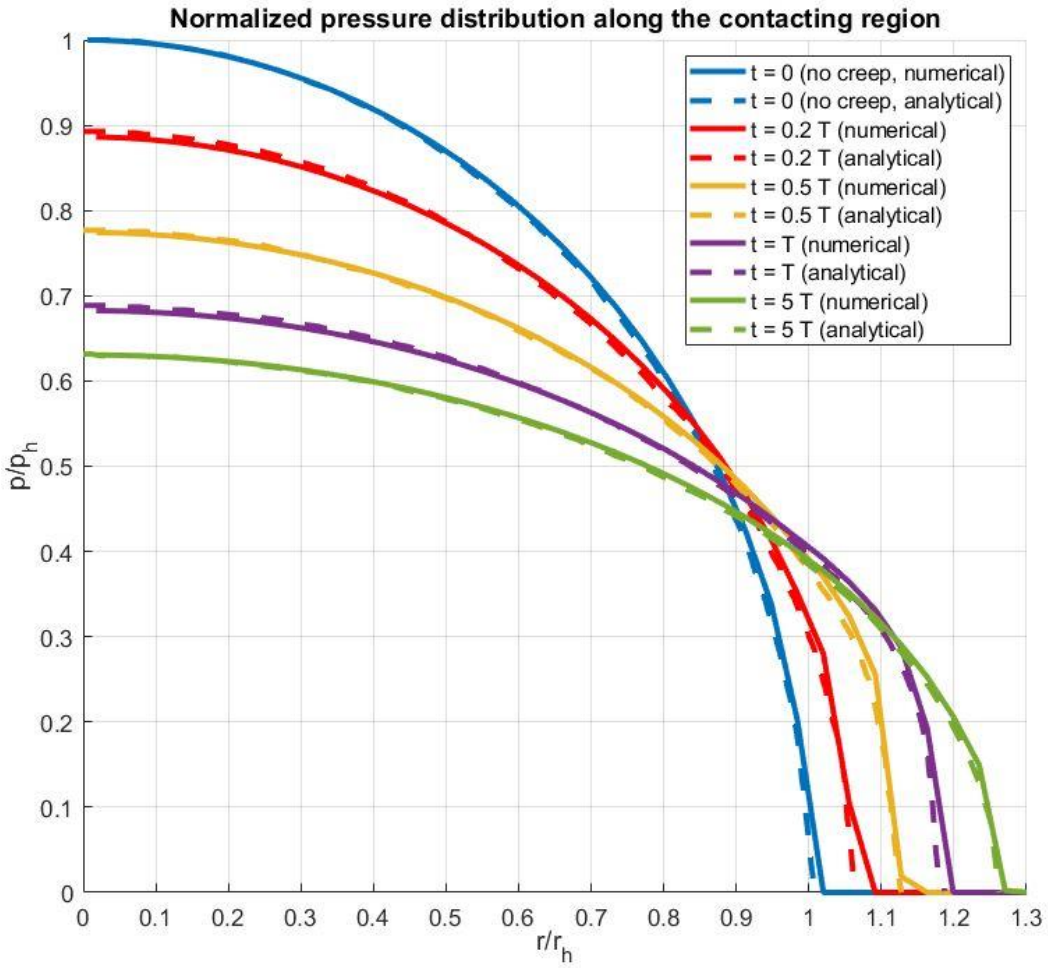

Figure 3.20 Comparison between analytical solutions (Lee and Radok, 1960; Johnson, 1985) and numerical solutions for the SLS model. p_h represents the maximum pressure when the time is zero (no creep, the solution is Hertzian contact solution), and r_h represents the radius of the contacting region when the time is zero.

The results in Figures 3.19 and 3.20 suggest that the difference between the numerical and analytical solutions is less than 10%. Therefore, the numerical results match well with the analytical results.

3.5 Limitations of the current numerical method

The numerical method provides a convenient approach to simulate visco-elastic deformations of rough fractures. However, the method has some limitations listed below:

(1): In the simulation, the contacting asperities deform visco-elastically. This implies that there is no upper limit for the compressive stress in the contacting cells. For some synthetic surface pairs, the compressive stress in a few contacting cells reaches 1.5 GPa. In reality, under such high compressive stresses, the cells may deform plastically, and the contact ratio will further increase.

Therefore, if plastic deformation is ignored, the compressive stress in the contacting cells may be overestimated, and the contact ratio may be underestimated.

(2): Asperity breakage or cracking is ignored. In reality, under high compressive stresses, the asperities may break, which will affect the contact ratio and contact stress distribution.

(3): The effect of shear stress on fracture visco-elastic deformations is not considered. In engineering applications, fractures may be subject to shear stresses, which may change the visco-elastic deformations.

To make the simulation more applicable, in the future, the effect of plastic deformation and shear stress could be considered.

3.6 Methods for generating synthetic rough fracture surfaces

Synthetic fracture surface pairs are generated based on Brown's probabilistic model (Brown, 1995). In this model, rough rock fracture surfaces can be approximated by a Gaussian height distribution and self-affine organization over a large range of length scales (Brown and Scholz, 1985a; Brown, 1995; Power et al., 1987). The rock fracture surface can be described by three parameters: Hurst exponent (H), root mean square roughness at a reference length scale (σ), and mismatch length scale (λ_{mis}) (Brown, 1995).

The surface roughness of rock fractures typically follows a self-affine fractal distribution (Mandelbrot, 1983; Brown and Scholz, 1985a; Odling, 1994). A self-affine surface can be described as:

$$z(x) \sim \varepsilon^{-H} z(\varepsilon x) \tag{3.39}$$

where z is the surface elevation, ε is a constant for x-direction scaling, and H is the Hurst exponent. The H value is between 0 to 1; and a larger H value corresponds to a smoother local surface profile, as shown in Figure 3.21.

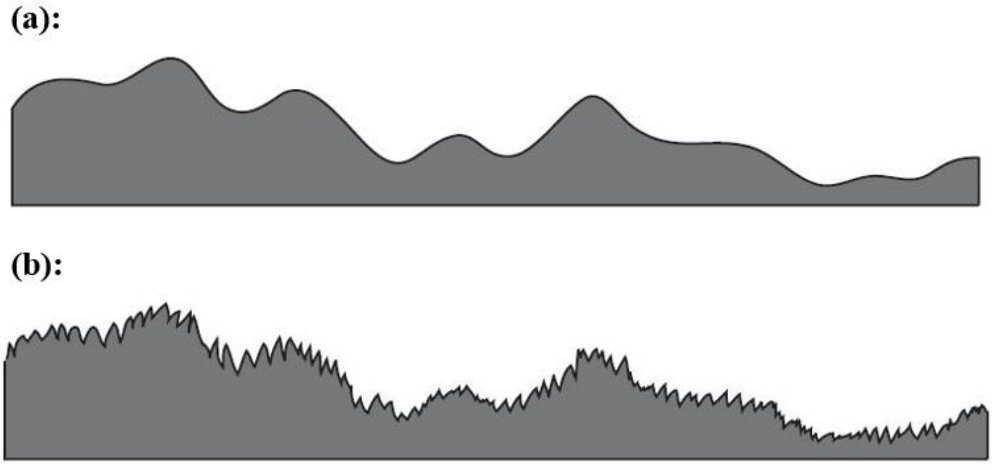

Figure 3.21 Schematic of two self-affine surfaces with different H values (Persson, 2006). (a): H = 1; (b): H = 0.

H can be well quantified from the power spectrum of the surface. The power spectrum is calculated by decomposing the surface into a sum of sinusoidal waves, each with its amplitude, phase, and wavelength. Figure 3.22 shows the process of wave decomposition. In the wave decomposition process, the Fourier transform is used to decompose the random rough surface into a series of sinusoidal wave components. The squared amplitude of each wave component (A^2) is defined as the power, and a plot of power versus the inverse of wavelength ($q = 2\pi/\lambda$) is defined as the power spectrum (see Figure 3.23 for a schematic). For self-affine fracture surfaces, the power spectrum C(q), can be related to the wavenumber (q):

$$C(q) \sim q^{-2(1+H)} \tag{3.40}$$

The upper frequency end, q_{max}, is defined as $q_{max} = 2\pi / \lambda_1$, where λ_1 is the smallest measurable size of surface scanning devices. The lower frequency end, q_{min}, is defined as $q_{min} = 2\pi / \lambda_L$, where λ_L is the surface length.

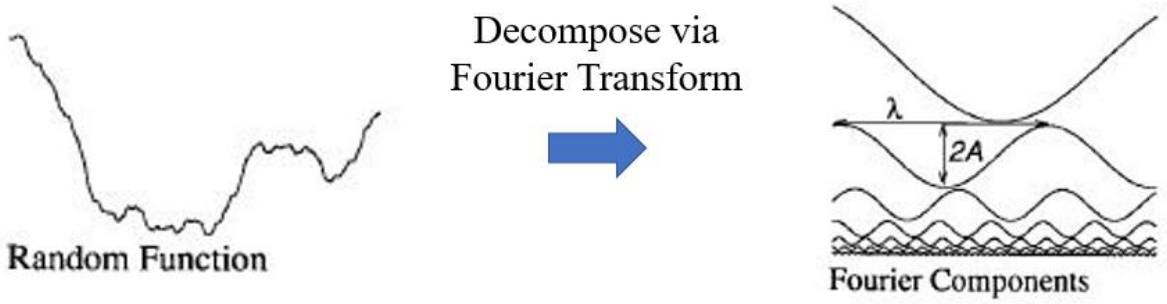

Figure 3.22 Schematic of surface profile breakdown (Brown, 1995). Each component is characterized by its wavelength (λ), amplitude (A), and phase (relative position of the first peak of the sinusoid to that of all others).

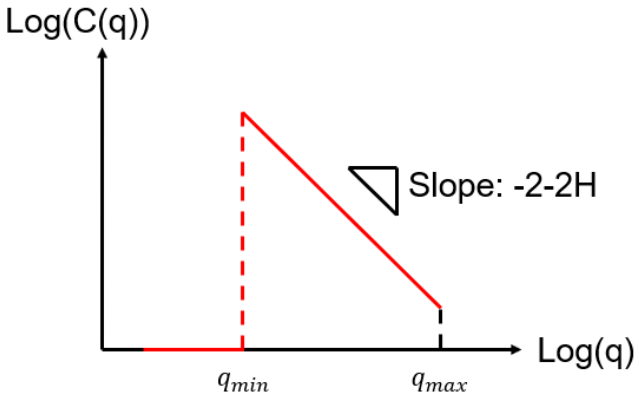

Figure 3.23 Schematic of the power spectrum. The horizontal axis is the frequency q (1/λ), and the vertical axis is the power C (A^2). The unit for q is (1/length).

The second parameter is the mismatch length λ_{mis}. As shown in Figure 3.22, each waveform can be completely described by three parameters: wavelength (λ), amplitude (A), and phase. In a natural rock joint, the two surfaces may not be perfectly matched; they may have relative shear displacements (Brown et al., 1986; Glover et al., 1998; Kang et al., 2016). Rock fracture surface measurement results from Brown (1995) and Matsuki et al. (1995) suggest that natural fractures are matched at long wavelengths, but the surfaces are not identical at short wavelengths. Based on these observations, Brown (1995) proposed the parameter of critical wavelength λ_{mis}, called the mismatch length scale. Above the mismatch length scale, the decomposed sinusoidal wavelengths are perfectly matched; they have the same phase, wavelength, and amplitude. Below the mismatch length scale, the decomposed sinusoidal wavelengths behave independently; they have an identical relationship between C and q, but independent phases. Figure 3.24 illustrates the concept of the mismatch length scale.

(a):

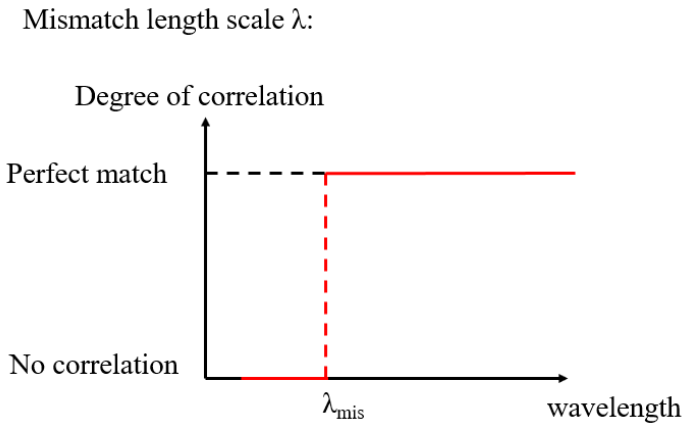

(b):

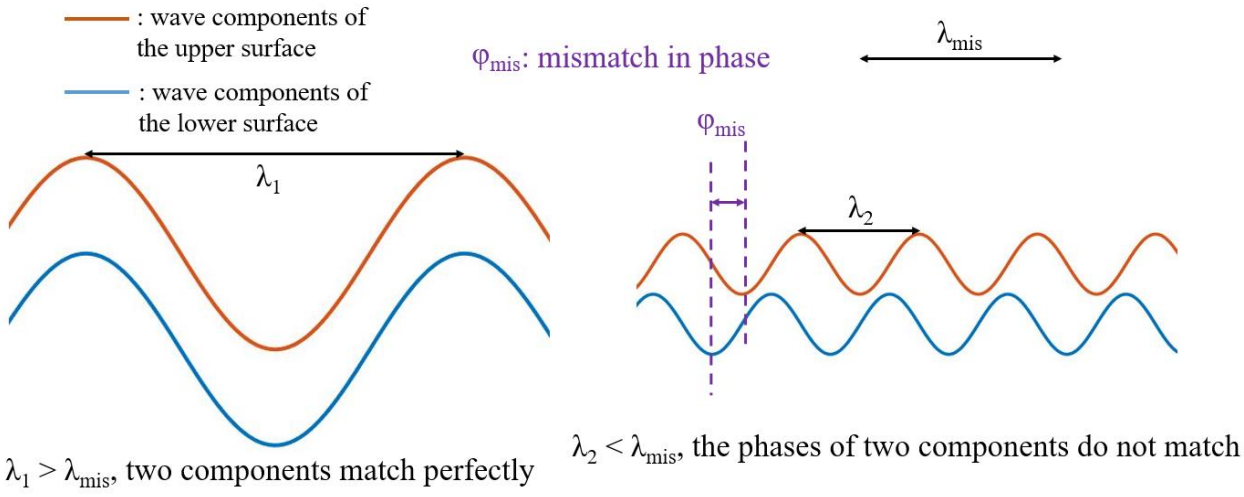

Figure 3.24 Schematic of mismatch length scale, λ_{mis}. (a): Degree of correlation with respect to the mismatch length, λ_{mis}; (b): Example of wave components with different wavelengths. λ_1, λ_2, and λ_{mis} represent three different wavelengths ($\lambda_1 > \lambda_{mis} > \lambda_2$, this is the length relationship). For

the left wave components, $\lambda_1 > \lambda_{mis}$, and the two components match perfectly. For the right wave components, $\lambda_2 < \lambda_{mis}$, and the phases of the two components do not match (they are independent). φ_{mis} represents the mismatch in phase between the two components.

The third parameter is the root mean square roughness (σ). This parameter is used to define the absolute scale of the surface height. The σ can be expressed as:

$$\sigma^2 = \int_{q_{min}}^{q_{max}} C(q)dq \tag{3.41}$$

After generating the surface profile, its root mean square value, σ_{ini}, is calculated. Then, the surface height is scaled linearly as:

$$z_{final} = z_{ini}\frac{\sigma_{final}}{\sigma_{ini}} \tag{3.42}$$

where z_{ini} is the initial surface height, z_{final} is the final surface height, and σ_{final} is the designated root mean square roughness. Figure 3.25 illustrates the concepts of z (surface height) and h (aperture).

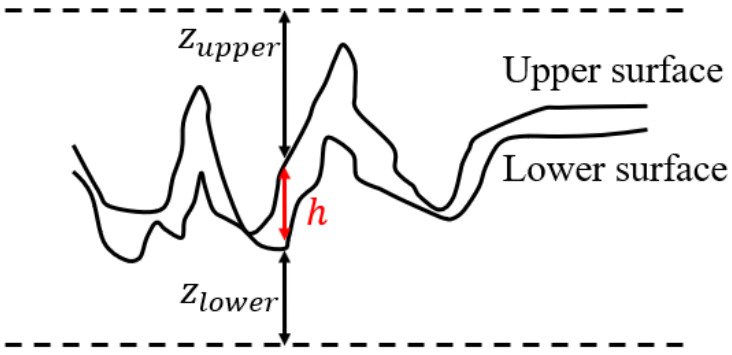

Figure 3.25 Schematic of z and h. z_{upper} represents the height of the upper surface, z_{lower} represents the height of the lower surface, and h represents the aperture (the gap between the two surfaces).

In this research, rough fracture surface pairs will be generated based on Brown's (1995) model. The Hurst exponent, root mean square roughness, and mismatch length scale will be varied systematically to investigate the effect of surface roughness parameters on fracture visco-elastic deformations.

3.7 Short conclusions

In this research, the loading stage of micro-indentation tests has been simulated using ABAQUS. An in-house numerical code has been developed to generate synthetic rock fracture surfaces based on Brown's (1995) model, and another code has been developed to simulate visco-elastic deformations of rough fractures. So far, the following conclusions can be drawn:

1) The loading stage of micro-indentation tests can be accurately simulated by using the linear elasticity and von Mises plasticity model in ABAQUS.
2) The visco-elastic deformation of rough fractures can be simulated. In this research, the Maxwell and SLS models are used. The numerically simulated results match the analytical results well.
3) Synthetic rock fracture surfaces can be generated by three parameters: Hurst exponent H, mismatch length scale λ_c, and root mean square roughness RMS.

The fracture surface generation results and visco-elastic deformation simulation results will be shown in Chapter 4.

4. Numerical Simulation Results

This chapter presents the numerical simulation results. The synthetic fracture surface generation results will be presented in Section 4.1. The creep simulation results for the Maxwell and the Standard Linear Solid (SLS) model will be shown in Sections 4.2 and 4.3, respectively. This will be followed by discussions in Section 4.4. Finally, this chapter finishes with conclusions in Section 4.5.

4.1 Surface generation results

As described in Section 3.6, synthetic rough fracture surfaces are generated based on Brown's model (Brown, 1995). Brown (1995) analyzed the surface profiles of 23 natural rock joints, and calculated the Hurst exponent (H), root mean square roughness (RMS), and mismatch length (λ_c) of each rock joint. The rock types include tuff, granodiorite, granite, basalt, chalk, and siltstone. Table 4.1 summarizes his analysis results. The RMS and λ_c are normalized by the profile length.

Table 4.1. Natural rock joint profiles analysis results (obtained from Brown, 1995).

Rock joint specimen	Profile length L (mm)	Hurst exponent (H)	Normalized RMS (RMS /L)	Normalized λ_c (λ_c/L)
Tuff	13.0	0.59 ± 0.33	0.00752	0.014-0.092
Tuff	13.0	0.55 ± 0.31	0.00525	0.039-0.205
Granodiorite	13.0	0.91 ± 0.40	0.01708	0.014-0.041
Granodiorite	13.0	0.68 ± 0.36	0.00854	0.010-0.062
Tuff	52.0	0.70 ± 0.25	0.01458	0.063-0.143
Tuff	52.0	0.83 ± 0.27	0.01350	0.019-0.072
Tuff	52.0	0.73 ± 0.26	0.01850	0.014-0.053
Basalt	13.0	0.85 ± 0.42	0.01792	0.022-0.078
Basalt	13.0	0.77 ± 0.39	0.01085	0.017-0.049
Sandstone	13.0	0.48 ± 0.32	0.00654	0.069-0.317
Chalk	26.0	0.59 ± 0.23	0.00400	0.007-0.015
Tuff	26.0	0.75 ± 0.32	0.00727	0.011-0.029
Tuff	26.0	0.77 ± 0.28	0.00565	0.018-0.092
Siltstone	13.0	0.52 ± 0.32	0.00349	0.059-0.205
Granite	13.0	0.49 ± 0.30	0.01546	0.100-0.461
Granite	13.0	0.51 ± 0.31	0.01446	0.053-0.270
Granite	13.0	0.79 ± 0.38	0.01569	0.055-1.000
Rhyolitic dike	13.0	0.66 ± 0.37	0.00758	0.021-0.048
Rhyolitic dike	13.0	0.60 ± 0.36	0.01569	0.020-0.076
Rhyolitic dike	13.0	0.64 ± 0.36	0.00665	0.014-0.032
Rhyolitic dike	13.0	0.66 ± 0.36	0.00514	0.139-1.000
Rhyolitic dike	13.0	0.65 ± 0.34	0.00688	0.029-0.084
Metasediment	13.0	0.64 ± 0.34	0.00654	0.050-0.125

Based on the results in Table 4.1, it can be concluded that the Hurst exponent is normally between 0.50 and 0.90; the normalized RMS (RMS / L) is normally between 0.005 and 0.015; and the normalized λ_c (λ_c / L) is normally between 0.02 and 0.2. The synthetic surface pairs described in Section 3.6 are generated based on the above values. Specifically, seven pairs of the synthetic surfaces are generated with three different H, RMS, and λ_c values. Table 4.2 summarizes the information of the seven pairs of the synthetic surfaces. For all the surfaces, the dimensions (profile lengths) in the x- and y-directions are 10 mm. Surface pair 2 is chosen as the reference surface pair. Its Hurst exponent H, normalized RMS (RMS / L) and normalized λ_c (λ_c / L) values fall in the middle of the range of these values listed in Table 4.1.

Table 4.2. Summary of the seven synthetic surfaces

Surface Pair No.	Profile length L (mm)	H	RMS		λ_c	
			RMS / L	Absolute value (μm)	λ_c / L	Absolute value (μm)
1	10	0.6	0.005	50	0.1	1000
2	10	0.8	0.005	50	0.1	1000
3	10	1.0	0.005	50	0.1	1000
4	10	0.8	0.005	50	0.2	2000
5	10	0.8	0.005	50	0.3	3000
6	10	0.8	0.010	100	0.1	1000
7	10	0.8	0.015	150	0.1	1000

Table 4.2 shows that in surface pairs 1, 2, and 3, the H value is varied; in surface pairs 2, 4, and 5, the λ_c value is varied; in surface pairs 2, 6, and 7, the RMS value is varied.

For each pair of the surfaces, the aperture field can be calculated. Figures 4.1, 4.2, and 4.3 show the effect of different H, λ_c, and RMS values on the aperture field, respectively. The following conclusions can be drawn:

1) From Figure 4.1, as H increases, the mean and standard deviation of the aperture decreases.
2) From Figure 4.2, as λ_c increases, the mean and standard deviation of the aperture increases.
3) From Figure 4.3, as RMS increases, the mean and standard deviation of the aperture increases. The magnitude of the aperture field scales linearly with the RMS value (this can be explained from Eqn. 3.42 in Section 3.6).

Table 4.3 summarizes the mean and standard deviation of the aperture field for the seven surface pairs. Each of the calculated aperture fields is implemented in the creep simulation code as the initial aperture field. The creep deformation of the aperture field is calculated as described in Sections 3.2 and 3.3.

Table 4.3. Mean and standard deviation of the aperture field for the seven surface pairs

Surface pair No.	H	RMS (μm)	λ_c (μm)	Mean aperture (μm)	Standard deviation of aperture (μm)
1	0.6	50	1000	63.41	14.29
2	0.8	50	1000	37.30	8.57

3	1.0	50	1000	21.89	5.14
4	0.8	50	2000	55.94	15.01
5	0.8	50	3000	66.10	20.12
6	0.8	100	1000	74.59	17.15
7	0.8	150	1000	111.89	25.72

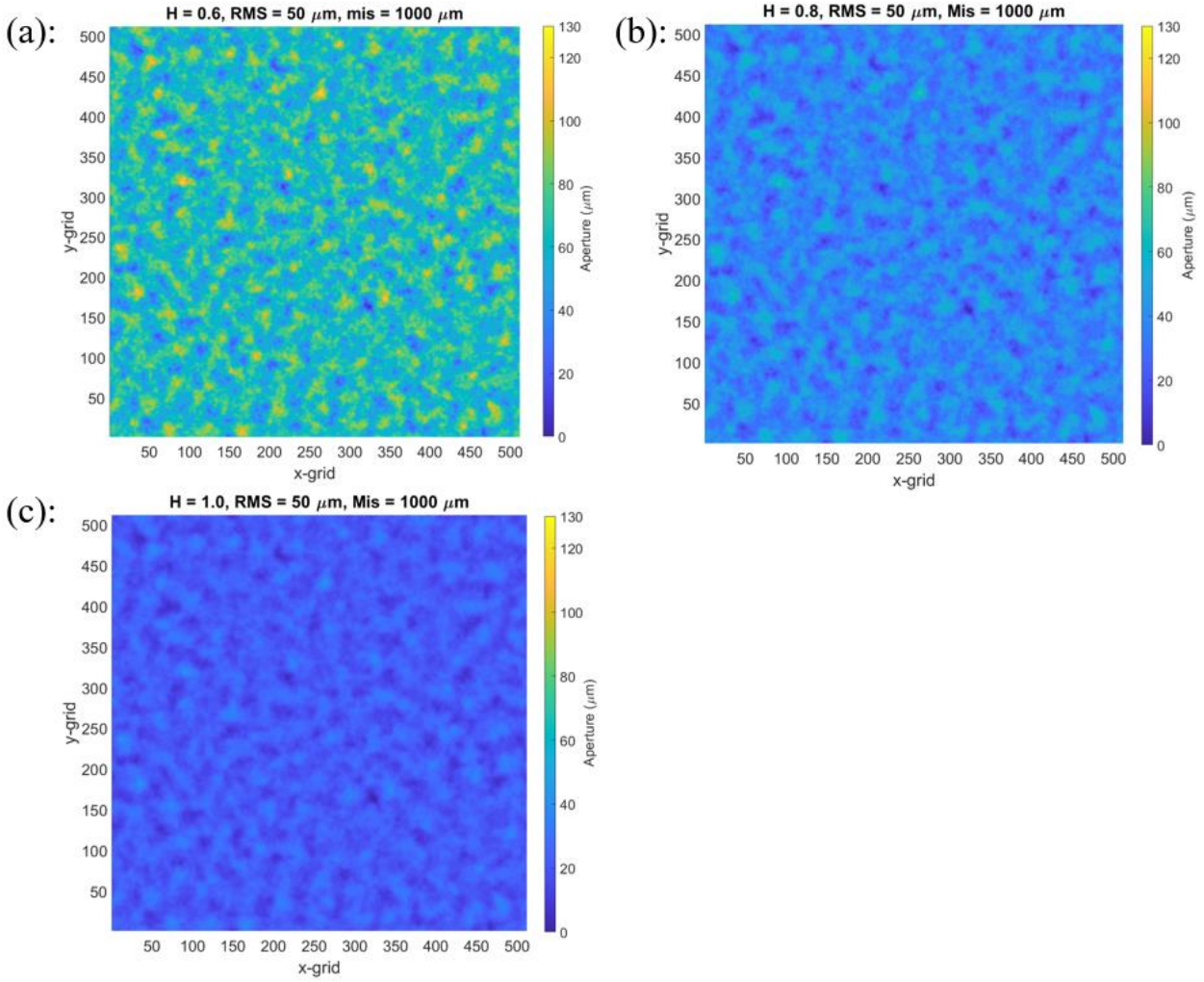

Figure 4.1. Effect of the H value on the aperture field. The RMS = 50 μm and λ_c = 1000 μm. The scale of the color bar is between 0 and 130 μm. The number of grids in the x- and y- direction is 512. (a): aperture field when H = 0.6, which corresponds to surface pair 1 in Table 4.2; (b): aperture field when H = 0.8, which corresponds to surface pair 2 in Table 4.2; (c): aperture field when H = 1.0, which corresponds to surface pair 3 in Table 4.2. The H value increases from sub-figure (a) to sub-figure (c).

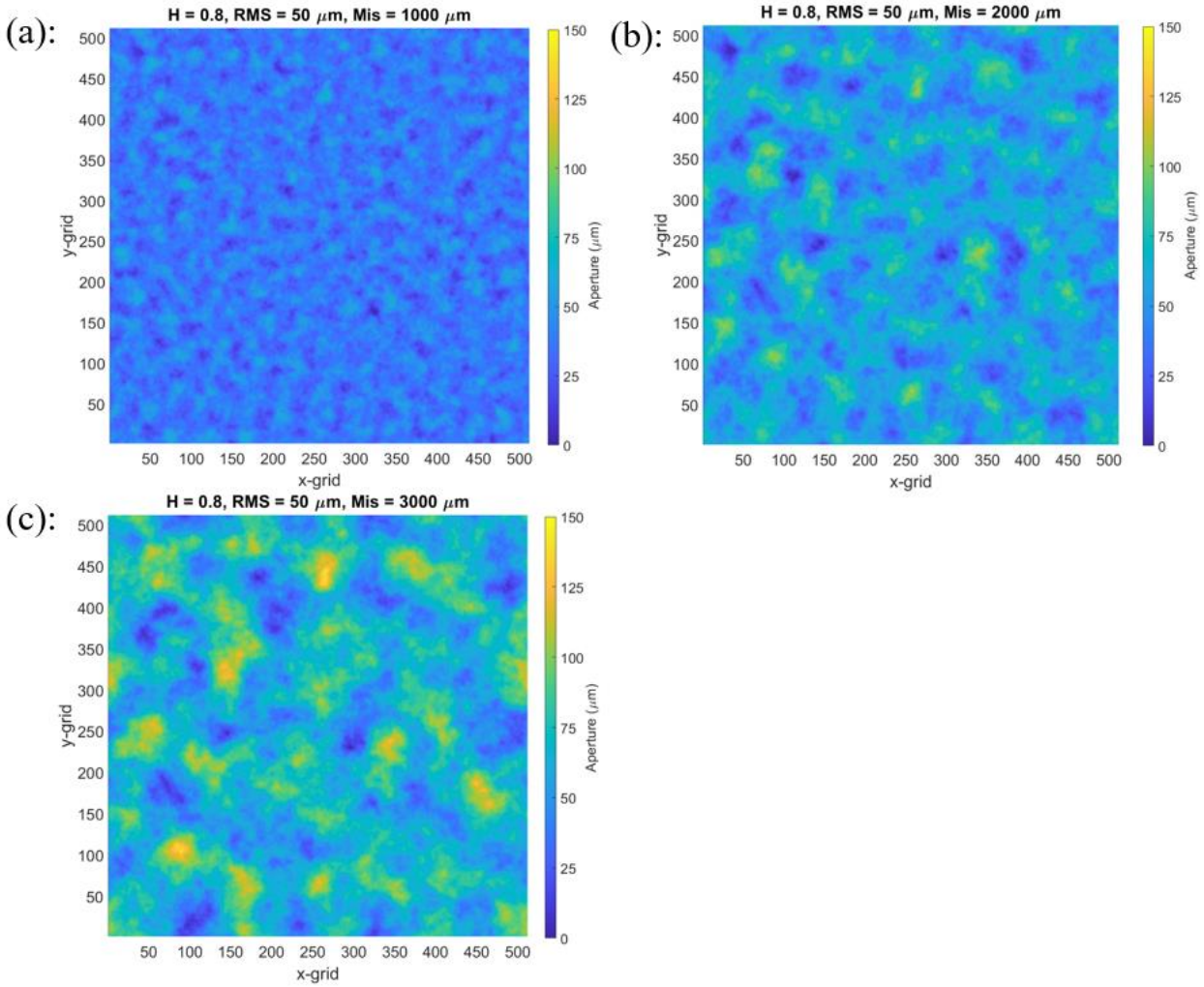

Figure 4.2. Effect of the λ_c value on the aperture field. The RMS = 50 μm and H = 0.8. The scale of the color bar is between 0 and 150 μm. The number of grids in the x- and y- direction is 512. (a): aperture field when λ_c = 1000 μm, which corresponds to surface pair 2 in Table 4.2; (b): aperture field when λ_c = 2000 μm, which corresponds to surface pair 4 in Table 4.2; (c): aperture field when λ_c = 3000 μm, which corresponds to surface pair 5 in Table 4.2. The λ_c value increases from sub-figure (a) to sub-figure (c).

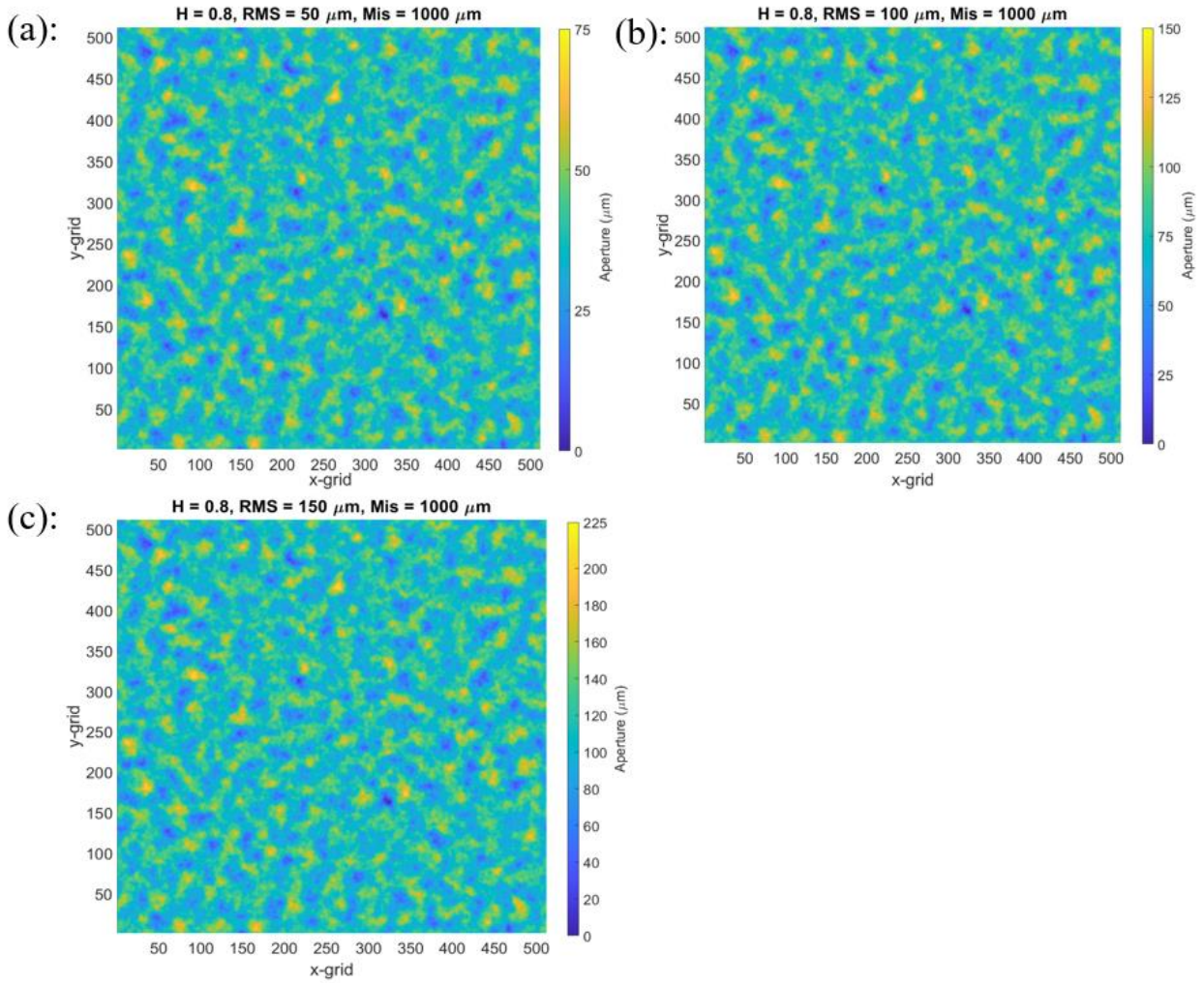

Figure 4.3. Effect of the RMS value on the aperture field. The H = 0.8 and λ_c = 1000 μm. The scale of the color bar (aperture value) is proportional to the RMS value. The number of grids in the x- and y- direction is 512. (a): aperture field when RMS = 50 μm, which corresponds to surface pair 2 in Table 4.2; (b): aperture field when RMS = 100 μm, which corresponds to surface pair 6 in Table 4.2; (c): aperture field when RMS = 150 μm, which corresponds to surface pair 7 in Table 4.2. The RMS value increases from sub-figure (a) to sub-figure (c).

As discussed in Section 3.6, in physics, a larger H value corresponds to a smoother local surface profile (see Figure 3.21), a larger λ_c value corresponds to a larger shear offset between two surfaces, and the RMS value defines the magnitude of surface elevation z (z scales linearly with the RMS value). The results in Figure 4.1 suggest that if the local surface profile is smoother, the average aperture value will be smaller; the results in Figure 4.2 indicate that if the offset between two surfaces increases, the average aperture value will be larger; the results in Figure 4.3 imply that if the H and λ_c values are constant (same local smoothness and surface offset), the average aperture value scales linearly with the RMS value.

4.2 Creep simulation results for the Maxwell model

The creep deformations of the seven surface pairs are calculated using the Maxwell model. Table 4.4 summarizes the input parameters. The parameters are obtained from the testing results of the Vaca Muerta Shale published by Mighani et al. (2019).

Table 4.4. Input parameters for the Maxwell model (see Section 3.4 for the model explanation)

Parameters	Value
Shear modulus, G (GPa)	7.0
Poisson's ratio, υ	0.25
Viscosity, η (GPa*s)	2.0×10^7
Relaxation time, $\tau = \eta / G$ (s)	2.857×10^6

The following parameters are also defined:

1) Macroscopic stress σ_1 = F / A, where F is the total force applied on the fracture surface, and A is the area of the fracture surface (10 mm * 10 mm).
2) Contact ratio (%) = (No. of contacting cells / No. of total cells) * 100. See the definition in Figure 3.14 in Section 3.2.

Figure 4.4 summarizes the effect of different H, λ_c, and RMS values on the creep deformation. In the simulation, σ_1 is fixed at 10 MPa. The initial values of the average aperture and contact area correspond to the elastic deformation. The time duration is from 0 to 2τ (τ is the relaxation time, which has been defined in Table 4.4 and Section 3.4).

(a) mean aperture

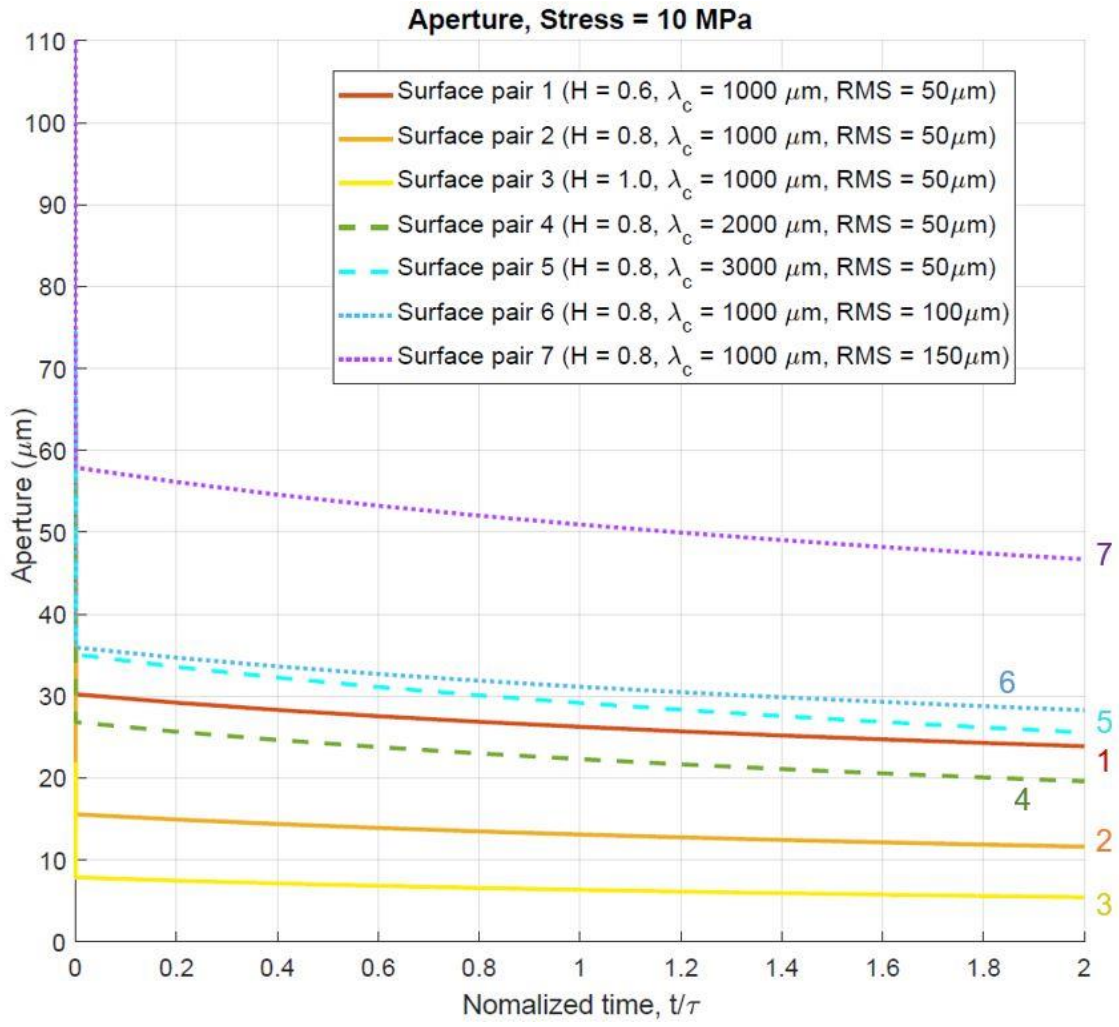

(b) contact ratio

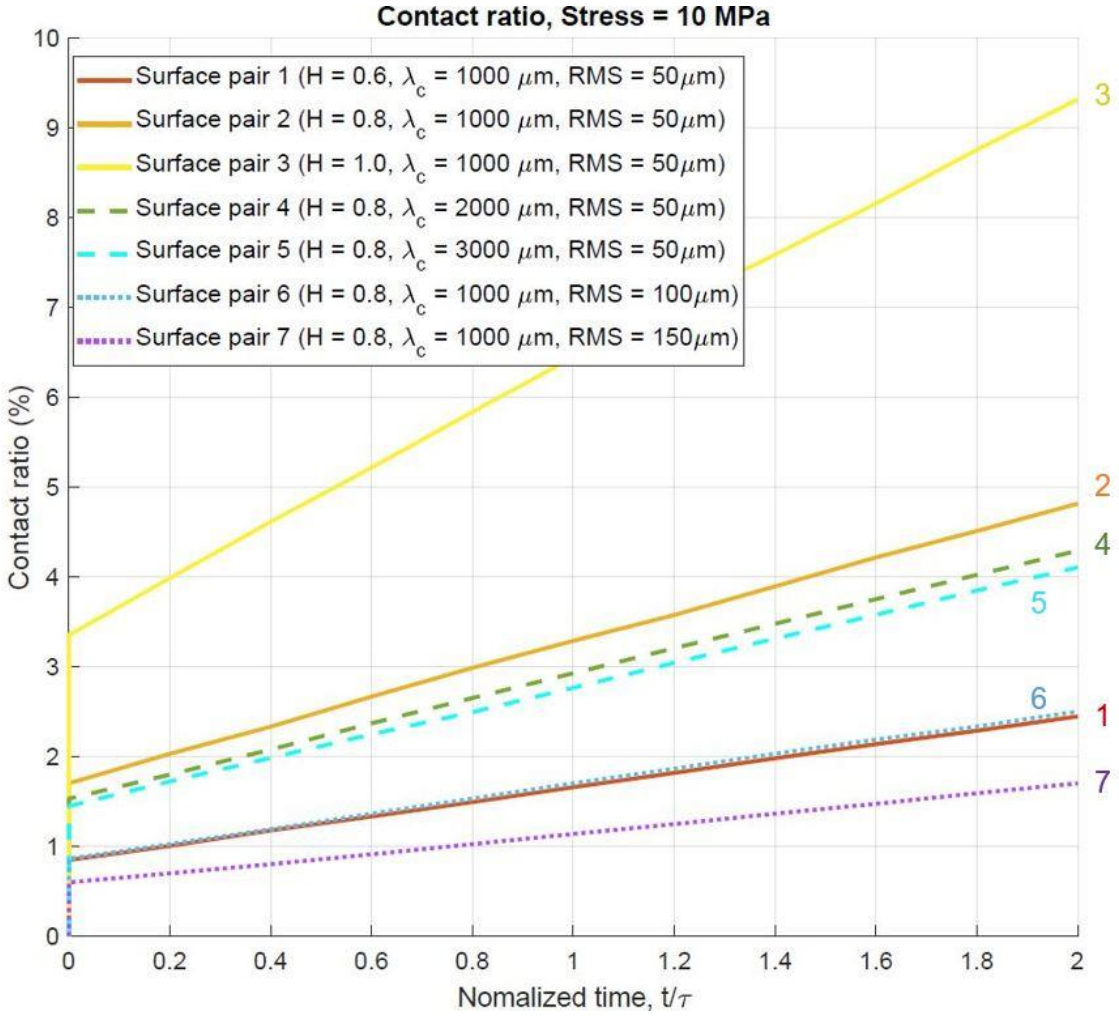

Figure 4.4. Creep deformation of the seven surface pairs (shown in Tables 4.2 and 4.3). The horizontal axis corresponds to the normalized time (time t divided by τ, and τ is the relaxation time). (a): mean aperture changing with time for the seven surface pairs; (b): contact ratio changing with time for the seven surface pairs.

The following conclusions can be drawn:

1) Based on the curves of Surface pairs 1, 2, and 3, when H increases, the average aperture decreases, and the slope of the curve in Figure 4.4 (b) increases. This indicates that the contact ratio increases faster with time.
2) Based on the curves of Surface pairs 2, 4, and 5, when λ_c increases, the average aperture increases, and the slope of the curve in Figure 4.4 (b) decreases. This indicates that the contact ratio increases slower with time.
3) Based on the curves of Surface pairs 2, 6, and 7, when RMS increases, the average aperture increases, and the slope of the curve in Figure 4.4 (b) decreases. This indicates that the contact ratio increases slower with time.
4) With the current surface parameters, macroscopic stresses, and the time durations, the contact ratio is generally less than 10%.

Table 4.5 summarizes the above conclusions.

Table 4.5. Conclusions for the Maxwell model simulation.

Parameters	Average aperture		Contact ratio	
	Initial value	Decrease rate	Initial value	Increase rate
H ↑	↓	↓	↑	↑
λ_c ↑	↑	↑	↓	↓
RMS ↑	↑	↑	↓	↓

Note: ' ↓ ' means decrease and ' ↑ ' means increase.

As described in Section 3.6, in physics, a larger H value corresponds to a smoother local surface profile (see Figure 3.21), a larger λ_c value corresponds to a larger shear offset between two surfaces, and the RMS value defines the magnitude of initial aperture field h (h scales linearly with the RMS value). In physics, the results in Figure 4.4 suggest that:

1) If the local surface profile is smoother (surface pairs 1, 2, and 3), the average aperture value during the creep stage will be smaller. In addition, for the same creep time, the area of contacting asperities will be larger.
2) If the shear offset between two surfaces is larger (surface pairs 2, 4, and 5), the average aperture value during the creep stage will be larger. In addition, for the same creep time, the area of contacting asperities will be smaller.
3) If the absolute value of the initial aperture field is larger (surface pairs 2, 6, and 7), the average aperture value during the creep stage will be larger. In addition, for the same creep time, the area of contacting asperities will be smaller.

Figure 4.5 compares the contact area and local contact stress before and after the creep stage. The white areas correspond to non-contacting areas, and the colored areas correspond to contacting areas. The input parameters are: H = 1.0, RMS = 50 μm, λ_c = 1000 μm, σ = 10 MPa, and the creep time duration = 2τ. The left figure corresponds to the stress distribution before the creep (the moment after the elastic deformation), and the right figure corresponds to the stress distribution after the time duration of 2τ. The scale of the color bar is 0 to 2000 MPa. After creep, the contact area increases, and the local contact stresses (the vertical stress in the contacting cells, see the definition of cell in Figure 3.14 in Section 3.2) decrease. The change of color between Figures 4.5 (a) and (b) may not be clearly visible; the decrease in local contact stress will be clearly shown in Section 4.4.3.

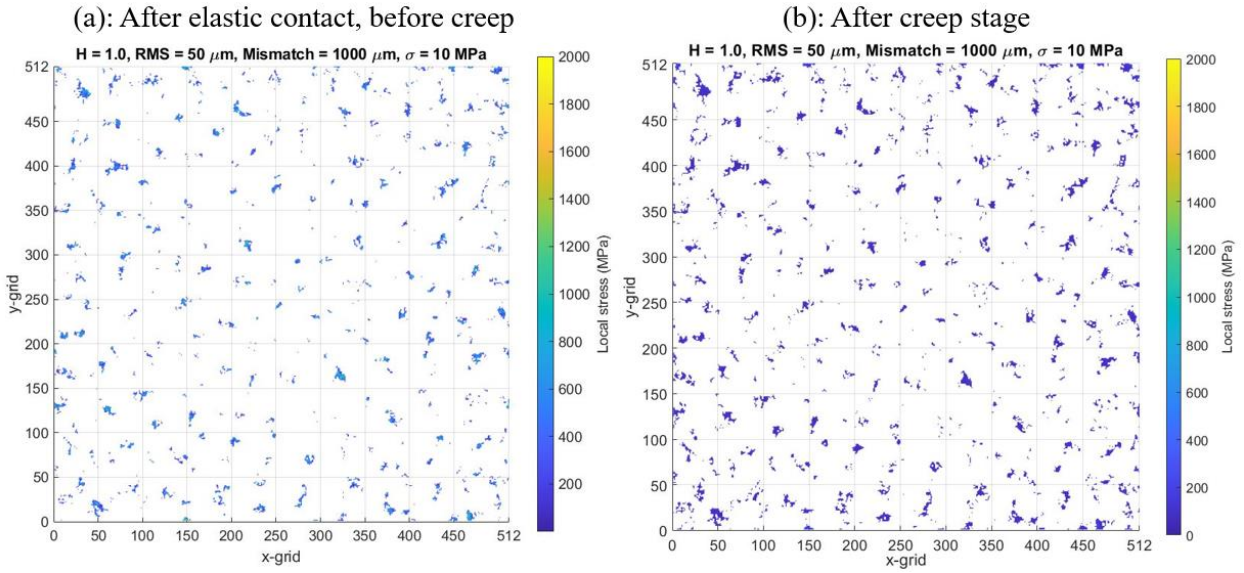

Figure 4.5. Contact area and local contact stress evolution. (a): contact area and local contact stress before creep (the moment after the elastic deformation); (b): contact area and local contact stress after creep (the time duration is 2τ). The number of grids in the x- and y- direction is 512.

4.3 Creep simulation results for the SLS model

The creep deformations of the seven surface pairs are also calculated by the SLS model. Table 4.6 summarizes the input parameters. For comparison purpose, the shear modulus and viscosity for the SLS model are identical to these of the Maxwell model.

Table 4.6. Input parameters for the SLS model (see Section 3.4 for the model explanation)

Parameters	Value
Shear modulus, G_1 (GPa)	7.0
Shear modulus, G_2 (GPa)	7.0
Poisson's ratio, υ	0.25
Viscosity, η (GPa*s)	2.0×10^7
Relaxation time, $\tau = \eta_2 / G_2$ (s)	2.857×10^6

Figure 4.6 summarizes the effect of different H, λ_c, and RMS values on the creep deformation. In the simulation, σ_1 is fixed at 10 MPa. The initial values of the average aperture and contact area correspond to the elastic deformation. The time duration is from 0 to 5τ (τ is the relaxation time, which has been defined in Table 4.4 and Section 3.4). Compared with the Maxwell model, the time duration is extended from 2τ to 5τ to better illustrate the decreasing creep rate.

(a) mean aperture

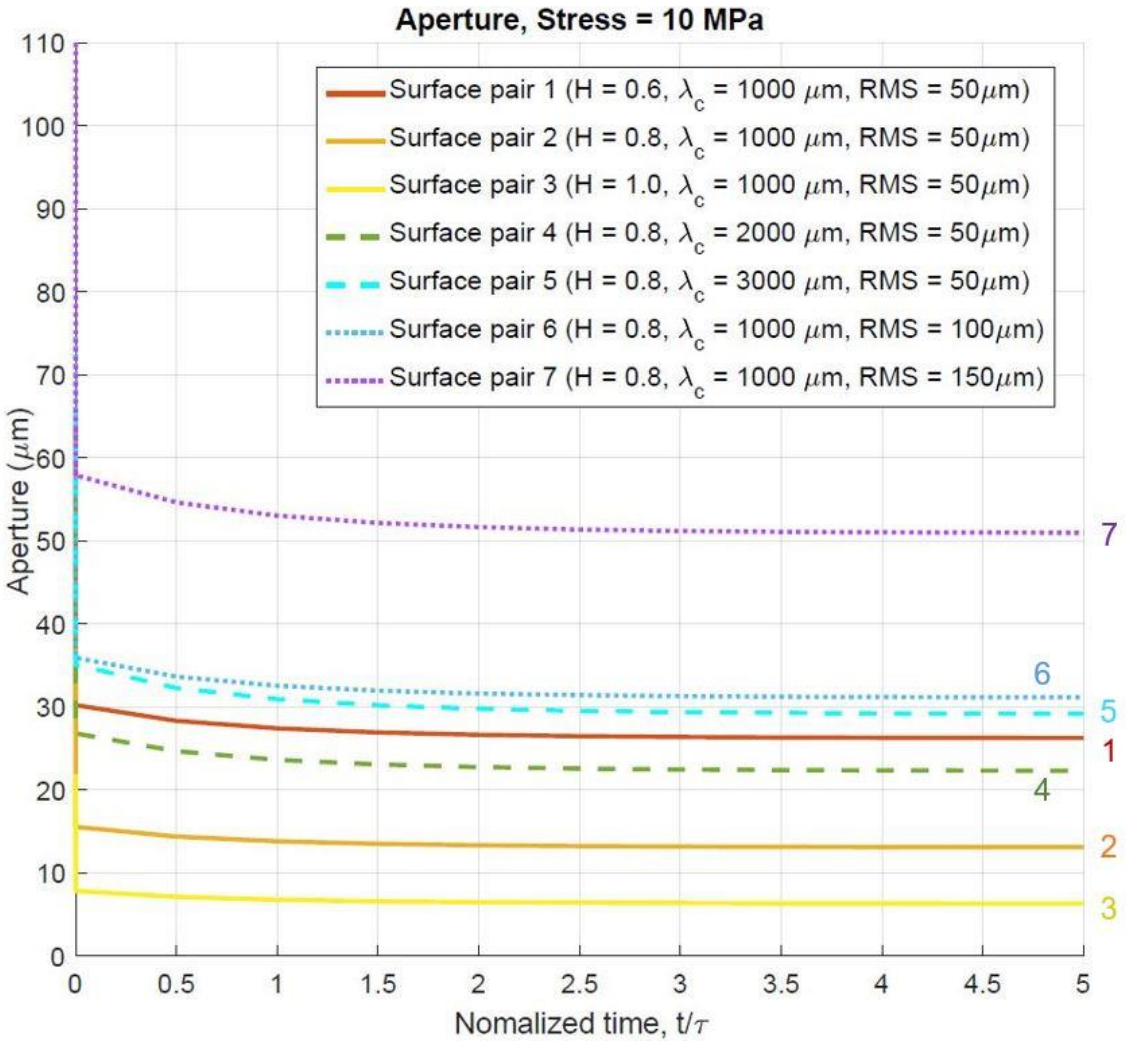

(b) contact ratio

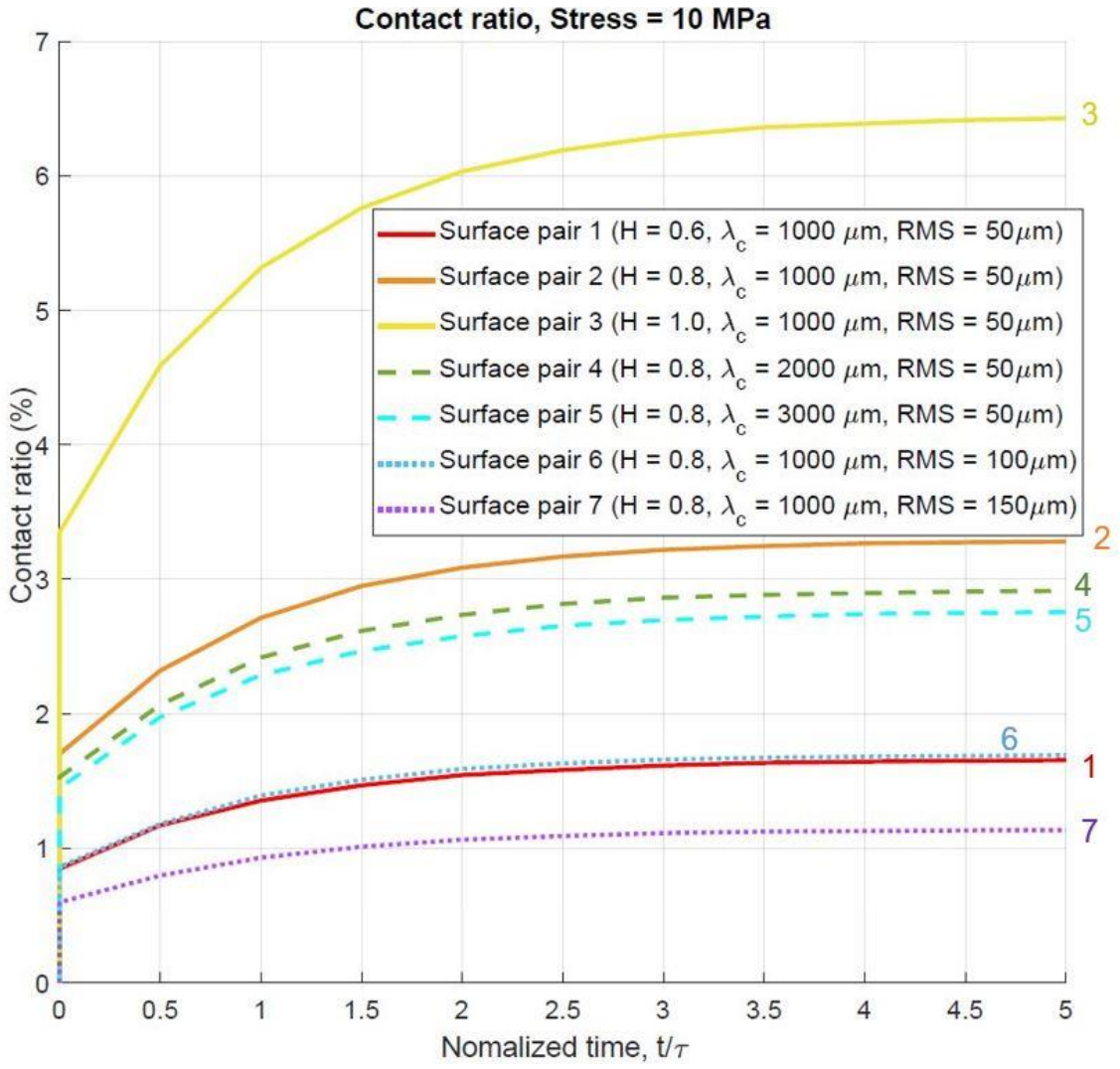

Figure 4.6. Creep deformation of the seven surface pairs (shown in Tables 4.2 and 4.3). The horizontal axis corresponds to the normalized time (time t divided by τ, and τ is the relaxation time). (a): mean aperture changing with time for the seven surface pairs; (b): contact ratio changing with time for the seven surface pairs.

The following conclusions can be drawn:

1) Based on the curves of Surface pairs 1, 2, and 3, when H increases, the average aperture decreases, and the slope of the curve in Figure 4.6 (b) increases. This indicates that the contact ratio increases faster with time.
2) Based on the curves of Surface pairs 2, 4, and 5, when λ_c increases, the average aperture increases, and the slope of the curve in Figure 4.6 (b) decreases. This indicates that the contact ratio increases slower with time.
3) Based on the curves of Surface pairs 2, 6, and 7, when RMS increases, the average aperture increases, and the slope of the curve in Figure 4.6 (b) decreases. This indicates that the contact ratio increases slower with time.

4) With the current surface parameters, macroscopic stresses, and the time durations, the contact ratio is generally less than 10%.
5) With the current surface parameters, macroscopic stresses, and the time durations, the creep rate (aperture decrease rate) decreases significantly with time. The main reason is that the SLS model assumes exponentially decreasing creep rate.

Table 4.7 summarizes the above conclusions. The effects of H, RMS, and λ_c on the creep rate under the SLS model are similar to those under the Maxwell model.

Table 4.7. Conclusions for the SLS model simulation.

Parameters	Average aperture		Contact ratio	
	Initial value	Decrease rate	Initial value	Increase rate
H ↑	↓	↓	↑	↑
λ_c ↑	↑	↑	↓	↓
RMS ↑	↑	↑	↓	↓

Note: ' ↓ ' means decrease and ' ↑ ' means increase.

As described in Section 3.6, in physics, a larger H value corresponds to a smoother local surface profile (see Figure 3.21), a larger λ_c value corresponds to a larger offset between two surfaces, and the RMS value defines the magnitude of initial aperture field h (h scales linearly with the RMS value). In physics, the results in Figure 4.6 suggest that:

1) If the local surface profile is smoother (surface pairs 1, 2, and 3), the average aperture value during the creep stage will be smaller. In addition, for the same creep time, the area of contacting asperities will be larger.
2) If the shear offset between two surfaces is larger (surface pairs 2, 4, and 5), the average aperture value during the creep stage will be larger. In addition, for the same creep time, the area of contacting asperities will be smaller.
3) If the absolute value of the initial aperture field is larger (surface pairs 2, 6, and 7), the average aperture value during the creep stage will be larger. In addition, for the same creep time, the area of contacting asperities will be smaller.

Figure 4.7 compares the contact area and local contact stress before and after the creep stage. The white areas correspond to non-contacting areas, and the colored areas correspond to contacting areas. The input parameters are: H = 1.0, RMS = 50 μm, λ_c = 1000 μm, σ = 10 MPa, and the creep time duration = 5τ. The left figure corresponds to the stress distribution before the creep (the moment after the elastic deformation), and the right figure corresponds to the stress distribution after the time duration of 5τ. The scale of the color bar is 0 to 2000 MPa. After creep, the contact area increases, and the local contact stresses (the vertical stress in the contacting cells, see the definition of cell in Figure 3.14 in Section 3.2) decrease (the color becomes darker). The change of color between Figures 4.7 (a) and (b) may not be clearly visible; the decrease in local contact stress will be clearly shown in Section 4.4.3.

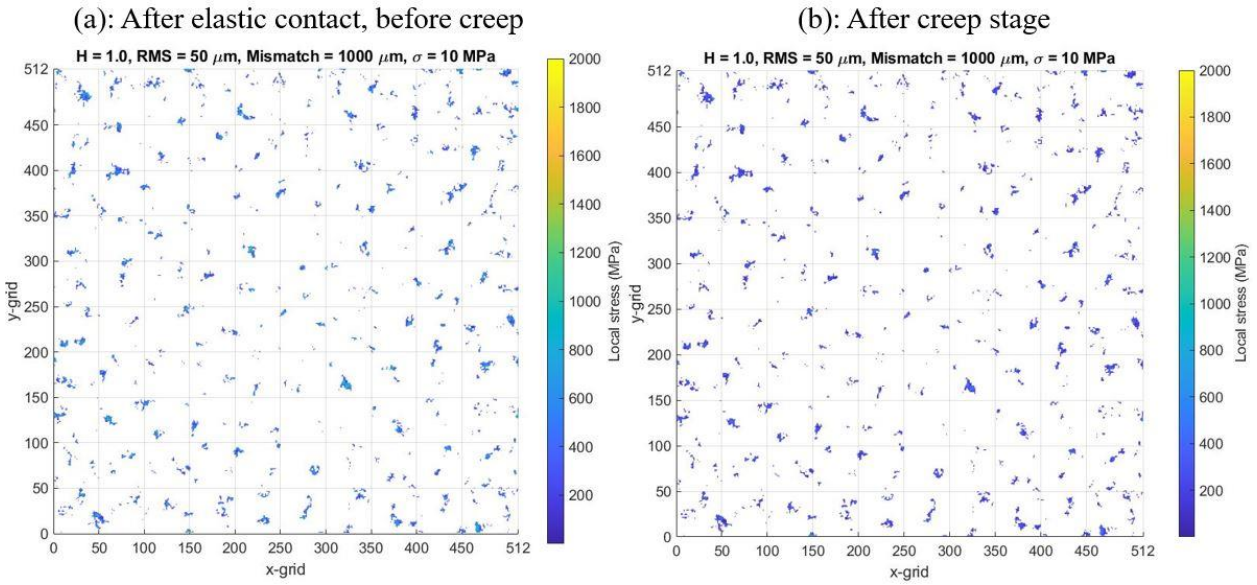

Figure 4.7. Contact area and local contact stress evolution. (a): contact area and local contact stress before creep (the moment after the elastic deformation); (b): contact area and local contact stress after creep (the time duration is 5τ). The number of grids in the x- and y- direction is 512.

4.4 Discussion for numerical results

4.4.1 Creep deformation normalization – the Maxwell model

The creep curves (mean aperture and contact ratio versus normalized time) under different H, λ_c, and RMS values can be normalized. For each surface pair (see Figures 4.1 to 4.3 for the surface pair plots), between time duration 0 and 2τ, the mean aperture, h, and the contact ratio, c, are normalized as:

$$h_{nor} = \frac{h_{elas}}{h_{elas-ref}} h \tag{4.1}$$

and

$$c_{nor} = \frac{c_{elas}}{c_{elas-ref}} c \tag{4.2}$$

where h_{nor} is the normalized mean aperture for each surface pair, h_{elas} is the mean aperture right after the elastic deformation (before creep) for each surface pair, $h_{elas\text{-}ref}$ is the mean aperture right after the elastic deformation for surface pair 2 (H = 0.8, RMS = 50 μm, and λ_c = 1000 μm), c_{nor} is the normalized contact ratio for each surface pair, c_{elas} is the contact ratio right after the elastic deformation (before creep) for each surface pair, and $c_{elas\text{-}ref}$ is the contact ratio right after the elastic deformation for surface pair 2. According to Eqn. 4.1, the unit of normalized aperture h_{nor} is the same as that of h, which is μm. Surface pair 2 is chosen because it is the reference surface pair for the seven fracture surface pairs.

Figure 4.8 summarizes the normalized mean aperture and contact ratio for different H, λ_c, and RMS values. σ_1 is fixed at 10 MPa, and the time duration is from 0 to 2τ.

(a) normalized mean aperture

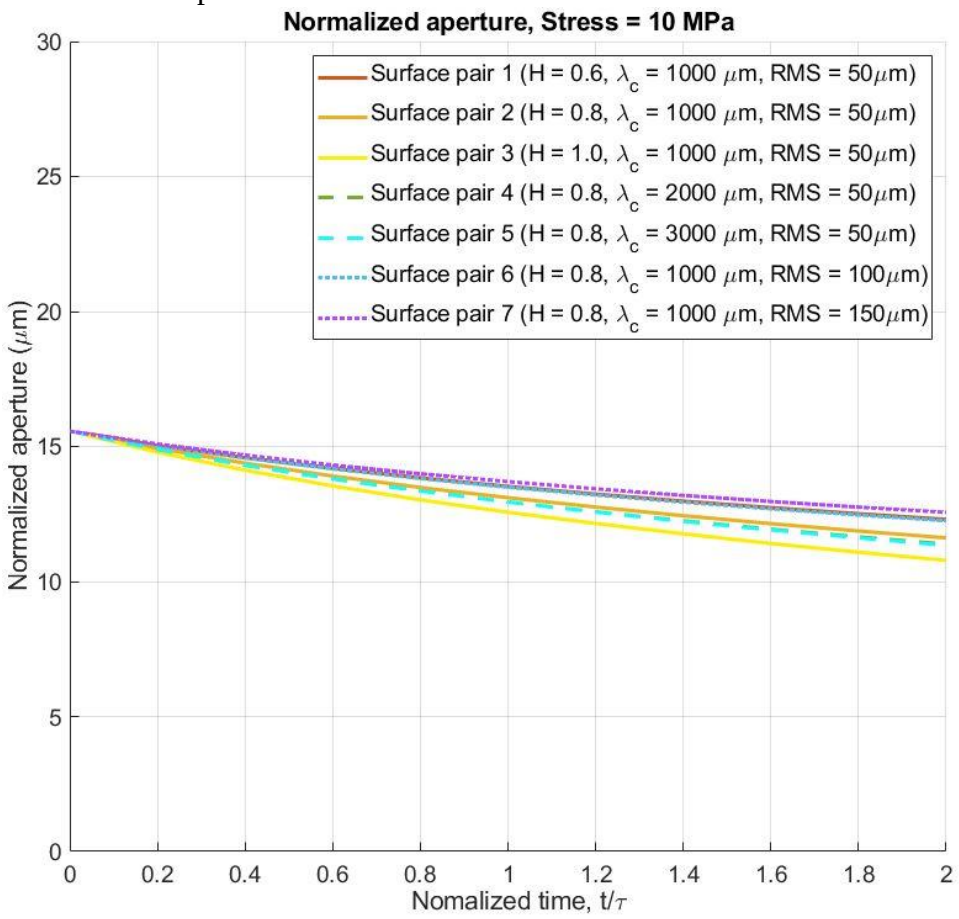

(b) normalized contact ratio

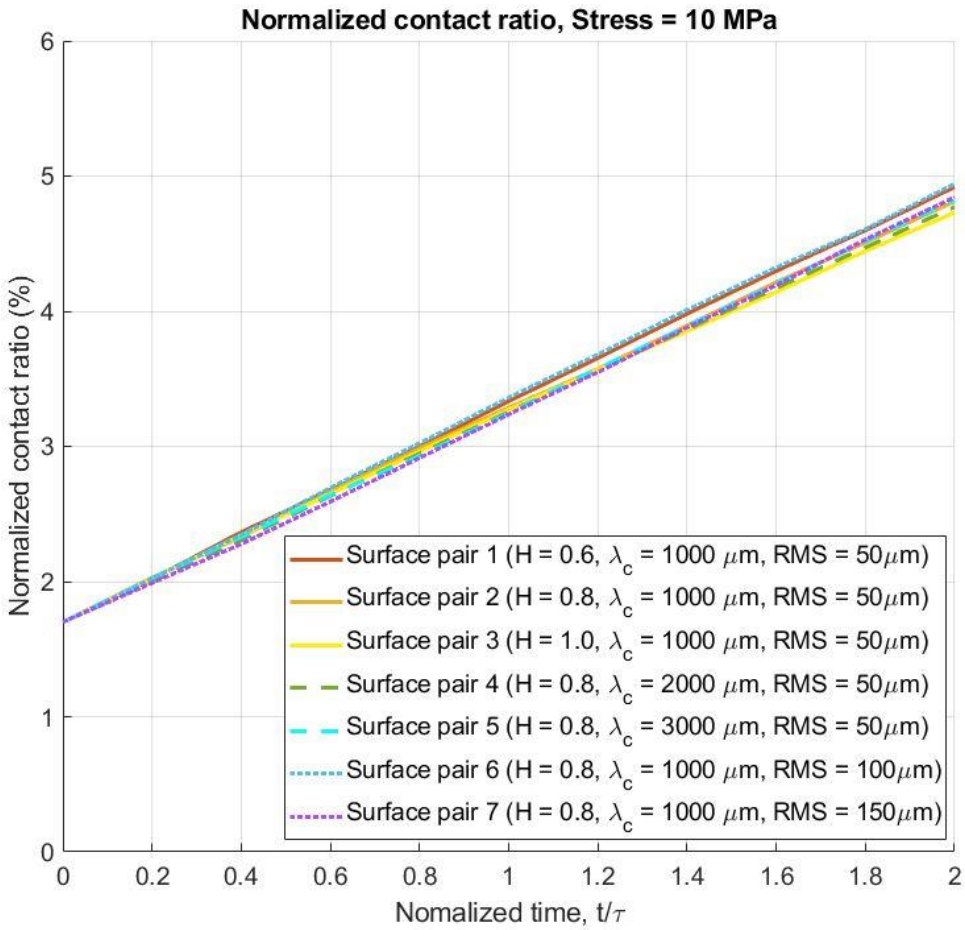

Figure 4.8. Normalized mean aperture and contact ratio of the seven surface pairs (shown in Tables 4.2 and 4.3). The time t is normalized by τ. (a): normalized mean aperture changing with time for the seven surface pairs; (b): normalized contact ratio changing with time for the seven surface pairs. The formulae for normalized mean aperture and normalized contact ratio are shown in Eqns. 4.1 and 4.2, respectively.

The results show that by normalizing the values as described in Eqns. 4.1 and 4.2, the curves for different surface parameters fall into a narrow region.

4.4.2 Creep deformation normalization – the SLS model

The creep curves (mean aperture and contact ratio versus normalized time) under different H, λ_c, and RMS values can be normalized similarly as described in Section 4.4.1. For each surface pair, between time duration 0 and 5τ, the mean aperture, h, and the contact ratio, c, are normalized as:

$$h_{nor} = \frac{h_{elas}}{h_{elas-ref}} h \tag{4.3}$$

and

$$c_{nor} = \frac{c_{elas}}{c_{elas-ref}} c \tag{4.4}$$

where h_{nor} is the normalized mean aperture for each surface pair, h_{elas} is the mean aperture right after the elastic deformation (before creep) for each surface pair, $h_{elas\text{-}ref}$ is the mean aperture right after the elastic deformation for surface pair 2 (H = 0.8, RMS = 50 μm, and λ_c = 1000 μm), c_{nor} is the normalized contact ratio for each surface pair, c_{elas} is the contact ratio right after the elastic deformation (before creep) for each surface pair, and $c_{elas\text{-}ref}$ is the contact ratio right after the elastic deformation for surface pair 2. Surface pair 2 is chosen because it is the reference surface pair for the seven fracture surface pairs.

Figure 4.9 summarizes the normalized mean aperture and contact ratio for different H, λ_c, and RMS values. σ_1 is fixed at 10 MPa, and the time duration is from 0 to 5τ.

(a) normalized mean aperture

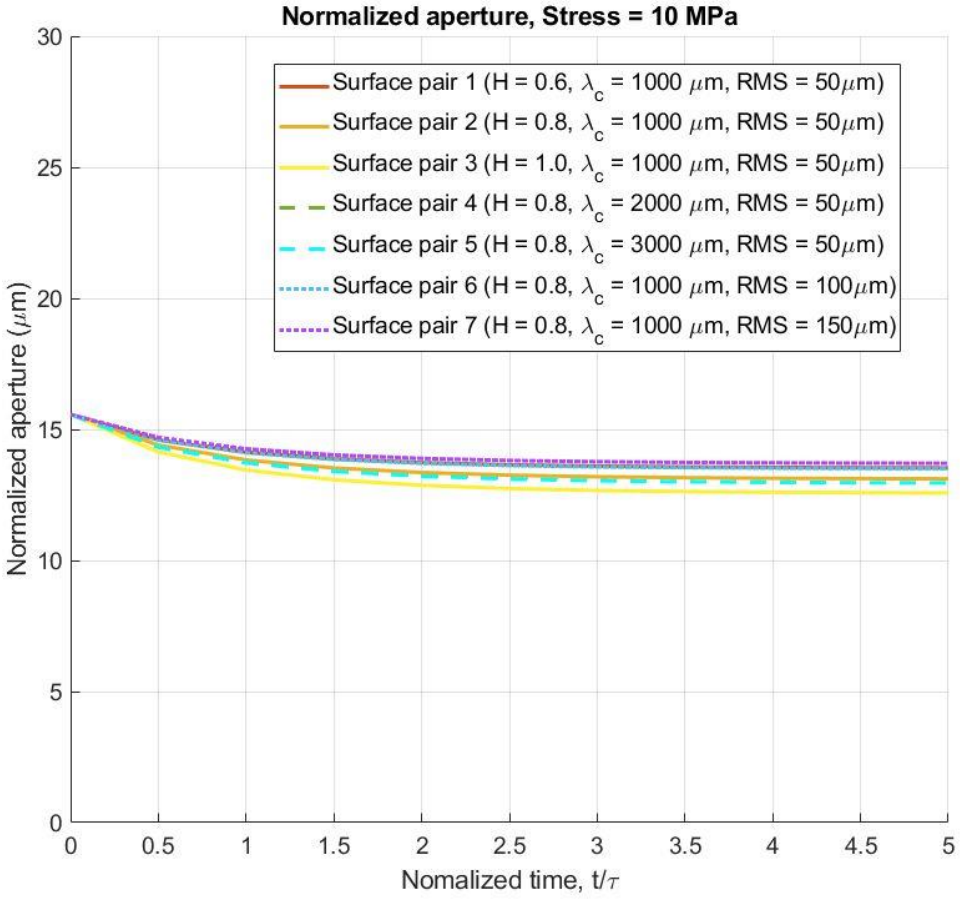

(b) normalized contact ratio

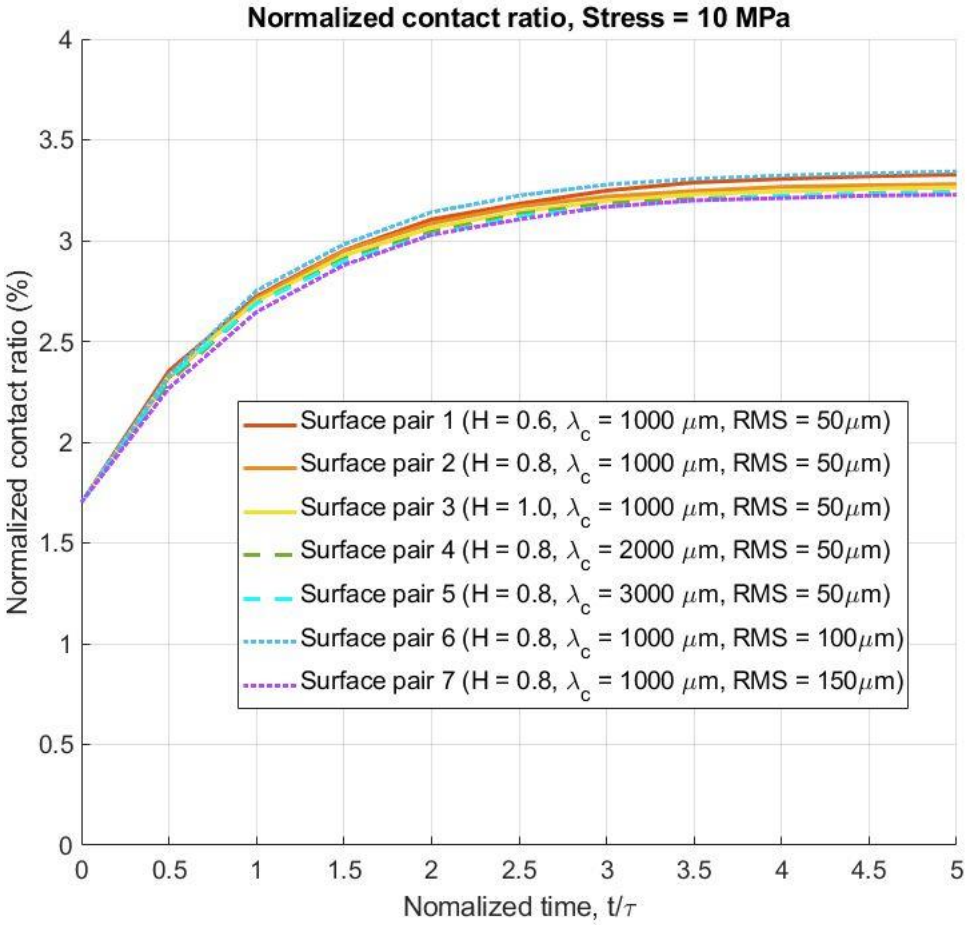

Figure 4.9. Normalized mean aperture and contact ratio of the seven surface pairs (shown in Tables 4.2 and 4.3). The time t is normalized by τ. (a): normalized mean aperture changing with time for the seven surface pairs; (b): normalized contact ratio changing with time for the seven surface pairs. The formulae for normalized mean aperture and normalized contact ratio are shown in Eqns. 4.3 and 4.4, respectively.

The results show that by normalizing the values as described in Eqns. 4.3 and 4.4, the curves for different surface parameters fall into a narrow region.

4.4.3 Contact pressure evolution during the creep stage – two examples

Figure 4.10 compares the histogram of local contact stress (only for the contacting cells, see the definition of cell in Figure 3.14) before and after the creep stage for surface pair 3 for the Maxwell model. The horizontal axis represents the local contact stress in each contacting cell, and the vertical axis represents the normalized frequency (the number of contacting cells within the stress range / the total number of contacting cells). The Maxwell model is used as the visco-elastic model, and the time duration is 2τ. Other input parameters are: H = 1.0, RMS = 50 μm, λ_c = 1000 μm, and σ = 10 MPa. The blue histogram corresponds to the local stress histogram before the creep (the moment right after the elastic deformation), and the orange histogram corresponds to the local

stress histogram after the time duration of 2τ. This plot implies that after creep, the local stresses in the contact region decrease significantly (the histogram shifts leftwards).

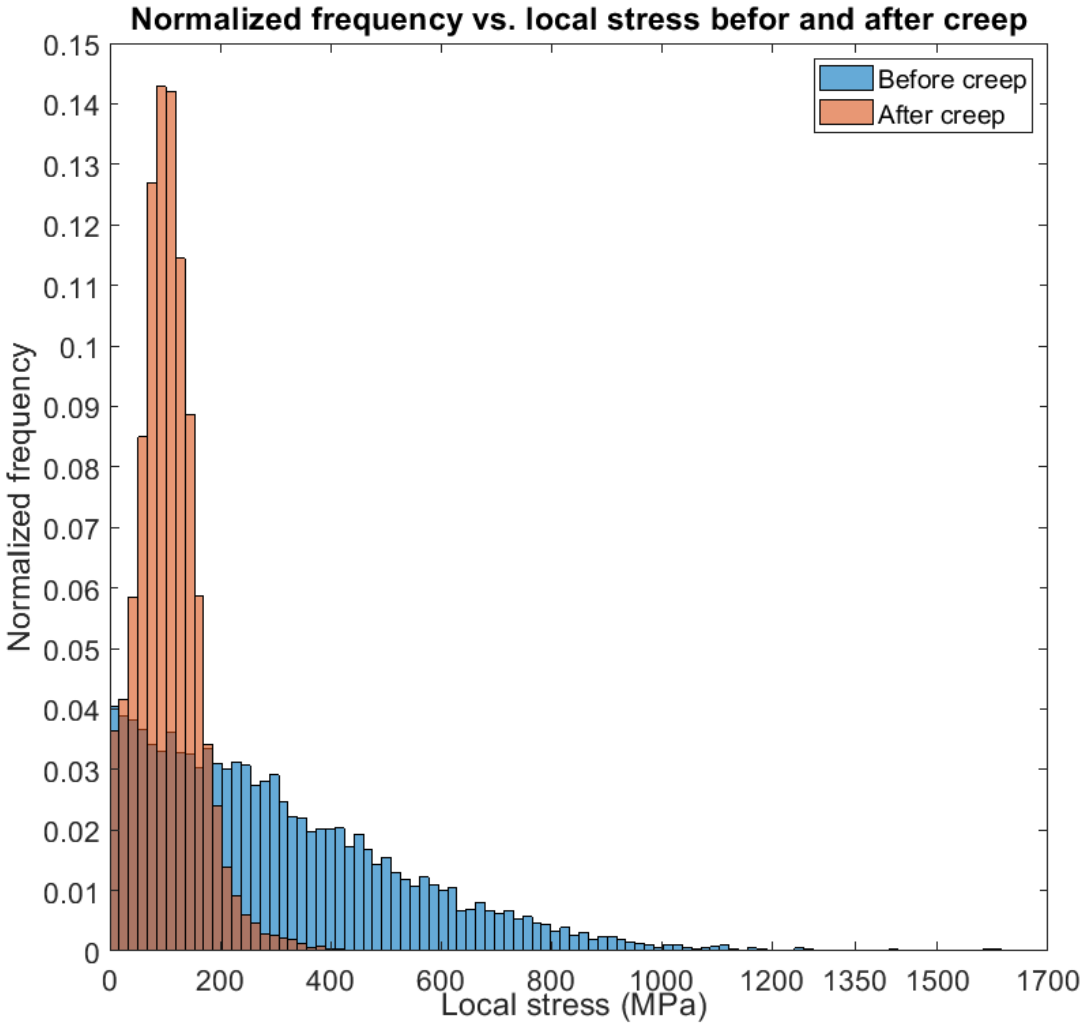

Figure 4.10. Histogram of local contact stress before and after the creep stage. The Maxwell model is used as the input, H = 1.0, RMS = 50 μm, λ_c = 1000 μm, σ = 10 MPa, and the time duration is 2τ.

Figure 4.11 compares the histogram of local contact stress (only for the contacting cells, see the definition of cell in Figure 3.14) before and after the creep stage for surface pair 3 for the SLS model. The horizontal axis represents the local contact stress in each contacting cell, and the vertical axis represents the normalized frequency (the number of contacting cells within the stress range / the total number of contacting cells). The SLS model is used as the visco-elastic model, and the time duration is 5τ. Other input parameters are: H = 1.0, RMS = 50 μm, λ_c = 1000 μm, and σ = 10 MPa. The blue histogram corresponds to the local stress histogram before the creep (the moment right after the elastic deformation), and the orange histogram corresponds to the local stress histogram after the time duration of 5τ. This plot implies that after creep, the local stresses in the contact region decrease (the histogram shifts leftwards).

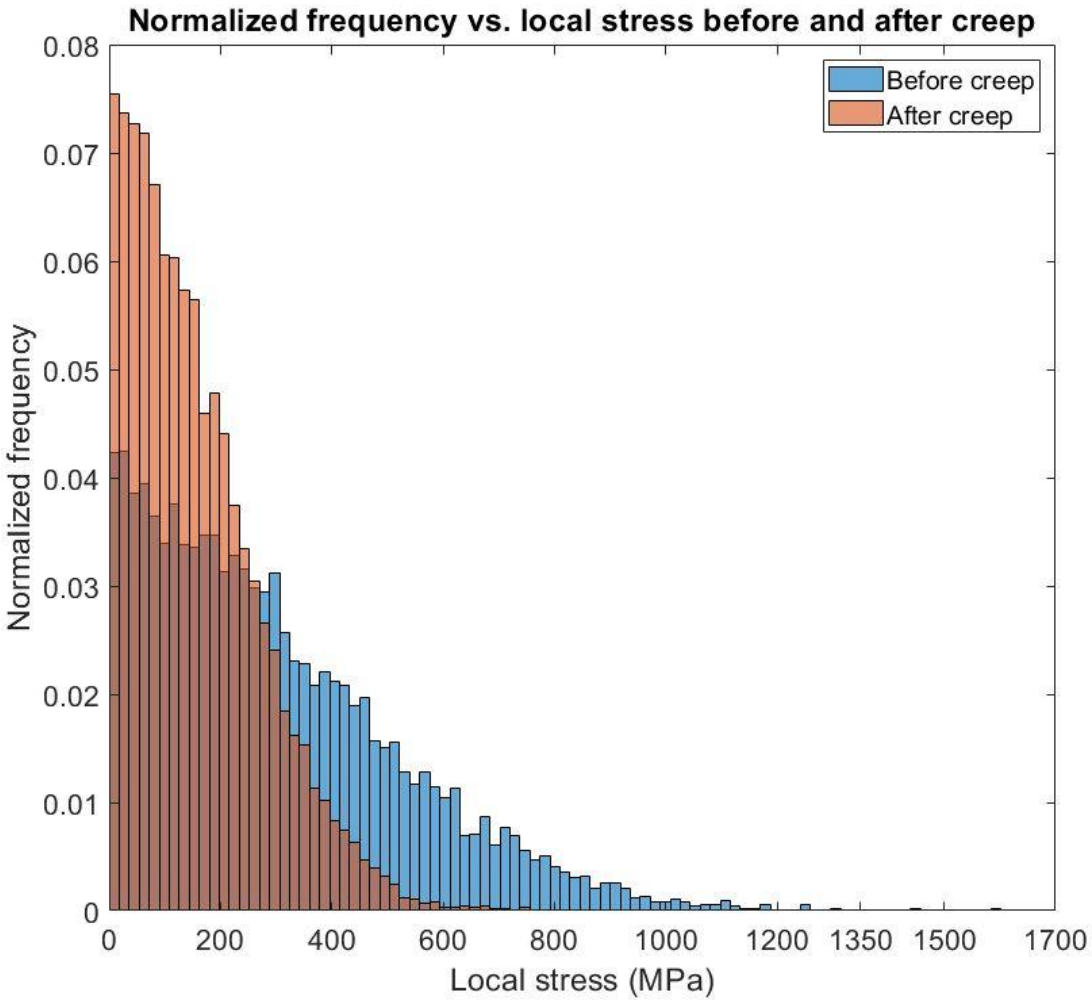

Figure 4.11. Histogram of local contact stress before and after the creep stage. The SLS model is used as the input, H = 1.0, RMS = 50 μm, λ_c = 1000 μm, σ = 10 MPa, and the time duration is 5τ.

From the histograms, it is worth noting that the local contact stress can be larger than 200 MPa. However, for both the Maxwell and SLS models, the input elastic modulus and viscosity are obtained from triaxial tests with confining and differential pressures less than 50 MPa. Therefore, if possible, creep data from triaxial tests with confining and differential pressures larger than 200 MPa should be used to obtain more accurate simulation results.

4.4.4 Parameters affecting the magnitude and shape of the creep curves

The applied macroscopic stress σ_1 significantly affects the magnitude of the creep curves. Figures 4.12 (a) and (b) show the average aperture value and the contact ratio respectively changing with macroscopic stress σ_1 using the Maxwell model; Figures 4.12 (c) and (d) show the average aperture value and the contact ratio respectively changing with macroscopic stress σ_1 using the SLS model. Surface 2 is chosen because it is the reference surface. The results in Figure 4.12 indicate that as

the macroscopic stress σ_1 increases, the average aperture value decreases and the contact ratio increases.

(a):

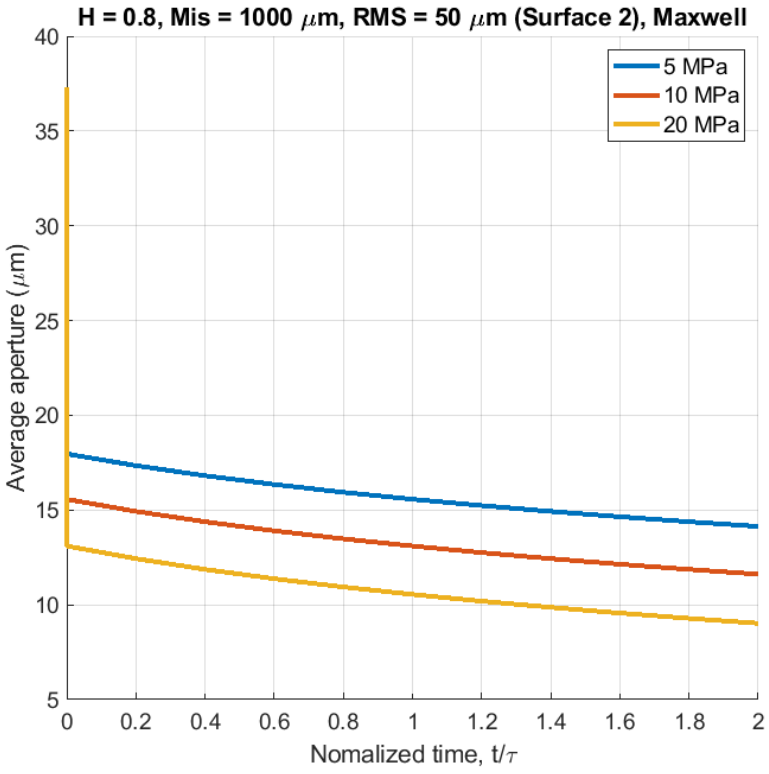

(b):

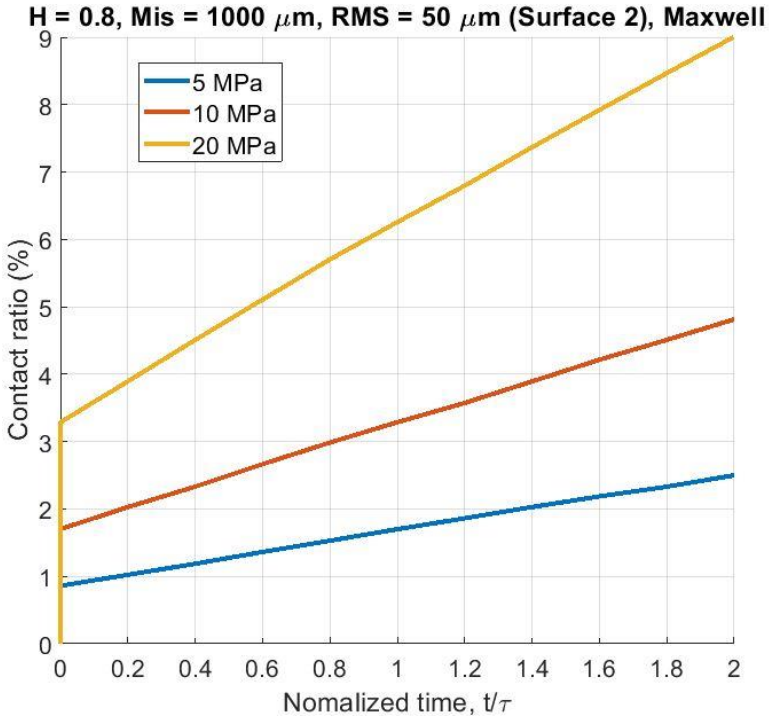

(c):

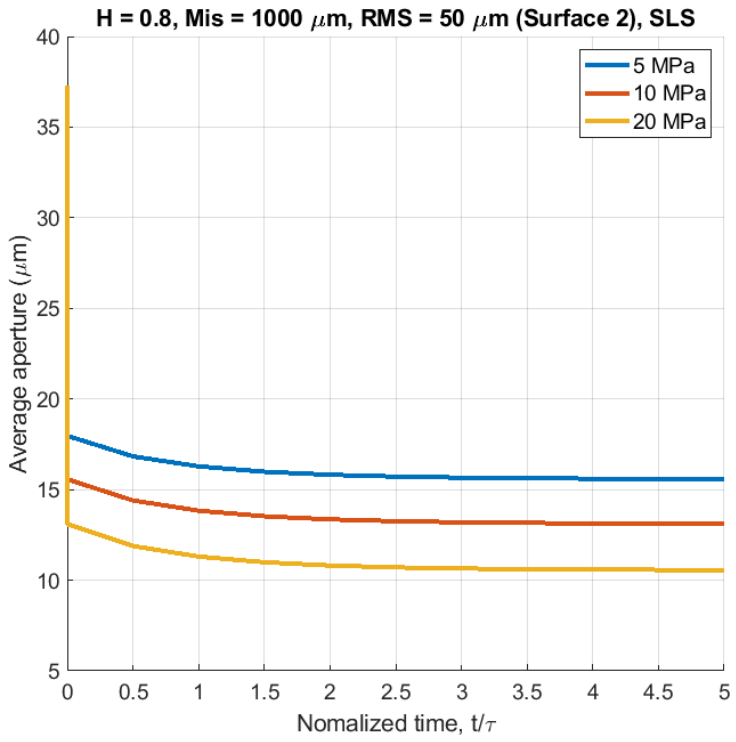

(d):

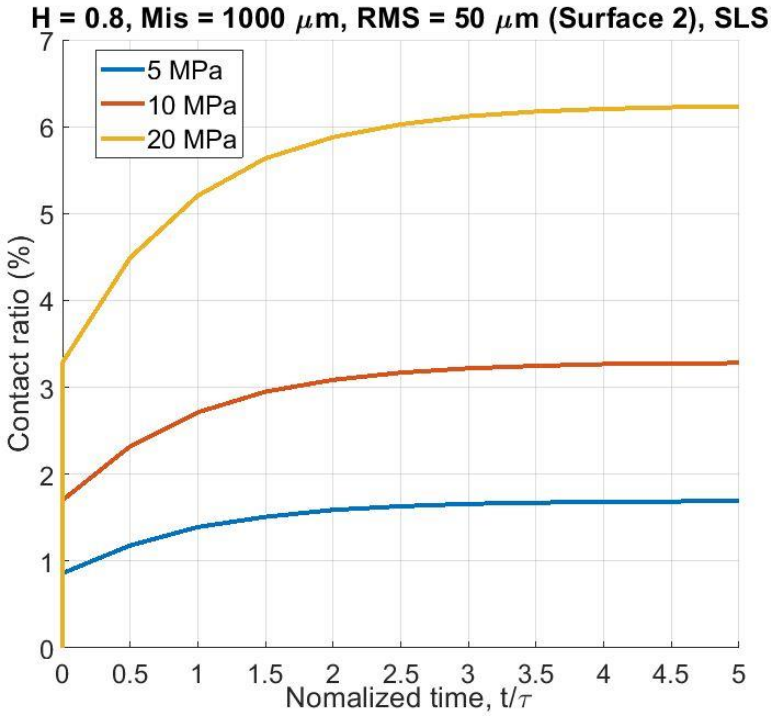

Figure 4.12. Creep curves changing with applied macroscopic stress σ_1. (a): average aperture value changing with macroscopic stress σ_1 using the Maxwell model; (b): average contact ratio changing

with macroscopic stress σ_1 using the Maxwell model; (c): average aperture value changing with macroscopic stress σ_1 using the SLS model; (d): average contact ratio changing with macroscopic stress σ_1 using the SLS model.

The visco-elastic model affects the shape of the creep curves. Figure 4.13 compares the contact ratio of surface 2 changing with time under 10 MPa macroscopic stress. The Maxwell model assumes a constant creep rate. As a result, the contact ratio curve is relatively more linear; the slope of the curve (which indicates the creep rate) does not change significantly with time. In contrast, the SLS model assumes a time-decaying creep rate. As a result, the contact ratio curve flattens with time; the slope of the curve decreases significantly with time.

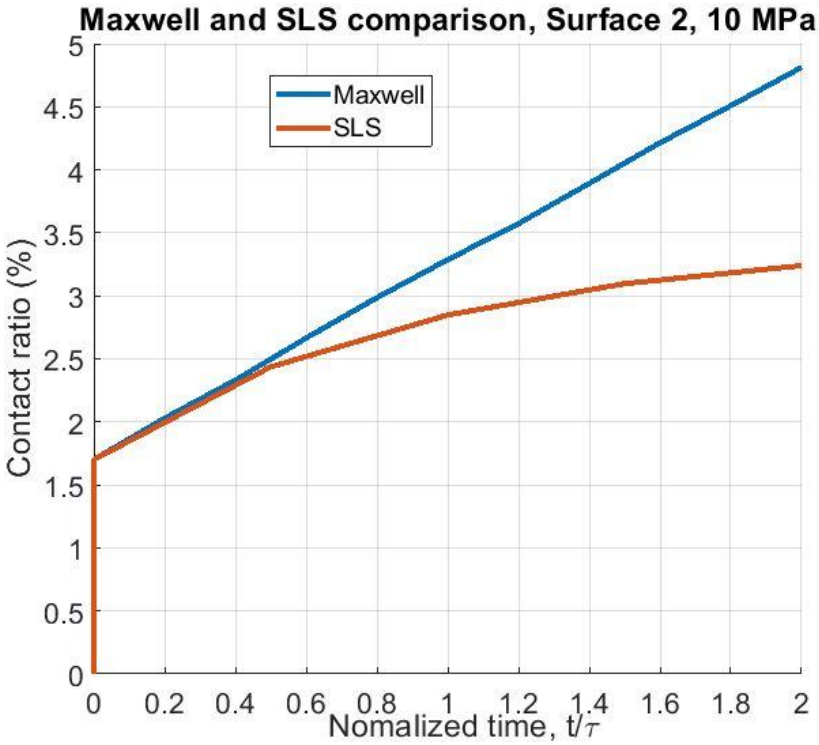

Figure 4.13 Contact ratio changing with time for surface 2 under 10 MPa macroscopic stress. The blue and red curves represent the Maxwell model and the SLS model, respectively.

4.5 Conclusions

In this numerical simulation, an in-house numerical code has been developed to generate synthetic rock fracture surfaces based on Brown's (1995) model, and another code has been developed to simulate visco-elastic deformations of rough fractures. Seven synthetic fracture surface pairs are generated using different values of the Hurst exponent H (0.6, 0.8, and 1.0), root mean square roughness RMS (50 μm, 100 μm, and 150 μm), and mismatch length λ_c (1000 μm, 2000 μm, 3000 μm). The visco-elastic deformations of the seven surface pairs are simulated based on the Maxwell and Standard Linear Solid (SLS) model. For both models, the following conclusions can be drawn:

4) When H increases (surface pairs 1, 2, and 3), the average aperture decreases, and the contact ratio increases faster with time (see Figures 4.4 and 4.6). This indicates that if the local surface profile is smoother, the average aperture value during the creep stage will be smaller. In addition, for the same creep time, the area of contacting asperities will be larger.
5) When λ_c increases (surface pairs 2, 4, and 5), the average aperture increases, and the contact ratio increases slower with time (see Figures 4.4 and 4.6). This implies that if the shear offset between two surfaces is larger, the average aperture value during the creep stage will be larger. In addition, for the same creep time, the area of contacting asperities will be smaller.
6) When RMS increases (surface pairs 2, 6, and 7), the average aperture increases, and the contact ratio increases slower with time (see Figures 4.4 and 4.6). This suggests that if the absolute value of the initial aperture field is larger, the average aperture value during the creep stage will be larger. In addition, for the same creep time, the area of contacting asperities will be smaller.
7) For the surface parameters (H between 0.6 and 1.0, RMS between 50 and 150 μm, λ_c between 1000 and 3000 μm), macroscopic stresses (between 5 and 20 MPa), and the time durations (2τ for the Maxwell model and 5τ for the SLS model) used in the simulation, the contact ratio is generally less than 10% (see Figures 4.4 (b) and 4.6 (b)).
8) The creep curves for different surface parameters can be normalized so the curves fall into a very narrow region (see Figures 4.8 and 4.9).
9) The magnitude of the creep curves is significantly affected by the applied macroscopic stress (see Figure 4.12). As the macroscopic stress increases, the average aperture value decreases, and the contact ratio increases.
10) The shape of the creep curves depends on the input visco-elastic model (see Figure 4.13). The Maxwell model assumes a constant creep rate. As a result, under current surface parameters, macroscopic stresses, and the time durations, the creep rate (aperture decrease rate) does not change significantly with time. On the contrary, the SLS model assumes a time-decaying creep rate. As a result, under current surface parameters, macroscopic stresses, and the time durations, the creep rate (aperture decrease rate) decreases significantly with time.

While the numerical results are very informative, future work would be beneficial. Currently the numerical code only simulates the deformation using the Maxwell and SLS models. Other visco-elastic models, such as the power law model and the Burgers model, could be implemented. In addition, as mentioned above, the code only considers the visco-elastic deformation, while in reality, ductile deformation or breakage of contacting asperities may occur. The code could be modified to simulate the visco-elasto-plastic deformation of fracture surfaces. Furthermore, the effect of shear stress on visco-elastic deformations could be simulated to make the simulation more applicable. Last but not least, the code calculates the creep deformation under dry conditions. Pressure solution equations can be added in addition to the elastic deformation code to simulate the fracture creep deformation under wet conditions.

5. Experimental Method

This chapter discusses the experimental methodology used in this research. Rock fracture flow tests, triaxial creep tests, micro-indentation tests, nano-indentation tests, and SEM-EDS (scanning electron microscopy – energy dispersive X-ray spectrometry) tests were conducted on Musandam limestone. In addition, the experimental setup and experimental procedure for each type of tests were different. Therefore, for each different type of test, the experimental setup, specimen preparation, and experimental procedure will be introduced separately. Before discussing the experiments, it is essential to introduce the rock information. Therefore, the basic information on Musandam limestone will be provided in Section 5.1, including the rock origin and the specimen retrieval method. Section 5.2 discusses the specimen preparation, experimental setup, and experimental procedure for rock fracture flow tests. In the rock fracture flow tests, the specimen total deformation (rock matrix + fracture) was measured. The results indicate that the specimen total deformation changed with time. However, the rock matrix and fracture deformation could not be distinguished from each other because the rock matrix deformation was not measured in the rock fracture flow tests. Therefore, to better understand the time effect on specimen deformation, the rock matrix and fracture deformation were investigated separately. To investigate the rock matrix time-dependent deformation, triaxial creep tests were conducted on intact rocks. As mentioned in Section 2.1.1, in triaxial creep tests, if the time duration is long enough, the creep behavior can be described by three sequential regimes: primary creep (decelerating rate), secondary creep (constant rate, or steady-state), and tertiary creep (accelerating rate). Section 5.3 introduces the specimen preparation, experimental setup, and experimental procedure for triaxial creep tests. To investigate the fracture deformation, micro- and nano-indentation creep tests were conducted because the size of fracture contacting asperities is similar to the size of micro- or nano-indentation tests. As mentioned in Section 2.2.1, in indentation creep tests, the indentation creep deformation increases with time, while the creep rate decreases. Section 5.4 introduces the device, experimental procedure, and data analysis methods for micro- and nano-indentation tests.

5.1 Rock materials

5.1.1 Rock origin

In this research, Musandam limestone was chosen as the rock material. Before discussing the experimental methodology for different types of tests, it is essential to introduce the rock material. The Musandam group comprises a sequence of carbonate sediments deposited in the area of the present Northern Emirates during the Jurassic and the Lower Cretaceous. The Musandam limestone formation underlies the UAE at the depth of approximately 1400 to 2800 meters, and outcrops in the Musandam Peninsula in Oman. Figures 5.1 and 5.2 show the location of Musandam groups and the geological cross-section, respectively. In this research, the Musandam limestone specimens were obtained from an outcrop quarry in Khasab City (26°11′N, 56°15′E) in the Musandam Peninsula.

Figure 5.1. Location of Musandam groups. The left figure shows the location of the Musandam outcrop (Google Map, 2020). The white region represents the Musandam Peninsula. The red rectangles at the bottom left and the top right show the location of Abu Dhabi and the outcrop, respectively. The top right figure shows the outcrop and the quarry, and the bottom right figure shows Block 1, from which samples for testing were taken (see Figures 5.3 and 5.4 for specimen retrieval).

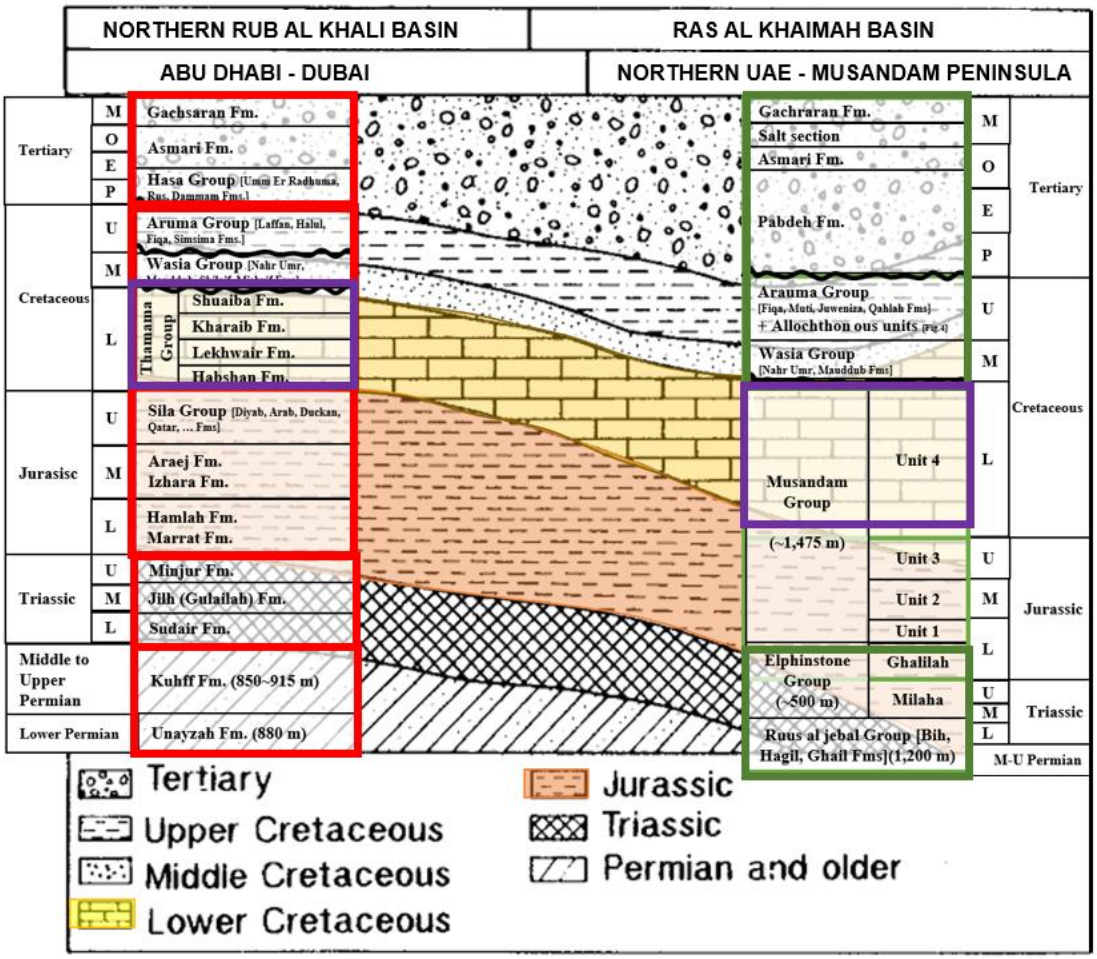

Figure 5.2. Geological cross-section of UAE and Musandam Peninsula (modified from Alsharhan and Nairn, 1986; Villamor Lora, 2018). The red rectangles represent the groups underlying Abu Dhabi and Dubai, and the green rectangles represent the groups underlying the Northern UAE and the Musandam Peninsula. The lower Cretaceous parts of the Musandam groups and the lower Cretaceous groups underlying Abu Dhabi are shown with the purple rectangles. The depth of the Musandam group is approximately 1400 to 2800 meters.

As shown in Figure 5.2, Alsharhan and Nairn (1986) and Richatean and Riche (1980) stated that the lower Cretaceous group underlying the Northern UAE and outcropping in the Musandam Peninsula (the lower Cretaceous part of the Musandam groups) shows good analogy with the lower Cretaceous group underlying Abu Dhabi. The XRD tests conducted in this research further proved the mineralogical analogy (this will be shown in Section 6.1). It is worth noting that the lower Cretaceous group underlying Abu Dhabi is one typical type of hydrocarbon reservoir rocks. Therefore, based on the geological profile and the mineralogical analogy, it is assumed that investigating the mechanical properties of Musandam limestone will benefit both the hydrocarbon extraction in Abu Dhabi and the geotechnical infrastructure construction in the Musandam Peninsula. Still, the mechanical properties of the Musandam group and the lower Cretaceous group underlying Abu Dhabi may be different. It appears that the mechanical properties of Musandam limestone have not been very well characterized so far. The mineralogy, deformation properties,

strength properties, creep properties, and indentation properties have not been systematically investigated. Therefore, in this research, the mechanical properties of Musandam limestone were systematically investigated.

To investigate the mechanical properties, two Musandam limestone blocks (Block 1: 0.50 m × 0.43 m × 0.11 m; Block 2: 0.31 m × 0.35 m × 0.22 m) from the above-mentioned quarry were sent to MIT. Then, Block 1 was cut into sub-blocks, as shown in Figure 5.3. Block 2 was also cut in a similar way, but no further experiments were so far conducted on it. It is worth noting that all the sub-blocks are characterized by two veins: a yellow vein (oriented horizontally) and a white vein (dipping steeply) (see Figure 5.4).

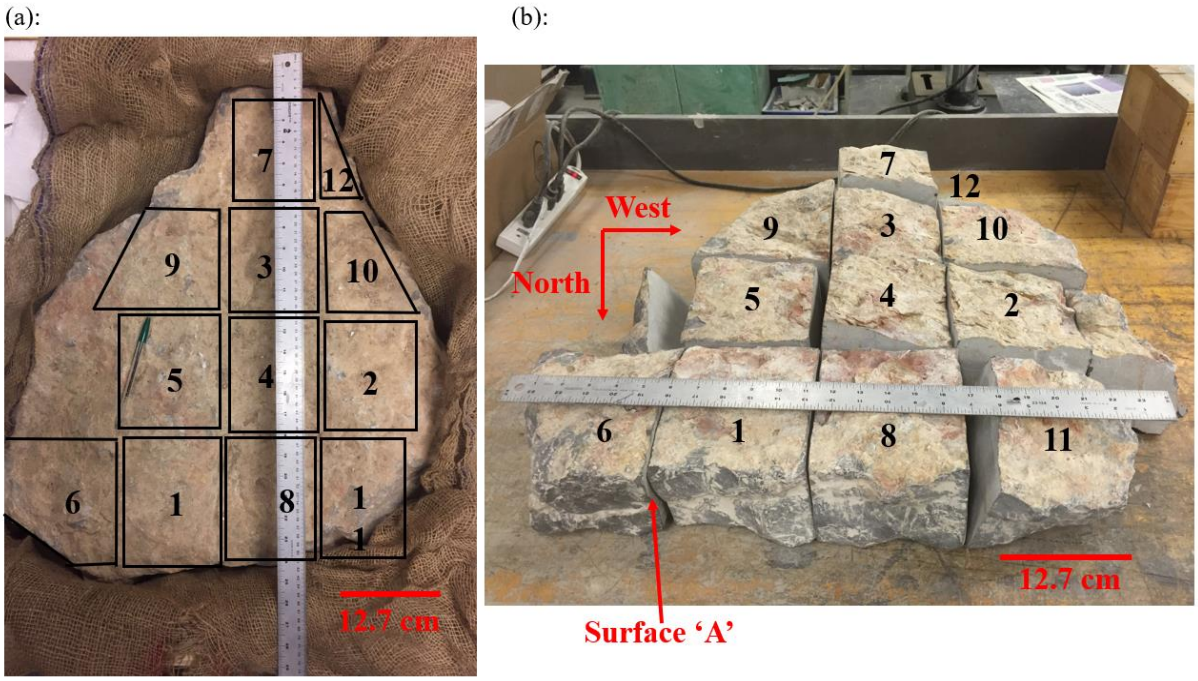

Fig. 5.3. Musandam limestone. (a): Block 1 before cutting; (b): Block 1 cut into sub-blocks.

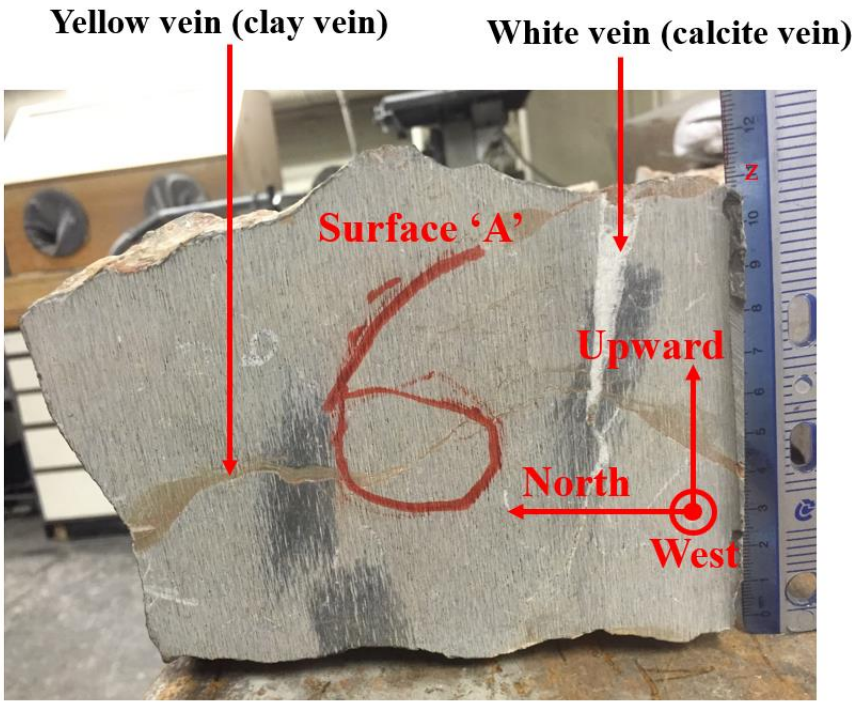

Figure 5.4. Sub-block '6' from Block 1. The 'west' direction is pointing perpendicularly out of the paper (also perpendicular to surface 'A').

5.2 Rock fracture deformation and flow tests

In this research, rock fracture flow tests were conducted using a computer-controlled triaxial system. In this section, the specimen preparation, experimental setup, experimental procedure, and data analysis procedure will be presented.

5.2.1 Specimen preparation

Cylindrical specimens with a diameter of 1.4 inches and a height of 2.8 inches were prepared from the sub-blocks. First, the cylindrical specimens were cored from the Musandam limestone sub-blocks. Water was used as the coring liquid. The coring direction was horizontal (either 'north' or 'west', see Figures 5.3 and 5.4), and the vertical axis of the cylindrical specimens corresponds to the horizontal coring direction. In addition, the drilled cores did not intersect with the yellow or the white vein. Figure 5.5 shows the coring machine. After coring, the two ends were flattened parallel and polished by a grinder, and the lateral surface was polished by a lathe. Figures 5.6 and 5.7 show the processes of end flattening and lateral surface polishing, respectively.

Figure 5.5 Picture of the coring machine.

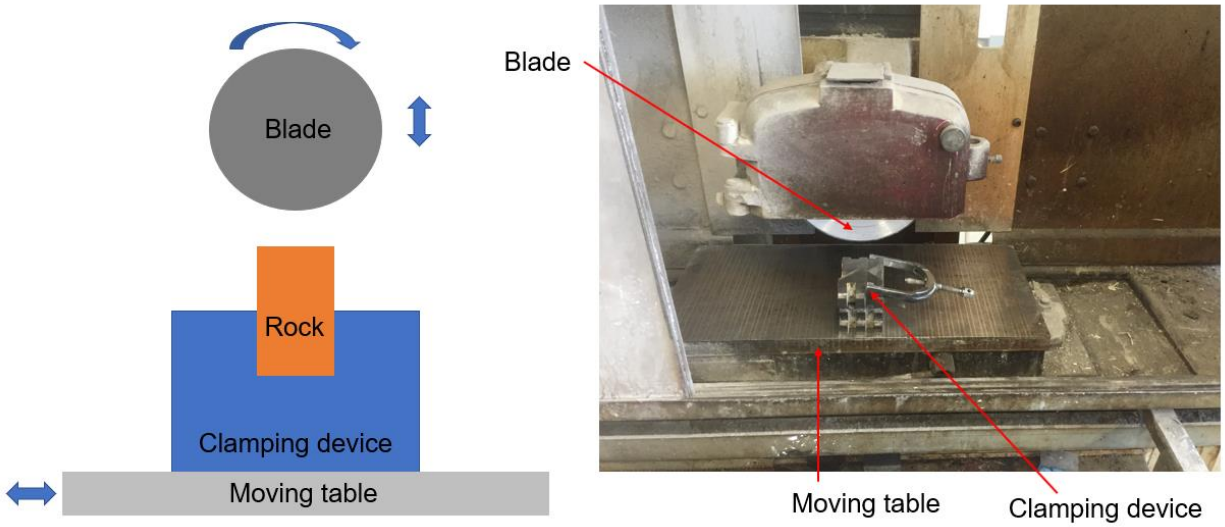

Figure 5.6 Schematic of flattening and polishing two ends. The left part shows the schematic, and the right part shows the picture of the machine. The rock specimen (not shown in the right figure) was clamped by a clamping device, and the clamping device was fixed on the moving table. The blade rotated and the moving table moved back and forth horizontally. As a result, the

end surface was ground horizontally and polished. The elevation of the blade could be adjusted, as shown by the blue vertical arrow in the left part.

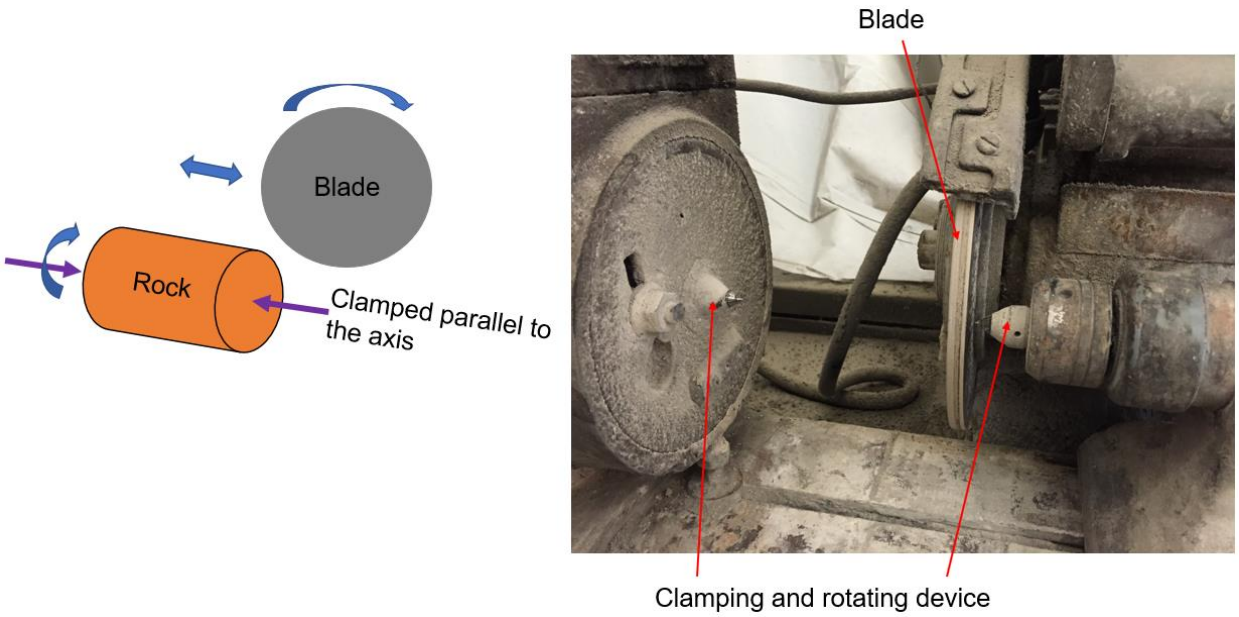

Figure 5.7 Schematic of lateral surface polishing. The left part shows the schematic, and the right part shows the picture of the machine. The rock specimen (not shown in the right figure) was clamped aligning its axis (shown by the purple arrows) and was rotating. The blade was rotating and was moved horizontally. As a result, the lateral surface was polished.

Then, 14 limestone cores were fractured by tensile splitting to obtain one major tensile crack in each of the specimens. Only specimens with one major fracture were accepted for further testing. Figures 5.8 (a) and (b) show the fracturing setup and one accepted specimen, respectively. In addition, 6 limestone cores were prepared with a polished saw-cut fracture. For each specimen, a major saw-cut fracture was created by a wetsaw, and the two fracture surfaces were polished by N120 sand paper (produced by Buehler). Figure 5.8 (c) shows the schematic for saw-cut fractures.

(a):

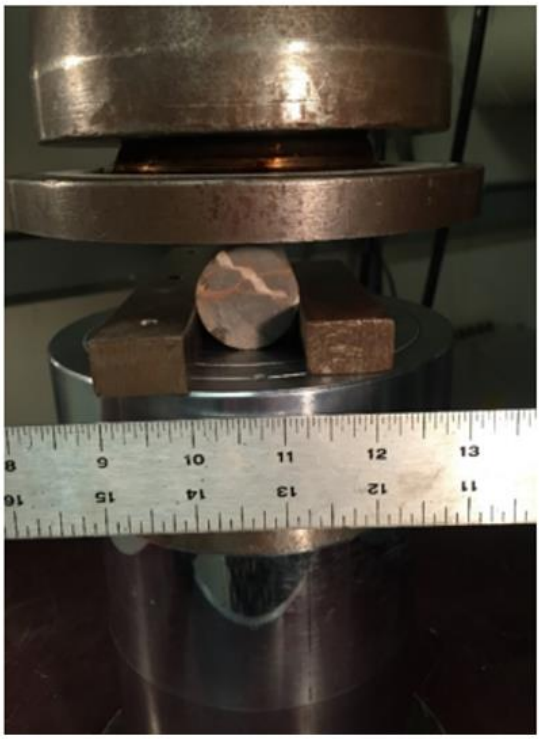

(b):

(c):

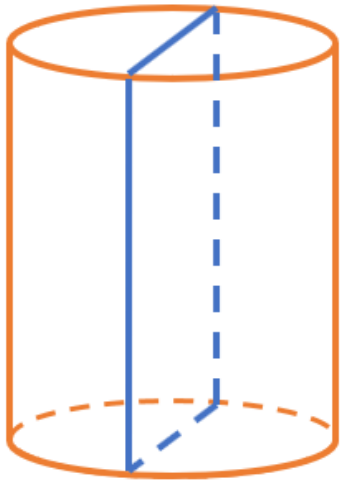

Figure 5.8. Illustration of fracture creation. (a): tensile fracturing setup of a limestone core; (b): the fractured core; (c): schematic for saw-cut fractures. The orange cylinder represents the rock core, and the blue plane represents the saw-cut fracture.

5.2.2 Experimental setup

A computer-controlled triaxial system was used to apply confining pressure and inject fluid into rock fractures. Figure 5.9 shows the schematic of the computer-controlled triaxial system. The triaxial system was originally designed by Sheahan and Germaine (1992) to measure the mechanical properties of soil. The system was upgraded for fracture flow tests by adding the specimen deformation measurement system, upgrading the capacity of the water injection PVA, and adding an outlet pressure transducer.

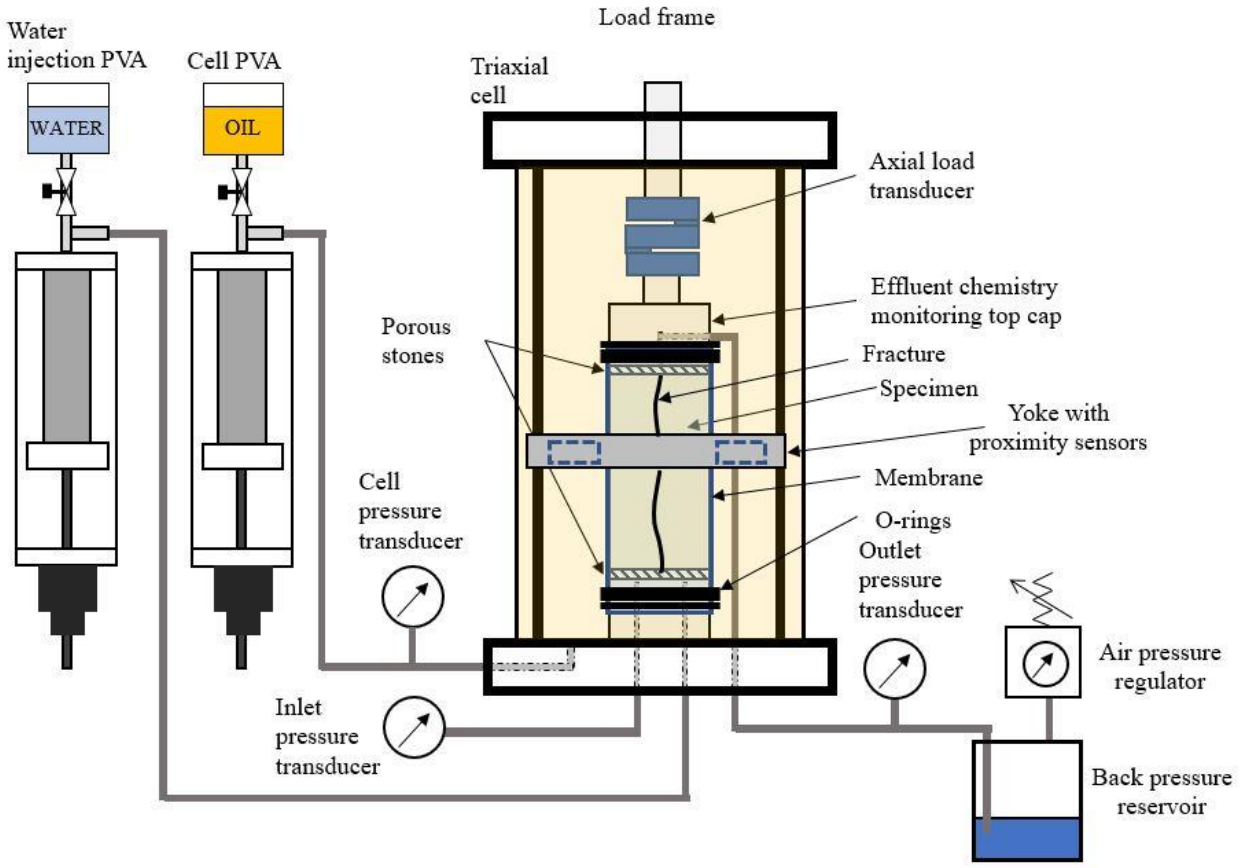

Figure 5.9. Triaxial test apparatus for confining pressure less than 1 MPa.

As shown in Figure 5.9, two proximity sensors (shown by two dashed blue rectangles) measured the specimen deformation (rock matrix + fracture) perpendicular to the fracture. The specimen was mounted between the bottom pedestal and the top cap with two porous stones. The porous stones were used to spread the fluid flow. The cell PVA was used to apply the confining pressure. The fractured specimen was sealed against the confining oil by two layers of membrane-sleeves, and the membrane-sleeves were stabilized in the top cap and bottom pedestal with three O-rings each. The axial stress was applied through the load transducer and the loading frame (the latter is not shown for simplification). Distilled water or a saturated limestone solution were used as fracture flow liquid, and the fracture flow liquid was injected by the water injection PVA from the bottom

to the top of the specimen. During each test, the flowrate, head difference, and specimen deformation (perpendicular to the fracture; measured by the proximity sensors) were measured.

5.2.3 Experimental procedure

Before each fracture flow experiment, the specimen was saturated with distilled water for 24 hours. The water was introduced to the system under vacuum. During the saturation stage, the back pressure was 136 kPa, and the confining pressure was 300 kPa.

Many factors affect rock fracture creep. Based on the literature (Elkhoury et al., 2013; Ameli et al., 2014; Deng et al., 2015), confining pressure, flowrate, and fracture surface roughness (tensile or polished saw-cut) affect fracture creep rate. In addition, the fracture creep is associated with four coupled mechanisms: mechanical compression, pressure solution, dissolution, and erosion. Investigating all these factors in one type of tests would make it very difficult to determine the effect of each individual factor. For this reason, two types of tests are conducted:

Type 1 experiments: the effects of confining pressure, flowrate, and fracture type (tensile and polished saw-cut) on fracture creep (permeability evolution) were investigated to obtain a qualitative relationship between the different factors (confining pressure, flowrate, and fracture type) and fracture permeability.

Type 2 experiments: as mentioned in Section 2.4.1, there are four different mechanisms contributing to permeability evolution: mechanical compression, pressure solution, dissolution, and erosion. It is still not well understood which mechanism dominates the permeability evolution. For example, by increasing the confining pressure, the fracture permeability will be reduced; this can be caused by enhanced mechanical compression of contacting asperities (shown in Figure 2.28) or enhanced pressure solution on contacting asperities (shown in Figure 2.29). The second type of experiments was designed to investigate the effect of different mechanisms on fracture creep. Between different experiments, the fluid type was changed to investigate to some extent the effect of different mechanisms; the confining pressure steps and the time duration for each step were identical.

For type 1 experiments, four tests will be reported and discussed. The effect of three different factors – confining pressure, flowrate, and fracture type (tensile and polished saw-cut) – on fracture permeability evolution were investigated. The three factors were systematically varied by keeping two constant and changing the third one (see Table 5.3 and Figure 5.10). For example, the effect of confining pressure was investigated by conducting tests 003 and 004. Between the two tests, only the confining pressure was varied; the flowrate and fracture type were the same.

Table 5.1. Test summary for type 1 experiments.

Test No.	Fracture type	Flowrate (μL/sec)	Confining pressure (kPa)	Back pressure (kPa)
001	Tensile	10	300	136
003	Tensile	2.5	500	136

004	Tensile	2.5	300	136
007	Polished saw-cut	2.5	300	136

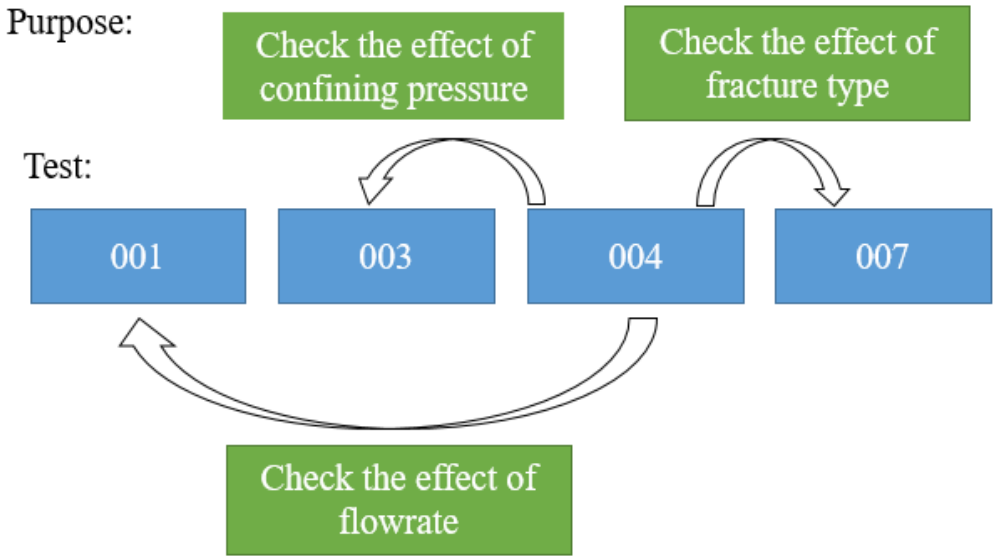

Figure 5.10 Objective of design of type 1 experiments

For type 2 experiments, four tensile fracture specimens were tested. Between different experiments, the fluid type was changed to get an initial understanding of the role of different mechanisms causing the creep (the creep is caused by the four mechanisms mentioned in the previous page and Section 2.1.4, not only mechanical compression). As shown in Figure 5.11, specimen 011 was tested under dry conditions, specimen 015 under saturated limestone solution conditions, specimen 014 under stagnant distilled water conditions, and specimen 013 under distilled water flow conditions. In the four tests, the dissolution, pressure solution, and erosion were not directly measured. Instead, the mechanical creep of the four specimens (rock matrix and fracture) was measured. The relative importance of dissolution, pressure solution, and erosion was tentatively interpreted from the relative magnitude of the mechanical creep. Table 5.2 summarizes the details of the four tests.

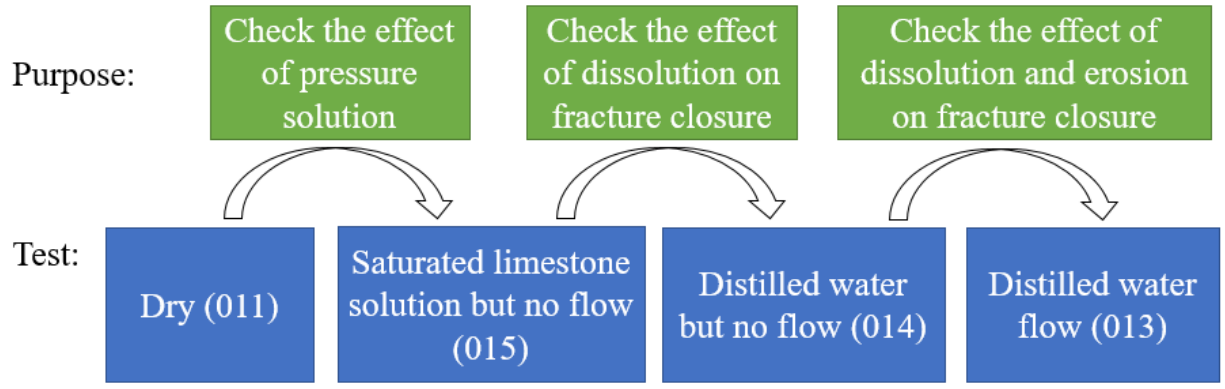

Figure 5.11 Objective of design of type 2 experiments

Table 5.2. Summary of the experimental conditions of the four specimens for type 2 experiments. The effective confining stress (confining pressure minus back pressure) steps were: 164 kPa (loading) → 364 kPa (loading) → 564 kPa (loading) → 364 kPa (unloading) → 164 kPa (unloading).

Specimen (test) No.	Fluid type	Time duration for each effective stress step (hr)					Back pressure (kPa)
		164 kPa, loading	364 kPa, loading	564 kPa, loading	364 kPa, unloading	164 kPa, unloading	
011	Dry	24	24	24	24	24	136
015	Stagnant saturated limestone solution	24	24	24	24	24	136
014	Stagnant distilled water	24	24	24	24	24	136
013	Distilled water, flow	24	24	24	24	24	136

5.2.4 Data analysis procedure

For type 1 experiments, the confining pressure, flowrate, and head difference were measured. The hydraulic aperture was computed based on the cubic law:

$$h = \sqrt[3]{\frac{12QL\mu}{\Delta pw}} \tag{5.1}$$

where Q is the flowrate, L is the specimen length, μ is the dynamic viscosity of the liquid, w is the specimen width, Δp is the pressure difference between water inlet and outlet. The cubic law is a

simplification but acceptable in the context of this research where the hydraulic aperture is used for comparison.

The averaged hydraulic aperture creep rate was computed as:

$$\overline{cr_{hy}} = \frac{h_{ini} - h_{fin}}{t} \tag{5.2}$$

where $\overline{cr_{hy}}$ is the averaged hydraulic aperture creep rate (unit: μm / day), t is the total duration of the experiment, h_{ini} is the initial hydraulic aperture (the averaged hydraulic aperture for the first fifteen minutes of the test), h_{fin} is the final hydraulic aperture (the averaged hydraulic aperture for the last fifteen minutes of the test). Positive hydraulic aperture creep indicates hydraulic aperture reduction.

The normalized averaged hydraulic aperture creep rate (unit:1/day), was also computed as:

$$\overline{cr_{hy-no}} = \frac{\overline{cr_{hy}}}{h_{ini}} \tag{5.3}$$

where $\overline{cr_{hy-no}}$ is the normalized averaged hydraulic aperture creep rate.

For type 2 experiments, in each effective confining stress step (see Table 5.4), the mechanical deformation (rock matrix and fracture) was computed based on the measured proximity probe readings. In each effective confining stress step, the mechanical deformation at the beginning was defined as zero. Contraction (fracture and rock matrix) was defined as positive mechanical deformation.

In addition, for specimen 013, the hydraulic aperture h (unit: μm), was calculated. The calculation method was the same as type 1 experiments.

5.3 Triaxial creep tests

In the rock fracture flow tests, the specimen total deformation (rock matrix + fracture) was measured. However, the rock matrix and fracture deformation could not be distinguished from each other because the rock matrix deformation was not measured. Therefore, to better understand the specimen deformation, the rock matrix and fracture deformation were investigated separately. To investigate the rock matrix deformation, triaxial creep tests were conducted on intact rock. This section introduces the specimen preparation, experimental setup, and experimental procedure for triaxial creep tests. To investigate the fracture deformation, micro- and nano-indentation tests were conducted because the size of fracture contacting asperities is similar to the size of micro- or nano-indentation tests. The device, experimental procedure, and data analysis methods for micro- and nano-indentation tests will be introduced in Section 5.4.

In this research, intact rock creep tests were conducted using another computer-controlled triaxial system (the NER AutoLab 3000, which will be introduced in Section 5.3.2). Under different experimental systems, the specimen preparation steps and sensors were different. In this section, the specimen preparation, experimental setup, and experimental procedure will be presented.

5.3.1 Specimen preparation

Cylindrical specimens with a diameter of 2 inches and a height of 4 inches were prepared from the sub-blocks. The specimen coring and polishing processes were similar to those described in Section 5.2.1. First, the cylindrical specimens were cored from the Musandam limestone sub-blocks. Water was used as the coring liquid. The coring direction was horizontal (either 'north' or 'west', see Figures 5.3 and 5.4), and the vertical axis of the cylindrical specimens corresponds to the horizontal coring direction. In addition, the drilled cores did not intersect with the yellow or the white vein. After coring, the two ends were flattened parallel and polished by the grinder shown in Figure 5.6, and the lateral surface was polished by the lathe shown in Figure 5.7.

Then, the cylindrical specimen was sealed from confining oil. As shown in Figure 5.12, a copper jacket (made by McMaster Carr, 0.003 inches thick) was attached to the specimen's circumferential surface. After soldering the copper jacket sleeve, two Viton tubes (made by Aero Rubber Company, Viton Type A) were used to seal the specimens. Figure 5.13 shows the schematic of sealing. The gaps between the copper jacket and the Viton tube were filled with epoxy (3M Scotch-Weld 2216 Gray B/A). After the epoxy cured, the specimen was placed into a confining vessel. The confining pressure inside the vessel was increased to 10 MPa to make the copper jacket attach firmly to the specimen surface.

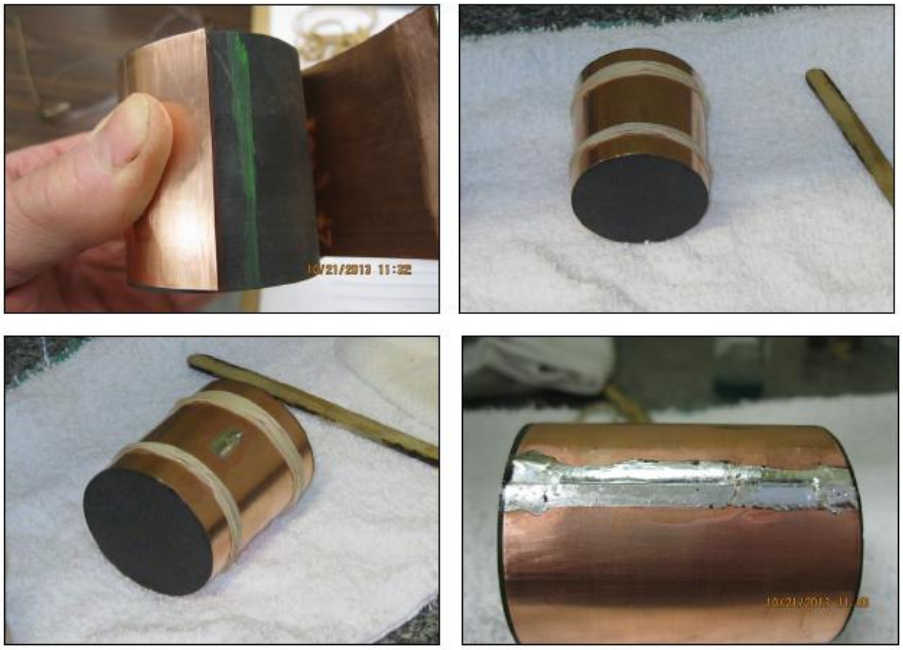

Figure 5.12 Copper jacket installation (Villamor Lora, 2015). First, a rectangular copper jacket sleeve was cut. Then, the sleeve was wrapped around the specimen's circumferential surface, and the two ends of the copper jacket sleeve were soldered together.

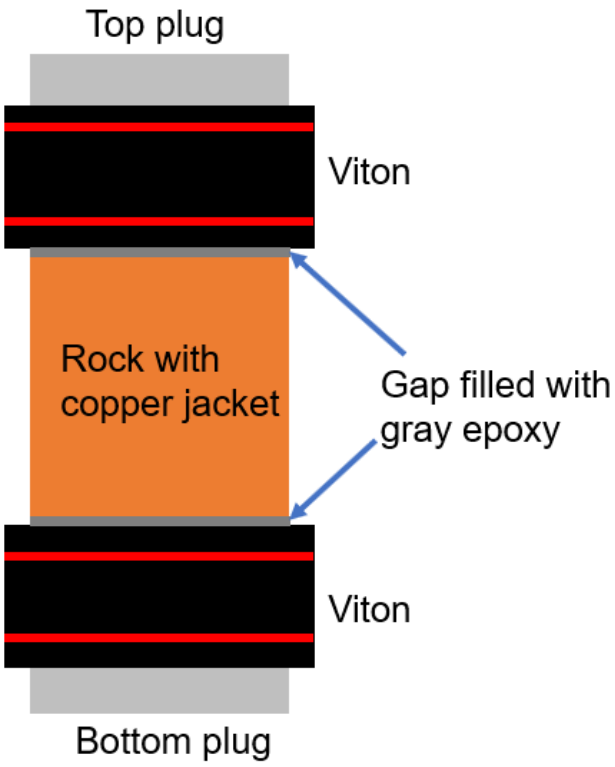

Figure 5.13 Schematic of sealing (I did not take a picture when I was sealing the specimen). The black rectangles represent the bottom and top Viton tubes. The red lines represent the steel wires. For each Viton tube, two steel wires were used. One wire is used to tighten the Viton tube to the rock specimen, and the other wire is used to tighten the Viton tube to the plug. The gap between the copper jacket and the Viton tube (shown by the two blue arrows) was filled with epoxy.

After the pressurization process, displacement measurement sensors were installed on the specimen. As shown in Figures 5.14 and 5.15, two axial strain gauges were glued on the middle of the copper jacket with a 180˚ azimuthal separation. Next to each axial strain gauge, one circumferential strain gauge was glued. The resistance for all the strain gauges was 120 Ω and the gauge factor was 2.09. In addition, two LVDT sensors, with a 180˚ azimuthal separation, were used to measure the axial displacement.

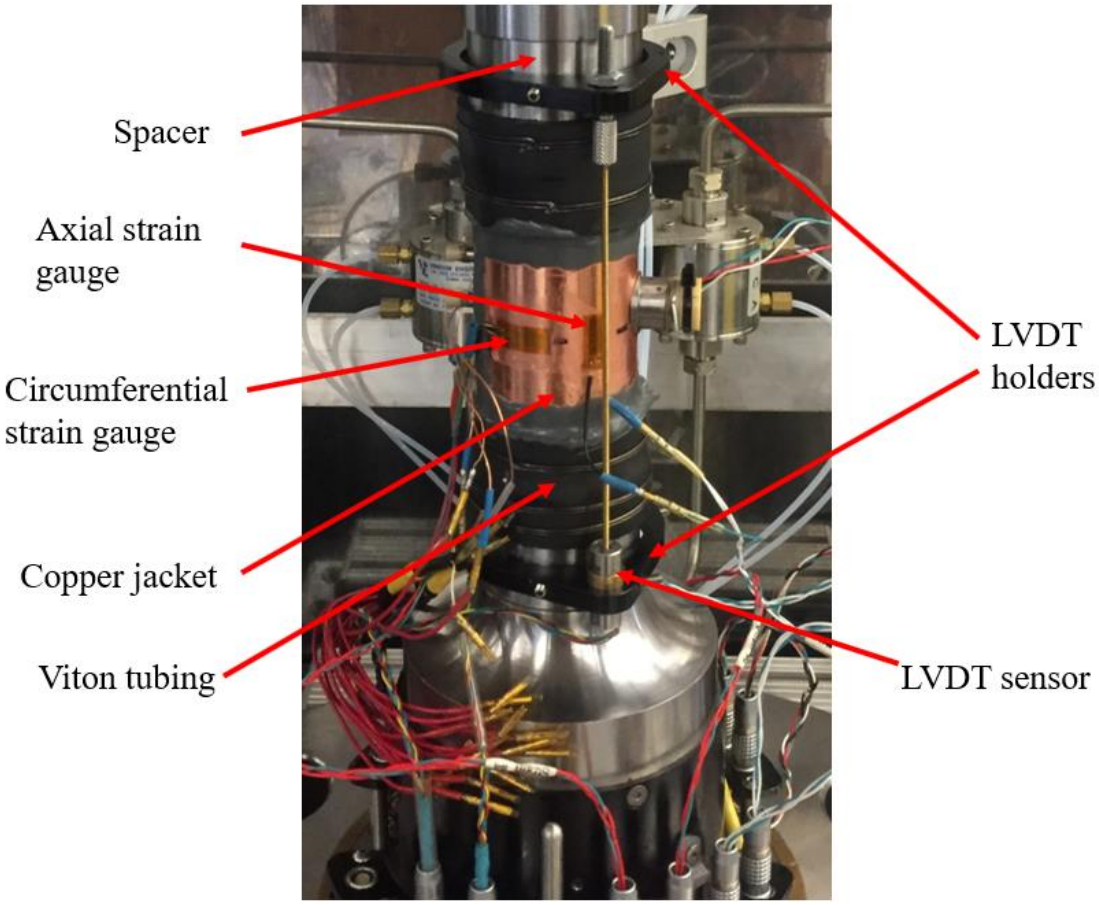

Figure 5.14. A photo of the specimen and sensors in the triaxial test.

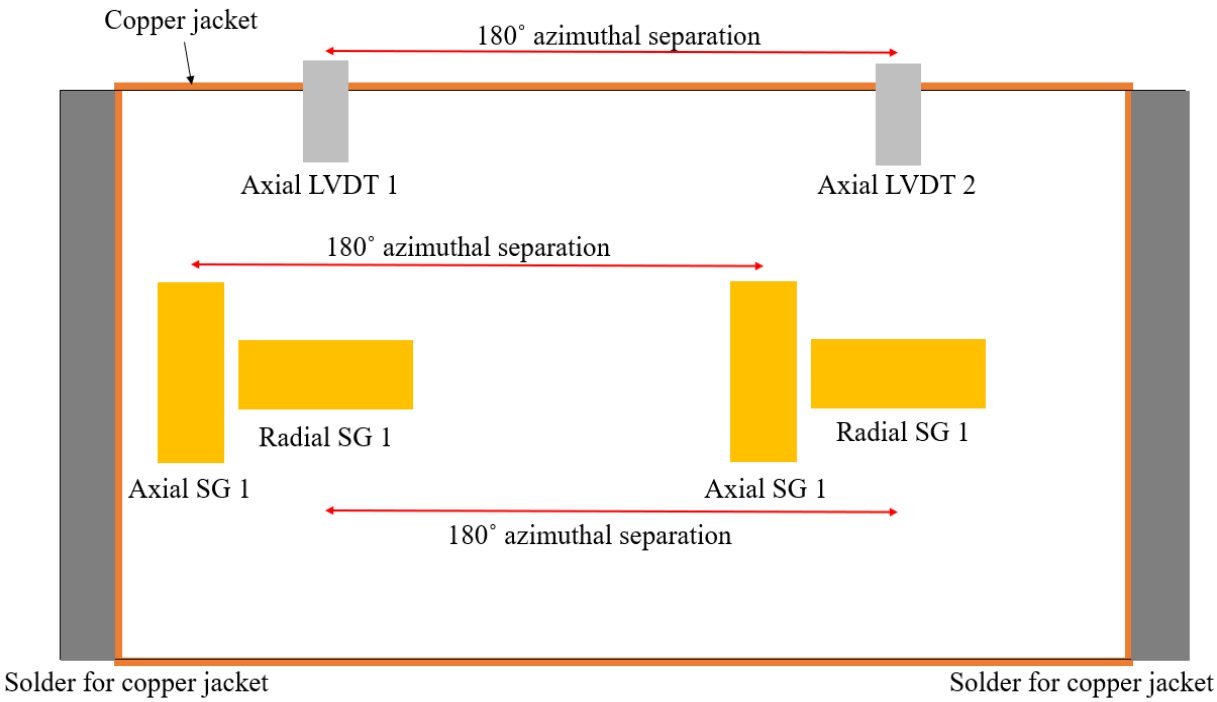

Figure 5.15. A schematic of the sensors in triaxial testing. The large orange rectangular box represents the edges of the copper jacket. The dark side bars represent the solder.

5.3.2 Experimental setup

Triaxial tests were conducted using the NER AutoLab 3000 triaxial cell of the MIT EAPS (Department of Earth, Atmospheric, and Planetary Sciences) Rock Mechanics Laboratory. Figure 5.16 shows the schematic of the NER triaxial cell. Hydraulic oil was used as confining fluid. The confining and axial stresses were both servo-controlled with control errors approximately ±0.09 and ±0.05 MPa, respectively (Mighani et al., 2019). During each test, the cylindrical specimen was kept under dry conditions (no pore pressure was applied).

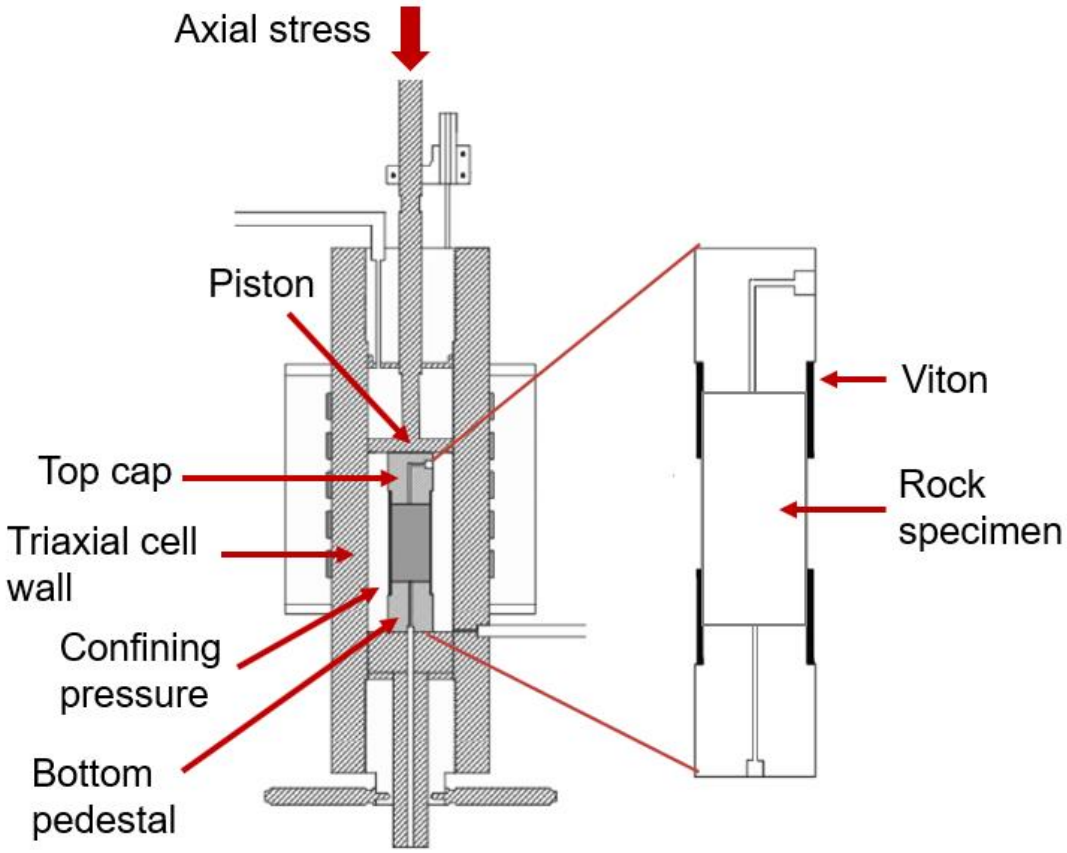

Figure 5.16 Schematic of the NER triaxial cell (modified from Villamor Lora et al., 2016).

5.3.3 Experimental procedure

In total, two triaxial creep tests were conducted. In each test, two loading stages were applied. In stage 1, the specimen was loaded by uniformly increasing the confining pressure; in stage 2, the confining pressure was kept constant, while the axial stress was varied. For both stages, the loading rates for the axial and confining stresses were 0.12 MPa/s. The data acquisition rate was 10 Hz. Figures 5.17 and 5.18 show the schematic of the stress steps for specimens 1 and 2, respectively. Tables 5.3 and 5.4 summarize the stress steps for specimens 1 and 2, respectively.

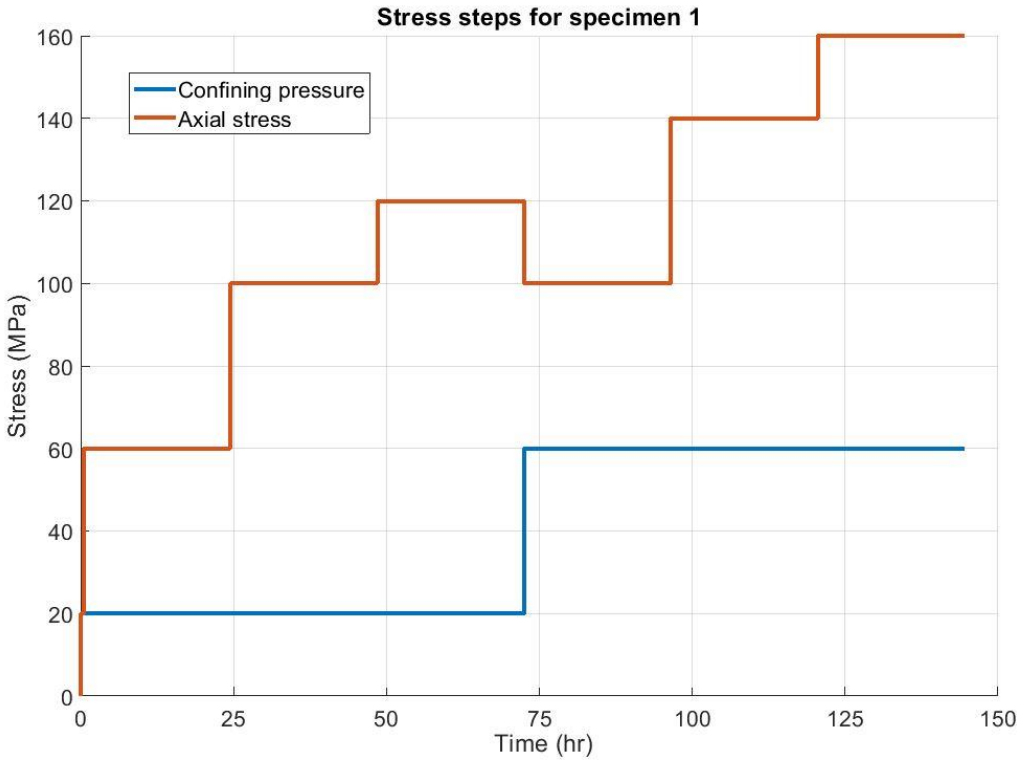

Figure 5.17 Stress steps for specimen 1.

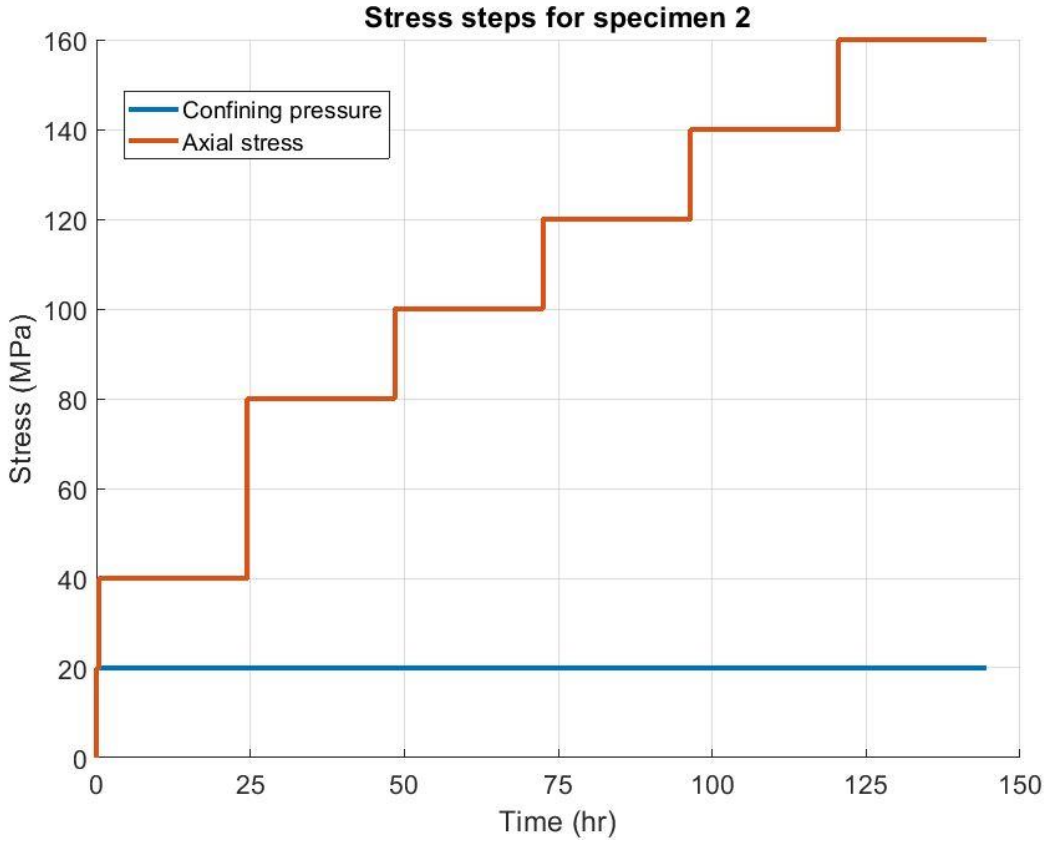

Figure 5.18 Stress steps for specimen 2.

Table 5.3. Summary of the stress steps for specimen 1.

Step No.	Time duration (hr)	Confining pressure (MPa)	Axial stress (MPa)	Differential stress (MPa)
1	0.5	20	20	0
2	24	20	60	40
3	24	20	100	80
4	24	20	120	100
5	24	60	100	40
6	24	60	140	80
7	24	60	160	100

Note: differential stress = axial stress – confining pressure.

Table 5.4. Summary of the stress steps for specimen 2.

Step No.	Time duration (hr)	Confining pressure (MPa)	Axial stress (MPa)	Differential stress (MPa)
1	0.5	20	20	0
2	24	20	40	20
3	24	20	80	60
4	24	20	100	80

5	24	20	120	100
6	24	20	140	120
7	24	20	160	140

Note: differential stress = axial stress – confining pressure.

During each stress step, the confining pressure and axial stress were measured by pressure transducers. The circumferential strain was measured by strain gauges, and the axial strain was measured by both LVDT and strain gauges.

5.4 Micro- and nano-indentation tests

As mentioned at the beginning of Section 5.3, to investigate the fracture deformation, micro- and nano-indentation tests were conducted because the size of fracture contacting asperities is similar to the size of micro- or nano-indentation tests. In this section, the specimen preparation, experimental procedure, and data analysis method will be described. In addition, the SEM-EDS test will be very briefly introduced.

5.4.1 Specimen preparation

As introduced in Section 2.2, to study small volumes of material and understand their mechanical properties at a micron scale, indentation tests are used. An indentation test consists of pushing an indenter with known geometry and mechanical properties perpendicularly to a horizontal polished material surface, at a certain loading or displacement rate. Indentation machines are capable of controlling the load acting on the indenter and continuously measuring the indentation penetration depth. Indenters with different tip geometries are used in indentation tests; in this research, a Berkovich indenter will be used. As shown in Figure 5.19, the Berkovich tip is a three-sided pyramid; geometrically, it is equivalent to a cone with a half-angle of 70.32˚.

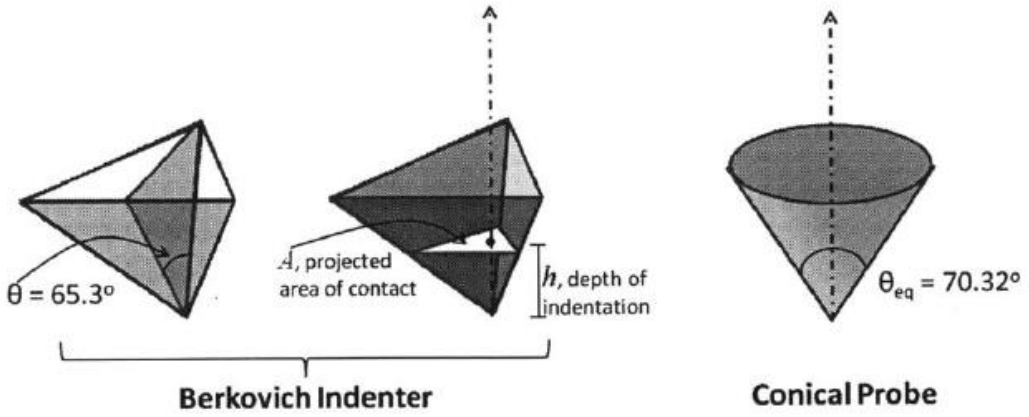

Figure 5.19 Schematic of the Berkovich tip (Brooks, 2013). To simplify the analysis, the Berkovich indenter is simplified as a conical probe. A conical probe with a half-angle θ_{eq} of

70.32˚ gives the same projected contact area at a given depth as the Berkovich tip. The projected contact area corresponds to the contact area projected on the horizontal surface.

Before introducing the experimental procedure, it is essential to introduce the specimen preparation. A 24.7 mm × 18.1 mm × 19.0 mm specimen was cut from the grey matrix in Sub-block '10' from Block 1. The specimen faces were flattened and polished using silicon carbide grinding paper (produced by Buehler) with different grit sizes. The sandpaper with the coarsest grit size was used first, and the finest size was used last. The order of the sandpaper grit size was: N60 → N120 → N220 → N320 → N400 → N600 → N800. Figure 5.20 shows the schematic of surface polishing.

Figure 5.20 Schematic of surface polishing. During polishing, the sandpaper was glued to the circular disc, and the circular disc was rotating. The rock specimen (shown by the orange rectangle) was pressed against the sandpaper. After polishing the surface for 10 minutes, the sandpaper was replaced by a new piece of sandpaper with a finer grit size, and the polishing was repeated.

5.4.2 Experimental procedure

After surface polishing, rectangular arrays of indentations were placed on the polished surface. In this research, both micro- and nano-indentation tests were conducted, and the time durations were 3-min and 6-hr. Table 5.5 summarizes the indentation tests. Figures 5.21 and 5.22 show the rectangular arrays of 3-min micro-indentation and nano-indentation, respectively.

Table 5.5 Summary of the indentation tests

Test type	No. of indents	Creep duration	Maximum load	Loading rate in loading and unloading stage
3-min micro-indentation	225 (15*15)	3 minutes	9 N	15 N/min
6-hr micro-indentation	8	6 hours	9 N	15 N/min

3-min nano-indentation	225 (15*15)	3 minutes	5 mN	18 mN/min
6-hr nano-indentation	9	6 hours	5 mN	18 mN/min

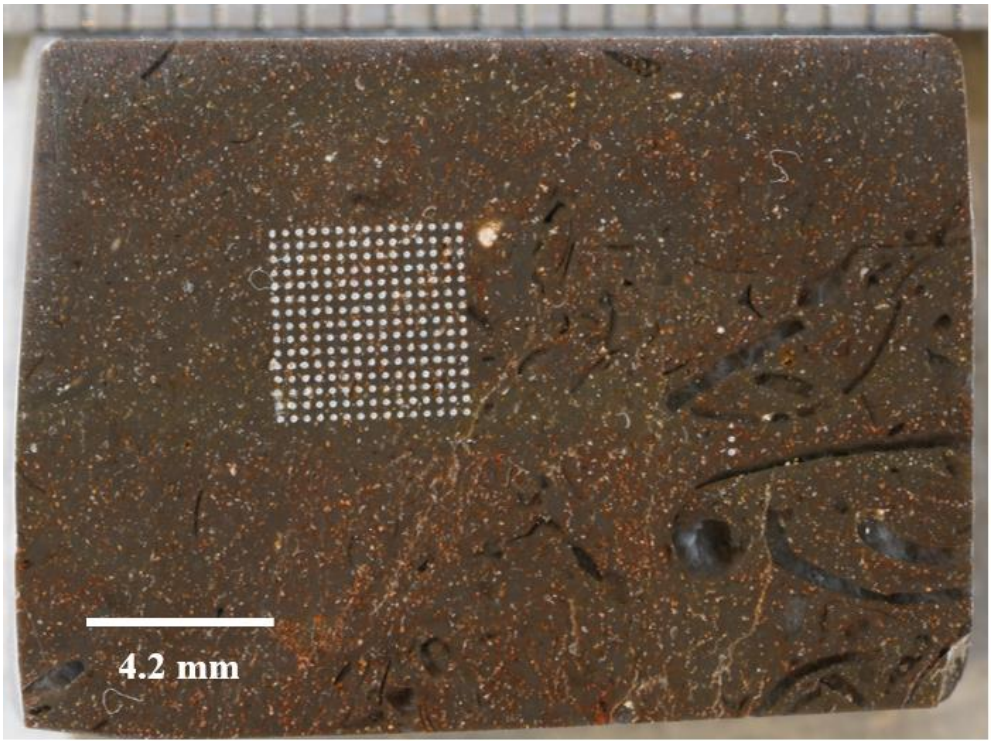

Figure 5.21. High-resolution camera image of the 3-min micro-indentation array. The white dots correspond to indentation locations. The spacing between each indent is 300 μm.

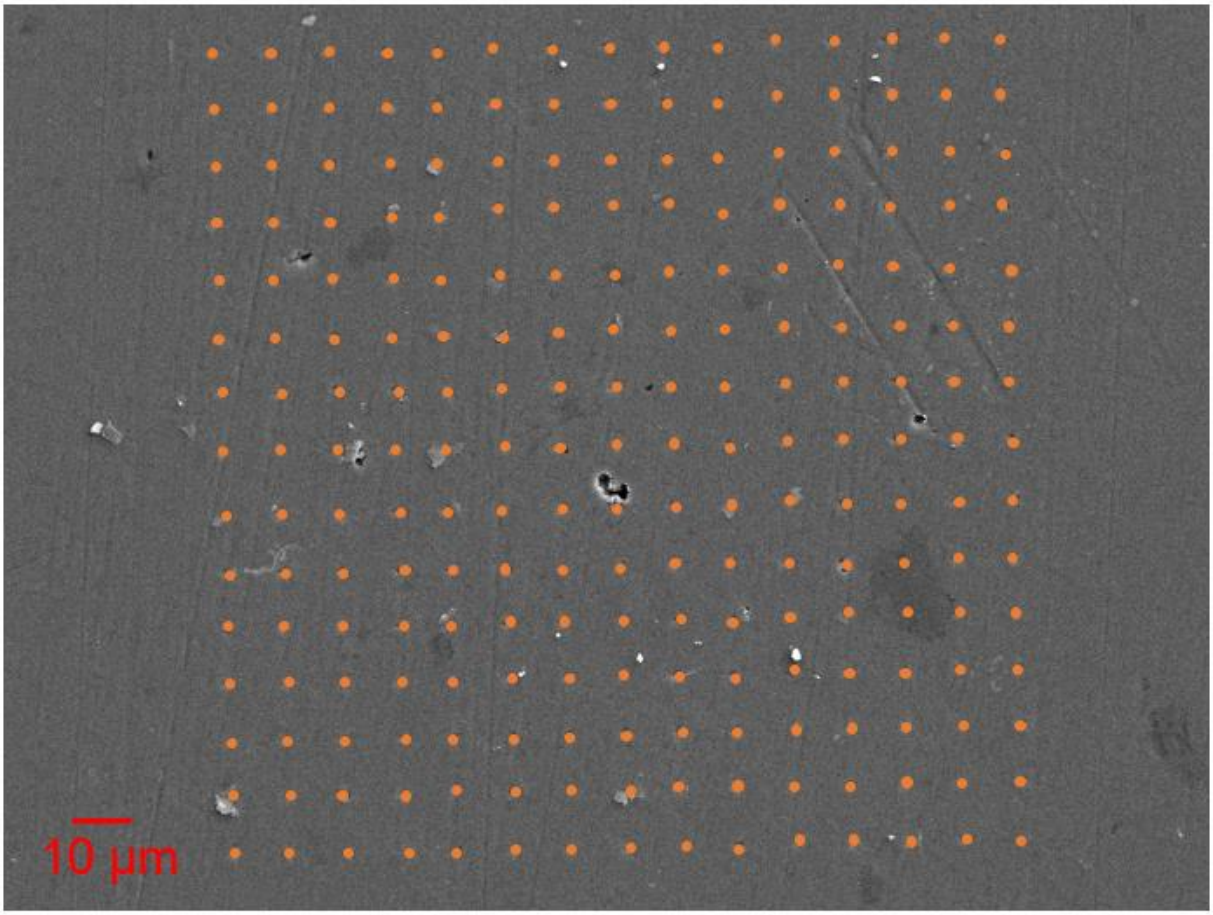

Figure 5.22. SEM image of the 3-min nano-indentation array. The spacing between each indent is 10 µm. The orange dots correspond to indentation locations.

Figure 5.23 shows the schematic of each indent. During each indent, the indentation load was increased from zero to the maximum load, then held at the maximum load, and finally decreased to zero. During the test, the load and indentation depth were monitored, with a data acquisition rate of 50 Hz. The micro-indentation tests were conducted using the Micro-Indentation Tester (MHT) made by the CSM-Instrument Company; the nano-indentation tests were conducted using the Anton Parr Ultra Nanoindentation Tester (UNHT) made by the CSM-Instrument Company.

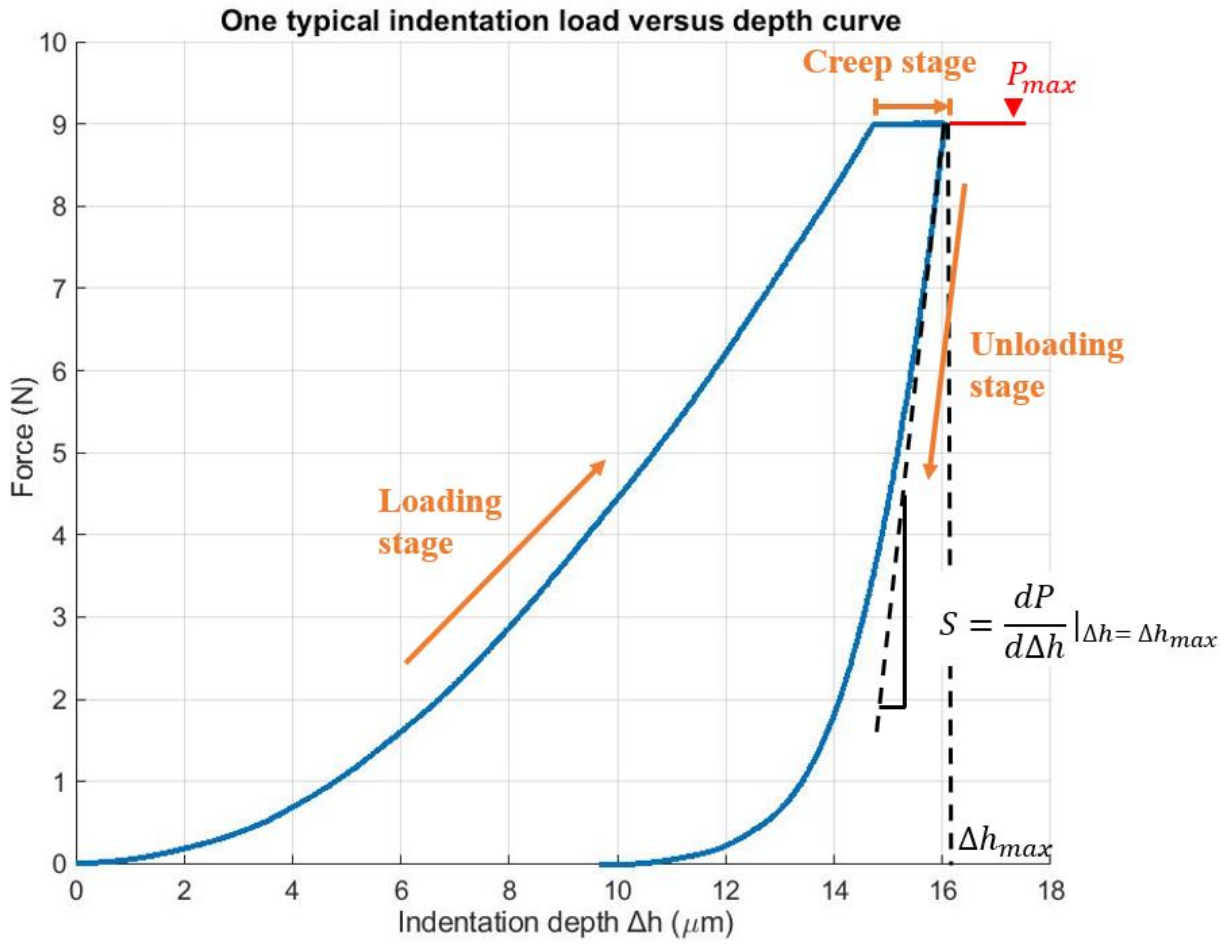

Figure 5.23. Load versus indentation depth curve from a typical micro-indentation test. P_{max} corresponds to the maximum force (load). The indentation depth Δh and slope S will be explained in Section 5.4.3.

5.4.3 Data analysis method

For micro- and nano-indentation tests, the indentation modulus M, indentation hardness H, and indentation creep modulus C can be calculated. Oliver and Pharr (1992) proposed a methodology to calculate the indentation modulus M and indentation hardness H for the Berkovich indenter. Their method can be applied to both micro- and nano-indentation tests.

Before introducing indentation modulus, M, it is essential to introduce a parameter, E_1, which is defined as:

$$E_1 = \beta \frac{S}{2a_u} \tag{5.4}$$

and

$$S = \frac{dP}{d\Delta h}|_{\Delta h = \Delta h_{max}} \tag{5.5}$$

where S is the initial slope of the unloading curve, P is the applied load, Δh is the indentation depth, β is a correction factor (1.05 in this study), and a_u is the radius of the contact area between the indented surface and the indenter at the beginning of unloading (see Figure 5.24). Figure 5.23 in Section 5.4.2 shows a typical indentation load versus depth curve and the above-mentioned parameters.

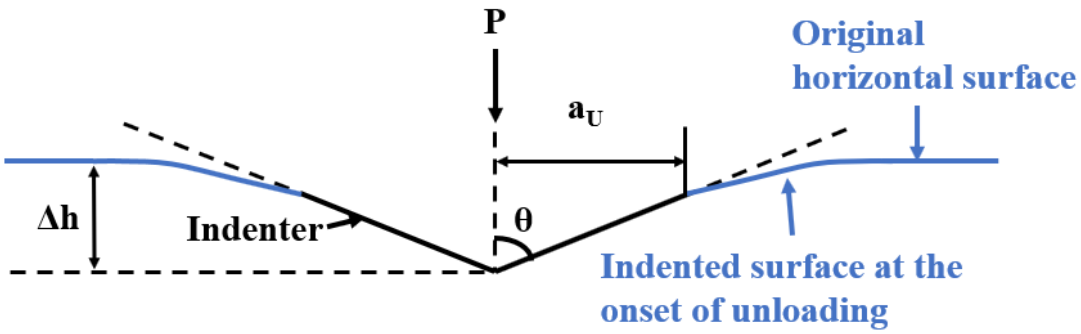

Figure 5.24. Illustration of indenter geometry and a_u. θ is the half-angle of the indenter (70.32˚ for Berkovich indenter).

If the indented material and the indenter are isotropic, the indentation modulus M can be calculated as:

$$M = \left(\frac{1}{E_1} - \frac{1}{M_{ind}}\right)^{-1} \tag{5.6}$$

where M_{ind} is the indentation modulus of the diamond indenter (1147 GPa) in this study.

The indentation hardness H can also be determined:

$$H = \frac{P_{max}}{\pi a_u^2} \tag{5.7}$$

where P_{max} is the maximum load. Here H is equivalent to the average compressive stress beneath the indenter.

Ulm and Vandamme (2009) proposed another parameter, the indentation creep modulus C, to quantify the material's creep behavior. Under the same indentation load, smaller C values correspond to larger creep deformation. Figure 5.25 shows a typical indentation creep curve (Δh versus t), where Δh is the indentation creep depth, and t is the creep time. The creep curve corresponds to the creep stage (when the load was constant) shown in Figure 5.23. From the creep curve in Figure 5.26, the indentation creep modulus C can be obtained:

$$C = \frac{P_{max}}{2a_u x_1} \tag{5.8}$$

where x_1 is obtained using curve fitting:

$$\Delta h = x_1 \, ln\,(x_2 t + 1) + x_3 t + x_4 \tag{5.9}$$

where x_1 (unit: length) and x_2 (unit: time^{-1}) are curve-fitted parameters characteristic of the tested material. x_3 and x_4 are related to the drifting of the indentation machine and are independent of testing materials. The material-independent property of x_3 will be explained in Figure 5.27. Ulm and Vandamme (2009) stated that in micro-indentation tests, the machine drifting is much less than the indentation creep depth. Therefore, x_3 and x_4 can be ignored in the analysis, and Eqn. 5.9 is reduced to:

$$\Delta h = x_1 \, ln \, (x_2 t + 1) \tag{5.10}$$

In Eqn. 5.10, Δh and t are measured in the indentation tests; while x_1 and x_2 are the unknown parameters. The x_1 and x_2 are fitted by the least square method.

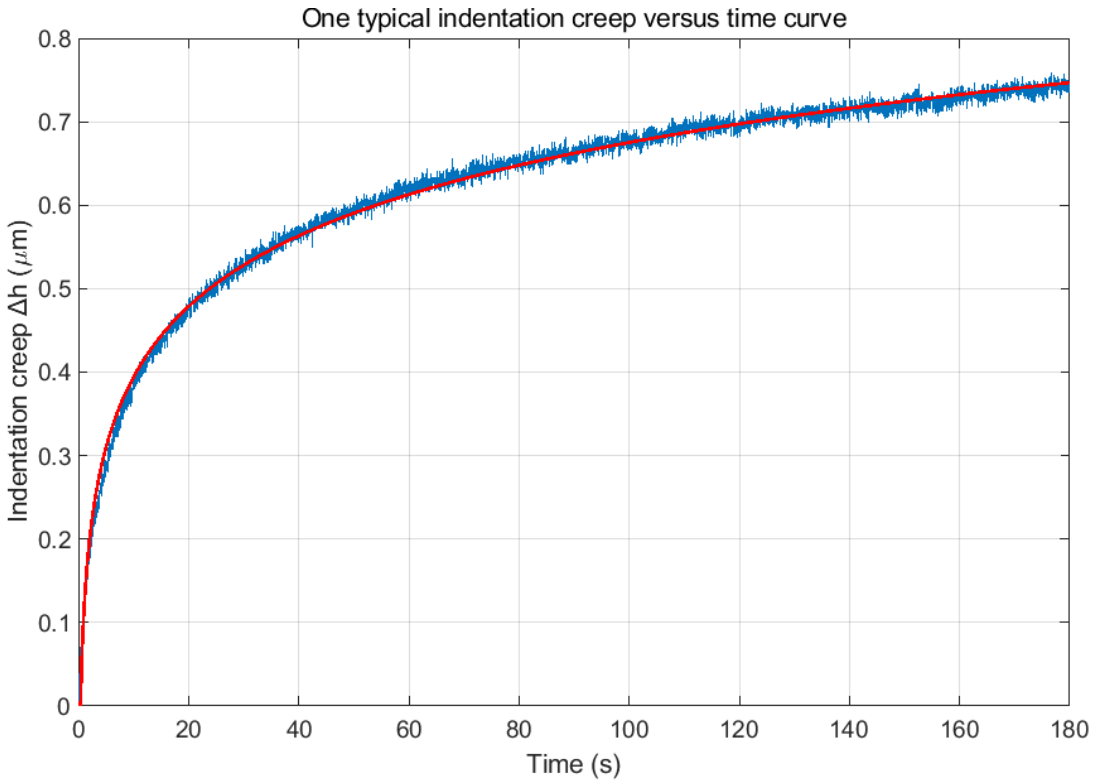

Figure 5.26. A typical indentation creep versus time curve. The blue curve corresponds to the measured data, and the red curve corresponds to the fitted curve based on Eq. 5.9.

However, for nano-indentation tests, Ulm and Vandamme (2009) stated that the machine drifting is comparable to the indentation depth. Therefore, when calculating x_1 (unit: length) and x_2 (unit: time^{-1}) (shown in Eqn. 5.9), the x_3 and x_4 terms must be considered. The x_3 and x_4 values are dependent on the machine type and the creep time duration, so the x_3 and x_4 values for the specific machine and designated time-duration need to be determined.

Vandamme and Ulm (2013) determined the x_3 and x_4 values of the UNHT machine (the nano-indentation machine used in this research) for 3-min nano-indentation tests. They performed 400 3-min nano-indentation tests on a concrete specimen. For each indentation test, they measured Δh and t values; the x_1, x_2, x_3, and x_4 values were fitted based on Eqn. 5.9 using the least square

method. They observed that for x_4, the average value is 1.27 nm and the standard deviation value is 1.92 nm.

Then, Vandamme and Ulm (2013) proved that the x_3 value is not material dependent. They plotted x_3 versus indentation modulus M, and x_3 versus indentation hardness H. Figures 5.27 (a) and (b) show the x_3 versus M and x_3 versus H, respectively. They stated that since the r^2 values in Figures 5.27 (a) and (b) are very small, the x_3 value is not related to M and H, and therefore, material independent.

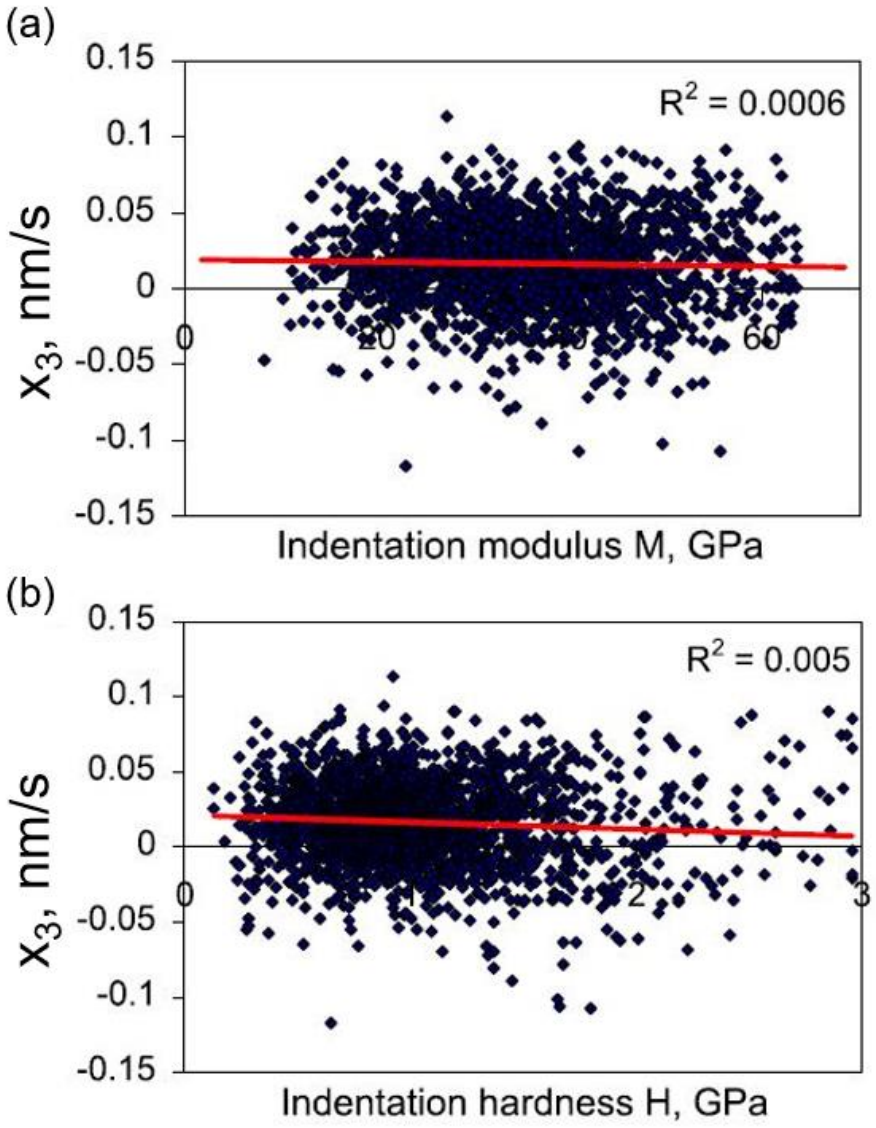

Figure 5.27. x_3 value versus (a): indentation modulus M; (b): indentation hardness H. The red lines are the fitted linear line.

Based on Figures 5.27 (a) and (b), Vandamme and Ulm (2013) stated that for most 3-min nano-indentation tests, the x_3 value is between -0.05 nm/s and 0.05 nm/s. In addition, the number of x_3 values larger than zero is approximately similar to that smaller than zero. Therefore, Ulm and

Vandamme (2013) stated that the average value of x_3 could be used. In this research, 0.005 nm/s was used as the average value of x_3.

Based on the above discussion, it can be concluded that to obtain the x_3 and x_4 values for a specific machine and a specific creep time duration, a lot of tests (at least 100) need to be conducted. This is not possible for 6-hr nano-indentation tests. Both Ulm's group and the manufacturer do not have the x_3 and x_4 values for 6-hr duration. Therefore, at this moment, for 6-hr nano-indentation tests, the x_1 and x_2 values cannot be determined based on Eqn. 5.9. As a result, the creep modulus C for 6-hr nano-indentation tests cannot be obtained.

5.4.4 Very brief introduction of the SEM-EDS (scanning electron microscopy – energy dispersive X-ray spectrometry) test

In this section, the principles of the SEM-EDS (scanning electron microscopy – energy dispersive X-ray spectrometry) test will be very briefly introduced. A detailed explanation of the SEM-EDS test could be found in Brooks (2013) and Slim (2016). SEM-EDS tests were conducted to obtain the element distribution of micro- and nano-indentation test regions. There are three basic parts to the operation of SEM: the evacuated tube, the electron gun, and the lenses. Figure 5.28 shows the schematic of an SEM device.

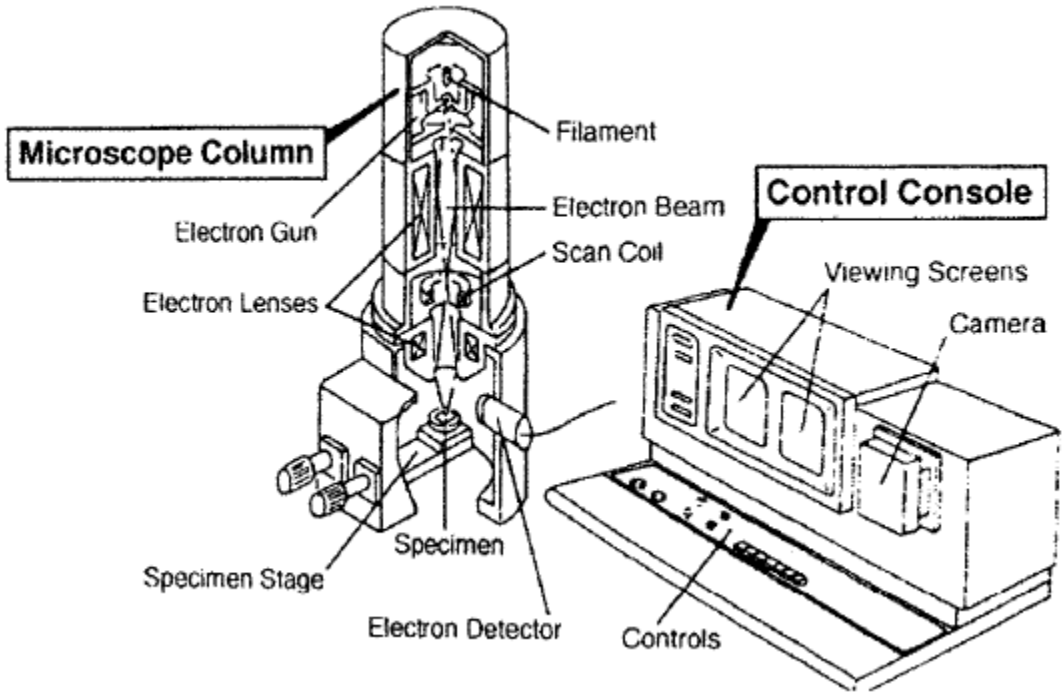

Figure 5.28 The schematic of an SEM device (from Brooks, 2013).

In an SEM test, the specimen is put inside the evacuated tube. An electron beam is produced by the electron gun and is accelerated through an electrical potential (normally between 2 kV and 30 kV). The electron lenses demagnify and redirect this beam to ultimately focus the beam onto the

specimen as a spot with a size of 10 nm. The electron beam enters the specimen surface and interacts with the atoms.

After the electron beam interacts with the atoms, X-rays with different energies will be reflected from the specimen surface (shown in Figure 5.29). The intensity of X-rays with different energies emitted from the specimen can be measured by an energy-dispersive spectrometer. Each chemical element has its peak X-ray intensity at a unique energy (energies). Therefore, by detecting the peak intensities of the X-rays and their corresponding energy, the chemical element of the surface can be obtained. Figure 5.30 shows an example of the X-ray spectrum of $CaCO_3$.

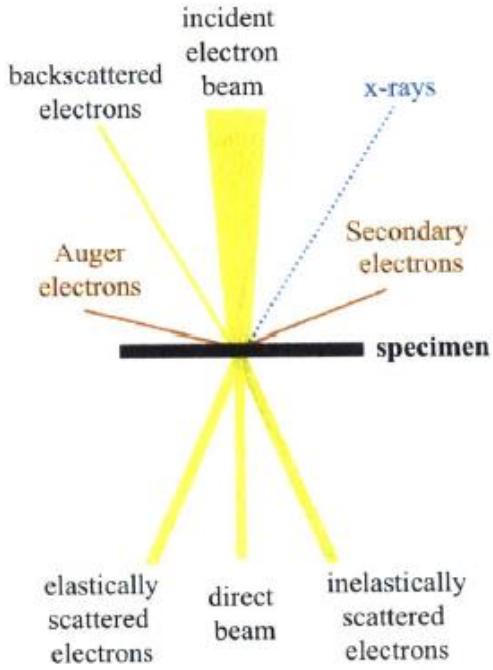

Figure 5.29 A schematic showing results of interactions between an SEM electron beam and material atoms (Slim, 2016). The incident electron beam corresponds to the electron beam generated by the electron gun. In the SEM-EDS technique, the reflected X-ray intensity and energy are detected; while the backscattered electrons, auger electrons, and secondary electrons are not detected.

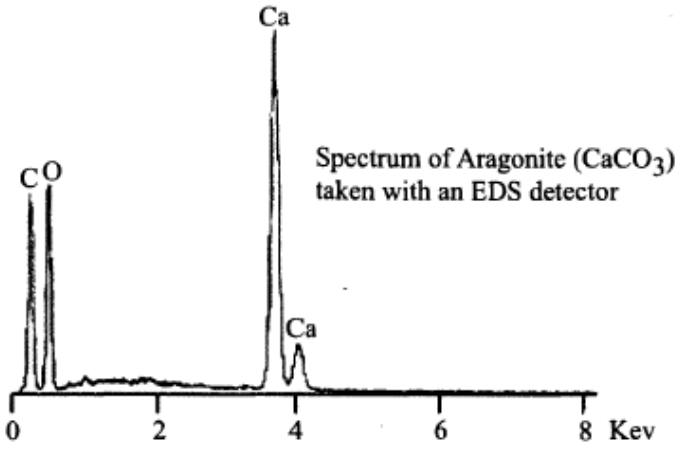

Figure 5.30 An aragonite spectrum taken with an EDS detector (Slim, 2016). The horizontal axis represents the energy (unit: Kev) of different X-rays, and the vertical axis (not shown) represents the X-ray intensity. For $CaCO_3$, three elements could be detected: Ca, C, and O.

6. Experimental Results

This chapter presents and discusses the experimental results of this research. Different types of tests are reported and discussed in following sections:

- Section 6.1 presents the mechanical properties of Musandam limestone, including the mineralogy, dissolution properties, and mechanical properties. The results will eventually provide a reference for numerical modeling on Musandam limestone.
- Section 6.2 shows the rock fracture creep tests. Rock fracture creep tests were conducted under different fluid conditions, including dry, stagnant saturated limestone solution, stagnant distilled water, and distilled water flow conditions. The rock specimen total creep deformation (rock matrix + fracture) was measured. The results prove that specimen creep under dry conditions (in which mechanical compression is the primary creep mechanism) is important.
- It is essential to understand rock creep behavior at the scale of contacting asperities because the creep of contacting asperities dominates the fracture-scale creep. According to Dieterich and Kilgore (1994), the scale of contacting asperities is generally between 100 nm and 100 μm. To cover the scale range, triaxial creep tests, micro-indentation tests, and nano-indentation tests were conducted.
- Section 6.3 shows the results of micro-indentation tests. 3-min and 6-hr micro-indentation creep tests were conducted.
- Section 6.4 presents the results of nano-indentation tests. 3-min and 6-hr nano-indentation creep tests were conducted.
- Section 6.5 discusses the results of triaxial creep tests on intact Musandam limestone specimens.
- Section 6.6 compares the different creep patterns between triaxial and indentation creep tests.

6.1 Mechanical properties of Musandam limestone

6.1.1 Rock Mineralogy

It is essential to understand the mineralogical composition of Musandam limestone because the mineralogical composition could significantly affect its mechanical properties. XRD (X-Ray Diffraction) tests and SEM-EDS tests were conducted.

Specifically, XRD tests were conducted on Musandam limestone (grey matrix only. Figure 5.4 in Section 5.1.1 shows the grey matrix, white vein, and yellow vein) and on one rock core from the Cretaceous group underlying Abu Dhabi (depth between 2662.85 and 2663.34 m, see the purple

rectangle in Figure 5.2 in Chapter 5). Table 6.1 summarizes the bulk mineralogy of the two types of rocks.

Table 6.1. Bulk mineralogy (weight %) by XRD tests

Rock type	Calcite	Dolomite	Quartz	Pyrite	Illite and Smectite	Kaolinite	Total
Musandam limestone (grey matrix only)	98.3	0.0	1.1	0.0	0.0	0.6	100
Core from reservoir	95.0	0.5	1.6	0.1	1.9	0.9	100

Based on Table 6.1, the mineralogical compositions of Musandam limestone and the Cretaceous group underlying Abu Dhabi are similar. The average specific gravity of Musandam limestone is 2.67, and the average porosity measured by the mercury intrusion method is 0.93%.

As shown in Figure 5.4 in Section 5.1.1, both white and yellow veins could be found in all the sub-blocks. SEM – EDS tests were conducted on thin sections that contain the grey matrix, the white vein, and the yellow vein. The results indicate that the grey matrix mainly consists of calcite, the yellow vein mainly of clay minerals, and the white vein mainly of calcite and quartz.

6.1.2 Dissolution properties

Musandam limestone may be subject to varying conditions related to water. In such conditions, pressure solution or chemical dissolution may occur. To understand the difference between pressure solution and chemical dissolution, it is essential to know the dissolution properties. The element concentration and electrical conductivity of saturated (equilibrated) limestone solutions were measured. The saturated limestone solutions were made by grinding small limestone pieces (from the grey matrix in Sub-block '3') into fine powder and mixing the powder with distilled water for 24 hours. The electrical conductivity was measured with electrical probes, and the element concentration was measured using the ICP (induced coupled plasma) technique (Yasuhara et al., 2015).

The electrical conductivity of the saturated limestone solution is 76 μS/cm. Table 6.2 summarizes the element concentration of the saturated limestone solution. The concentration of seven elements was measured. The dissolution properties will not be further discussed in this thesis since this thesis focuses on the mechanical properties.

Table 6.2. Element concentration of Musandam limestone matrix solution based on ICP.

Element type of limestone solution	Concentration (ppm)
Calcium (Ca)	23.63

Summation of the concentration of six other elements (Fe, Al, Na, K, Mg, Si)	≈2.30

6.1.3 Overview of the strength properties – uniaxial and triaxial testing

Two uniaxial compression tests and three triaxial tests were conducted (see also Figures 6.1 and 6.2 for the results) on Musandam limestone to measure the strength and elastic properties. Table 6.3 summarizes the failure strengths for different tests, and Figure 6.1 plots the failure strengths against confining pressures.

Table 6.3. Failure strengths at different confining pressures (CPs)

Confining pressure (MPa)	Failure strength (MPa)	Number of tests
0	74.28	2
20	157.40	1
60	349.60	1
100	504.40	1

Note: the failure strength at zero confining pressure is the averaged failure strength of the two tests.

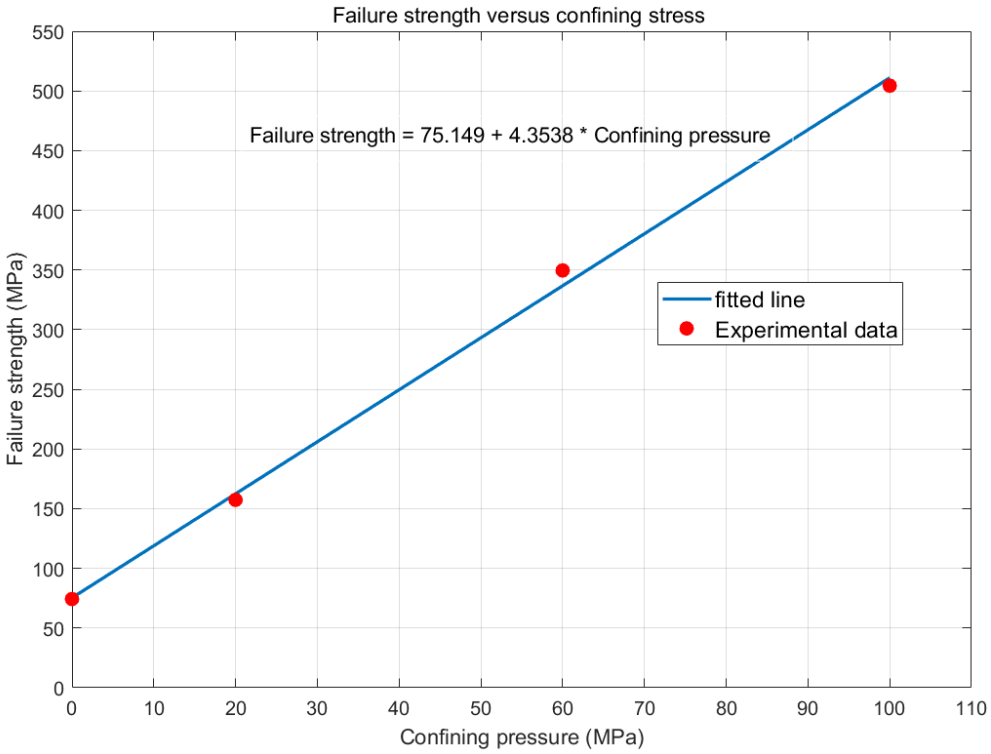

Figure 6.1. Failure strength versus confining pressure.

Based on the measured failure strengths and their corresponding confining pressures, the linear Coulomb parameters – cohesion and friction angle – were obtained. By plotting the failure

strengths against confining pressures and using linear regression, the intercept S and slope n were obtained. According to Zoback (2007),

$$\varphi = \tan^{-1}\left(\frac{n-1}{2\sqrt{n}}\right) \tag{6.1}$$

and

$$c = \frac{S}{2\sqrt{n}} \tag{6.2}$$

where c is the cohesion and φ is the friction angle. From Figure 6.1, n = 4.3538 and S = 75.149 MPa. Therefore, **c = 18MPa**, and **φ = 39**°. It is worth noting that under confined conditions, for each confining pressure, only one test was conducted. While more tests would be desirable, the results in Figures 6.1 and 6.2 show strong consistency.

Figure 6.2 plots the Mohr circles and the fitted linear Coulomb line.

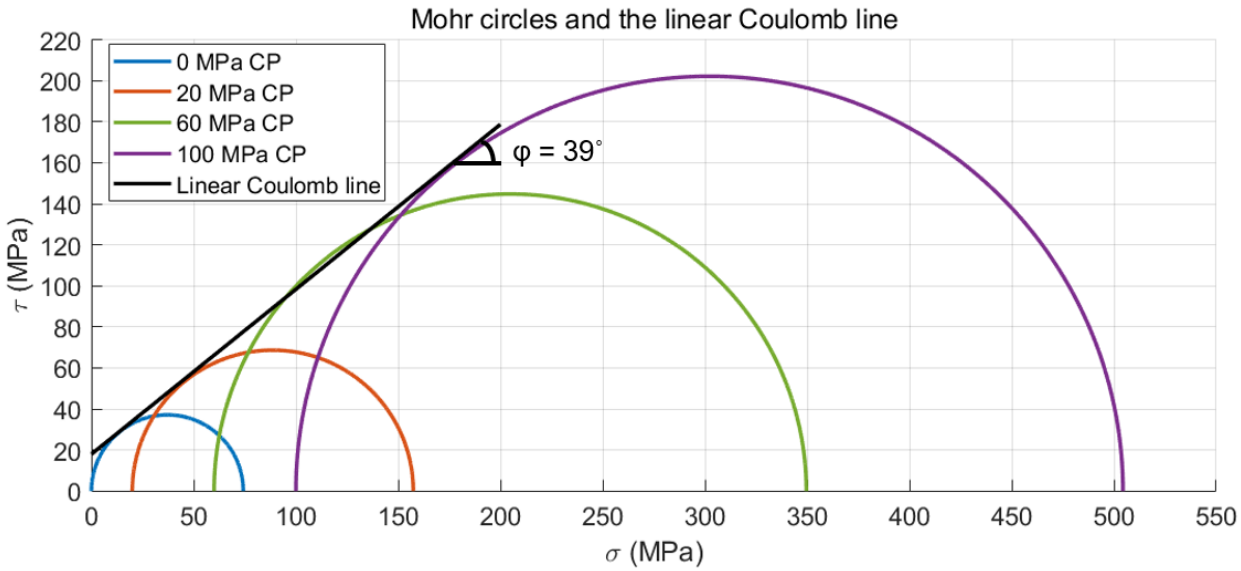

Figure 6.2. Mohr circles based on Table 6.1 and the linear Coulomb line based on Figure 6.2.

6.1.4 Elastic properties changing with confining pressure

The deformation of Musandam limestone specimens was also measured. In the uniaxial compression tests, two extensometers were used to measure the axial displacement. In the triaxial tests, the axial displacement was measured by both axial strain gauges and LVDT sensors; the radial strain was measured by radial strain gauges (see Figure 5.14 for a photo and Figure 5.15 for a schematic in Section 5.3).

When the axial stress was less than 70% of the ultimate strength, the stress-strain curves were approximately linear for all confining pressures. The elastic modulus and Poisson's ratio were computed as:

$$E = \frac{\Delta\sigma}{\Delta\varepsilon_{axial}} \tag{6.3}$$

$$\nu = -\frac{\Delta\varepsilon_{radial}}{\Delta\varepsilon_{axial}} \tag{6.4}$$

where $\Delta\sigma$ is the axial stress increment between 40% and 60% of ultimate compressive strength, $\Delta\varepsilon_{axial}$ and $\Delta\varepsilon_{radial}$ are the corresponding axial and radial strain increments, respectively (ISRM, 1979). In the strain increment calculation, the two axial and radial strain gauge readings and the two LVDT readings were averaged. The calculated elastic modulus is denoted as $E_{'50'}$). Figures 6.3 to 6.6 show the stress-strain curves for specimens under 0 MPa confining pressure, 20 MPa confining pressure, 60 MPa confining pressure, and 100 MPa confining pressure, respectively.

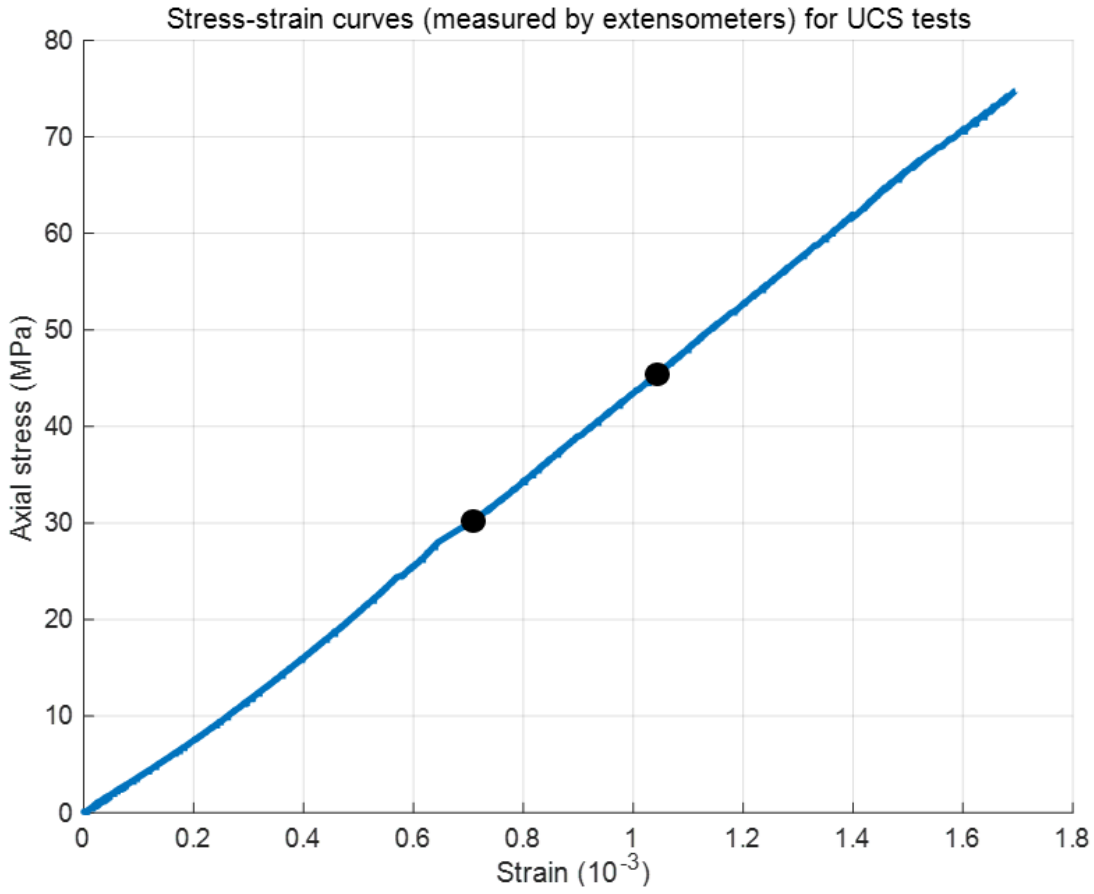

Figure 6.3 Axial strain (measured by extensometers) changing with axial stress for uniaxial compression tests. The two black dots show the segment used for elastic modulus calculation. The elastic modulus is 43.84 GPa.

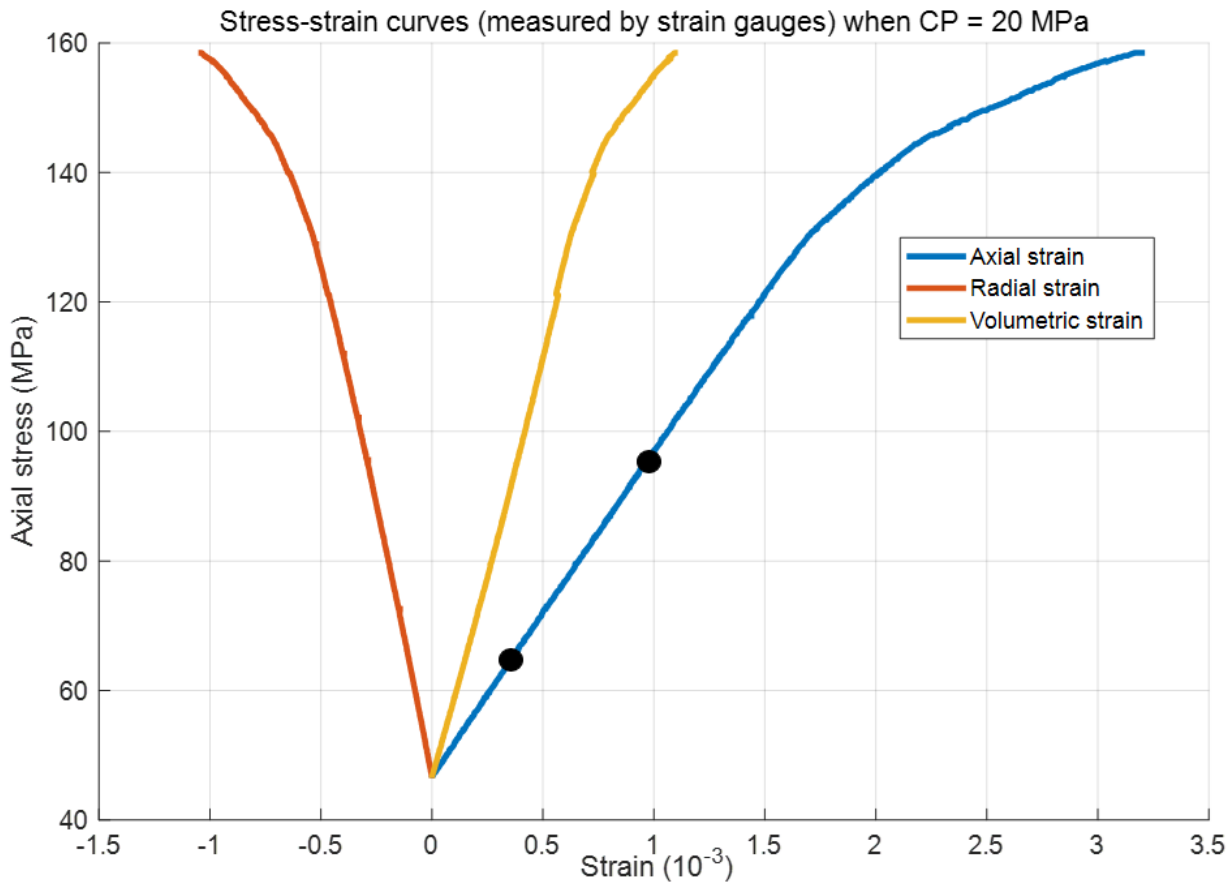

Figure 6.4 Axial, radial, and volumetric strain values (measured by strain gauges) changing with axial stress when the confining pressure was 20 MPa. The two black dots show the segment used for elastic modulus calculation. The elastic modulus is 57.35 GPa.

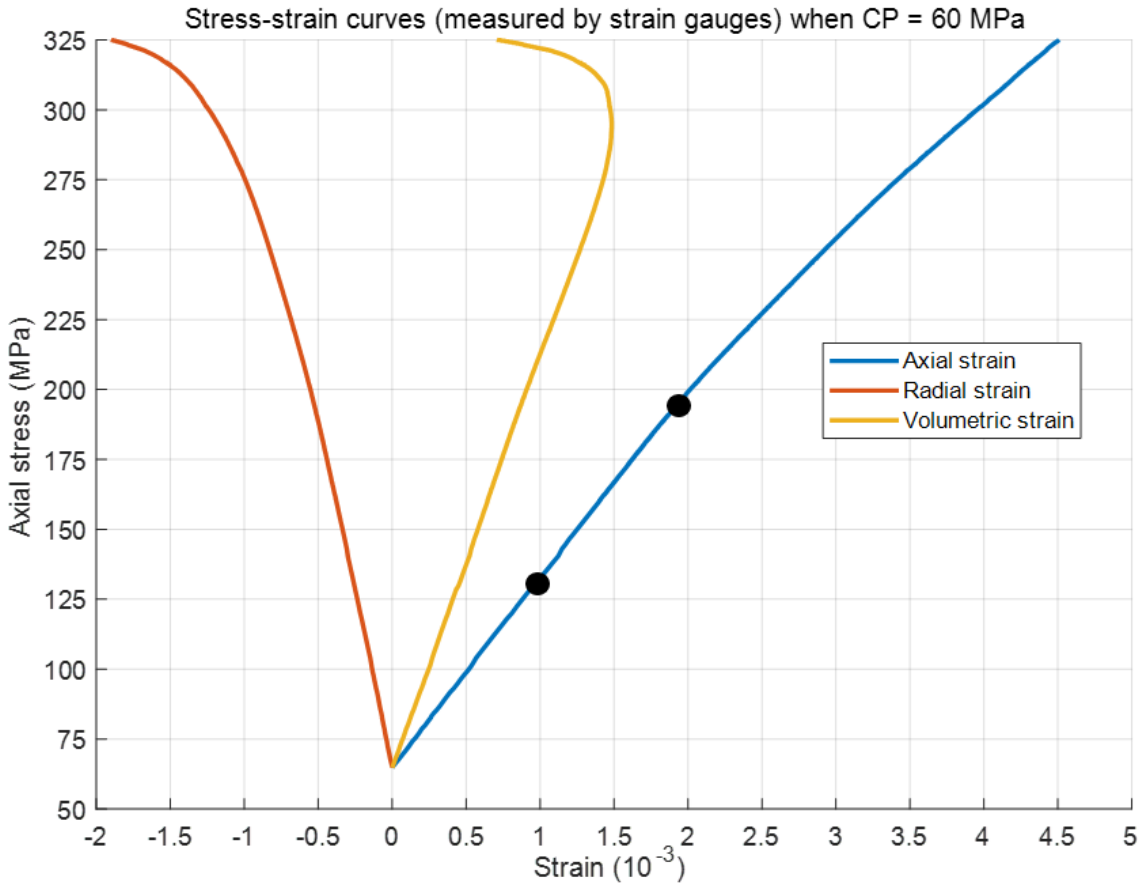

Figure 6.5 Axial, radial, and volumetric strain values (measured by strain gauges) changing with axial stress when the confining pressure was 60 MPa. The two black dots show the segment used for elastic modulus calculation. The elastic modulus is 68.11 GPa.

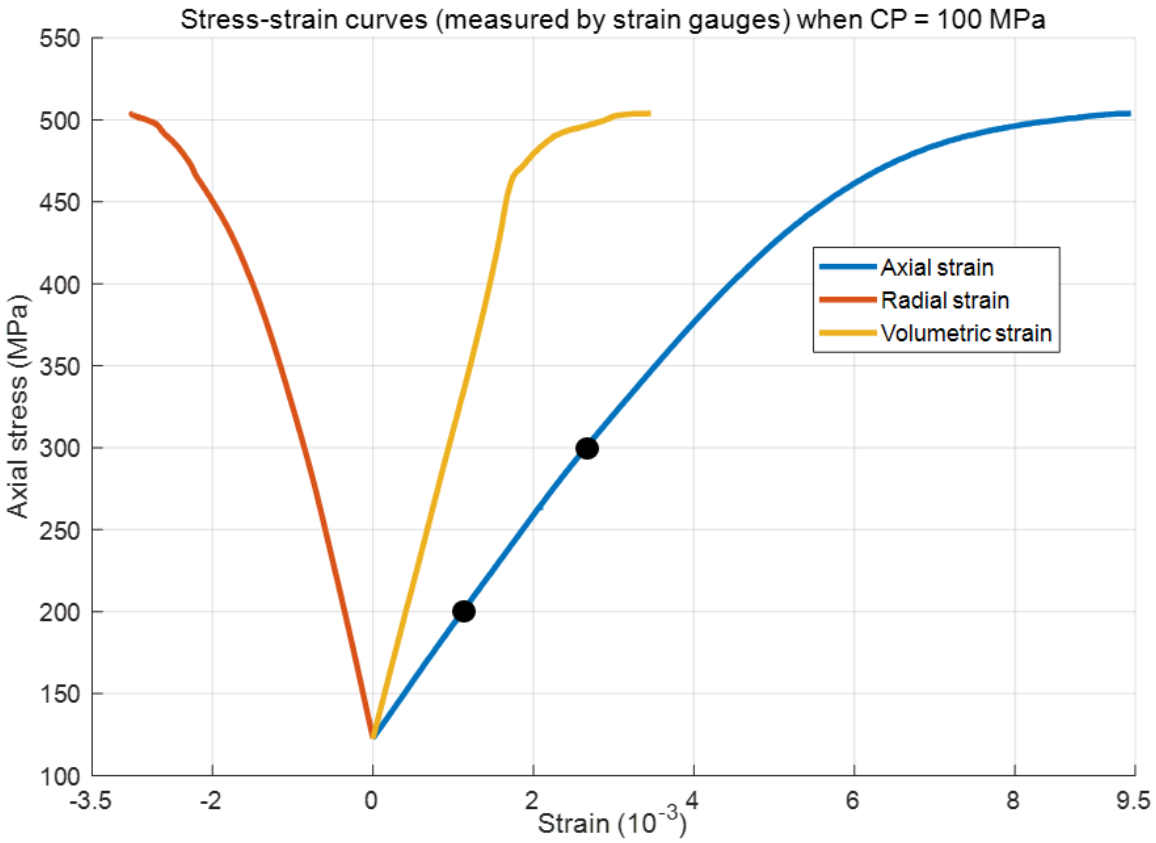

Figure 6.6 Axial, radial, and volumetric strain values (measured by strain gauges) changing with axial stress when the confining pressure was 100 MPa. The two black dots show the segment used for elastic modulus calculation. The elastic modulus is 68.87 GPa.

Table 6.4 summarizes the elastic properties (E_{50} and ν) changing with confining pressures, and Figure 6.7 plots the E_{50} versus confining pressures for different types of sensors. Figure 6.7 suggests that the E_{50} increased when the confining pressure was increased from 0 to 60 MPa, and stabilized when the confining pressure was between 60 and 100 MPa. In contrast, based on Table 6.4, the Poisson's ratio did not change significantly with confining pressure.

Table 6.4. E_{50} and ν changing with confining pressure.

CP (MPa)	Elastic modulus by strain gauge (GPa)	Poisson's ratio by strain gauge	Elastic modulus by extensometer or LVDT (GPa)
0	-	-	43.84
20	57.35	0.29	55.13
60	68.11	0.30	68.06
100	68.87	0.30	67.11

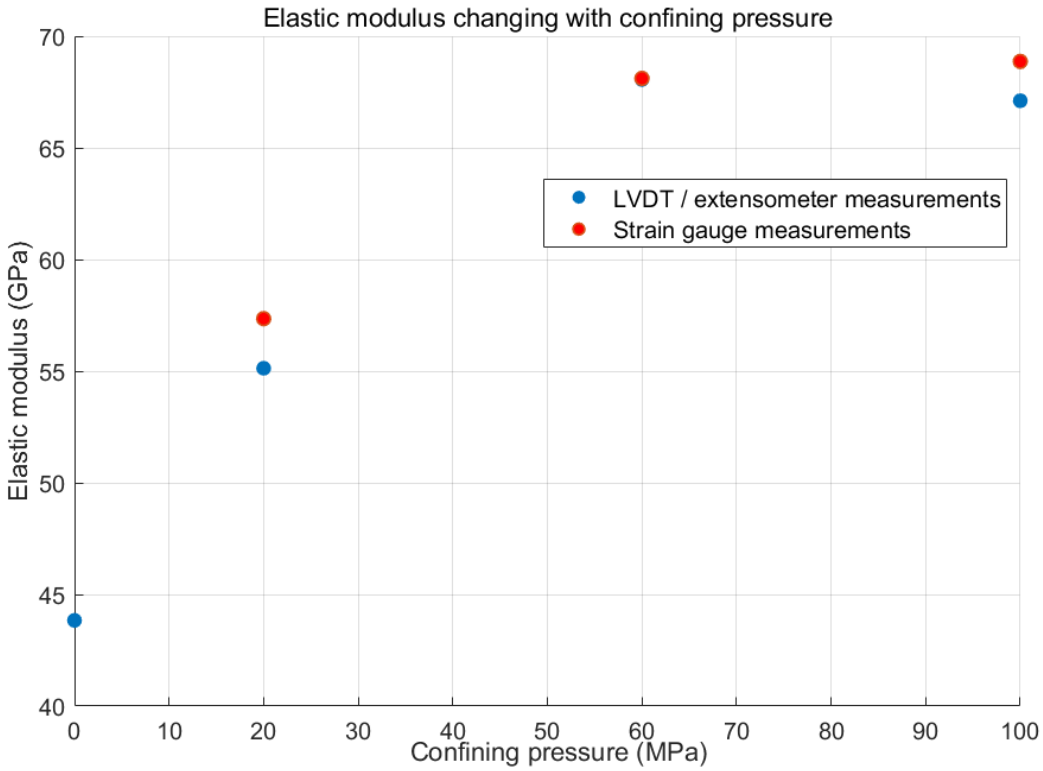

Figure 6.7. E_{50} changing with confining pressure.

The P-wave velocity (V_p) of the rock was also measured at room temperature and unconfined conditions, as illustrated in Figure 6.8. For the z-direction, the P-wave intersected the yellow vein perpendicularly; while for the x- and y-directions, the P-wave did not intersect the yellow vein. As a result, the V_p in the z-direction was smaller than those in the x- or y-directions, while the V_p in the x- and y-directions were similar. The averaged V_p in the x- and y-directions was 5324 m/s, and in the z-direction was 4619 m/s. Since the bedding planes are horizontal (x-y plane), the smaller V_p in the z-direction may be affected both by the bedding planes and the yellow vein.

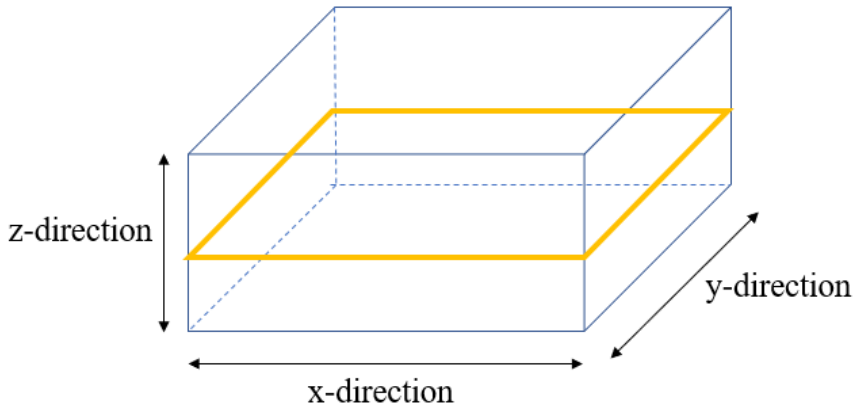

Figure 6.8. Schematic of specimens used in P-wave velocity measurements. The yellow rectangle represents the yellow clay vein.

The dynamic elastic modulus E_d can be computed from the P-wave velocity:

$$V_p = \sqrt{\frac{E_d(1-\nu_d)}{\rho(1-2\nu_d)(1+\nu_d)}} \tag{6.5}$$

where ν_d is the dynamic Poisson's ratio, and ρ is the density (2.62 g/cm^3). By assuming ν_d = 0.3 (the same as the Poisson's ratio measured in the triaxial tests), the E_d in z- and horizontal direction are 41.52 and 55.17 GPa, respectively. As shown by V_p, the smaller E_d in the vertical direction is partially due to the horizontal bedding planes or the horizontal yellow clay vein. Since the P-wave velocity was measured under unconfined conditions, the derived E_d values are valid only under these conditions.

Table 6.5 summarizes the axial stress and strain at final failure and yield initiation (when the specimen started to deform non-linearly). The values in Table 6.5 could also be found in Figures 6.3 to 6.6.

Table 6.5. Axial stress and strain at final failure and yield initiation

CP (MPa)	Final failure state		Yield initiation state	
	Axial stress (MPa)	Axial strain (10^{-3})	Axial stress (MPa)	Axial strain (10^{-3})
0	74.28	1.68	74.28	1.68
20	157.40	3.21	132.42	1.76
60	349.60	4.49	313.86	4.25
100	504.40	9.41	435.89	5.26

6.1.5 Comparison of mechanical properties between Musandam limestone and other limestones – elastic properties

The elastic properties of Musandam limestone are compared with those of other types of limestones. To extend the results to similar formations, the limestone rocks used for comparison are those from eastern Saudi, UAE, and Oman. Table 6.6 compares the elastic moduli and Poisson's ratios of different types of limestone.

Table 6.6. Elastic moduli and Poisson's ratios of different types of limestone (no confining pressure was applied)

Reference	Limestone formation	Limestone location	Elastic modulus (GPa)	Poisson's ratio	Dominant minerals	Porosity (%)
Mahmood et al. (2018)	-	Eastern Saudi	~48.3	~0.25	Calcite (> 98%)	-

Ameen et al. (2009)	Jubaila Formation	Eastern Saudi, Ghawar Field	~33	~0.19	Calcite (> 98%)	~12.0
Al-Shayea (2004)	Khuff Formation	Eastern Saudi	~35	~0.22	Calcite (> 99%)	~5.4
Alnuaim and Hamid (2019)	Jubaila and Arab Formation	Eastern Saudi, Riyadh	~50.1	~0.24	Calcite (91.5%), feldspar (3.8%), dolomite (1.3%).	~4.1
This thesis	Musandam Formation	Musandam Peninsular, Oman	43.84	-	Calcite (98.3%)	0.93

Note: '- 'means that the value or formation was not reported.

According to Table 6.1, calcite makes up of 98.3% of the mass for Musandam limestone. Therefore, the mineralogical composition of Musandam limestone is similar to those of the limestone rocks reported by Mahmood et al. (2018), Ameen et al., (2009), and Al-Shayea (2004). Under unconfined conditions, the elastic modulus of Musandam limestone is slightly larger than those reported by Ammen et al. (2009) and Al-Shayea (2004), while slightly smaller than that reported by Mahmood et al. (2018).

6.1.6 Comparison of mechanical properties between Musandam limestone and other limestones – strength properties

Similar to Section 6.1.5, the limestone rocks used for comparison are those from eastern Saudi, UAE, and Oman. It appears that the information on the cohesion and friction angle of different types of limestone is limited. However, some literature reported the uniaxial compressive strength (UCS). Therefore, Table 6.7 compares the unconfined compressive strength (UCS) of different types of limestone.

Table 6.7. Uniaxial compressive strengths of different types of limestone

Reference	Limestone formation	Limestone location	UCS (MPa)	Dominant minerals	Porosity (%)
Arman et al. (2014)	Lower Oligocene Asmari Formation	Southeastern UAE (Al Ain City)	~36.2	Calcite (> 95%), dolomite (~1.3%), quartz (~0.5%)	~6.2
Arman and Paramban (2020)	Dammam Formation	Southeastern UAE	~91.2	Calcite (> 98%)	~1.20

Wang (2011)	Shah Simsima Formation	Southeastern UAE	~55.3	-	~12.4
Ameen et al. (2009)	Jubaila Formation	Eastern Saudi, Ghawar Field	~33	Calcite (> 98%)	~12.0
Al-Shayea (2004)	Khuff Formation	Eastern Saudi	~76.2	Calcite (> 99%)	~5.4
Alnuaim and Hamid (2019)	Jubaila and Arab Formation	Eastern Saudi	~130.7	Calcite (91.5%), feldspar (3.8%), dolomite (1.3%).	~4.1
Mahmood et al. (2018)	-	Eastern Saudi	~69.0	Calcite (> 98%)	-
El-Aal (2015)	Sulaiy Formation	Eastern Saudi	~65.26	Calcite (> 98%)	~5.2
This thesis	Musandam Formation	Musandam Peninsular, Oman	74.28	Calcite (98.3%)	0.93

Note: '- 'means that the value or the location was not reported.

Since calcite makes up 98.3% of the mass for Musandam limestone, the mineralogical composition of Musandam limestone is similar to those of the other limestone rocks in Table 6.7 with calcite more than 98%. Based on Table 6.7, for similar mineralogical compositions, the porosity has a significant effect on the UCS – the UCS decreases with increasing porosity.

6.2 Rock fracture creep experimental results

6.2.1 Type 1 experimental results

As discussed in Section 5.2, for rock fracture creep, two types of experiments were conducted. The details of the experimental procedures have been shown in Section 5.2.3. Here, the experimental procedures of both types of experiments are briefly summarized.

In type 1 experiments, the effects of confining pressure, flowrate, and fracture type (tensile and polished saw-cut) on fracture creep (permeability evolution) were investigated to obtain a qualitative relationship between the different factors (confining pressure, flowrate, and fracture type) and fracture permeability. Four tests are reported and discussed in this section. The three factors were systematically varied by keeping two constant and changing the third one (see Table 6.8 and Figure 6.9). For example, the effect of confining pressure was investigated by conducting tests 003 and 004. Between the two tests, only the confining pressure was varied; the flowrate and fracture type were the same.

Table 6.8. Test summary for type 1 experiments.

Test No.	Fracture type	Flowrate (μL/sec)	Confining pressure (kPa)	Back pressure (kPa)
001	Tensile	10	300	136
003	Tensile	2.5	500	136
004	Tensile	2.5	300	136
007	Polished saw-cut	2.5	300	136

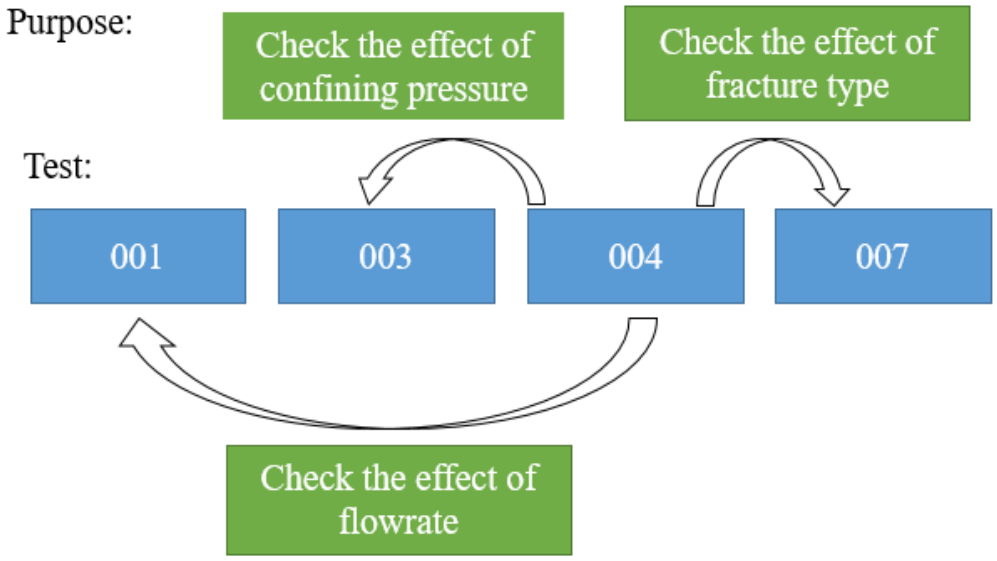

Figure 6.9 Objective of design of type 1 experiments.

Type 2 experiments were designed to investigate the effect of different mechanisms on fracture creep. As mentioned in Section 2.4.1, there are four different mechanisms contributing to permeability evolution: mechanical compression, pressure solution, dissolution, and erosion. It is still not well understood which mechanism dominates the permeability evolution. Between different experiments, the fluid type was changed to get an initial understanding of the role of different mechanisms causing the creep (the creep is caused by the four mechanisms mentioned above, not only mechanical compression); the confining pressure steps and the time duration for each step were identical. Four tensile fracture specimens were tested. As shown in Figure 6.10, specimen 011 was tested under dry conditions, specimen 015 under saturated limestone solution conditions, specimen 014 under stagnant distilled water conditions, and specimen 013 under distilled water flow conditions. In the four tests, the dissolution, pressure solution, and erosion were not directly measured. Instead, the mechanical creep of the four specimens (rock matrix and fracture) was measured. The relative importance of dissolution, pressure solution, and erosion was tentatively interpreted from the relative magnitude of the mechanical creep. Table 6.9 summarizes the details of the four tests.

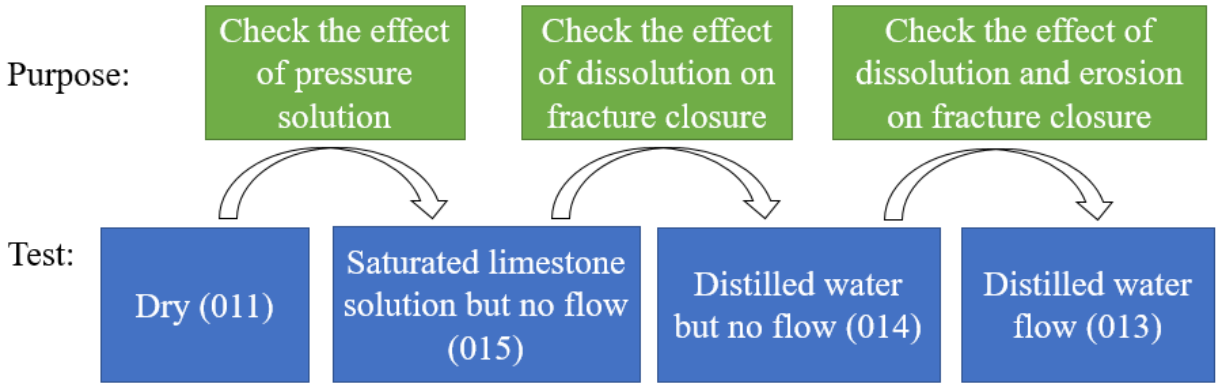

Figure 6.10 Objective of design of type 2 experiments

Table 6.9 Summary of the experimental conditions of the four specimens for type 2 experiments. The effective confining stress (confining pressure minus back pressure) steps were: 164 kPa (loading) → 364 kPa (loading) → 564 kPa (loading) → 364 kPa (unloading) → 164 kPa (unloading).

Specimen (test) No.	Fluid type	Time duration for each effective stress step (hr)					Back pressure (kPa)
		164 kPa, loading	364 kPa, loading	564 kPa, loading	364 kPa, unloading	164 kPa, unloading	
011	Dry	24	24	24	24	24	136
015	Stagnant saturated limestone solution	24	24	24	24	24	136
014	Stagnant distilled water	24	24	24	24	24	136
013	Distilled water, flow	24	24	24	24	24	136

For type 1 experiments, the hydraulic aperture, averaged hydraulic aperture creep rate, and normalized averaged hydraulic aperture creep rate for different tests are calculated and are summarized in Table 6.10. Figures 6.11, 6.12, and 6.13 plot the hydraulic aperture changing with time. Below, the hydraulic aperture, averaged hydraulic aperture creep rate, and normalized averaged hydraulic aperture creep rate are defined again.

The hydraulic aperture was computed based on the cubic law (this has been introduced in Section 2.3):

$$h = \sqrt[3]{\frac{12QL\mu}{\Delta pw}} \tag{6.6}$$

where Q is the flowrate, L is the specimen length, μ is the dynamic viscosity of the liquid, w is the specimen width, Δp is the pressure difference between water inlet and outlet. The cubic law is a simplification but acceptable in the context of this research where the hydraulic aperture is used for comparison.

The averaged hydraulic aperture creep rate was computed as:

$$\overline{cr_{hy}} = \frac{h_{ini} - h_{fin}}{t} \tag{6.7}$$

where $\overline{cr_{hy}}$ is the averaged hydraulic aperture creep rate (unit: μm / day), t is the total duration of the experiment, h_{ini} is the initial hydraulic aperture (the averaged hydraulic aperture for the first fifteen minutes of the test), h_{fin} is the final hydraulic aperture (the averaged hydraulic aperture for the last fifteen minutes of the test). Positive hydraulic aperture creep indicates hydraulic aperture reduction (closure).

The normalized averaged hydraulic aperture creep rate (unit:1/day), was also computed as:

$$\overline{cr_{hy-no}} = \frac{\overline{cr_{hy}}}{h_{ini}} \tag{6.8}$$

where $\overline{cr_{hy-no}}$ is the normalized averaged hydraulic aperture creep rate.

Table 6.10. Averaged hydraulic aperture creep rate and normalized averaged hydraulic aperture creep rate for type 1 experiment.

Test	Flowrate (μL/sec)	Hydraulic aperture (μm)		Averaged hydraulic aperture creep rate (μm/day)	Normalized averaged hydraulic aperture creep rate (μm/day)
		Initial	End		
001	10	34.40	15.92	9.24	0.27
003	2.5	16.11	5.52	5.25	0.33
004	2.5	32.09	21.45	4.73	0.15
007	2.5	18.50	15.71	1.16	0.06

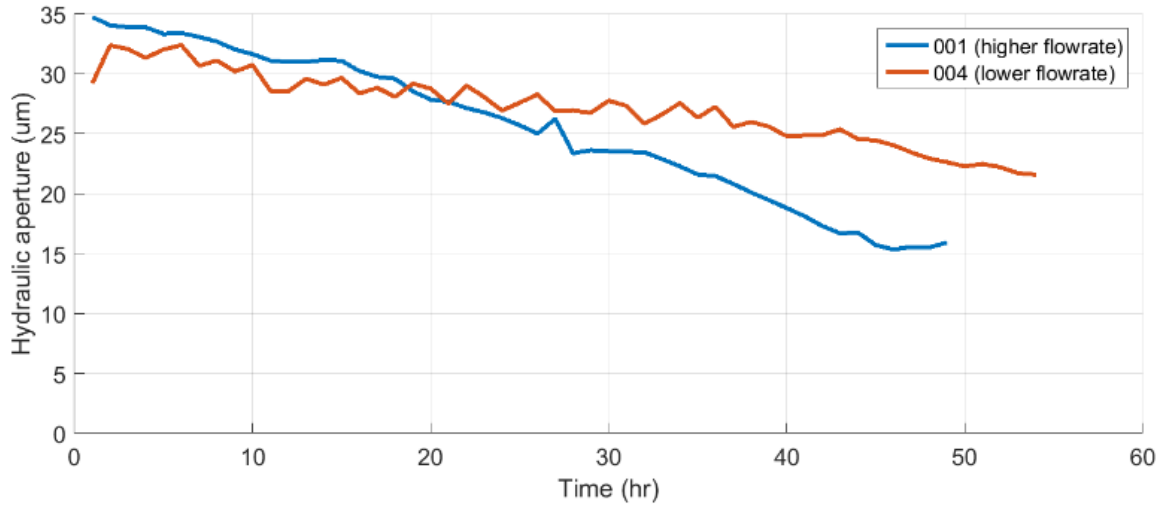

Figure 6.11. Hydraulic aperture changing with time for tests 001 (higher flowrate, 10 µL/sec, shown by the blue curve) and 004 (lower flowrate, 2.5 µL/sec, shown by the orange curve). The confining pressure and fracture type (both tensile fractures) were identical.

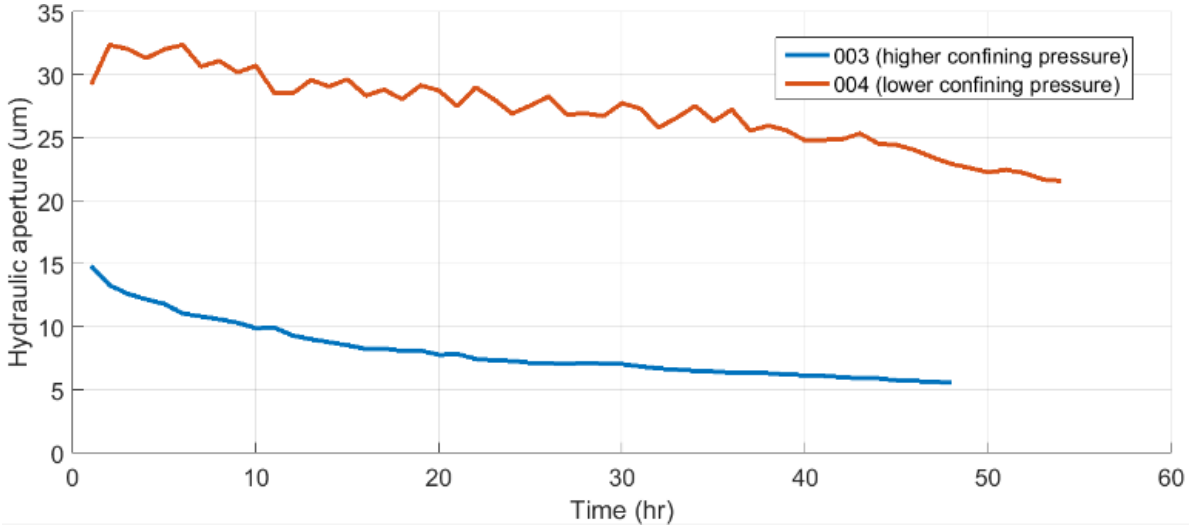

Figure 6.12. Hydraulic aperture changing with time for tests 003 (higher confining pressure, 500 MPa, shown by the blue curve) and 004 (lower confining pressure, 300 MPa, shown by the orange curve). The flowrate and fracture type (both tensile fractures) were identical.

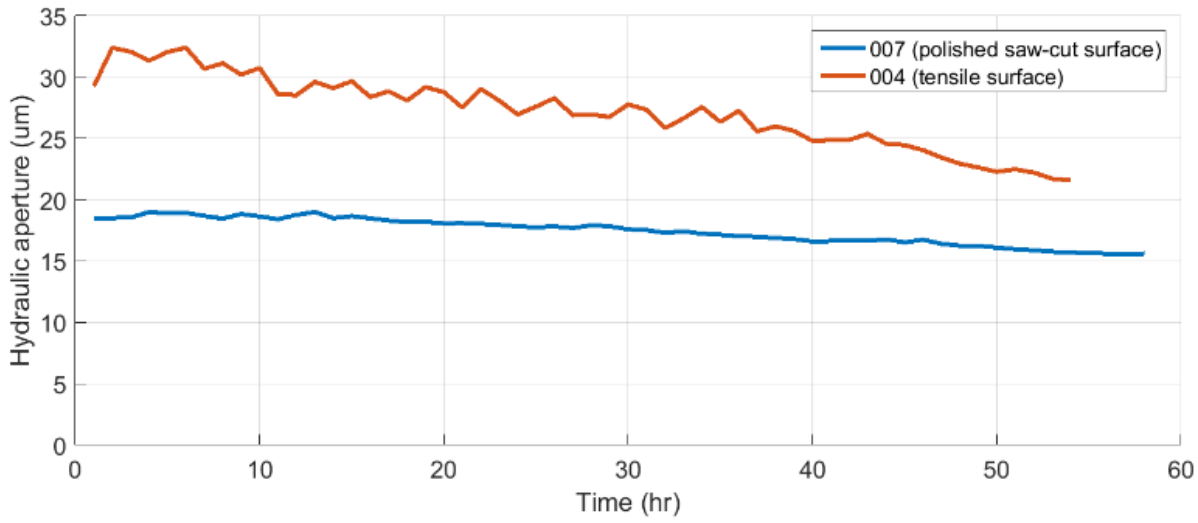

Figure 6.13. Hydraulic aperture changing with time for tests 004 (tensile fracture, shown by the orange curve) and 007 (polished saw-cut fracture, shown by the blue curve). The fracture surface of the tensile fracture is rougher. The confining pressure and flowrate were identical.

Based on the above results, the observations can be summarized:

(i). Increasing the confining pressure, increasing the flowrate, and increasing the surface roughness leads to greater hydraulic aperture reduction.

(ii). At a high confining pressure (500 kPa), the hydraulic aperture decreases relatively faster initially, and slower near the end of the test, compared to low confining pressure (300 kPa).

6.2.2 Type 2 experimental results

6.2.2.1 Results – Mechanical deformation

Figures 6.14, 6.15, 6.16, 6.17, 6.18 summarize the mechanical deformation of the four specimens for each effective stress step (see Table 6.9), respectively. The mechanical deformation (rock matrix and fracture) was computed based on the measured proximity probe readings (See Figure 5.9 in Section 5.2 for the schematic of the proximity probe). In each effective confining stress step, the mechanical deformation at the beginning was defined as zero. Contraction (fracture and rock matrix) was defined as positive mechanical deformation.

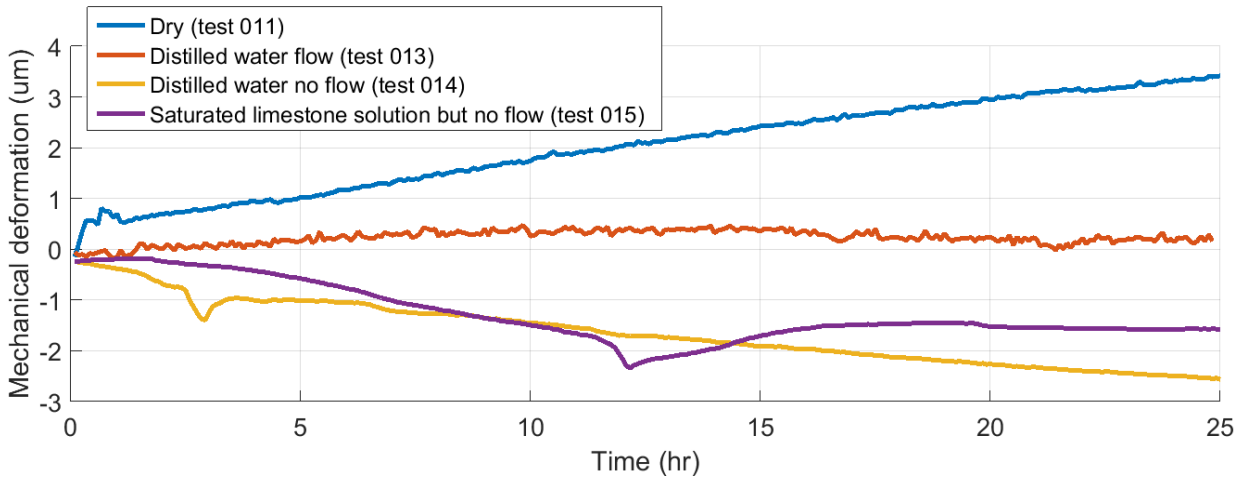

Figure 6.14. Specimen mechanical deformation (fracture and rock matrix) of the four tests under 164 kPa effective confining stress (loading). Positive mechanical deformation corresponds to specimen contraction, while negative mechanical deformation corresponds to specimen expansion.

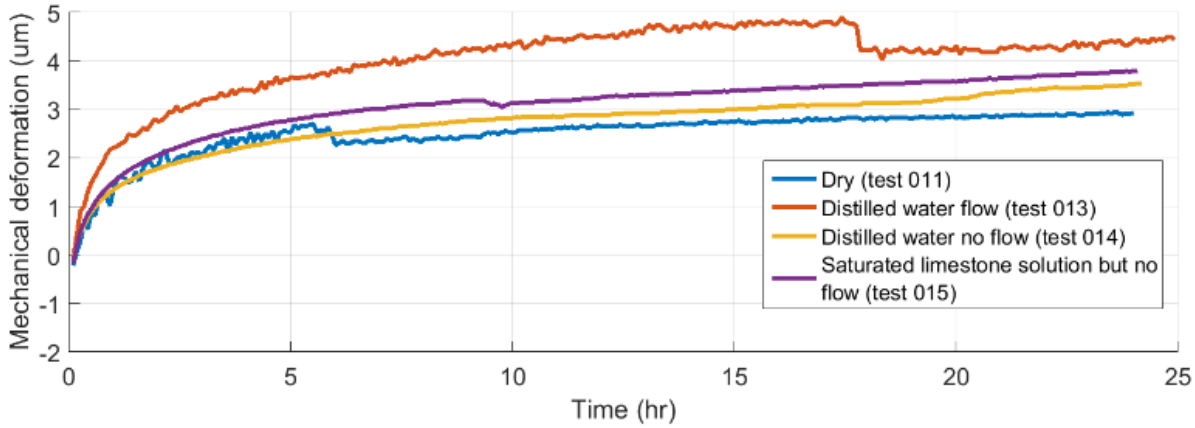

Figure 6.15. Specimen mechanical deformation (fracture and rock matrix) of the four tests under 364 kPa effective confining stress (loading). Positive mechanical deformation corresponds to specimen contraction.

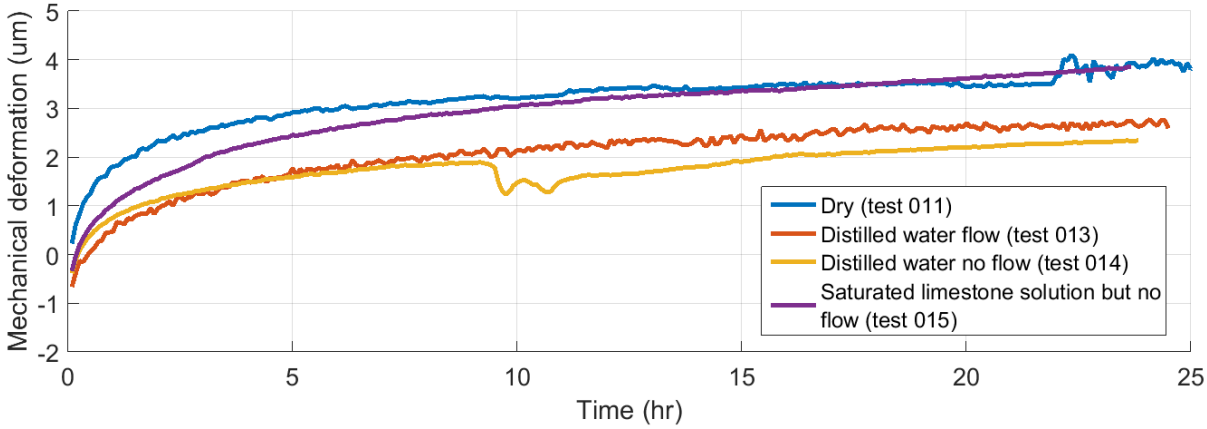

Figure 6.16. Specimen mechanical deformation (fracture and rock matrix) of the four tests under 564 kPa effective confining stress (loading). Positive mechanical deformation corresponds to specimen contraction.

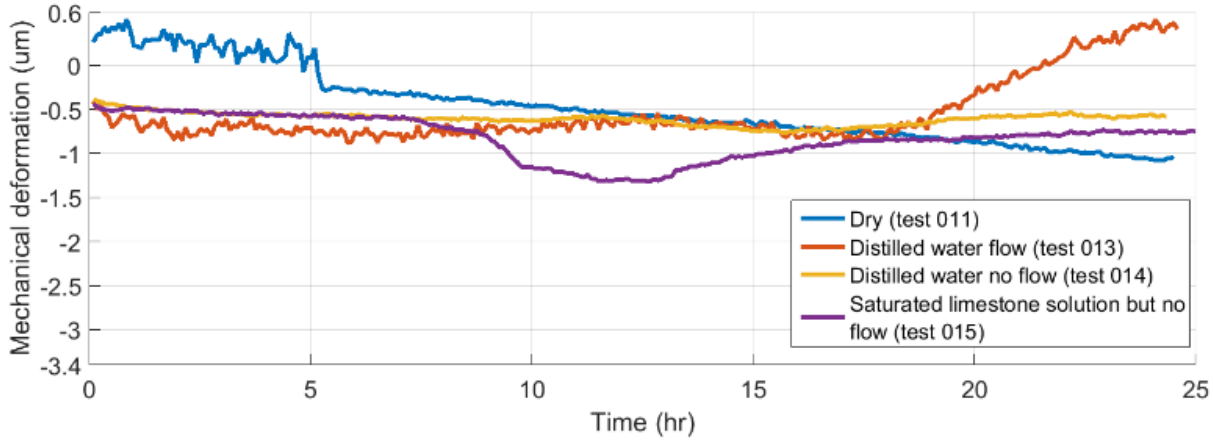

Figure 6.17. Specimen mechanical deformation (fracture and rock matrix) of the four tests under 364 kPa effective confining stress (unloading). Positive mechanical deformation corresponds to specimen contraction.

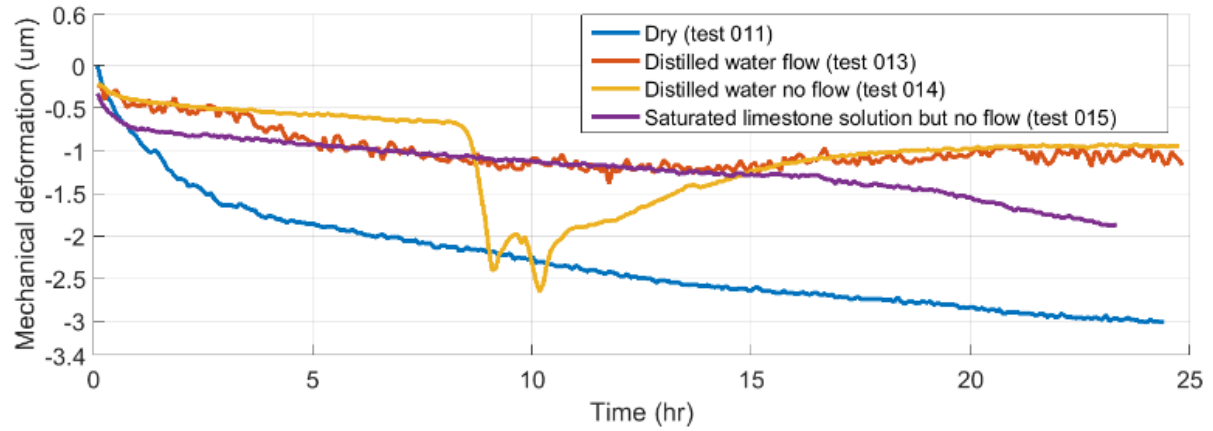

Figure 6.18. Specimen mechanical deformation (fracture and rock matrix) of the four tests under 164 kPa effective confining stress (unloading). Positive mechanical deformation corresponds to specimen contraction.

For the loading steps, the following observations can be made:

(i). When the effective confining pressure is 164 kPa, the dry specimen contracts with time. The specimen under distilled water flow condition does not deform significantly. However, the specimens under stagnant saturated limestone solution and stagnant distilled water condition expand with time.

(ii). When the effective confining pressure is 364 kPa, all four specimens contract with time. The specimens contract relatively faster initially, and relatively slower near the end. The specimen under distilled water flow condition shows the largest contraction. Furthermore, the magnitude of

contraction of the specimen under dry condition is comparable to that of specimens under other conditions, which indicates that the effect of mechanical compression is not negligible.

(iii). When the effective confining pressure is 564 kPa, all four specimens contract with time. The specimens contract relatively faster initially, and relatively slower near the end. Also, the specimens under the dry condition and stagnant saturated limestone solution show relatively larger contraction than the other two. The relatively larger contraction of the specimen under dry condition indicates that the effect of mechanical compression is not negligible.

For the unloading steps, the following observations can be made:

(i). When the effective confining pressure is 364 kPa, the dry specimen expands with time. However, the three specimens under wet conditions expand first, then contract. The specimen under distilled water flow condition contracts the most.

(ii). When the effective confining pressure is 164 kPa, the dry specimen and the specimen under stagnant saturated limestone solution expand with time. On the contrary, two specimens under distilled water conditions (both with and without flow) expand first, then contract.

6.2.2.2 Interpretation – Mechanical deformation

Based on the above observations, it is possible to tentatively interpret:

For the loading steps:

(i). (Corresponds to the first observation statement in the loading section) The dry specimen contracts, while the three other specimens do not contract. This indicates that the presence of water may cause the specimens to expand. One possible explanation is that the minerals (particularly the clay) may expand under wet conditions. Interestingly, the two specimens under stagnant water conditions show more expansion than the specimen under distilled water flow condition. Erosion caused by water flow may be an explanation. As introduced by Figure 2.32 in Section 2.4.1, under water flow conditions, surface erosion may occur; as a result, some particles may detach from fracture surfaces, and the released particles may be transported downstream. If the contacting asperities are detached and transported away, the fracture aperture may be reduced. The decrease in fracture aperture corresponds to specimen contraction if the rock matrix creep can be ignored (specimen deformation = fracture deformation + rock matrix deformation).

(ii). (Corresponds to the second and third observation statements in the loading section) An increase of effective confining pressure (164 kPa to 364 kPa, or 164 kPa to 564 kPa) causes specimens to contract. Increasing the effective confining pressure may compress the contacting asperities of the fracture surface.

For the unloading steps:

(This corresponds to the second observation statement in the unloading section) The two specimens under distilled water conditions expand first and then contract, while the other two specimens expand with time. This difference can be explained by dissolution. Dissolution of

fracture surfaces may occur under distilled water conditions, but will not occur under dry condition or saturated limestone solution condition.

In both loading and unloading stages, the effect of mechanical compression is important (shown by the blue curves from Figures 6.14 to 6.18). It is worth noting that the four specimens have different fracture surface geometries. As shown in Figure 4.4 in Section 4.2 and Figure 4.6 in Section 4.3, fracture surface geometry has a dominant effect on the magnitude of fracture creep. Therefore, the variation in surface geometry of the four specimens may influence the magnitude of creep, which is indicated by the magnitude of the measured mechanical deformation (I think it is enough to mention one conclusion in the numerical results chapter. Please let me know if more information is required).

6.2.2.3 Results – Hydraulic aperture

Under the distilled water flow condition (specimen 013), the hydraulic aperture keeps decreasing at each confining pressure step. Figure 6.19 shows the hydraulic aperture changing with confining pressure and time. During unloading, the hydraulic aperture does not go back to the hydraulic aperture of the corresponding loading steps, which indicates permanent deformation of the fracture surfaces. Figures 6.17 and 6.18 show the mechanical deformation during unloading for the flow test, and Figure 6.19 shows the hydraulic aperture during unloading. Based on Figures 6.17, 6.18, and 6.19, it is worth noting that during unloading, the hydraulic aperture decreases with time, but the specimen expands first and then contracts. In data interpretation, it is assumed that the rock matrix deformation is negligible. With this assumption, the measured specimen deformation is the fracture deformation, which is also the change of fracture mechanical aperture. Furthermore, if the parallel plate assumption is valid (the parallel plate assumption is explained by Figure 2.18 in Section 2.3), the fracture deformation corresponds to the change in hydraulic aperture: fracture contraction corresponds to hydraulic aperture decrease, and vice versa. Therefore, if the rock matrix deformation is negligible and the parallel plate assumption is valid, specimen contraction (which is also mechanical aperture decrease) corresponds to hydraulic aperture decrease, and vice versa. However, according to experimental data, during the unloading stress steps, the hydraulic aperture decreases with time, but the mechanical aperture first increases and then decreases. This indicates that either the parallel plate assumption or the negligible rock matrix deformation assumption may not be valid.

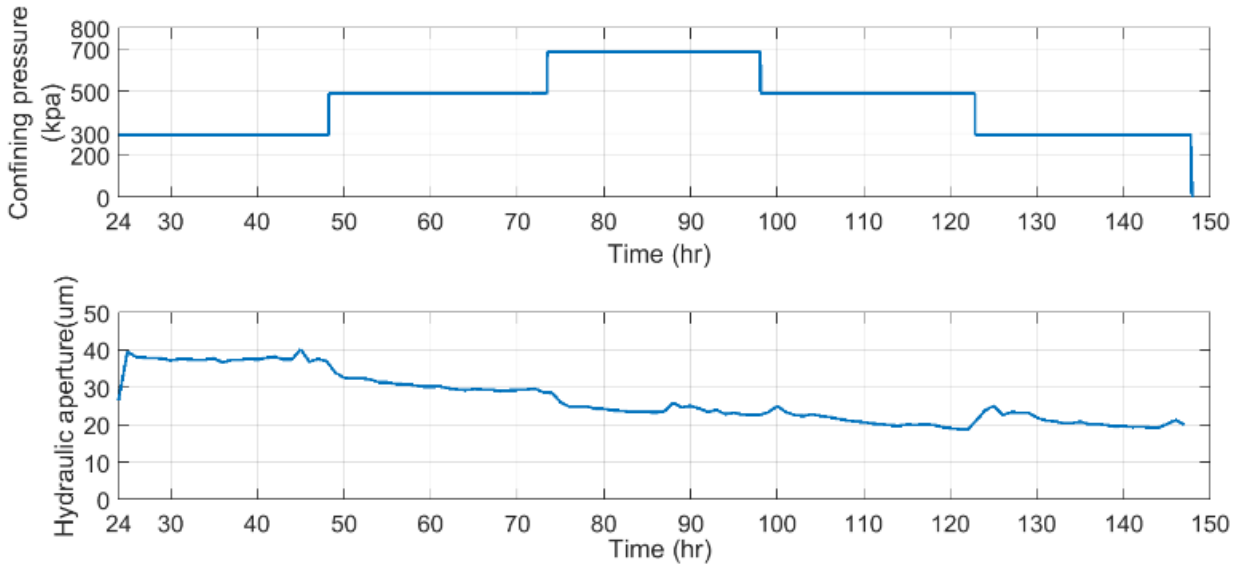

Figure 6.19. Hydraulic aperture changing with confining pressure and time for specimen 013 (distilled water flow condition). The flowrate is 2.5 μL/sec and the back pressure is 136 kPa.

6.2.3 Summary and conclusion of types 1 and 2 experimental results

Section 6.2 reports on an initial set of experiments in which the time-dependent fracture flow was investigated. Specifically, in type 1 tests, the effect of different factors on fracture hydraulic aperture (confining pressure, flowrate, and fracture type) was studied. Fracture flow tests were conducted under uniform stress ($\sigma_1 = \sigma_2 = \sigma_3$) and under distilled water flow conditions. The results of four tests were discussed. The three factors were systematically varied by keeping two constant and changing the third one. In type 2 tests, the effect of different mechanisms affecting fracture aperture (mechanical compression, pressure solution, dissolution, and erosion) was explored. Between different experiments, the fluid type was changed to get an initial understanding of the role of different mechanisms causing the creep; the confining pressure steps and the time duration for each step were identical. Four tensile fracture specimens were tested. As shown in Figure 6.10, specimen 011 was tested under dry conditions, specimen 015 under saturated limestone solution conditions, specimen 014 under stagnant distilled water conditions, and specimen 013 under distilled water flow conditions.

For type 1 tests, it can be concluded that increasing the confining pressure or the flowrate or the surface roughness each leads to greater hydraulic aperture reduction. Contributing to the hydraulic aperture reduction may be all possible mechanisms (mechanical compression, pressure solution, dissolution, and erosion), but differentiating between their effects is not possible.

Type 2 tests were included to shed more light on the underlying mechanism. Partial information can be obtained with the present setup in which only the specimen deformation (both the matrix and fracture deformation) is measured. It is assumed that the rock matrix deformation is negligible, so, therefore, the measured specimen deformation is the change of fracture mechanical aperture.

It appears that during loading, at lower (164 kPa) effective confining pressure, water causes the mechanical aperture to increase. On the contrary, at higher (364 kPa and 564 kPa) effective confining pressures, the mechanical aperture of all specimens decreases. Also, during both loading and unloading, the effect of mechanical compression is not negligible. For the test under distilled water flow, it is worth noting that during unloading, the mechanical aperture increases first and then decreases, while the hydraulic aperture keeps decreasing with time. However, as stated in Section 6.2.2.1, the specimen deformation was measured but the rock matrix deformation was not measured. Therefore, to accurately determine the fracture deformation, the rock matrix deformation should be measured together with the specimen deformation.

Overall the experimental results show the effect of different external conditions and fracture geometry on hydraulic aperture and specimen (matrix and fracture) deformation. So far, a distinct determination of possible mechanisms (mechanical compression, pressure solution, dissolution, and erosion) on fracture deformation is not possible. However, the experiments indicate in which way future research can be conducted. Practically, the results of series 1 are relevant in providing information on fracture flow behavior that can be used in engineering designs. In addition, the effect of mechanical compression on fracture creep is not negligible, and it appears that there is not much work systematically studying the creep mechanism caused by mechanical compression. Therefore, the effect of mechanical compression on fracture creep should be systematically studied.

6.3 Micro-indentation test results

6.3.1 3-min micro-indentation creep test results

6.3.1.1 Results summary

225 (15 * 15) 3-min micro-indentation tests were conducted as shown in Table 5.5 in Section 5.4.2. The indentation modulus M, indentation hardness H, and indentation creep modulus C were calculated based on the methods described in Section 5.4.3.

Table 6.11 summarizes the average and standard deviation for H, C, and M. Figure 6.20 plots the histograms for H, C, and M. Figure 6.21 plots M versus H, M versus C, C versus H, and M / H versus C.

Table 6.11. Summary of 3-min micro-indentation properties

Property	Average (GPa)	Standard deviation (GPa)
H	1.71	0.13
C	917.92	88.12
M	64.97	2.30

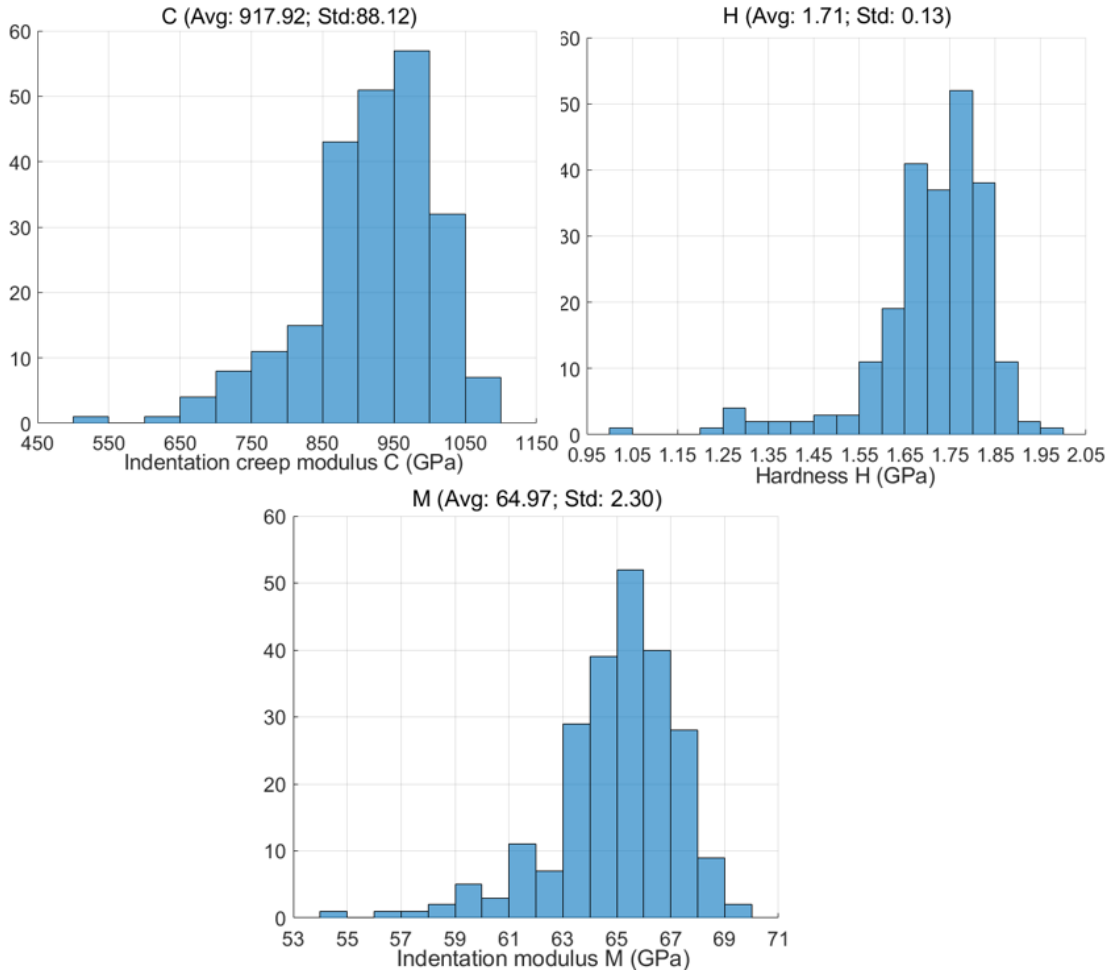

Figure 6.20. Histograms for C, H, and M. The vertical axis corresponds to the number of counts.

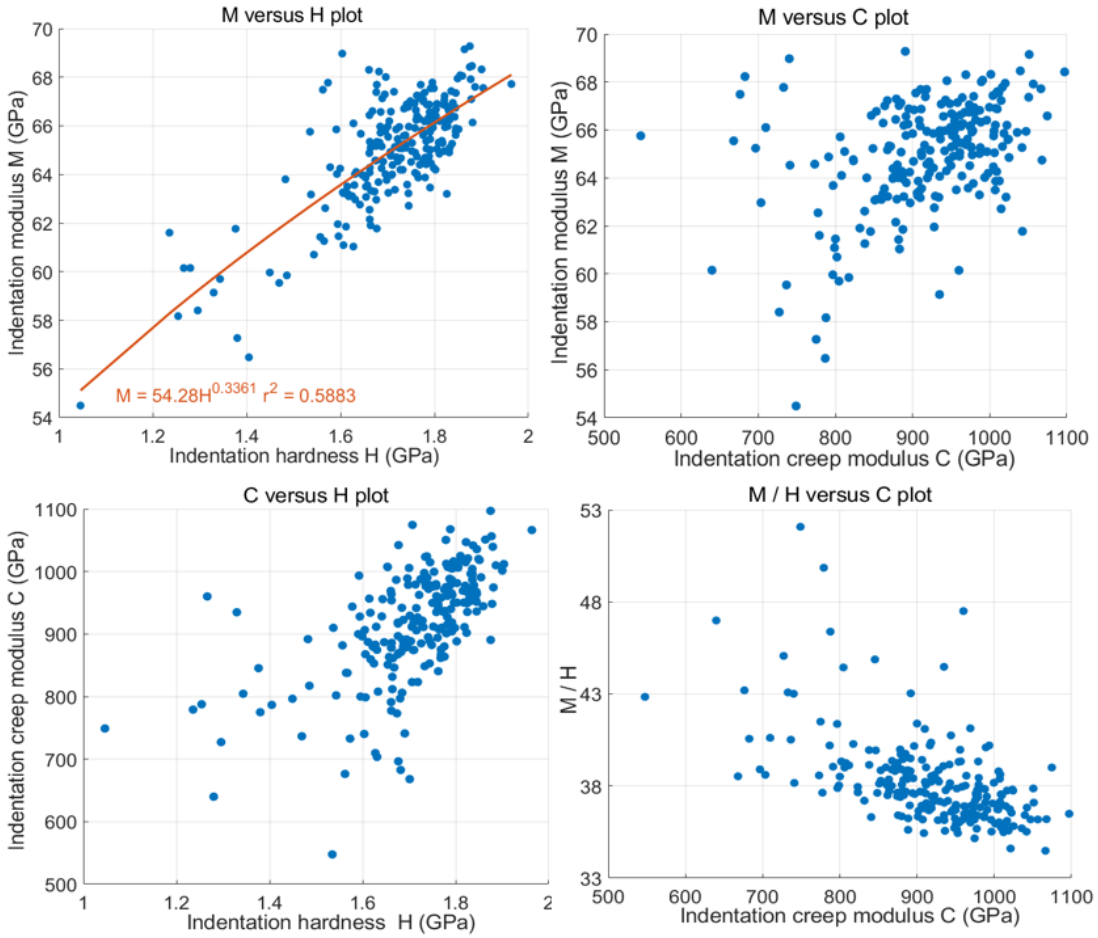

Figure 6.21. Plots for M versus H, M versus C, C versus H, and M /H versus C. The red line in the M versus H plot shows the power function relation between M and H.

Power function relation analysis (using the least square method) was conducted for the relationship between C and H, C and M, M and H, and M / H versus C. The results indicate that neither C and H, nor C and M, nor M and H, nor M / H and C are strongly related. For example, the relation between M and H is the strongest among the three above-mentioned combinations and is shown in Figure 6.21. $M = 54.28H^{0.3361}$, with $r^2 = 0.5883$.

6.3.1.2 Comparison of Triaxial and Micro-indentation Properties

Modulus

Triaxial and micro-indentation tests differ in specimen scale, stress conditions, and loading geometry. However, it is still useful to compare the mechanical properties obtained by the two different tests. Figure 6.22 compares the measured elastic moduli of micro-indentation and triaxial tests, by plotting the measured elastic modulus changing with measurement size and confining

pressure (the purpose of Figure 6.22 is only to compare the effect of measurement size on the measured elastic moduli). The measurement size for the LVDTs is the specimen length (101.6 mm), for strain gauges is the strain gauge length (6.6 mm), and for dynamic elastic modulus is the length of sub-blocks (the distance between the acoustic transmitter and receiver sensor is the length of sub-blocks, which is 140 mm). The blue error bar corresponds to micro-indentation test results, the yellow, red, green, and black dots correspond to triaxial test results, and the purple dot corresponds to P-wave velocity measurement results. When the confining pressure was less than 20 MPa, the elastic moduli measured by triaxial tests (shown by the yellow dots and the green dot) are less than those measured by micro-indentation tests (shown by the blue error bar); when the confining pressure was higher than 60 MPa, the elastic moduli measured by triaxial tests (shown by the red and black dots) are slightly larger than those measured by micro-indentation tests.

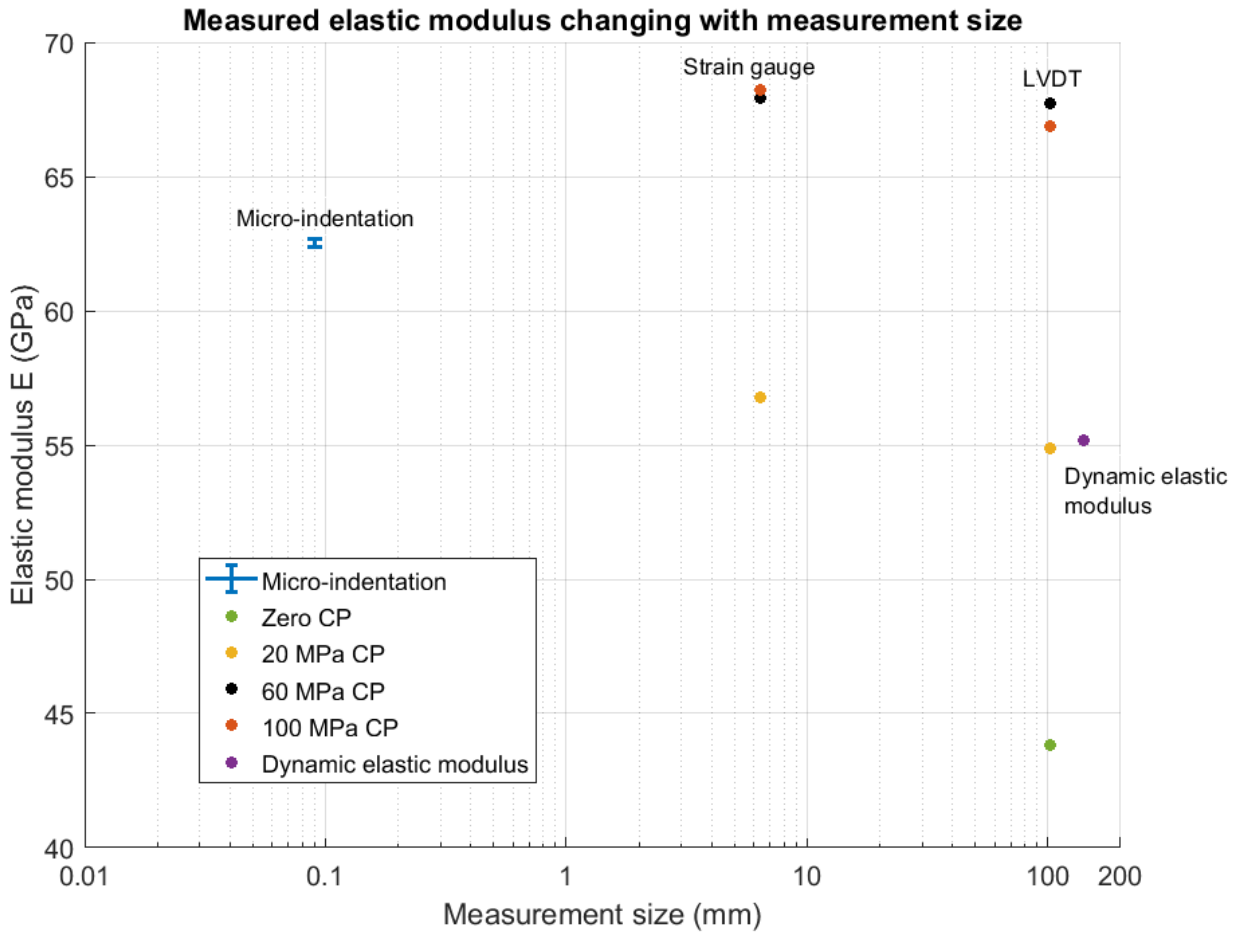

Figure 6.22. Measured elastic moduli changing with measurement size and confining pressures. For micro-indentation tests, the average elastic modulus E_1 (see Table 6.11) and the ± standard deviation are plotted. For triaxial tests, the E_{50} values under different confining pressures are plotted. The 'dynamic elastic modulus' corresponds to the average elastic modulus measured by P-wave velocity in the horizontal direction of sub-blocks.

Yield Strength

The yield strength results also suggest a scale dependence. As discussed in Section 2.2.3, Tabor (1948) conducted many indentation tests on metals. Bowden and Tabor (1950) stated that when using the conical indenters with a half-angle of 70.26˚ (geometry equivalent to the Berkovich indenter), the hardness can be *empirically* related to the material yield strength:

$$H = 3\sigma_Y \tag{6.9}$$

where σ_Y is the yield strength.

According to Table 6.11, the average indentation hardness of Musandam limestone was 1710 MPa. Thus, based on Eq. 6.9, the yield strength should be 570 MPa. However, the yield strength measured by triaxial tests was lower than that predicted by micro-indentation. For example, in triaxial tests, when the confining pressure was 100 MPa, the yield strength was 504 MPa.

6.3.2 6-hr micro-indentation creep test results

According to Table 5.5 in Section 5.4.2, in total 8 6-hr micro-indentation tests were conducted. For each indentation test, one indent was made. The 8 indentation tests were conducted in two series; each series has four tests (so four indents in each series). Figure 6.23 shows the schematic of the 6-hr micro-indentation test array. Figures 6.24 and 6.25 plot the indentation creep depth Δh versus time curves for the first and second series of tests, respectively. The indentation creep depth corresponds to the creep stage of the indentation test, and the concept of the creep stage is explained in Figures 5.23 and 5.26 in Section 5.4.

Figure 6.23 Schematic of the 6-hr micro-indentation test array. The eight indents form an array. Each blue circle corresponds to one indent.

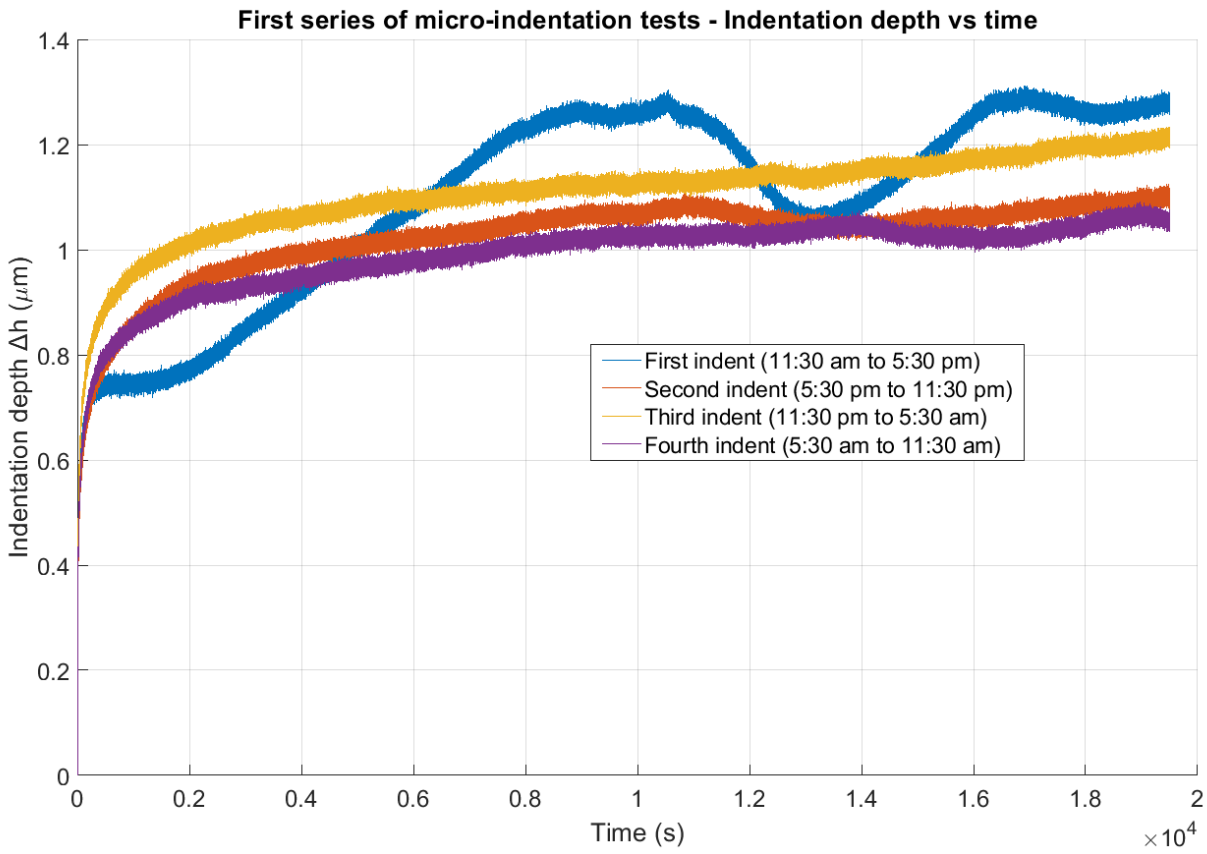

Figure 6.24. Indentation depth Δh versus time curves for the first series of micro-indentation tests. Four tests were conducted.

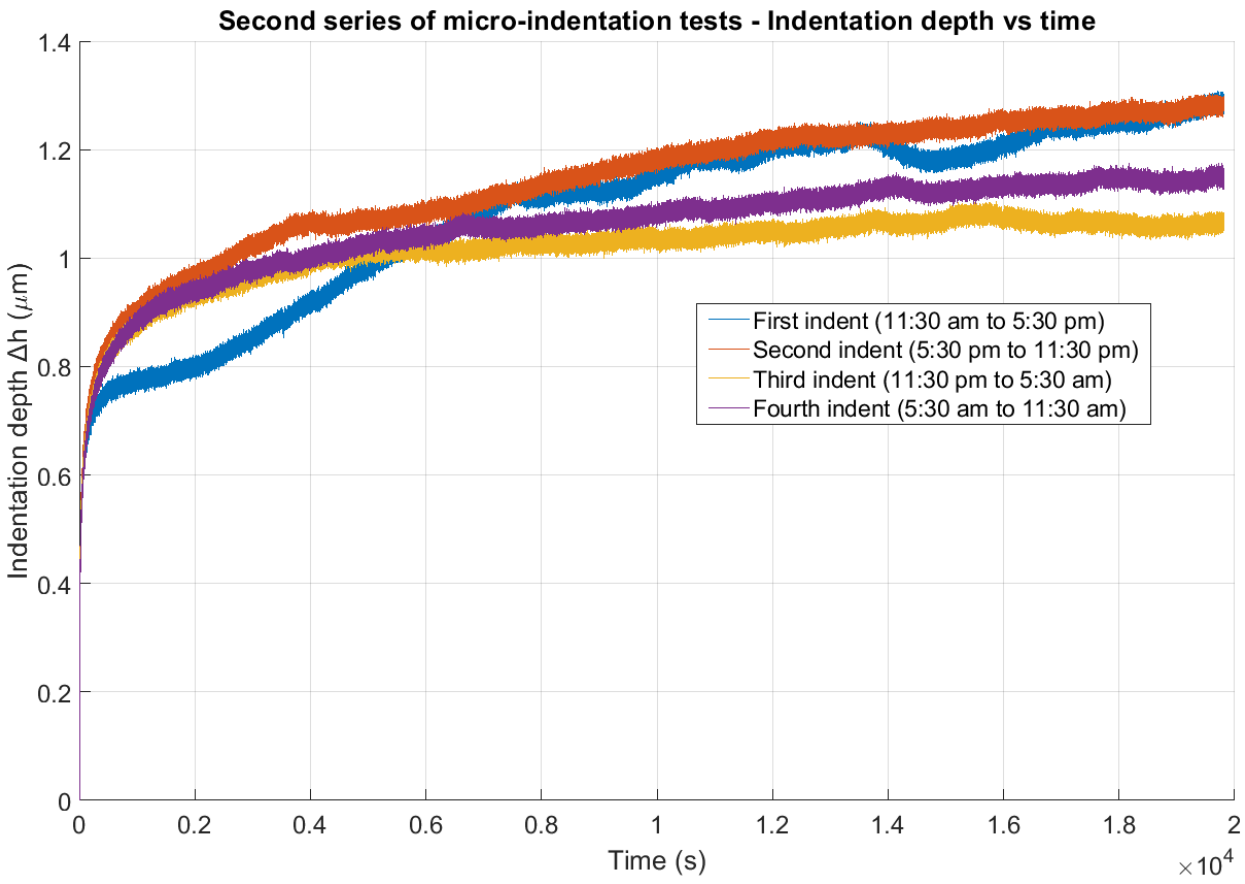

Figure 6.25. Indentation depth Δh versus time curves for the second series of micro-indentation tests. Four tests were conducted.

Figures 6.24 and 6.25 show that for the first indent (shown by the blue curve) in each series, the measured indentation depth fluctuated significantly with time. During the creep stage, the indentation load was held a constant. Thus, if the indenter and the specimen surface are stable, the measured indentation depth should not fluctuate significantly. The significant fluctuation might be caused by disturbances during the day time, since the micro-indentation device was very close to the main corridor in Building 1, and the time duration for the first indent was from 11:30 am to 5:30 pm. Due to the significant fluctuation, the data for the first indent in each series were not used for further analysis. In other words, the data for the second, third, and fourth indents in each series were used for further analysis and discussion (so in total the data for six indents were used), and the corridor disturbance was ignored.

The indentation modulus M, indentation hardness H, and indentation creep modulus C were calculated based on the methods described in Section 5.4.3.

Table 6.12 summarizes the average and standard deviation for H, C, and M. Figure 6.26 plots M versus H, M versus C, C versus H, and M / H versus C. Figure 27 plots the histograms for H, C, and M.

Table 6.12. Summary of 3-min and 6-hr micro-indentation properties

Testing type	Property	Average (GPa)	Standard deviation (GPa)
6-hr micro-indentation tests	H	1.63	0.11
	C	1272.17	218.09
	M	65.89	1.92
3-min micro-indentation tests	H	1.71	0.13
	C	917.92	88.12
	M	64.97	2.30

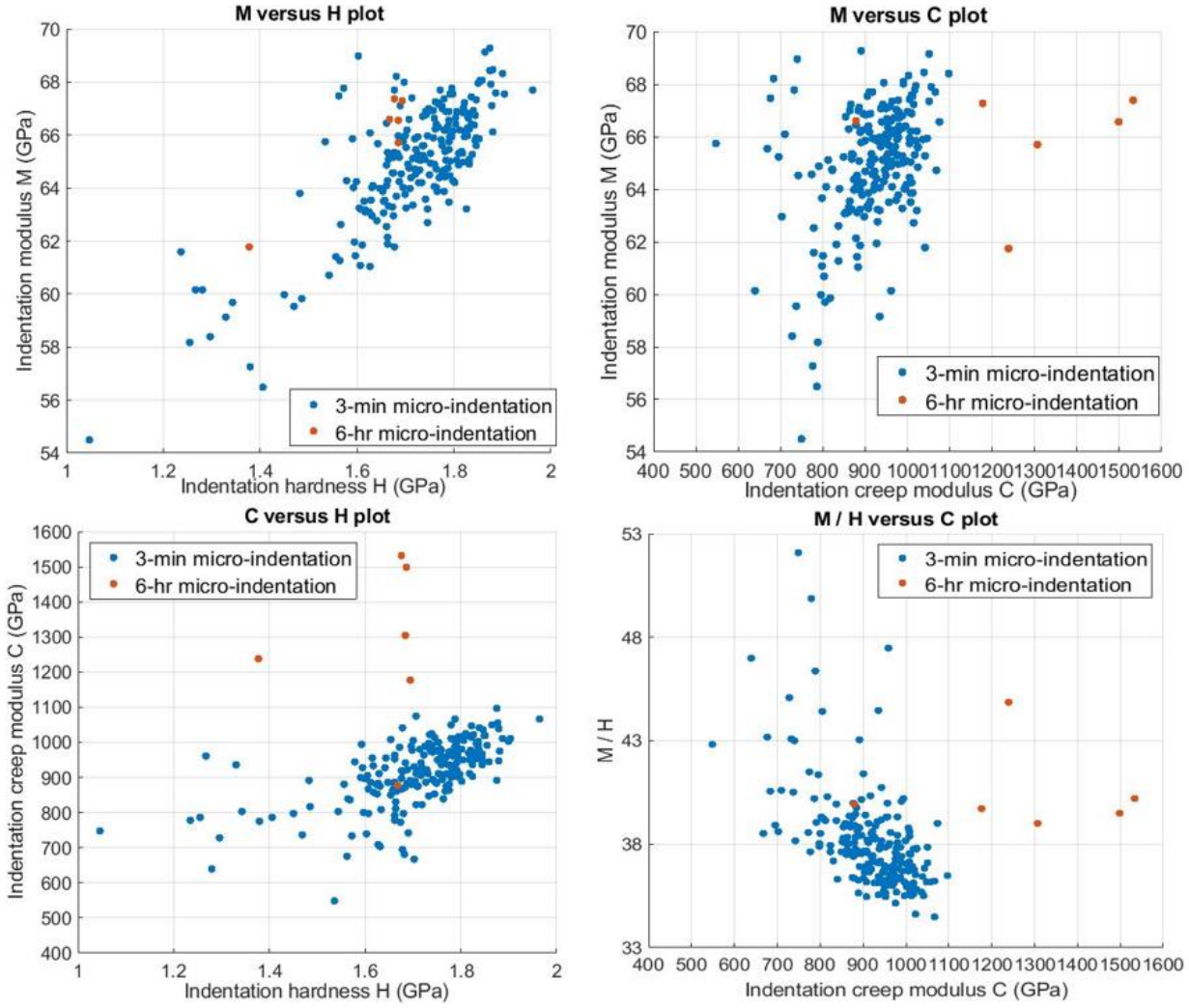

Figure 6.26. Plots for M versus H, M versus C, C versus H, and M /H versus C. The blue dots represent 3-min micro-indentation tests, and the red dots represent 6-hr micro-indentation tests.

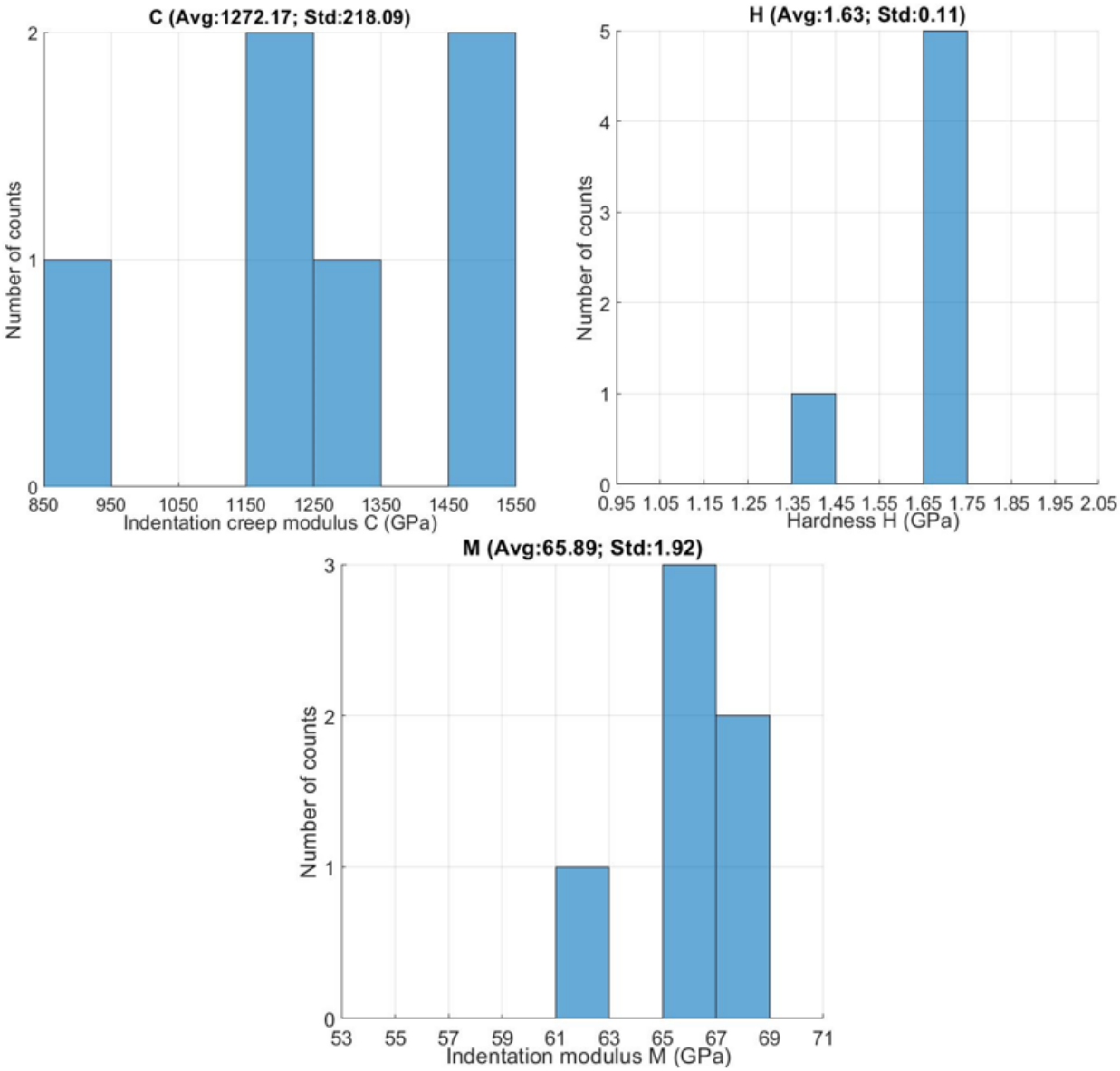

Figure 6.27. Histograms for C, H, and M for 6-hr micro-indentation tests. The vertical axis corresponds to the number of counts.

From Table 6.12 and Figure 6.26, one can conclude that the indentation hardness H and indentation modulus M measured by 6-hr micro-indentation are similar to those measured by 3-min micro-indentation. However, the creep modulus C measured by 6-hr micro-indentation is much larger than that measured by 3-min micro-indentation. As discussed in Section 2.2.1, under the same indentation load, a larger creep modulus C corresponds to a slower creep rate with time. This indicates that the micro-indentation creep rate reduced as the time duration was increased from 3-min to 6-hr.

Figures 6.29 and 6.30 further illustrate the decrease in the creep rate in 6-hr micro-indentation creep tests. In order to compare the 3-min and 6-hr results, the 3-min measurement needs to be

extended to 6 hours with the following procedures. This was done by using the 6-hr curves and taking the first three minutes of this test. The procedures could be divided into three steps:

Step 1 (shown by Figure 6.28 (a)): For each 6-hr indent, the creep depth Δh for six hours (see the blue curve in Figure 6.28 (a)) was measured. In this step, the first three minutes of the blue curve, Δh_{3min}, was obtained (see the red curve in Figure 6.28 (a)).

Step 2 (shown by Figure 6.28 (b)): The $x_{1\text{-}3}$ and $x_{2\text{-}3}$ values were calculated from the first 3-min measurement (Δh_{3min}) of the 6-hr results:

$$\Delta h_{3min} = x_{1-3}\, ln\,(x_{2-3} t_1 + 1) \tag{6.10}$$

Eqn. 6.10 was the same as Eqn. 5.10 in Section 5.4.3. In Eqn. 6.10, Δh_{3min} was the first three minutes of the blue curve, and Δh_{3min} is shown by the red curves in Figures 6.28 (a) and 6.28 (b). t_1 was the time, with a duration of 3 minutes (see the horizontal axis in Figure 6.28(b)). $x_{1\text{-}3}$ and $x_{2\text{-}3}$ were the unknown parameters and they were fitted by the least square method.

Step 3(shown by Figure 6.28 (c)): The Δh_{ext} was calculated as:

$$\Delta h_{ext} = x_{1-3}\, ln\,(x_{2-3} t + 1) \tag{6.11}$$

In Eqn. 6.11, the $x_{1\text{-}3}$ and $x_{2\text{-}3}$ values were obtained in step 2. The time duration of t was six hours. Figure 6.28 (c) compares the extended curve Δh_{ext} with the measured curve. The green curve corresponds to Δh_{ext}, and the blue curve is the measured creep curve (the same as the blue curve in Figure 6.28 (a)).

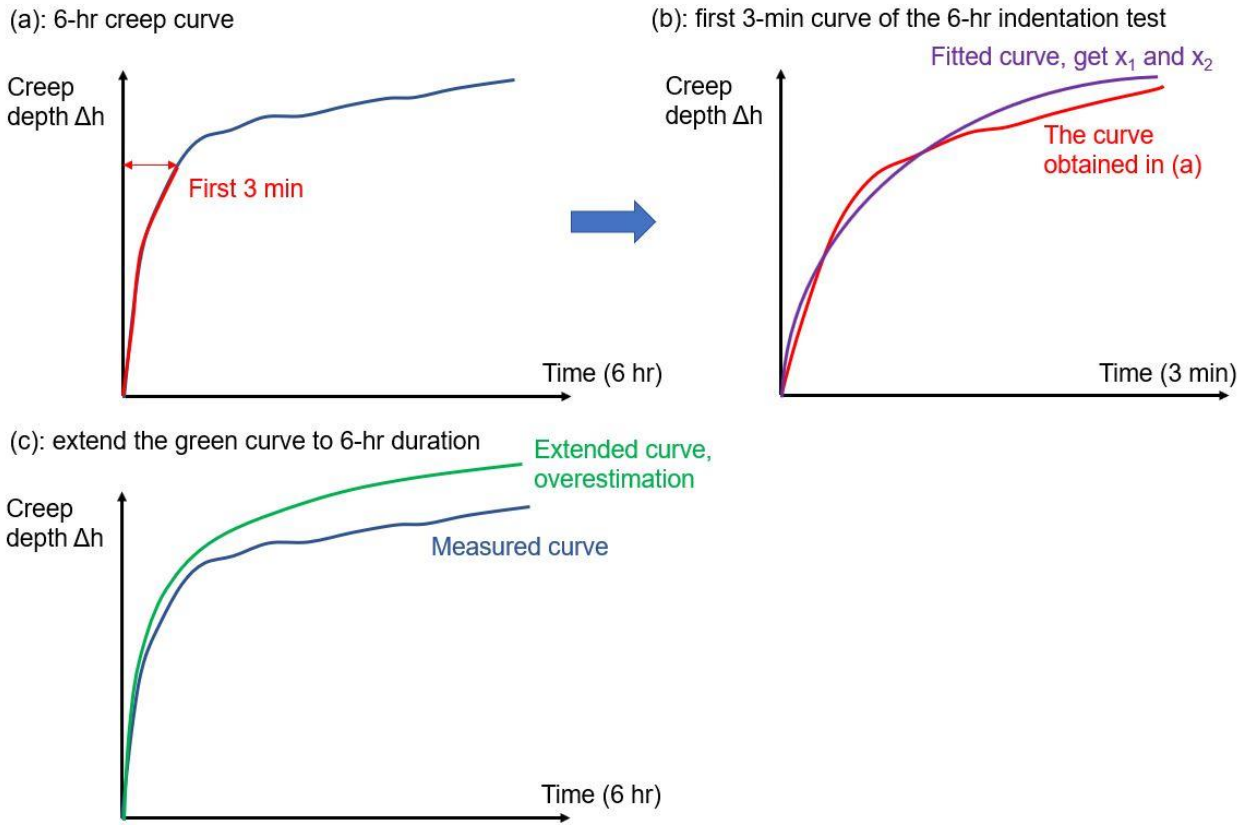

Figure 6.28 Illustration of the curve extension process of one 6-hr micro-indent. The green and purple curves are the fitted curves, and the blue and red curves are measured data. (a): The creep curve for the first 3 minutes was obtained (shown by the red curve); (b): Using curve fitting to obtain $x_{1\text{-}3}$ and $x_{2\text{-}3}$ based on the red curve. Eqn. 6.10 was used. The fitted curve is shown by the purple curve; (c): Calculating Δh_{ext} based on Eqn. 6.11. The time duration was 6 hours. The $x_{1\text{-}3}$ and $x_{2\text{-}3}$ values were obtained from (b). Δh_{ext} is shown by the green curve.

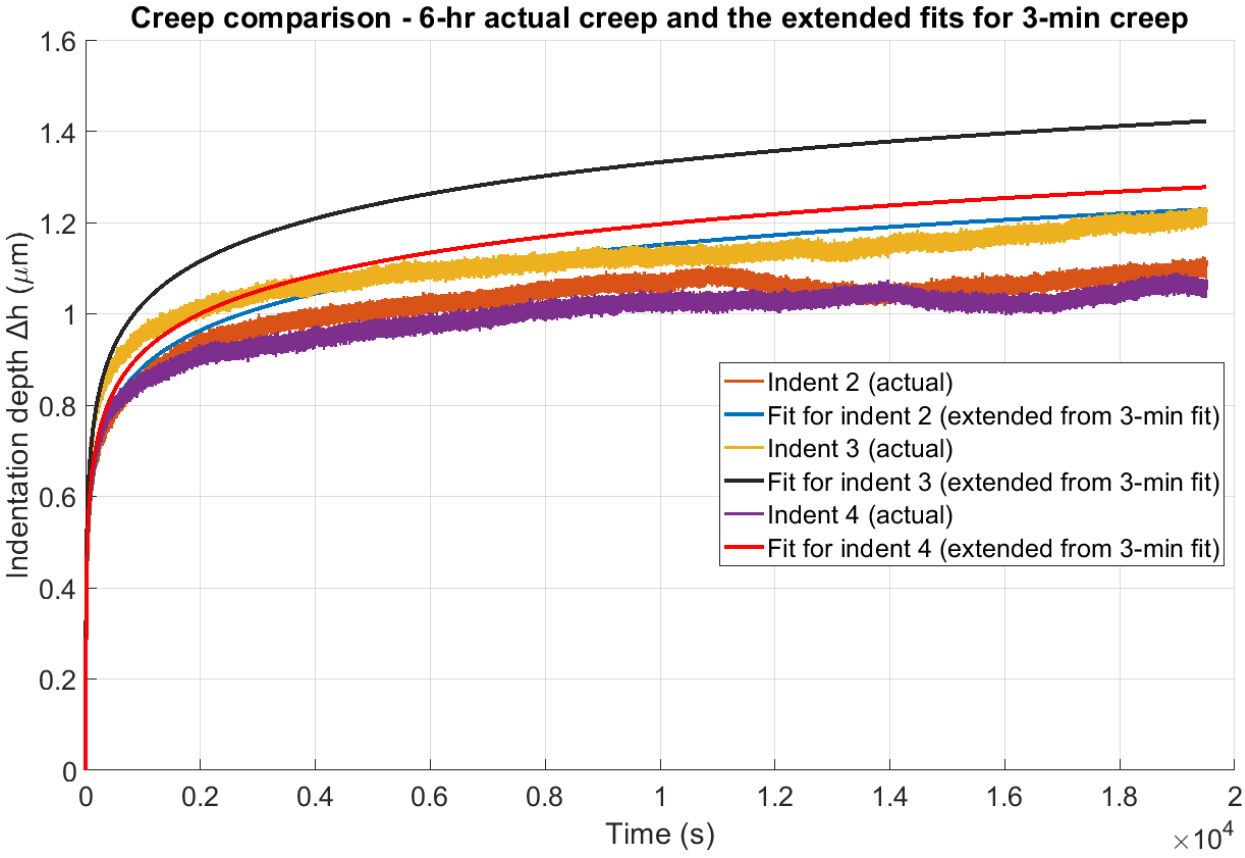

Figure 6.29 Comparison of 6-hr actual creep curves (Δh versus time) and 3-min extended curves (Δh_{ext} versus time) for the first series of 6-hr micro-indentation tests. The orange and blue curves represent the Δh and Δh_{ext} for indent 2, respectively; the yellow and black curves represent the Δh and Δh_{ext} for indent 3, respectively; the purple and red curves represent the Δh and Δh_{ext} for indent 4, respectively. The curve extension procedure is explained in Figure 6.28.

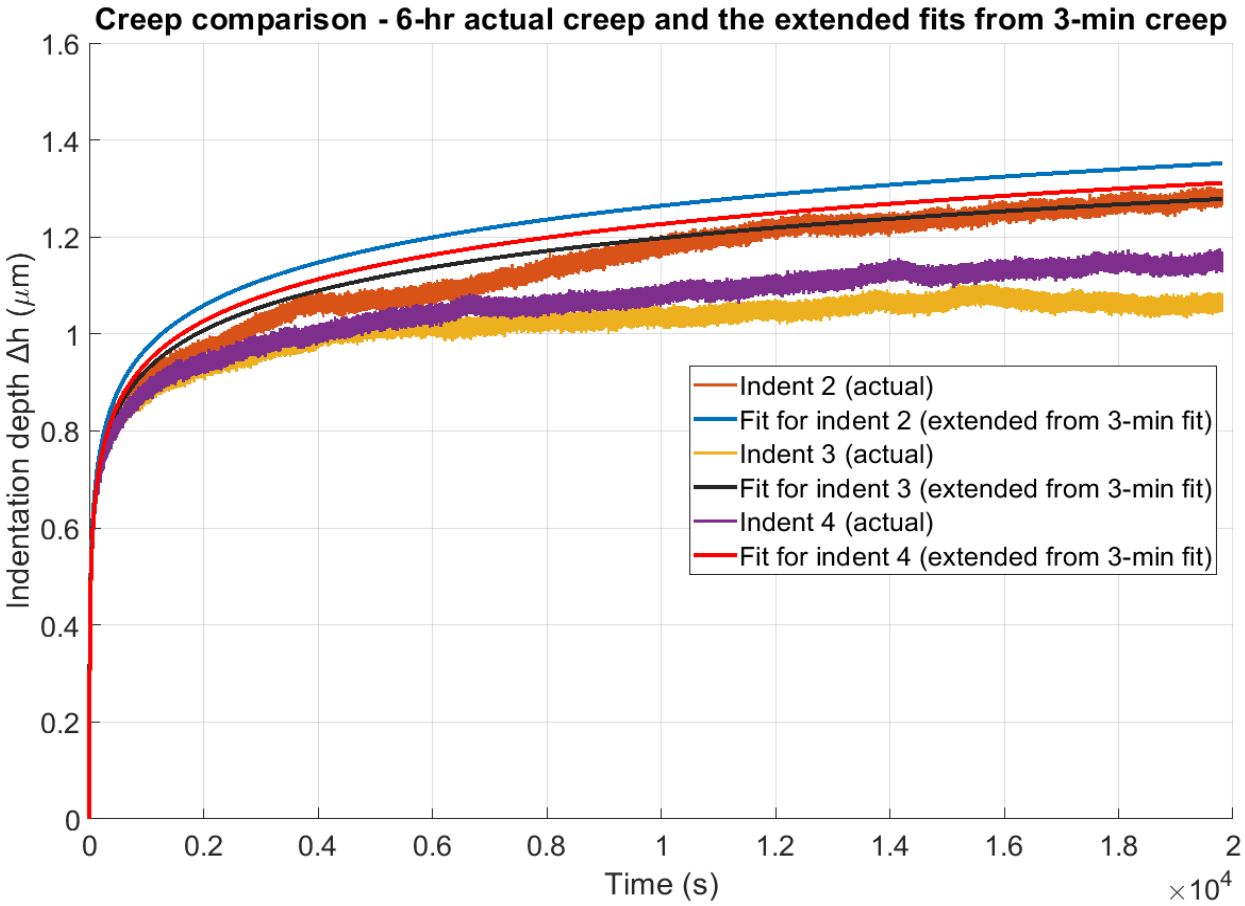

Figure 6.30 Comparison of 6-hr actual creep curves (Δh versus time) and 3-min extended curves (Δh_{ext} versus time) for the second series of 6-hr micro-indentation tests. The orange and blue curves represent the Δh and Δh_{ext} for indent 2, respectively; the yellow and black curves represent the Δh and Δh_{ext} for indent 3, respectively; the purple and red curves represent the Δh and Δh_{ext} for indent 4, respectively. The curve extension procedure is explained in Figure 6.28.

Figures 6.29 and 6.30 show that for all the indentation locations in both series, the Δh_{ext} value is larger than the Δh value. This implies that the 6-hr creep deformation will be overestimated if it is predicted from the 3-min creep deformation. Practically, to obtain the micro-indentation creep behavior for a specific time duration, creep tests at the specific time duration need to be conducted; it may not be accurate to use short-term creep behavior to predict long-term creep behavior.

6.3.3 Preliminary results for SEM-EDS tests

As mentioned in Section 5.4.4, SEM-EDS tests were conducted to measure the element distribution of the micro-indentation test region, and the element distribution is shown in Figure 6.31. The spatial distribution of eight elements, Ca, Al, Si, Fe, Mg, Na, K, and C, was obtained. Each element has a unique color. Table 6.13 summarizes the area percentage of the eight above-

mentioned elements in the scanned region shown in Figure 6.31. Based on Table 6.13, Ca, C, and Si are the three dominant elements.

(a):

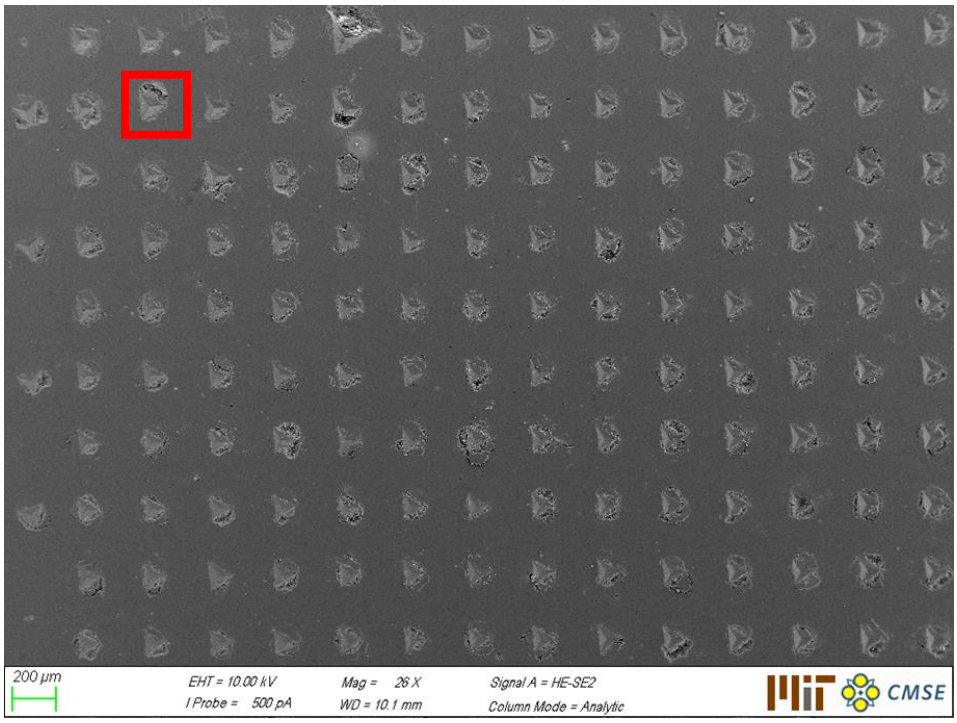

(b):

Ca:

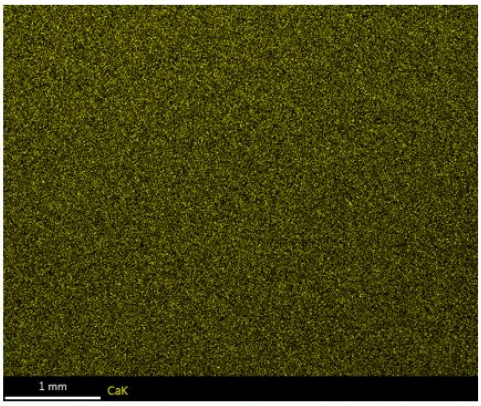

C:

Si:

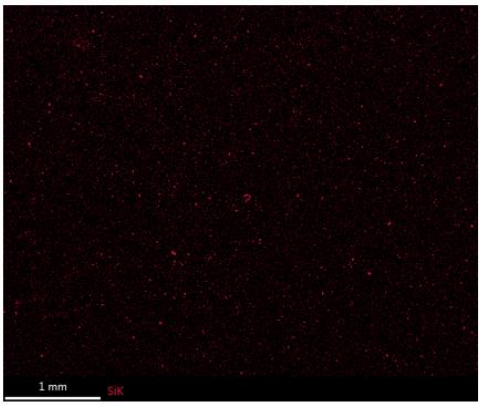

Al:

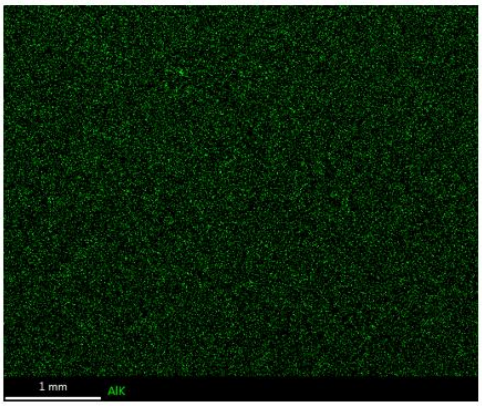

(c):

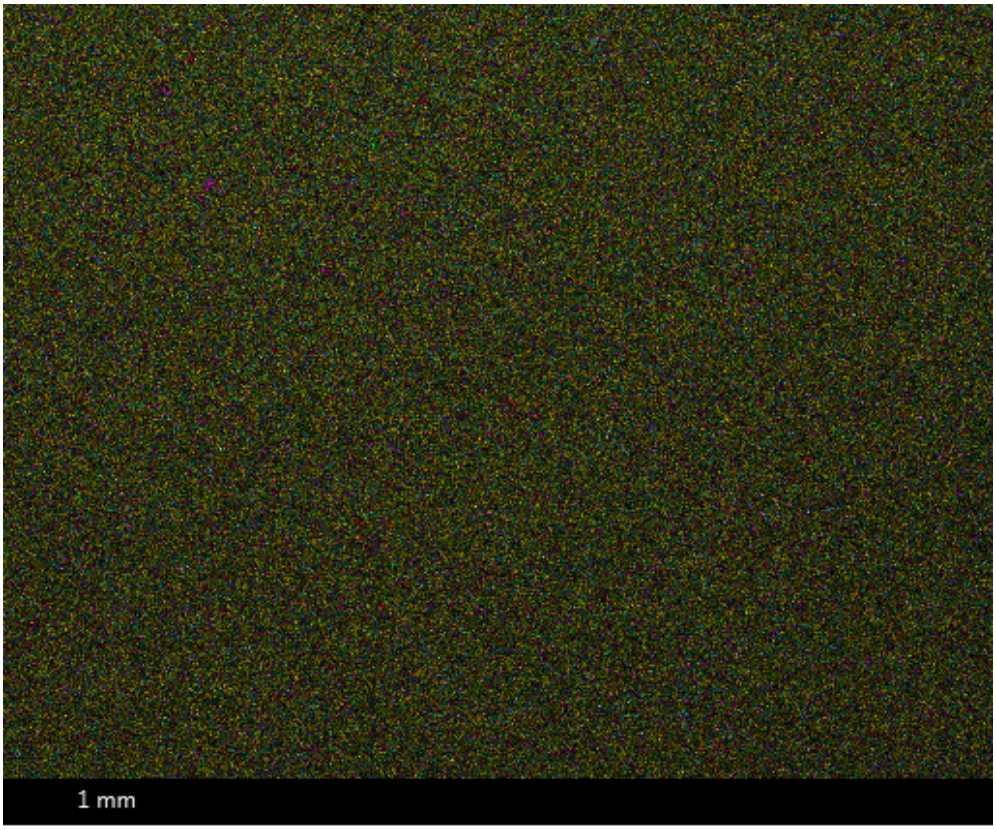

Figure 6.31. SEM-EDS images of the micro-indentation region. (a): SEM image of the micro-indentation test region. The maximum image zone area is 10 rows * 14 columns of the micro-indents. (b): the SEM-EDS image of calcium, carbon, silicon, and aluminum. Each element has a unique color. The four elements are evenly distributed within the scanned region. (As we discussed, we will leave it as what it is) (c): the SEM-EDS image of all the eight elements. Each element has a unique color, and the image is an overlay of all different colors. Based on the image, different colors are well mixed, indicating that the element distribution at the size of micro-indentation is homogeneous.

Table 6.13. The area percentage of the elements of the scanned region in Figure 6.31

Element type	Area (%)
Ca	77.95
C	12.45
Si	3.20
Al	1.45
Fe	1.80
Na	1.36
Mg	1.64
K	0.15

Figure 6.31 indicates that at the micro-indentation scale, the element distribution is homogeneous.

Figure 6.32 shows the element distribution in one indent (one micro-indentation test). The region of Figure 6.32 is shown by the red rectangle in Figure 6.31 (a). The spatial distribution of eight elements, Ca, Al, Si, Fe, Mg, Na, K, and C, was obtained. Each element has a unique color. Table 6.14 summarizes the area percentage of the eight above-mentioned elements in the scanned region shown in Figure 6.32. Based on Table 6.14, Ca, C, and Si are the three dominant elements. Also, the area percentages of the eight elements in Tables 6.13 and 6.14 are similar.

(a):

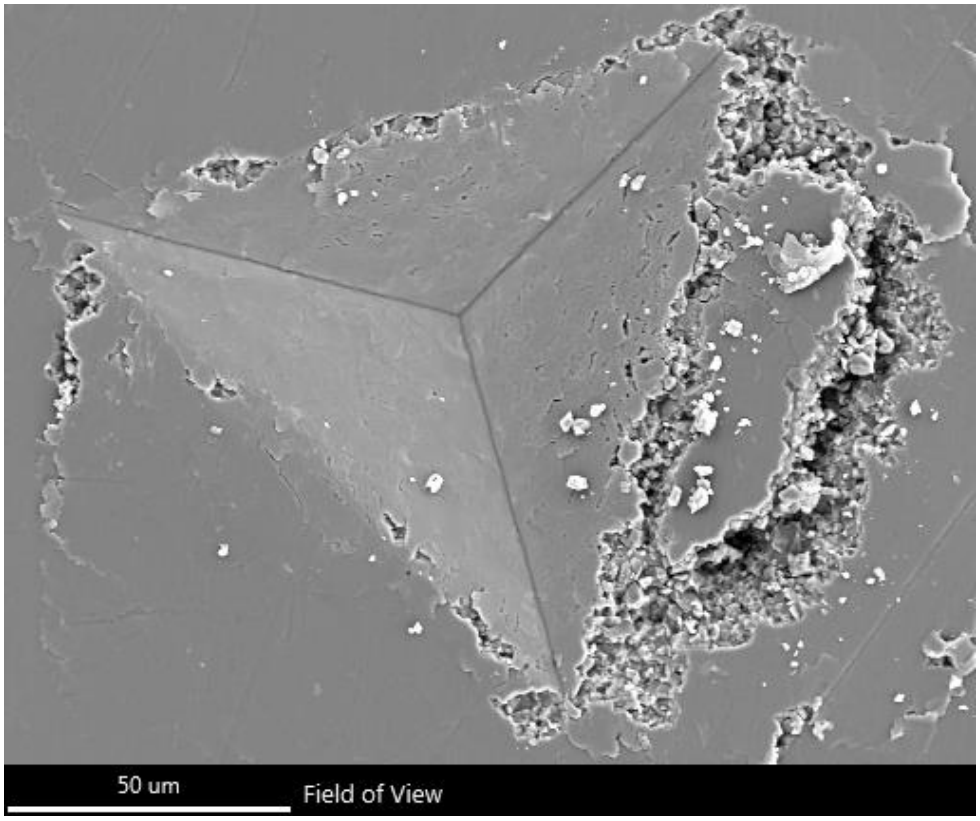

(b):

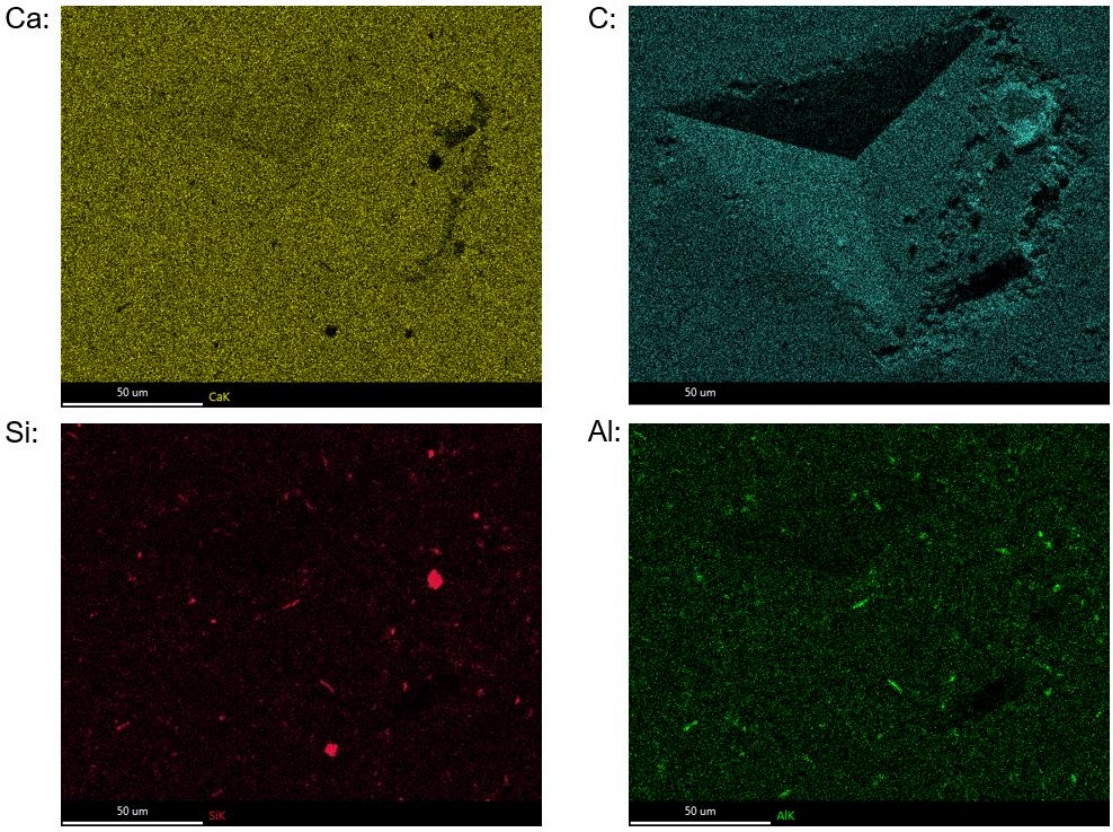

(c):

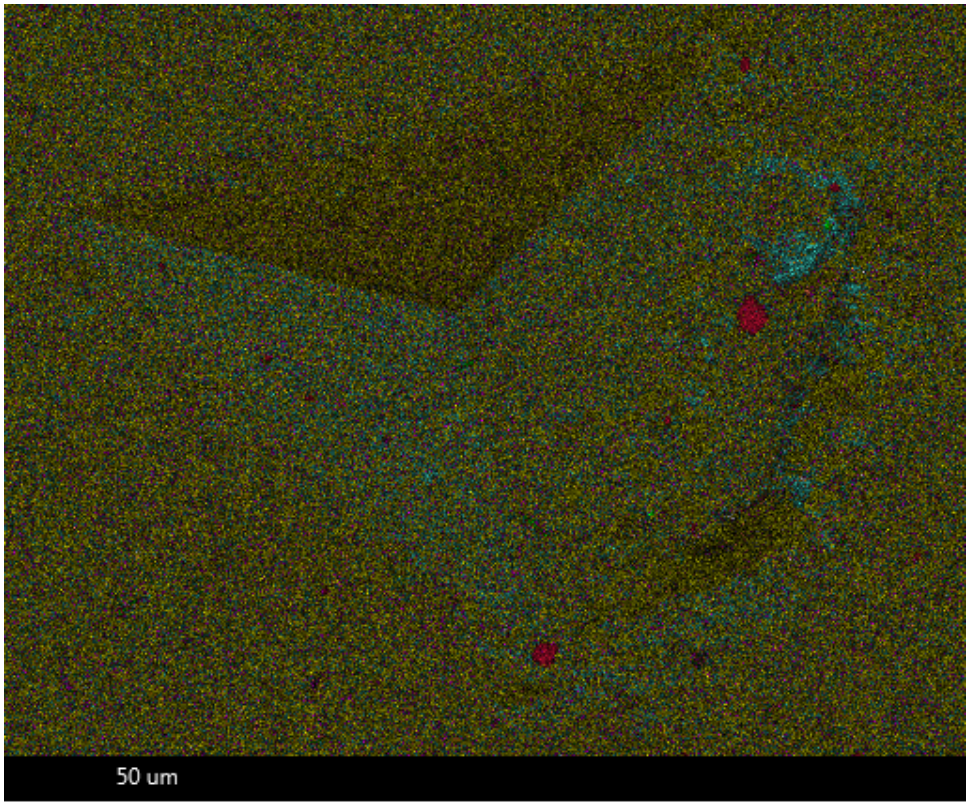

Figure 6.32. SEM-EDS images of one indent (one micro-indentation test). (a): SEM image of the one micro-indent region. (b): the SEM-EDS image of calcium, carbon, silicon, and aluminum. Each element has a unique color. The calcium, carbon, and aluminum elements are evenly distributed, while there are a few silicon intrusions. (It is difficult to see the regions. The images were generated by the SEM device during scanning. The image quality could not be improved because they were generated by the device) (c): the SEM-EDS image of all the eight elements. Each element has a unique color, and the image is an overlay of all different colors. Based on the image, different colors are well mixed, indicating the element distribution at the size of micro-indentation is not very heterogeneous.

Table 6.14. The area percentage of the elements of the scanned region in Figure 6.32.

Element type	Area (%)
Ca	79.69
C	11.98
Si	2.67
Al	1.33
Fe	1.52
Na	1.23
Mg	1.52
K	0.07

Figure 6.32 indicates that at the scale of one indent, the element distribution is also homogeneous.

6.3.4 Summary of micro-indentation test results

The experimental results yielded the following conclusions:

1) The average values for indentation modulus M, indentation hardness H, and indentation creep modulus C are 64.97 GPa, 1.71 GPa, and 917.92 GPa, respectively.

2) The yield strength measured by triaxial tests (504 MPa) is lower than that measured by micro-indentation tests (570 MPa).

3) When the confining pressure was less than 20 MPa, the elastic modulus measured in triaxial tests (43.84 to 57.35 GPa) is less than that measured in micro-indentation tests (64.97 GPa); when the confining pressure was higher than 60 MPa, the elastic modulus measured by triaxial tests (67.11 to 68.87 GPa) is similar to that measured by micro-indentation tests (64.97 GPa).

4) The 6-hr creep deformation will be overestimated if it is predicted from the 3-min creep deformation. Practically, to obtain the micro-indentation creep behavior for a specific time duration, creep tests at the specific time duration need to be conducted; it may not be accurate to use short-term micro-indentation creep behavior to predict long-term micro-indentation

creep behavior.

5) At the micro-indentation scale, the element distribution is homogeneous.

6.4 Nano-indentation test results

6.4.1 3-min nano-indentation creep test results

6.4.1.1 Results summary

According to Table 5.5 in Section 5.4.2, 225 (15 * 15) 3-min nano-indentation tests were conducted (one indent was made for each test). The indentation modulus M, indentation hardness H, and indentation creep modulus C were calculated based on the methods described in Section 5.4.3. The discussion for the rest of Section 6.4.1.1 will be limited to the results from the grey matrix, and this will be explained in Section 6.4.2.

Table 6.15 summarizes the average and standard deviation for H, C, and M. Figure 6.33 plots the histograms for H, C, and M. Figure 6.34 plots M versus H, M versus C, C versus H, and M / H versus C.

Table 6.15. Summary of 3-min nano-indentation properties

Property	Average (GPa)	Standard deviation (GPa)
H	2.28	0.40
C	1235.50	328.61
M	65.58	6.90

(a):

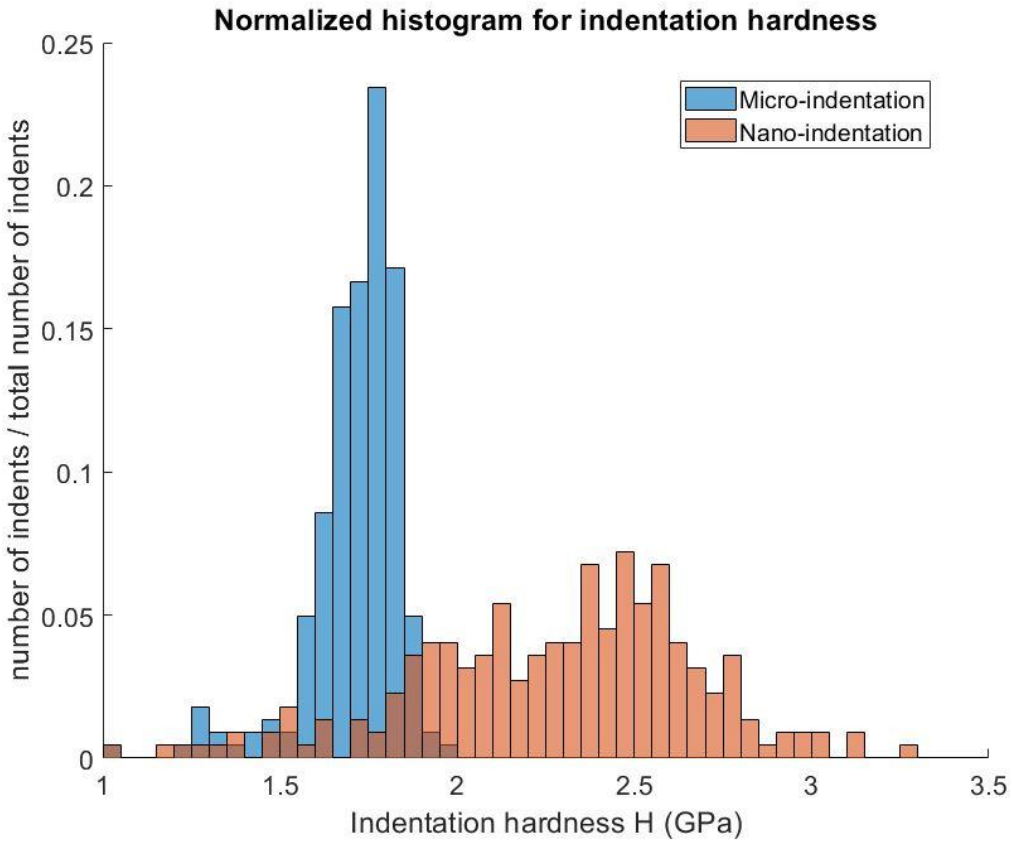
Normalized histogram for indentation hardness
Micro-indentation
Nano-indentation
number of indents / total number of indents
Indentation hardness H (GPa)
0.25
0.2
0.15
0.1
0.05
0
1
1.5
2
2.5
3
3.5

(b):

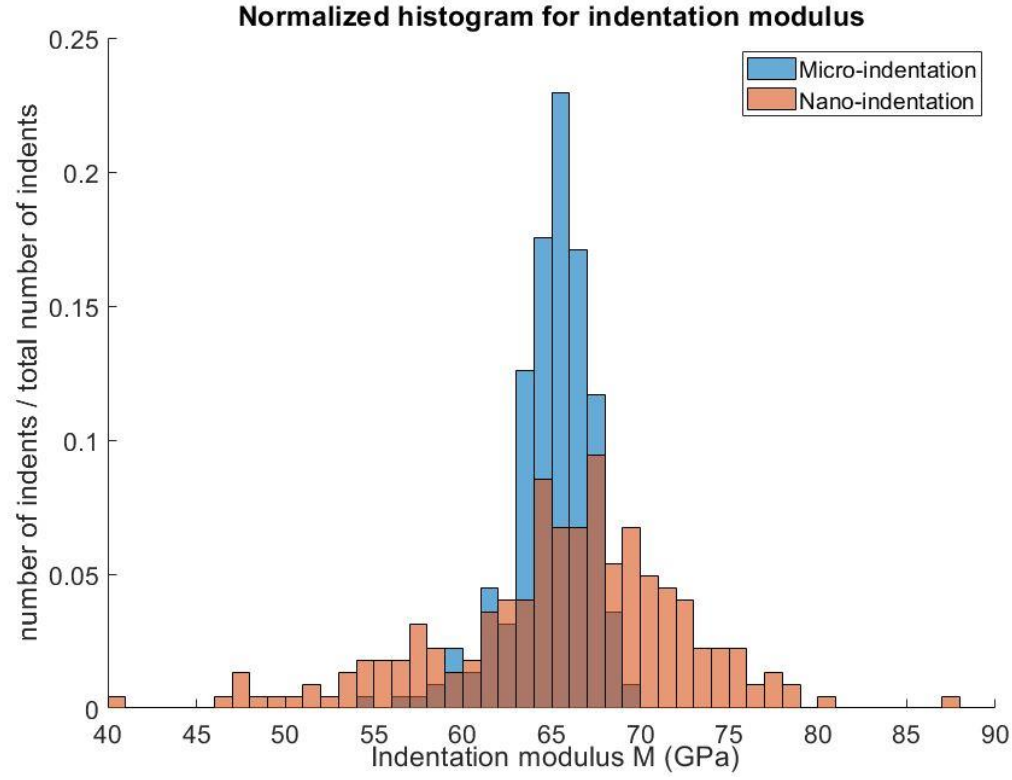
Normalized histogram for indentation modulus
Micro-indentation
Nano-indentation
number of indents / total number of indents
Indentation modulus M (GPa)
0.25
0.2
0.15
0.1
0.05
0
40
45
50
55
60
65
70
75
80
85
90

(c):

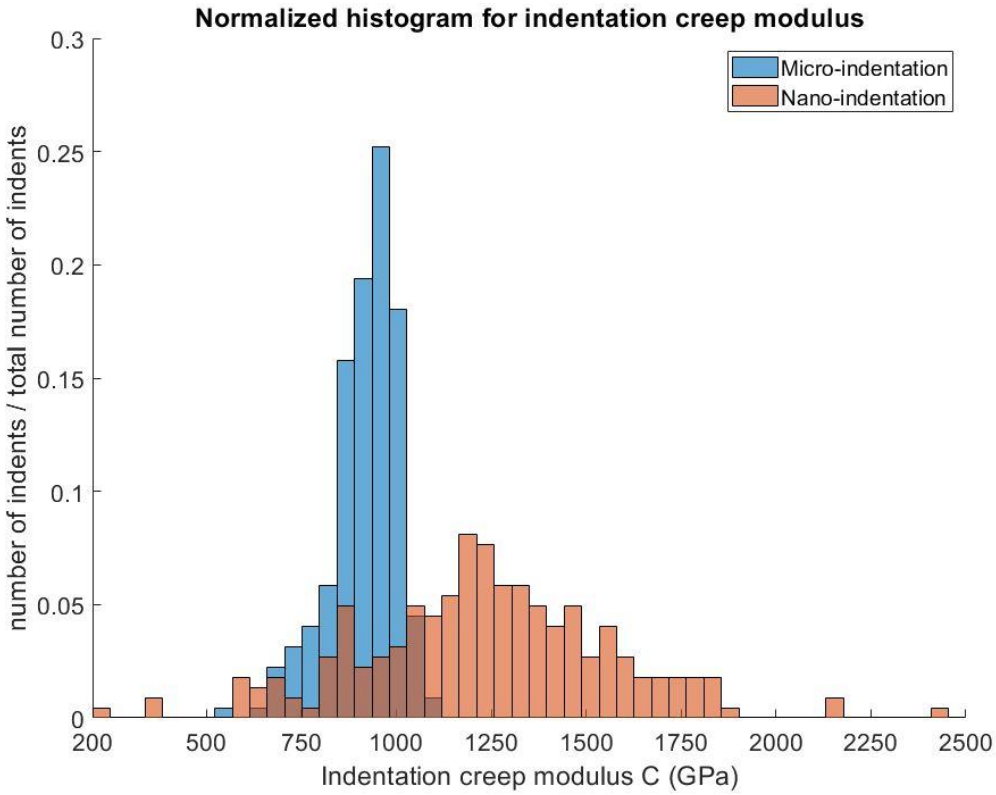

Figure 6.33. Normalized histograms for C, H, and M for 3-min micro- and nano-indentation tests. (a): normalized histograms for H; (b): normalized histograms for M; (c): normalized histograms for C. The blue bars and orange bars represent the values for micro-indentation and nano-indentation tests, respectively. The vertical axis corresponds to the number of counts / total number of indentation tests.

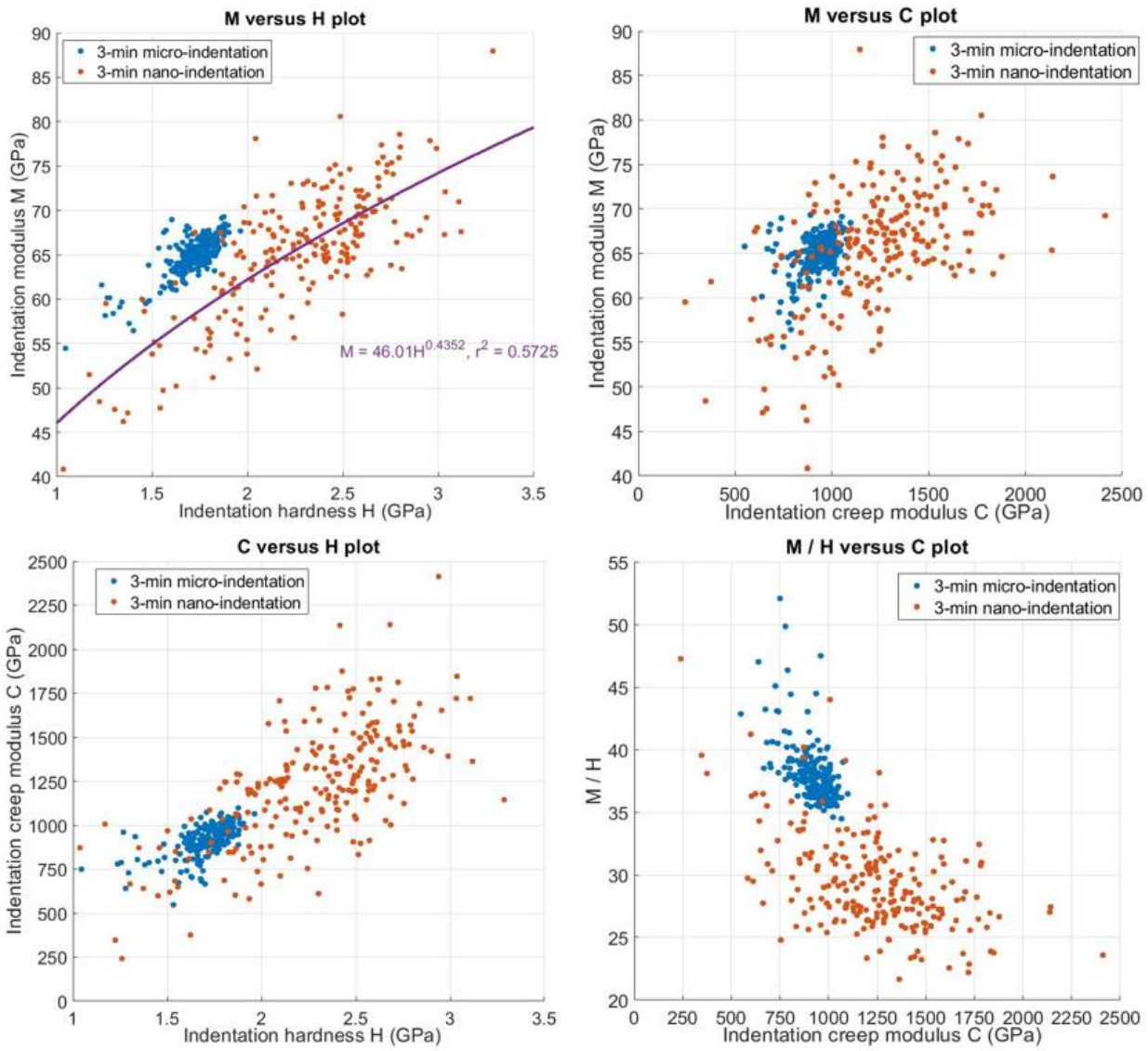

Figure 6.34. Plots for M versus H, M versus C, C versus H, and M /H versus C. The blue dots represent 3-min micro-indentation points, and the orange dots represent 3-min nano-indentation points. The purple line in the M versus H plot shows the power function relation between M and H for 3-min nano-indentation tests.

Power function relation analysis (using the least square method) was also conducted between C and H, C and M, M and H, and M / H versus C for 3-min nano-indentation tests. The results indicate that neither C and H, nor C and M, nor M and H, nor M / H and C are strongly related. For example, the relation between M and H is the strongest among the three above-mentioned combinations and is shown in Figure 6.34. $M = 46.01H^{0.4352}$, with $r^2 = 0.5725$.

By comparing the C, H, and M values between 3-min micro- and nano-indentation tests, the observations can be summarized:

(i) For indentation hardness H, as shown in Figure 6.33 (a), the average value and standard

deviation value from nano-indentation tests are larger than those from micro-indentation tests. Larger standard deviation corresponds to more widely spread vertical bars.

(ii) For indentation modulus M, as shown in Figure 6.33 (b), the average values of micro- and nano-indentation tests are similar, but the standard deviation value from nano-indentation tests is larger than that from micro-indentation tests. Larger standard deviation corresponds to more widely spread vertical bars.

(iii) For indentation creep modulus C, as shown in Figure 6.33 (c), the average value and standard deviation value from nano-indentation tests are larger than those from micro-indentation tests. Larger standard deviation corresponds to more widely spread vertical bars.

(iv) Dieterich and Kilgore (1994; 1996) and Vogler et al. (2016) stated that the size of contacting asperities in a fracture is closer to that of micro-indentation compared to that of nano-indentation. Therefore, to model the behavior of contacting asperities in a fracture, micro-indentation results should be used.

So far, convincing explanations for the three above-mentioned observations are not possible. Some postulations are proposed below.

(i) The relatively large variation obtained from nano-indentation tests may be due to the size effect. According to Bernabe (2019), limestone may be composed of calcite (larger grain, stronger) and micrite (smaller grain, weaker). As shown in Figure 6.35, for micro-indentation, the indenter size may be much larger than the grain size of calcite or micrite. Therefore, for each indent, the measured H, M, and C values are the values of calcite and micrite averaged by their volume ratios. As a result, the values obtained from micro-indentation tests show less variation. On the contrary, for nano-indentation, the indenter size may be comparable or smaller than the grain size of calcite or micrite. Thus, for each indent, the measured H, M, and C values are the values of single grains. As a result, the values obtained by nano-indentation tests show larger variation.

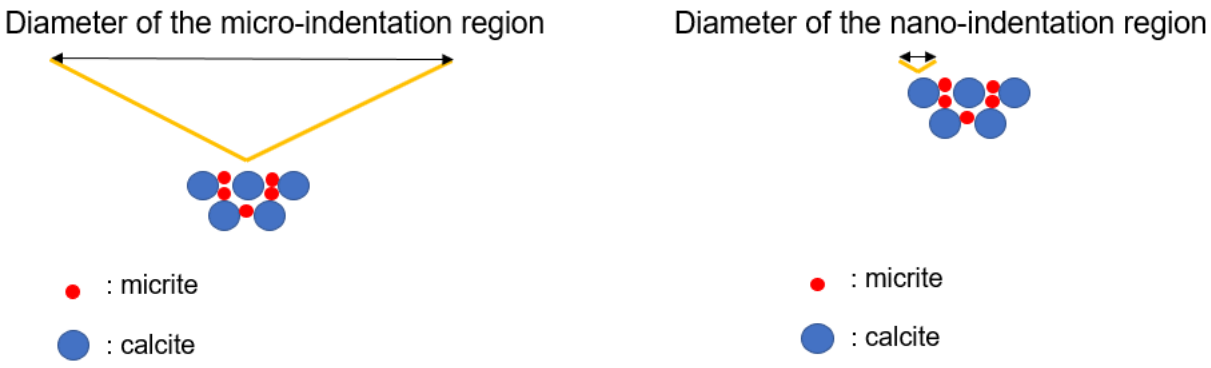

Figure 6.35 Schematic of micro- and nano-indentation size compared with grain sizes. The left and right figures represent micro- and nano-indentation tests, respectively. In each figure, the

yellow triangle represents the size of the indenter. The grain size of Musandam limestone was not measured, so the above schematic is hypothesized.

(ii) The larger average of H and C obtained by nano-indentation tests may be due to errors in contact area measurement. A few research groups in material science and tribology (Iost et al., 1996; Qian et al., 2005; Huang et al., 2006) have reported that for both brittle materials (i.e. fused silica) and metals, the H and C values measured by nano-indentation tests are larger than those measured by micro-indentation tests. They hypothesized that in nano-indentation tests, the radius of the contact area (see the explanation of a_u in Figure 5.24 in Section 5.4.3) may be underestimated. As shown in Eqns. 5.7 and 5.8 in Section 5.4.3, an underestimation of a_u leads to an overestimation of H or C.

6.4.1.2 Comparison of indentation properties between Musandam limestone and other limestones

The indentation properties of Musandam limestone are compared with those of other types of limestone. It appears that not much literature exists on the indentation properties of limestone rocks from eastern Saudi or UAE or Oman. Therefore, the indentation properties of Musandam limestone are compared with those of other types of limestone worldwide, and the results are shown in Table 6.16. It appears that most literature discusses the nano-indentation properties; the micro-indentation properties of different types of limestone have not been extensively researched.

Table 6.16. Indentation properties of different types of limestone (Berkovich indenter was used)

Reference	Limestone formation	Limestone location	Average H (GPa)	Average M (GPa)	Indentation size (Micro- or nano-indentation)	Porosity (%)
Mighani et al. (2018)	-	Abu Dhabi	~0.93	~32.0	Nano	~13.0
Shukla et al. (2015)	Salem Formation (Indiana limestone)	Indiana, USA	~0.86	~47.7	Nano	~15.6
Boulenouar et al. (2017)	Altmühltal Formation (Solnhofen limestone)	Solnhofen, German	~2.51	~54.0	Nano	~3.0
Kalo (2017)	Dogger and Keuper Formation	Near Paris	~1.51	~33.4	Nano	~8.1
Lebedev et al. (2017)	-	Eastern France (Savonnièr-es)	-	~23.2	Nano	~25.0

Vialle et al. (2018)	Oolite Blanche Formation	Eastern part of Paris Basin	-	~21.1	Nano	~15.0
This paper	Musandam Formation	Musandam Peninsular, Oman	2.28	65.58	Nano	0.93

Note: '- 'means that the value or the location was not reported.

Based on Table 6.16, the porosity has a strong effect on the indentation modulus M and hardness H - the indentation modulus M and hardness H decrease with increasing porosity. The porosity for Musandam limestone is much smaller than that of other types of limestone rocks; and as a result, the indentation modulus M and hardness H of Musandam limestone is larger than those of other types of limestone rocks.

6.4.1.3 Comparison of Triaxial and Micro-, and Nano-indentation Properties

Modulus

Triaxial, micro-indentation, and nano-indentation tests differ in specimen scale, stress conditions, and loading geometry. However, it is still useful to compare the mechanical properties obtained by the three different tests. Figure 6.36 compares the measured elastic moduli of nano-indentation, micro-indentation, and triaxial tests, by plotting the measured elastic modulus changing with measurement size and confining pressure (the purpose of Figure 6.36 is only to compare the effect of measurement size on the measured elastic moduli). The measurement size for the LVDT is the specimen length (101.6 mm), for strain gauge it is the strain gauge length (6.6 mm), and for dynamic elastic modulus is the length of sub-blocks (the distance between the acoustic transmitter and receiver sensor is the length of sub-blocks, which is 140 mm). The red and blue error bars correspond to nano- and micro-indentation test results, respectively; the yellow, red, green, and black dots correspond to triaxial test results, and the purple dot corresponds to P-wave velocity measurement results. When the confining pressure was less than 20 MPa, the elastic moduli measured by triaxial tests (shown by the yellow dots and the green dot) are less than those measured by micro-indentation tests (shown by the blue error bar) or nano-indentation tests (shown by the dark red error bar); when the confining pressure was higher than 60 MPa, the elastic moduli measured by triaxial tests (shown by the red and black dots) are slightly larger than those measured by micro-indentation tests or nano-indentation tests. Between the scale of micro- and nano-indentation (the radii of contact area are 90 μm and 2 μm, respectively), there is not much difference in elastic modulus.

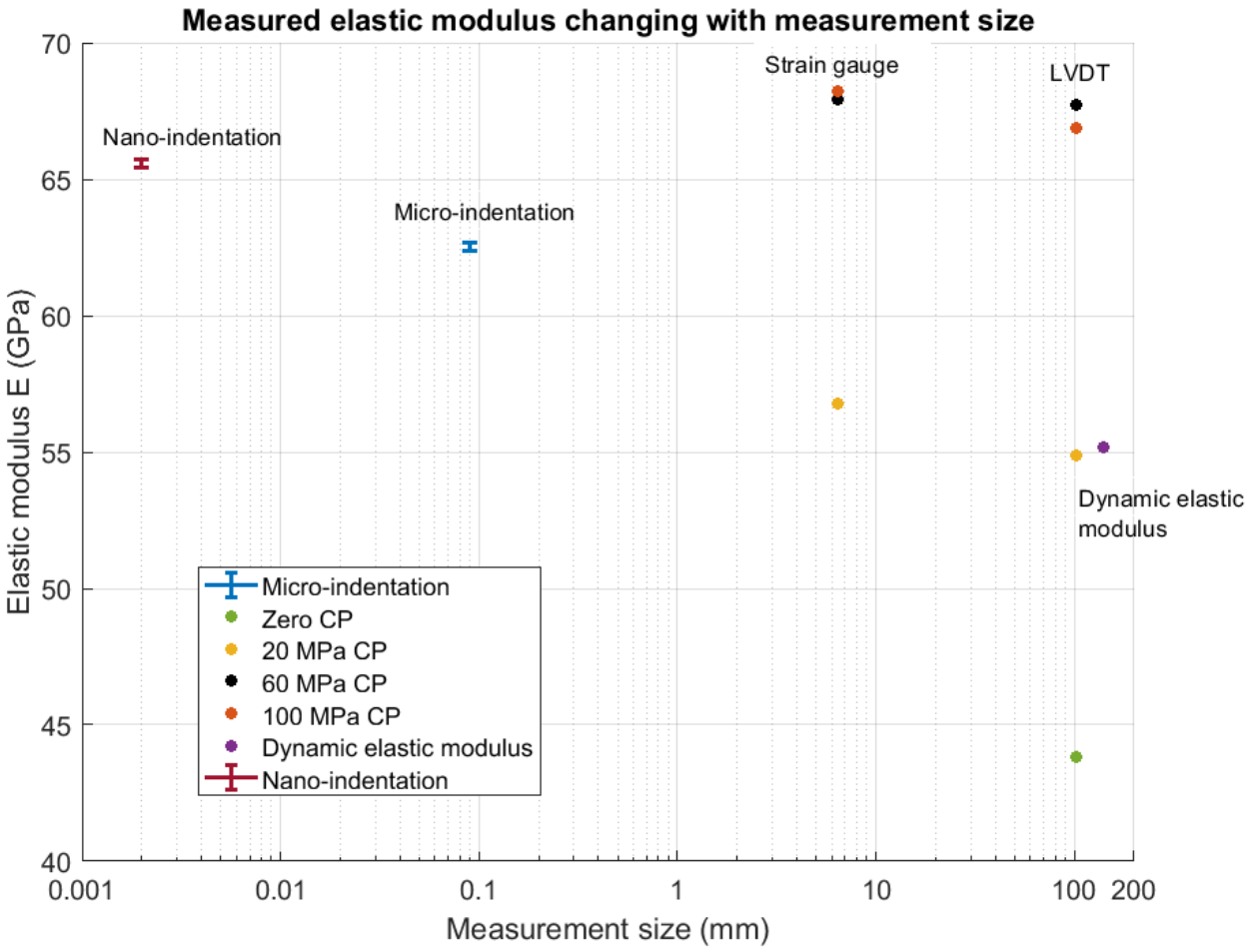

Figure 6.36. Measured elastic moduli changing with measurement size and confining pressures. For micro-indentation tests, the average elastic modulus E_1 (see Table 6.11) and the ± standard deviation are plotted; for nano-indentation tests, the average elastic modulus E_1 (see Table 6.15) and the ± standard deviation are plotted. For triaxial tests, the E_{50} values under different confining pressures are plotted. The 'dynamic elastic modulus' corresponds to the average elastic modulus measured by P-wave velocity in the horizontal direction of sub-blocks.

6.4.2 Preliminary results for SEM-EDS tests for 3-min nano-indentation

As mentioned in Section 5.4.4, SEM-EDS tests were conducted to measure the element distribution of the 3-min nano-indentation test region, and the element distribution is shown in Figure 6.37. The spatial distribution of eight elements, Ca, Al, Si, Fe, Mg, Na, K, and C, was obtained. Each element has a unique color. Table 6.17 summarizes the area percentage of the eight above-mentioned elements in the scanned region shown in Figure 6.37. Based on Table 6.17, Ca, C, and Si are the three dominant elements.

(a):

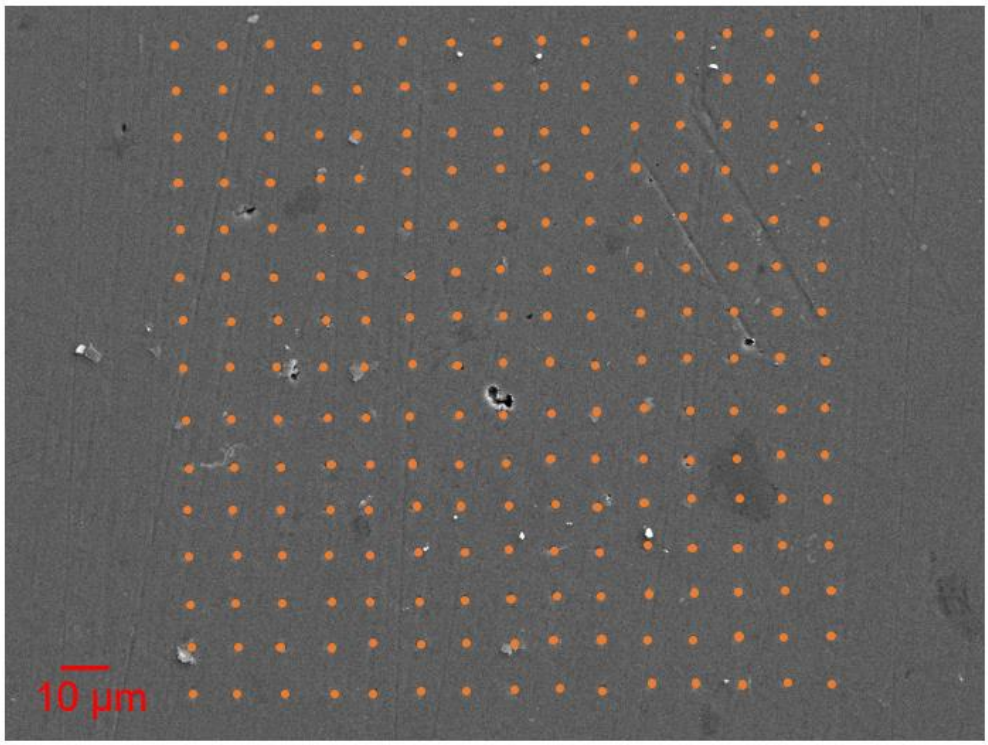

(b):

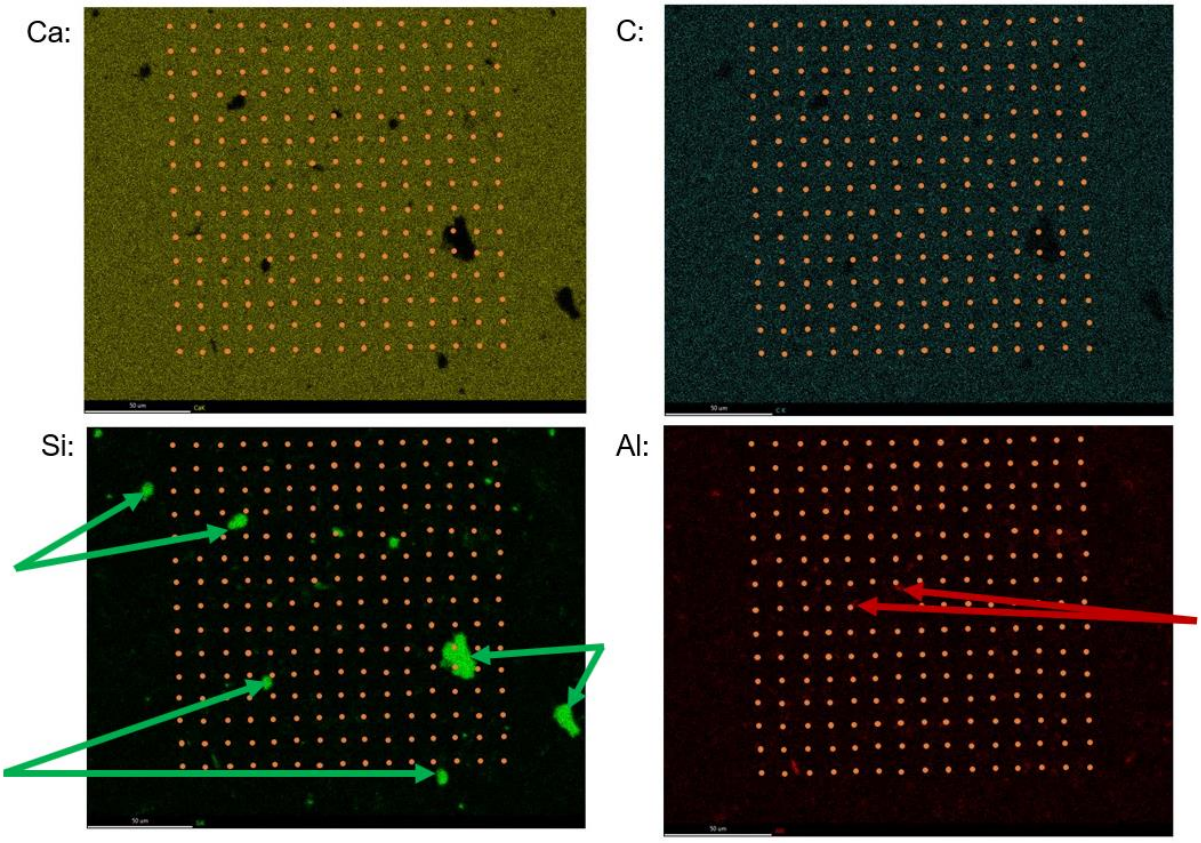

(c):

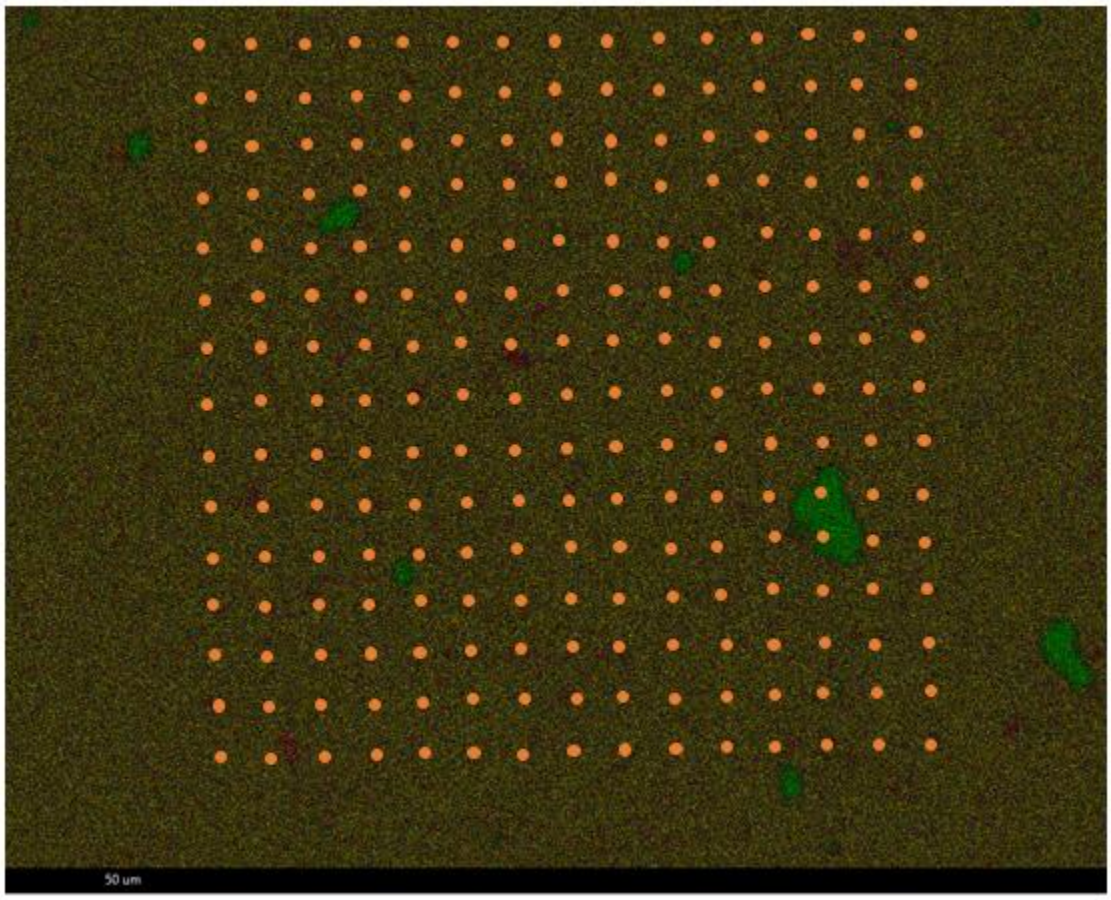

Figure 6.37. SEM-EDS images of the nano-indentation region. (a): SEM image of the nano-indentation test region. The orange dots represent the nano-indents. (b): the SEM-EDS image of calcium, carbon, silicon, and aluminum. Each element has a unique color. Calcium, silicon, and aluminum elements correspond to yellow, green, and red color, respectively. For most regions, calcium and carbon are the two dominant elements. There are some regions where silicon is the only dominant element; there are two regions where silicon and aluminum are the two dominant elements (It is difficult to see the regions. The images were generated by the SEM device during scanning. The image quality could not be improved because they were generated by the device). The regions where silicon is the only dominant element are shown by green arrows, and the regions where both silicon and aluminum are two dominant elements are shown by red arrows. (c): the SEM-EDS image of all the eight elements. Each element has a unique color, and the image is an overlay of all different colors. Based on the image, for most regions, calcium and carbon are the two dominant elements. There are some regions where silicon is the only dominant element.

Table 6.17. The area percentage of the elements of the scanned region in Figure 6.37.

Element type	Area (%)
Ca	67.89

C	23.39
Si	3.66
Al	1.58
Fe	0.38
Na	1.11
Mg	1.92
K	0.07

Based on Figure 6.37, for most regions, calcium and carbon are the two dominant elements. Specifically, three types of regions can be identified:

(i). Region A (see the yellow regions of sub-plot 'Ca' in Figure 6.37 (b)): calcium and carbon are the two dominant elements. It contains 221 indents. Therefore, calcite is the dominant mineral in region A.

(ii). Region B (see the green regions and green arrows in sub-plot 'Si' in Figure 6.37 (b)): silicon is the only dominant element. It contains 2 indents.

(iii). Region C (see the red regions and red arrows in sub-plot 'Al' in Figure 6.37 (b)): silicon and aluminum are the two dominant elements. It contains 2 indents.

For the nano-indents in regions A, B, and C, the indentation hardness H, indentation modulus M, and indentation creep modulus C were calculated. The H, M, and C for region A are summarized in Table 6.15. Tables 6.18 summarizes the volume fraction, H, M, and C values for regions A, B, and C.

Table 6.18. H, M, and C values for regions A, B and C.

Region (dominant element)	Volume fraction (%)	Indent No.	H (GPa)	M (GPa)	C (GPa)
A (calcite dominates)	97.90	-	2.28	65.58	1235.50
B (silicon dominates)	1.78	1	7.26	64.83	4574.67
		2	11.93	112.66	25570.1
C (silicon and aluminum dominate)	0.32	1	1.50	53.85	966.76
		2	1.45	59.91	598.80

Note: the values in region A are the averaged values from 221 indents.

Based on Table 6.18, two observations can be made:

(1): The H, M, and C values of indents in region B are much larger than those of the indents in region A. This indicates that the mineral in region B is much stronger and stiffer compared with calcite. Since silicon is the only dominant element and the values of H, M, C are high, it is postulated that silicate is the dominant mineral in region B.

(2): The H, M, and C values of indents in region C are smaller than those of the indents in region A. This indicates that the mineral in region C is relatively softer and weaker compared with calcite.

Since both silicon and aluminum are the two dominant elements, it is postulated that region C mainly consists of clay minerals.

The indentation modulus M obtained in 3-min nano-indentation tests were upscaled using the Hashin-Shtrikman (HS) method. The HS method determines the effective elastic moduli of composites (at least two different minerals) by minimizing the elastic potential energy of the composite. To apply the HS method, the elastic moduli and the volume fractions of different minerals need to be measured. The details could be found in Hashin and Shtrikman (1962). Here, the elastic modulus is equivalent to the indentation modulus M. Based on the indentation moduli and volume fractions shown in Table 6.18, the upscaled indentation modulus M was determined as 65.97 GPa, which is very similar to the indentation modulus M of region A. As shown in Table 6.11, the average indentation modulus M measured by 3-min micro-indentation tests is 64.97 GPa. Therefore, the M upscaled by the HS method and the M measured from 3-min micro-indentation tests are similar. The details of the calculation are shown in Appendix 2.

6.4.3 6-hr nano-indentation creep test results

According to Table 5.5 in Section 5.4.2, in total 9 6-hr nano-indentation tests were conducted. Figure 6.38 shows the schematic of the 6-hr nano-indentation test matrix. Figures 6.41 plots the indentation creep depth Δh versus time curves for the nine indents. The indentation creep depth corresponds to the creep stage of the indentation test, and the concept of creep stage is explained in Figures 6.39 and 6.40 below. It is worth noting that Figures 6.39 and 6.40 use one 3-min nano-indentation test as the example. (Due to significant fluctuation, if one 6-hr nano-indentation test is shown in Figure 6.39, Figure 6.39 will become very messy) Ideally, in the creep stage, the creep depth Δh should increase with time, and the creep curve should not fluctuate abruptly.

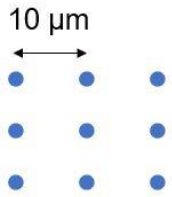

Figure 6.38 Schematic of the 6-hr nano-indentation test matrix. The nine indents form a 3 * 3 matrix. Each blue circle corresponds to one indent.

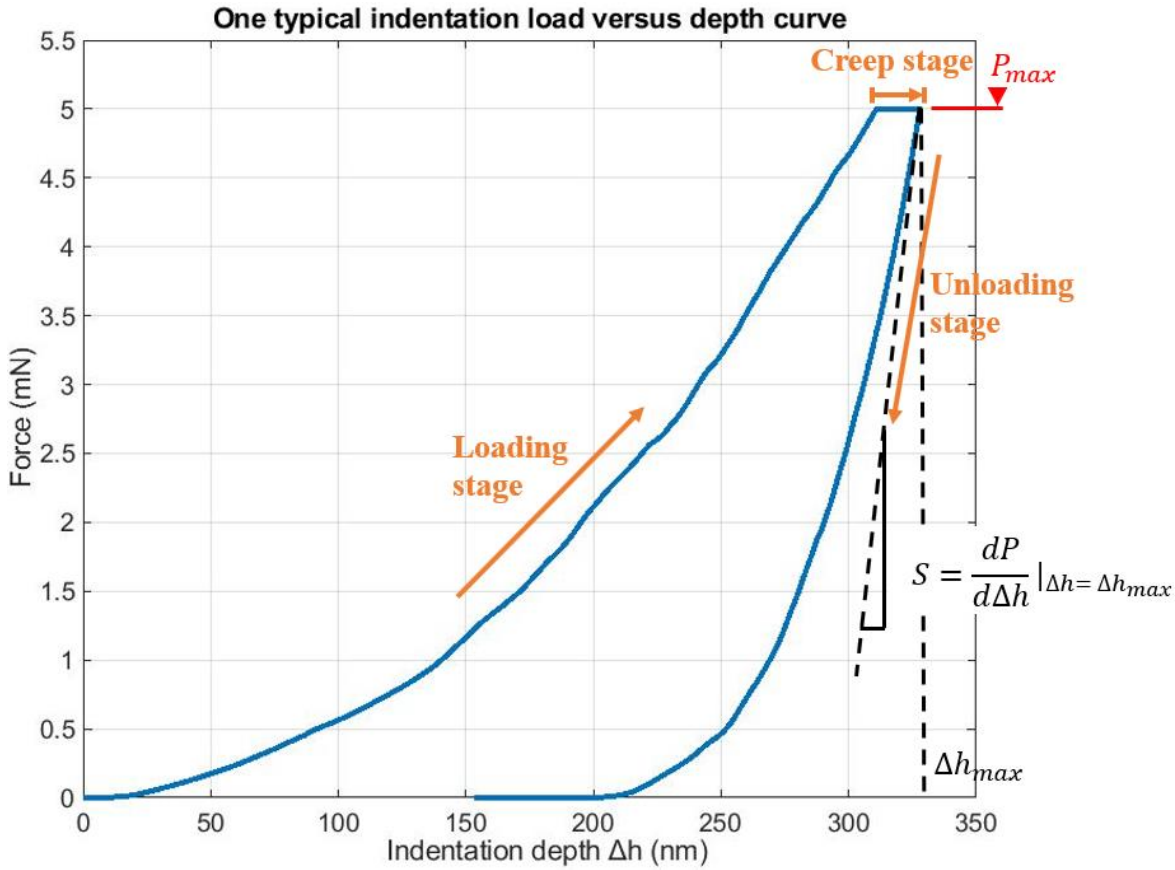

Figure 6.39. Load versus indentation depth curve from a typical 3-min nano-indentation test. P_{max} corresponds to the maximum force (load). The indentation depth Δh and slope S have been explained in Section 5.4.3.

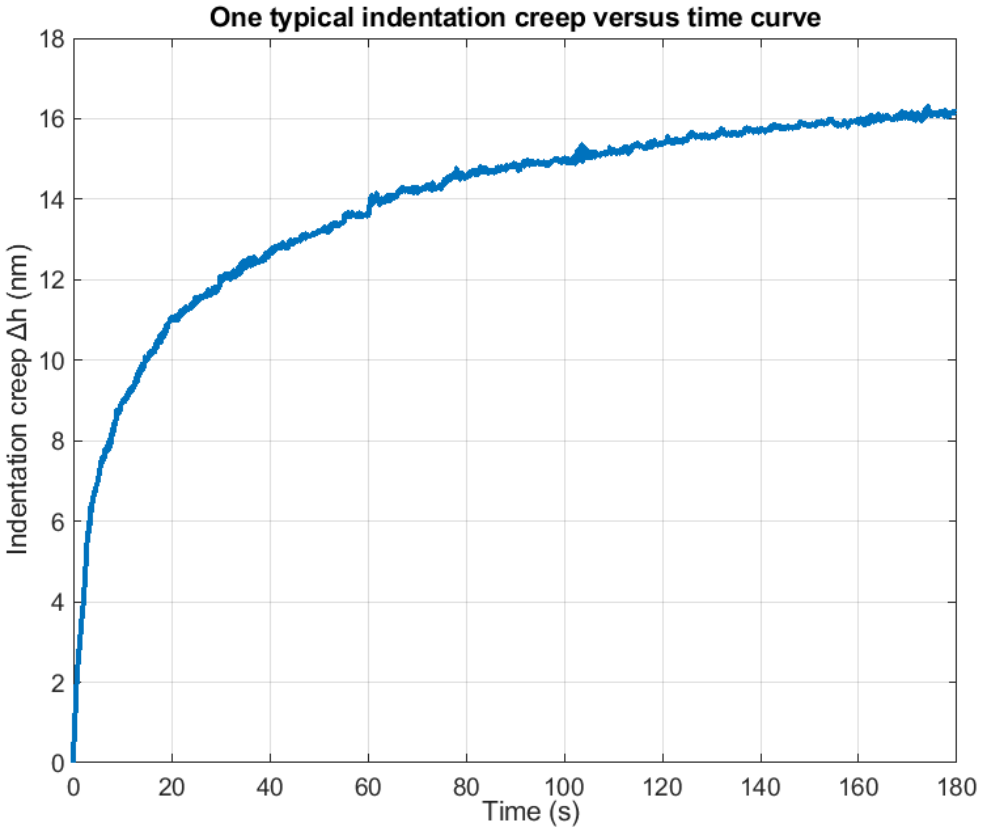

Figure 6.40. A typical indentation creep versus time curve for a 3-min nano-indentation test. The blue curve corresponds to the measured data.

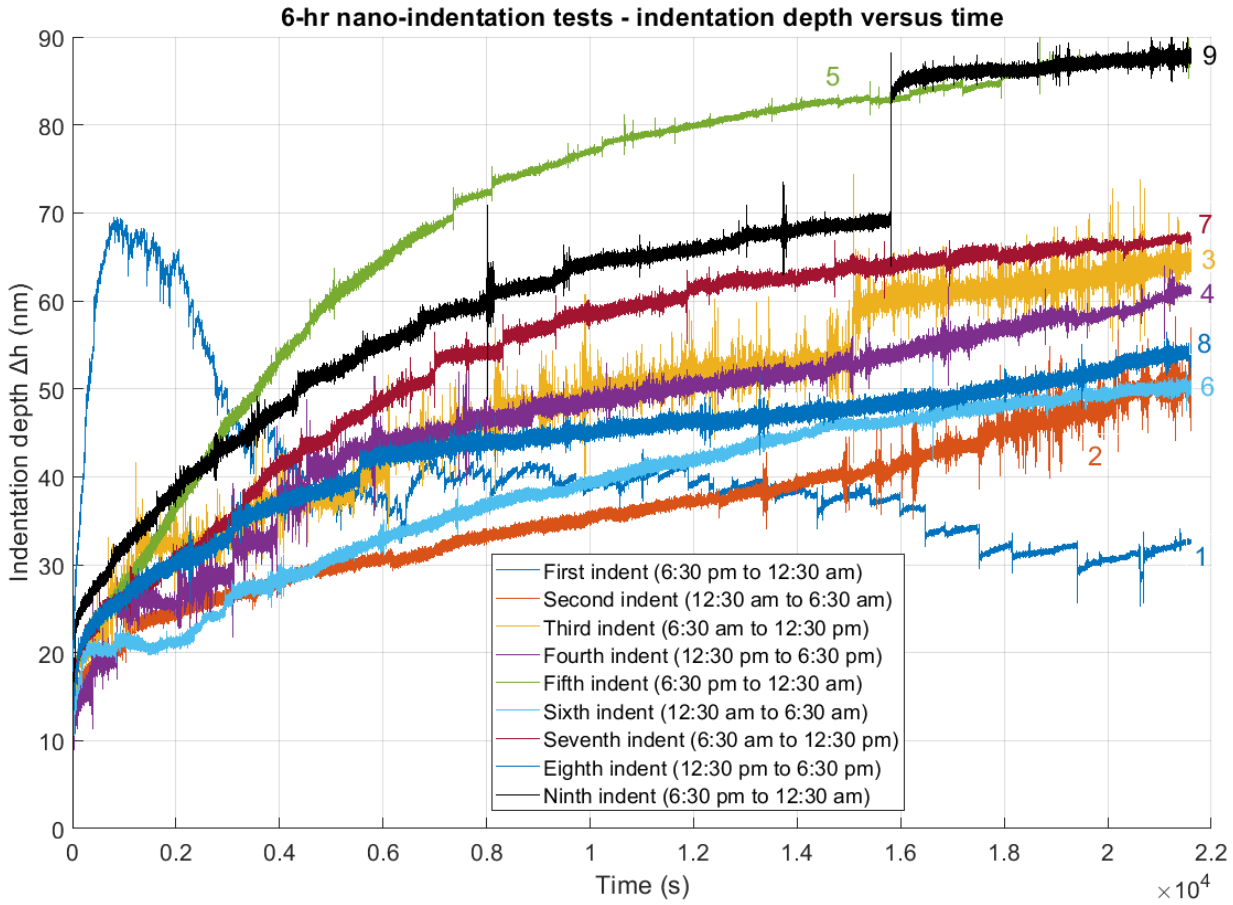

Figure 6.41. Indentation depth Δh versus time curves for the 6-hr nano-indentation tests. Nine tests were conducted (so nine indents were made). The creep of the first indent (the blue curve in which Δh increased rapidly to 70 nm and then decreased with time) might not be correctly measured. Each indentation curve is marked with the corresponding indent number.

Figure 6.41 shows that for some of the indents, the measured indentation depth fluctuated significantly with time. During the creep stage, the indentation load was held as a constant. There are three possible reasons for the fluctuation:

(i). Drifting of the machine. As discussed in Section 5.4.3, for nano-indentation tests, the machine drifting is not negligible because the magnitude of machine drift is comparable to that of indentation depth. However, both Ulm's group and the manufacturer do not have the machine drift data for the 6-hr duration. Therefore, the machine drift for this experiment could not be obtained.

(ii). Disturbance during the daytime. The nano-indentation device was close to the main corridor in Building 1.

(iii). Crushing of minerals or collapse of pores below the indent.

For 6-hr nano-indentation tests, the measured indentation depth Δh can be expressed as:

$$\Delta h = \Delta h_{ind} + \Delta h_{mach} \tag{6.12}$$

where Δh_{ind} is the creep of the indent, and Δh_{mach} is the machine drift. Since the 6-hr machine drift Δh_{mach} could not be obtained, the 6-hr indent creep Δh_{ind} could not be determined. As discussed in Section 5.4.3, to calculate the indentation modulus M, indentation hardness H, and indentation creep modulus C, the indent creep Δh_{ind} needs to be correctly determined. Since the Δh_{ind} for 6-hr nano-indentation tests cannot be obtained, the H, M, and C for 6-hr nano-indentation tests could not be calculated.

Although the Δh_{ind} for the 6-hr duration cannot be determined, the Δh_{ind} for the first three minutes can be determined because the machine drift Δh_{mach} for the first three minutes was provided by Ulm and Vandamme (2009). As discussed in Section 5.4.3, for the first three minutes of nano-indentation tests, the measured indentation depth can be expressed as:

$$\Delta h = x_1 \, ln \, (x_2 t + 1) + x_3 t + x_4 \tag{6.13}$$

where x_1 (unit: length) and x_2 (unit: time^{-1}) are curve-fitted parameters characteristic of the tested material. x_3 and x_4 are related to the drifting of the indentation machine and are independent of testing materials. From Eqns. 6.12 and 6.13, $\Delta h_{ind} = x_1 \, ln \, (x_2 t + 1)$ and $\Delta h_{mach} = x_3 t + x_4$. For 3-min duration, Ulm and Vandamme (2009) reported that x_3 = 0.005 nm/s and x_4 = 0.

In order to compare the 3-min and 6-hr results, the 3-min measurement needs to be extended to 6 hours with the following procedures. This was done by using the 6-hr curves and taking the first three minutes of this test. The procedures could be divided into three steps:

Step 1 (shown by Figure 6.42 (a)): For each 6-hr indent, the creep depth Δh for six hours (see the blue curve in Figure 6.42 (a)) was measured. In this step, the first three minutes of the blue curve, Δh_{3min}, was obtained (see the red curve in Figure 6.42 (a)).

Step 2 (shown by Figure 6.42 (b)): The $x_{1\text{-}3}$ and $x_{2\text{-}3}$ values were calculated from the first 3-min measurement (Δh_{3min}) of the 6-hr results:

$$\Delta h_{3min} = x_{1-3} \, ln \, (x_{2-3} t_1 + 1) + x_3 t_1 \tag{6.14}$$

Eqn. 6.14 was the same as Eqn. 5.9 in Section 5.4.3. In Eqn. 6.14, Δh_{3min} was the first three minutes of the blue curve, and Δh_{3min} is shown by the red curves in Figures 6.42 (a) and 6.42 (b). t_1 was the time, with a duration of 3 minutes (see the horizontal axis in Figure 6.42 (b)). $x_{1\text{-}3}$ and $x_{2\text{-}3}$ were the unknown parameters and they were fitted by the least square method. Ulm and Vandamme (2009) reported that x_3 is 0.005nm/s.

Step 3 (shown by Figure 6.42 (c)): The Δh_{ext} was calculated as:

$$\Delta h_{ext} = x_{1-3} \, ln \, (x_{2-3} t + 1) \tag{6.15}$$

In Eqn. 6.15, the $x_{1\text{-}3}$ and $x_{2\text{-}3}$ values were obtained in step 2. The time duration of t was six hours. Figure 6.42 (c) compares the extended curve Δh_{ext} with the measured curve. The green curve corresponds to Δh_{ext}, and the blue curve is the measured creep curve (the same as the blue curve in Figure 6.42 (a)).

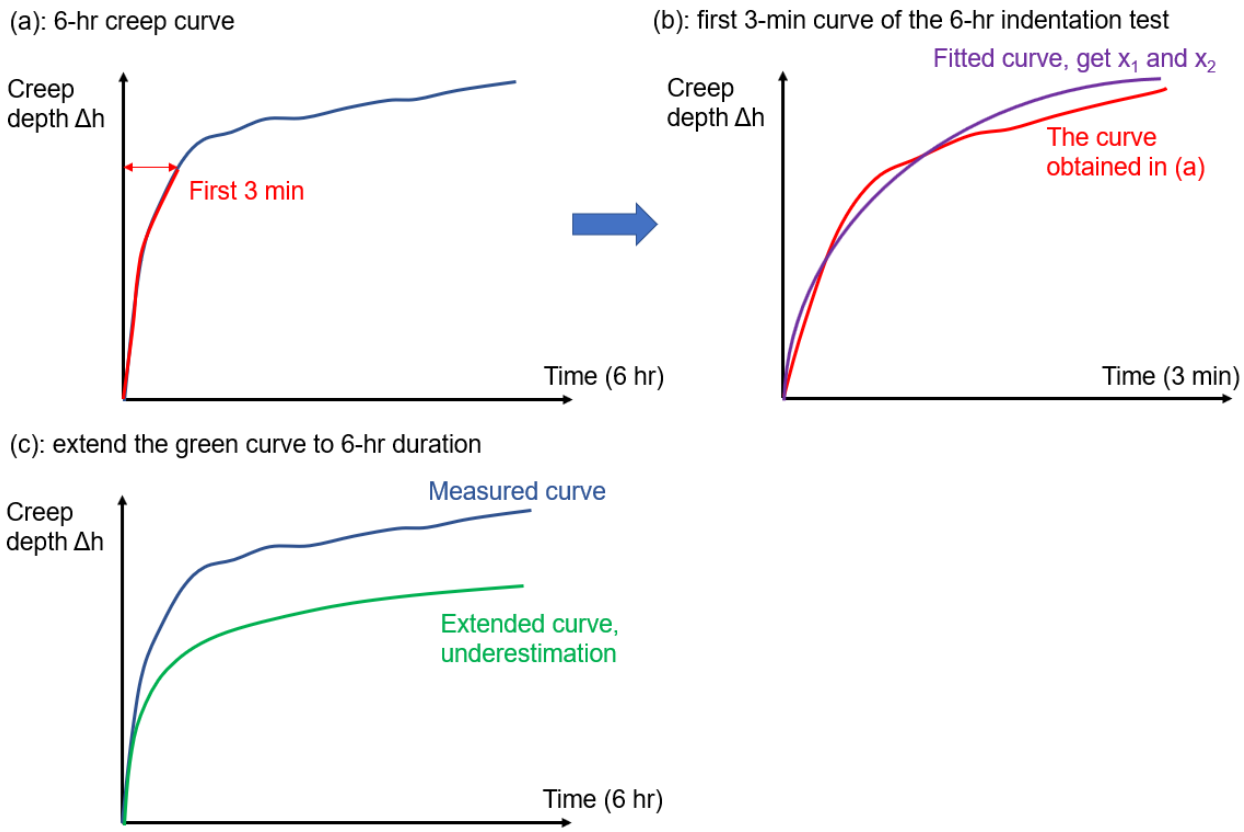

Figure 6.42 Illustration of the curve extension process of one 6-hr micro-indent. The green and purple curves are the fitted curves, and the blue and red curves are measured data. (a): The creep curve for the first 3 minutes was obtained (shown by the red curve); (b): Using curve fitting to obtain $x_{1\text{-}3}$ and $x_{2\text{-}3}$ based on the red curve. Eqn. 6.14 was used. The fitted curve is shown by the purple curve; (c): Calculating Δh_{ext} based on Eqn. 6.15. The time duration was 6 hours. The $x_{1\text{-}3}$ and $x_{2\text{-}3}$ values were obtained from (b). Δh_{ext} is shown by the green curve.

For all the indents, the Δh_{ext} value is larger than the Δh value. Figure 6.43 compares the Δh and Δh_{ext} for three nano-indentation locations (if I plot all nine locations, I will plot 18 different curves, and the plot will look extremely messy). This implies that the 6-hr creep deformation will be underestimated if it is predicted from the 3-min creep deformation. Practically, to obtain the nano-indentation creep behavior for a specific time duration, creep tests at the specific time duration need to be conducted; it may not be accurate to use short-term creep behavior to predict long-term creep behavior.

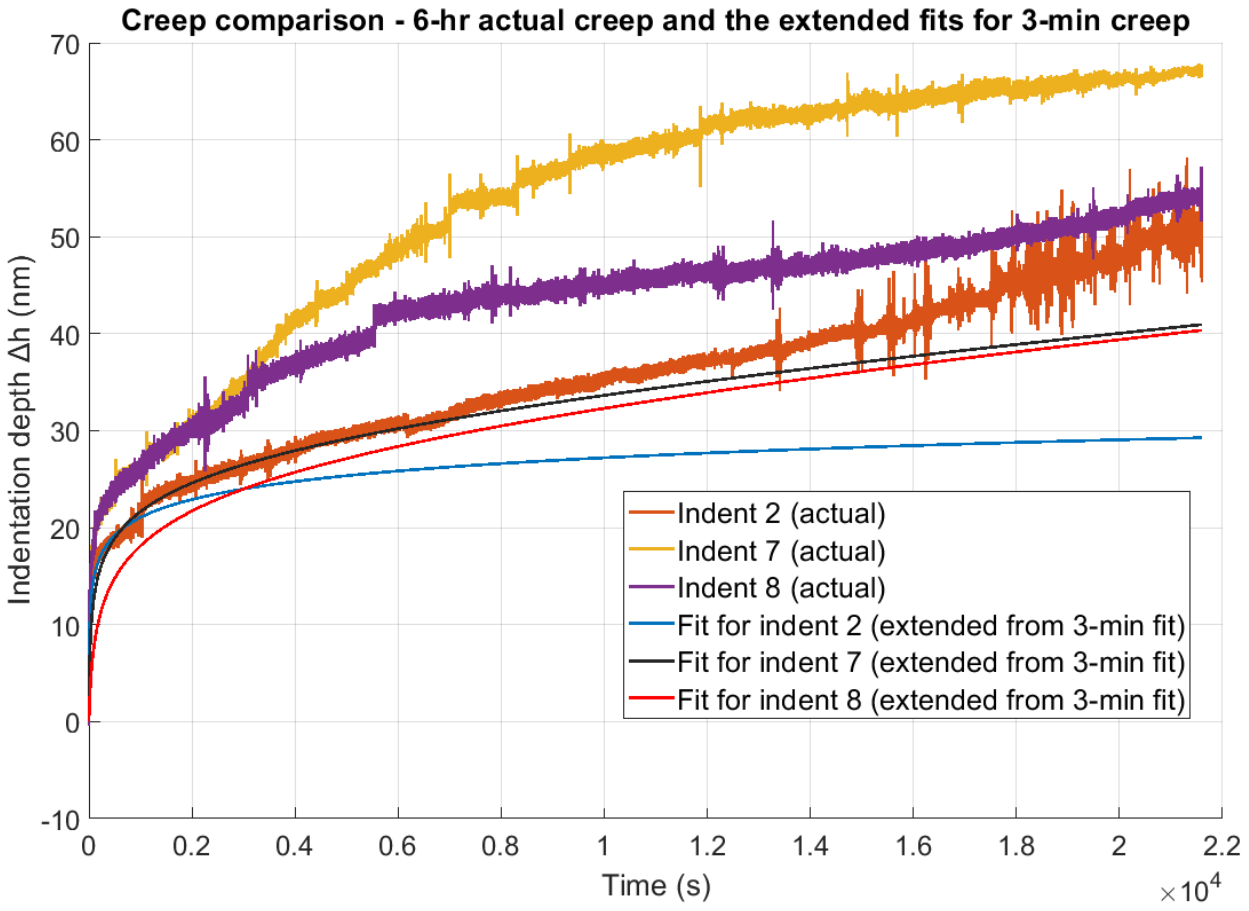

Figure 6.43 Comparison of 6-hr actual creep curves (Δh versus time) and 3-min extended curves (Δh_{ext} versus time) for three 6-hr nano-indentation tests. The orange and blue curves represent the Δh and Δh_{ext} for indent 2, respectively; the yellow and black curves represent the Δh and Δh_{ext} for indent 7, respectively; the purple and red curves represent the Δh and Δh_{ext} for indent 8, respectively. The curve extension procedure is explained in Figure 6.42.

6.4.4 Summary of nano-indentation test results

The experimental results yielded the following conclusions:

1) The average values for indentation modulus M, indentation hardness H, and indentation creep modulus C are 65.58 GPa, 2.28 GPa, and 1235.50 GPa, respectively.

2) 3-min micro- and nano-indentation tests are compared. Indentation hardness H: the average value and standard deviation value from nano-indentation tests are larger than those from micro-indentation tests. Indentation creep modulus C: the average value and standard deviation value from nano-indentation tests are larger than those from micro-indentation tests. Indentation modulus M: the average values of micro- and nano-indentation tests are similar, but the standard deviation from nano-indentation tests is larger than that from micro-indentation tests. So far, convincing explanations of the different H, C, M values between nano-

and micro-indentation tests could not be obtained; two hypotheses have been proposed.

3) For most nano-indentation regions, calcium and carbon are the two dominant elements. There are some regions where silicon is the only dominant element. At the micro-indentation scale, the element distribution is not very heterogeneous.

4) Due to machine drifting, the 6-hr nano-indentation creep deformation could not be accurately measured. Before measuring the long-term nano-indentation creep behavior, the machine drifting problem needs to be solved.

5) Between different types of limestone, the nano-indentation modulus M and hardness H increase with decreasing porosity.

6.5 Intact rock creep test results

6.5.1 Experimental results

As discussed in Section 5.3.3, triaxial creep tests were conducted on two intact limestone specimens. Figure 5.17 and Table 5.5 summarize the stress steps for specimen 1, and Figure 5.18 and Table 5.6 summarize the stress steps for specimen 2. Multiple stress steps were applied on both specimens. For each step, the axial strain was measured by both LVDTs and axial strain gauges, and the radial strain was measured by radial strain gauges. Figures 5.14 and 5.15 in Section 5.3.3 show a picture and a schematic of the sensors, respectively.

Figures 6.44, 6.45, and 6.46 plot the axial strain changing with time, total strain changing with time, and stress steps changing with time for specimen 1, respectively; Figures 6.47, 6.48, and 6.49 plot the axial strain changing with time, total strain changing with time, and stress steps changing with time for specimen 2, respectively. Compression is defined as positive.

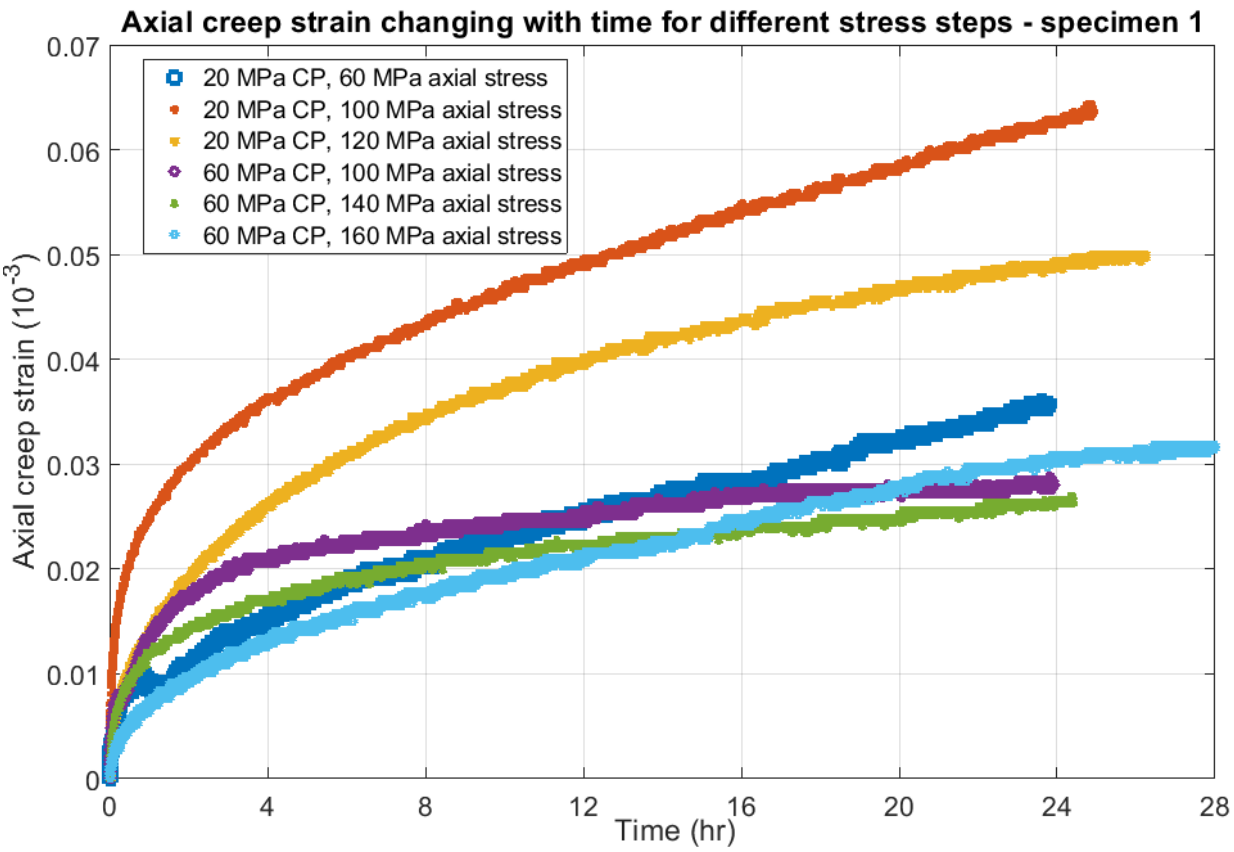

Figure 6.44 Axial strain changing with time during different stress steps for specimen 1. For each stress step, at time zero, the axial creep strain was set as zero.

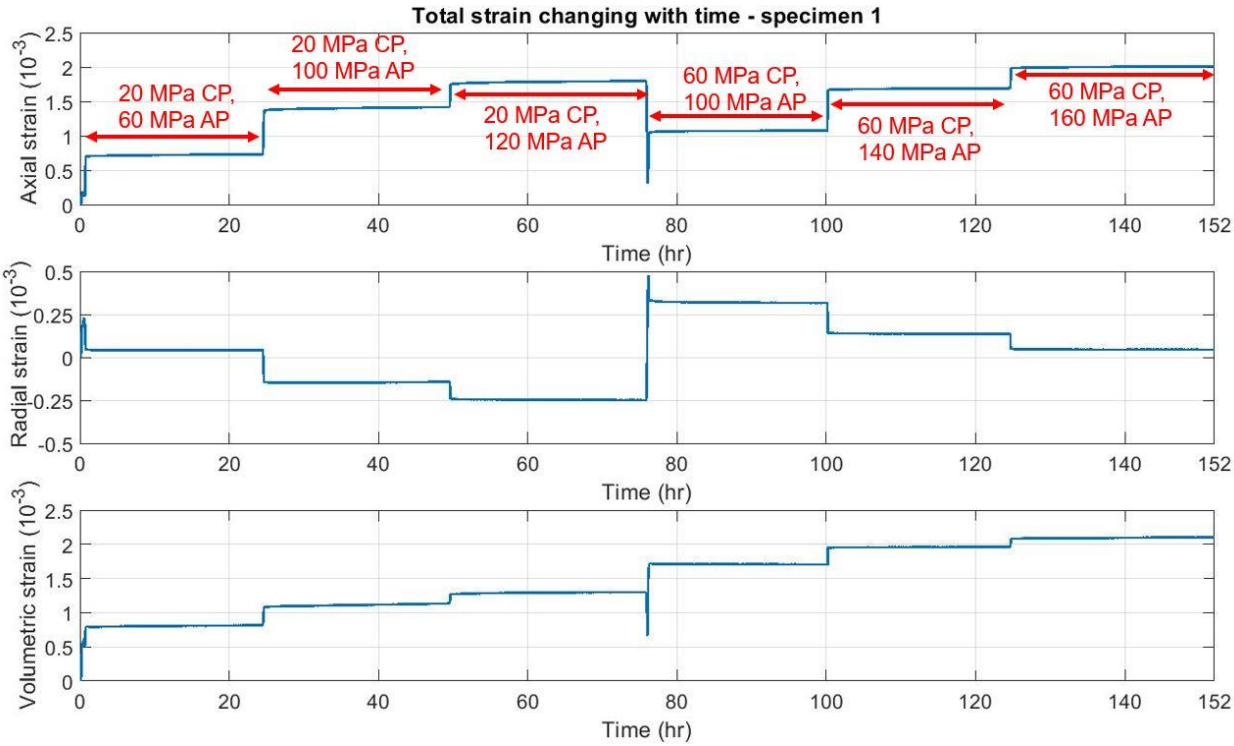

Figure 6.45 Total strain changing with time during different stress steps for specimen 1. The stress steps are shown in Figure 6.46. (a): axial strain; (b): radial strain; (c): volumetric strain (= axial strain + 2* radial strain). ‘AP’ and ‘CP’ correspond to axial stress and confining pressure, respectively. The strain at the beginning of the experiment is defined as zero.

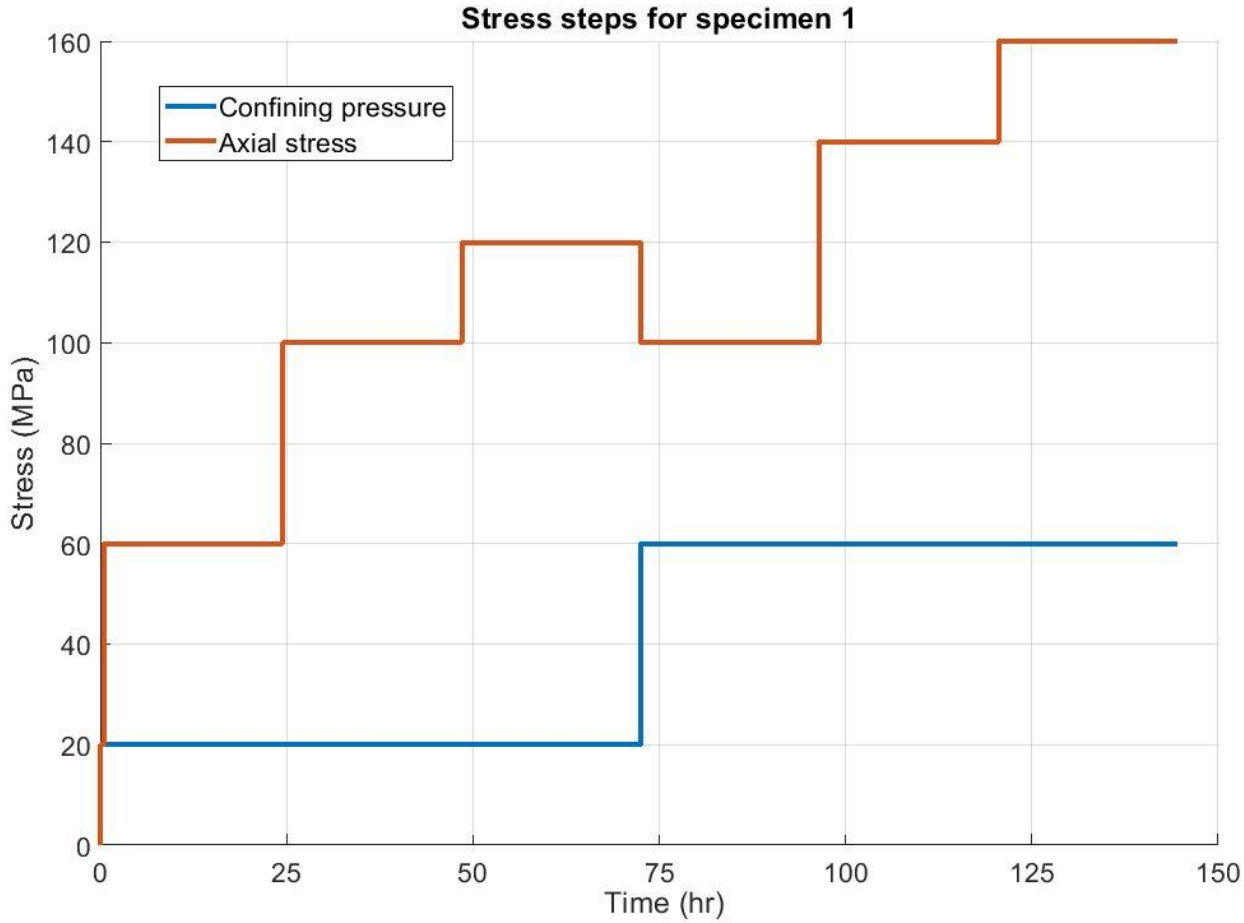

Figure 6.46 Stress steps applied to specimen 1.

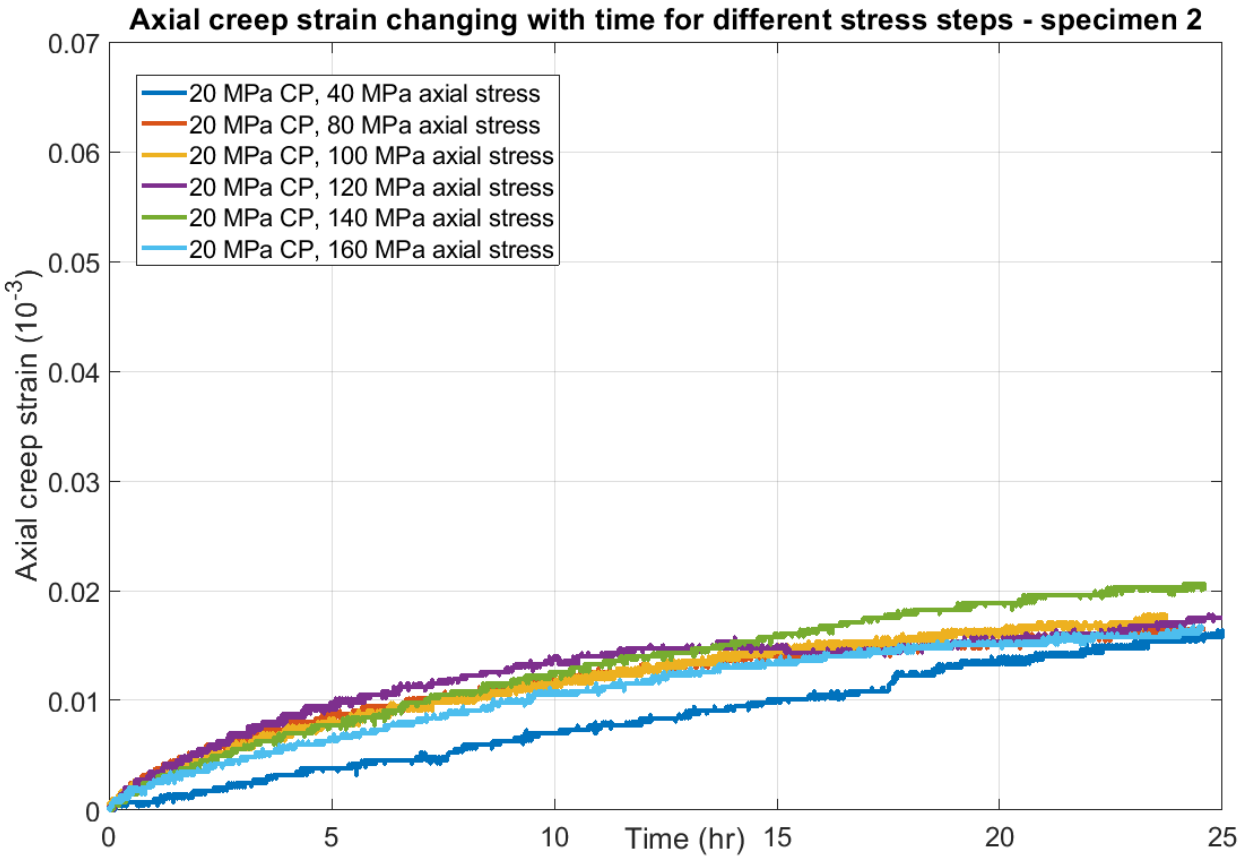

Figure 6.47 Axial strain changing with time during different stress steps for specimen 2. For each stress step, at time zero, the axial creep strain was set as zero.

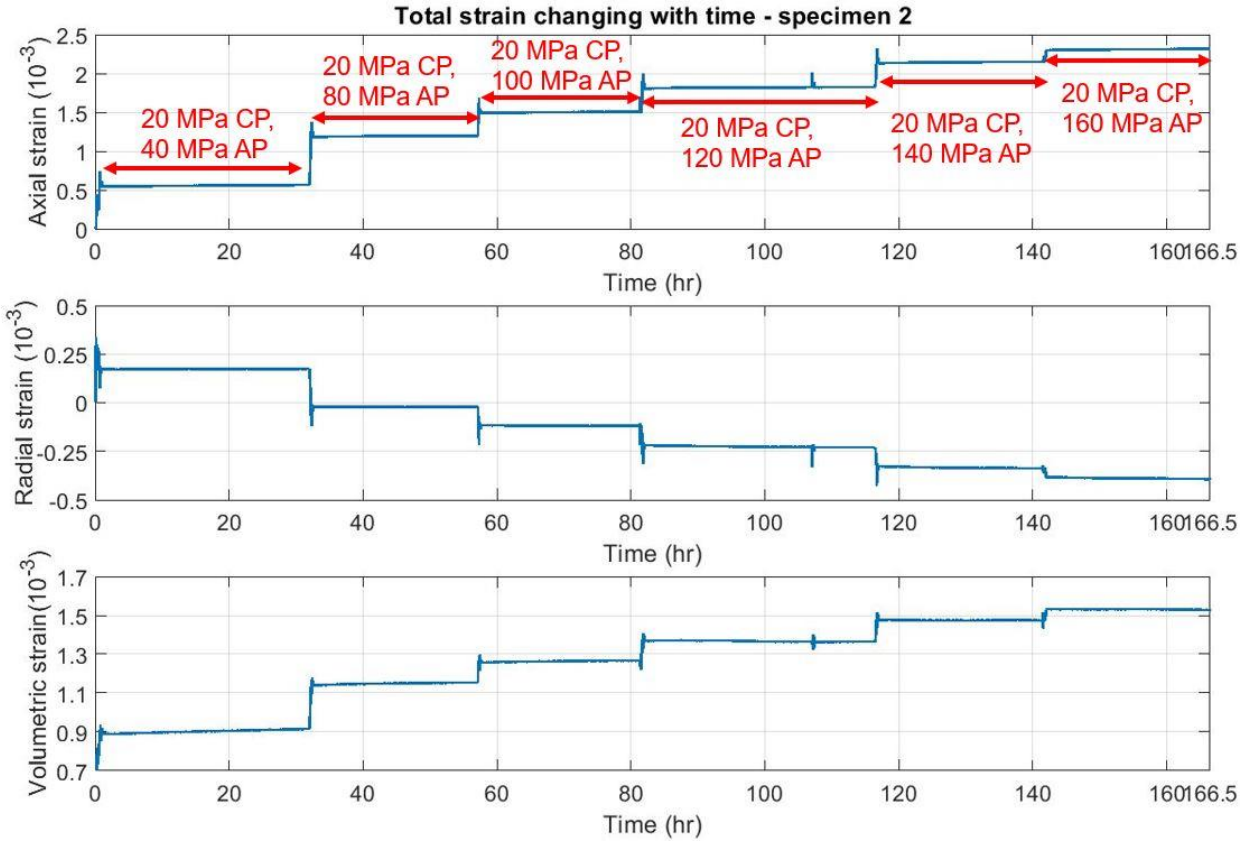

Figure 6.48 Total strain changing with time during different stress steps for specimen 2. The stress steps are shown in Figure 6.49. (a): axial strain; (b): radial strain; (c): volumetric strain (= axial strain + 2* radial strain). 'AP' and 'CP' correspond to axial stress and confining pressure, respectively. The strain at the beginning of the experiment is defined as zero. The spikes of the strain value were caused by axial stress oscillations. At the beginning of each axial stress step, the axial stress was oscillated to measure the elastic modulus and Poisson's ratio. Figure 6.50 shows the schematic of the stress oscillations.

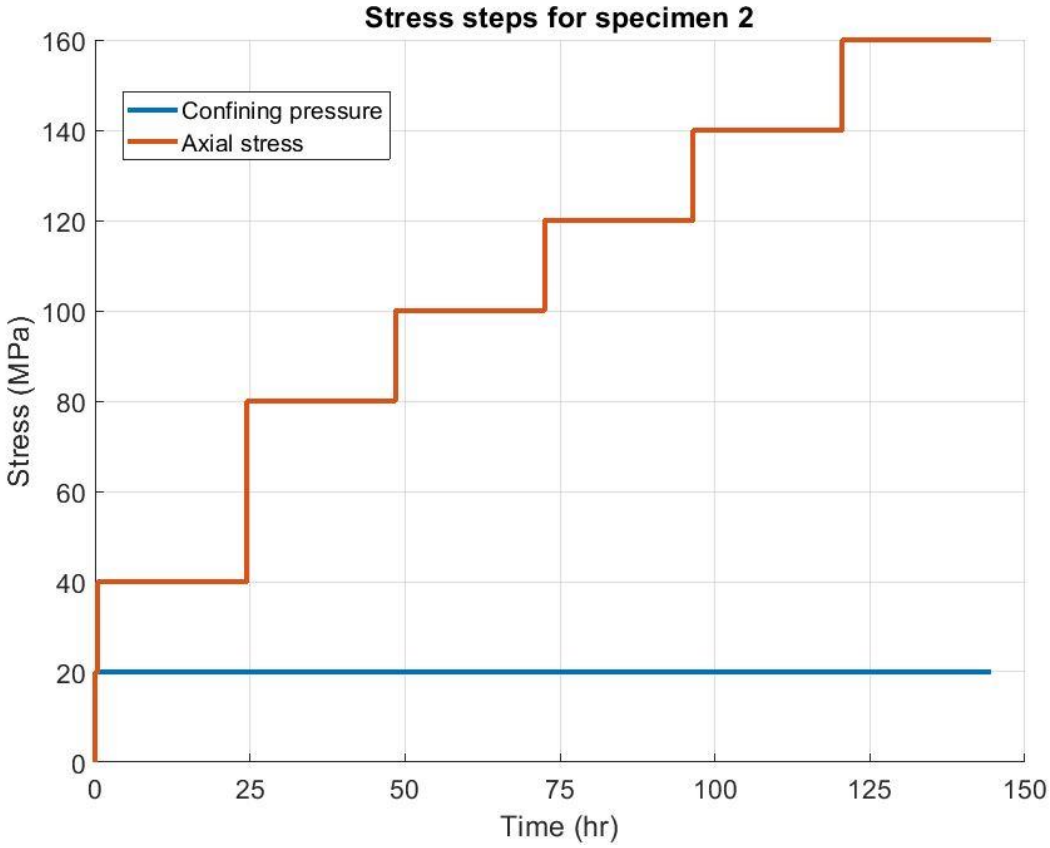

Figure 6.49 Stress steps applied to specimen 2.

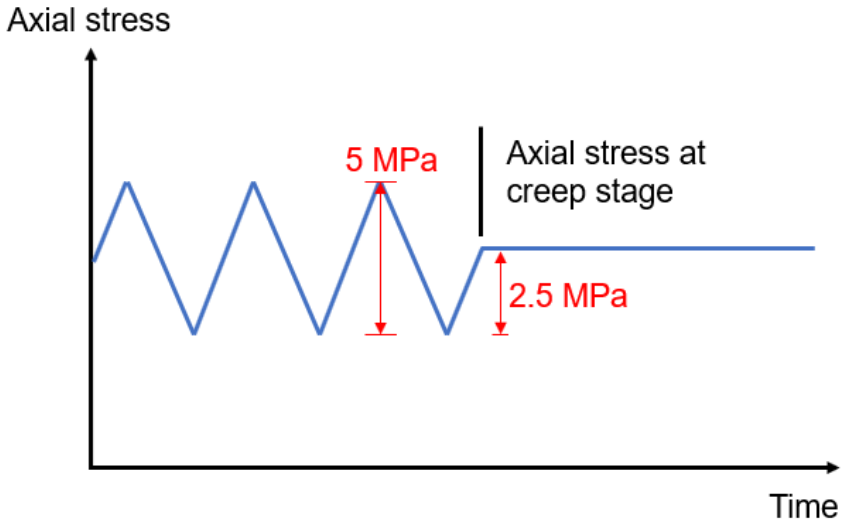

Figure 6.50 Schematic of axial stress oscillations. To obtain the elastic properties at a certain axial stress level, the stress-strain behavior at that stress level needs to be obtained. One method to obtain the stress-strain behavior is oscillating the axial stress. By oscillating the axial stress, the specimen strain will be obtained. Based on the stress-strain behavior, the elastic properties can be calculated. At the beginning of each axial stress step, the axial stress was oscillated to

measure the elastic modulus and Poisson's ratio of the specimen, while the confining pressure was fixed. The loading and unloading rates of the axial stress were 0.12 MPa/s. The magnitude of axial stress oscillation was 5 MPa. Table 6.19 summarizes the E and ν values obtained by the stress oscillations.

Table 6.19 Summary of E and ν values obtained by the stress oscillations.

Stress conditions	E (GPa)	ν
20 MPa CP, 40 MPa AP	67.75	0.30
20 MPa CP, 80 MPa AP	68.10	0.30
20 MPa CP, 100 MPa AP	67.73	0.30
20 MPa CP, 120 MPa AP	68.59	0.30
20 MPa CP, 140 MPa AP	68.82	0.30
20 MPa CP, 160 MPa AP	69.51	0.30

Figures 6.51 and 6.52 plot the creep rates changing with the time of specimens 1 and 2, respectively. The creep rate was calculated based on one-hour interval. For every hour, one creep rate was calculated. Therefore, for 24-hr duration, 24 creep rates were obtained. Eqn. 6.16 shows the calculation method of creep rate for every hour $\dot{\varepsilon}$:

$$\dot{\varepsilon} = \frac{\varepsilon_{ini} - \varepsilon_{fin}}{1\ hr} \tag{6.16}$$

where ε_{ini} is the initial axial creep strain at the beginning of the one-hour duration, and ε_{fin} is the final axial creep strain at the end of the one-hour duration. In Figures 6.51 and 6.52, the creep rate at time = 0.5 hr represents the creep rate between 0 and the first hour; the creep rate at time = 1.5 hr represents the creep rate between the first and second hour, and so on.

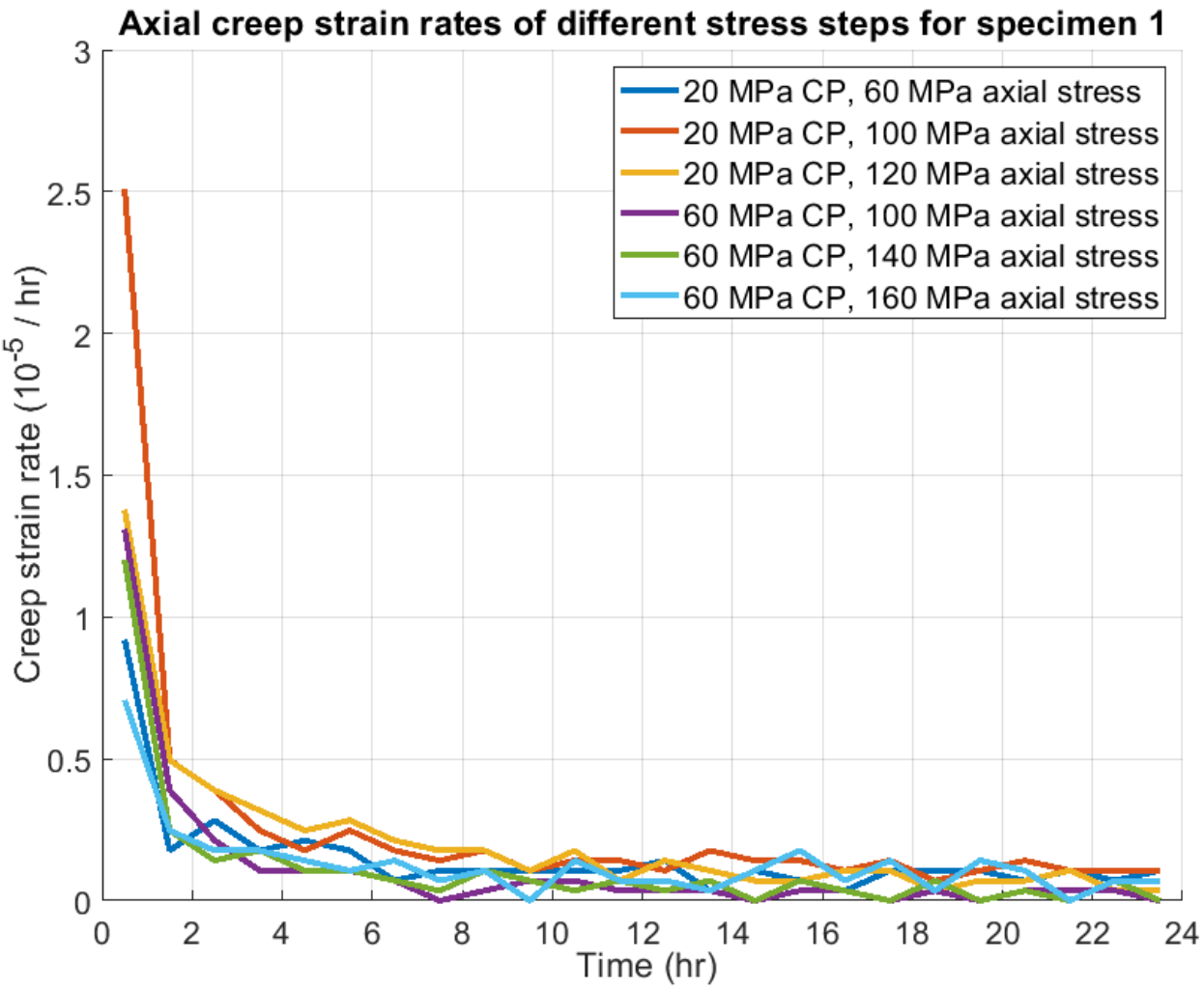

Figure 6.51 Axial creep strain rate changing with time during different stress steps for specimen 1. Different curves represent different stress steps. The stress steps are shown in Figure 6.46.

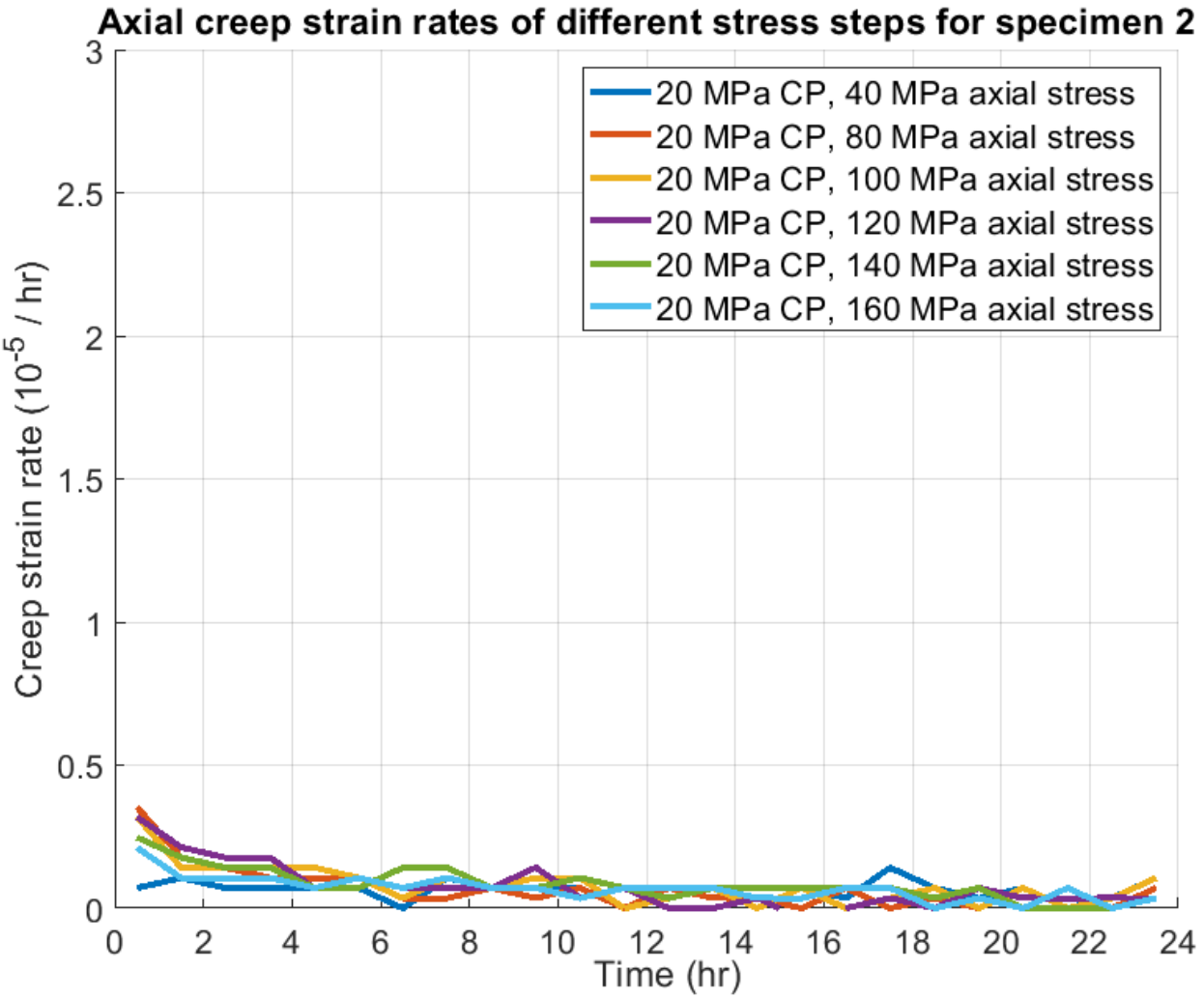

Figure 6.52 Axial creep strain rate changing with time during different stress steps for specimen 2. Different curves represent different stress steps. The stress steps are shown in Figure 6.49.

Based on Figures 6.44, 6.45, 6.46, and 6.51, for specimen 1, the observations can be summarized:

(i). For 24-hr duration, the creep strain kept increasing with time, while the creep rate decreased with time. In other words, for 24-hr duration, the creep was still in the primary stage, and had not reached the steady-state stage (see Figure 1 in Section 2.1.1 for the definitions of primary and steady-state stages).

(ii) Under the same differential stress (axial stress – confining pressure), the creep rate decreased with increasing confining pressure (see Figure 6.46 for the stress steps). For instance, the creep rate under 20 MPa confining pressure and 100 MPa axial stress (the differential stress was 80 MPa) was larger than that under 60 MPa confining pressure and 140 MPa axial stress (the differential stress was also 80 MPa). Figure 6.53 below compares the creep rate for the two above-mentioned stress steps. This implies that when predicting creep rate, the confining pressure needs to be considered. The predicted creep rate should decrease with increasing confining pressure under the same differential stress.

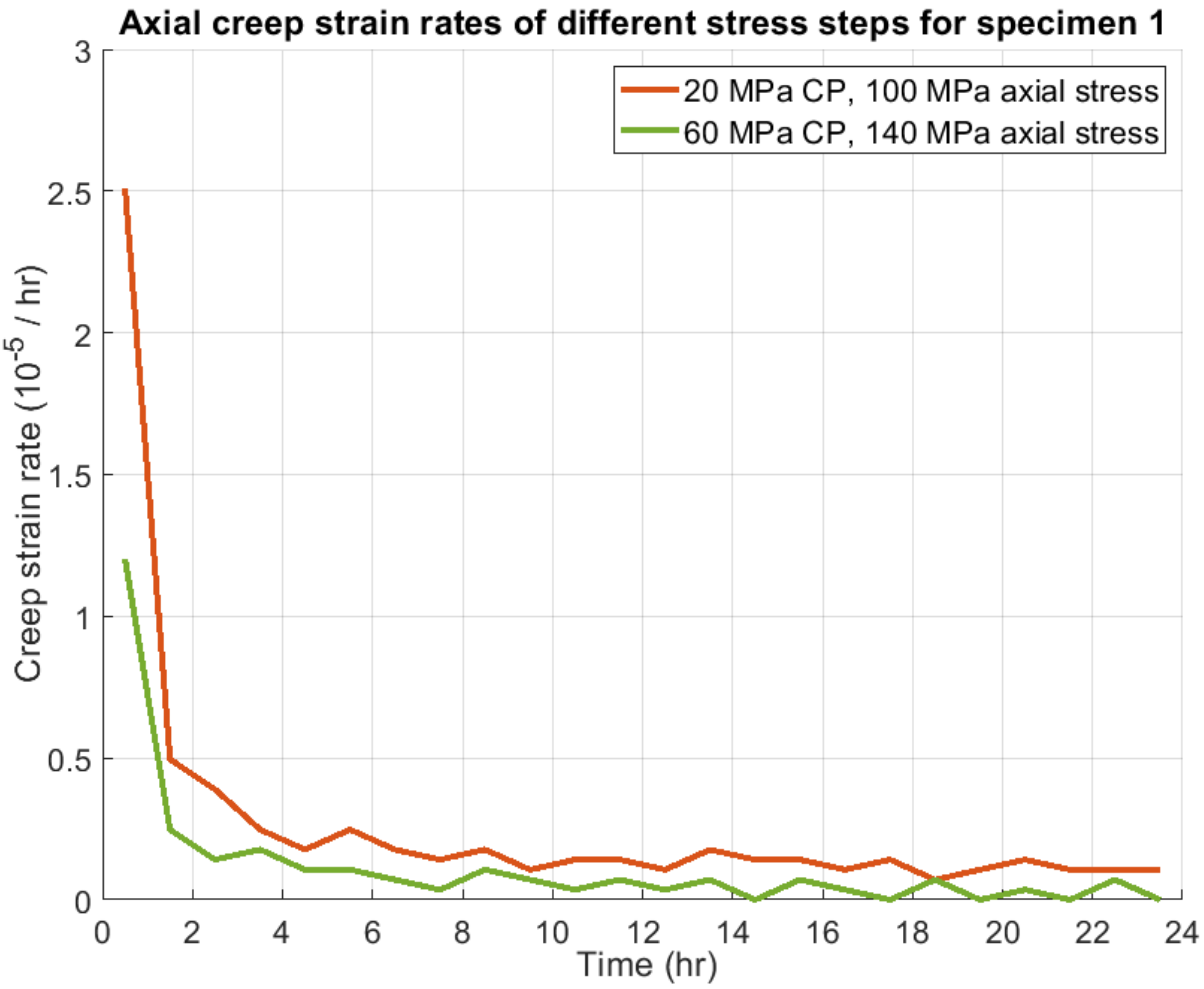

Figure 6.53 Axial creep strain rate changing with time during two stress steps for specimen 1. Different curves represent different stress steps.

Based on Figures 6.47, 6.48, 6.49, and 6.52, for specimen 2, the observations can be summarized:

(i). For 24-hr duration, the creep strain kept increasing with time, while the creep rate decreased with time. In other words, for 24-hr duration, the creep was still in the primary stage, and had not reached the steady-state stage (see Figure 1 in Section 2.1.1 for the definitions of primary and steady-state stages).

(ii). In general, under the same confining pressure, the creep rate increased with increasing axial stress. This implies that when predicting creep rate, the axial stress needs to be considered. The predicted creep rate should increase with increasing axial stress under the same confining pressure.

It is worth noting that the magnitudes of creep strain of specimen 2 were smaller than those of specimen 1, while the elastic moduli of the two specimens were similar. For example, under 20 MPa confining pressure and 100 MPa axial stress, after 24 hours, the total creep strain for specimens 1 and 2 is $6.3 * 10^{-5}$ and $1.7 * 10^{-5}$, respectively. Figure 6.54 plots the creep rates for specimens 1 and 2 under 20 MPa confining pressure and 100 MPa axial stress. The elastic moduli of specimens 1 and 2 were 67.61 GPa and 68.14 GPa, respectively. Despite similar elastic moduli,

the magnitudes of creep strain for the two specimens were different (the creep rate of specimen 1 is at least twice of that of specimen 2). The difference in creep strain might be caused by different loading histories (see the stress steps in Figures 6.46 and 6.49 for specimens 1 and 2, respectively). For specimen 1, before the stress step of 20 MPa confining pressure and 100 MPa axial stress, only one stress step was applied; for specimen 2, before the stress step of 20 MPa confining pressure and 100 MPa axial stress, two stress steps were applied.

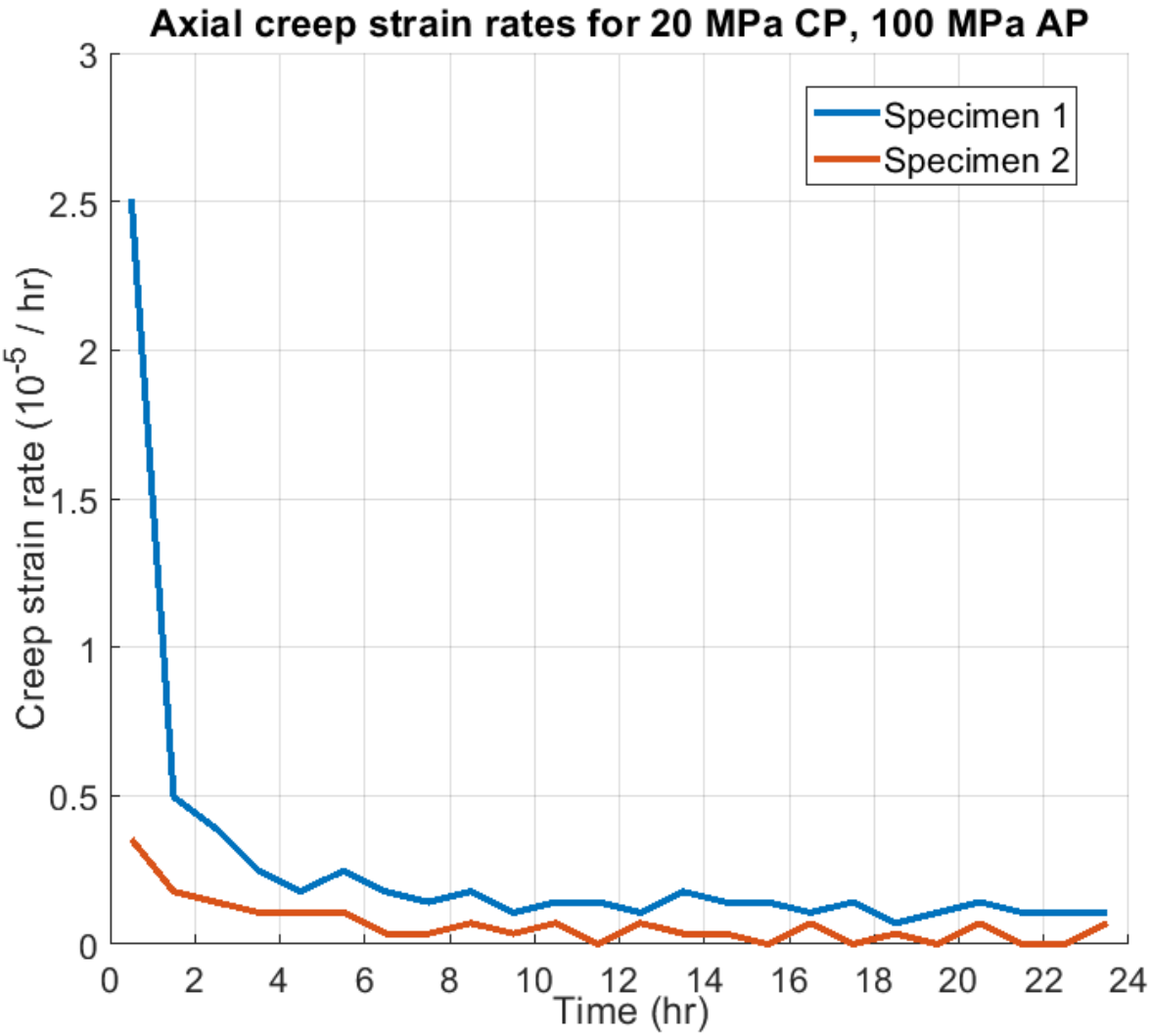

Figure 6.54 Axial creep strain rates changing with time for 20 MPa confining pressure, 100 MPa axial stress.

6.5.2 Curve fitting results

In this research, for each stress step, the measured axial creep strain ε was empirically related to time t by curve fitting. Two types of formulae were tried, and the least square method was used during the curve fitting.

The first formula (power law) can be expressed as:

$$\varepsilon(t) = At^n,\ 0 < n < 1 \tag{6.17}$$

where A and n are curve-fitted parameters.

The second formula (natural log of time law) can be expressed as:

$$\varepsilon(t) = A\ ln\ t\ + b \tag{6.18}$$

where A and b are curve-fitted parameters.

Table 6.20 and 6.21 summarize the curve fitting results of the power law for specimens 1 and 2, respectively. Figures 6.55 and 6.56 plot the curve fitting results of the power law for specimens 1 and 2, respectively.

Table 6.20 Summary of curve fitting results of power law for specimen 1

Stress step	n	ln A	r^2
20 MPa CP, 60 MPa AP	0.4167	-4.7130	0.9803
20 MPa CP, 100 MPa AP	0.2909	-3.7204	0.9964
20 MPa CP, 120 MPa AP	0.3958	-4.2300	0.9908
60 MPa CP, 100 MPa AP	0.2444	-4.2900	0.9357
60 MPa CP, 140 MPa AP	0.2628	-4.4554	0.9873
60 MPa CP, 160 MPa AP	0.4667	-4.9910	0.9959

Table 6.21 Summary of curve fitting results of power law for specimen 2

Stress step	n	ln A	r^2
20 MPa CP, 40 MPa AP	0.8189	-6.8192	0.9761
20 MPa CP, 80 MPa AP	0.5038	-5.6297	0.9687
20 MPa CP, 100 MPa AP	0.5647	-5.7808	0.9925
20 MPa CP, 120 MPa AP	0.5271	-5.6306	0.9228
20 MPa CP, 140 MPa AP	0.6785	-5.9686	0.9844

20 MPa CP, 160 MPa AP	0.6179	-6.0213	0.9927

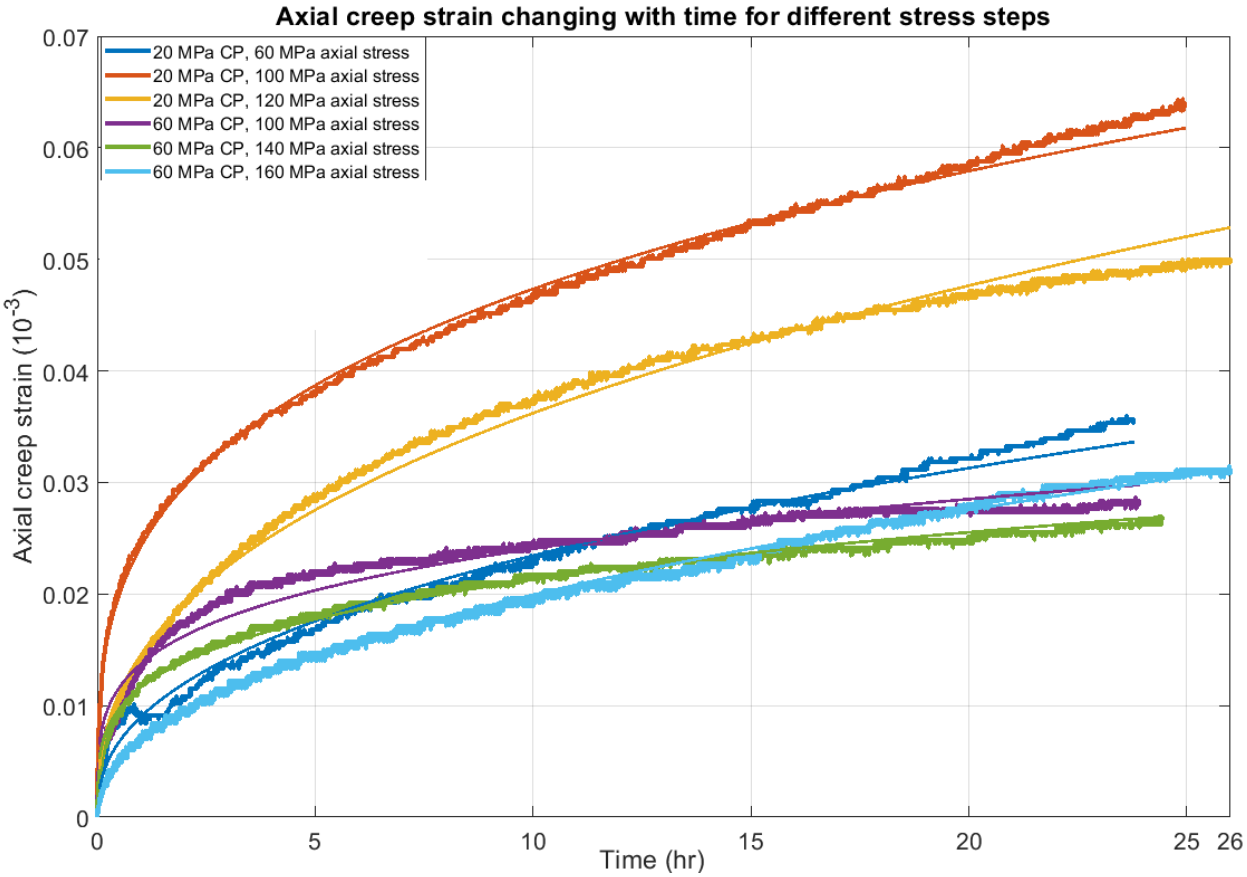

Figure 6.55 Axial creep strain changing with time during different stress steps for specimen 1. For each stress step, at time zero, the axial creep strain was set as zero. The curves with fluctuations are real measurements, and the smooth curves are fitted by the power law. The power law is shown in Eqn. 6.17, and the curve-fitted parameters are summarized in Table 6.20.

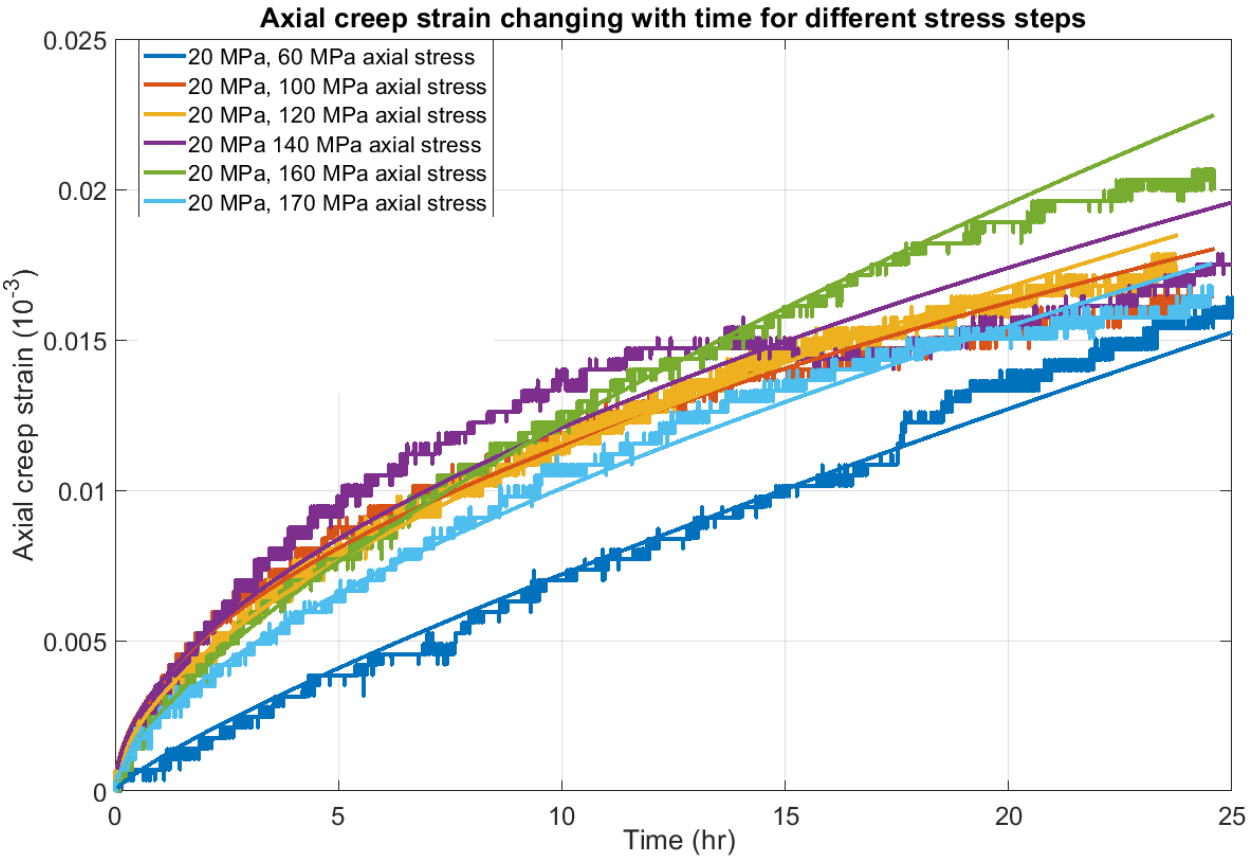

Figure 6.56 Axial creep strain changing with time during different stress steps for specimen 2. For each stress step, at time zero, the axial creep strain was set as zero. The curves with fluctuations are real measurements, and the smooth curves are fitted by the power law. The power law is shown in Eqn. 6.17, and the curve-fitted parameters are summarized in Table 6.21.

Based on Figures 6.55 and 6.56, the power law can reasonably fit the measured creep curves at different stress steps.

The natural log of time law (see Eqn. 6.18) was also tried. Figures 6.57 and 6.58 plot the axial creep strain changing with the natural log of time for specimens 1 and 2, respectively. According to Eqn. 6.18, if the natural log of time law fits the creep curves, the creep strain should change linearly with ln (time) in Figures 6.57 and 6.58. However, as shown by Figures 6.57 and 6.58, the creep strain for different stress steps does not change linearly with the natural log of time. Therefore, the natural log of time law could not reasonably fit the measured creep curves.

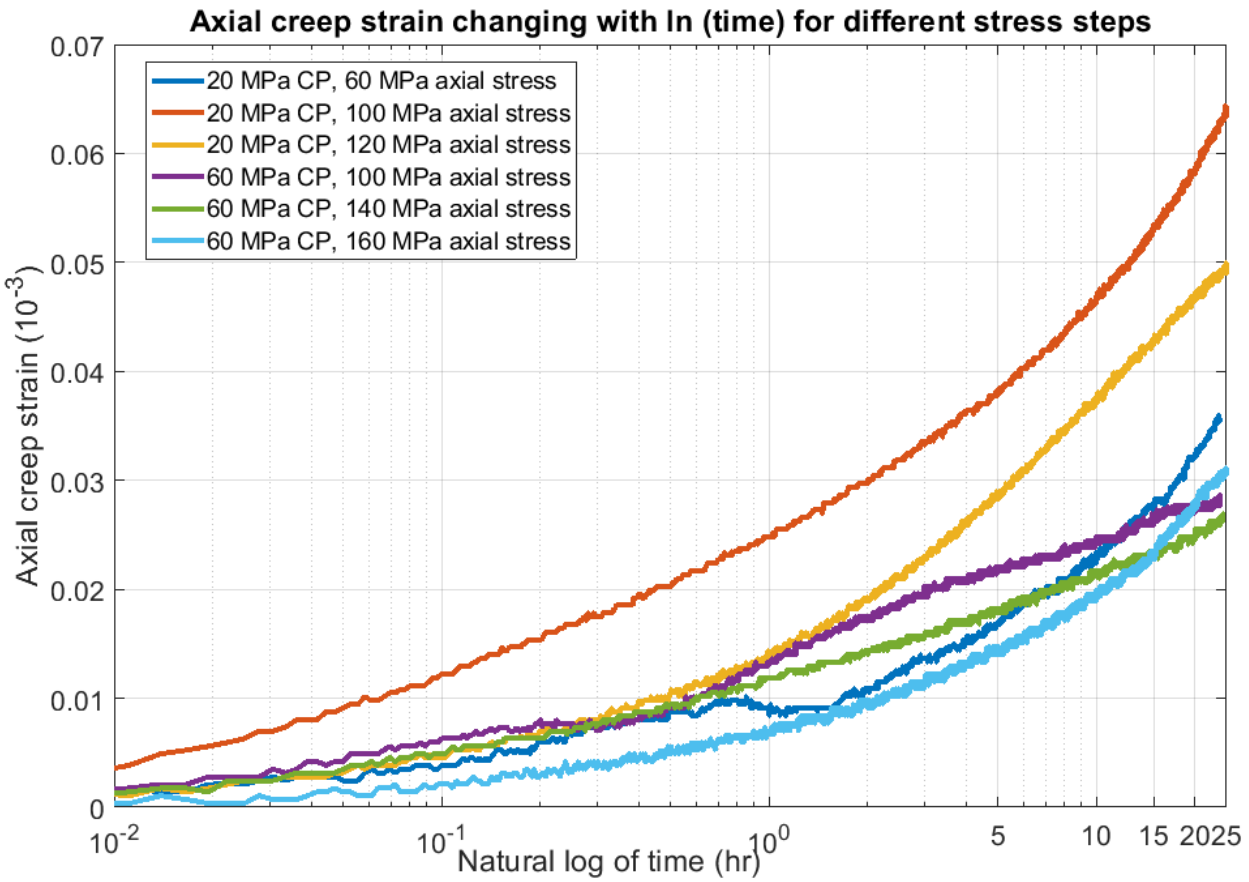

Figure 6.57 Axial creep strain changing with ln (time) during different stress steps for specimen 1. For each stress step, at time zero, the axial creep strain was set as zero. The axial creep strain did not increase linearly with ln (time).

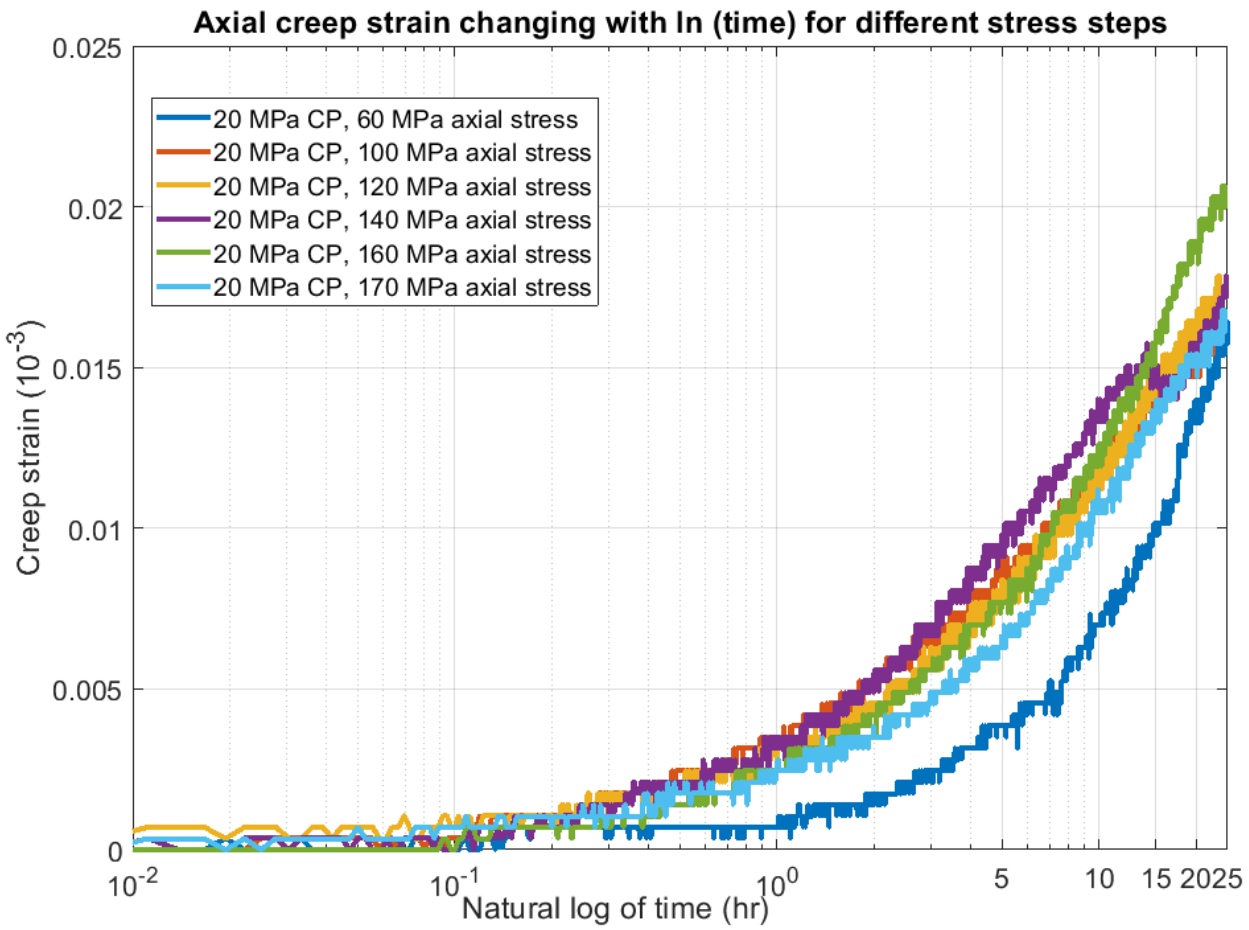

Figure 6.58 Axial creep strain changing with ln (time) during different stress steps for specimen 2. For each stress step, at time zero, the axial creep strain was set as zero. The axial creep strain did not increase linearly with ln (time).

6.6 Comparison of creep patterns in triaxial and indentation tests

6.6.1 Creep pattern comparison

In this section, the creep patterns of triaxial and indentation tests will be compared to show the effect of size on creep behavior. To show the size effect, it is important to keep the time durations for different tests the same. As discussed in Sections 6.3 and 6.4, in indentation tests, the results from 3-min micro-indentation tests, 3-min nano-indentation tests, and 6-hr micro-indentation tests were useful. To compare the creep pattern, the results from 6-hr micro-indentation tests were compared with the results from triaxial creep tests. In triaxial creep tests, the time duration for each stress step was 24 hours. To keep the time durations identical, for each stress step, the results of the first six hours of the triaxial tests were used for comparison.

Figures 6.59 and 6.60 plot the axial strain changing with time for specimens 1 and 2 in triaxial creep tests, respectively. For each stress step, the result from the first six hours is shown.

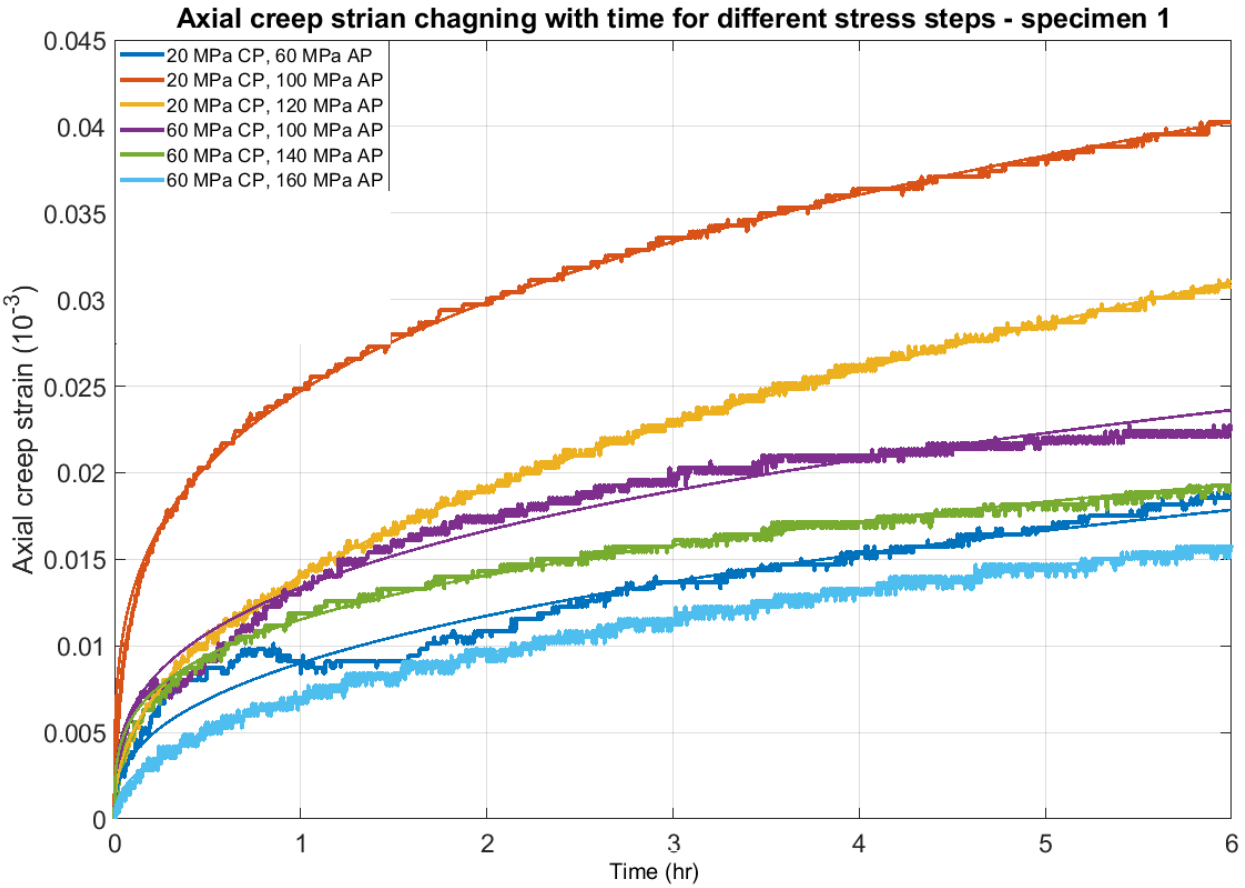

Figure 6.59. Axial creep strain changing with time during different stress steps for specimen 1. For each stress step, at time zero, the axial creep strain was set as zero. The curves with fluctuations are real measurements, and the smooth curves are fitted by the power law (explained in Eqn. 6.17).

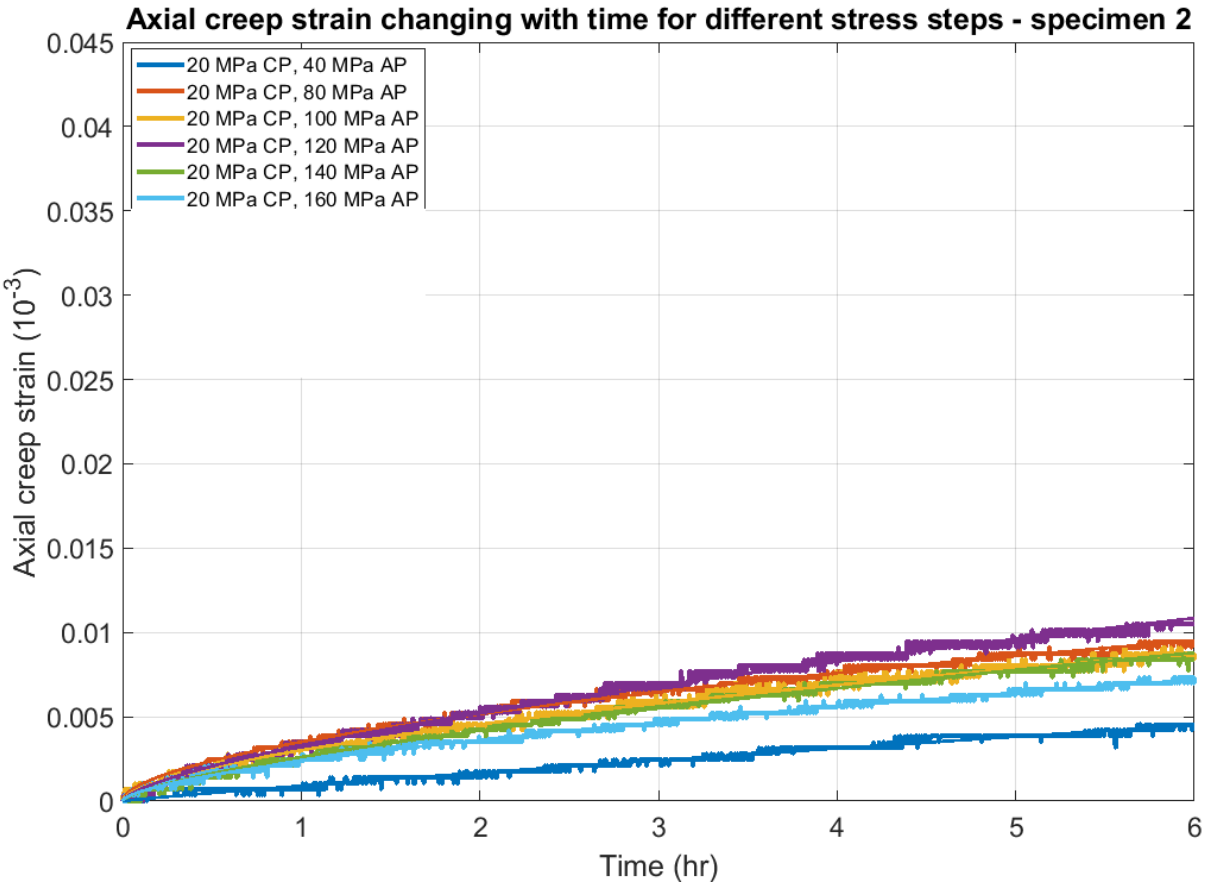

Figure 6.60. Axial creep strain changing with time during different stress steps for specimen 2. For each stress step, at time zero, the axial creep strain was set as zero. The curves with fluctuations are real measurements, and the smooth curves are fitted by the power law (explained in Eqn. 6.17).

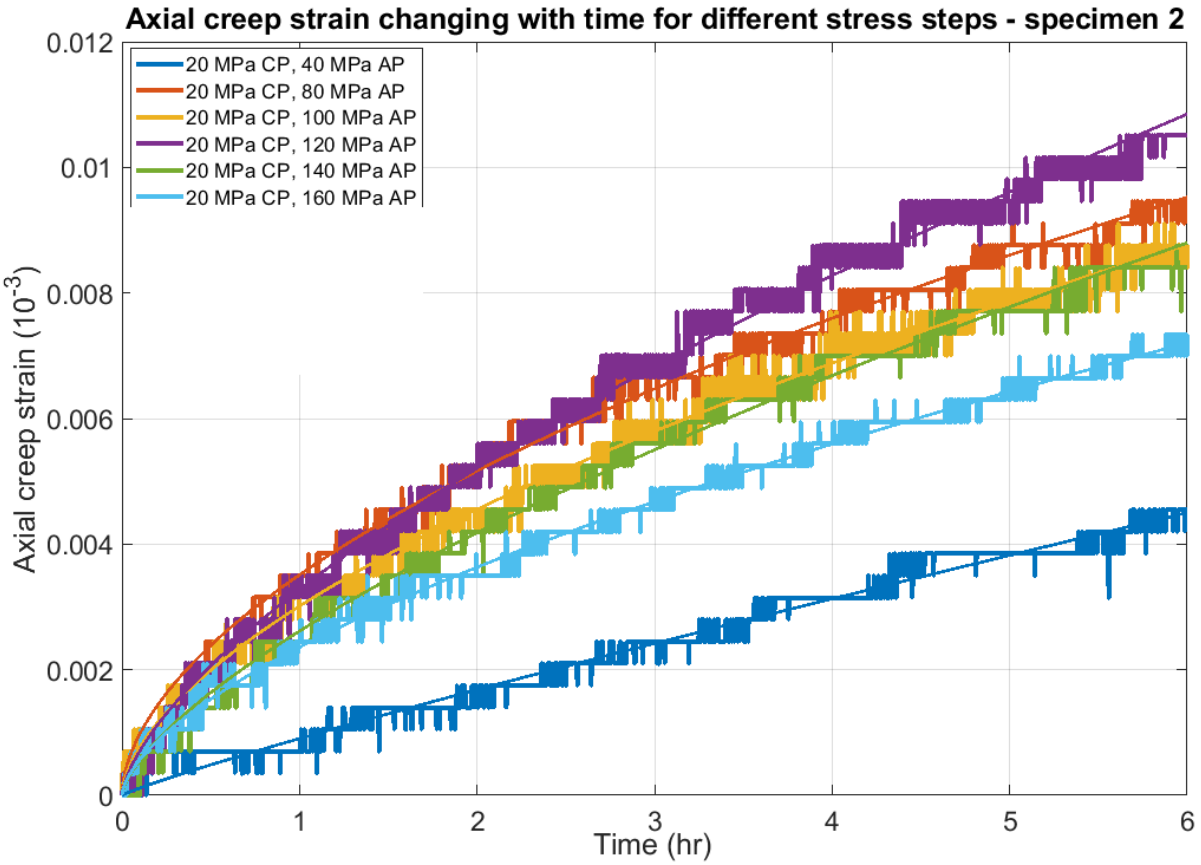

Figure 6.61. Axial creep strain changing with time during different stress steps for specimen 2. For each stress step, at time zero, the axial creep strain was set as zero. The curves with fluctuations are real measurements, and the smooth curves are fitted by the power law (explained in Eqn. 6.17). Compared with Figure 6.57, the scale of the vertical axis is reduced to better illustrate the goodness of curve fitting.

Based on Figures 6.59 and 6.61, the power law can reasonably fit the measured creep curves at different stress steps. The natural log of time law (see Eqn. 6.18) was also tried. Figures 6.62 and 6.63 plot the axial creep strain changing with the natural log of time for specimens 1 and 2, respectively. According to Eqn. 6.18, if the natural log of time law fits the creep curves, the creep strain should change linearly with ln (time) in Figures 6.62 and 6.63. However, as shown by Figures 6.62 and 6.63, the creep strain for different stress steps does not change linearly with ln (time). Therefore, the natural log of time law could not reasonably fit the measured triaxial creep curves.

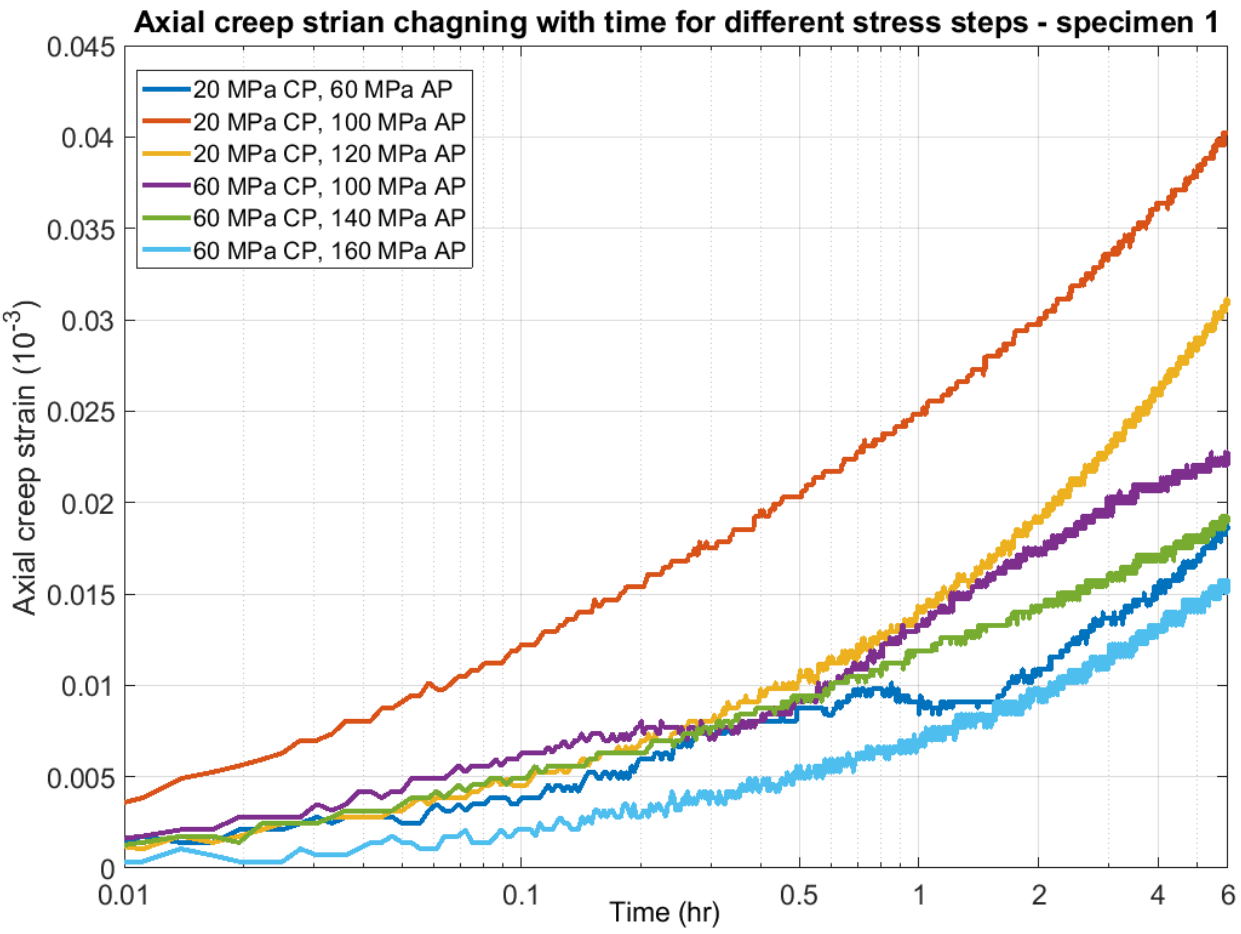

Figure 6.62 Axial creep strain changing with ln (time) during different stress steps for specimen 1. For each stress step, at time zero, the axial creep strain was set as zero. The axial creep strain did not increase linearly with ln (time).

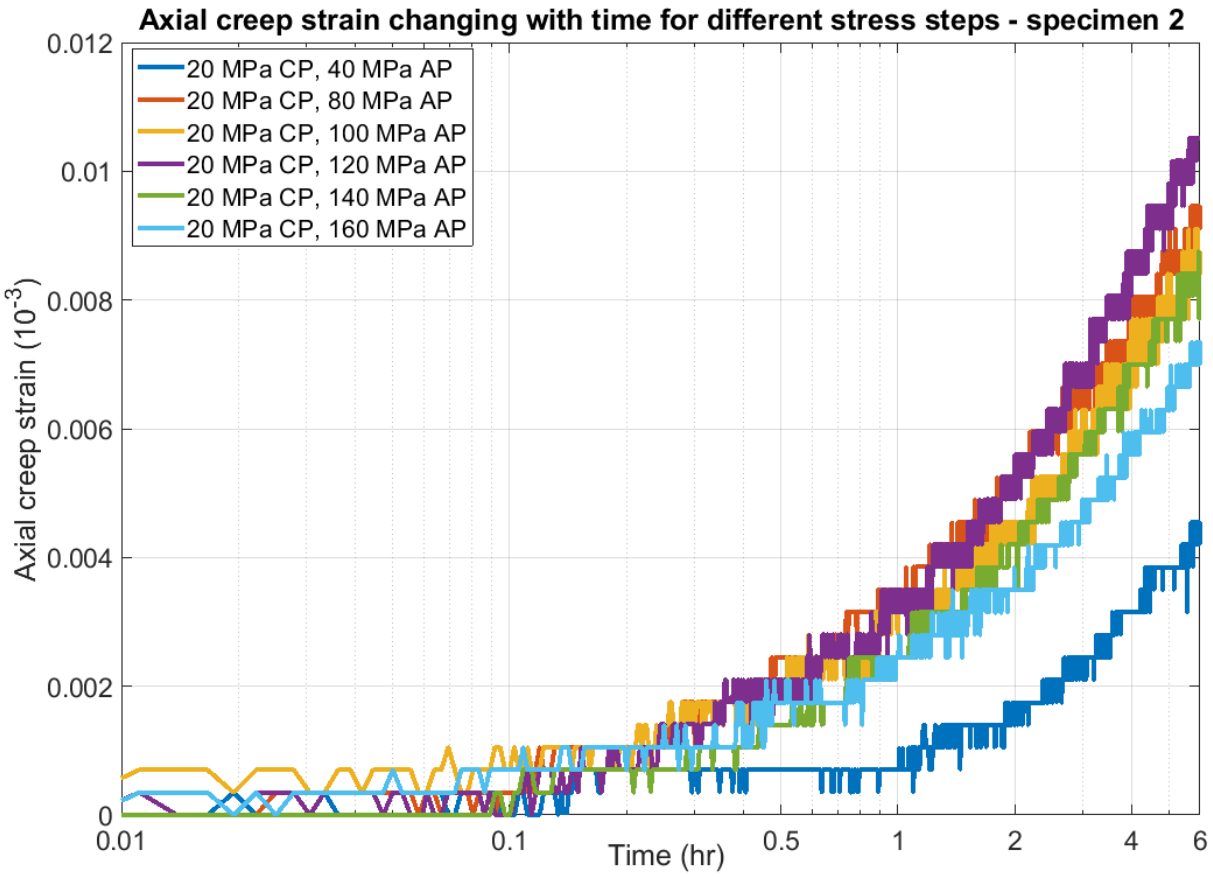

Figure 6.63 Axial creep strain changing with ln (time) during different stress steps for specimen 2. For each stress step, at time zero, the axial creep strain was set as zero. The axial creep strain did not increase linearly with ln (time).

Figures 6.64 and 6.65 plot the indentation creep depth Δh changing with the natural log of time for the first and second series of 6-hr micro-indentation tests, respectively. According to Eqn. 6.18, if the natural log of time law fits the creep curves, the creep strain should change linearly with ln (time) in Figures 6.64 and 6.65. As shown by Figures 6.64 and 6.65, the indentation creep depth Δh for different indents changes quite linearly with ln (time). Therefore, the natural log of time law reasonably fits the measured indentation creep curves.

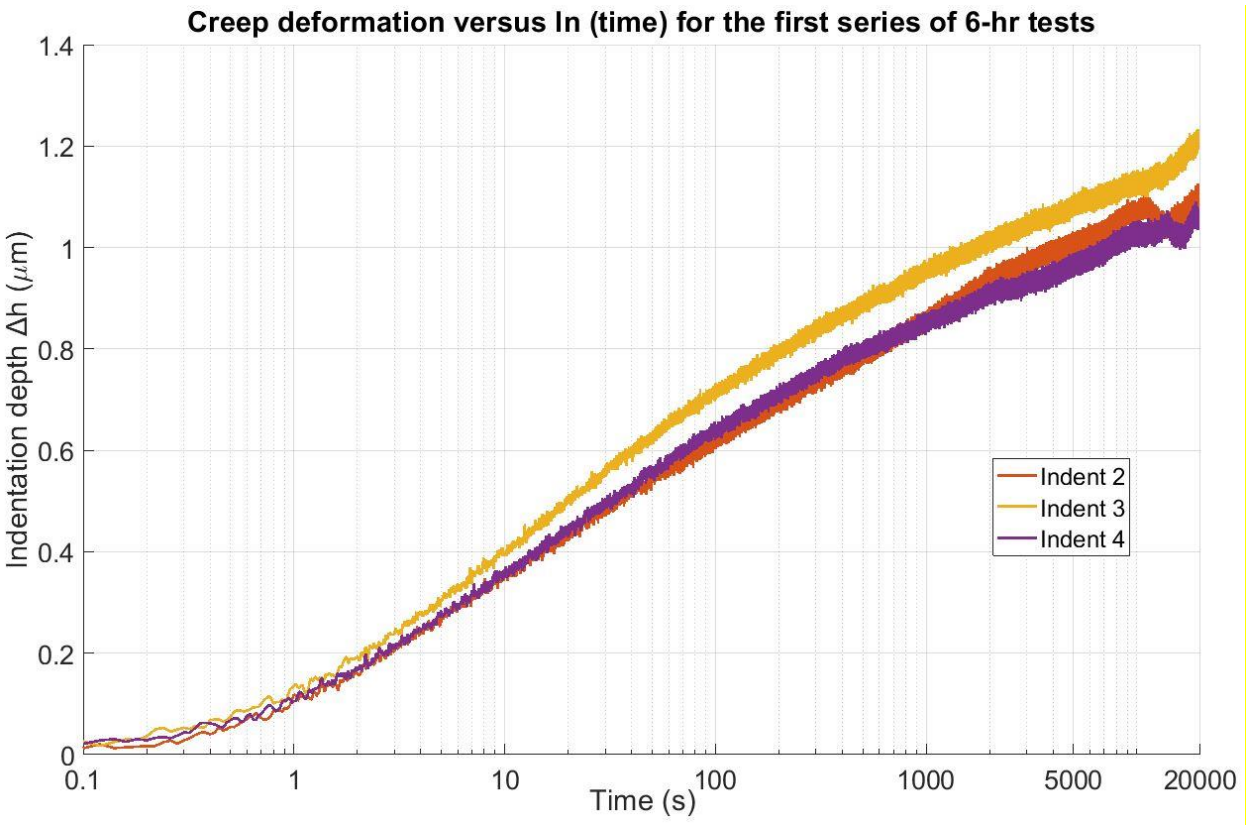

Figure 6.64 Indentation creep depth Δh changing with ln (time) for the first series of 6-hr micro-indentation tests. The creep depth Δh increases linearly with ln (time).

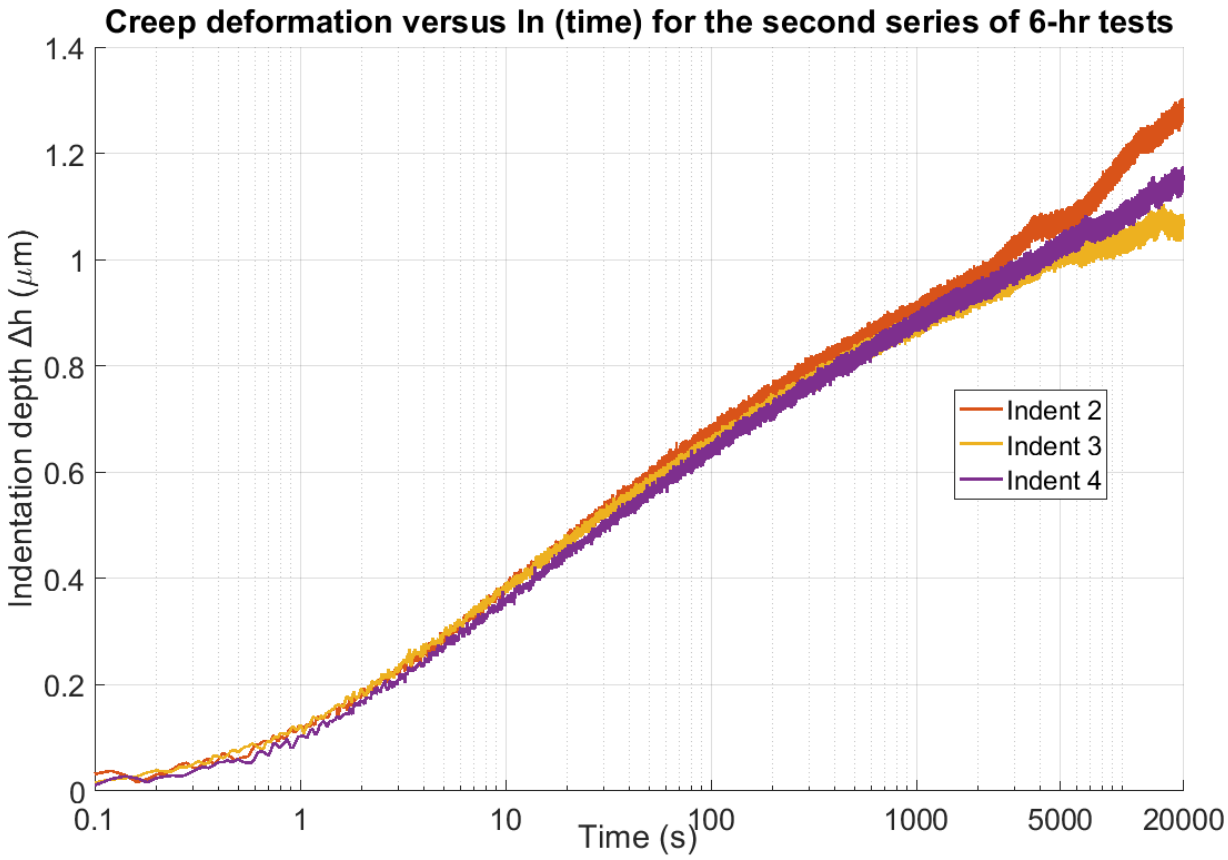

Figure 6.65 Indentation creep depth Δh changing with ln (time) for the second series of 6-hr micro-indentation tests. The creep depth Δh increases linearly with ln (time).

Based on Figures 6.62 and 6.63, for triaxial creep tests, the natural log of time law does not fit the creep curves well. In contrast, according to Figures 6.64 and 6.65, for 6-hr micro-indentation tests, the natural log of time law fits the creep curves reasonably well. Thus, the creep patterns between triaxial and 6-hr micro-indentation creep tests are different. The possible reasons for different patterns will be explained in Section 6.6.2.

6.6.2 Possible explanations for the differences

The specimen scales and stress conditions between triaxial and indentation creep tests are different. Table 6.22 summarizes the differences in specimen scales and stress conditions.

Table 6.22 Differences in specimen scales, stress conditions, and time durations.

Test type	Specimen scale	Stress condition
Triaxial creep (each axial stress step)	50.4 mm in diameter	Uniform, at MPa level
Micro-indentation	80 μm in indentation diameter	Non-uniform, at GPa level beneath the indenter

Nano-indentation	2.1 μm in indentation diameter	Non-uniform, at GPa level beneath the indenter

Based on Table 6.22, the specimen scales and stress conditions of indentation and triaxial creep tests are different. The differences in scales and stress conditions may cause different creep patterns. In this section, the difference in stress conditions will be further explained.

Figures 6.66 (a) and (b) plot the vertical stress distribution and von Mises stress distribution beneath the indenter, respectively, at the end of the loading stage in micro-indentation tests. The stress distribution in micro-indentation tests cannot be measured; it can only be obtained via numerical simulation. As shown in Figure 6.66 (a), the vertical stress beneath the indenter exceeds 1 GPa, and the stress distribution is non-uniform. According to Figure 6.66 (b), the von Mises stress beneath the indenter exceeds 500 MPa, and the stress distribution is non-uniform. In contrast, the axial stress of triaxial tests (see the stress steps in Figures 6.46 and 6.49) does not exceed 160 MPa, and the stress distribution is uniform. Different stress states between triaxial and indentation creep tests may partially explain the different creep patterns.

(a):

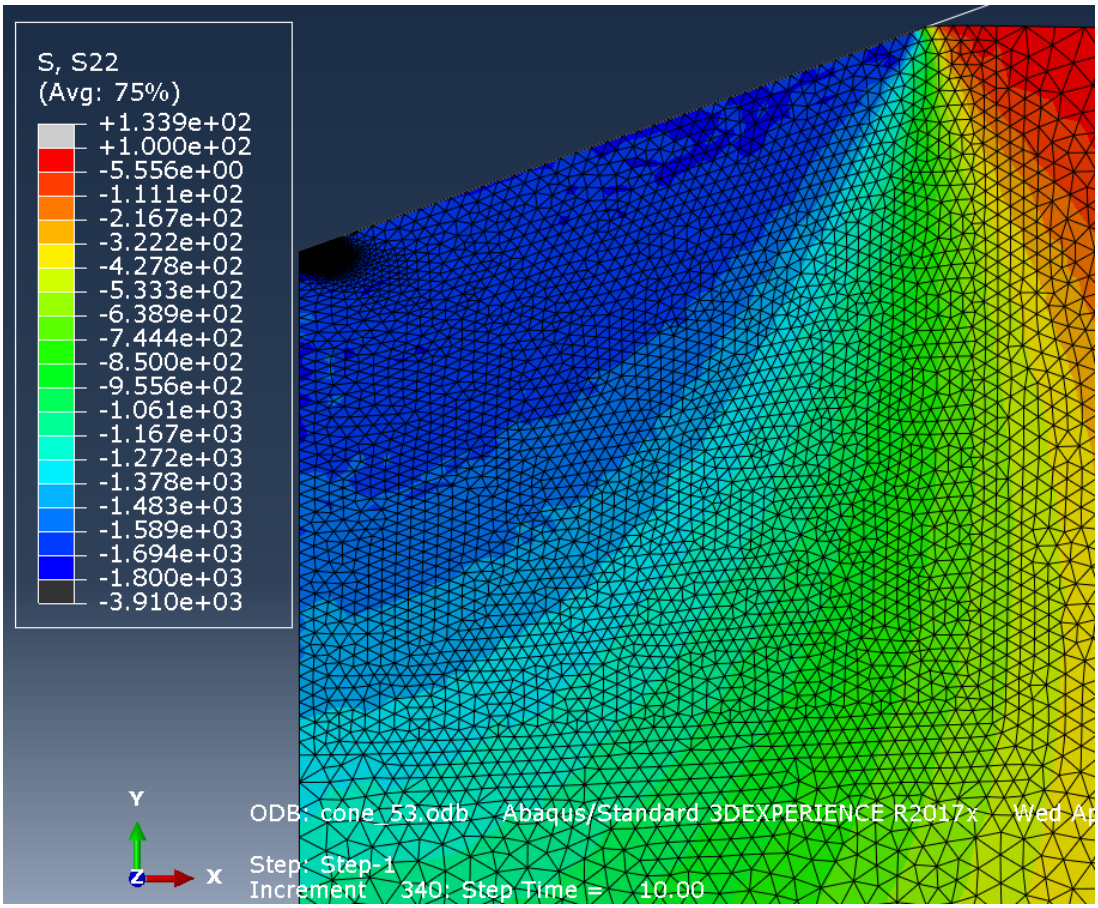

(b):

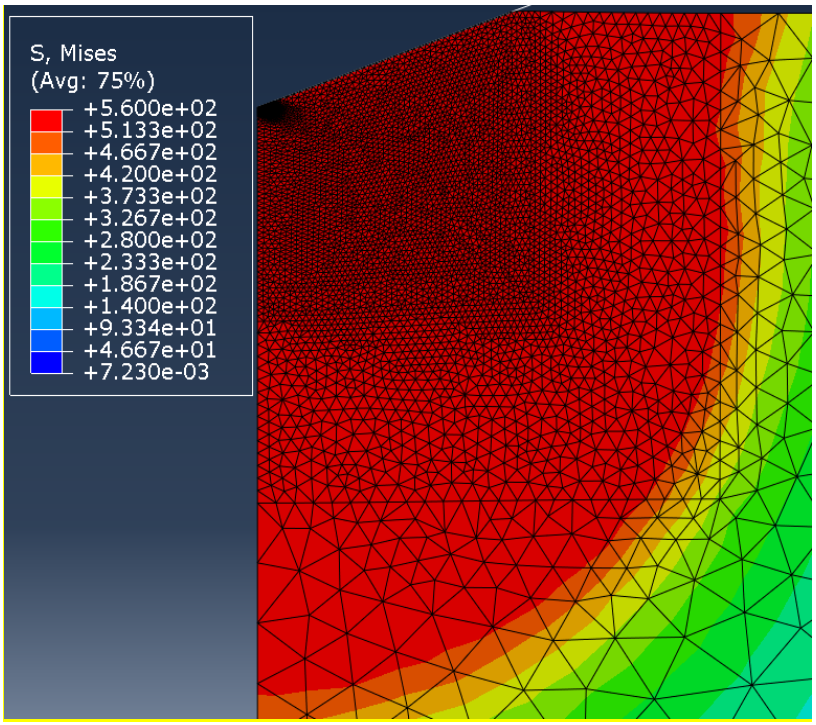

Figure 6.66 Stress distribution beneath the indenter. The unit is MPa. (a): Vertical stress distribution beneath the indenter. The vertical direction is shown by the 'Y' axis in the bottom left of the figure. In ABAQUS, tension is defined as positive. (b): Von Mises stress distribution beneath the indenter. The maximum von Mises stress is 560 MPa, which corresponds to the red color.

In addition, triaxial creep tests were conducted on only two specimens. To obtain more reliable conclusions, more triaxial creep tests should be conducted.

6.7 Conclusions and future recommendations

6.7.1 Summary and conclusions

In this research, the mechanical properties of Musandam limestone were measured. Rock fracture deformation and flow tests, micro-indentation tests, nano-indentation tests, and triaxial creep tests were conducted on Musandam limestone. Based on the testing results, the following main conclusions can be drawn:

1) When the confining pressure is less than 100 MPa, a linear Coulomb envelope can be used to describe the yield strength of Musandam limestone. The cohesion is 18 MPa and the friction angle is 39˚.

2) For Musandam limestone fractures, the effect of mechanical compression on fracture creep behavior is significant.

3) In 3-min micro- and nano-indentation tests, for indentation hardness H, the average and standard deviation from nano-indentation tests are larger than those from micro-indentation tests; for indentation creep modulus C, the average and standard deviation from nano-indentation tests are larger than those from micro-indentation tests; for indentation modulus M, the average of micro- and nano-indentation tests are similar, but the standard deviation from nano-indentation tests is larger than that from micro-indentation tests.

4) For micro-indentation, the 6-hr creep deformation will be overestimated if it is predicted from the 3-min creep deformation. Practically, to obtain the micro-indentation creep behavior for a specific time duration, creep tests at the specific time duration need to be conducted; it may not be accurate to use short-term micro-indentation creep behavior to predict long-term micro-indentation creep behavior.

5) Due to machine drifting, the 6-hr nano-indentation creep deformation could not be accurately measured. Before measuring the long-term nano-indentation creep behavior, the machine drifting problem needs to be solved.

6) The creep patterns between triaxial and indentation creep are different. The indentation creep curves followed the natural log of time law, while the triaxial creep curves did not follow it. The difference can be explained by different stress conditions.

6.7.2 Future experiments recommendations

While the results are very informative, future work would be beneficial. Specifically:

1) To address (1) in Section 6.7.1, triaxial tests could be conducted at confining pressures greater than 100 MPa to obtain the strength properties under confining pressures greater than 100 MPa.

2) To address (3) in Section 6.7.1, the SEM technique could be used to measure the grain size. The difference in H, M, and C between 3-min micro- and nano-indentation tests may be partially explained by the size difference.

3) To address (5) in Section 6.7.1, the 6-hr machine drifting should be measured.

4) To address (6) in Section 6.7.1, more triaxial creep tests could be conducted on intact rock specimens to obtain a better understanding of the triaxial creep patterns. However, triaxial creep and indentation creep differ in specimen scales and stress conditions. To link the different creep patterns between triaxial and indentation creep, theoretical or numerical work is required.

7. Comparison of numerical and experimental results

This short chapter compares the numerical simulation and experimental results of fracture creep under dry conditions. The numerical and experimental results will be compared in Section 7.1, followed by discussions in Section 7.2.

7.1 Comparison of numerical and experimental results

In this research, only one fracture creep deformation test under dry conditions has been conducted. The fracture creep deformation test results are compared with numerical simulation results. Figure 7.1 shows the flowchart of what is presented in this section.

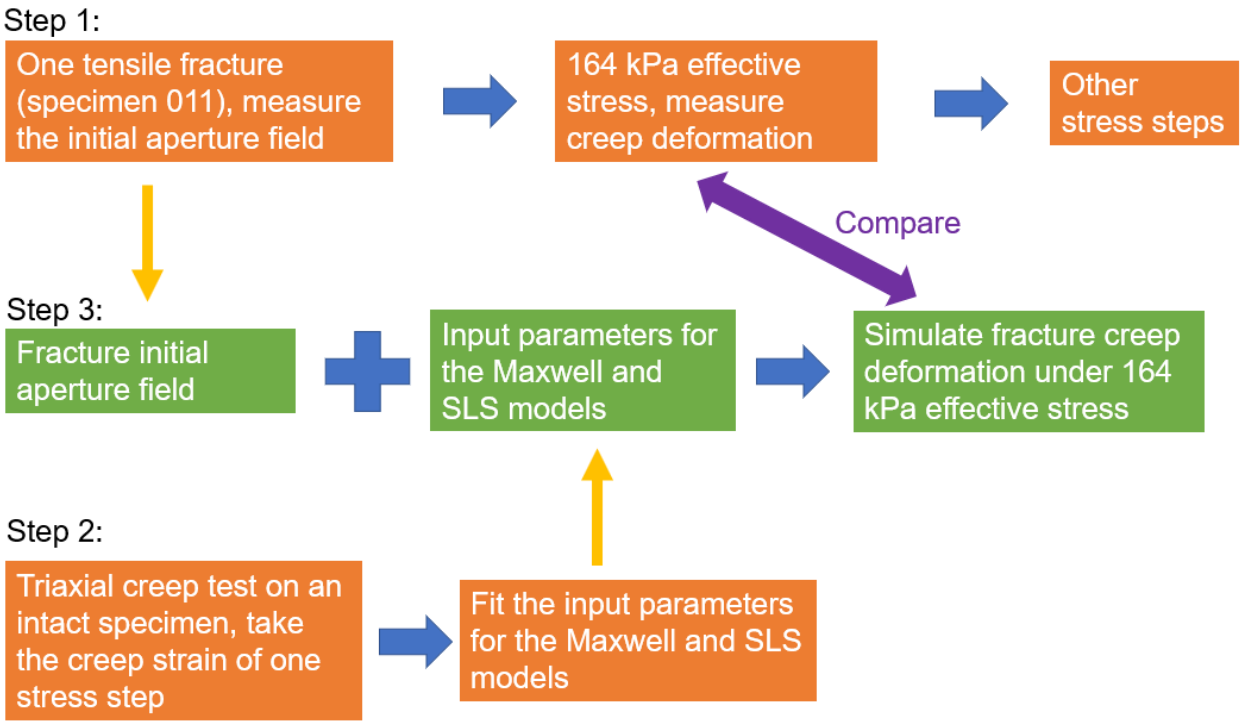

Figure 7.1 Flowchart of what is presented in this section. The orange and green boxes correspond to experimental and numerical work, respectively. The yellow arrows show the experimental steps, which provide input parameters for numerical simulation. The purple arrow illustrates the comparison between numerical and experimental results.

As shown in Figure 7.1, the work in this section can be summarized in three steps.

Step 1: in this step, one Musandam limestone tensile fracture (specimen 011) is created, and the initial aperture field is measured. Then, multiple stress steps are applied to the fracture specimen under dry conditions, and the creep deformation is measured. The effective stress steps are: 164 kPa (loading) → 364 kPa (loading) → 564 kPa (loading) → 364 kPa (unloading) → 164 kPa (unloading). Section 6.4 shows the details of the experimental results. The creep deformation

measured in the first stress step (164 kPa effective stress, loading) is used for comparison with numerically simulated fracture visco-elastic deformation.

Step 2: in this step, triaxial creep tests are conducted on intact Musandam limestone specimens. The input parameters for the Maxwell and Standard Linear Solid (SLS) models are fitted to the creep strain of one stress step. Steps 1 and 2 are not related; the purpose of step 2 is to provide input parameters for the Maxwell and SLS models.

Step 3: in this step, the fracture creep is simulated numerically and compared with the measured creep. As described in Section 3.3, two input components are required to simulate visco-elastic deformation of rough fractures: the fracture aperture field, and the input parameters for visco-elastic constitutive models (i.e. the Maxwell model, the SLS model). The fracture aperture field is obtained in step 1, and the input parameters for visco-elastic constitutive models are obtained in step 2.

The details of steps 1 and 2 are explained in Sections 7.1.1 and 7.1.2, respectively. The results of step 3 are shown in Section 7.1.3.

7.1.1 Step 1: fracture creep experiment

In this research, only one fracture creep deformation test under dry conditions has been conducted. The fracture is a tensile fracture created on Musandam limestone, and the specimen preparation steps have been shown from Figures 5.5 to 5.8 in Section 5.2. The fracture creep test is conducted using the low-pressure triaxial system, and the schematic of the triaxial system is shown in Figure 5.9 in Section 5.2. Before the test, the fracture surface profiles are measured by a profilometer. Based on the measured fracture surface profiles, the aperture field before the experiment can be calculated. Figure 7.2 shows the aperture field before the test. The mean aperture and the standard deviation values are 86.73 μm and 16.11 μm, respectively.

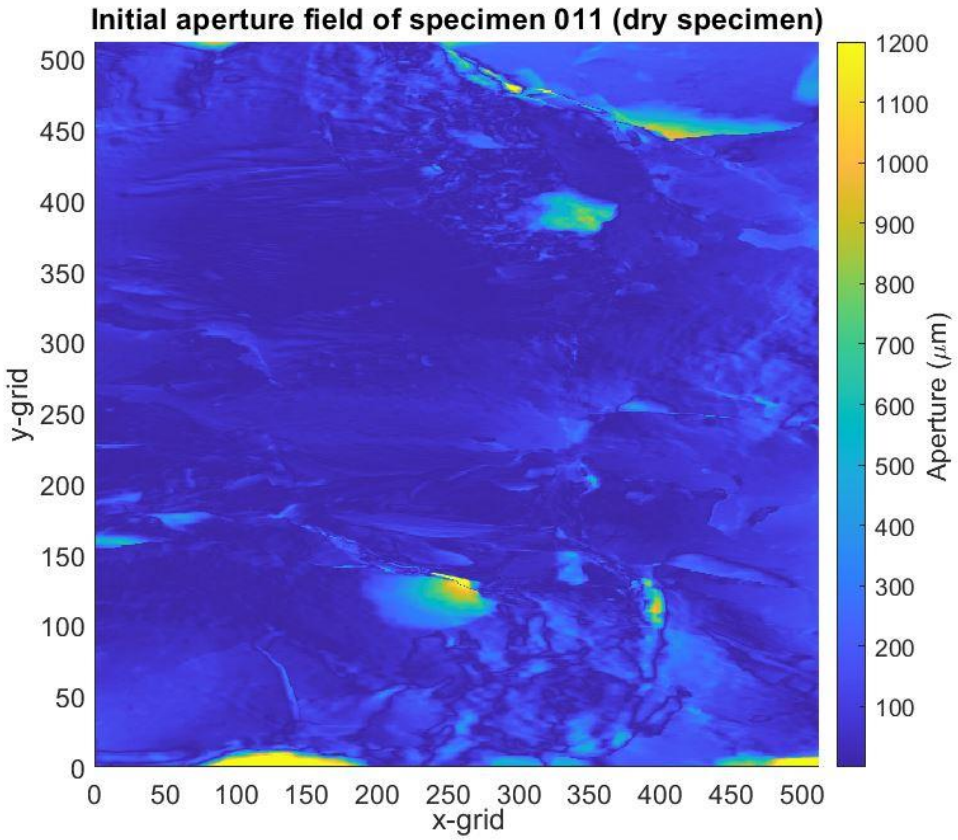

Figure 7.2 Aperture field before the stress step. The number of grids in the x- and y- direction is 512. The unit of the aperture is μm.

During the creep test, the fractured specimen is under uniform stress ($\sigma_1 = \sigma_2 = \sigma_3 = 164$ kPa), and the fracture closure is measured by proximity sensors (see Figure 5.9 for a schematic). The stresses are held for 24 hours. The measured fracture closure changing with time will be plotted later (when compared with numerical results). At the end of this stress step, the fractured specimen is not removed from the triaxial cell for surface scanning. Instead, new stress steps are applied to the specimen. Therefore, only the initial aperture field before the stress step can be obtained.

7.1.2 Step 2: Obtaining the input parameters from triaxial creep tests

In this research, the numerical code uses the Maxwell model and the Standard Linear Solid (SLS) model as visco-elastic constitutive models. The input parameters for the two models (component (ii)) are obtained using curve fitting against triaxial test results on intact rock specimens.

Before showing the curve fitting results, it is important to briefly review the two models. Both visco-elastic models have been explained in detail in Sections 2.1.3.2 and 3.4. Figures 7.3 (a) and (b) show the schematic for the Maxwell and SLS model, respectively.

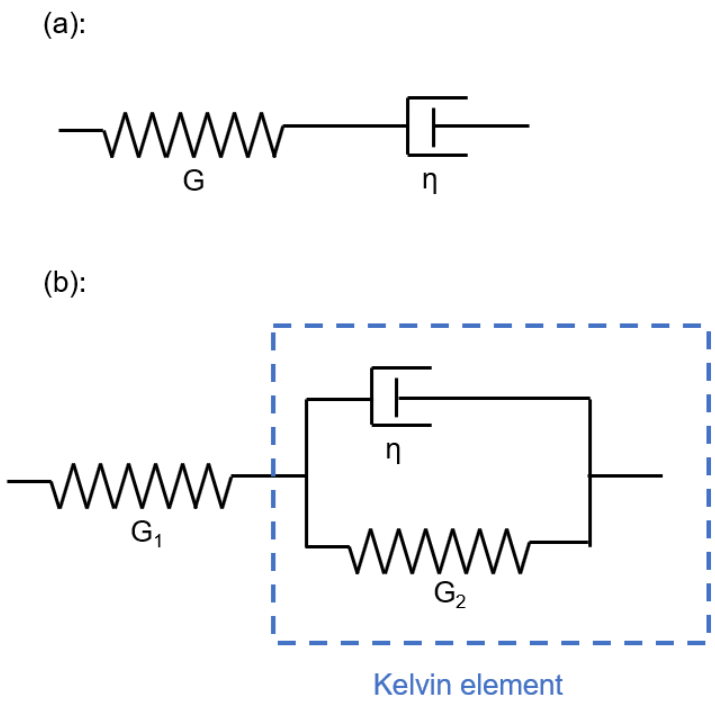

Figure 7.3 (a): Schematic of the Maxwell model; (b): Schematic of the SLS model.

The Maxwell model consists of a spring and a dashpot in series. The spring represents elasticity, with a shear modulus of G; and the dashpot represents viscosity, with a viscosity of η (unit: time * pressure). Under constant differential stress (axial stress – confining pressure) σ_0, the strain can be expressed as:

$$\varepsilon_{total} = \varepsilon_{elas} + \varepsilon_{time} \tag{7.1}$$

$$\varepsilon_{elas} = \sigma_0\left(\frac{1}{G}\right) \tag{7.2}$$

$$\varepsilon_{time} = \sigma_0\left(\frac{t}{\eta}\right) \tag{7.3}$$

where ε_{total} is the total strain, ε_{elas} is the elastic strain (occurs instantaneously when the stress σ_0 is applied and is not time-dependent), ε_{time} is the time-dependent strain, and t is the time. The elastic strain corresponds to the strain of the spring, and the time-dependent strain corresponds to the strain of the dashpot. For the elastic strain calculation, the shear modulus G and Poisson's ratio υ values are obtained from triaxial strength tests. Table 6.4 summarizes the elastic properties obtained from triaxial strength tests. The elastic properties measured under 100 MPa confining pressure are used: the shear modulus G_1 is 26.15 GPa and the Poisson's ratio υ is 0.30. For the time-dependent strain calculation, the viscosity η is obtained from triaxial creep tests. Eqn. 7.3 is fitted to measured data (strain vs. time plot), and η is determined by curve fitting.

The SLS model consists of a spring and a Kelvin element in series. The Kelvin element has a shear modulus of G_2, and a viscosity of η (unit: time * pressure); and the spring has a shear modulus of

G_1. The Kelvin element represents time-dependent deformation, while the spring represents instantaneous elastic deformation. Under constant differential stress (axial stress – confining pressure) σ_0, the strain can be related to σ_0 as:

$$\varepsilon_{total} = \varepsilon_{elas} + \varepsilon_{time} \tag{7.4}$$

$$\varepsilon_{elas} = \sigma_0\left(\frac{1}{G_1}\right) \tag{7.5}$$

$$\varepsilon_{time} = \sigma_0\left(\frac{1-e^{-\frac{tG_2}{\eta}}}{G_2}\right) \tag{7.6}$$

where ε_{total} is the total strain, ε_{elas} is the elastic strain (occurs instantaneously when the stress σ_0 is applied and is not time-dependent), ε_{time} is the time-dependent strain, and t is the time. The elastic strain corresponds to the strain of the spring, and the time-dependent strain corresponds to the strain of the Kelvin element. For the elastic strain calculation, the shear modulus G_1 and Poisson's ratio υ values are obtained from triaxial strength tests. Table 6.4 summarizes the elastic properties obtained from triaxial strength tests. The elastic properties measured under 100 MPa confining pressure are used: the shear modulus G_1 is 26.15 GPa and the Poisson's ratio υ is 0.30. For the time-dependent strain calculation, the parameters for the Kelvin element (η and G_2) are obtained from triaxial creep tests. Eqn. 7.6 is fitted to measured data (strain vs. time plot), and G_2 and η are determined by curve fitting.

As described in Section 6.5, triaxial creep tests are conducted on two intact Musandam limestone specimens. Figures 7.4 and 7.5 show the stress steps for specimens 1 and 2, respectively. The data from the stress step of 60 MPa confining pressure (CP) and 160 MPa axial pressure (AP) of specimen 1 is chosen to fit the visco-elastic models, because the axial stress of this stress step is the largest. The above-mentioned stress step is shown by the green box in Figure 7.4.

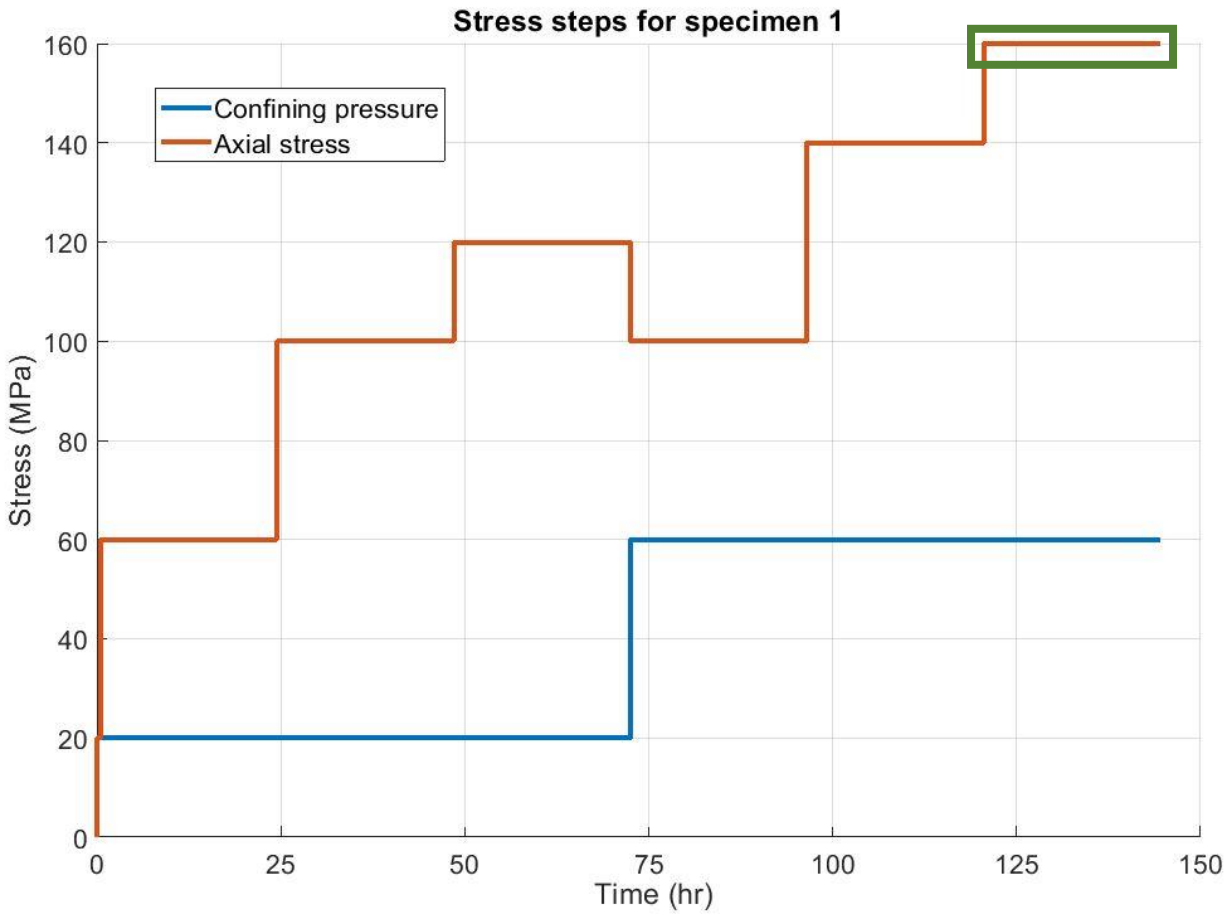

Figure 7.4 Stress steps for specimen 1 (no fracture, intact specimen) in triaxial creep tests.

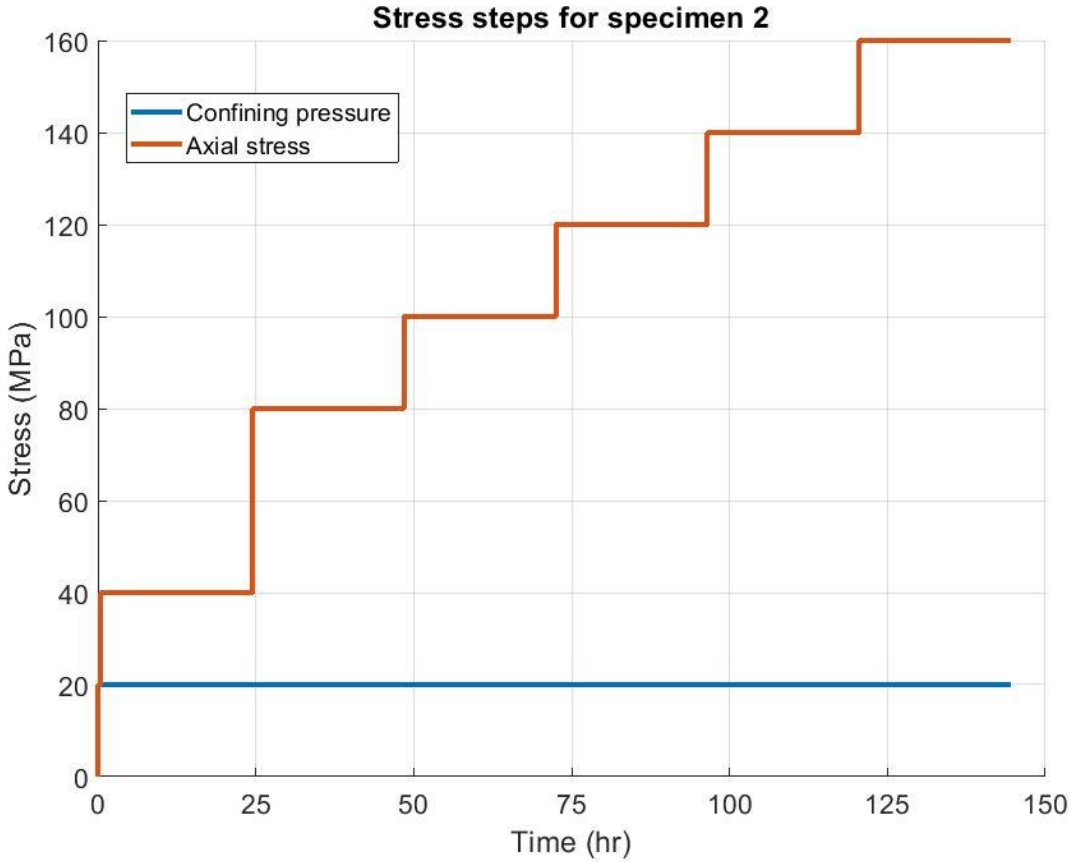

Figure 7.5 Stress steps for specimen 2 (no fracture, intact specimen) in triaxial creep tests.

Figure 7.6 plots the measured creep strain changing with time for the 60 MPa CP, 160 MPa AP stress step. For the Maxwell model, Eqn. 7.3 is fitted to the measured curve by the least square method. The viscosity parameter η is obtained by curve fitting. For the SLS model, Eqn. 7.6 is fitted to the measured curve by the least square method. The parameters of the Kelvin element, G_2 and η, are obtained by curve fitting.

The curves fitted from the Maxwell and SLS models are also plotted in Figure 7.6. In addition, the input parameters (fitted from the measured curve) for the Maxwell and SLS models are summarized in Tables 7.1 and 7.2, respectively.

Table 7.1. Input parameters for the Maxwell model (η is obtained from the measured creep curve)

Parameters	Value
Shear modulus, G_1 (GPa)	26.15
Poisson's ratio, υ	0.30
Viscosity, η (GPa*s)	2.41×10^8
Relaxation time, $\tau = \eta / G$ (s)	9.230×10^6
R^2 in the curve fitting	0.601

Table 7.2. Input parameters for the SLS model (G_2 and η are obtained from the measured creep curve)

Parameters	Value
Shear modulus, G_1 (GPa)	26.15
Poisson's ratio, υ	0.30
Shear modulus, G_2 (GPa)	3.23
Viscosity, η (GPa*s)	1.05×10^8
Relaxation time, $\tau = \eta / G_2$ (s)	4.016×10^6
R^2 in the curve fitting	0.943

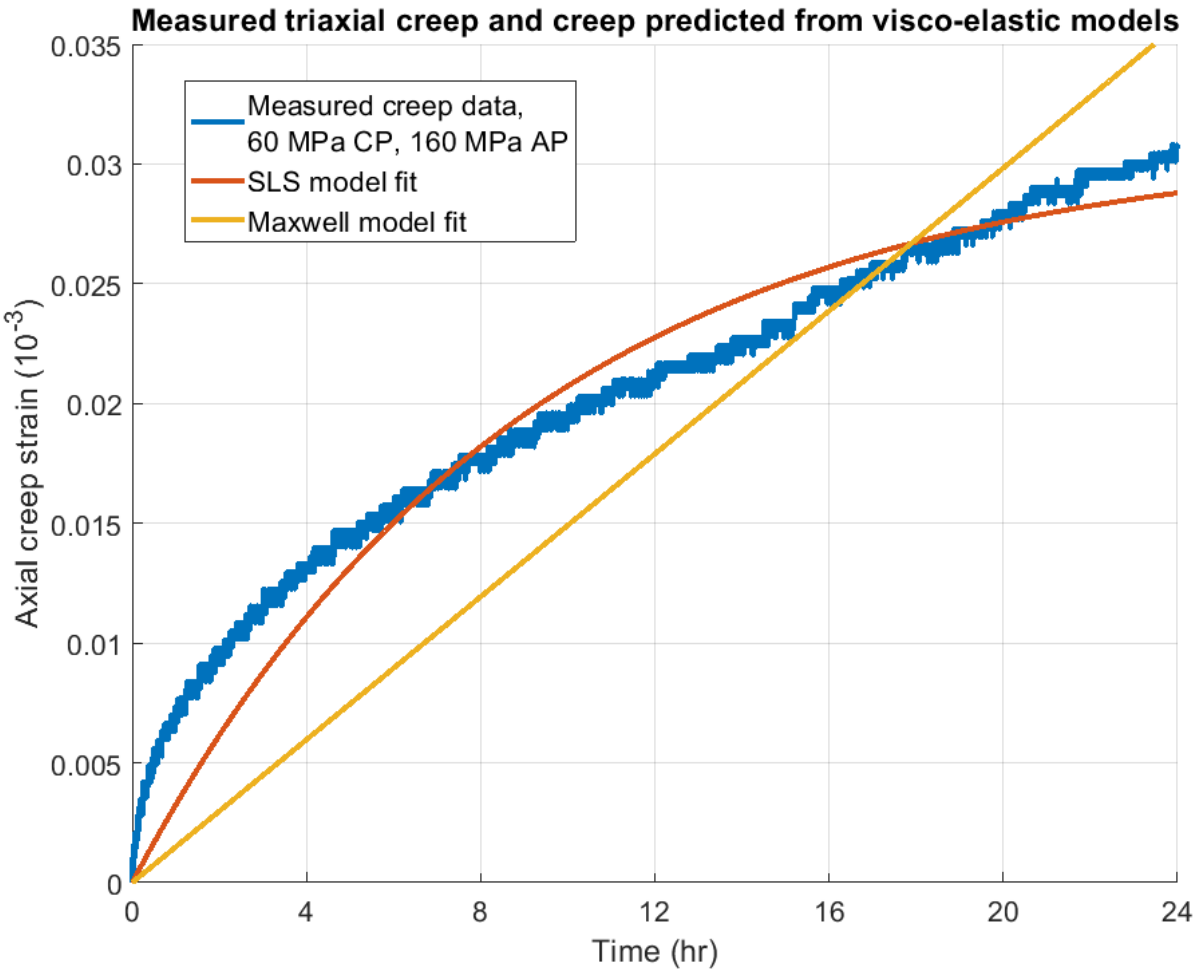

Figure 7.6 Comparison between the measured creep curve and the curves fitted from the Maxwell and SLS models. The experiment is a triaxial creep test on an intact Musandam limestone specimen, and the stress step is shown by the green box in Figure 7.4. For the measured creep curve, at time zero, the creep strain is set as zero.

7.1.3 Step 3: Comparison of numerical and experimental results – fracture creep

As shown in Figure 7.1, to simulate visco-elastic deformation of rough fractures, two input components are required: the fracture aperture field, and the parameters for visco-elastic constitutive models. For the Maxwell model, the aperture field (shown in Figure 7.2) and the parameters shown in Table 7.1 are used as the input components; for the SLS model, the aperture field (shown in Figure 7.2) and the parameters shown in Table 7.2 are used as the input components. The visco-elastic deformation changing with time is calculated by the numerical code, and the numerically simulated visco-elastic deformation is compared with the measured fracture creep deformation in Figure 7.7. Figure 7.8 plots the same results as Figure 7.7; in Figure 7.8, the scales of the vertical axes are identical.

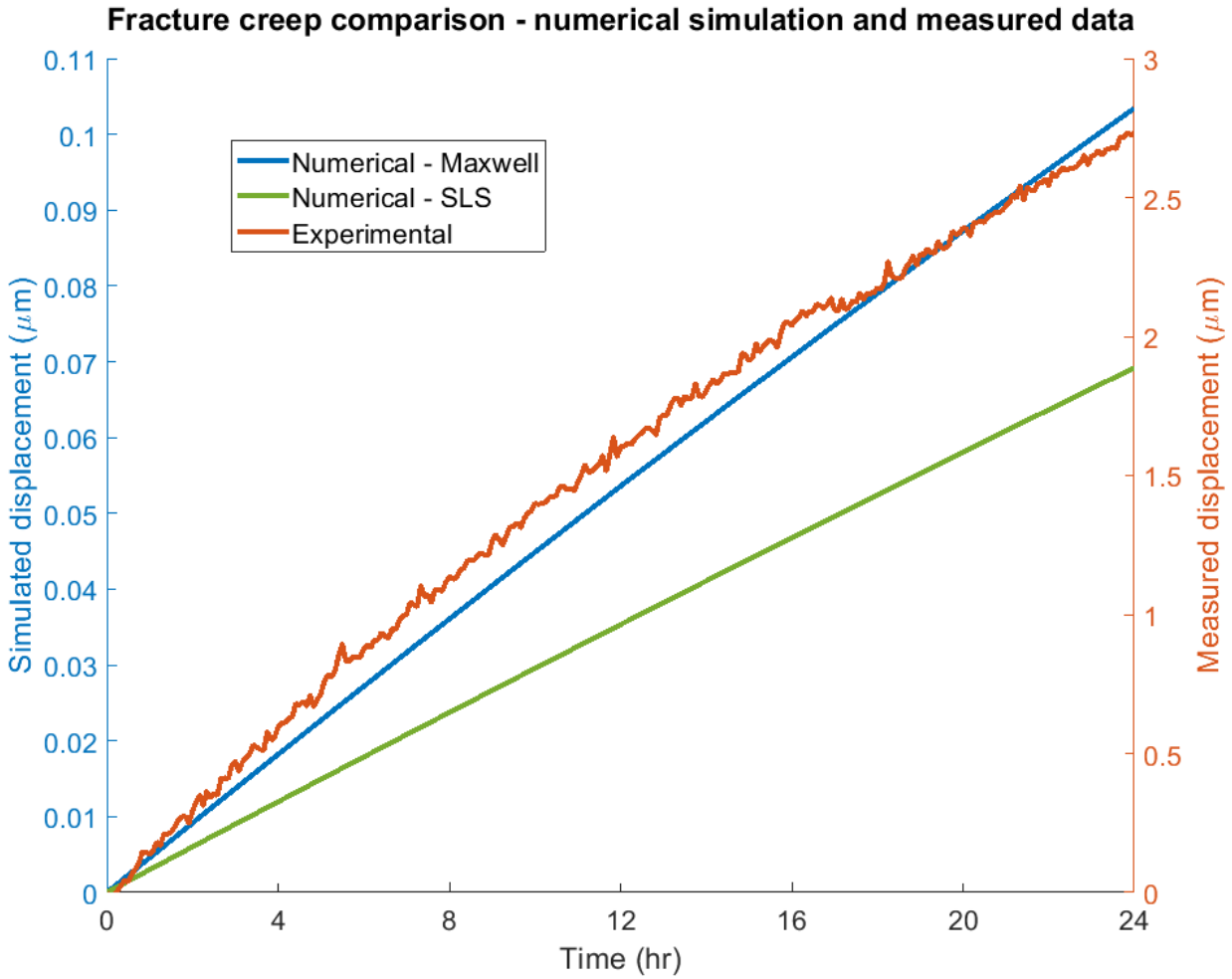

Figure 7.7 Comparison of numerically simulated visco-elastic displacements and measured creep displacement. The experiment is a creep test on a rock fracture (see the details in Section 7.1.1). The red curve represents the experimental results, and the blue and green curves represent the results of Maxwell model simulation and SLS model simulation, respectively.

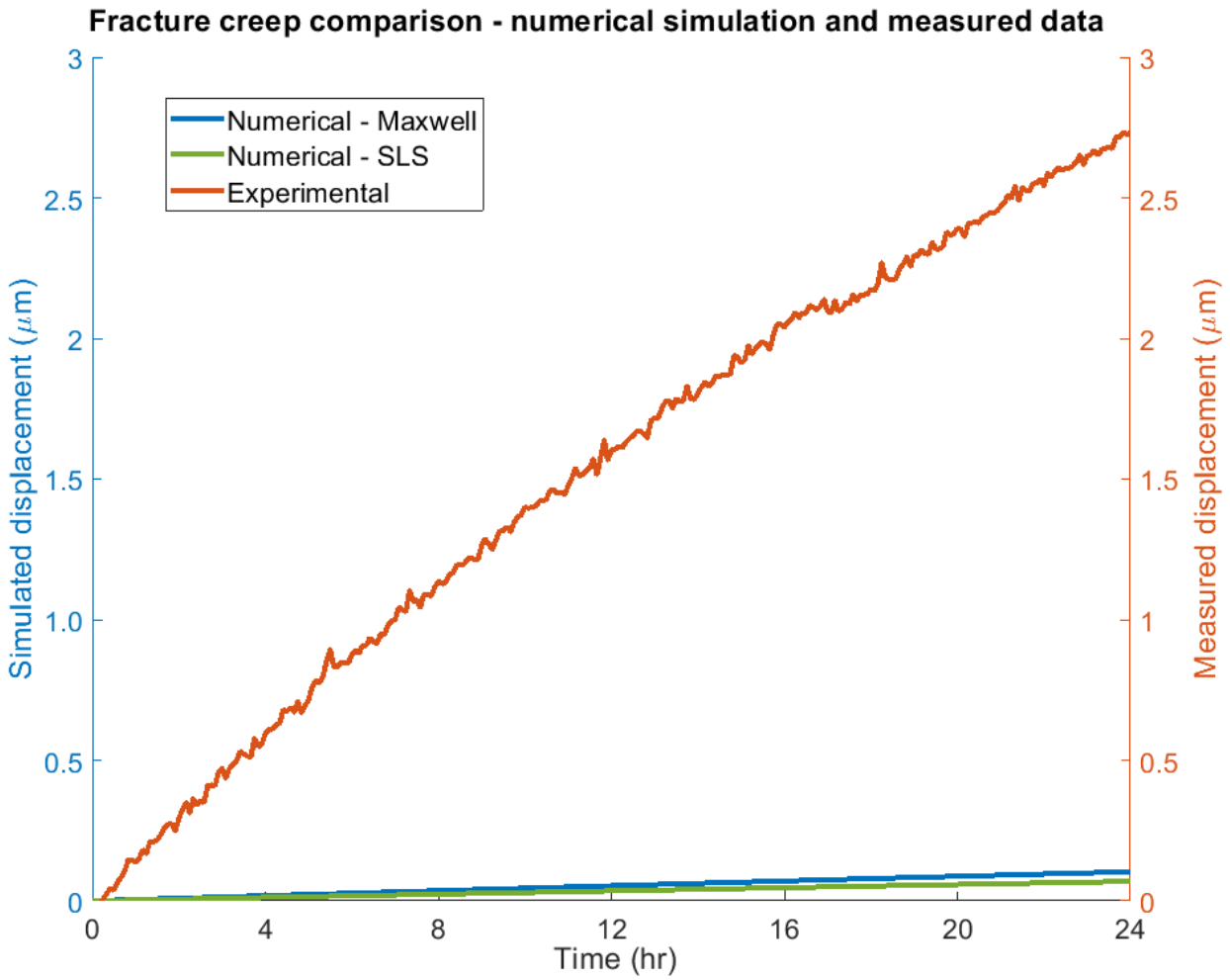

Figure 7.8 Comparison of numerically simulated visco-elastic displacements and measured creep displacement. The data in Figures 7.7 and 7.8 are identical.

Based on Figure 7.7, after 24 hours, the measured creep displacement is 2.73 μm, the simulated creep displacement using the Maxwell model is 0.1035 μm, and the simulated creep displacement using the SLS model is 0.0693 μm. Thus, the measured creep displacement is much larger than the simulated visco-elastic deformation.

It is worth noting that in Figure 7.6, the SLS model fits the measured data better; while in Figure 7.7, the Maxwell model fits the measured data better. The deviation may be due to different types of experiments. In Figures 7.6 and 7.7, the measured data are obtained from a triaxial creep test on an intact rock specimen and from a fracture creep test, respectively. The stress states between the triaxial creep test and contacting asperities in a rock fracture are different, and this will be further explained in Section 7.2.

The difference between numerically simulated results and measured results may be due to two possible reasons. First, the assumptions of the code may not be realistic. In reality, plastic deformation or shearing may occur. Secondly, the input parameters for the visco-elastic models may not be correct. The possible reasons will be further discussed in Section 7.2.

7.2 Discussions on the comparison results

To explain the difference between the numerical and experimental results, four hypotheses are proposed below.

(1): In the simulation, the contacting asperities deform visco-elastically. This implies that there is no upper limit for the compressive stress in the contacting cells. As shown in Figures 4.10 and 4.11 in Section 4.4.3, the compressive stress in a few contacting cells exceeds 1 GPa. In reality, under such high compressive stresses, the rock asperities may deform ductilely, and the compressive stress may not further increase after a threshold value. Therefore, if the ductile deformation is ignored, the compressive stress in the contacting asperities may be overestimated; the contact ratio (area of contacting asperities / total fracture surface area) may be underestimated. Due to force balance (force = pressure * area), an overestimation in contacting stress leads to an underestimation in the area of contacting asperities.

(2): Asperity breakage or cracking is ignored in the numerical model. In reality, under high compressive stresses, the asperities may break, which will affect the aperture field and the contact stress.

(3): The shear displacement between contacting asperities is ignored in the numerical model. As shown in Figure 7.9, when applying normal stress (shown by the blue arrows) to a rough fracture, shear displacements between contacting asperities may occur (shown by the red arrows). The shear displacements may also contribute to fracture creep.

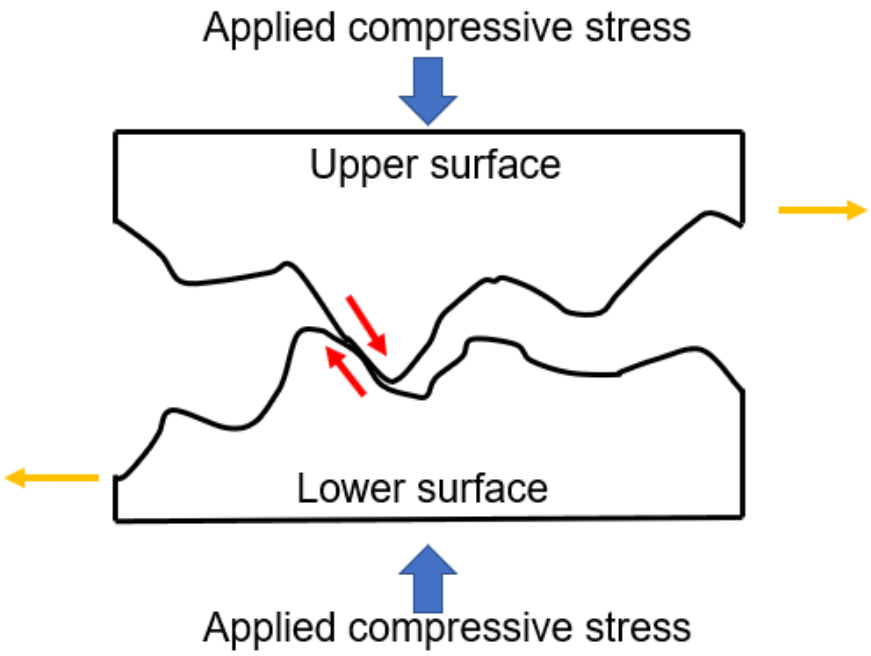

Figure 7.9 Schematic of shearing between contacting asperities. The red arrows represent the shear displacements between contacting asperities. The shear displacement between contacting asperities may lead to the shear displacement between the two fracture surfaces (show by the orange arrows).

(4): The creep rate at contacting asperities may be underestimated if the input parameters of visco-elastic models are fitted from triaxial tests. The size of fracture contacting asperities is comparable to that of micro-indentation tests and is smaller than that of triaxial tests. Therefore, the stress states in micro-indentation tests may better represent the stress states of fracture contacting asperities. However, the magnitude of stresses in micro-indentation tests is much larger than those of triaxial tests. Figure 7.10 (the same as Figure 3.8) shows the ABAQUS simulation of the von Mises stress distribution at the end of the loading stage in micro-indentation tests (the stress distribution in micro-indentation tests cannot be measured; it can only be obtained via numerical simulation). Based on Figure 7.10, the von Mises stress beneath the indenter exceeds 500 MPa, and the stress distribution is non-uniform. In contrast, the axial stress of the triaxial test (the stress step shown in the green box in Figure 7.3) is 160 MPa. Since the stresses in the triaxial test are much less than the stresses in the micro-indentation test, the creep rate using the input parameters fitted from the triaxial data may be underestimated.

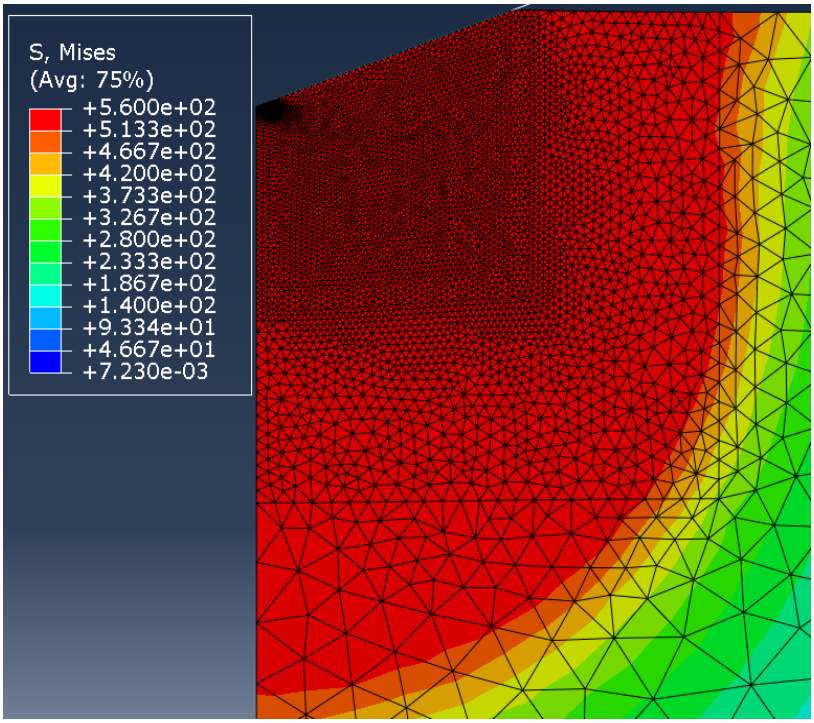

Figure 7.10 Von Mises stress distribution beneath the indenter. The maximum von Mises stress is 560 MPa, which corresponds to the red color. The unit is MPa.

Based on the discussion above, visco-elastic deformation only accounts for part of the fracture mechanical deformation under dry conditions. In future, to accurately simulate the fracture mechanical creep under dry conditions, the plastic deformation of contacting asperities needs to be considered. In addition, since the size of contacting asperities in a fracture is closer to that of

micro-indentation tests compared with that of triaxial tests, the input parameters for the fracture-scale numerical model should be obtained from micro-indentation test results.

8. Conclusions and future recommendations

8.1 Summary of experiments and numerical modeling

Rock fracture creep is a coupled process of four mechanisms: mechanical compression, pressure solution, dissolution, and erosion. Under dry conditions, creep caused by mechanical compression is the only mechanism suggesting that it should be systematically studied. However, there is not much work systematically studying the creep caused by mechanical compression.

In this thesis, creep caused by mechanical compression was investigated both numerically and experimentally. Specifically, the goal of this thesis is to (1): understand the creep behavior of rock at the scale of fracture contacting asperities; (2) build numerical models to simulate the creep behavior caused by mechanical compression at the fracture scale. An experimental component and a numerical component were implemented to achieve the first and second objectives, respectively.

The effect of time and scale on rock creep behavior was investigated experimentally. The experimental research was done on Musandam Limestone, the reservoir formation underlying Abu Dhabi, which is of primary interest to the sponsor of this research, ADNOC. The elastic and strength properties of Musandam limestone were obtained from triaxial and indentation tests. To study the effect of size on creep behavior, triaxial creep tests, micro-indentation tests, and nano-indentation tests were conducted. The creep patterns from triaxial, micro-indentation, and nano-indentation tests were compared. In addition, to study the effect of time duration on rock creep behavior, micro- and nano-indentation tests at different time durations (3-min and 6-hr) were conducted. For the experiments, the results can be summarized as follows:

1) When the confining pressure was less than 100 MPa, a linear Coulomb envelope could be used to describe the yield strength of Musandam limestone with cohesion of 18 MPa and friction angle of 39˚.

2) For Musandam limestone fractures, the magnitude of creep under dry conditions was comparable to that under other conditions. Under dry conditions, mechanical compression was the primary creep mechanism. This suggested that the effect of mechanical compression on fracture creep was not negligible.

3) 3-min micro- and nano-indentation tests showed that:

    - Indentation hardness H: the average and standard deviation from nano-indentation tests were larger than those from micro-indentation tests.
    - Indentation creep modulus C: the average and standard deviation from nano-indentation tests were larger than those from micro-indentation tests.
    - Indentation modulus M: the average of micro- and nano-indentation tests were similar, but the standard deviation from nano-indentation tests was larger than that from micro-indentation tests.

4) For micro-indentation, the 6-hr creep deformation would be overestimated if it was predicted from the 3-min creep deformation. Practically, to obtain the micro-indentation creep behavior for a specific time duration, creep tests at the specific time duration need to

be conducted; it may not be accurate to use short-term micro-indentation creep behavior to predict long-term micro-indentation creep behavior.

5) Due to machine drifting, the 6-hr nano-indentation creep deformation could not be accurately measured. Before measuring the long-term nano-indentation creep behavior, the machine drifting should be measured.

6) The creep patterns of triaxial and indentation creep were different. The indentation creep curves followed the natural log of time law, while the triaxial creep curves did not follow the natural log of time law.

An in-house numerical code was developed to simulate the fracture-scale creep caused by mechanical compression. The fracture mechanical creep consists of two components: visco-elastic deformation and visco-elasto-plastic deformation. In this numerical study, initial steps were taken – the numerical code simulated the visco-elastic deformation of rough fractures. In addition, another numerical code was developed to generate synthetic fracture surfaces based on Brown's (1995) model. In this model, a rock fracture surface was completely described by three parameters: the Hurst exponent, the mismatch length, and the root mean square roughness. The three parameters were varied systematically to investigate the effect of surface geometry on fracture visco-elastic deformation. In addition, the numerical simulation results were compared with experimental results. For numerical modeling of fracture-scale visco-elastic deformation, the results can be summarized as follows:

1) When H increased:

    - The average aperture decreased (before and during the creep stage). This indicated that if the local surface profile was smoother, the average aperture before and during the creep stage would be smaller.
    - The contact ratio increased faster with time. This indicated that if the local surface profile was smoother, with the same creep time duration, the area of contacting asperities would be larger.

2) When λ_c increased:

    - The average aperture increased (before and during the creep stage). This implied that if the shear offset between two surfaces was larger, the average aperture before and during the creep stage would be larger.
    - The contact ratio increased slower with time. This implied that if the shear offset between two surfaces was larger, with the same creep time duration, the area of contacting asperities would be smaller.

3) When RMS increased:

    - The average aperture increased (before and during the creep stage). This suggested that if the absolute value of the initial aperture field was larger, the average aperture before and during the creep stage would be larger.
    - The contact ratio increased slower with time. This suggested that if the absolute

value of the initial aperture field was larger, with the same creep time duration, the area of contacting asperities would be smaller.

4) With the surface parameters (H between 0.6 and 1.0, RMS between 50 and 150 μm, λ_c between 1000 and 3000 μm), macroscopic stresses (between 5 and 20 MPa), and the time durations (2τ for the Maxwell model and 5τ for the Standard Linear Solid (SLS) model. τ was the relaxation time and was defined as the ratio of viscosity to shear modulus) used in the simulation, the contact ratio was generally less than 10%.

5) The creep curves (average aperture changing with time and contact ratio changing with time) for different surface parameters could be normalized so the curves fell into a very narrow region. The curves were scaled linearly so the average aperture and contact ratio after elastic deformation (before creep) were the same.

6) The magnitude of the creep curves was significantly affected by the applied macroscopic stress. Before and during the creep stage, as the macroscopic stress increased, the average aperture decreased, and the contact ratio increased.

7) The shape of the creep curves depended on the input visco-elastic model. The Maxwell model assumed a constant creep rate. As a result, under current surface parameters, macroscopic stresses, and the time durations, the creep rate (aperture decrease rate) did not change significantly with time. In contrast, the SLS model assumed a time-decaying creep rate. As a result, under current surface parameters, macroscopic stresses, and the time durations, the creep rate (aperture decrease rate) decreased significantly with time.

8) Visco-elastic deformation only accounted for part of the fracture mechanical deformation under dry conditions. To accurately simulate the fracture mechanical creep under dry conditions, the plastic deformation of contacting asperities needs to be considered.

8.2 Conclusions from experiments and numerical modeling

8.2.1 Experimental work

Musandam limestone fracture creep tests were conducted under different fluid conditions, including dry, stagnant saturated limestone solution, stagnant distilled water, and distilled water flow conditions. The rock specimen total creep deformation (rock matrix + fracture) was measured. The results proved that specimen creep under dry conditions (in which mechanical compression was the primary creep mechanism) was important. This indicated that the mechanical compression mechanism was important in fracture creep deformation.

Four different types of indentation tests were conducted on Musandam limestone: 3-min micro-indentation tests, 6-hr micro-indentation tests, 3-min nano-indentation tests, and 6-hr nano-indentation tests. For the first three types of indentation tests, the indentation hardness H, indentation modulus M, and indentation creep modulus C for each indent were determined. The C, H, M values obtained from 3-min micro-indentation tests and 3-min nano-indentation tests were compared. For indentation hardness H, the average and standard deviation from nano-indentation

tests were larger than those from micro-indentation tests; for indentation creep modulus C, the average and standard deviation from nano-indentation tests were larger than those from micro-indentation tests; for indentation modulus M, the average of micro- and nano-indentation tests were similar, but the standard deviation from nano-indentation tests was larger than that from micro-indentation tests. As explained in Section 6.4, the relatively large variation obtained from nano-indentation tests might be due to the size effect. The larger average of C and H obtained by nano-indentation tests might be due to errors in contact area measurement – in nano-indentation tests, the contact area between the indenter and the rock surface might be underestimated. As a result, the C and H values might be overestimated. Further investigation is required to explain the differences in the C, H, and M values.

The results of 3-min micro-indentation tests were compared with those of 6-hr micro-indentation tests. The indentation creep modulus C of 6-hr micro-indentation tests was larger than that of 3-min micro-indentation tests. Under the same load, a larger creep modulus C corresponded to a slower creep rate. This indicates that the 6-hr creep deformation would be overestimated if it was predicted from the 3-min creep deformation. Practically, to obtain the micro-indentation creep behavior for a specific time duration, creep tests at the specific time duration need to be conducted; it may not be accurate to use short-term micro-indentation creep behavior to predict long-term micro-indentation creep behavior.

The results of 3-min nano-indentation tests were compared with those of 6-hr nano-indentation tests. The measured indentation creep consisted of both indent creep and machine drift. For the 6-hr duration, the machine drift was not measured so the indent creep could not be determined. To determine the indent creep for long-duration nano-indentation tests, the machine drift for the specific time duration needs to be measured.

Triaxial creep tests were conducted on two intact Musandam limestone specimens. Multiple stress steps were applied to each specimen, and the time duration for each stress step was 24 hours. For each stress step, the creep rate decreased with time. This implied that for each stress step, the specimens had not reached steady-stage creep stage after 24 hours; the specimens were still in the primary creep stage. Between different stress steps, in general, under the same confining pressure, the creep rate increased with increasing axial stress. Between the two specimens, under the same stress condition (same axial stress and confining pressure), the creep rate of specimen 1 was more than twice of the creep rate of specimen 2. The difference in the creep rate might be due to varied loading histories. To compare the creep rate between different specimens, the loading history should be the same.

The creep patterns of triaxial tests were compared with those of indentation tests. The indentation creep curves followed the natural log of time law (the creep deformation changed linearly with the natural log of time); while the triaxial creep curves did not follow it. The difference might be due to different stress conditions. In indentation tests, the stresses beneath the indenter could reach the magnitude of GPa; while in triaxial tests, the axial stress did not exceed 160 MPa.

8.2.2 Numerical work

An in-house numerical code was developed to generate synthetic fracture surfaces based on Brown's (1995) model. In this model, a rock fracture surface was completely described by three

parameters: the Hurst exponent H, the mismatch length λ_c, and the root mean square roughness RMS. The three parameters were varied systematically to generate seven synthetic surfaces with different geometries. Conceptually, a larger H value corresponded to a smoother local surface profile, a larger λ_c value corresponded to a larger shear offset between two surfaces, and the RMS value defined the magnitude of surface elevation. The surface generation results suggested that if the local surface profile was smoother, the average aperture value would be smaller; if the offset between two surfaces increased, the average aperture value would be larger; if the H and λ_c values were constant (same local smoothness and surface offset), the average aperture value scaled linearly with the RMS value.

Another in-house numerical code was developed to simulate visco-elastic deformation of rough fractures. The seven synthetic surfaces were used as rough surfaces. If H increased, two conclusions could be summarized:

1) The average aperture decreased before and during the creep stage. Conceptually, if the local surface profile was smoother, the average aperture before and during the creep stage would be smaller.

2) The contact ratio increased faster with time. Conceptually, if the local surface profile was smoother, with the same creep time duration, the area of contacting asperities would be larger.

If λ_c value increased, two conclusions could be summarized:

1) The average aperture increased before and during the creep stage. Conceptually, if the shear offset between two surfaces was larger, the average aperture before and during the creep stage would be larger.

2) The contact ratio increased slower with time. Conceptually, if the shear offset between two surfaces was larger, with the same creep time duration, the area of contacting asperities would be smaller.

If RMS value increased, two conclusions could be summarized:

1) The average aperture increased before and during the creep stage. Conceptually, if the absolute value of the initial aperture field was larger, the average aperture before and during the creep stage would be larger.

2) The contact ratio increased slower with time. Conceptually, if the absolute value of the initial aperture field was larger, with the same creep time duration, the area of contacting asperities would be smaller.

The factors affecting the shape and magnitude of the creep curves (average aperture changing with time and contact ratio changing with time) were also investigated. Three different macroscopic stresses (5 MPa, 10 MPa, and 20 MPa) and two visco-elastic constitutive models (the Maxwell and Standard Linear Solid models) were used. The results indicated that the magnitude of the creep curve was significantly affected by the applied macroscopic stress. Before and during the creep stage, as the macroscopic stress increased, the average aperture value decreased, and the contact ratio increased. In addition, the shape of the creep curves was affected by the visco-elastic models. The Maxwell model assumed a constant creep rate. As a result, under current surface parameters, macroscopic stresses, and the time durations, the creep rate (aperture decrease rate) did not change

significantly with time. In contrast, the SLS model assumed a time-decaying creep rate. As a result, under current surface parameters, macroscopic stresses, and the time durations, the creep rate (aperture decrease rate) decreased significantly with time. With the surface parameters (H between 0.6 and 1.0, RMS between 50 and 150 μm, λc between 1000 and 3000 μm), macroscopic stresses (between 5 and 20 MPa), and the time durations (2τ for the Maxwell model and 5τ for the Standard Linear Solid (SLS) model) used in the simulation, the contact ratio was generally less than 10%. This suggested that most regions were still non-contact regions (no contacting pressure, aperture greater than zero).

The numerically simulated fracture visco-elastic deformation was compared with the measured fracture creep. One Musandam limestone tensile fracture was created, and the initial aperture field was measured. Then, the creep deformation of the fractured specimen under dry conditions and 164 kPa uniform stress was measured. The numerical code simulated the fracture visco-elastic deformation using two input components. The first was the measured initial aperture field; the second was the input parameters for the Maxwell and SLS models, and these parameters were obtained from a triaxial creep test on an intact Musandam limestone specimen. The measured creep deformation was 26.4 times and 39.4 times the creep deformation predicted by the Maxwell and SLS models, respectively.

The difference might be due to plastic deformation of contacting asperities or the input parameters of the visco-elastic models. The size of contacting asperities in a fracture was comparable to that of micro-indentation tests and was smaller than that of triaxial tests. Therefore, the stress states in micro-indentation tests might better represent the stress states of contacting asperities in a fracture.

The loading stage of micro-indentation tests was simulated using ABAQUS to obtain the stress states. The results suggested that in the loading stage of a micro-indentation test, the combination of linear elasticity and von Mises criterion provided a good fit of the micro-indentation test results. This implied that to accurately simulate the deformation of contacting asperities in a fracture, plastic deformation should be considered. In the simulation, the input parameters were obtained from a triaxial creep test on an intact rock specimen. However, the ABAQUS simulation indicated that the stresses in the triaxial test were much less than the stresses in the micro-indentation test. Therefore, the creep rate using the input parameters fitted from the triaxial data might be underestimated. The input parameters for the fracture-scale numerical model should be obtained from micro-indentation test results.

8.3 Recommendations for future work

To accurately simulate the fracture mechanical creep under dry conditions, the plastic deformation of contacting asperities, including ductile deformation and breakage, needs to be considered. In addition, since the size of fracture contacting asperities is closer to that of micro-indentation tests compared with that of triaxial tests, the input parameters for the fracture-scale numerical model should be obtained from micro-indentation tests results.

The numerical code can be modified to simulate the effect of shear stress. In natural conditions, rock fractures may be subject to shear stress; the shear stress may further deform the contacting asperities and change the aperture value. Therefore, it would be beneficial to simulate the fracture mechanical creep under both normal and shear stresses.

The numerical code can also be extended to wet conditions. Given the aperture field, the current numerical code can calculate contact stress distribution. Based on contact stress distribution, the pressure solution rate in contacting asperities can be determined; and with the pressure solution rate, the aperture change caused by the pressure solution can be obtained.

For the experiments, more triaxial creep tests on intact specimens should be conducted. In this thesis, due to time constraints, only two triaxial creep tests were conducted. The data would be more persuasive if more tests can be repeated.

In addition, for 6-hr nano-indentation tests, the machine drifting should be measured. In nano-indentation tests, the measured creep is the summation of indent creep and machine drift. However, the 6-hr machine drift of the nano-indentation machine is unknown. As a result, the indent creep could not be determined. It would be beneficial to measure the 6-hr machine drifting so the indent creep can be determined.

References

1. AlDajani, O. A. (2017) *Fracture and hydraulic fracture initiation, propagation, and coalescence in shale, SM Thesis*, Massachusetts Institute of Technology.
2. Alnuaim, A., Hamid, W., Alshenawy, A. (2019) Unconfined compressive strength and Young's modulus of Riyadh limestone, *Electronic Journal of Geotechnical Engineering*, 2019 (24.03), 707-717.
3. Alsharhan, A. S., Nairn, A. E. M. (1986). A review of the Cretaceous formations in the Arabian Peninsula and Gulf: Part I. Lower Cretaceous (Thamama Group) stratigraphy and paleogeography. *Journal of Petroleum Geology*, 9(4), 365-391.
4. Al-Shayea, N. A. (2004) Effects of testing methods and conditions on the elastic properties of limestone rock, *Engineering Geology*, 74, 139–156.
5. Ameen, M. S., Smart, B. G. D., Somerville, J. M., Hammilton, S., Naji, N. A. (2009) Predicting rock mechanical properties of carbonates from wireline logs (A case study: Arab-D reservoir, Ghawar field, Saudi Arabia), *Marine and Petroleum Geology*, 26, 430–444.
6. Ameli, P., Elkhoury, J. E., Morris, J. P., Detwiler, R. L. (2014) Fracture permeability alteration due to chemical and mechanical processes: a coupled high-resolution model, *Rock Mechanics and Rock Engineering*, 47(5), 1563-1573.
7. Andrews, D. J. (1988) On modeling closure of rough surfaces in contact, *Eos Trans, AGU, 69*, 1426-1427.
8. Arman, H., Hashem, W., El Tokhi, M., Abdelghany, O., El Saiy, A. (2014) Petrographical and geomechanical properties of the lower Oligocene limestones from Al Ain City, United Arab Emirates, *Arabic Journal of Science and Engineering*, 39, 261–271.
9. Arman, H., Paramban, S. (2020) Correlating natural, dry, and saturated ultrasonic pulse velocities with the mechanical properties of rock for various sample diameters, *Applied Sciences*, 10, 9134.
10. Aristorenas, G. V. (1992) *Time-dependent behavior of tunnels excavated in shale, PhD Thesis*, Massachusetts Institute of Technology.
11. Bandis, S. C., Lumsden, A.C., Barton, N. R. (1983) Fundamentals of rock joint deformation, *International Journal of Rock Mechanics and Mining Sciences*, 20: 249-268.
12. Barton, N., Brandis, S., Bakhtar, K. (1985) Strength, deformation and conductivity coupling of rock joints, *International Journal of Rock Mechanics and Mining Sciences Geomechanical Abstract*, 22.
13. Bear, J. (1972) *Dynamics of Fluids in Porous Media*, Dover Publications, Inc, New York.
14. Beeler, N., Hickman, S. (2004) Stress-induced, time-dependent fracture closure at hydrothermal conditions, *Journal of Geophysical Research*, 109, B02211.
15. Bernabé, Y., Evans, B. (2007) Numerical modelling of pressure solution deformation at axisymmetric asperities under normal load, *Geological Society, London, Special Publications*, 284(1), 185–205.
16. Bland, D. R. (1960) *The Theory of Linear Viscoelasticity*, Pergamon, Oxford and New York.
17. Bowden, F. P., Tabor, D. (1950) *The Friction and Lubrication of Solids*, New York: Oxford University Press.
18. Boulenouar, A., Mighani, S., Pourpak, H., Bernabe, Y., Evans, B. (2017) Mechanical properties of Vaca Muerta shales from nano-indentation tests, *51st US Rock Mechanics/Geomechanics Symposium*.
19. Brantut, N., Heap, M., Meredith, P., Baud, P. (2013) Time-dependent cracking and brittle creep in crustal rocks: A review, *Journal of Structural Geology*, 52, 17-43.

20. Brooks, Z. (2013) *Fracture process zone: microstructure and nanomechanics in quasi-brittle materials, PhD Thesis,* Massachusetts Institute of Technology.
21. Brown, S. R., Scholz, C. H. (1985a) Broad bandwidth study of the topography of natural rock surfaces, *Journal of Geophysical Research*, 90(B14), 12,575–12,582.
22. Brown, S. R., Scholz, C. H. (1985b) Closure of random elastic surfaces in contact, *Journal of Geophysical Research*, 90(B7), 5531–5545.
23. Brown, S. R. (1995) Simple mathematical model of a rough fracture, Journal of Geophysical Research, 100, 5941-5952.
24. Brown, S. R., Caprihan, A., Hardy, R. (1998) Experimental observation of fluid flow channels in a single fracture, *Journal of Geophysical Research*, 103(B3), 5125-5132.
25. Carey, J. W., Frash, L. P., Ickes, T. (2018) Experimental investigation of shear fracture development and fluid flow in dolomite, *52nd U.S. Rock Mechanics/Geomechanics Symposium*, Seattle, U. S. A.
26. Chen, W. W., Wang, Q. J., Huan, Z., Luo, X. (2011) Semi-analytical viscoelastic contact modeling of polymer-based materials, *Journal of Tribology*, vol.133, no.4, Article ID 041404.
27. Chester, F., Chester, J., Kronenberg, A., Hajash, A. (2007) Subcritical creep compaction of quartz sand at diagenetic conditions: Effects of water and grain size, *Journal of Geophysical Research*, 112, B06203.
28. Cook, N. G. W., Jeager, J. C., Zimmerman, R. W. (2006) *Fundamentals of Rock Mechanics, Fourth Edition*, Wiley Blackwell.
29. Cottrell, A. H. (1952) The time laws of creep, *Journal of Mechanics and Physics of Solids*, 1, 53-63.
30. Deng, H., Fitts, J. P., Crandall, D., McIntyre, D., Peters, C. A. (2015) Alterations of fractures in carbonate rocks by CO_2-acidified brines. *Environmental Science and Technology*, 49(16), 10226-10234.
31. Deng, H., Voltolini, M., Molins, S., Steefel, C., DePaolo, D., Ajo-Franklin, J., Yang, L. (2017) Alteration and erosion of rock matrix bordering a carbonate-rich shale fracture, *Environmental Science and Technology*, 51, 8861-8868.
32. Detwiler, R. L., Rajaram, H. (2007) Predicting dissolution patterns in variable aperture features: Evaluation of an enhanced depth-averaged computational model, *Water Resources Research*, 43(4).
33. Detwiler, R. L. (2008) Experimental observations of deformation caused by mineral dissolution in variable-aperture fractures, *Journal of Geophysical Research*, 113, B08202.
34. Dieterich, J. H., Kilgore, B. D. (1994) Direct observation of frictional contacts: new insights for state-dependent properties, PAGEOPH, 143, No. 1/2/3.
35. Dieterich, J. H., Kilgore, B. D. (1996) Imaging surface contacts: power law contact distributions and contact stresses in quartz, calcite, glass and acrylic plastic, *Tectonophysics*, 256, 219-239.
36. Durham, W. B., Bourcier, W. L., and Burton, E. A. (2001) Direct observation of reactive flow in a single fracture, *Water Resources Research*, 37(1), 1–12.
37. El Aal, A. A. (2015) Geomechanical aspects and suitability of the limestone (Sulaiy limestone formation) for foundation bedrock, Sulaiy region, Saudi Arabia, *Journal of Geology and Geophysics*, 4, 230.
38. Elkhoury, J. E., Ameli, P., Detwiler, R. L. (2013) Dissolution and deformation in fractured carbonates caused by flow of CO_2-rich brine under reservoir conditions, *International Journal of Greenhouse Gas Control*, 16, S203–S215.

39. Evans, B. E. (2020) Personal communication.
40. Evans, B. E., Dresen, G. (1991) Deformation of earth materials – six easy pieces, rheology of rocks, *Reviews of Geophysics*, 29, Part 2, Supplementary support, 823-843.
41. Evans, B. E., Kohlstedt, D. L. (1995) Rheology of rocks, in *Rock Physics and Phase Relations – A Handbook of Physical Constants, American Geophysical Union*, Washington, D. C., 148-165.
42. Fan, L. F., Ma, G. W., Wong, L. N. Y (2012) Effective viscoelastic behavior of rock mass with double-scale discontinuities, *Geophysical Journal International*, 191, 147-154.
43. Fillot, N., Iordanoff, I., Berthier, Y. (2007) Modelling third body flows with a discrete element method – a tool for understanding wear with adhesive particles, *Tribology International*, vol 40, 6, 973 – 981.
44. Gale, J., Macleod, R., LeMessurier, P. (1990) Site characterization and validation – Measurement of flowrate, solute velocities and aperture variation in natural fractures as a function of normal and shear stress, Stage 3, Stripa Project, *Technical Report TR 90-11*, SKB, Stockholm.
45. Garcia-Rios, M., Luquot, L., Soler, J. M., Cama, J. (2017) The role of mineral heterogeneity on the hydrogeochemical response of two fractured reservoir rocks in contact with dissolved CO_2. *Applied Geochemistry*, 84, 202-217.
46. Geng, Z., Bonnelye, A., Chen, M., Jin, Y., Dick, P., David, C., et al. (2018) Time and temperature dependent creep in Tournemire shale, *Journal of Geophysical Research: Solid Earth*, 123, 9658-9675.
47. Gentier, S., Billaux, D., van Vliet, L. (1989) Laboratory testing of the voids of a fracture, *Rock Mechanics and Rock Engineering*, 22, 149-157.
48. Gentier, S., Hopkins, D., Riss, J. (2013) Role of fracture geometry in the evolution of flow paths under stress, *Dynamics of fluids in fractured rock, American Geophysical Union*, 169-184.
49. Germaine, J. T., Germaine, A. V. (2009) *Geotechnical Laboratory Measurements for Engineers*, John Wiley & Sons, Inc.
50. Goldstein, J. I., Newbury, D. E., Michael, J. R., Ritchie, N. W. M., Scott, J. H. J., Joy, D. C. (2018) *Scanning Electron Microscopy and X-ray Microanalysis*, Fourth Edition, Springer.
51. Goodman, R. E. (1976) *Methods of Geological Engineering in Discontinuous Rocks*, West Publishing Company, New York.
52. Greenwood, J. A., Williamson, J. B. P. (1966) Contact of nominally flat surfaces, *Proceedings of the Royal Society of London. Series A, Mathematical and Physical Sciences*, 295:300-319.
53. Griggs, D. T. (1939) Creep of rocks, *Journal of Geology*, 47, 225-251.
54. Hakami, E., Barton, N. (1990) Aperture measurements and flow experiments using transparent replicas of rock joints, *Proceedings of International Symposium on Rock Joints*, Leon, Norway, 383-390.
55. Hakami, E., Gentier, S. (1995) Characterisation of fracture apertures – methods and parameters, *Proceedings of the Eighth International Congress of the ISRM*, Tokyo, Japan.
56. Hansen, A., Schmittbuhl, J., Batrouni, G. G., De Oliveira F. A. (2000) Normal stress distribution of rough surfaces in contact, *Geophysical Research Letters*, 27:3639-3642.
57. Hashin, Z., Shtrikman, S. (1962) On some variational principles in anisotropic and nonhomogeneous elasticity, *Journal of the Mechanics and Physics of Solids*, 10, 335 – 342.
58. Heap, M., Brantut, N., Baud, P., Meredith, P. G. (2015) Time-dependent compaction band formation in sandstone, *Journal of Geophysical Research: Solid Earth*, 120, 4808-4830.

59. Herrmann, F. J., Bernabe, Y. (2004) Seismic singularities at upper-mantle phase transitions: a site percolation model, *Geophysical Journal International*, 159, 949 – 960.
60. Hertz, H. (1882a) Uber die Beruhrung fester elasticher Korper (On the contact of elastic solids), J. reine und angewandte Mathematik, 92, 156-171. (For English translation, see *Miscellaneous Papers by H. Hertz*, Eds. Jones and Schott, London: Macmillan, 1896.).
61. Hertz, H. (1882b) Uber die Beruhrung fester elasticher Korper and uber die Harte (On the contact of rigid elastic solids and on hardness), Verhandlungen des Vereins zur Beforderung des Gewerbefleisses, Leipzig, Nov. 1882. (For English translation, see *Miscellaneous Papers by H. Hertz*, Eds. Jones and Schott, London: Macmillan, 1896.).
62. Hopkins, D. L., Cook, N. G., Myer, L. R. (1987) Fracture stiffness and aperture as a function of applied stress and contact geometry, *21st U.S. Rock Mechanics/Geomechanics Symposium.*
63. Hopkins, D. L. (1991) The effect of surface roughness on joint stiffness, aperture, and acoustic wave propagation, *PhD thesis, University of California, Berkeley*.
64. Ishibashi, T., McGuire, T. P., Watanabe, N., Tsuchiya, N., Elsworth, D. (2013) Permeability evolution in carbonate fractures: Competing roles of confining stress and fluid PH, *Water Resources Research*, 49, 2828-2842.
65. IRSM (1979) Suggested methods for determining the uniaxial compressive strength and deformability of rock materials, *International Journal of Rock Mechanics and Mining Sciences Geomechanics Abstract*, 16, 135-140.
66. Iwano, M., Einstein, H. H. (1995) Laboratory experiments on geometric and hydromechanical characteristics of three fractures in granodiorite, *Proceedings of the Eighth International Congress of the ISRM*, Tokyo, Japan.
67. Iwano, M. (1995) *Hydromechanical characteristics of a single rock joint, PhD Thesis*, Massachusetts Institute of Technology.
68. Jacq, C., Nelias, D., Lormand, G. Girodin, D. (2002) Development of a three-dimensional semi-analytical elastic-plastic contact code, *Journal of Tribology*, 124:653-667.
69. Jeffreys, H. (1958) A modification of Lmnitz's law of creep in rocks, *Geophysical Journal of the Royal Astronomical Society*, 1, 321-334.
70. Johnson, K. L. (1985) *Contact Mechanics*, Cambridge University Press, London.
71. Kang, H., Germain, J. T., Einstein, H. H. (2019) Creep behavior of Musandam limestone fractures under confining pressures less than 1 MPa, *53rd U.S. Rock Mechanics/Geomechanics Symposium*, New York, U. S. A.
72. Kang, H., AlDajani, O., Germain, J. T., Einstein, H. H. (2020) Experimental investigation of the mechanical properties of Musandam limestone, Submitted to *Rock Mechanics and Rock Engineering*.
73. Kang, H., Einstein, H. H., Brown, S. R., Germaine, J. T. (2020) Numerical simulation for rock fracture visco-elastic creep under dry conditions, *Journal of Geofluids*.
74. Kang, P., Brown, S., Juanes, R. (2016) Emergence of anomalous transport in stressed rough fractures, *Earth and Planetary Science Letters*, 454:46-54.
75. Kalo, K. (2017) Microstructural characterization and micromechanical modeling of oolitic porous rocks. *PhD thesis in Civil Engineering, Université de Lorraine.*
76. Kemeny, J. (1991) A model for non-linear rock deformation under compression due to sub-critical crack growth, *International Journal of Rock Mechanics and Mining Sciences & Geomechanical Abstracts*, 28(6), 459-467.
77. Kling, T., Vogler, D., Pastewka, L., Amann, F., Blum, P. (2018) Numerical simulations and validation of contact mechanics in a granodiorite fracture, *Rock Mechanics and Rock*

Engineering, 51:2805-2824.
78. Lang, P. S., Paluszny, A., Zimmerman, R. W. (2015) Hydraulic sealing due to pressure solution contact zone growth in siliciclastic rock fractures, *Journal of Geophysical Research: Solid Earth*, 120, 4080 – 4101.
79. Lang, P. S., Paluszny, A., Zimmerman, R. W. (2016) Evolution of fracture normal stiffness due to pressure dissolution and precipitation, *International Journal of Rock Mechanics and Mining Sciences*, 88:12-22.
80. Lebedev, M., Zhang, Y., Sarmadivaleh, M., Barifcani, A., Al-Khdheeawi, E., Iglauer, S. (2017) Carbon geosequestration in limestone: Pore-scale dissolution and geomechanical weakening, *International Journal of Greenhouse Gas Control*, 66, 106–119.
81. Lee, E. H., Radok, J. R. M. (1960) The contact problem for viscoelastic bodies, ASME Journal of Applied Mechanics, 27, pp. 438–444.
82. Lehner, F., Leroy, Y. (2004) Sandstone compaction y intergranular pressure solution, *Mechanics of Fluid Saturated Rocks*, 89, 115-168.
83. Li, B., Zhao, Z., Jiang, Y., Jing, L. (2015) Contact mechanism of a rock fracture subjected to normal loading and its impact on fast closure behavior during initial stage of fluid flow experiment. *International Journal for Numerical and Analytical Methods in Geomechanics*, 39:1431–1449.
84. Li, B. (2019) *Micro-seismic and Real Time Imaging of Fractures and Microfractures in Barre Granite and Opalinus Clayshale, PhD Thesis*, Massachusetts Institute of Technology.
85. Li, W. (2019) *Experimental and Theoretical Studies of Reactive Transport Processes in Soluble Porous Rocks, PhD Thesis*, Massachusetts Institute of Technology.
86. Liu, S. B., Wang, Q., Liu, G. (2000) A Versatile Method of Discrete Convolution and FFT (DC-FFT) for Contact Analyses, *Wear*, 243, pp. 101–111.
87. Liu, G., Zhu, J., Yu, L., Wang, Q. (2001) Elasto-plastic contact of rough surfaces, *Tribology Transactions*, vol 44, 3, 437 – 443.
88. Lomnitz, C. (1956) Creep measurements in igneous rocks, *Journal of Geology*, 64, 473-479.
89. Love, A. E. H. (1929) Stress produced in a semi-infinite solid by pressure on part of the boundary, *Philosophical Transactions of Royal Society*, A228, 337, 54-59.
90. Ludwik, P. (1909) *Elemente der Teknologischen Mechanik (Elements of Engineering Mechanics)*, Springer, Berlin.
91. Mahmood, T., Carmargo, O. E. M., Al-Gawas, A. H., Al-Hawas, K. A., Nashar, A. R., Deshenenkov, I., Planchart, C. A. (2018) Integrated 3D geomechanics model to characterize the in situ stress rotations and their implications on the mechanical behavior of the natural fractures and drilling operations: a case study for a carbonate reservoir, *Saudi Arabia, Saudi Aramco Journal of Technology Winter 2018*, 14-28.
92. Mandelbrot, B. B. (1983) *The fractal geometry of nature*, W. H. Freeman & Company, San Francisco.
93. McGuire, T. P., Elsworth, D., Karcz, Z. (2013) Experimental measurements of stress and chemical controls on the evolution of fracture permeability, *Transport in Porous Media*, 98(1), 15–34.
94. Mighani, S., Mok, U., Pec, M., Evans, B. (2018) Can we use nanoindentation to derive the poroelastic parameters of microporous rocks? – experimental evidence, *52nd U.S. Rock Mechanics/Geomechanics Symposium*, Seattle, US.
95. Mighani, S., Bernabe, Y., Boulenouar, A., Mok, U., Evans, B. (2019) Creep deformation in Vaca Muerta Shale from nanoindentation to triaxial experiments, *Journal of Geophysical*

Research: Solid Earth, 124, 7842-7868.
96. Morgan, S. P. (2015) *An experimental and numerical study on the fracturing processes in Opalinus shale, PhD Thesis*, Massachusetts Institute of Technology.
97. Myer, L. R. (2000) Fractures as collections of cracks, *International Journal of Rock Mechanics*, 37, 231-243.
98. Neretnieks, I. (2014) Stress-mediated closing of fractures: Impact of matrix diffusion, *Journal of Geophysical Research: Solid Earth*, 119, 4149–4163.
99. Noiriel, C., Gouze, P., Made, B. (2013) 3D analysis of geometry and flow changes in a limestone fracture during dissolution. *Journal of Hydrology*, 486, 211-223.
100. Odling, N. E. (1994) Natural fracture profiles, fractal dimension and joint roughness coefficients, *Rock Mechanics and Rock Engineering*, 27, 135-153.
101. Oliver, W. C., Pharr, G. M. (1992) An improved technique for determining hardness and elastic-modulus using load and displacement sensing indentation experiments, *Journal of Materials Research*, 7, 1564.
102. Pei, L., Hyun, S., Molinari, J. F., Robbins, M. O. (2005) Finite element modeling of elasto-plastic contact between rough surfaces, *Journal of Mechanics of Physics and Solids*, vol 53, 11, 2385 – 2409.
103. Persson, B. N. J., Albohr, O., Tartaglino, U., Volokitin, A. I., Tosatti, E. (2005) On the nature of surface roughness with application to contact mechanics, sealing, rubber friction and adhesion, *Journal of Physical Condensed Matter*, 17(1), R1–R62.
104. Polak, A., Elsworth, D., Liu, J., Grader, A. S. (2004) Spontaneous switching of permeability changes in a limestone fracture with net dissolution, *Water Resources Research*, 40, W03502.
105. Polonsky, I. A., Keer L. M. (1999) A numerical method for solving rough contact problems based on the multi-level multi-summation and conjugate gradient techniques, Wear, 231:206-219.
106. Pyrak-Nolte, L. J., Morris, J. P. (2000) Single fractures under normal stress: the relation between fracture specific stiffness and fluid flow, *International Journal of Rock Mechanics and Mining Sciences*, 37: 245-262.
107. Pyrak-Nolte, L. J., Nolte, D. D. (2016) Approaching a universal scaling relationship between fracture stiffness and fluid flow, *Nature Communications*, 7:10663.
108. Ricateau, R., Riche, P. H. (1980). Geology of the Musandam Peninsula (Sultanate of Oman) and its surroundings. *Journal of Petroleum Geology*, 3(2), 139-152.
109. Robertson, E. C. (1964) Viscoelasticity of rocks, in *State of Stress in the Earth's Crust*, W. R. Judd edited, Elsevier, New York, 181-233.
110. Sahlin, F., Larsson, R., Almqvist, A., Lugt, P. M., Marklund, P. (2010) A mixed lubrication model incorporating measured surface topography. Part 1: theory of flow factors, *Proceedings of the Institution of Mechanical Engineers, Part J: Journal of Engineering Tribology*, 224(4), 335-351.
111. Shukla, P., Taneja, S., Soundergeld, C., Rai, C. (2015) Nanoindentation measurements on rocks, Fracture*, Fatigue, Failure and Damage Evolution, Volume 5: Proceedings of the 2014 Annual Conference on Experimental and Applied Mechanics*, Greenville, US.
112. Slim, M. I. (2016) *Creep properties of source rocks using indentation: the role of organic matter on texture and creep rates, PhD Thesis*, Massachusetts Institute of Technology.
113. Sone., H., Zoback, M. D. (2014) Time-dependent deformation of shale gas reservoir rocks and its long-term effect on the in situ state of stress, *International Journal of Rock Mechanics*

and Mining Sciences, 69, 120-132.
114. Spinu, S., Cerlinca, D. (2017) Modelling of rough contact between linear viscoelastic materials, *Modelling and Simulation in Engineering*, vol.2017, Article ID 2521903.
115. Stanley, H. M., Kato, T. (1997) An FFT-based method for rough surface contact, *Journal of Tribology*, 119:481–485.
116. Tian, X., Bhushan, B. (1996) A numerical three-dimensional model for the contact of rough surfaces by variational principle, *Journal of Tribology*, 118:33-42.
117. Ting, T. C. T. (1966) The contact stresses between a rigid indenter and a viscoelastic half-space," *ASME Journal of Applied Mechanics*, 33, pp. 845–854.
118. Ting, T. C. T. (1968) Contact problems in the linear theory of viscoelasticity," *ASME Journal of Applied Mechanics*, 35, pp. 248–254.
119. Vandamme, M., Tweedie, C., Constantinides, G., Ulm, F-J, Van Vliet, K. J. (2011) Quantifying plasticity-independent creep compliance and relaxation of viscoelastoplastic materials under contact loading, *Journal of Materials Research*, 27:302-312.
120. Vandamme, M., Ulm, F.-J. (2013) Nanoindentation investigation of creep properties of calcium silicate hydrates, *Cement and Concrete Research*, 52, 38-52.
121. Vialle, S., Pazdniakou, A., Adler, P. M. (2018) Prediction of the macroscopic mechanical properties of carbonate from nano-indentation tests, *52nd U.S. Rock Mechanics/Geomechanics Symposium*, Seattle, US.
122. Villamor Lora, R. 2018. Personal communication.
123. Wang, D. (2011) Experimental study of mechanical properties of Shah Simsima rocks, *MS Thesis in the Petroleum Institute, UAE*.
124. Wang, L., Cardenas, M. B. (2016) Development of an empirical model relating permeability and specific stiffness for rough fractures from numerical deformation experiments, *Journal of Geophysical Research: Solid Earth*, 121:4977-4989.
125. Wang, Z. J., Wang, W. Z., Hu, Y. Z., Wang, H. (2010) A numerical elastic-plastic contact model for rough surfaces, *Tribology Transactions*, 53:224-238.
126. Watanabe, N., Hirano, N., Tsuchiya, N. (2008) Determination of aperture structure and fluid flow in a rock fracture by high-resolution numerical modeling on the basis of a flow-through experiment under confining pressure, *Water Resources Research*, 44: W06412.
127. Witherspoon, P. A., Wang, J. S., Iwai, K., Gale, J. E. (1980). Validity of cubic law for fluid flow in a deformable rock fracture. *Water resources research*, 16(6):1016-1024.
128. Wu, W., Sharma, M. M. (2017) A model for the conductivity and compliance of unpropped and natural fractures, *SPE Journal*, 22(06): 1893-1914.
129. Yasuhara, H., Kinoshita, N., Ohfuji, H., Takahashi, M., Ito, K., and Kishida, K. (2015) Long-term observation of permeability in sedimentary rocks under high-temperature and stress conditions and its interpretation mediated by microstructural investigations, *Water Resources Research*, 51.
130. Yasuhara, H., Elsworth, D. (2004) Evolution of permeability in a natural fracture: Significant role of pressure solution, *Journal of Geophysical Research*, 109, B03204.
131. Yasuhara, H., Polak, A., Mitani, Y., Grader, A., Halleck, P., Elsworth, D. (2006) Evolution of fracture permeability through fluid rock reaction under hydrothermal conditions, *Earth and Planetary Science Letters*, 244(1–2), 186–200.
132. Zhang, J., Standifird, W., Roegiers, J. C., Zhang, Y. (2007) Stress-dependent permeability in fractured media: from lab experiments to engineering applications, Rock Mechanics and Rock Engineering, 40 (1), 3 – 21.

133. Zhang, J. (2019) *Applied Petroleum Geomechanics*, Elsevier.
134. Zhao, Y., Wang, Y., Wang, W. et al. (2017) Modeling of non-linear rheological behavior of hard rock using triaxial rheological experiment, *International Journal of Rock Mechanics and Mining Sciences*, 2017, 93: 66-75.
135. Zhao, Y., Zhang, L., Wang, W. et al. (2018) Separation of elastoviscoplastic strains of rock and a nonlinear creep model, *International Journal of Geomechanics*, 18(1): 04017129.
136. Zhao, Z., Liu, L., Neretnieks, I., Jing, L. (2014) Solute transport in a single fracture with time-dependent aperture due to chemically medicated changes, *International Journal of Rock Mechanics and Mining Sciences*, 66, 69–75.
137. Zimmerman, R. W., Bodvarsson, G. S. (1996) Hydraulic conductivity of rock fractures, *Transport in Porous Media*, 23, 1-30.
138. Zoback, M. D. (2007) *Reservoir Geomechanics*, Cambridge University.
139. Zoback, M. D., Kohli, A. H. (2019) *Unconventional Reservoir Geomechanics*, Cambridge University.
140. Zou, L., Li, B., Mo, Y., Cvetkovic, V. (2020) A high-resolution contact analysis of rough-walled crystalline rock fractures subject to normal stress, *Rock Mechanics and Rock Engineering*, 53:2141-2155.

Appendix A1

In this Appendix, the conjugate gradient (CG) method proposed by Polonsky and Keer (1999) is shown step by step. It is an iterative method.

Before the start of iteration, the process needs to be initialized. First, the initial pressure distribution field $p_{i,j}$, which satisfy Eqns. 3.11, 3.12, and 3.17, is chosen. Variables δ and G_{old} are defined and initialized by setting $\delta = 0$ and $G_{old} = 1$. The accuracy goal ε_0 is also set to zero. Then, the iteration step begins.

First, the deformation at each cell, $u_{i,j}$, is calculated by Eqn. 3.16:

$$(u_e)_{i,j} = FFT^{-1}\left[FFT\left(K_{i,k,j,l}\right) \times FFT(p_{k,l})\right] \tag{A1.1}$$

Then, the gap distribution $g_{i,j}$ is calculated and its mean value $\bar{g}$ is adjusted as follows:

$$g_{i,j} = -u_{i,j} - h_{i,j},\ (i,j) \in I_g \tag{A1.2}$$

$$\bar{g} = \frac{1}{N_c} \sum_{(k,l)\in I_c} g_{k,l} \tag{A1.3}$$

$$g_{i,j} \leftarrow g_{i,j} - \bar{g},\ (i,j) \in I_g \tag{A1.4}$$

where N_c corresponds to the number of elements in I_c, $h_{i,j}$ is the aperture field (defined in Figures 3.11 and 3.25), I_c corresponds to the elements which are in contact (the set of all elements (i,j) for which $p_{i,j} > 0$), and I_g corresponds to the set of all elements. For the new $g_{i,j}$, the summation

$$\mathrm{G} = \sum_{(i,j)\in I_c} g_{i,j}^2 \tag{A1.5}$$

is calculated, which is used to calculate the new conjugate direction $t_{i,j}$:

$$t_{i,j} \leftarrow t_{i,j} + \delta(G/G_{old})t_{i,j},\ (i,j) \in I_c \tag{A1.6}$$

$$t_{i,j} = 0,\ (i,j) \notin I_c \tag{A1.7}$$

The new $t_{i,j}$ is the direction in which the next step will be made in the multidimensional space of elemental pressures. If $\delta = 0$, $t_{i,j}$ will coincide with the steepest decent direction. The current value of G is then stored for the next iteration:

$$G_{old} \leftarrow G \tag{A1.8}$$

A convolution of $K_{i,k,j,l}$ with $t_{k,l}$ is then calculated:

$$r_{i,j} = \sum_{(k,l)\in I_g} K_{i,k,j,l} t_{k.l}\,, (i,j) \in I_g \tag{A1.9}$$

The mean value of $r_{i,j}$ is then adjusted as follows:

$$\bar{r} = \frac{1}{N_c} \sum_{(k,l)\in I_c} r_{k,l} \tag{A1.10}$$

$$r_{i,j} \leftarrow r_{i,j} - \bar{r},\ (i,j) \in I_g \tag{A1.11}$$

The distribution of $r_{i,j}$ is used to calculate the length of the step that will be made in the direction $t_{i,j}$:

$$\tau = \frac{\sum_{(i,j)\in I_c} g_{i,j} t_{i,j}}{\sum_{(i,j)\in I_c} r_{i,j} t_{i,j}} \tag{A1.12}$$

At this point, the current $p_{i,j}$ are stored for the subsequent error estimation:

$$p_{i,j}^{old} = p_{i,j},\ (i,j) \in I_g \tag{A1.13}$$

after which the solution is updated by making a step of the length τ in the direction $t_{i,j}$:

$$p_{i,j} \leftarrow p_{i,j} + \tau t_{i,j},\ (i,j) \in I_c \tag{A1.14}$$

Next, the boundary condition of Eqn. 3.12 is satisfied by setting all negative $p_{i,j}$ to zeros.

The set of all non-contact cells at which the two surfaces overlap is then determined:

$$I_{ol} = \left\{(i,j) \in I_g :\ p_{i,j} = 0, g_{i,j} < 0\right\} \tag{A1.15}$$

If $I_{ol} = \emptyset$, then δ is set to unity. Otherwise, δ is set to zero, and the pressures at the overlapping cells are corrected:

$$p_{i,j} \leftarrow p_{i,j} - \tau g_{i,j},\ (i,j) \in I_{ol} \tag{A1.16}$$

It can be shown that $\tau > 0$ at all times. Hence, all the cells in I_{ol} will enter I_c after the correction in Eqn. A1.16. Next, the current contact load is calculated and the force balance condition is enforced:

$$P = \sum_{(i,j)\in I_g} p_{i,j} \tag{A1.17}$$

$$p_{i,j} \leftarrow (P/P_0) p_{i,j},\ (i,j) \in I_g \tag{A1.18}$$

where P_0 is the load applied normal to the fracture surface. Then, the current relative error is estimated:

$$\varepsilon = \frac{1}{P_0} \sum_{(i,j)\in I_g} \left| p_{i,j} - p_{i,j}^{old} \right| \tag{A1.19}$$

If $\varepsilon > \varepsilon_0$, another iteration is performed. Otherwise, the iteration process is stopped.

Appendix A2

In this Appendix, the indentation modulus M and indentation creep modulus C obtained in 3-min nano-indentation tests are upscaled using the Hashin-Shtrikman (HS) method. Before conducting the upscaling, it is important to briefly introduce the HS method.

The HS method determines the effective elastic moduli of composites (at least two different minerals) by minimizing the elastic potential energy of the composite. To apply the HS method, the elastic moduli and the volume fraction of different minerals need to be given. The details could be found in Hashin and Shtrikman (1962). If the composite consists of two minerals, the upper bound of bulk modulus, K_{upper}, and shear modulus, G_{upper}, can be written as:

$$K_{upper} = K_1\left[1 + \frac{p_2(K_2-K_1)}{p_1(K_2-K_1)a_1+K_1}\right] \tag{A2.1}$$

and

$$G_{upper} = G_1\left[1 + \frac{p_2(G_2-G_1)}{p_1(G_2-G_1)b_1+G_1}\right] \tag{A2.2}$$

and

$$a_1 = \frac{3K_1}{3K_1+4G_1} \tag{A2.3}$$

and

$$b_1 = \frac{6(K_1+2G_1)}{5(3K_1+G_1)} \tag{A2.4}$$

where K_1 and G_1 denote the bulk and shear moduli, respectively, of the stiffer mineral; K_2 and G_2 denote the bulk and shear moduli, respectively, of the softer mineral. p_1 and p_2 are the volume fractions of the stiffer and softer mineral, respectively.

Similarly, the lower bound of bulk modulus, K_{lower}, and shear modulus, G_{lower}, can be written as:

$$K_{lower} = K_2\left[1 + \frac{p_1(K_1-K_2)}{p_2(K_1-K_2)a_2+K_2}\right] \tag{A2.5}$$

and

$$G_{lower} = G_2\left[1 + \frac{p_1(G_1-G_2)}{p_2(G_1-G_2)b_2+G_2}\right] \tag{A2.6}$$

and

$$a_2 = \frac{3K_2}{3K_2+4G_2} \tag{A2.7}$$

and

$$b_2 = \frac{6(K_2+2G_2)}{5(3K_2+G_2)} \tag{A2.8}$$

Based on the SEM-EDS scanning images of the nano-indentation grid (see Figure 6.37 in Section 6.4.2), there are three different regions: in region A, the dominant mineral is calcite; in region B, the dominant mineral is silicate; in region C, the dominant minerals are clayey minerals. The volume fractions, indentation moduli M, and indentation creep moduli C for the three regions are summarized in Table A2.1:

Table A2.1. Volume fractions, indentation moduli M, indentation creep moduli C for the three regions.

Region (dominant mineral)	Volume fraction (%)	Averaged M (GPa)	Averaged C (GPa)
A (calcite)	97.90	65.58	1235.50
B (silicate)	1.78	88.75	15072.39
C (clayey minerals)	0.32	56.88	797.78

To apply Eqns. A2.1 to A2.8, the Poisson's ratio needs to be measured so the bulk modulus K can be calculated from M ($K = M/(3-6v)$). The Poisson's ratios for the three regions were not measured by indentation tests. In triaxial tests, the Poisson's ratio of the rock (with a diameter of 50.8 mm and a length of 101.6 mm) was measured as 0.3. It is assumed that the Poisson's ratios of the three regions are 0.3.

In the nano-indentation area, three regions were observed. However, Eqns. A2.1 to A2.8 considers to minerals. Therefore, regions A and B are first homogenized into an effective medium. In the effective medium, regions A and B are the two different minerals. The bulk and shear moduli of the effective medium are calculated. Then, the effective medium will be mixed with region C.

Mighani et al. (2017) stated that since the creep modulus C characterizes the creep compliance in shear, it can be interpreted as the shear contact creep modulus. The upper and lower bounds of C can be calculated based on Eqns. A2.2 and A2.6.

After calculation, the upper and lower bounds of bulk modulus K are 54.97 GPa and 54.91 GPa, respectively; the upper and lower bounds of shear modulus G are 25.37 GPa and 25.34 GPa, respectively; the upper and lower bounds of creep modulus C are 1380.47 GPa and 1257.71 GPa, respectively. Table A2.2 summarizes the upper and lower bounds for the bulk modulus K, shear modulus G, indentation modulus M, and creep modulus C.

Table A2.2 Upper and lower bounds for K, G, C, and E

Parameter	Upper bound	Lower bound
K (GPa)	54.97	54.91
M (GPa)	65.97	65.89
G (GPa)	25.37	25.34
C (GPa)	1380.47	1257.71

Note: the upper and lower bounds of M are calculated based on the upper and lower bounds of K, respectively. The Poisson's ratio v is assumed to be 0.3, and M = K*3*(1-2v).